Functional Metal Oxide Coatings from Molecular Precursors for Energy Applications

Victor Riesgo Gonzalez

Yusuf Hamied Department of Chemistry

University of Cambridge

Gonville and Caius College

March 2023

This dissertation is submitted for the degree of *Doctor of Philosophy*

Declaration

This thesis is the result of my own work and includes nothing which is the outcome of work done in collaboration except as declared in the Preface and specified in the text. I further state that no substantial part of my thesis has already been submitted, or is being concurrently submitted for any such degree, diploma or other qualification at the University of Cambridge or any other University or similar institution except as declared in the Preface and specified in the text. It does not exceed the prescribed word limit for the relevant Degree Committee.

Victor Riesgo Gonzalez, July 2023

Name: Víctor Riesgo González. **Thesis title:** Functional Metal Oxide Coatings from Molecular Precursors for Energy Applications.

Abstract

The ability to create and optimise new interfaces is essential to develop and optimise materials for use in sustainable energy storage and conversion technologies. In this thesis, the solution-deposition of coatings from molecular precursors is explored as a promising approach towards this end. First, a facile method for the deposition of electrocatalytically active zirconium-based films for photoelectrochemical water oxidation is developed. The films were derived from three novel alkoxy cage compounds containing Zr and a first-row transition metal (Co, Fe or Cu). The deposition of a Co-doped ZrO_2 coating onto the $BiVO_4$ photoanode lowers its onset potential by 0.12 V to 0.21 V vs. the reversible hydrogen electrode (RHE) and increases the maximum photocurrent density by ~50% to 2.41 mA cm^{-2} compared to the uncoated $BiVO_4$. In the next chapter, a new solution deposition method to coat the Li-ion battery cathode $LiNi_{0.8}Mn_{0.1}Co_{0.1}O_2$ (NMC811) with Al_2O_3 using aluminium isopropoxide (AIP) is developed. High-field solid-state nuclear magnetic resonance spectroscopy (SSNMR) probes the formation of γ-$LiAlO_2$ at 600 °C and doping of aluminium into NMC811 starting at 500 – 600 °C. NMC811 coated with amorphous Al_2O_3 (200 – 400 °C) had a capacity retention comparable to pristine NMC811, while higher annealing temperatures led to more crystalline coatings and surface Al-doping which were found to increase the rate of degradation of NMC811 upon cycling. Finally, $LiAlO_2$ coatings are deposited onto NMC811 using heterobimetallic alkoxides: $LiAl[(OCH_2Ph)_4]$, $LiAl[(O^iPr)_4]$ and $LiAl[(O^tBu)_4]$. The later showing the most promise as a coating precursor due to its high solubility in tetrahydrofuran (THF), low temperature decomposition (283 °C) and reaction with hydroxyl groups present on the surface of NMC811. This coating was tested on polycrystalline NMC811 (PC-NMC811) and Al_2O_3 coated single-crystal NMC811 (Al_2O_3|SC-NMC811). Significant improvements in capacity retention (17.2 % more C/2 capacity retained after 107 cycles vs. Al_2O_3|SC-NMC811) were seen in the $LiAlO_2$|Al_2O_3|SC-NMC811 system. Furthermore, coating PC-NMC811 that was previously degraded by soaking in water improved the capacity retention (50.1 % more capacity retention at C/2 after 215 cycles vs. uncoated PC-NMC811 soaked in water and annealed at 400 °C) suggesting that the combination of a $LiAlO_2$ coating and subsequent annealing step can recover NMC811 surfaces that have been previously degraded by soaking in water.

Acknowledgements

I feel incredibly lucky to have been supervised by two great scientists and human beings: Prof. Dominic S. Wright and Prof. Clare P. Grey. Their guidance and support far exceeded any expectation, and I will always be indebted to them for accepting me in their groups. I also want to thank everyone who, over the course of my PhD, has contributed to this research and my development as a scientist: David S. Hall, who helped me with the XPS measurements and electrochemistry work, as well as with helpful discussions on the research project and beyond. Katharina Märker and Christopher O'Keefe, for teaching me solid-state NMR and for helping me with the measurements and data interpretation. Svetlana Menkin for helpful discussions on electrochemistry. Chloe Coates for teaching me how to do Rietveld refinements. Subhajit Bhattacharjee and Xinsheng Dong for their help with the (photo)electrochemical measurements, and the synthesising of 3d transition metal doped Zr-oxo alkoxy cages. I would also like to thank Darren Ould, as by collaborating with him I gained experience in sodium-ion battery electrolytes, and thermal characterisation. I should also acknowledge the Faraday Institution for giving me the PhD scholarship that made this work possible. Furthermore, I want to extend my thanks to all the Grey and Wright group members for making the lab a stimulating and enjoyable place of work. Finally, I would like to thank my parents, Toni and Isabel, whose love and support throughout my life allowed me to be where I am now and without whom none of this would have been possible. I also want to thank Lucia, for her advice and support and for always being there when things were difficult and my friends in Cambridge and in Spain who have encouraged me along this journey.

List of Patents

"Electrode Coating Method and Coated Electrode" UK Patent Application. GB2112283.3. **V. Riesgo-Gonzalez,** J. Slaughter, D. S. Wright, C. P. Grey.

List of Publications

Riesgo-González, V.; Hall, D. S.; Maerker, K.; Slaughter, J.; Wright, D. S., Grey, C. P. Effect of Annealing on the Structure, Composition and Electrochemistry of NMC811 Coated with Al_2O_3 Using an Alkoxide Precursor. *Chem. Mater.* **2022***, 34,* 9722−9735. https://doi.org/10.1021/acs.chemmater.2c02580.

Riesgo-González, V.; Bhattacharjee, S.; Dong, X.; Hall, D. S.; Andrei, V.; Bond, A. D.; Grey, C. P.; Reisner, E.; Wright, D. S. Single-Source Deposition of Mixed-Metal Oxide Films Containing Zirconium and 3d Transition Metals for (Photo)Electrocatalytic Water Oxidation. *Inorg. Chem.* **2022**, *61* (16), 6223–6233. https://doi.org/10.1021/acs.inorgchem.2c00403.

Ould, D. M. C.; Menkin, S.; Smith, H. E.; **Riesgo-González, V.**; Jónsson, E.; O'Keefe, C. A.; Coowar, F.; Barker, J.; Bond, A. D.; Grey, C. P.; Wright, D. S. Sodium Borates: Expanding the Electrolyte Selection for Sodium-Ion Batteries. *Angew. Chem. Int. Ed.* **2022**, 61. https://doi.org/10.1002/anie.202202133.

Congrave, D. G.; Drummond, B. H.; Gu, Q.; Montanaro, S.; Francis, H.; **Riesgo-González, V.**; Zeng, W.; Matthews, C. S. B.; Dowland, S.; Wright, I. A.; Grey, C. P.; Friend, R. H.; Bronstein, H. A Solution-Processable near-Infrared Thermally Activated Delayed Fluorescent Dye with a Fused Aromatic Acceptor and Aggregation Induced Emission Behavior. *J. Mater. Chem. C.* **2022**, 10, 4831. https://doi.org/10.1039/D1TC04753A.

Fang, W.; Muller, R.; Jethwa, R. B.; **Riesgo-González, V.**; Li, N.; Pike, S. D.; Bond, A. D.; Luo, H.-K.; Zhang, C.; Wright, D. S. Titanium Compounds Containing Naturally Occurring Dye Molecules. *Dalton Trans.* **2021**, 50, 17202. https://doi.org/10.1039/D1DT03377H.

Contents

Chapter 1: Introduction 1

1.1. Abstract 1

1.2. Overview of Electrochemical Energy Storage and Conversion Technologies 2

1.3. Precursor Chemistry: From Molecular Structure to Deposition Properties 6

1.4. Precursor Approach to Photoelectrocatalytic Materials 9

1.4.1. Applications in Electrocatalysis and Photocatalysis 10

1.4.2. Precursor-derived Coatings for Photoelectrocatalytic Water Splitting 15

1.5. Rechargeable Batteries 20

1.5.1. Electrode Materials from Single-source Precursors 20

1.5.2. Aluminium Oxide and Lithium Aluminate as Coatings for Cathode Materials 22

1.5.3. Other Coatings for Cathode Materials 28

1.6. Conclusions and Outlook 30

1.7. Aims of the Thesis 31

Chapter 2: Single-source Deposition of Mixed-metal Oxide Films Containing Zirconium and 3d Transition Metals for (Photo)electrocatalytic Water Oxidation 35

2.1. Abstract 35

2.2. Introduction 36

2.3. Synthesis and Characterization of the Catalyst Precursors 39

2.4. Coating Deposition and (Photo)electrocatalytic Testing 46

2.4.1. Fabrication of the Catalyst 46

2.4.2. Electron Microscopy Study of the Deposited Films 47

2.4.3. Surface Characterisation by X-ray Photoelectron Spectroscopy (XPS) 49

2.4.4. Electrochemical Characterisation 54

2.5. Photoelectrochemical Studies 62

2.6. Conclusions and Outlook 64

Chapter 3: The Effect of Annealing on the Structure, Composition and Electrochemistry of NMC811 Coated with Al_2O_3 Using an Alkoxide Precursor 65
3.1. Abstract 65
3.2. Introduction 66
3.3. Coating Deposition 69
3.4. Electron Microscopy Study of the Morphology and Composition of the Coatings 71
3.5. Powder XRD Characterisation of Al_2O_3 Coated NMC811 Materials 78
3.6. Investigating the Surface Chemistry of Coated NMC811 with XPS 81
3.7. Solid-state NMR Characterisation 86
3.8. Electrochemical Testing 97
3.9. Conclusions 104
Chapter 4: Recovery of Long-term Capacity of NMC811 by Coating with Lithium Aluminate Using Mixed-metal Alkoxides 107
4.1. Abstract 107
4.2. Introduction 108
4.3. Precursor Synthesis 113
4.4. Precursor Thermolysis 118
4.4.1. Thermogravimetric Analysis 118
4.4.2. Powder X-ray Diffraction 120
4.4.3. Solid-state NMR 122
4.5. Coating NMC811 with $LiAlO_2$ 124
4.5.1. Coating Deposition 124
4.5.2. XPS Characterisation 129
4.5.3. Solid-state NMR Characterisation 133
4.5.4. Powder XRD Characterisation of the Pristine and Coated Materials 139
4.5.5. Electrochemical Testing 144
4.6. Conclusions 155

Chapter 5: Conclusions and Future Work 157
Chapter 6: Experimental Details 163
6.1. Experimental Details for Chapter 2 163
6.1.1. Synthesis and Characterisation of Precursors 1, 2 and 3 163
6.1.2. Characterisation of the Catalysts 165
6.2. Experimental Details for Chapter 3 166
6.2.1. Reagents and Materials 166
6.2.2. Characterisation of the Pristine and Coated NMC811 166
6.2.3. Electrode Fabrication and Cell Assembly 168
6.3. Experimental Details for Chapter 4 169
6.3.1. Reagents and Materials 169
6.3.2. Synthetic Procedures 169
6.3.2. Characterisation of the NMC811 Materials 171
6.3.3. Electrode Fabrication, Cell Assembly and Electrochemical Cycling 173
Appendix A: X-ray Diffraction 174
A1. Refinements of the Single-Crystal XRD Data (Chapter 2) 174
A1.1. Precursor 1: [{$Zr_4(\mu_4\text{-}O)(OEt)_{15}$}$Co^{II}Cl$] 174
A1.2. Precursor 2: [{$Zr_4(\mu_4\text{-}O)_2(EtO)_{16}$}$(Fe^{III}Cl)_2$] 174
A1.3. Precursor 3: [{$Zr_4(\mu_4\text{-}O)_2(EtO)_{16}$}{$(Cu^{II}Cl)_2(OEt)$}$_2$] 174
A1.4. Crystallographic Data and Refinement of Complexes 1, 2 and 3. 176
A2. PXRD Rietveld Refinements (Chapter 3) 178
A2.1. Pristine NMC811 178
A2.2. Al_2O_3 Coated NMC811 Annealed at 200 º C 178
A2.3. NMC811 Al_2O_3 Coated and Annealed at 500 º C 179
A2.4. NMC811 Al_2O_3 Coated and Annealed at 800 º C 179
A2.5. Uncoated NMC811 Annealed at 400 ºC under Air 180
A2.6. Uncoated NMC811 Annealed at 800 ºC under Air 181

A2.7. Al_2O_3 Coated NMC811 Annealed at 800 ºC under Oxygen 181
A3. PXRD data and Rietveld Refinements (Chapter 4) 182
A3.1. Precursor Thermolysis: Rietveld Refinement Parameters 182
A3.2. Diffraction Patterns and Refinements of NMC811 Materials (Chapter 4) .. 183
Appendix B: Electron Microscopy and Elemental Analysis by X-ray Spectroscopy .. 195
B1. Characterisation of the Catalyst Films using SEM-EDS (Chapter 2) 195
B1.1. EDS Analysis of CoZr Electrode before Catalysis: 195
B1.2. EDS Analysis of CoZr Electrode after Catalysis 198
B1.3. EDS Analysis of CuZr Electrode before Catalysis 200
B1.4. EDS Analysis of CuZr Electrode after Catalysis 202
B1.5. EDS Analysis of FeZr Electrode before Catalysis 204
B1.6. EDS Analysis of FeZr Electrode after Catalysis 206
B1.7. Summary of the EDS Results and Dopant : Zr Ratio 207
B.2. Characterisation of the Pristine and Al_2O_3 Coated NMC811 (Chapter 3) 208
B2.1. SEM Images 208
B2.2. High-resolution TEM Images 213
B.2.3. Coating Thickness Measurements with TEM 219
B.2.4. SEM-EDS Characterisation 221
B2.5. STEM-EDS Characterisation 231
B2.6. XRF Characterisation 241
B3. Characterisation of the NMC811 Materials Discussed in Chapter 4 242
B3.1. Scanning Electron Microscopy Images 242
B3.2. EDX Analysis 250
B3.2.1. Polycrystalline NMC811 250
B3.2.2. Single-crystal NMC811 252
Appendix C: Spectroscopy 254
C1. XPS Survey Spectra of the Catalysts Discussed in Chapter 2 254

C2. XPS Survey Scans and Fitting Parameters for the High-resolution Al 2p Region (Chapter 3) 255
C3. Fitting of the High-resolution XPS Spectra in Chapter 4 257
C4. Fitting Parameters 1GHz Solid-state ^{27}Al NMR Measurements (Chapter 3) 259
C5. Solution NMR Spectra (Chapter 4) 260
C6. Solid-state NMR Spectra from Chapter 4 270
C6.1. ^{1}H SSNMR Measurements 270
C6.2. ^{7}Li SSNMR Measurements 272
C6.3. ^{27}Al SSNMR Measurements 275
C6.4. Fittings of the SSNMR Spectra of the Precursors 276
Appendix D: Electrochemistry 278
D1. Determination of Ohmic Resistance, R_{Ω}, for IR Correction in Chapter 2 278
D2. Long–term Galvanostatic Cycling of Al_2O_3-coated NMC811 in Chapter 3 279
D3. Long-term Cycling of the NMC811 Materials Discussed in Chapter 4 280
D3.1. Polycrystalline NMC811 Materials 280
D3.2. Single-crystal NMC811 Materials 281
References 282

List of Abbreviations

AA-CVD: Aerosol assisted chemical vapour deposition

ALD: Atomic layer deposition

AIP: Aluminium isopropoxide

ASAP: Atmospheric solids analysis probe

CA: Chronoamperometry

CAM: Cathode active material

CB: Conduction band

CFP: Carbon fibre paper

CCCV: Constant current constant voltage

CEI: Cathode-electrolyte interphase

CV: Cyclic voltammetry

DEC: Diethyl carbonate

DFT: Density functional theory

DMSO: Dimethyl sulfoxide

DRS: Diffuse reflectance spectroscopy

EC: Ethylene carbonate

ECSA: Electrochemical surface area

EDS: Energy dispersive X-ray spectroscopy

EELS: Electron energy loss spectroscopy

EIS: Electrochemical impedance spectroscopy

EPR: Electron paramagnetic resonance

EXAFS: Extended X-ray Absorption Fine Structure

FT-IR: Fourier transform infrared spectroscopy

FWHM: Full width half maximum

FY: Faradaic Yield

FTO: Fluorine doped tin oxide

GC: Glassy carbon

GI-XRD: Grazing incidence X-ray diffraction

HER: Hydrogen evolution reaction

HR-TEM: High-resolution transmission electron microscopy

ICP-OES: Inductively coupled plasma optical emission spectroscopy

ITO: Indium tin oxide

LCO: Lithium cobalt oxide

LMR: Lithium and manganese rich

LNO: Lithium nickel oxide

LSV: Linear sweep voltammetry

LTO: Lithium titanium oxide

MAS: Magic angle spinning

MATPASS: Magic-angle turning and phase-adjusted sideband separation

MS: Mass spectrometry

MOF: Metal organic framework

MW: Microwave

NMC: Lithium nickel manganese cobalt oxide

OER: Oxygen evolution reaction

PEC: Photoelectrochemical

PLD: Pulsed-laser deposition

POT: Polyoxotitanate

PXRD: Powder X-ray diffraction

PVDF: Polyvinylidene difluoride

RHE: Reversible hydrogen electrode

RDE: Rotating disk electrode

SAXS: Small angle X-ray scattering

SEI: Solid-electrolyte interphase

SEM: Scanning electron microscopy

SC: Single crystal

SoC: State of charge

SSNMR: Solid-state nuclear magnetic resonance

SSP: Single-source precursor

STEM: Scanning transmission electron microscopy

TEOS: Tetraethyl orthosilicate

TGA: Thermogravimetric analysis

THF: Tetrahydrofuran

TM: Transition metal

TMA: Trimethyl aluminium

UCV: Upper cut-off voltage

UV: Ultraviolet

VB: Valence band

WOC: Water oxidation catalyst

WRC: Water reduction catalyst

XANES: X-ray absorption near edge structure

XRD: X-ray diffraction

XRF: X-ray fluorescence

XPS: X-ray photoelectron spectroscopy

Chapter 1: Introduction

1.1. Abstract

Developing technologies for sustainable energy storage and conversion such as (photo)electrocatalysis and lithium-ion batteries for electric vehicles face significant challenges for their commercialisation. The stability of key solid-liquid interfaces essential for their function needs to be improved to achieve long-term operation. Meanwhile, better catalytic efficiency and ionic transport would enhance the performance of these devices. Synthetic methods to functionalise and protect surfaces and create completely new interfaces are therefore needed to improve current and future energy systems. In this introduction, the use of molecular precursors is reviewed as a promising strategy for the fabrication of functional coatings to address these problems. First, a brief overview of energy conversion and storage is provided, with a focus on batteries and photoelectrocatalysis, followed by an introduction to the chemistry of molecular precursors and their solution deposition. Next, the applications of this method in the areas of electrocatalysis, photocatalysis and solar fuel production are reviewed in depth. Methods to achieve control of the crystallinity, phases formed, and nanostructure of the catalysts are discussed. Synthesis of photoelectrodes and the deposition of protective coatings for these is then covered. The applications of this approach in the lithium-ion battery field are then discussed in detail, both as a method for the fabrication of electrode materials and as a coating / surface doping approach. In this introduction, the relationships between synthesis, deposition conditions, structure, morphology, and function are emphasised. Furthermore, by broadly reviewing the progress in using molecular precursors to functionalise and protect energy materials it is hoped that the common features become highlighted to promote the transfer of methods across adjacent areas.

1.2. Overview of Electrochemical Energy Storage and Conversion Technologies

Climate change, caused by anthropogenic emission of greenhouse gases, is one of the defining challenges of our time. To reduce and eventually completely stop the production of greenhouse gases, the infrastructure for energy storage and conversion needs to be reinvented at a global scale to rely on renewable resources instead of fossil fuels. When this goal is placed in the context of a world in which there is an increasing growth of population and industrialisation, the need to develop sustainable energy systems becomes obvious. Furthermore, our ability to find and extract fossil fuels continues to improve, reducing their cost, and the energy technologies under development need to be competitive to eventually displace fossil fuels.[1]

This challenge can be divided into three main aspects: transportation,[2] stationary storage,[3] and sustainable manufacturing.[4] For transportation, lithium-ion batteries and fuel cells are being considered as the two main options. Challenges of implementing fuel cells include their reliance on expensive Pt group catalysts, and the need to store hydrogen gas inside a vehicle at high pressure.[1] On the other hand, they present advantages such as higher energy density and the fast refuelling time compared to current lithium-ion battery technology.[5] Batteries display excellent overall efficiency and are straightforward to implement compared to fuel cells that would require the installation of a hydrogen infrastructure. However, the high costs of transition metals used in the cathode, safety issues, short cycle life, low energy, and power density place challenges for their commercialisation. Due to their complementary characteristics, lithium-ion batteries and fuel-cells are likely to coexist in the future of transportation for different applications with lithium-ion batteries employed for light-duty vehicles and fuel cells in heavy-duty and long-distance transportation.[5] Furthermore, research efforts are being directed at the development of batteries that have higher energy densities and rely on more abundant elements such as metal-sulphur and metal-air batteries which may overcome the limitations currently faced by the lithium-ion battery.[2,6,7]

Due to the intermittent nature of renewable energy sources, stationary energy storage is needed to be able to access the electrical energy on demand.[3] Technologies being considered towards this end include lithium and sodium ion batteries, redox-flow batteries, compressed air in air-tight caverns, pumped hydroelectric, thermal energy storage and solar fuels.[8] The latter requires the development of suitable photoelectrocatalysts with good kinetics and based on earth abundant elements. Similar

requirements are needed for the design of electrocatalysts for the sustainable production of industrially relevant chemicals and fuels such as hydrogen, hydrogen peroxide, methanol, and ammonia.[4,9,10]

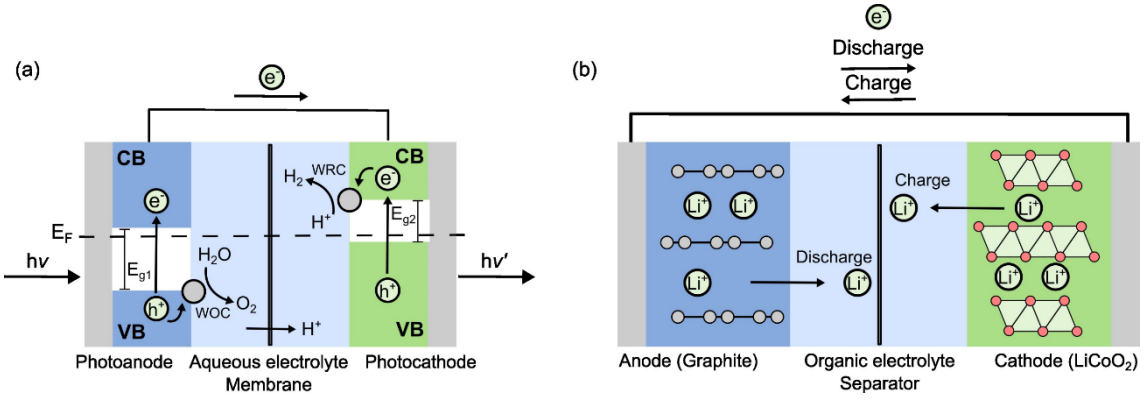

Figure 1.1: Schemes showing the working principle of (a) a photoelectrocatalytic water splitting cell, adapted from [11]. (b) A conventional lithium-ion battery.

A photoelectrochemical water-splitting cell is an energy conversion device (Figure 1.1a) that irreversibly transforms H_2O into H_2 and O_2 via a light-driven electrocatalytic process. In one of its most simple forms, it consists of two semiconductors with different bandgaps E_{g1} and E_{g2} (E_{g1}>E_{g2}) which are termed the photoanode and the photocathode, respectively. When a photon is absorbed, an electron is promoted from the valence band (VB) to the conduction band (CB) generating an electron hole in the VB of each photoelectrode. In the photocathode, the electrons drift to the semiconductor – liquid junction to drive the hydrogen evolution reaction (HER) at the water reduction catalyst (WRC). Similarly, the electron holes drift to the surface of the photoanode to drive the water oxidation reaction (WOR) at the water oxidation catalyst (WOC). The electrons photogenerated at the photocathode travel via an external circuit to the photoanode where they recombine with the electron holes in the valence band.[11]

A lithium-ion battery is a rechargeable electrochemical cell for energy storage (Figure 1.1b). It consists of a positive electrode (cathode) and a negative electrode (anode) with different chemical potentials which are separated by an electrolyte that can be a liquid or a solid. The anode is typically graphite, and the cathode a layered metal oxide such as $LiCoO_2$. Crucially, the redox reactions (Co^{4+}/Co^{3+} in $LiCoO_2$) that take place at the electrodes need to be reversible for the electrochemical cell to be rechargeable and the layered structure of the electrode materials needs to allow the reversible intercalation / deintercalation reactions.[2,6,7,12,13] The electrodes are kept apart using a polymeric separator which is permeable to the electrolyte. The function of the electrolyte is to allow

the transport of lithium ions between the cathode and the anode and to prevent electrical contact between the electrodes so that the electronic part of the reaction needs to take place through an external circuit. The electrolyte operates beyond its thermodynamic stability window by forming passivating layers on the surface of the electrodes.[14] These new interphases are essential to achieve kinetic stability of the electrolyte in the operating voltage window since they are ionically conductive but electrically insulating, limiting further electrolyte degradation.[14] At the graphite anode, the reduction of the electrolyte leads to the formation of a 10–50 nm thick layer containing both organic (Li_2CO_3 and polyolephines) and inorganic (Li_2O and LiF) species known as solid-electrolyte interphase (SEI).[14] Similarly, cathode-electrolyte interphase (CEI) layers containing LiF, Li_xPF_y, $Li_xPO_yF_z$ and organic polymeric species grow on cathode surfaces due to electrolyte oxidation, although they are thinner (3–7 nm) and grow at a slower rate compared to the SEI.[15,16]

Clearly, lithium-ion batteries and (photo)electrolysers serve different functions and are complementary. Significant progress is needed in both areas to obtain sustainable energy systems competitive with fossil fuels. Furthermore, there are advantages in discussing these two technologies together as fruitful crossover between these two research areas may inspire materials innovation. For example, more efficient multifunctional, heterogeneous catalysts are needed in future battery technologies such as Li-S,[17] and metal-air batteries.[18] Moreover, there are similarities in the interfacial challenges that these two approaches face.

As we have seen, one of the major obstacles for lithium-ion battery implementation in transportation is its low energy density which limits driving ranges. To address this problem, Ni-rich cathodes of the form $Li[Ni_{0.8}Mn_{0.1}Co_{0.1}]O_2$ (NMC811) have been developed. The increased Ni content leads to higher discharge capacities but also to poorer cycle life due to interfacial phenomena such as electrolyte oxidation, oxygen evolution followed by the formation of a reduced NiO rock salt insulating layer and the formation of surface impurities such as Li_2CO_3 and LiOH with exposure to air and moisture.[19] Photoelectrodes have also faced significant interfacial challenges. Corrosion processes, which can be promoted by light irradiation at an applied voltage, limit the pH range at which these materials can be used.[20,21] Furthermore, photoanodes like $BiVO_4$ have a bandgap of the required energy for the oxidation of water and can act as good light absorbers but suffers from poor charge carrier mobility which leads to charge

accumulation and promotes recombination, reducing the efficiency of the cell.[22] This problem could be solved by improving charge extraction on the surface.[22] Photocathode p-Si also has a suitable bandgap for HER and excellent light-harvesting properties. However, it forms a passivating SiO_2 layer on the surface in contact with air, unless the surface is protected by a coating layer.[23]

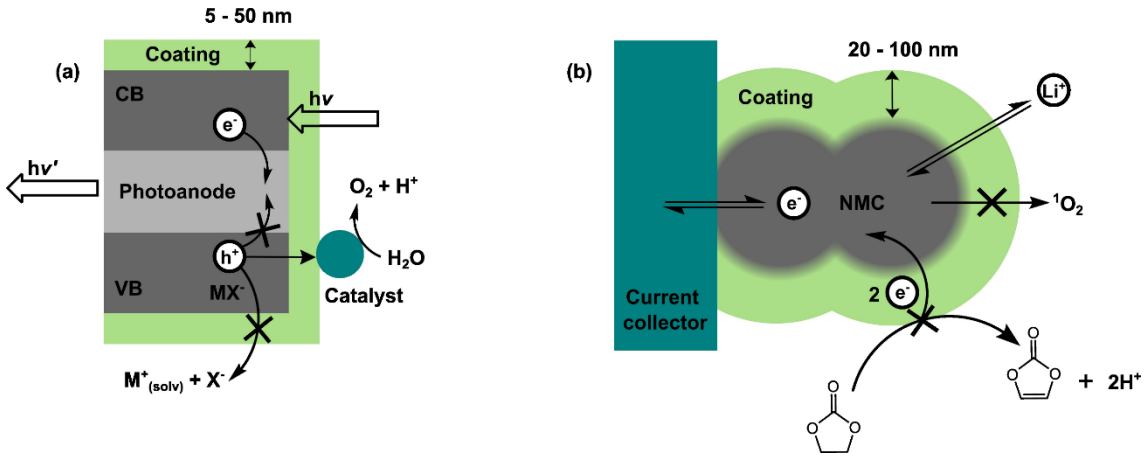

Figure 1.2: Schemes showing optimised coatings for (a) a photoanode in a water splitting cell, and (b) a lithium-ion battery cathode (NMC).

In this context, coatings could act as new electrode-electrolyte interphases that improve the long-term performance of lithium-ion batteries and photoelectrolysers. Figure 1.2 shows two examples of optimised coatings for these applications. Coatings are usually deposited onto lithium-ion battery cathodes such as NMC to slow down their rate of degradation (Figure 1.2b).[24–26] This can be achieved by limiting electrolyte oxidation which occurs either by direct reaction between the electrolyte and NMC or following the release of singlet oxygen at high voltages.[27] Therefore, the coating should be able to decrease the amount of singlet oxygen that reaches the electrolyte,[28] and provide a passive interface that does not react with the electrolyte under operating conditions. Importantly, it should be a Li-ion conductor but electrically insulating to prevent electrolyte oxidation. Most of the surface should be coated to maximise its effects but full surface coverage is not essential, since the NMC particles will crack during the first charge-discharge cycles, exposing new surfaces to the electrolyte.[29]

The effectiveness of the coating will also depend on its thickness. If it is less than 1 nm thick, electron tunnelling may take place compromising its ability to prevent electrolyte oxidation.[14] Furthermore, a thin (5–10 nm) coating may not prevent singlet-oxygen from reaching the electrolyte, as the diffusion length from the surface of the cathode is

shortened.[28] Although a sufficiently ionically conductive coating should not affect the cyclability of the cathode, a thick coating would reduce the energy density of the material, since it is not electrochemically active. Therefore, the aim is to obtain a coating of an intermediate thickness (e.g., 50–100 nm) that is a good ionic conductor. Furthermore, good adhesion and surface compatibility with the cathode particles is required in order to withstand the volume changes that the particles undergo during cycling and to prevent coating delamination. This could be achieved by controlled diffusion of the coating into the bulk of the cathode by annealing, which could also stabilise the lattice in the near-surface region.[30,31] Finally, since the amount of electrolyte oxidised is proportional to the surface area of the material, the coating should be non-porous.

Like in the lithium-ion battery area, coatings are applied to photoelectrodes to improve their compatibility with the electrolyte (Figure 1.2a). Towards this end, the coating should be stable at the operating pH and voltage and conformal to mitigate corrosion.[20,21,32] However, unlike coatings for Li-ion battery cathodes, it needs to be electrically conductive for the redox processes to take place at the semiconductor-liquid junction. It should also be transparent and thin enough to allow light transmission.[20,21,32] Furthermore, catalytic properties towards the process of interest are required, to enhance the interfacial kinetics of the photoelectrode, minimising the accumulation of charge carriers at its surface by acting as a co-catalyst.[20,21,32–35] This should limit surface charge recombination, improving the efficiency of the device.[33,35,36]

Since the desired properties of the coating will depend on the specific application, versatile deposition methods that allow good control of the coating properties at multiple length-scales are needed. Furthermore, simple, and scalable methods to modify these surfaces are highly desirable. In this context, molecular precursors emerge as a promising approach to deposit thin films from solution and create functional interphases in energy materials.

1.3. Precursor Chemistry: from Molecular Structure to Deposition Properties

There are advantages in using molecular precursors to form solid state materials over conventional synthetic routes for some applications. Since single-source precursors can be prepared with the desired ratio of metal elements in their structure, and thermolysis reactions require lower temperatures than conventional ceramic routes, this often allows the low-temperature synthesis of oxides including amorphous oxides with well-defined compositions.[37] Furthermore, by carefully selecting the synthesis and decomposition

conditions, the morphology of the products can be controlled allowing the formation of nanostructured materials and coatings. Since the precursor can usually be dissolved in organic solvents, this allows processing by methods such as spray coating, dip coating, spin coating, drop-casting, and aerosol-assisted chemical-vapour deposition (AA-CVD).[38,39] This enables coating of a wide variety of substrates including flexible materials, particles and electrodes.[38,39]

Using molecular precursors also presents some drawbacks that should be considered. First, even though the fabrication of the material from the precursor is usually a simple one-step process, the complexity lies in the synthesis of the precursor molecule which may not be trivial and also it may not be possible to obtain in good yield.[37] Furthermore, the costs associated with the synthesis of the precursor should be considered when evaluating its feasibility for the fabrication of a material at scale.[37] Finally, although there have been examples of air-stable complexes used as precursors, many of these precursors are air- and moisture-sensitive and require storage under inert atmosphere which could make them impractical for some applications.[40]

Figure 1.3 shows the most common types of molecular precursors used in the area of energy materials. Alkoxides (Figure 1.3a) can be monometallic or contain multiple metals allowing the deposition of mixed-metal oxides. They tend to have poor stability and be moisture sensitive. Organometallic compounds (Figure 1.3c) are also moisture sensitive, but they have less tendency to dimerise which makes them more volatile and better suited for vapor deposition processes. Oxo-bridge clusters (Figure 1.3b and d) such as oxo-alkoxide clusters and ligand-stabilised cubane cages can allow more control of the inter-metal ratios if a dopant element is present. Furthermore, the pre-assembled M-O-M bridges can help lower the temperature of oxide formation. The oxo-alkoxide cages which form by partial hydrolysis of the simple alkoxide are soluble in common organic solvents but the alkoxy groups in the periphery hydrolyse readily which makes them suitable for low temperature deposition onto surfaces bearing -OH groups before calcination. Finally, bidentate ligands (Figure 1.3e) can be used to stabilise main group / transition metal adducts, but care should be taken when decomposing these precursors as longer heating times may be required to eliminate the carbon residues and the multiple bonds may decompose at different rates.[37]

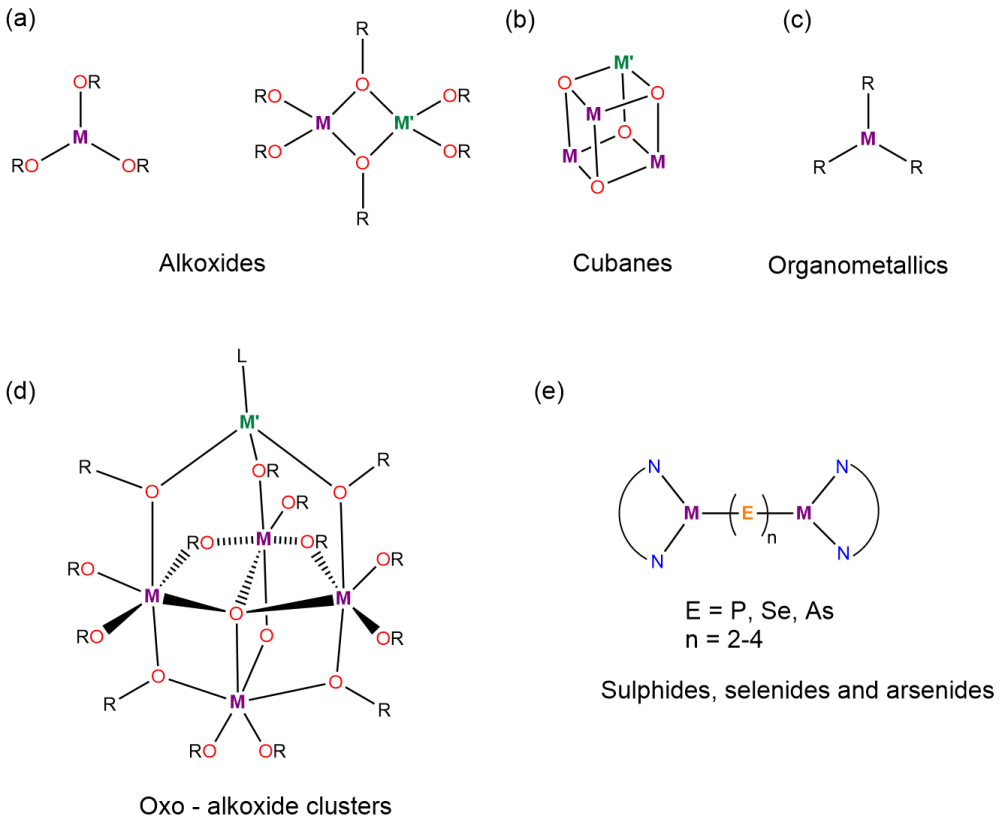

Figure 1.3: Structural motifs commonly used for molecular precursors to energy materials. (a) Alkoxide molecules, including both simple and heterobimetallic alkoxides. (b) Cubane precursors which are cage compounds containing one or more metallic elements typically bonded by oxygen. (c) Organometallic precursors containing reactive C-M bonds. (d) Oxo-alkoxide clusters which are metal-oxo alkoxy cages that can also be heterobimetallic and can be structurally regarded as molecular fragments of extended oxide solids. (e) Sulphide, selenide, and arsenide complexes.

Having outlined the main types of precursors available, the solution deposition methods for the formation of the solid material from those will be discussed. The possible deposition reactions are classified in Figure 1.4. Depending on the driving force for the decomposition of the molecule these can be divided in three categories; thermolysis or the heat-induced elimination or oxidation of the ligands (Figure 1.4a), reaction with a solvent (solvolysis) which most commonly is water (hydrolysis) to remove the organic ligands and form the oxide (Figure 1.4b), and oxidation of the precursor molecule onto an electrode surface under anodic conditions (Figure 1.4c).

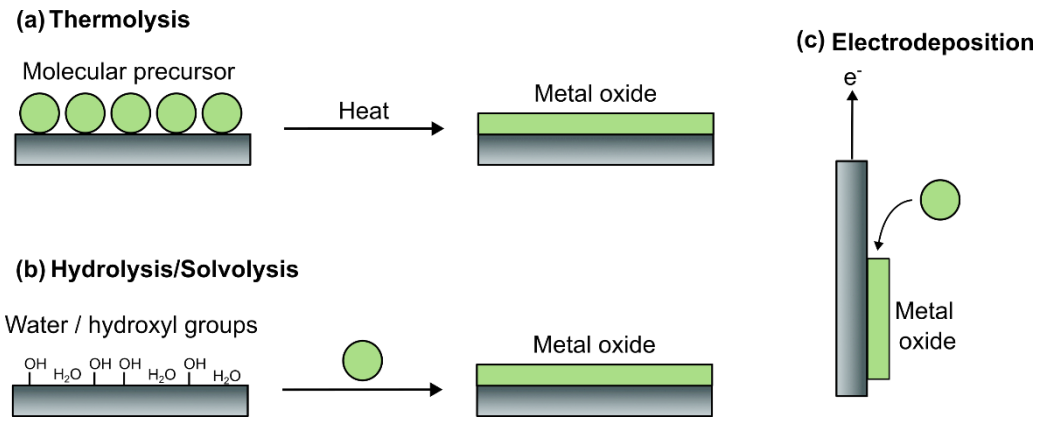

Figure 1.4: Solution deposition classified by the driving force for the reaction. (a) Decomposition of the precursor caused by heat. (b) The chemical reaction between the surface water or other solvent suitable for this reaction as well as by hydroxyl groups on surfaces. (c) Electrochemical oxidation of the precursor at the surface of an electrode to form a solid (typically oxide) phase.

A wealth of molecular precursors has been synthesised over the years and multiple reviews on the topic exist.[37,41–43] However, most of these studies and reviews have focused on the synthesis, characterisation and decomposition of the precursors and not so much on their application for energy materials with the exception of Panda et. al. who reviewed the use of molecular precursors to fabricate nanomaterials for water splitting.[44] Therefore in this introduction, the key results in the precursor-based approach to the synthesis of energy-related materials will be reviewed, not only focusing on the precursor chemistry but also on the structure-property relationships and the merits and limitations of the approach in terms of the performance of the materials. The discussion will focus on materials and composites for lithium-ion batteries and (photo)electrocatalysis. These two are rarely discussed together but the advances in the two areas can inform each other and are often transferrable.

1.4. Precursor Approach to Photoelectrocatalytic Materials

The molecular precursor approach has been extensively used for the synthesis of (photo)electrocatalysis layers, either for the deposition of the active catalyst or the surface functionalization of active materials.[45,46] It has allowed the optimisation of the number of active sites and composition of these materials, thereby realising electrocatalysts containing earth abundant elements that approach the performance of Pt and Ru in basic media or exhibit useful properties such as bifunctionality - the ability to act as both a WOC and a WRC.[45,46]

1.4.1. Applications in Electrocatalysis and Photocatalysis

In this section previous work on the synthesis of electrocatalysts using molecular precursors will be reviewed. Synthetic strategies that allow control of the resulting phase, defects, crystallinity, and nanostructure of the product are reviewed.

1.4.1.1. Access to Different Phases

Metal oxides can exist in multiple phases, and often it is found that one phase has a much higher activity towards a particular electrocatalytic transformation than others. By changing the atmosphere in which the thermolysis of a molecular precursor is performed, it is possible to favour the formation of a specific phase of the oxide product. In one report, three phases of nanostructured manganese oxide are prepared by calcining Mn(II) oxalate under different atmospheres.[47] Mn_2O_3 was obtained under air, Mn_3O_4 under N_2 and MnO under vacuum. As expected, the Mn_2O_3 performed best in chemical water oxidation experiments using ceric ammonium nitrate due to the higher oxidation state of Mn. The MnO phase showed better chemical water oxidation activity than Mn_3O_4 owing to its transformation to the amorphous, oxidised MnO_x phase during chemical water oxidation. This trend was also observed in photochemical water oxidation studies.[47]

Another strategy to control the phase of the oxide is by introducing small amounts of another element during its synthesis, often termed a 'dopant'.[40] This can be done by high-temperature routes, which rely on diffusion for the mixing of the dopant with the host material. However, this can lead to inhomogeneous doping and the formation of thermodynamic products or secondary phases. On the other hand, by introducing the dopant in a heterobimetallic precursor, the elements required to form the doped oxide are already mixed at atomic level and in the desired stoichiometry. As an example, a Mn-doped titanium oxo-alkoxy cage was synthesised by a solvothermal route and decomposed by thermolysis at 500 °C forming a Mn-doped rutile (TiO_2) as a major product, with a small amount of anatase and α-MnO_2 at lower temperature.[40] Rutile does not normally crystallise under these conditions, and it was considered whether factors such as the formation of low surface-area TiO_2 could lead to the low-temperature stabilisation of rutile (which has a higher surface enthalpy than anatase).[48,49] However, this is unlikely since the thermolysis of SSPs often leads to the formation of high surface-area oxides.[50,51] Therefore, the authors hypothesised that the Mn doping could be stabilising the structure at lower temperatures.[40]

Finally, unusual phases can be accessed from precursor-derived precatalysts after activation. MnS nanocubes were prepared by hot injection of the precursor $[Mn(pyHS)_6](OTf)_2$ in oleic acid. During OER the precatalyst converts to β-MnOOH, which is a metastable phase and was unexpected as most literature reports the formation of the more stable δ-MnO_2 phase.[52]

1.4.1.2. Control of Oxygen Vacancies

A route to oxides with a high concentration of defects is synthesis under kinetic control conditions. Although these phases may be metastable, molecular precursors can allow their preparation by low temperature thermolysis at varying heating rates. In one study, a $[CH_3ZnOCH(CH_3)_2]_4$ precursor was synthesised and shown to be useful in preparing ZnO catalysts with different amounts of oxygen defects as determined by electron paramagnetic resonance spectroscopy (EPR) by changing the heating rate during thermolysis and by using different ligands.[53] The effect of the oxygen vacancies on the hydrogenative conversion of CO to methanol was investigated (Figure 1.5) and a correlation was found between the amount of vacancies and the catalytic activity providing experimental evidence of the vacancies being the active sites.[53]

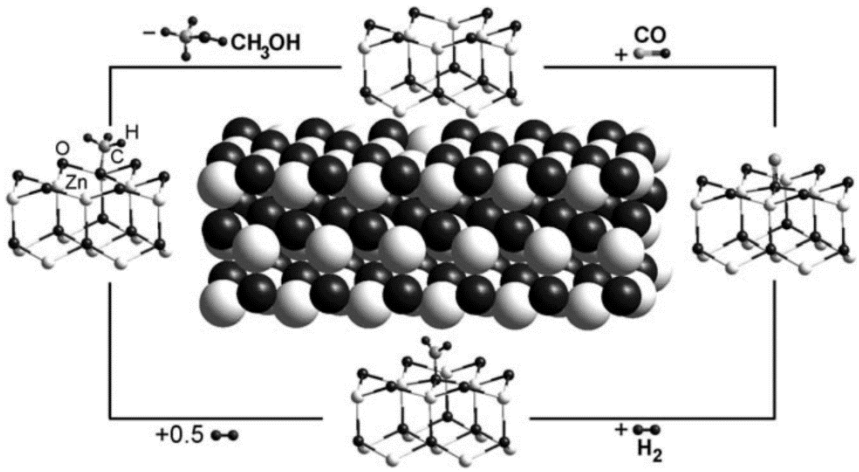

Figure 1.5. Scheme showing the mechanism of CO hydrogenation on ZnO. An oxygen vacancy is depicted as the active site where chemisorption of CO takes place. Reproduced from reference [53].

By hydrolysing a series of manganese complexes of the form $[Mn^{III}_4O_2(PhCOO)_9(H_2O)]N(n\text{-}Bu)_4$ it was possible to obtain amorphous manganese oxide that performed well as a WOR catalyst.[54] A detailed extended X-ray absorption fine structure (EXAFS) study revealed that the oxide presented a high number of structural defects, μ-oxo bridges and two different oxidation states of Mn (III and IV), all known requirements for highly active MnO_x OER catalysts. However, when a phosphate buffer was used during

hydrolysis to control the pH, a smaller number of μ-oxo bridges were found and an average Mn(III) oxidation state. It was hypothesised that the phosphate anion is bridging the Mn units leading to a poorer performance due to the absence of bridging oxygens.[54]

1.4.1.3. Synthesis of Amorphous Catalysts

Another important structural factor influencing the performance of the catalyst is the degree of crystallinity. While conventional ceramic routes often lead to crystalline materials, the use of molecular precursors make well defined amorphous materials accessible and allow a greater control of the degree of crystallinity of the product. In one report, a β-diketiminato cyclo-P4 dicobalt(I) complex with a Co_2P_4 core was shown to form crystalline or an amorphous CoP depending on whether in was decomposed by pyrolysis or by hot injection in oleic acid (Figure 1.6).[55] The amorphous material performed better than the crystalline in terms of current density and onset potential due to the larger surface area and the ease in which the amorphous material is transformed into CoO_x (which is the actual catalyst), which was attributed to easier P dissolution for the amorphous CoP.[55]

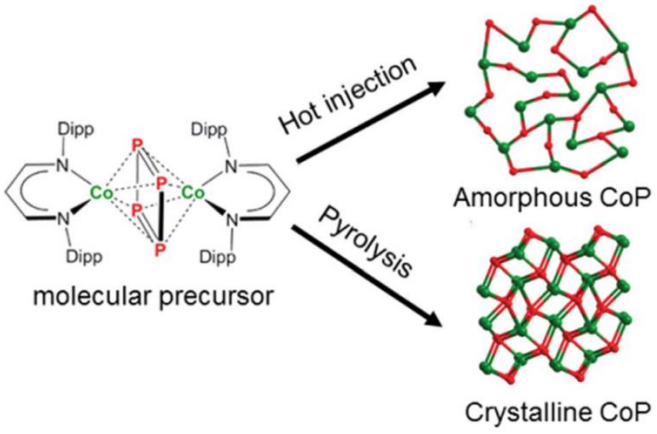

Figure 1.6. A molecular precursor can yield an amorphous or crystalline phosphide depending on the decomposition method, allowing testing of the effect of crystallinity on the activity of the material. Reproduced from reference [55].

In another study, a single-source precursor (SSP) for the synthesis of $ZnTiO_3$ was prepared using *p*-carboxybenzaldehyde oxime as a linker between the Zn(II) and $Ti(O^iPr)_3$ moieties.[50] The oxide $ZnTiO_3$ was then obtained by sol-gel processing of the precursor. The structural evolution of this material with increasing annealing temperature was followed by in-situ small-angle X-ray scattering (SAXS). For comparison, a sample was prepared using two precursors with similar ligand environments. It was found that

the SSP leads to a single-phase material at low temperatures, but the dual source led to two phases. At high temperature, the evolution of both converges once the organic ligands have been removed. Both products annealed at 550 °C were tested for photocatalytic degradation of methylene blue. The SSP derived $ZnTiO_3$ had better performance due to larger surface area which is derived from its more porous structure compared to the dual-source material.[50]

1.4.1.4. Synthesis of Nanostructured Electrocatalysts

Precursors have been recently used to synthesise catalysts with specific morphologies, including nanomaterials. For example, cobalt oxalate was used for the scalable synthesis of cobalt nanochains using an inverse micelle approach followed by thermolysis.[45] The catalyst exhibited bifunctional activity, being able to catalyse both the OER under neutral and basic pH and HER under basic pH conditions, showing similar HER performance to the Pt/C benchmark catalyst in terms of electrochemical half-way potential in the linear-sweep voltammetry (LSV).[45] This approach is not restricted to oxides, nanostructured pnictides such as Fe_2P_3[46] and FeAs[56] and one chalcogenide, $FeSe_2$[57] were synthesised from molecular precursors. Fe_2P_3 nanoparticles were obtained by hot injection of a diiron triphosphide complex with a $Fe^{II}P_3Fe^{III}$ core and asymmetric cyclo P(2+1) ligands in oleylamine forming highly monodisperse nanocrystals of 2-5 nm.[46] These are deposited onto Ni foam by electrophoresis and tested for both OER and HER in 1 M KOH. The catalyst displayed excellent performance towards OER with better kinetics (lower Tafel slope) and lower overpotential compared to benchmark IrO_2, RuO_2 and Pt as well as being stable over 14 h in a chronoamperometric (CA) test.[46] The presence of a reversible redox process at 1.2-1.4 V in the LSV suggested the surface oxidation of Fe leading to disordered $Fe(OH)_2$/FeOOH. This was confirmed by transmission electron microscopy (TEM), X-ray photoelectron spectroscopy (XPS), Fourier-transform infrared spectroscopy (FT-IR) and inductively-coupled plasma optical emission spectroscopy (ICP-OES) which indicated that Fe_2P_3 acts as a precatalyst and that the active disordered $Fe(OH)_2$/FeOOH forms after activation under anodic conditions.[46] The catalyst was bifunctional as it also shown HER activity without oxidation and phosphorus dissolution. It was suggested that P acts as a base and Fe as a hydride acceptor facilitating H_2 evolution.[46] The work on 2Fe-2As and $FeSe_2$ led to very similar conclusions.[56,57] Finally, sacrificial templating agents can also be used to achieve nanostructured materials upon thermolysis of the precursor. In one study, a titanium oxo-alkoxy cage was deposited onto

graphene oxide nanoflakes that acted as a sacrificial templating agent for the synthesis of TiO_2 with 2D morphology.[58] High surface area was achieved which was favourable for photocatalytic H_2 production.[58]

1.4.1.5. Structure Retention and Electrodeposition

The effect of molecular structure on the electrodeposition properties has been studied in some detail. While many of the molecular catalysts retain their nature during HER, most decompose under OER conditions to form a solid-state material which is the actual catalyst. This property has been used for the synthesis of solid-state electrocatalysts under anodic conditions by electrodeposition.[59] Nickel complexes using bidentate and tridentate ligands of the form $[Ni^{II}(H_2L)_2](NO_3)_2$ and $[Ni_4^{II}(HL)_4(OAc)_4]$ with H_2L = 2,6-pyridinemethanol have been used for the electrodeposition of an amorphous Ni oxohydride under basic conditions (pH=12).[59] It was found that both complexes decompose slowly into nickel hydroxide with increasing cyclic voltammetry (CV) cycles and that the generated hydroxide is dispersed in solution by the ligands.[59] At positive enough potentials electrodeposition takes place by forming the nickel oxyhydroxide active catalyst on the electrode without the need for a buffer solution.[59] Other studies have used a Ni_4O_4 ligand-stabilised structure for the deposition of well dispersed NiO nanoparticle formation onto mesoporous silica by thermolysis of the precursor.[60] Compared to $Ni(OAc)_2$, the Ni_4O_4 precursors form smaller, highly monodisperse nanoparticles that showed higher activity towards methane conversion ($CH_4 + CO_2 \rightarrow 2\ H_2 + 2\ CO$). This effect was attributed to the close proximity of the Ni atoms in the preformed precursors.[60]

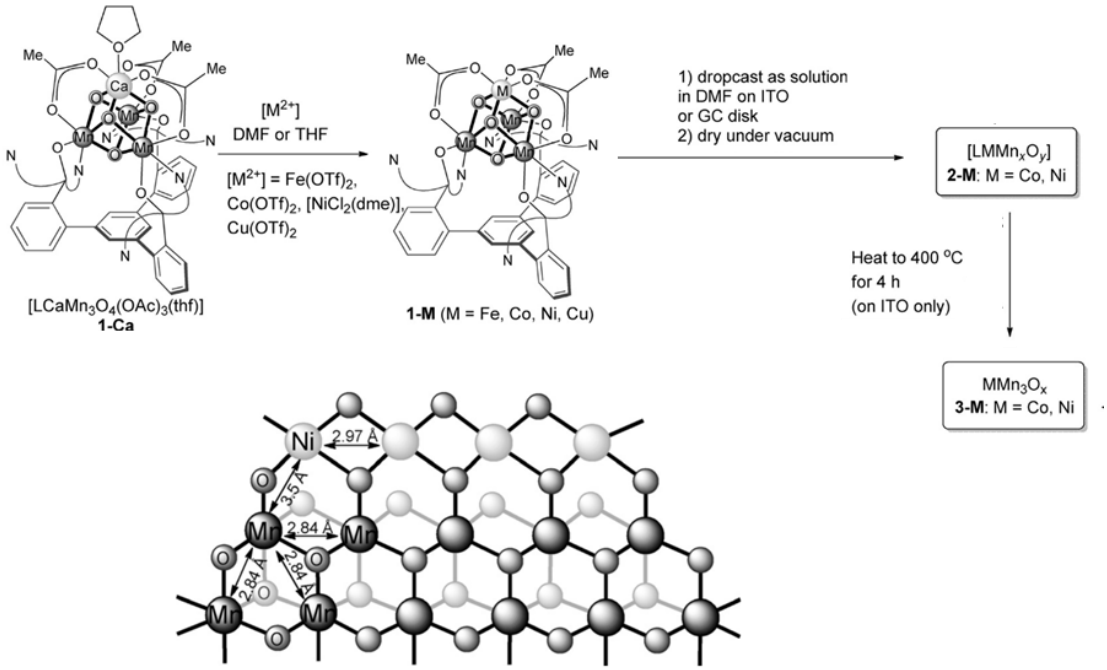

Figure 1.7. Transmetalation reaction to form the [MMn_3O_4] precursors and method for their deposition on ITO together with the extended structure of the thermolyzed Ni-Mn precursor as determined by EXAFS. Adapted from reference [61].

The cubane motif has also been used to prepare heterobimetallic precursors. In recent work, a [$CoMn_3O_4$] and a [$NiMn_3O_4$] mixed metal Mn oxido cubanes were synthesised and their structural evolution with thermolysis and/or OER studied by X-ray spectroscopy techniques (Figure 1.7).[61] It was found that while the [$CoMn_3O_4$] precursor is a pre-catalyst it transforms during OER to form an active CoO_x catalyst accompanied by Mn dissolution, [$NiMn_3O_4$] maintains the same Ni : Mn stoichiometry as before catalysis and the cube motif is also mostly retained.[61] When the drop-casted Ni-Mn film was subjected to an annealing step before catalysis an extended mixed-metal oxide phase with lower OER activity was formed.[61] This work suggests that low- temperature deposition aids the retention of the molecular structure even after electrocatalysis which may enhance the activity of the catalyst.

1.4.2. Precursor-derived Coatings for Photoelectrocatalytic Water Splitting

1.4.2.1. Synthesis of Photoanodes from Molecular Precursors

Photoanodes are semiconducting, light-absorbing materials with the required bandgap to drive a photocatalytic transformation such as water oxidation. A successful photoanode should consist of inexpensive, abundant elements, possess high charge carrier separation efficiencies, fast electron transfer kinetics and long-term stability under the required pH

conditions.[20] In the last decade, the use of multijunction devices incorporating complementary light-absorbers and directly interfacing components in wireless systems has progressed rapidly.[62,63] As these technologies evolve it becomes important to find ways to deposit these films at scale using simple solution methods. Furthermore, the main technical challenge that current photoanode materials face is their poor stability in aqueous solutions and sluggish kinetics.[20] Both of these problems can be addressed by the deposition of a suitable metal-oxide coating that can prevent the contact of the photoanode with the electrolyte solution and act as a co-catalyst enhancing the kinetics of the photocatalytic reaction.[20]

In this context, TiO_2 emerges as a promising photoanode material for water oxidation due to its non-toxicity and abundance. However, its large bandgap (3.2 eV) and fast recombination of electrons and holes, which leads to low utilization of the light spectrum, limits its practical use.[64] To lower the bandgap of TiO_2, dopants can be introduced.[64] The dopants allow a reduction in bandgap by introducing additional donor or acceptor energy states in between the valence band and the conduction band.[64] This led to an interest in the synthesis of heterobimetallic titanium oxo alkoxy clusters to use as precursors to doped TiO_2. These clusters acted both as a model system for bulk doped titania and as SSPs that could be decomposed by thermolysis or hydrolysis to yield an atomically well mixed doped TiO_2 at lower temperatures. This synthetic method for doped TiO_2 favours substitutional doping, or the substitution of Ti sites by dopant atoms, which is a prerequisite for injection of additional energy levels between the valence and the conduction bands.[51]

An example of this approach was the fabrication of Ce-doped TiO_2 using titanium oxo-alkoxy clusters containing varying amounts of cerium.[65] Three cages with different Ti:Ce ratios were synthesised; $[Ti_{28}O_{38}(OEt)_{38}(EtOH)_{1.4}CeCl]$, $[Ti_8O_7(HOEt)(OEt)_{21}Ce]$ and $[\{Ti_2O(OEt)_8\}(EtOH{\cdot}CeCl)]_2$. When decomposed by hydrolysis in EtOH followed by calcination at 150 °C in air Ce^{III} doped TiO_2, Ce^{III} titanate / anatase and $Ce_2Ti_2O_7$ / TiO_2 formed, respectively. High Ce content led to phase segregation while low Ce content led to the formation of Ce doped TiO_2 with different degrees of crystallinity depending on the amount of dopant. Interestingly, the $Ce_2Ti_2O_7$ / TiO_2 composite was air-stable, and XPS / energy dispersive X-ray spectroscopy (EDS) provided evidence of a core-shell structure that could be stabilising the air-sensitive $Ce_2Ti_2O_7$ in air. Furthermore, the composite showed broadband absorption and far superior photocatalytic activity for the

degradation of an organic dye compared to the other two Ce doped TiO_2 materials. Similarly an α-Mn_2O_3/Mn-TiO_2 composite with a bandgap of 1.80 eV, which could have applications in photocatalysis, was synthesised by thermolysis of $[Ti_{18}MnO_{30}(OEt)_{20}(MnPhen)_3]$ (Phen = 1,10-Phenantroline) at 600 °C.[40]

The composite may also form in-situ from a doped TiO_2 phase. In one example, $[Ti_{12}O_{15}(OiPr)_{17}]^+(CoBr)_6Ti_{15}O_{24}(OiPr)_{18}Br]^-$ and $[(CoI)Ti_{11}O_{14}(OiPr)_{17}]$ were synthesised under solvothermal conditions and used to deposit a Co doped TiO_2 precatalyst by drop-casting a dichloromethane solution of the precursors onto fluorine-doped tin oxide (FTO) followed by room-temperature drying and washing with water. [66] The amorphous Co-doped TiO_2 film undergoes an activation process at positive potentials leading to a CoO_x active catalyst embedded in a TiO_2 matrix which confers it stability in a chronoamperometric test compared to a control $Co(NO_3)_2$ sample. Furthermore, EDS results show the Co migration and P enrichment in crack areas of the material pointing at a new electrodeposited Co-P_i layer, similar to those reported by Nocera et. al.[66,67]

More recently a Mo doped TiO_2 was synthesised by spray-pyrolysis of $[Ti_4Mo_2O_8(OEt)_{10}]_2$. Part of the Mo sublimes after annealing at 650 – 800 °C leading to the formation of a porous structure.[51] A combination of XPS, Raman, EDS and EPR showed that the rest of the Mo is doping the TiO_2.[51] The properties of the resulting film are strongly dependent on the annealing temperature with 700 ºC being optimal leading to a nanostructure with larger surface area, which results from the sublimation of Mo as well the presence of mostly anatase which has more favourable electronic properties compared to rutile (such as reduced electron – hole recombination). An improved efficiency was seen in the photoelectrochemical testing of Mo-doped TiO_2 annealed at 700 °C which was attributed to the substitution of Ti(IV) by Mo(V/VI) which lowered the bandgap and to the presence of oxygen vacancies, which aided charge transport.

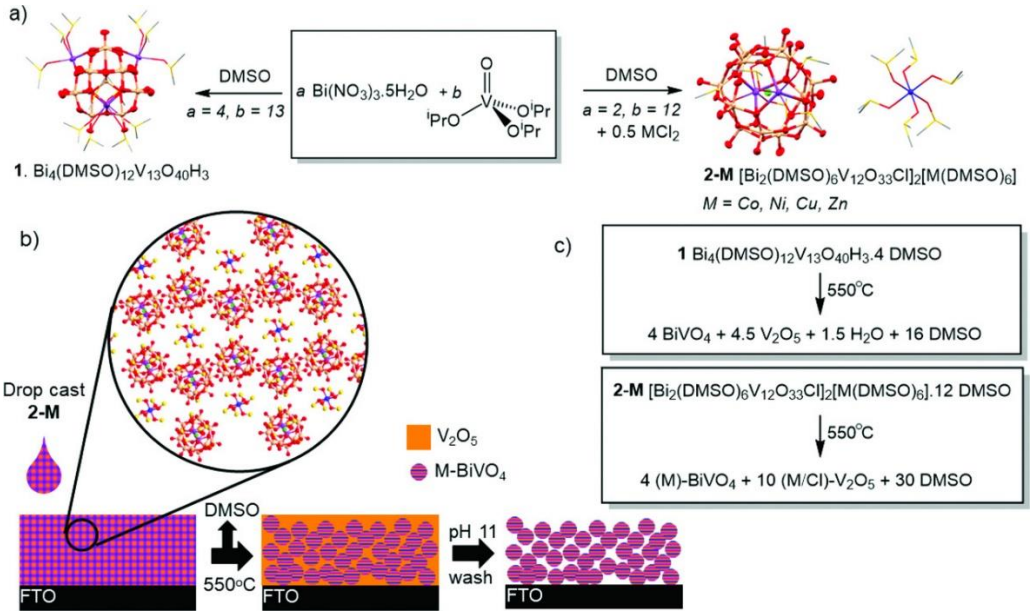

Figure 1.8. Synthesis and deposition of doped $BiVO_4$. (a) Depending on the stoichiometry of the reaction, oxo-alkoxy cages containing Bi and V in different ratios can be obtained. (b) Drop casting of a solution of the precursor in dimethyl sulfoxide (DMSO) onto FTO glass, followed by drying and removal of V_2O_5 impurities by washing. (c) Thermolysis reactions of the two $BiVO_4$ precursors. Reproduced from reference [22].

$BiVO_4$ is another promising photoanode material with an adequate bandgap energy for water oxidation as well as good light absorption properties.[68] Challenges for its implementation include its low carrier diffusion lengths which lead to charge recombination and low efficiencies, and the difficulties associated with scaling-up its thin-film deposition for practical water-splitting devices.[68,69] SSPs for the deposition of doped $BiVO_4$ have been synthesised to help solve these problems, since doping $BiVO_4$ could improve charge separation and having SSPs that are soluble in organic solvents should allow film deposition by drop-casting onto FTO which should be easily scalable (Figure 1.8).[22] It was possible to incorporate Co, Ni, Cu and Zn into the precursor clusters which formed doped $BiVO_4$ upon thermolysis. All the doped $BiVO_4$ samples had higher photocurrent densities compared to the bare $BiVO_4$ with the Zn and Co doped $BiVO_4$ showing the best performance as determined by LSV, CV and CA.[22] These improvements were attributed to a change in morphology and defect states induced by the dopant.[22] Co doped $BiVO_4$ films of 25 cm^2 and 300 cm^2 were prepared by drop-casting and tested, demonstrating the potential of this approach for scaling-up.[22] Nevertheless, the 300 cm^2 test showed reduced current densities, which was attributed to resistive losses in the FTO substrate, indicating that further technical challenges need to be addressed in the scaling-up of these photoanodes.[22]

1.4.2.2. Coatings for Photoelectrocatalysis

Coating photoelectrodes with an active catalyst embedded in a protective matrix can improve their performance and lifetime.[70] The cocatalyst can assist in charge extraction, reducing recombination losses, and the coating can protect the material against corrosion.[70] Furthermore, the precursor solution can penetrate porous materials leading to a cocatalyst layer by decomposition with a high concentration of active sites due to the large surface area.[60]

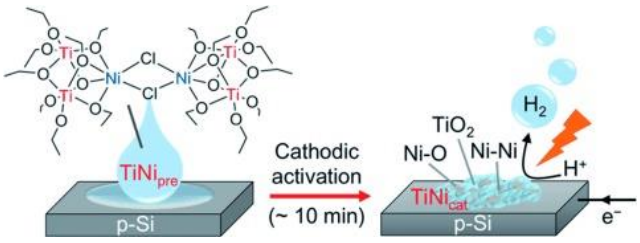

Figure 1.9. Example of using a POT cage to deposit a doped TiO_2 film capable of water splitting. Reproduced with permission from reference [23].

SSPs have been used to coat water splitting materials to form more favourable interfaces, for example, p-Si which is a promising HER photocathode due to its excellent light absorption properties and bandgap position.[23] However, it shows poor stability in aqueous media and slow kinetics for the HER reaction.[23] By drop-casting a solution of $[\{Ti_2(OEt)_9(NiCl)\}_2]$ in toluene followed by drying and cathodic activation, p-Si can be coated with a TiO_2 amorphous layer containing Ni-O and Ni^0 species as determined by XANES (Figure 1.9).[23] Photoelectrochemical measurements showed an increase in photocurrent density, lower onset potentials and improved stability at near neutral pH (pH = 9.2) compared to TiO_2 deposited from $Ti(O^iPr)_4$ and to a TiO_2 / Ni film formed by electrodeposition of Ni over the TiO_2 coating.[23] Furthermore, it approached a benchmark Pt coated p-Si in performance but achieved slightly lower current densities due to kinetic limitations in the Ni doped TiO_2 catalyst.[23] This same precursor has also been used to stabilise the surface of photoanode materials. In one study, WO_3 was coated with amorphous Ni-doped TiO_2.[71] This photoanode is a light-harvesting n-type semiconductor with a band structure suitable for OER but presents several drawbacks such as chemical instability at neutral or basic pH, poor kinetics, and poor selectivity.[71] By spin-coating a $[\{Ti_2(OEt)_9(NiCl)\}_2]$ solution onto nanostructured WO_3, it was possible to stabilise the material to perform OER under basic conditions.[71] Furthermore, higher current densities were observed, which was attributed to less charge recombination caused by TiO_2 acting

as a charge separation layer and to the improved OER kinetics resulting from the surface NiO_x catalyst.[71]

1.5. Rechargeable Batteries

1.5.1. Electrode Materials from Single-source Precursors

Using SSPs as starting materials for battery electrodes has been explored in the literature to obtain new nanoparticulate electrode materials and thin film electrodes. TiO_2[72,73] and SnS[74] anodes as well as $LiCoO_2$,[75,76] $NaCoO_2$,[77] $Na_2Mn_2FeO_6$,[78] and $LiCo_{0.5}Ni_{0.5}O_2$[79] cathodes have been prepared by this route. A SSP precursor for the deposition of $LiCoO_2$ was prepared by reacting $LiN(SiMe_3)_2$ and $Co(N(SiMe_3)_2)_2$ in toluene or THF and addition of HOAr (where OR = OC_6H_4Me-2, $OC_6H_4(OCHMe_2)$-2, $OC_6H_3(Me)_2$-2,6, OC_6H_3-$(OCHMe_2)_2$-2,6) which afforded the heterobimetallic complex $[Co[(\mu\text{-}OAr)_2Li(solv)_x]_2$ by crystallisation.[75] Spin coating of pyridine / toluene solutions of these complexes over Si wafers yielded a thin film of $LiCoO_2$ as determined by grazing incidence X-ray diffraction (GI-XRD).[75] Interestingly, the pyridine adducts led to better film morphology compared to THF which was attributed to better wetting properties of pyridine.[75] The electrochemical measurements were carried out using an open cell in an Ar-filled glovebox with lithium metal as both the reference and the counter electrode and LP40 (1 M $LiPF_6$ in a 1:1 (vol.) solution in diethyl carbonate (DEC) / ethylene carbonate (EC)) as the electrolyte. CV scans at 1 mV/s between 3.2 and 4.4 V showed that the oxide could be charged-discharged reversibly 9 times and PXRD revealed that the structure of the thin-film electrode was largely unaffected by the CV scans.[75] In a second study, complexes of the form $[Li(H_2O)M(N_2H_3CO_2)_3]_{0.5}H_2O$ with M = Ni, Co were synthesised by reacting the metal salt with hydrazinecarboxylate ($N_2H_3CO_2^-$) which was prepared by reaction of hydrazine with dry ice.[80] The compounds crystallise in a 2D bilayer structure with a $P2_1$ space group.[80] When thermolyzed at 700 ºC they produce $LiCoO_2$ (LCO) in air or $LiNiO_2$ (LNO) in oxygen. CV and galvanostatic cycling vs. Li gave the expected results for LCO and LNO although the cycling stability of the materials was poor and further optimisation of the electrode fabrication process was needed.[80] In a further development, volatile complexes that contained Li and Co in the desired ratio to form LCO were synthesised using bidentate oxygen donor ligands.[76] By using the asymmetric tert-butyl acetoacetate ligand (^{t}BuOC(=O)CHC(=O)Me = tbaoac) it was possible to obtain a tetranuclear heterobimetallic structure that crystallised in a centrosymmetric triclinic space group.[76] Thermolysis of this precursor led to the formation of LCO at only

280 ºC in air.[76] This synthesis was later extended to sodium-ion battery cathodes, by thermolyzing the complex $Na_2Co_2(tbaoac)_6(THF)_2$ giving Na_xCoO_2 with a P_2 space group at 750 ºC and in a O'3 space group at 450 ºC (Figure 1.10).[77]

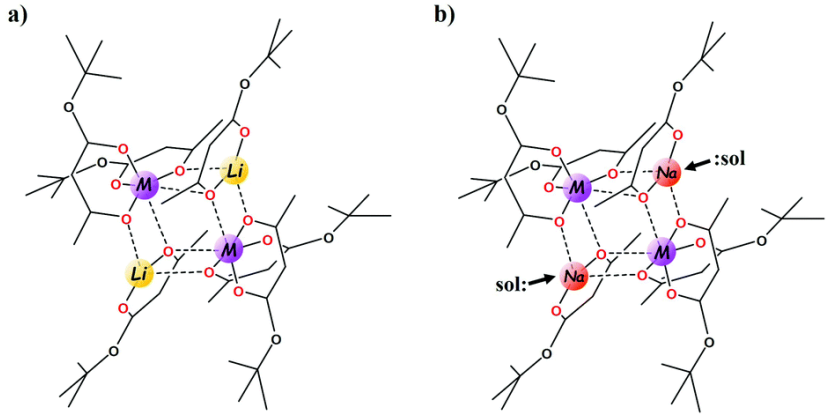

Figure 1.10. Molecular structures of the heterobimetallic precursors to the cathode materials $LiCoO_2$ (a) and $NaCoO_2$ (b). Reproduced from reference [77]. Sol = solvent molecule.

Heterotrimetallic precursors are being targeted as ternary and quaternary oxides become more common battery cathodes.[78,79] By reaction of $CoCl_2$, $NiCl_2$ and $Li(tbaoac)_6$ (tbaoac = ^{t}BuOC(=O)CHC(=O)Me) either in the solid state or in solution it is possible to obtain a $Li_2CoNi(tbaoac)_6$ trimetallic complex that decomposes at 450 ºC under air forming phase pure $LiCo_{0.5}Ni_{0.5}O_2$.[79] Due to the similar X-ray scattering factors of Ni and Co, it was not possible to fully resolve the structure from single-crystal (SC) XRD alone but mass spectroscopy (MS) revealed that the product is a mixture of the trimetallic and bimetallic species.[79] Later on, the true heterotrimetallic precursor [$Mn^{II}(ptac)_3$-Na-$Fe^{III}(acac)_3$-$NaMn^{II}(ptac)_3$] (ptac = 1,1,1 – trifluoro – 5,5 – dimethyl – 2,4 – hexanedionate) was synthesised by reaction of Na(ptac) with $Fe^{II}Cl_2$ and $Mn^{III}(acac)_3$ either in the solid-state or in hexane.[78] This precursor decomposes forming phase pure, partially amorphous P2 $Na_2Mn_2FeO_6$ at 600 ºC and crystalline material at 750 ºC.[78]

1.5.2. Aluminium Oxide and Lithium Aluminate as Coatings for Cathode Materials

The development of new electrode-electrolyte interphases displaying tailored properties such as high ionic conductivity, electronic insulation, (electro)chemical stability towards the electrolyte, desired thickness, good adhesion and flexibility is a promising avenue towards improving the performance of batteries.[14,81] Efforts to control the characteristics of these interphases include the use of electrolytes and electrolyte additives that form optimised layers upon decomposition, and the coating of electrodes with metallic, metal oxides, phosphates, fluorides and polymeric layers, often described as artificial SEIs,[14,81] to control the subsequent interfacial processes occurring upon battery cycling.

It is very common to use monometallic molecular precursors to coat electrode materials for lithium-ion batteries. The aim is usually to prevent reactions between the electrode and the electrolyte that could cause degradation of the electrode surface[82] or the dissolution of active electrode material[83] in order to improve the capacity retention of (most commonly) the cathode with long-term cycling. Furthermore, coatings can aid the processing of the materials by improving their stability towards air and moisture. Several reviews have been written on coating cathode materials.[25,26,84–88] Some work has also been done on coating anode materials following the same approach.[89–93] In contrast to photoelectrocatalysis, a much narrower variety of precursor types (mainly alkoxides) and solution deposition methods has been used in this area. Instrumental deposition methods such as ALD and CVD [94] and well as mechanochemical [95] or sol-gel coating in aqueous solutions using inorganic salts [96] have also been frequently employed but are outside the scope of this introduction.

Aluminium oxide is the archetypical coating material for lithium-ion battery cathodes. Other coatings have been deposited from solution using molecular precursors (MgO, SiO_2, SnO_2, ZrO_2, TiO_2 and ZnO),[25,26,84–88] and some examples will be discussed in the next section. Early work on Al_2O_3 coatings focused on coating $LiCoO_2$ (LCO) with the aim of improving capacity retention (Figure 1.11).[97,98] These coatings were prepared following a sol-gel route using aluminium ethylexano diisopropoxide, $Al(OOC_8H_{15})(OC_3H_7)_2$, as a precursor.[97] A solution of the precursor in isopropanol with the required concentration to achieve 5 % wt. of aluminium in the final product was reacted with LCO.[97] The product was annealed under air at 400, 500 and 700 ºC.

Annealing at 700 ºC led to complete diffusion of the coating into the LCO forming an Al-doped LCO surface.[97] The material had enhanced capacity retention when cycling in half cells under harsh conditions (between 2.75 and 4.4 V).[97] PXRD and CV studies showed that the aluminium substitution improved the structural stability of LCO. The hexagonal to monoclinic phase transition peak disappeared from the CV and less change in lattice parameters is seen before and after cycling in the PXRD.[97] Testing in full cells led to similar conclusions, enhancement in capacity retention and suppression of *c*-lattice parameter expansion was seen together with an increased discharge voltage at higher C-rates.[98]

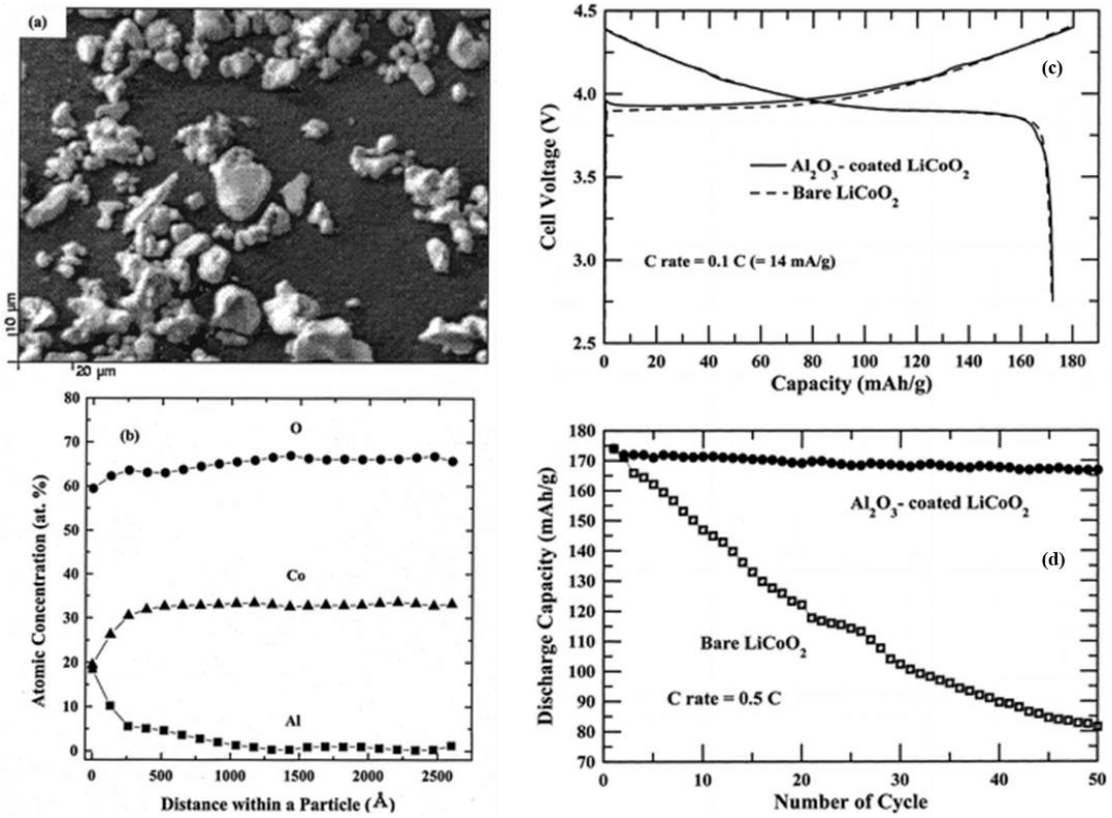

Figure 1.11. Coating LCO with Al_2O_3 by a sol-gel route using aluminium ethylexano diisopropoxide. (a) SEM image of the coated LCO. (b) Auger profile of elemental content showing the aluminium as a function of depth. (c) Voltage profiles of the coated and bare LCO. (d) Capacity retention of the coated and pristine LCO in half cells over 50 cycles. Adapted from reference [98].

Similarly, the lithium excess material $Li[Li_{0.05}Ni_{0.4}Co_{0.15}Mn_{0.4}]O_2$ ($Li_{1+x}Ni_yCo_zMn_{1-x-y-z}O_2$ with x= 0.05, y=0.4 and z=0.15) was coated with Al_2O_3 using AIP in EtOH by slow evaporation over 2 days at 80 °C under aerobic conditions.[82] Two wt. %s of precursor were used (0.23 wt. % and 2.5 wt. %) and both samples were calcined at 400 °C under air. It was observed that the morphology and thickness of the resulting coatings depended

strongly on the amount of precursor used with small amounts of precursor leading to a thin homogeneous coating (5 nm) and large amounts producing a thicker coating (10 nm) and large aggregates. The cathode material coated with a thin layer showed enhanced capacity retention at 60 °C and high cycling rates in full cells. No Al_2O_3 reflections were seen in the PXRD for both samples suggesting that the coatings were amorphous or in too low amounts to be detected. In-situ PXRD did not show any significant change in the evolution of the bulk structure with cycling between the coated and uncoated samples, so it was concluded that the difference in cycling was due to interfacial reactions. This was further confirmed by the lower impedance build-up measured for the coated materials and the lower amount of HF detected after cycling due to the HF-scavenging properties of the coating.[82] Although the coating reactions described so far were carried out in organic solvents, using water would be more desirable due to its lower environmental impact. By reaction of a carboxylic acid with the mineral boehmite in water, carboxylate alumoxanes can be prepared.[99] These precursors can be used to coat the $LiCoO_2$ (LCO) which is suspended in an aqueous solution of the precursor by sonication followed by slow evaporation. This treatment improves the capacity retention of LCO, especially after a calcination step is introduced due to the surface Al doping and densification of the coating.[99]

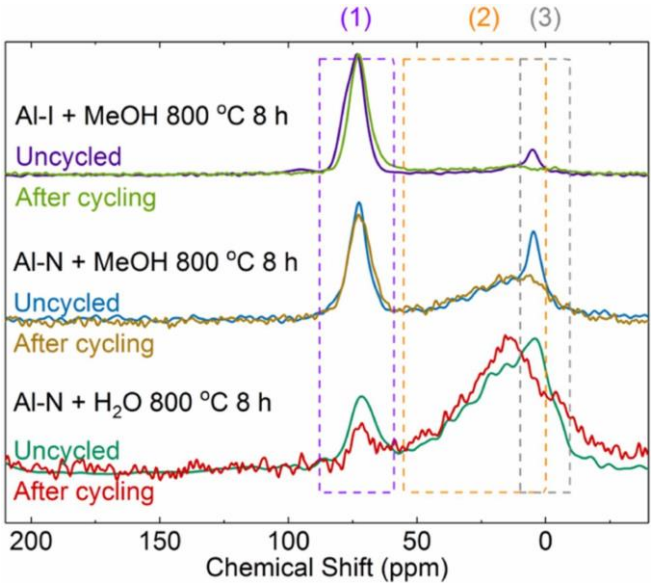

Figure 1.12. ^{27}Al SSNMR spectra of NMC532 coated with aluminium oxide using aluminium isopropoxide (AIP) in methanol, $Al(NO_3)_3$ in methanol, and $Al(NO_3)_3$ in water before and after galvanostatic cycling in half cells. Reproduced from reference [100].

A lot of the coating work has focused on improving the capacity of $Li[Ni_xMn_yCo_{1-x-y}]O_2$ materials (NMC) which are interesting as new generation cathode materials due to their higher capacities and lower costs compared to LCO, which stem from their lower cobalt content. To understand the effect of deposition conditions on the structure of the coating and its effect on the performance of NMC, various combinations of precursor, solvents, annealing temperatures and precursor wt. % were systematically tested for Al_2O_3-coated $Li[Ni_{0.5}Mn_{0.3}Co_{0.2}]O_2$ (NMC532, Figure 1.12).[100] Aluminium nitrate, aluminium chloride, aluminium acetate, and aluminium isopropoxide (AIP) were tested in water, methanol, ethanol, and xylene. The coated NMCs were characterised by SSNMR, SEM, TEM and galvanostatic cycling in half cells and full cells. It was found that coating in water produces a loosely attached layer that needs to be annealed to high temperatures to condense and create better adhesion to the particles. Water also led to more lithium extraction from the particles compared to organic solvents which had a negative impact on the electrochemistry. Using organic solvents and Al nitrate led to clusters of small particles after annealing at 400 ºC in air although annealing at higher temperatures led to more homogeneous, denser coatings. Interestingly, coating with AIP either in MeOH or xylene produced a dense, homogeneous coating without annealing. Higher temperatures led to better capacity retention in general due to the increased surface coverage but lower specific capacities, probably due to the diffusion of inactive Al^{3+} ions into the bulk of NMC532. Finally, the nature of the precursor also affected the amount of α-$LiAlO_2$ and γ-$LiAlO_2$ formed with annealing at 800 ºC. AIP produced mainly γ-$LiAlO_2$ but Al nitrate produce a mixture of both in H_2O or MeOH as determined by SSNMR (Figure 1.12).[100]

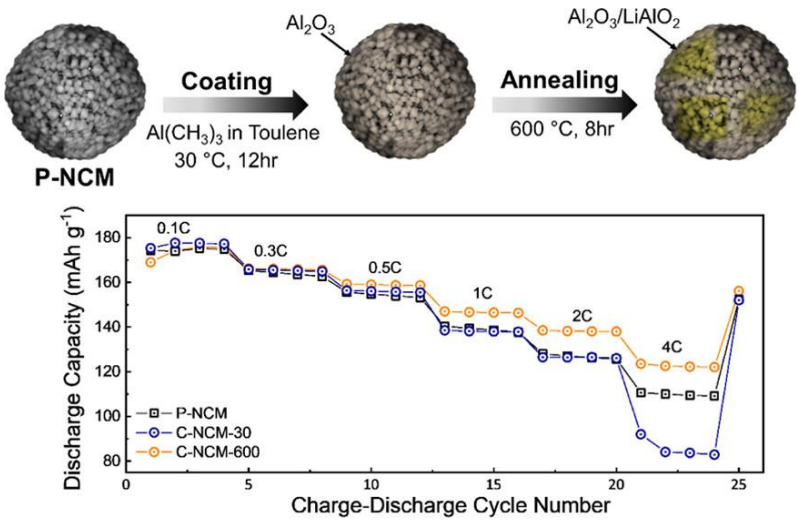

Figure 1.13. Reaction scheme for the coating of NMC701515 with Al_2O_3 / $LiAlO_2$ using trimethyl aluminium (TMA) as precursor and effect of the coating on the rate-capability of the cells. Adapted from reference [101].

More recently, trimethyl aluminium (TMA) has been used as a precursor to Al_2O_3 coatings in Ni-rich NMC (Ni > 70 %).[101–103] This work, which was inspired by ALD Al_2O_3 coatings in which TMA is normally employed, shows that organometallic precursors can be used to coat NMC with Al_2O_3 by reacting them with adsorbed water and -OH bearing species present on the surface.[102] The coating reactions were carried out under aerobic conditions by reacting TMA with NMC at 30 ºC for 12 h in toluene followed by drying under vacuum at room temperature,[102] 200 ºC[103] or 600 ºC.[101] SEM-EDS and XPS confirmed the presence of an aluminium containing layer on top of the NMC.

Performance improvements in terms of capacity retention and impedance build-up were seen in full cells for NMC811[102] without annealing and in half cells for NMC701515 with annealing.[103] It should be noted that these studies were conducted using wet NMC so the enhancement of performance caused by these coatings is compared to a previously degraded NMC (therefore introducing a potential false-positive in the conclusions concerning improved performance of the coated samples).[102] In the case of NMC701515, the effect of annealing at 600 ºC for 8 h on the performance of the coated NMC was also studied. XPS has shown that the annealing step increased the amount of Li on the surface slightly and the growth of a 4-coordinate aluminium environment could be seen by SSNMR. Based on this evidence, it was concluded that a $LiAlO_2$ phase (in which aluminium occupies 4-coordinate sites) was forming. Electrochemical testing in half cells showed that both the annealed and the as-coated samples had improved capacity retention.

The annealed sample presented an improved rate capability (Figure 1.13), and the coating / annealing did not increase the activation energy for charge transport as determined by temperature-dependent EIS which was explained by the better conductivity of the $LiAlO_2$ compared to Al_2O_3.[101]

Coating in hydrothermal conditions may lead to the low-temperature crystallisation of a coating or the formation of different morphologies. In one example, a solution of AIP in ethanol is hydrolysed by adding deionised water to produce a sol.[104] Addition of NMC532 and reaction of the mixture in hydrothermal conditions produces $LiAlO_2$ nanosheets on the surface of the NMC.[104] The Li impurities on the surface of the NMC may dissolve in water, forming LiOH that reacts with $Al(OH)_3$ forming $LiAl(OH)_4$ that then coats the NMC in the hydrothermal reaction. Further annealing steps allows the diffusion of Al^{3+} into the material as determined by cross-section SEM-EDS. This modified NMC532 showed better capacity retention and rate capability than the pristine NMC in half cells.[104] In another report, NMC622 coating was performed using a sol-gel approach with aluminium(III) *sec*-butoxide, ethyl acetoacetate, water and ethanol. For the synthesis of the Li-rich coating LiOMe was also introduced. The mixture is heated at 150 ºC for 15 h in an autoclave and then dried without a calcination step. Similar capacity retention was seen for the coated and uncoated materials in half cells using a 4.5 – 4.7 V upper cut-off voltage (UCV) but the presence of $LiAlO_2$ could not be determined unambiguously from the available XPS data.[105]

Sublimation has also been used as a method to deposit coatings from molecular precursors onto Ni-rich NMC. A $LiAlO_2/Al^0@Al_2O_3$ coating was prepared by sublimation of $(H_2AlO^tBu)_2$ onto NMC851005.[106] The as-formed $Al^0@Al_2O_3$ reacts with surface Li species to form $LiAlO_2$ at 180 ºC, temperature at which the sublimation process takes place. The remaining Al-H bonded species present are oxidised under air. This coating method resulted in an inhomogeneous coating and low specific capacities when large amounts of precursor were used. However, reducing the amount of precursor led to improved capacity retention and less resistance build-up.[106]

Finally, some studies did not find Al_2O_3 coatings effective in increasing the lifetime of the cathode material.[96,107] In one study, the effectiveness of Al_2O_3 coatings and Al doping in increasing the lifetime of a Li-rich, Mn-rich layered oxide (LMR) was investigated.[107] Al_2O_3 was deposited using $Al(OEt)_3$ in ethanol and the Al^{3+} was doped using a dry-particle fusion process.[107] Similar capacity retention for the coated and

uncoated material but higher bulk electrical resistance for the coated material were measured. The coating could not prevent the voltage fade or the cycle-induced transformation to spinel that this material undergoes and is one major cause of the loss in capacity.[107] This contrasts with work from other groups that found LMR materials can attain longer cycle life by coating with aluminium oxide and which showed by post-mortem XRD that there was less spinel phase forming in the coated material after cycling.[108] However the coating conditions were quite different in this second report. They used AIP in EtOH at 80 ºC for 4 h followed by a hydrothermal treatment at 80 ºC for 20 h and a calcination step at 500 ºC for 4 h.[108]

1.5.3. Other Coatings for Cathode Materials

Several studies have explored the use of niobium oxides as coatings for cathode materials. In recent work, NMC811 was coated using $Nb(OEt)_5$ in ethanol (stirred overnight and evaporated at 80 °C) followed by annealing under pure oxygen at temperatures ranging between 400 and 800 °C.[30,31] Synchrotron PXRD and neutron diffraction showed that the coating is composed of $LiNbO_3$ / Li_3NbO_4 by reaction of the $Nb(OEt)_5$ with Li-bearing impurities present on the surface of NMC.[30,31] These lithium-rich species should be good ionic conductors and not increase the polarization between charge and discharge or damage the rate capability. When heating at T > 600 °C Nb substitutes Mn in the lattice. It was found through electrochemical testing in half cells that coating at low temperatures led to the stabilisation of the surface with better rate capability and less first-cycle discharge capacity loss. On the other hand, doping led to stabilisation of the lattice, which improved capacity retention (Figure 1.14).[30,31] Interestingly, $LiNbO_3$ coatings derived from alkoxide solutions have also been used to stabilise the cathode-electrolyte interphase in solid-state batteries.[109] In one study, $LiNbO_3$ was coated on NMC622 by reaction with Li(OEt) and $Nb(OEt)_5$ in a 2:1 molar ratio in ethanol followed by annealing under air at 300 °C for 2h. This treatment led to the formation of a homogeneous coating formed of 15 nm particles composed of an amorphous $LiNbO_3$ core and a Li_2CO_3 shell. The coating improved the capacity retention of the solid-state battery by suppressing the interfacial oxidation of the solid-state electrolyte.[109] $LiTaO_3$ outperformed $LiNbO_3$ as a coating for NMC820612 in solid-state batteries due to its better ability to suppress transition metal migration and reaction with the sulphide decomposition products coming from the solid electrolyte at the interface.[110] However, both Ta- and Nb-based coatings proved effective in increasing the cycling

performance and rate capability of the battery, particularly when a combined coating and doping approach was used.[110]

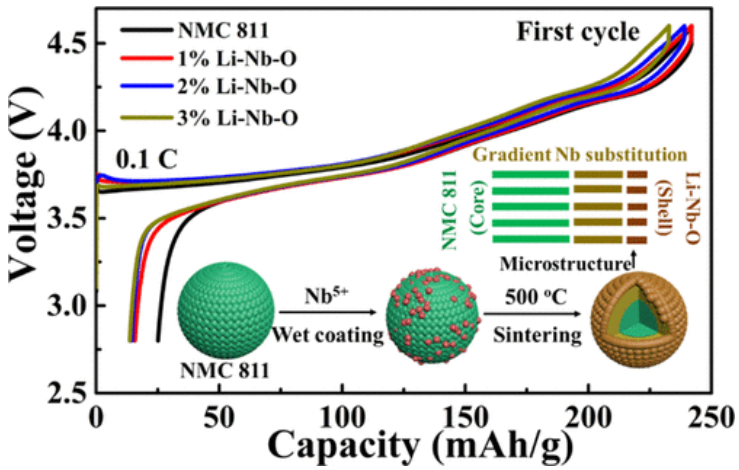

Figure 1.14. Wet chemical method used to deposit a Li-Nb-O coating on NMC811 using $Nb(OEt)_5$. Sintering at 500 °C leads to the diffusion of Nb into the near surface regions of the particle. The first-cycle capacity loss is reduced by coating, by physically separating the NMC811 from the electrolyte solution and by the Nb-induced lattice stabilisation. Reproduced from reference [30].

Zirconium oxides have also been employed to coat lithium-ion battery cathodes. NMC811 can be coated with ZrO_2 by reaction in a $Zr(OEt)_4$ solution followed by annealing under oxygen.[111] It was found that annealing at T > 700 °C led to the full diffusion of the coating into the NMC whereas annealing at lower temperatures produced a surface coating layer with some Zr diffusion in the near-surface regions with the Zr^{4+} ions preferentially substituting the Ni sites according to a DFT calculation.[111] Regardless of the annealing temperature, the coated samples performed better in half cell electrochemical cycling than the pristine NMC, showing less voltage hysteresis and less impedance growth with cycling.[111] Finally, nanobeam electron diffraction studies suggested that Zr doping may suppress the formation of spinel phases in the cycled NMC.[111] $Li[Ni_{1/3}Mn_{1/3}Co_{1/3}]O_2$ was also coated with ZrO_2 using a sol-gel route with $Zr(O^iPr)_4$ as a precursors.[112] A thin 25 nm layer was formed with no doping observed in this case after heating the NMC to 450 °C judging by the lack of change in the lattice parameters.[112] Cycling in half cells between 3–4.5 V showed improved capacity retention and less impedance growth with cycle number. Finally, mixed Zr-La oxide coatings were also synthesised by a dual-precursor route with a sol-gel process.[113] A conformal, 20 nm thick coating layer was formed on NMC622 by mixing it with Zr *n*-butoxide and $La(NO_3)_3$ in EtOH followed by evaporation. The coated NMC622 showed improved

capacity retention in half cells using harsh cycling conditions (4.5 V upper cut-off voltage).[113]

Another popular coating material is TiO_2.[114–117] Coating cathode materials with TiO_2 using alkoxides has led to similar conclusions as those for the other coatings. For example, NMC622 was stabilised at high voltages (4.4–4.6 V) by coating with TiO_2 using a $Ti(OBu)_4$ solution in EtOH with slow hydrolysis by dropwise addition of a water / EtOH mixture.[118] Annealing at 500 °C for 5 h led to partial diffusion of the TiO_2 coating into NMC622 as determined by Rietveld refinement and electron energy loss spectroscopy (EELS). Leakage current curves showed that the coated material underwent less parasitic reactions with the electrolyte when held at 4.2 V, explaining its better long-term cycle stability.[118] Furthermore, in an interesting variation of the sol-gel coating synthesis, an amorphous TiO_2 layer was deposited onto NMC622 from a $Ti(O^nBu)_4$ solution in anhydrous EtOH under inert atmosphere.[119] The dropwise addition of a H_2O/NH_3 mixture modulated the heterogeneous nucleation of the TiO_2 film on the NMC surfaces allowing conformal TiO_2 coatings to be synthesised. The amorphous nature of the coating allowed good ionic conductivity and better rate capability in NMC622 / $Li_4Ti_5O_{12}$ (LTO) full cells.[119]

1.6. Conclusions and Outlook

Many of the challenges faced by electrochemical energy storage and conversion technologies such as lithium-ion batteries and (photo)electrocatalysts are related to interfacial phenomena. Lithium-ion battery cathodes are reactive with air and moisture forming surface impurities, oxidise the electrolyte and undergo transitions to reduced, inactive surface phases. Photoelectrodes are often chemically unstable at the required pH for (photo)electrolysis and show poor kinetics. Synthetic methods to create more favourable interphases through functional coatings are therefore urgently needed. Fortunately, a large library of molecular precursors already exists, and different classes of molecules can be used depending on the targeted deposition method, material, and application. Furthermore, this introduction highlights the complex relationship that exist between the structure of the molecule, the decomposition method, and the final properties of the material.

Studies in the area of electrocatalysis have demonstrated the potential of molecular precursors to produce functional catalytic films. The increased control over the phase, morphology and crystallinity gained through this approach led to an improved

understanding of the electrocatalysis in oxide, phosphide, sulphide, and arsenide materials. Amorphous catalysts outperformed crystalline counterparts, nanoparticulate materials deposited electrophoretically displayed superior activities owing to the large surface areas, unstable photoanodes were protected from corrosion and their kinetic properties enhanced through catalytic coating layers. These studies highlighted the need to study the structural evolution of the catalysts during operation and found that it was highly dependent on the preparation method.

In the battery area, coatings have been applied onto cathode materials to stabilise their surfaces and improve their cycle life and rate capabilities. Using a wide variety of sol-gel methods and alkoxide or organometallic precursors, optimised coatings have been prepared. Furthermore, introducing an annealing step after coating has become a common strategy to achieve surface doping by diffusion of the coating into the bulk of the material. The dopant stabilises the lattice of the cathode and the coating limits the extent of parasitic reactions between the electrode and the electrolyte. Exciting developments in the coating of more unstable Ni-rich cathodes are taking place with heavier, more positive transition metals (Nb, Zr) proving effective in the stabilisation of the Ni-rich NMC lattice. Furthermore, the area is seeing impressive progress in the synthesis of conductive coatings that can improve the rate capability as well as the application of coatings to solid-state battery electrodes.

It is anticipated that this approach will continue to play an important role in the development of future materials for photoelectrocatalysis. Furthermore, countless opportunities to apply molecular precursors exists in the battery area. The synthesis of electrode materials from SSPs is still in its infancy, however, it is highly interesting as it could allow the large-scale preparation of thin-film and nanostructured electrodes that could be less prone to mechanical cracking with electrochemical cycling or display beneficial surface properties. Separators could be functionalised to scavenge damaging electrolyte degradation side-products and interrupt deleterious crosstalk effects between electrodes. Finally, HER and OER catalysts for metal-air batteries could be developed.[18]

1.7. Aims of the Thesis

Although significant work has been done in the area of solution coating of energy materials, there are several problems that still need addressing. In electrocatalysis most of the studies have focused on depositing active catalysts from molecular precursors. Meanwhile, the deposition of co-catalyst and protective layers onto active

(photo)electrodes has received much less attention. Most of this work has been done on doped TiO_2 using Ti-oxo cages doped with various 3d-transition metal (TM) ions. Therefore, while the role of different dopants on the electrocatalytic and optical properties of TiO_2 has been well explored, the effect of changing the host transition metal has been less well so. Chapter 3 will address those issues by developing Zr-oxo alkoxy clusters similar to the Ti analogues and a solution deposition method to obtain electrocatalytically active 3d-TM doped ZrO_2 coatings as well as by testing the effect of these coatings on the photoelectrocatalytic water oxidation activity of $BiVO_4$.

In the Li-ion battery area, a current challenge is to increase the lifetime of Ni-rich NMC cathodes such as NMC811, with surface treatments being a promising strategy towards this end. Although there have been examples of using molecular precursors for the deposition of coatings these have been mostly confined to lower Ni-content NMC and using sol-gel methods which lead to rough, thick coatings or organometallic ALD-like solution deposition methods using flammable organometallic precursors. Furthermore, existing methods to deposit ternary (heterobimetallic) oxides onto cathode materials from solution use a dual-source approach which can lead to heterogeneous deposition of the two oxides. Finally, there is some debate as to whether oxide coatings (such as Al_2O_3 coatings) have any beneficial effect on the capacity retention of high Ni-content NMC materials such as NMC811. Since Al is widely abundant (and therefore cheap) and non-toxic, these problems will be addressed in Chapters 3 and 4 by developing precursors and deposition methods to obtain Al-based coatings for NMC811.

First a safe and scalable solution deposition method to coat NMC811 with Al_2O_3 using aluminium isopropoxide will be developed in Chapter 3. The coated NMC811 will be annealed at 200-800 °C to obtain coatings with varying degrees of crystallinity and surface Al doping. Electrochemical testing of those will shed light on the effect of Al_2O_3 coatings on the capacity retention of NMC811. Following on from there, the use of SSPs for the solution deposition of $LiAlO_2$ onto NMC811 will be explored in Chapter 4 as a scalable route towards well-defined heterobimetallic coatings. The effect of $LiAlO_2$ on the capacity retention of NMC811 will be studied to ascertain if further gains in capacity retention could be obtained by coating with $LiAlO_2$ compared to Al_2O_3. Different NMC811 surfaces (Al_2O_3 coated, uncoated-water treated and pristine) and NMC811 with various morphologies (polycrystalline and monolithic NMC811) will be coated with

$LiAlO_2$ to gain understanding of the underlying mechanism of action of these coatings and of the best performance conditions.

Chapter 2: Single-source Deposition of Mixed-metal Oxide Films Containing Zirconium and 3d Transition Metals for (Photo)electrocatalytic Water Oxidation

2.1. Abstract

The fabrication of mixed-metal oxide films holds promise for the development of practical photoelectrochemical catalyst coatings but currently presents challenges in terms of homogeneity, cost, and scalability. In this chapter, a straightforward and versatile approach to produce catalytically active zirconium-based films for electrochemical and photoelectrochemical water oxidation is reported. Mixed-metal oxide catalyst films are derived from novel single-source precursors (SSPs) which are oxide cage compounds that contain Zr and a 3d transition metal (TM) such as Co, Fe and Cu. Of all of the materials explored, the Zr-based film doped with Co on fluorine-doped tin oxide (FTO) coated glass exhibits the highest electrocatalytic O_2 evolution performance in alkaline medium and an operational stability of above 18 h. The deposition of this film onto a $BiVO_4$ photoanode significantly enhances its photoelectrochemical activity towards solar water oxidation, lowering the onset potential by 0.12 V to 0.21 V vs. RHE and improving the maximum photocurrent density by ~50% to 2.41 mA cm^{-2} for the CoZr-coated $BiVO_4$ photoanodes compared to bare $BiVO_4$.

2.2. Introduction

Hydrogen gas is widely used in industry for petroleum refining, float-glass production, and the synthesis of fertilizers. In the future, it is also considered as a more widespread fuel for energy storage, transport and more sustainable manufacturing.[120] Therefore, it is likely to hold an essential role in achieving a zero carbon economy, but there is a need to develop clean and efficient ways to produce it at scale and at low cost. Water electrolysis and photoelectrochemical (PEC) water splitting are promising technologies towards this end,[121–124] but in order to work they require the use of an effective catalyst to improve the kinetics of the water splitting process, particularly water oxidation, which otherwise would suffer from large overpotentials. Currently, noble metals are used towards this end, but their high cost is one of the main limitation to the development of this promising technologies. In addition, the current efficiency of water electrolysers is only around 60-80%,[125] meaning that a significant amount of electricity (generated in the future by renewable infrastructure) is lost. It is possible to reduce the costs of electrocatalysis by replacing the noble metals with more earth-abundant elements, such as first-row transition metals (TM). However, this leads to low efficiencies due to the sluggish kinetics of the four-electron water oxidation reaction as well as faster degradation.[126–130] Although significant progress in the fabrication of noble-metal free oxygen evolution reaction (OER) catalysts has been achieved,[131–138] the challenges of high overpotential, low stability, and complex electrode fabrication techniques still persist. It is therefore desirable to develop noble-metal free OER catalysts that show enhanced performance as well as methods for their production at scale.

This development of OER catalysts has direct implications in the field of PEC water splitting, where sunlight is used to drive the water splitting process thereby achieving an integrated approach to sustainable hydrogen production. Towards this end, PEC catalysts for light-driven water oxidation are being developed,[123] n-type semiconductors with an optimum band-gap for water oxidation being commonly used.[139,140] The $BiVO_4$ photoanode is particularly promising as it allows unassisted tandem PEC water oxidation due to its early onset potential.[141,142] However, it suffers from rapid charge recombination that hampers its photoactivity.[143,144] The deposition of a co-catalyst layer on top of $BiVO_4$ overcomes this problem by allowing better charge extraction, decreasing recombination losses, and increasing stability under operation.[143,145] Integrating co-catalysts with $BiVO_4$ is therefore emerging as a promising strategy to produce solar-driven water oxidation devices with improved performance.[146–148]

The limitations of the available deposition routes to the catalytic layer are a major obstacle in the fabrication of these composite catalysts for PEC. These can be classified as electrodeposition, photodeposition and wet chemistry routes. Electrodeposition[149,150] suffers from sensitive voltage protocols, scalability issues, and inability for the direct deposition on semiconductors. Photodeposition[151] requires UV-irradiation and wet chemistry[152] is usually followed by high temperature treatments to obtain the desired material. Furthermore, both photodeposition and wet-chemistry approaches typically require the use of excess catalyst reagents. An easily scalable, simpler route towards the fabrication of these films is therefore urgently needed.

In this context, the use of mixed-metal single-source precursors (SSPs) presents a unique opportunity for the facile deposition of metal oxides onto a variety of substrates, including photoactive semiconducting electrodes that show a high catalytic activity towards water oxidation.[153,154] The simple approach of drop-casting, spin-coating or spray-coating the precursor solutions onto the substrate affords the formation of a catalytic film providing a low-cost and easily scalable approach to the fabrication of catalysts for the water-splitting reaction.[154–156] This deposition process can be mediated by labile groups such as alkoxy groups at the periphery of the precursor molecules. Alkoxide groups hydrolyse in the presence of ambient air providing the means by which thin films of material can be deposited directly from solution. This enables the single-step deposition of a co-catalyst layer over semiconductors such as Si, WO_3, and $BiVO_4$. The deposited mixed-metal oxide films not only provide efficient electrocatalysts involving active first-row TMs but can also protect the semiconductor electrode from corrosion. Furthermore, the homogeneous distribution of the active dopants in the inert host material can potentially improve the metal-atom utilization by increasing the number of available active sites.[157]

Consequently, the applications of polyoxotitanium cages as SSPs for the deposition of TM-doped titania has been previously explored, both in regard to their use in pollution control and water splitting.[148,154–156,158] Analogous Zr-based SSPs, on the other hand, are virtually unexplored for the fabrication of mixed-metal oxide coatings for (photo)electrocatalysis. This is surprising given that Zr is non-toxic, forms a moisture-stable oxide, and is the eleventh most abundant metal in the earth's crust. Zirconia (ZrO_2)-based systems are therefore attractive hosts for redox-active first-row TMs. Furthermore, the high charge-to-size ratio of Zr^{4+} gives it a strong Lewis acid character,[159–161] which may help to stabilize reaction intermediates during catalysis, similar to the way in which

Ca^{2+} acts as a Lewis acid to stabilize water oxidation intermediates in the heterometallic $CaMn_4$ clusters in photosystem II.[162–166]

Although the fabrication of 3d-TM-doped zirconia catalysts using SSPs has not been explored previously, doping ZrO_2 is common in other contexts. In the area of structural ceramics, small amounts of Y_2O_3 are incorporated during the synthesis of ZrO_2 to increase its strength and fracture toughness by stabilising the cubic phase at lower temperatures, avoiding the deleterious volume expansion and cracking associated with the tetragonal to monoclinic phase transitions that takes place upon cooling pure ZrO_2.[167,168] In the area of electrocatalysis, Zr borides and phosphides containing 3d-TMs have been prepared and tested as water-splitting catalysts in the context of intercalation of active species that act as confined catalytic centers.[169–173] Oxides such as $CoFe_2O_4$ have also been doped with Zr accessing different morphologies with increased surface area.[174] These methods for the fabrication of Zr-based mixed-metal films usually require annealing at high temperatures for the solid-state reaction of the precursors,[173,175] or multi-step synthetic routes for the incorporation of the dopant.[172,176] Moreover, MOFs containing a variety of transition-metals acting as active sites have also been employed in electrocatalysis.[177,178] However, these usually present their own challenges, such as poor conductivity and stability, and are difficult to scale-up. In contrast to all of these approaches, film deposition from solution using SSPs allows the room-temperature deposition of mixed-metal oxide films in a one-step process using scalable methods such as drop-casting or spin-coating.[153]

With this background in mind, three different Zr-based mixed-metal SSPs have been developed in the current study and their activity towards electrochemical water oxidation and as co-catalysts for PEC water oxidation has been investigated. The precursors allow a simple and scalable approach to the deposition of 3d-transition metal doped ZrO_2 (Figure 2.1). A substrate can be coated simply by adding a precursor solution by drop casting or spin-coating, followed by solvent evaporation and hydrolysis of the cages leading to an amorphous Zr-based film. This one-step process is easy to scale-up and more cost effective than instrumental film deposition techniques such as atomic-layer deposition. The precursors are Zr-based cage compounds incorporating 3d TMs in their structures. The drop-casting of the precursors affords the first examples of room-temperature deposition of TM-doped amorphous ZrO_2 films (abbreviated as MZr where M = Co, Fe, and Cu). The CoZr system on FTO-coated glass substrate (FTO|CoZr) showed the highest electrocatalytic activity out of the three catalysts tested in alkaline

medium and improved the photoactivity of $BiVO_4$ under neutral pH substantially. This work demonstrates the suitability of the SSP approach for the facile synthesis of technologically relevant complex metal oxides. Furthermore, it highlights the role of the TM co-catalyst in the design of efficient water-splitting catalyst films.

2.3. Synthesis and Characterization of the Catalyst Precursors

We employed a one-step synthetic approach to the new complexes $[\{Zr_4(\mu_4\text{-}O)(EtO)_{15}\}Co^{II}Cl]$ (**1**), $[\{Zr_4(\mu_4\text{-}O)_2(EtO)_{16}\}(Fe^{III}Cl)_2]$ (**2**) and $[\{Zr_4(\mu_4\text{-}O)_2(EtO)_{16}\}\{(Cu^{II}Cl)_2(OEt)\}_2]$ (**3**), in which $Zr(OEt)_4$ is reacted with the corresponding first-row TM salt (MCl_2; M = Co, Fe, Cu) in a 5:1 molar ratio in EtOH under solvothermal conditions (see Chapter 6, section 6.1.1). The stoichiometry used was based on previous studies of polyoxotitanium cage precursors of this type, but it was found that the same cages are generated regardless of the stoichiometry used (but in lower yields). The formation of oxo-cage compounds in these reactions has been ascribed to the presence of trace water in the solvent or starting materials or to scavenging of O-atoms from the EtOH solvent (with the formation of diethyl ether) under the solvothermal conditions used.[179] The products **1**-**3** were obtained as crystals after workup in 11-62% yield and characterized by infrared (Figure 2.4), solution and solid-state UV-visible spectroscopy (Figure 2.5), elemental (C, H) analysis and single-crystal X-ray diffraction (SC-XRD) (Figures 2.1–2.3).

SC-XRD data were collected and analysed with help from Dr. Andrew Bond. The resulting structures of **1**, **2** and **3** are shown in Figure 2.1. Their compositions reveal a 4:1 ratio of Zr:Co in **1**, 4:2 ratio of Zr:Fe in **2** and 1:1 ratio of Zr:Cu in **3**, showing that the reaction stoichiometry has little or no bearing on the molecular ratio or structure of the complex formed. Instead, it appears that the coordination preference and ionic size of the 'dopant' metal ions (Co^{2+}, Fe^{2+} and Cu^{2+}) have the greatest effect on the structure. Previous work has led to similar conclusions regarding the structures of heterometallic polyoxotitanium complexes containing Co^{2+}, Cu^{2+} and Fe^{2+}.[154,158]

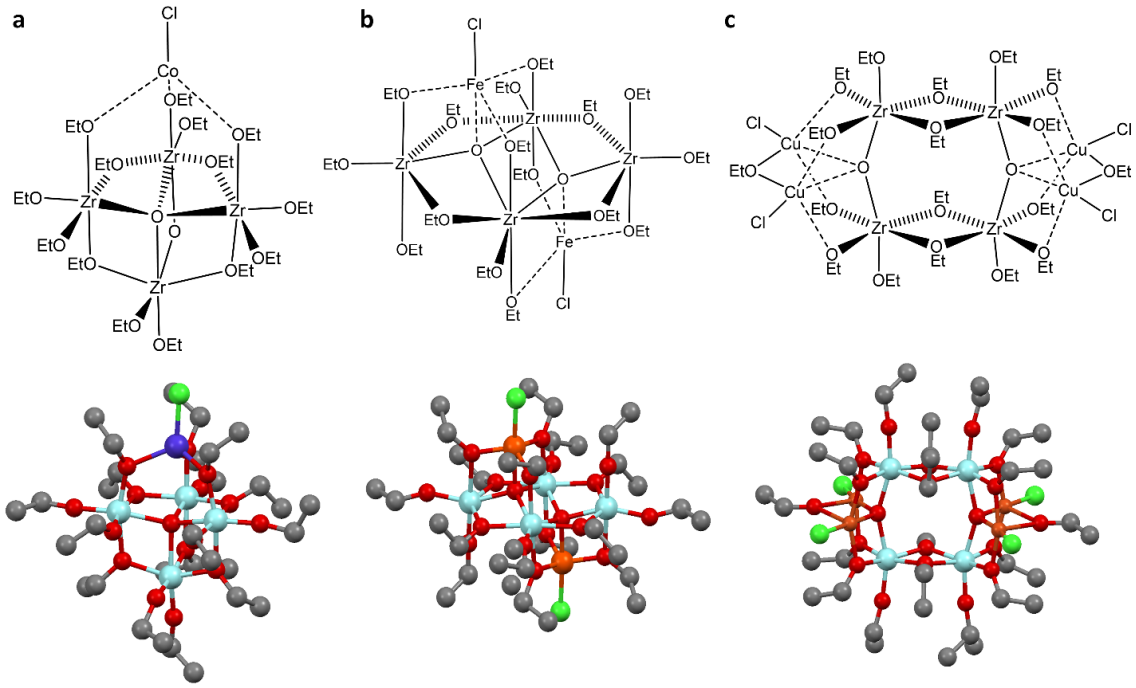

Figure 2.1. Molecular structures of the SSPs. **(a)** [{$Zr_4(\mu_4\text{-}O)(OEt)_{15}$}$Co^{II}Cl$] (**1**). H-atoms and one of the disordered CoCl sites (present in 50:50 ratio with the site shown) have been omitted for clarity. **(b)** [{$Zr_4(\mu_4\text{-}O)_2(EtO)_{16}$}$(Fe^{III}Cl)_2$] (**2**). H-atoms and the lattice THF molecules have been omitted for clarity. **(c)** [{$Zr_4(\mu_4\text{-}O)_2(EtO)_{16}$}{$(Cu^{II}Cl)_2(OEt)$}$_2$] (**3**). H-atoms and lattice EtOH molecules have been omitted for clarity. For selected bond lengths and angles see Table 2.1.

Compound **1** (Figure 2.1a) is isostructural with the series of 3d-TM complexes [{$Ti_4(\mu_4\text{-}O)(OEt)_{15}$}$M^{II}Cl$] with M = Co, Cu, Fe.[180,181] Its crystal structure is fully isomorphous with the Co and Fe titanium complexes, and also with the zirconium-based ZnCl complex [{$Zr_4(\mu_4\text{-}O)(EtO)_{15}$}$Zn^{II}Cl$] (**1**_Zn) reported previously.[182] The SC-XRD refinement of **1**_Zn was noted by the authors to be problematic, and the refinement of **1** in the present work was similarly problematic. For **1**_Zn there was some ambiguity as to the correct space group, and the refinement was quite poor with an *R*-factor of *ca* 15%. The diffraction pattern of **1** showed similar features. The best description in this case was produced with space group *C*2/*c*. The complex is situated on a crystallographic 2-fold rotation axis (passing through atoms O1 and O5), which necessitates 50% site occupancy for atoms Co1 and Cl1 (Figure 2.2). The ethoxide groups are in general poorly resolved and the displacement parameters of all C atoms are large. The conclusion from detailed analysis of the SC-XRD data for **1** and **1**_Zn is that this structural type is prone to twinning/stacking disorder. However, the chemical identity of **1**, and in particular the presence of only one CoCl group per complex, is clear.

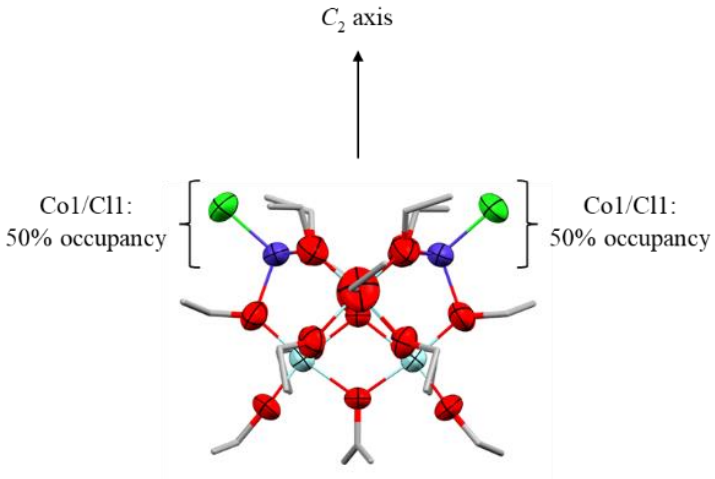

Figure 2.2. Crystal structure of complex **1**. Significant twinning/stacking disorder was observed, but the average structure of the complex could be resolved using a C2/c space group with 50 % occupancy of the atoms Co1 and Cl1 and a C_2 rotation axis passing through O1 and O5.

The complex can be regarded as being constructed from a $[\{Zr_4(\mu_4\text{-}O)(OEt)_{15}\}]^-$ anion and a single $[Co^{II}Cl]^+$ fragment. The Co^{2+} ion is coordinated by three of the EtO^- groups of the anion together with a Cl^- ligand, resulting is a distorted tetrahedral metal geometry (with all of the Zr^{4+} centers having six-coordinate, distorted-octahedral geometries).

The structures of **2** and **3** (Figure 2.1b, c and Figure 2.3) are unprecedented in relation to the known family of related alkoxy first-row mixed-metal polyoxozirconium cages, which generally contain Zr_2 or Zr_3 units.[183–186] Refinement of $[\{Zr_4(\mu_4\text{-}O)_2(EtO)_{16}\}(Fe^{III}Cl)_2]\cdot 2THF$, denoted **2**·2THF, was largely straightforward.. The THF molecule (one in the asymmetric unit, two per centrosymmetric complex **2**) is quite poorly resolved. Eliminating this problematic THF molecule from the refinement model and applying *SQUEEZE* led to some improvement in the *R*-factors ($R1 = 0.032$, $wR2 = 0.083$), but inclusion of THF was finally preferred for chemical clarity.

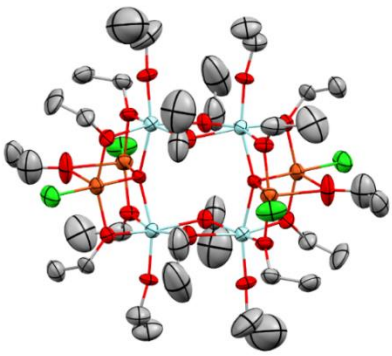

Figure 2.3. Crystal structure of **3**. The complex consists in a $[Zr_4(\mu_2\text{-}O)_2(EtO)_{16}]^{4-}$ rectangular unit with two $[(CuCl)_2(\mu_2\text{-}OEt)]^+$ at either side leading to an overall charge of -2.

Data collection for **3** was carried out on several crystals taken from different batches, in all cases giving comparable results. The crystals appear to be twinned, and the final refinement is based on a 2-component refinement. The refinement produced good *R*-factors and a well-defined centrosymmetric complex with formula $[\{Zr_4(\mu_4\text{-}O)_2(EtO)_{16}\}\{(Cu^{II}Cl)_2(OEt)\}_2]$ (Figure 2.3). The X-ray data indicate that **3** consists of a $[Zr_4(\mu_2\text{-}O)_2(EtO)_{16}]^{4-}$ anion, which coordinates two $[(CuCl)_2(\mu_2\text{-}OEt)]^+$ units at either side of its rectangular Zr_4 unit. This leaves an overall 2– charge on the complex, with no apparent charge-balancing cation(s) within the crystal structure. Possibilities for charge balance include protonation of two of the ethoxide ligands, or exchange of Cl^- /EtO^- by H_2O. The Cu^{2+} ions have pseudo-tetrahedral coordination geometries, with all the Zr^{4+} centers having distorted octahedral environments. The structure contains additional electron density in spaces between the complexes, which is modelled as one disordered ethanol molecule per void. Detailed crystallographic analysis led to the conclusion that any isolated charge-balancing cation in this site (*e.g.,* Na^+ or H_3O^+) is unlikely on the basis of the clearly hydrophobic environment of the channels.

Table 2.1. Selected bond-lengths for **1**, **2** and **3**.

Precursor	**Bond**	**Bond length / Å**
CoZr (**1**)	Zr•••Zr	3.459(2)–3.525(2)
	Terminal Zr-O(Et), Zr-bridging Zr-O(Et)	1.866(10)-2.202(8)
	$Zr\text{-}O_{oxo}$	2.213(3)-2.234(5)
	Co-O(Et)	1.965(10)-2.196(12)
	Co-Cl	2.242(7)
	Zr···Zr···Zr	59.36(3)-61.29(4)
FeZr (**2**)	Zr···Zr	3.537(1)
	Terminal Zr-O(Et), Zr-bridging Zr-O(Et)	2.149(3)-2.287(3)
	$Zr\text{-}O_{oxo}$	2.113(3)-2.173(3)
	$Fe\text{-}O_{oxo}$	1.992(3)
	Fe-O(Et)	1.915(3)-1.967(3)
	Fe-Cl	2.246(1)
	Zr···Zr···Zr	62.11(1)-117.89(1)
CuZr (**3**)	Zr···Zr [$Zr(\mu_3\text{-}O)Zr$]	4.172(1)
	Zr···Zr [$Zr(\mu_2\text{-}OEt)_2$]	3.496(2)
	Zr-O(Et)	1.905(6)-1.907(5)
	Zr-bridging Zr-μ-O(Et)	2.145(6)-2.158(7)
	$Zr\text{-}O_{oxo}$	2.136(5)-2.152(5)
	$Cu\text{-}O_{oxo}$	2.051(6)-2.066(6)
	Cu-O(Et)(bridging Zr)	1.943(6)-1.948(6)
	Cu-OEt (bridging Cu)	2.439(8)-2.490(8)
	Cu-Cl	2.202(3)-2.208(3)
	Zr···Zr···Zr	88.83(2)-91.17(2)

The three precursors **1**, **2** and **3** show very similar FT-IR spectra (Figure 2.4). They present a broad feature at 500–715 cm^{-1} which corresponds to the metal-oxo framework υ(MO),[187] the region corresponding to C-O stretching shows distinct bands. One υ(CO) at ca. 950 cm^{-1} which is assigned to the terminal -OEt ligands and one broader band at 1000–1250 cm^{-1} which corresponds to μ_2-OEt ligands. The bending and stretching modes of the C-H bonds are seen at 1250–1500 cm^{-1} and 2750–3000 cm^{-1}, respectively (in overlap with those of Nujol). Finally, IR bands corresponding to TM-Cl bond, which typically appear at 100–300 cm^{-1} are not visible in the spectral window available.[188] Overall, FT-IR supports the presence of metal-oxo alkoxy cages in good agreement with the SC-XRD data.

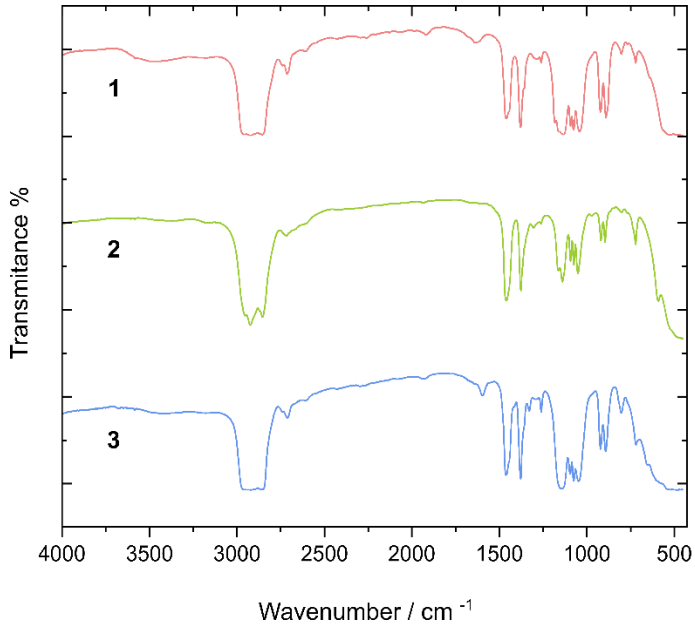

Figure 2.4. FTIR spectra of complexes **1**-**3**. The three complexes show very similar features with bands corresponding to υ(C-O) and υ(M-O) bonds as expected from the SC-XRD data.

The solution UV-vis and diffuse-reflectance spectroscopy (DRS) UV-vis spectra of the solids are presented in Figure 2.5. DRS UV-vis allowed the observation of weak absorptions that were not seen in solution UV-vis because of the low solubility of the compounds. The absorption bands at 280–300 nm are attributed to the Zr-O cage backbone.[189] Direct evidence of the presence of Co^{2+} in **1** is observed in the UV-vis spectrum (Figure 2.5a), showing three bands in the visible region (561, 600 and 658 nm) which correspond to the three allowed transitions from the ^4A ground state to the three ^4T states for a tetrahedral d^7 ion (i.e., in a tetrahedral coordination geometry). The presence of Cu^{2+} in **3** (Figure 2.1c) is supported by the observation of a single visible absorption band at ca. 690 nm in the solid-state UV-DRS spectrum, which corresponds to the weak-field $^2T \rightarrow {}^2E$ for a tetrahedral d^9 ion and is in agreement with previously reported

titanium-oxo cages containing Ti^{4+}.[180] The C_{2h}-symmetric molecular structure of **2** contains a $[Zr_4(\mu_3\text{-}O)_2(EtO)_{16}]^{4-}$ anion with the same composition as the anion in **3**, but a very different arrangement. In **2**, each of the oxo-anions bridge three of the four Zr^{4+} ions within the boundary of the rhombic Zr_4 unit (rather than being located at two opposite edges of a rectangular metal framework). The Fe^{3+} cations have distorted trigonal bipyramidal geometries, each being coordinated by an oxo-atom of the core, by three terminal EtO^- groups and by a terminal Cl^- ligand. This is consistent with the absence of any absorption band in the visible region in the UV-vis spectrum of **2** due to the presence of high-spin d^5 Fe^{3+} cations in a complex in which d-d electronic transitions are spin-forbidden.

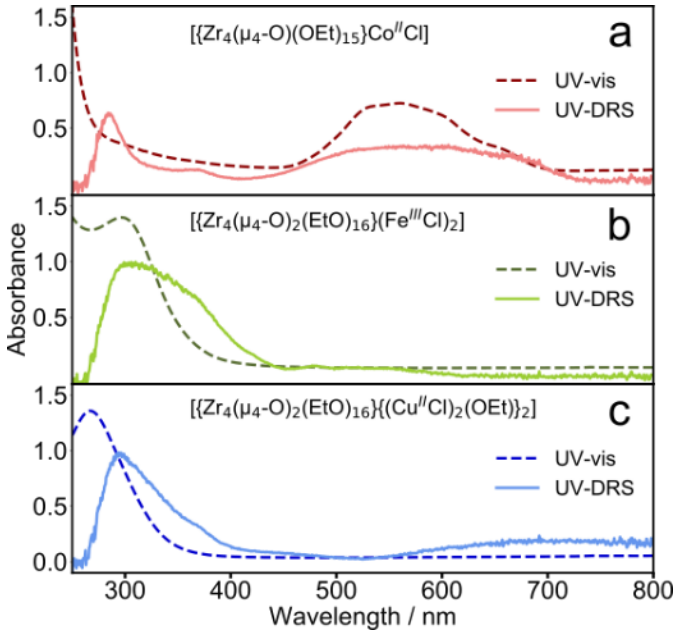

Figure 2.5. Solution UV-Vis and DRS UV-Vis spectra of precursors **1**, **2** and **3**. The solution UV-Vis spectra were recorded in dry EtOH (conc. 0.08 mmol/L). The data show the expected absorption bands for tetrahedral d^7 and d^9 configurations, indicating the presence of Co^{2+}, and Cu^{2+}, respectively. Furthermore, the lack of absorption bands in the visible region of **2** is consistent with the presence of trigonal bipyramidal Fe^{3+} with a d^5 configuration.

2.4. Coating Deposition and (Photo)electrocatalytic Testing

2.4.1. Fabrication of the Catalyst

Electrocatalyst films were prepared by drop-casting a SSP solution (60 µL, 0.26 mol/L) onto a clean, preheated (40 ºC) FTO-coated glass substrate. The resulting films are designated as FTO|MZr (M = Co, Fe and Cu). FTO-coated glass substrates were thoroughly cleaned by sonication in MilliQ water, acetone, and isopropanol (20 minutes in each), followed by UV-ozone treatment for 15 minutes. In order to obtain a uniform deposition, 20 µL of the saturated catalyst solution (concentration 0.26 mol/L) was carefully pipetted onto a clean preheated (40 ºC) FTO-coated glass substrate (effective area 1 cm^2) and dried for 15 minutes under ambient conditions. This process was repeated two more times, for a total of 60 µL of solution. Thereafter, 20 µL of a 1:1 Nafion:EtOH mixture was uniformly pipetted over the catalyst layer and dried overnight under ambient conditions (Figure 2.6). The amorphous nature of the films was confirmed by powder X-ray diffraction (PXRD) which did not show any peaks between 5 to 80 2θ degrees. The same drop-casting procedure was followed when preparing the carbon-fibre paper, graphite paper and indium tin oxide (ITO) coated glass substrates which were used to test the effect of different substrates on the electrocatalytic activity of the materials.

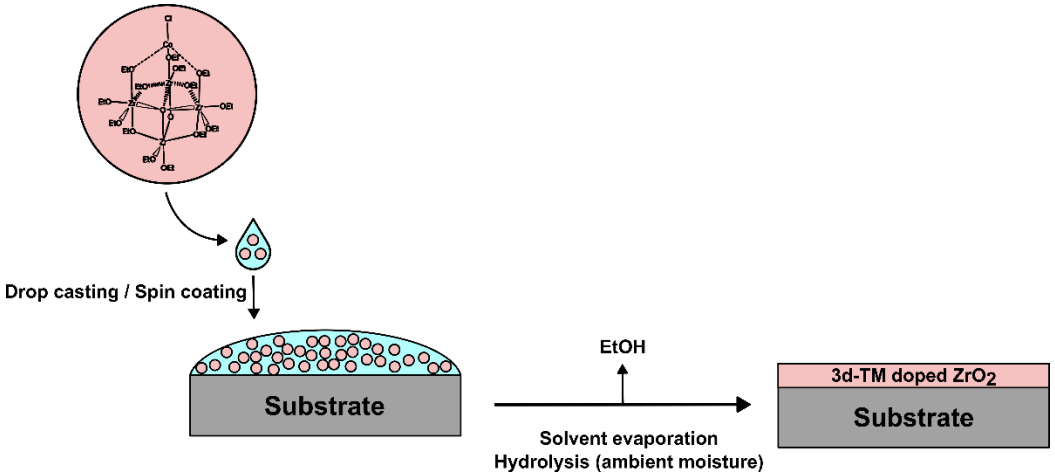

Figure 2.6. Scheme of the coating deposition method used in this work. The electrocatalyst is prepared by drop-casting a precursor solution over the surface of the substrate. For the deposition of the co-catalyst layer on the photoanode for photoelectrolysis, the precursor solution was spin-coated onto $BiVO_4$ to obtain a thin, homogeneous film. The solvent evaporates under air and the precursor is hydrolysed by ambient moisture leading to an amorphous 3d-TM doped zirconium oxide coating.

2.4.2. Electron Microscopy Study of the Deposited Films

Scanning electron microscopy (SEM) images and energy dispersive X-ray spectroscopy (EDS) maps presented in Figure 2.7 show the morphologies and elemental compositions of the films deposited on FTO coated glass. SEM images show that the deposition process leads to rough films on top of the substrate. The morphologies of the films vary significantly depending on the region of the sample, being composed of fragments of material that show large differences in size ranging from 1–250 μm for each of the electrodes. EDS maps confirm the presence of zirconium and the dopant element evenly distributed throughout the deposited layer.

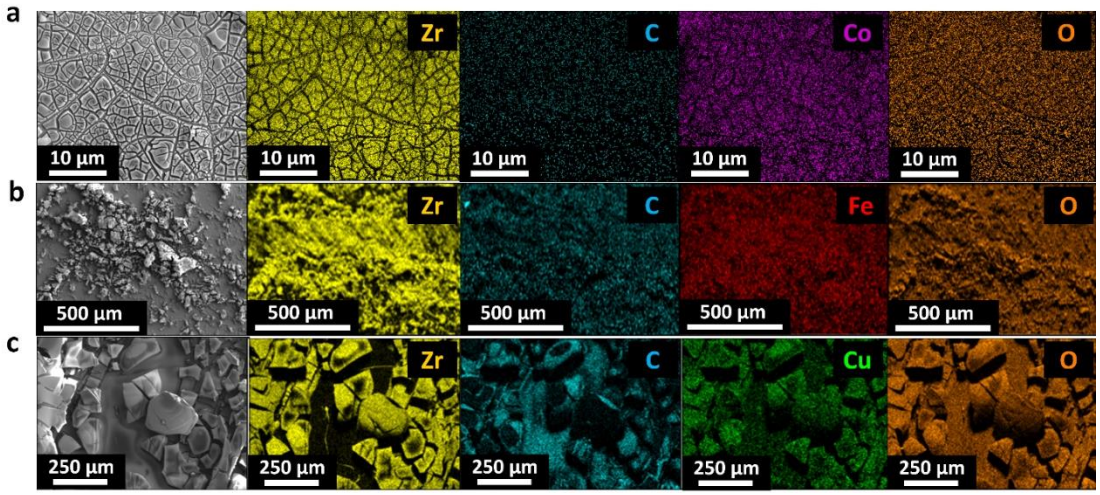

Figure 2.7. SEM images and corresponding EDS elemental mapping of the three systems: **(a)** FTO|CoZr, **(b)** FTO|FeZr and **(c)** FTO|CuZr.

To obtain quantitative information about the composition of the catalysts, multiple EDS spectra were measured for each of the samples. The atomic ratios were calculated from these data and are shown in Figure 2.8. The similar levels of dopant content detected on different points of the sample confirm that this deposition approach leads to doped zirconia films that are homogeneous in composition (See Tables B1-B7, Appendix B). The catalysts have lower dopant (Co, Fe and Cu) content than the precursor molecules used as SSPs, suggesting that a fraction of the dopant remains in solution during the deposition process and is not incorporated into the films. Nevertheless, there is a significant amount of dopant incorporated into the materials and a correlation between dopant level in the precursor and the catalyst, with precursors containing higher dopant content leading to a larger amount of dopant in the catalyst film. The presence of 3d-TMs and the correlation between the amount of dopant on the catalyst film and the dopant : Zr ratio of the parent precursor was further confirmed by inductively coupled plasma optical

emission spectroscopy (ICP-OES) which showed values of 0.4 mol/cm^2 of Co, and 0.5 mol/cm^2 of Fe and Cu. Finally, the catalyst compositions after the chronoamperometric (CA) water oxidation test (Figure 2.15c) were studied following the same methodology to investigate the stability of the catalysts and possible metal dissolution. Within error, there are similar levels of dopant present before and after catalysis for the three materials. For the FTO|CuZr system, a slight decrease in Cu content after catalysis is observed while for the FTO|FeZr system the Fe content remains the same, within error, before and after catalysis. The EDS analysis of the FTO|CoZr system showed a slight increase in the Co:Zr ratio after catalysis. These results do not support Zr dissolution as similar Zr atomic % values are detected before and after catalysis (for CoZr 12.2 ±1.0 and 15.2 ±1.8 atomic % of Zr were detected, Table B1 and B2, Appendix B). Alternatively, this enrichment in surface Co might be explained by a surface reconstruction process.[190,191]

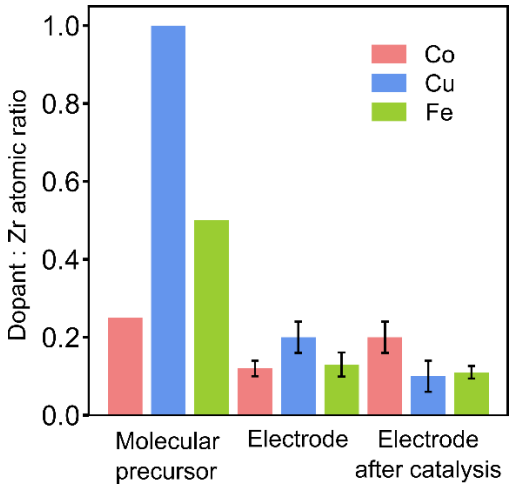

Figure 2.8. Dopant-to-zirconium atomic ratios for the molecular precursors, determined from their crystal structure, and the catalyst films deposited onto FTO glass, determined by EDS. The dopant content of the catalyst is lower but dependent on that of the precursor. The metal dissolution during operation is dependent on the combination of elements present.

2.4.3. Surface Characterisation by X-ray Photoelectron Spectroscopy (XPS)

2.4.3.1. Calibration of the XPS Spectra

The spectra were charge-corrected by setting the adventitious carbon alkyl (C–H, C–C) peak to 284.8 eV (Figure 2.9). The calibration method followed conventional practices.[192] Measured XPS binding energies were adjusted to compensate for the shift that arises from accumulated electrostatic charge by setting the alkyl hydrocarbon C 1s peak (from adventitious carbon) to the binding energy of 284.8 eV. This was performed fitting four peaks corresponding to alkyl (C–H, C–C), ethers and alcohols (C–O–C,C–OH), carbonyl (C=O), and esters and carbonates (O–C=O); the peaks were constrained to have equal width and their spacing was 1.5 eV, 3.0 eV and 4–5 eV, relative to the alkyl peak, respectively.[192] The C 1s region in the samples prepared in Nafion showed a larger number of carbon chemical environments, as well as overlap with the K 2p peak from potassium inclusions in the Nafion from exposure to KOH solution. A C–F peak was added and its width was allowed to vary freely, while its position was set at ~8 eV above the alkyl peak. The K 2p was fitted as a single peak with freely varied width and a position set at ~11 eV above the alkyl peak (Figure 2.9b).

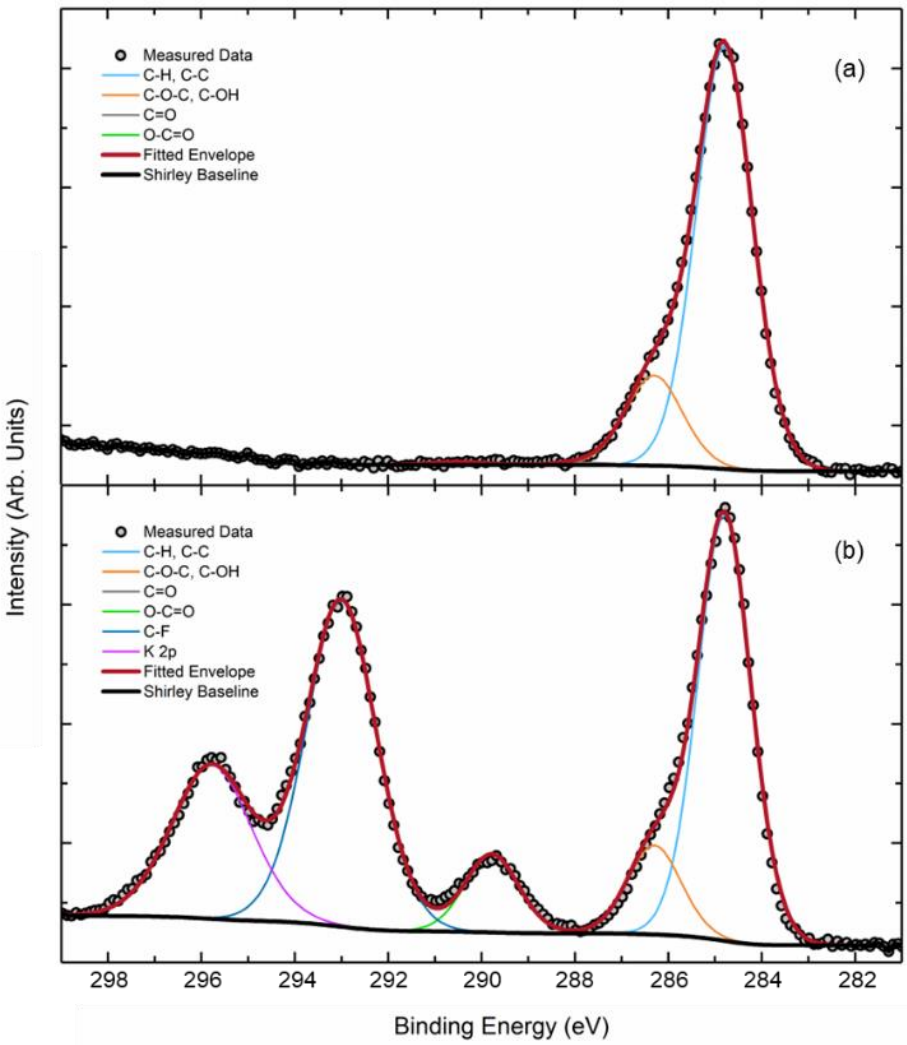

Figure 2.9. (a) Fitted C 1s region of the CoZr sample, demonstrating the peaks used for charge compensation of free-standing catalyst materials in this work. (b) Fitted C 1s region of the FeZr/Nafion sample, demonstrating the peaks used for charge compensation of catalyst materials prepared with Nafion and immersed in aqueous KOH.

2.4.3.2. XPS Investigation of the Surface Species

After charge correction, XPS was applied to the deposited films to investigate the chemical species present on the surfaces (Figures 2.10-2.12). The Zr 3d region was fitted by constraining the $3d_{5/2}$ and $3d_{3/2}$ spin-orbit pairs to have equal peak width and a fixed area ratio of 3:2 (Figure 2.10). In all cases, it was found that the region fitted very well using two chemical environments (i.e., four peaks in total). The lower binding-energy $3d_{5/2}$ components were centred at 182.2–182.3 eV for all three films and the spin-orbit splitting was in the region 2.37–2.39 eV, consistent with reported values for the Zr(IV) oxide, ZrO_2 (182.8 ± 0.6 eV and ~2.43 eV, respectively).[193] The higher binding-energy (BE) $3d_{5/2}$ component had more variability between samples and was centred at 183.81, 183.15, and 183.59 eV for the FTO|CoZr, FTO|CuZr, and FTO|FeZr samples, respectively.

Table 2.2. XPS fitting parameters for the Zr 3d region, measured at a pass energy of 20 eV.

Sample	**Zr $3d_{5/2}$ Peak 1 / eV**	**FWHM / eV**	**$3d_{5/2}$ – $3d_{3/2}$ Splitting / eV**	**Zr $3d_{5/2}$ Peak 2 / eV**	**FWHM / eV**	**$3d_{5/2}$ – $3d_{3/2}$ Splitting / eV**	**Peak 2 Area %**
CoZr/Nafion	182.26	1.36	2.37	183.81	2.24	2.27	27.9
CuZr/Nafion	182.19	1.40	2.39	183.15	1.92	2.31	22.7
FeZr/Nafion	182.22	1.31	2.37	183.59	1.76	2.38	31.6

The higher BE peaks are above the binding energy range expected for a metal alloy (e.g., Zr-Co alloys and alloy films, BE ≅ 178.9 eV).[194] Thus, they are attributed to mixed-metal oxides, supported by the presence of the respective TM counterparts (Co 2p, Cu 2p, and Fe 2p spectra are shown in Figure 2.12). The fitted XPS peak parameters are summarized in Table 2.2.

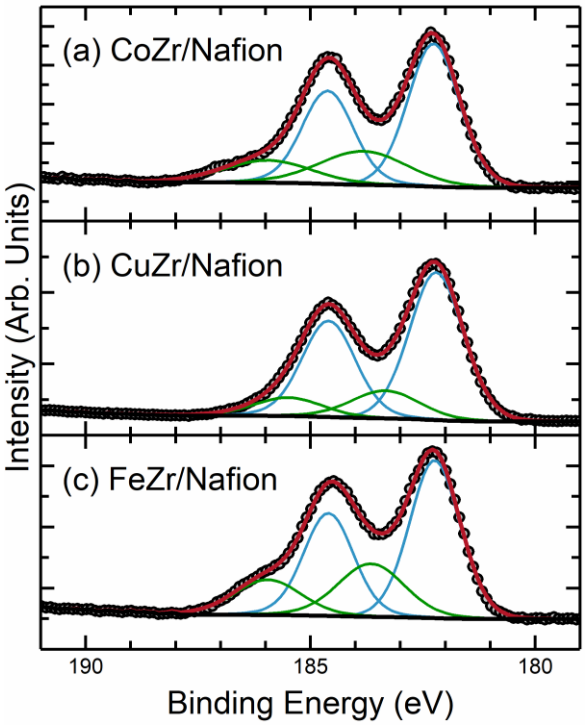

Figure 2.10. High-resolution XPS of the Zr 3d region for (a) FTO|CoZr (b) FTO|CuZr and (c) FTO|FeZr samples. The spectra were fitted using two spin-orbit $3d_{5/2}/3d_{3/2}$ pairs (i.e., four peaks total).

High-resolution F 1s and O 1s spectra of were also collected (Figure 2.11). The F 1s spectra (Figure 2.11, a-c) shown a single chemical environment centred at 685 eV for all the samples, as expected for fluorinated polymers like Nafion,[195] confirming that the coating of the catalyst film with Nafion by drop-casting was successful.

Table 2.3. XPS fit parameters for the O 1s region, measured at a pass energy of 20 eV.

	Lattice oxygen			**Hydroxides - Defects**			**Organic species (C-O)**		
Sample	**B.E. / eV**	**FWHM**	**Area %**	**B.E. / eV**	**FWHM**	**Area %**	**B.E. / eV**	**FWHM**	**Area %**
CoZr/ Nafion	530.50	1.95	28	532.05	1.67	48	532.63	1.67	24
CuZr/ Nafion	530.05	1.53	27	531.60	1.85	59	532.67	1.85	14
FeZr/ Nafion	530.48	1.93	27	532.01	1.61	49	532.54	1.61	24

The O 1s spectra (Figure 2.11, d-f, and Table 2.3) was fitted to three components corresponding to lattice oxygen (M-O) species, hydroxides and defects, and organic species (C-O) following common practice and similarly to previous literature reports on O1s fitting of ZrO_2.[196] The lattice oxygen peak was allowed to vary between 531 and 528 eV, while the other two components were constrained to 533–531 eV. The FWHM of the lattice oxygen peak was constrained between 0.5 and 3, and the other two peaks (which were set to have the same FWHM) were allowed to vary between 1 and 2. The two lower B.E. peaks are assigned to the lattice and hydroxide / defects contribution from the ZrO_2. These results show the presence of mostly hydroxides or oxides with high concentration of defects, as expected for an amorphous ZrO_2 deposited by hydrolysis.[197] The surface content of organic species bearing C-O groups is estimated to be between 14–24 % (Table 2.3), and is explained by the presence of Nafion and residual ethoxide groups from the hydrolysis of the precursors.

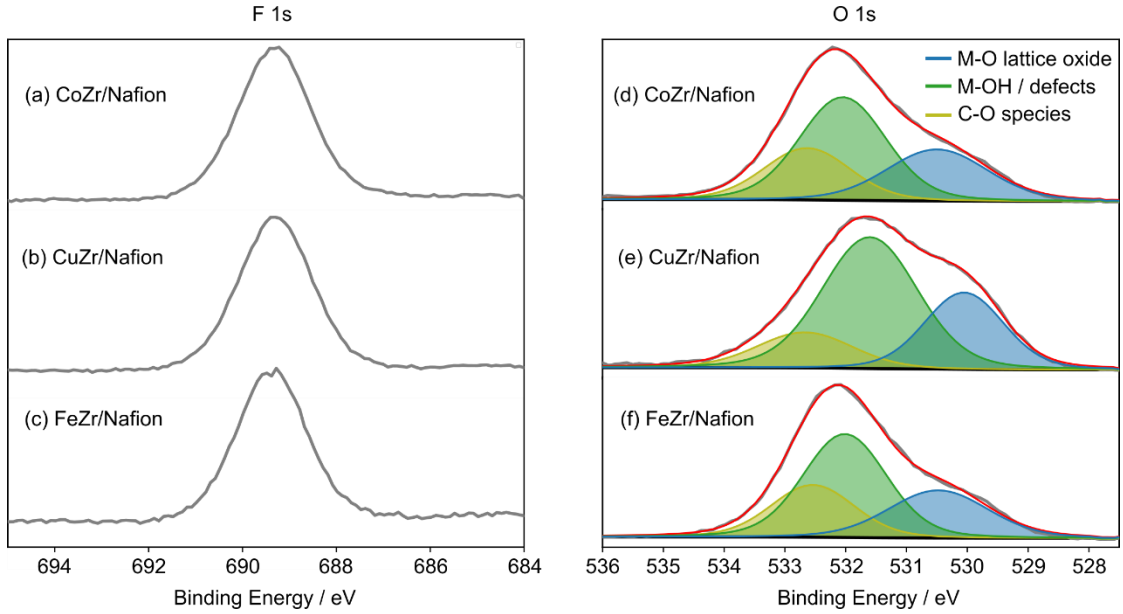

Figure 2.11. F 1s and O 1s spectra of the samples for (a, d) CoZr/Nafion, (b, e) CuZr / Nafion and (c, f) FeZr / Nafion.

The high-resolution XPS regions of the 3d transition metal dopants Co 2p, Cu 2p and Fe 2p was also measured (Figure 2.12). The low dopant content led to a poor resolution which precluded fitting of the spectra. These results are consistent with the findings from EDS, i.e., that the metal ratios in the deposited films are lower from those of the precursors. It is important to note that the analysis depth of XPS is significantly lower (order of a few nm) than EDS. The Co 2p spectrum presents one environment with two peaks corresponding to the $2p_{1/2}$ and $2p_{3/2}$ components. The $2p_{3/2}$ component is centred at

780 eV which is consistent with literature values for CoO_x species and not with metallic Co^0 which would appear at lower binding energies.[198] Inspection of the Cu 2p and Fe 2p spectra led to similar conclusions; the position of the peaks falls in the expected values for oxides.[198,199]

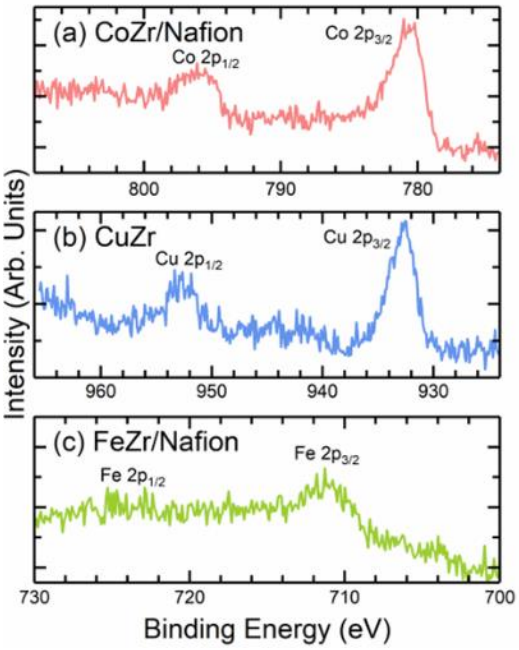

Figure 2.12. Transition metal regions of the XPS spectra. a) FTO|CoZr b) FTO|CuZr and c) FTO|FeZr samples.

2.4.4. Electrochemical Characterisation

The deposited films were then tested for electrocatalytic activity towards the OER in collaboration with Subhajit Bhattacharjee, Xinsheng Dong, Dr Virgil Andrei, and Prof. Erwin Reisner. The electrochemical measurements were performed using an Ivium Compactstat Electrochemical Analyzer and a two-compartment cell separated by a Selemion anion exchange membrane in alkaline conditions. 1 M $KOH_{(aq)}$ was used as the electrolyte solution, which was purged with N_2 before the experiments. The FTO|MZr (M = Co, Fe, Cu) catalyst, $Ag/AgCl_{sat}$ and platinum mesh were used as the working, reference, and counter electrodes, respectively. Prior to the measurements (except in the 4 h chronoamperometric test, Figure 2.17), the working electrode was subjected to CV scans between 0.8 V and 2.0 V vs. RHE at a scan rate of 100 mV s^{-1} for 20 cycles in order to activate it and remove surface impurities.[200] Linear sweep voltammetry (LSV) measurements were performed at a lower scan rate of 5 mV s^{-1} for all the three systems in order to minimize the capacitive current. Unless mentioned otherwise, all the potentials reported have been converted from the $Ag/AgCl_{sat}$ to the reversible hydrogen electrode (RHE) scale using Equation 1, where pH of 1 M KOH (aq.) was estimated to be 14.[201]

$$E_{(RHE)} = E_{(Ag/AgCl)} + E^{0}_{(Ag/AgCl)} + 0.059 \times pH \quad (1)$$

The potential of the saturated Ag/AgCl electrode was taken as $E^{0}_{Ag/AgCl} = 0.197\ V_{NHE}$. To account for the uncompensated solution resistance and other Ohmic losses, the measured potentials were *IR*-corrected using equation 2, where R_{Ω} was determined from the Bode Plots of the respective catalysts (Figure D1) following Equation 2.

$$E_{IR-corrected} = E_{applied} - IR_{\Omega} \quad (2)$$

The double-layer capacitance (C_{dl}) was determined by performing CV scans at different scan rates in the non-faradaic region (Figure 2.13). The slope of the current versus scan rate plot yields the C_{dl}, according to equation 3:

$$I = C_{dl}\left(\frac{dV}{dt}\right) \quad (3)$$

The electrochemically active surface area (ECSA) was determined from the C_{dl} by dividing the C_{dl} by the specific capacitance C_s (C_s = 40 μF cm^{-2}) known from literature.[202,203]

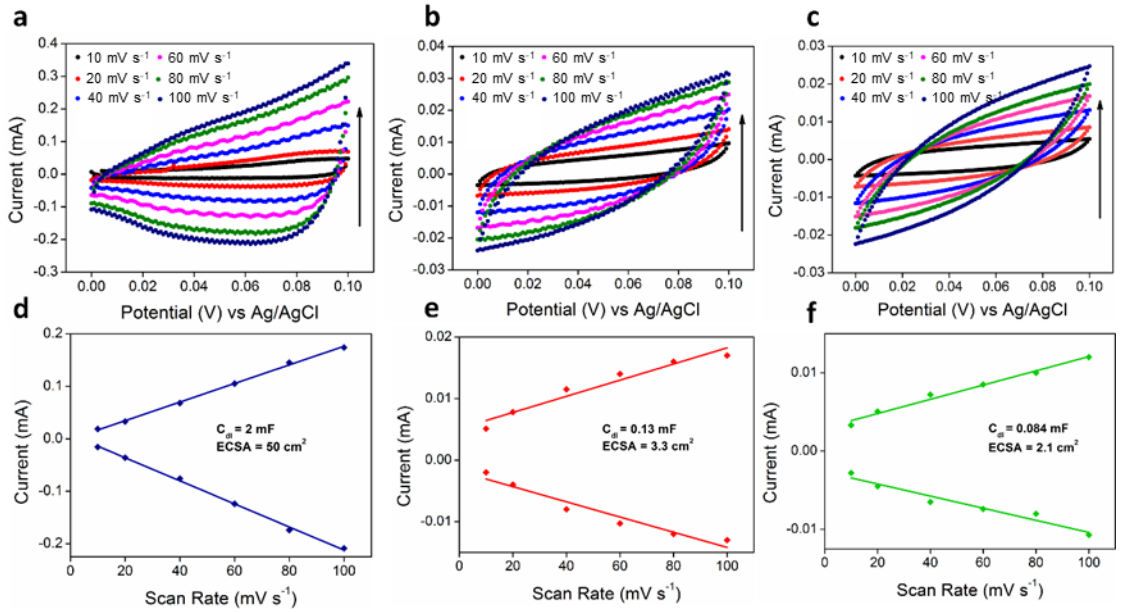

Figure 2.13. Electrochemically active surface area measurements. Top panel: CV plots of the (a) CoZr, (b) FeZr and (c) CuZr systems recorded at different scan rates. Bottom panel: Plot of current (recorded at a fixed potential) as a function of scan rate for (d) CoZr, (e) FeZr and (f) CuZr systems.

LSV measurements were taken in the direction of increasing potential (Figure 2.14 and 2.15 a-b). The CuZr film initially shows very similar behaviour to the blank FTO glass substrate, whilst the FeZr film gives an anodic current that is significantly greater than this 'background' level (by a factor on the order of 2–5 times). Meanwhile, the

FTO|CoZr film shows a much higher current density at all potentials. Given that the data in Figures 2.14 and 2.15 is normalized to the geometric area, it was considered whether the differences are attributable to changes in the surface roughness and charges in the surface electrochemical double layer. From the relative ECSAs evaluated using this method (Figure 2.13), the CoZr has a surface roughness of approximately 25 times CuZr. Therefore, the differences in current densities observed in the LSV between the CoZr sample and the other two can be attributed to differences in surface area (Figures 2.14 and 2.15). Between the FeZr and CuZr there is much less difference in ECSA (FeZr shows approximately 1.6 times the ECSA of CuZr). Surface roughness is therefore considered a significant component of the differences in their electrochemical behaviour, but there are likely additional factors. The presence of redox processes before the catalytic wave in the cobalt and copper catalysts are consistent with the surface oxidation of the TM.[135,203,204] These anodic waves are seen at ~1.15 V_{RHE} for the CoZr film (Figure 2.14) and at ~1.4 V_{RHE} for the CuZr film (Figure 2.15). Interestingly, this feature was not observed in the FeZr film.

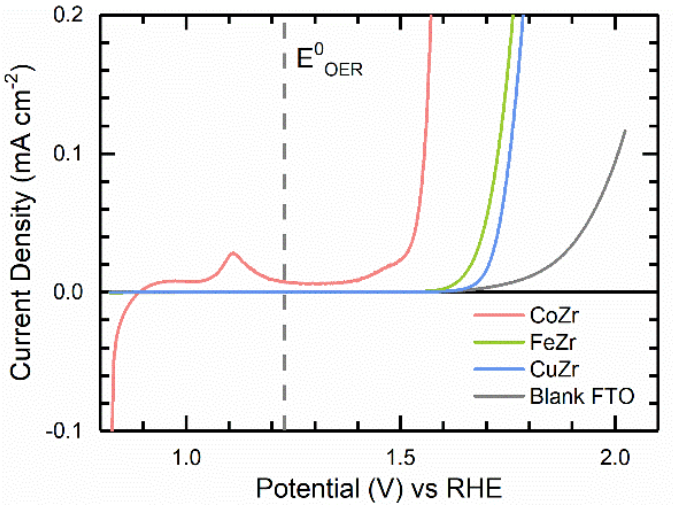

Figure 2.14. Linear sweep voltammetry (LSV) was measured on the untreated FTO glass (grey) and on the FTO|CoZr (red), FTO|FeZr (green), and FTO|CuZr (blue) coatings (scan rate 5 mV s^{-1}). The CoZr film presents an anodic wave at ~1.15 V_{RHE}, below the OER standard potential.

The activity of the catalysts towards water oxidation was then evaluated in terms of their onset potentials and Tafel slopes. The three catalysts are active towards water oxidation with the FTO|CoZr film showing the best performance while FTO|CuZr and FTO|FeZr showing lower activities. The potential vs. RHE of the FTO|CoZr film at current densities of 1 mA cm^{-2} is 0.3 V lower than that of the FTO|CuZr and FTO|FeZr films which are both very close (Figure 2.15a). The FTO|CoZr film exhibits OER

overpotentials of ~372 mV and ~430 mV vs. RHE at current densities of 1 mA cm^{-2} and 10 mA cm^{-2}, respectively. The FTO|FeZr and FTO|CuZr systems, however, fail to achieve high current densities and show higher overpotentials of ~ 670 mV and 693 mV vs. RHE at a current density of 1 mA cm^{-2}. Furthermore, the Tafel slope of FTO|CoZr film was 54 mV dec^{-1}, 15-20 mV dec^{-1} lower than for the other two catalysts. The FTO|CoZr catalyst also shows an activity comparable to some of the best-performing zirconium-based systems reported that also show onset potentials below 1.6 V vs. RHE and Tafel slopes of the order of 50 mV dec^{-1} (Table 2.4).[172,174] Although it is worth noting that direct comparison of catalysts based on these metrics can be difficult due to differences in the measurement conditions,[137] it is nevertheless an encouraging observation. More importantly, these findings confirm the higher intrinsic activity of cobalt compared with copper and iron as active sites for the water oxidation reaction. While this is in good agreement with previous studies that have shown cobalt oxides to have a higher intrinsic activity than other 3d TM oxides,[133,205] this work represents a first examination of the role of 3d TMs as catalytic sites incorporated in an inert host material.

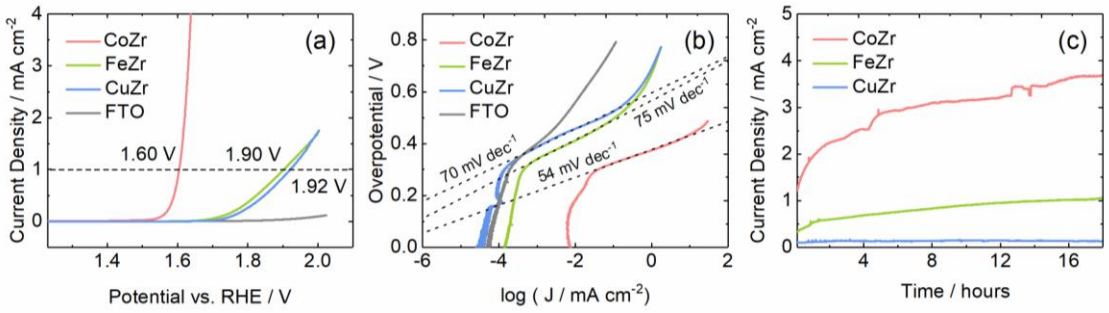

Figure 2.15. (a) Linear sweep voltammetry (LSV) was measured on the untreated FTO glass (grey) and on the FTO|CoZr (red), FTO|FeZr (green), and FTO|CuZr (blue) coatings (currents normalized to geometric surface area of the electrodes, i.e., 1 cm^2; scan rate 5 mV s^{-1}) and the corresponding (b) Tafel plots and linear fittings. (c) 18 h chronoamperometric (CA) tests were performed at a constant potential of 1.8 V for the FTO|CuZr and FTO|FeZr and 1.6 V for FTO|CoZr owing to the earlier onset of oxygen evolution of the later. Measurements were performed in degassed 1 M $KOH_{(aq)}$ solutions at room temperature.

At high potentials, a deviation from Tafel behaviour is observed (Figure 2.15b). This is attributed to diffusion limitations and local pH changes that can take place near the electrode under these conditions. Finally, the stability of the catalysts during operation was tested (Figure 2.15c). The stability tests for each catalyst were done using chronoamperometry (CA) by applying a constant bias of 1.6 V vs RHE for CoZr and 1.8 V vs RHE for FeZr and CuZr, for 18 h. It was found that the choice of 3d-TM dopant has an important effect on the stability of the catalyst. No significant degradation was found in the FTO|CoZr and in FTO|FeZr systems which undergo an activation process showing an increase in current density of 78 and 76%, respectively, during the first 18 h of operation. On the other hand, a 7% decrease in current density for the FTO|CuZr system is seen which is explained by the dissolution of copper, as supported by EDS (Figure 2.8) which shows a decrease in copper content after catalysis.

In order to gain a better understanding of the role of the substrate and versatility of SSP deposition for the water oxidation reaction, CoZr films were drop-casted onto three other substrates (graphite paper, carbon-fibre paper, and ITO-coated glass) and studied for electrochemical activity as shown in Figure 2.16. The electrochemical performance for FTO and graphite paper was found to be similar, whereas the ITO-coated glass substrate showed lower activity. A lower onset potential and high current density was observed in the case of the carbon-fibre paper as the three-dimensional porous network provides a high surface area for catalyst deposition, resulting in a high ECSA value of 203.7 cm^2.

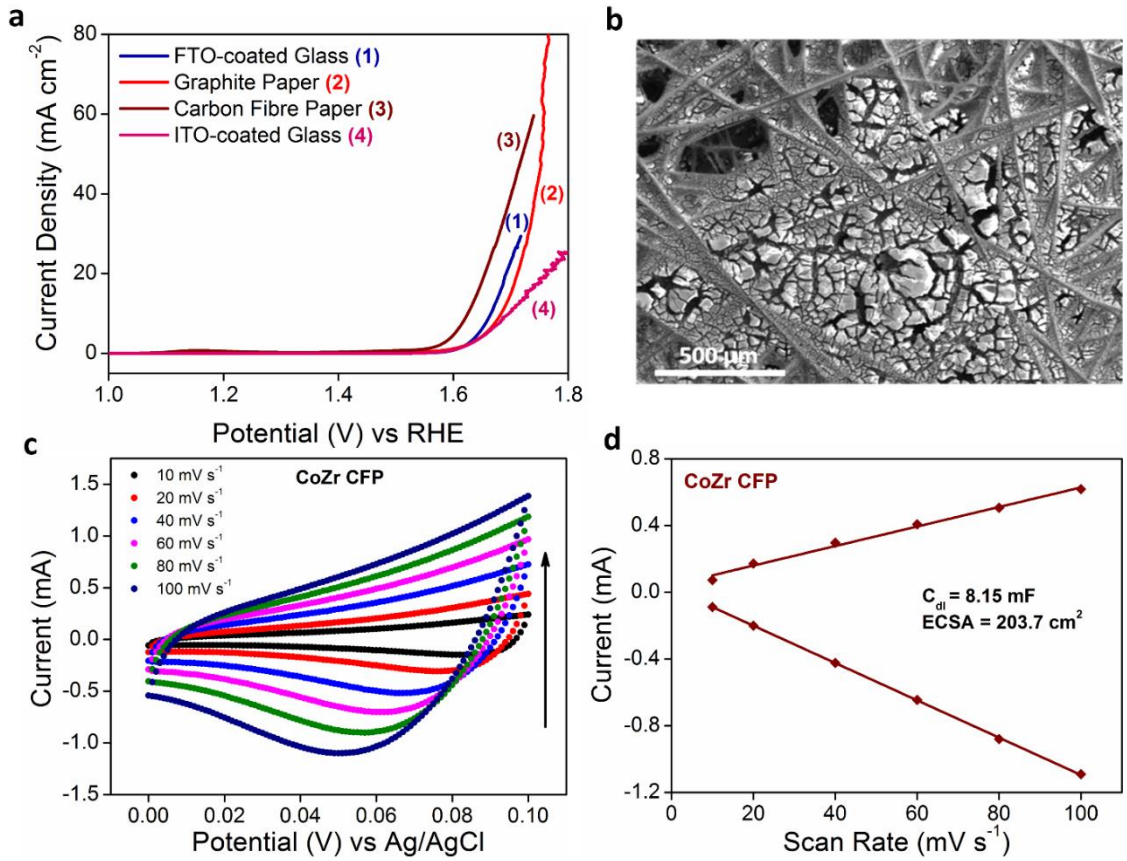

Figure 2.16. Substrate comparison experiments for OER: (a) LSV polarization curves recorded at a scan rate of 5 mV s^{-1} for the best performing CoZr system on different substrates in 1 M KOH (pH 14) at 25˚C. The overpotentials (vs. RHE) at 10 mA cm^{-2} are estimated to be: ~430 mV (on FTO), ~453 mV (on graphite foil), ~390 mV (on carbon-fibre paper) and ~469 mV (on ITO). (b) SEM image of CoZr drop-casted on carbon-fibre paper. (c) ECSA measurements: CV plots of CoZr deposited on carbon-fibre paper recorded at different scan rates. (d) Plot of current (recorded at fixed potential) as a function of scan rate for CoZr on carbon-fibre paper.

The O_2 quantification was then conducted for the best performing CoZr system in the anodic compartment of a gas-tight (photo)electrochemical cell (Figure 2.17). A constant potential was applied for 4 h. The O_2 baseline was also recorded before and after the chronoamperometry. The amount of oxygen in solution was obtained using Henry's law.

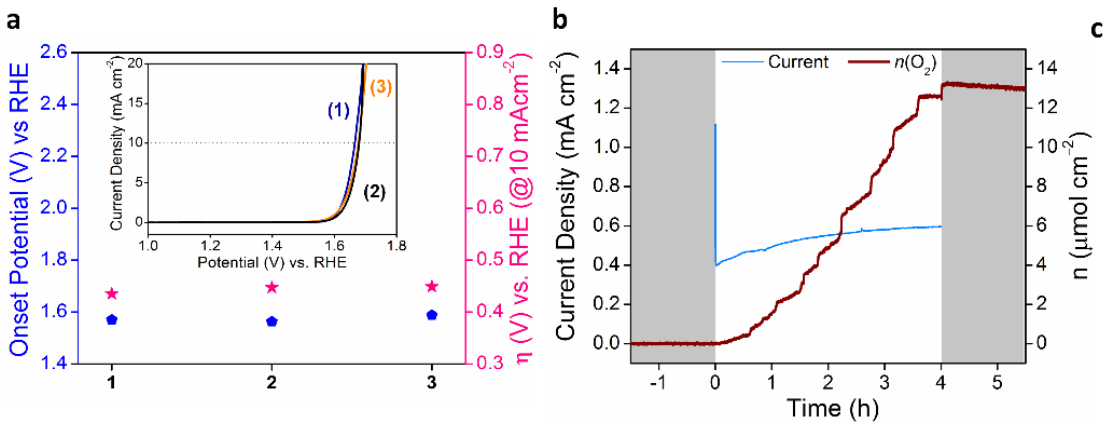

Figure 2.17. (a) Reproducibility plots of the best performing FTO|CoZr system with the (inset) OER LSV polarization curves indicating the consistency in the OER onset potential and the overpotential at a current density of 10 mA cm^{-2}. (b) Example of O_2 evolution on an FTO|CoZr sample and corresponding current trace. Chronoamperometry is performed for 4 h at 1.6 V vs. RHE in a 1 M KOH aqueous solution, without initial CV activation, with the grey areas indicating the O_2 baseline measurements.

No initial CV catalyst activation was performed for the O_2 evolution measurements, to aid the product quantification by avoiding additional O_2 generation before the start of electrolysis. Three separate FTO|CoZr samples produced 12.6 ± 2.7 µmol cm^{-2} O_2 over 4 h at 1.6 V vs. RHE, with an average Faradaic yield (FY) of 57 ± 14% and a steady-state current density of 0.59 ± 0.27 mA cm^{-2} (recorded after 0.5 h under operation). The low FY suggested secondary electrochemical processes (such as oxidation of low valent Co species in the matrix, H_2O_2 production, etc.) contributing to the overall current density. The broader distribution in the values is due to morphological variations introduced during catalyst drop-casting.

Table 2.4. Comparison of synthesis procedures and performance metrics of literature bimetallic and trimetallic catalysts with the materials reported in this work.

Material	**Substrate**	**Fabrication**	**Onset Potential / V vs. RHE**	**Overpotential (mV vs. RHE)**	**Tafel slope / mV dec^{-1}**
CoFeZr nanosheet [174]	Ni foam	Hydrothermal (160 ºC; 15 h)	~1.46*	264 @20 mA cm^{-2}	54.2
Co/ZrP [169]	RDE	solution route	~1.61*	451 @3 mA cm^{-2}	79
Fe/Co-MOF [206]	FTO	Hydrothermal (120 ºC; 24 h)	~1.55*	410 @10 mA cm^{-2}	101
Co(Ox)P@PNC [207]	Si & Cu foil	PLD+NP deposition	1.5	349 @10 mA cm^{-2}	75.3
$Co_{0.89}Ca_{0.11}$-CP [208]	GC	solution route	~1.55*	-	58.3
$CoFeO_x$ [209]	FTO	electrodeposition	~1.51*	240 @10 mA cm^{-2}	-
Amorphous Co Phylosilicate [210]	CFP	Hydrothermal + annealing (200 ºC; 24 h)	~1.53*	367 @10 mA cm^{-2}	60
$Co_{2-x}V_xO_4$ [211]	GC	solution route	-	240 @10 mA cm^{-2}	45
$FeCo_2O_4$ [212]	GC	MW-assisted solvothermal	1.57	-	83.2
3DOM Ce-$LaCoO_3$-0.05 [213]	RDE	Multi-step solution route + calcination	~1.56*	440 @10 mA cm^{-2}	83
CoZr	FTO	Drop-cast SSP solution	1.56	372 @1 mA cm^{-2} 430 @10 mA cm^{-2}	53
FeZr	FTO	Drop-cast SSP solution	1.77	670 @1 mA cm^{-2}	362
CuZr	FTO	Drop-cast SSP solution	1.81	693 @1 mA cm^{-2}	478

* *Onset potentials estimated from the LSV curves.*

2.5. Photoelectrochemical Studies

In addition to their high electrocatalytic activity, SSPs also allow more facile photoelectrode assembly compared to complex (photo)electrochemical deposition procedures. Accordingly, the CoZr film was evaluated as a suitable co-catalyst for solar-driven water oxidation by integrating it with the well-known light absorber $BiVO_4$.[139,140] The $BiVO_4$ photoanodes were prepared according to a previous report.[141] For the PEC studies, 20 µL of a CoZr saturated solution were diluted using a 1:1 THF:EtOH mixture to different concentrations, 0.13, 0.052, 0.026, 0.013, and 0.0065 mol/L, corresponding to 1:2, 1:5, 1:10, 1:20 and 1:40 dilutions, respectively, and spin-coated over $BiVO_4$ at 2000 rpm for 10 s with an acceleration of 2000 rpm/s. The dilution and spin-coating were necessary to yield a uniform thin-layer deposition and avoid light blockage leading to poor light-absorption by the $BiVO_4$. A 1:1 Nafion:EtOH mixture (20 µL) was then spin-coated over the FTO|$BiVO_4$|CoZr photoanode and dried overnight under ambient conditions. Spin-coating yielded a fine and uniform layer of CoZr over the $BiVO_4$ without compromising its ability to absorb light (Figure 2.18).

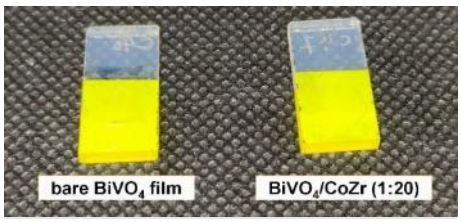

Figure 2.18. Images of (left) a bare $BiVO_4$ film and (right) a $BiVO_4$ film over which CoZr (1:20) has been spin-coated. The images reveal that the deposition of CoZr is uniform and does not occlude light transmission.

$BiVO_4$ is a photoanode with suitable onset potential for tandem water splitting applications which operates under pH-neutral conditions. Therefore, a 0.1 M potassium borate (KBi) buffer (pH 8.5) with 0.1 M K_2SO_4 as supporting electrolyte was used for the PEC measurements. FTO|$BiVO_4$ and FTO|$BiVO_4$|CoZr photoanode were used as working electrodes. The PEC performance of the different samples produced by spin-coating using different concentrations of **1** is shown in Figure 2.19. It was observed that the PEC performance increases with dilution of the solution of **1**, with photocurrent densities (at 1.23 V vs. RHE) increasing from 1.64 mA cm^{-2} for a 1:2 (0.13 mol/L) sample to 2.41 mA cm^{-2} for a 1:20 (0.013 mol/L) sample. The FTO|$BiVO_4$|CoZr (1:20) film showed the highest PEC activity with an early onset potential of 0.21 V vs. RHE, while

bare $BiVO_4$ showed a maximum photocurrent density of only 1.62 mA cm^{-2} at 1.23 V vs. RHE and a higher onset potential of 0.33 V vs. RHE.

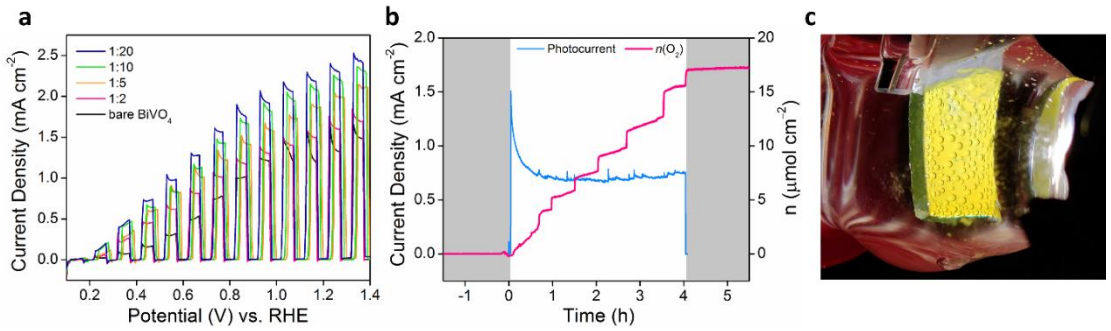

Figure 2.19. PEC responses of the FTO|$BiVO_4$|CoZr system recorded in 0.1 M potassium borate (KBi), 0.1 M K_2SO_4 (pH 8.5) buffer solution at 25˚C without stirring. **(a)** Forward CV scans recorded under chopped simulated solar light irradiation (AM 1.5G, 100 mW cm^{-2}, 1 Sun) for the system with varying dilution ratios of the CoZr precursor solution. **(b)** Light-driven O_2 evolution on a $BiVO_4$|CoZr (1:20, 0.013 mol/L) photoanode and corresponding photocurrent. The sample is maintained for 4 h at 1.23 V vs. RHE in a 0.1 M KBi, 0.1 M K_2SO_4 (pH 8.5) buffer solution, under continuous irradiation. Grey areas indicate no irradiation. **(c)** Photograph of a typical FTO|$BiVO_4$|CoZr working electrode in operation under illumination.

The PEC O_2 detection was conducted for the best performing 1:20 CoZr diluted sample (Figure 2.19b). A triplicate of the $BiVO_4$|CoZr (1:20) samples sustained a steady-state photocurrent of 0.71 ± 0.06 mA cm^{-2}, producing 17.1 ± 0.3 µmol cm^{-2} O_2 with a FY of 72 ± 6 % over the course of 4 h at 1.23 V vs. RHE, with the smaller variation in performance and improved Faradaic yield owing to the more homogeneous catalyst deposition. The stepwise increase in the detected oxygen amount could be traced back to O_2 bubble formation and release from the surface of the photoanode, which supports the influence of gas trapping on the observed Faradaic yield. The presence of active Co sites over the $BiVO_4$ surface helps to reduce the onset potential for water oxidation and facilitates the extraction of holes from the valence band of the $BiVO_4$ generated upon illumination. This improves the photocurrent density by significantly reducing the charge recombination processes.[144,146] However, spin-coating of more concentrated solutions produced thicker CoZr layers, which results in poor light absorption by the $BiVO_4$ layer and reduces the efficiency of charge transport to the electrolyte interface. Moreover, increasing the dilution to 1:40 reduces the photocurrent density owing to the decrease in the Co active sites (Figure 2.20).

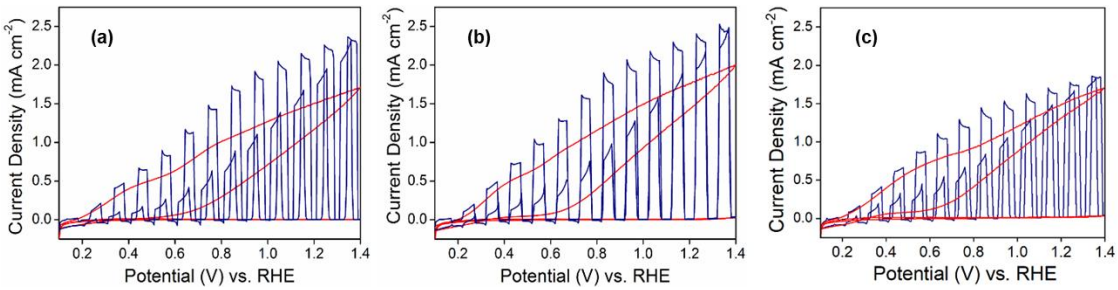

Figure 2.20. EC responses of FTO|$BiVO_4$|CoZr system recorded in 0.1 M KBi, 0.1 M K_2SO_4 (pH 8.5) buffer solution at 25 ℃ without stirring. CV scans under chopped, continuous and no artificial sunlight irradiation (AM 1.5G, 1000 W m^{-2}) of the photoanode with **(a)** 1:10 diluted CoZr, **(b)** 1:20 diluted CoZr and **(c)** 1:40 diluted CoZr spin-coated over the $BiVO_4$ layer. The wave at approximately 1 V vs. RHE in (a) is owing to the absence of stirring[141].

2.6. Conclusions and Outlook

Three novel Zr-based cages containing copper, iron, and cobalt as "dopants" have been synthesised and their structures are strongly dependent on the coordination characteristics of the dopant atoms. These precursor molecules are versatile reagents for the low-cost fabrication of catalytically active doped-zirconia films over a wide variety of substrates. EDS and XPS analysis show that these films are indeed zirconia doped with 3d-TMs. All of them show activity towards water oxidation with the FTO|CoZr system having lower Tafel slopes and onset potentials compared to FTO|CuZr and FTO|FeZr. This demonstrates the essential role of the dopant in the catalytic activity of these materials and confirms the higher intrinsic activity of cobalt compared to iron and copper ions as active sites in an inert zirconia matrix. Finally, the integration of the CoZr film with $BiVO_4$ by spin-coating led to a significant enhancement in the photoelectrocatalytic performance of this material, lowering the onset potentials by 0.1 V and increasing the photocurrent densities by 1.2 mA cm^{-2}, proving that SSPs represent a simple yet effective approach for the deposition of catalytically active films that can act on their own or as co-catalysts enhancing the activity of known materials. This method represents a step forward in the development of large-scale multijunction devices that could incorporate electrocatalysts, light absorbers and spectral converters that will allow an efficient utilization of sunlight for chemical energy storage.

Chapter 3: The Effect of Annealing on the Structure, Composition and Electrochemistry of NMC811 Coated with Al_2O_3 Using an Alkoxide Precursor

3.1. Abstract

Nickel-rich layered oxides are promising positive electrode materials for lithium-ion batteries due to their high capacity and decreased cobalt content. The application of surface coatings is a common approach to slowing or potentially stopping deleterious reactions at the electrode-electrolyte interphase of lower-Ni content layered oxides. However, their efficacy on Ni-rich $LiNi_{0.8}Mn_{0.1}Co_{0.1}O_2$ (NMC811) is less certain and knowledge on how to design effective coatings with favourable properties is sparse. In this chapter, a convenient solution-based deposition method for the synthesis of aluminium oxide coatings on NMC811 secondary particles is developed. This is followed by an investigation of the effect of annealing temperature on the structure and electrochemical lifetime of the coated materials. Using energy dispersive X-ray spectroscopy (EDS) and X-ray fluorescence spectroscopy (XRF), the amount and distribution of aluminium oxide on the cathode particles was determined. Changes in the coating phase and composition as a function of annealing temperature are tracked with solid-state nuclear magnetic resonance (SSNMR) and X-ray photoelectron spectroscopy (XPS). ^{27}Al magic-angle spinning (MAS) NMR spectroscopy at very high field (23.5 T) provides direct evidence that after annealing up to 400 °C, 4-, 5- and 6-coordinate aluminium is present, here assigned to an amorphous alumina coating, but after annealing to 600 ºC, a γ-$LiAlO_2$-like coating is observed. The critical temperature at which aluminium doping into the bulk of NMC811 occurs is determined for the first time. Surface/bulk doping starts to occur in the range 500–600 °C, with considerable bulk doping being found at 800 °C. The onset of Al diffusion coincides with the decrease in capacity retention, contradicting previous studies and giving new insight into the relationship between lifetime and lithium-ion conductivity.

3.2. Introduction

Developing cathodes with higher capacities and lower costs is a key challenge in lithium-ion battery research. The strategy most widely used in batteries designed for the electric vehicle (EV) market is to replace Co by Ni in the parent cathode material, $LiCoO_2$ (LCO). $LiNiO_2$ (LNO) achieves higher capacities at similar voltages compared to LCO, and Ni is also cheaper and associated with fewer environmental/mining concerns than Co. On the other hand, the stability of LNO is worse than that of LCO, particularly as more Li is removed during battery operation. This has led to the development of a wide range of $Li[Ni_xMn_yCo_z]O_2$ (NMC) compounds to improve upon the stability of LNO whilst maintaining high capacities.[214,215] For example, by synthesizing and testing NMC materials with varying amounts of nickel, Noh et al. found that higher nickel content led to higher capacity but at the cost of faster capacity fade and safety issues.[216] Subsequent studies of Ni-rich materials such as NMC811 ($Li[Ni_xMn_yCo_z]O_2$ where x = 0.8 and y = z = 0.1) have shown that degradation becomes particularly pronounced when cycling to upper cut-off voltages where more than 80% of Li is removed (above 4.2 V for NMC811 vs. graphite).[217,218] Accordingly, excellent lifetimes are achievable in NMC811/graphite cells operated under more moderate conditions (*e.g.*, 3.00–4.06 V and 20–30 °C).[219] Improvements in battery lifetime can also be attained by modifying the NMCs through surface coatings[102,103,220–226] or by using electrolyte additives.[227–229] Even with these strategies, it is not yet clear whether it is possible to obtain satisfactory performance at temperatures above 25 ºC or with increased voltage windows for practical applications.

One proposed major mechanism for degradation of NMC materials is related to the exergonic loss of lattice oxygen at delithiated states of charge and the formation of densified phases such as spinel (M_3O_4, with M = Ni, Mn and Co) and rock-salt (MO) on the surface of the cathode particles upon exposure to the electrolyte.[230,231] These insulating and electrochemically inactive layers grow with cycling, particularly at high voltages, leading to a decrease in capacity.[232] One potential strategy to tackle this problem is to coat the surface of NMC, forming a new interphase able to prevent electrolyte oxidation and rock-salt formation. Towards this end, a plethora of coating materials has now been investigated. Some of the most common materials used to coat NMC cathode particles include metal oxides such as Al_2O_3,[102,103,220] TiO_2,[233] ZrO_2[226] and SiO_2,[221] but also metal phosphates and fluorides like $AlPO_4$,[234] $FePO_4$,[222] AlF_3,[223] CaF_2,[235] and $LiAlF_4$.[224] These coatings can be deposited using vapor-deposition techniques such as

atomic layer deposition (ALD) [225,236,237] or solution-based methods which do not require sophisticated equipment and tend to be easier to scale-up.[101–103,220,238]

Al_2O_3 has a number of desirable properties compared to other oxides that make it stand out as a coating material. Aluminium is non-toxic and the most abundant metallic element in the Earth's crust. Al_2O_3 coatings lead to the in situ formation of $LiPO_2F_2$, a well-known electrolyte additive, by reaction with $LiPF_6$ and, in contrast to other oxide coatings such as Nb_2O_5 and TiO_2, it has been shown to inhibit the reactions involving ethylene carbonate (EC), which limits a cascade of degradation mechanisms.[236,239] Despite Al_2O_3 being one of the most extensively studied cathode coating materials, there is still a need for practical methods to synthesize Al_2O_3-coated nickel-rich particles. There is also a limited understanding of the effects of synthetic conditions, such as annealing temperature, on the structural and electrochemical properties of the coated materials. Coatings are proposed to mitigate the degradation of the outer surface of the cathode by scavenging acidic species present in the electrolyte and by limiting transition metal dissolution, while also decreasing the rate of electrolyte oxidation.[240] Surface doping may suppress the near-surface rearrangements that lead to rock-salt formation and growth without sacrificing specific capacity, as bulk doping with aluminium increases the thermal stability and capacity retention of lower nickel-content NMCs by delaying oxygen loss and retarding transformation to spinel phases.[241–244] However, these hypotheses still need further experimental verification. While some previous studies have found that the Al_2O_3 coatings improved capacity retention in NMCs with a 70% nickel content or lower, there is more divergence of opinions about the effect that Al_2O_3 coatings have on the degradation of NMC cathodes with 80% nickel or higher. For example, Han et al. found that Al_2O_3 coatings had a negative effect in the overall capacities and capacity retention in NMC811 cathodes and that annealing further deteriorated performance, which they ascribed to the diffusion of aluminium cations from the coating into the bulk of the material.[245] Others, like Neudeck et al., observed an increase in capacity retention after coating NMC811 with Al_2O_3 from solution using trimethyl aluminium (TMA) as a precursor.[102]

Several coating methods have been developed to deposit Al_2O_3 coatings onto cathode materials. Atomic layer deposition (ALD) is one of the most common methods to coat NMCs and LCO with a layer of Al_2O_3 and generally leads to improvement in capacity retention and stability.[225,239,246,247] Another possibility is to use solution-based coating

methods ('wet-chemistry'), with early work in this area showing that the deposition of Al_2O_3 coatings onto LCO has a positive effect on capacity retention. Cho et al. coated LCO with Al_2O_3 using an alkoxide precursor (aluminium ethylhexanodiisopropoxide) solution in isopropanol following a sol-gel route.[97,248] The coating process was explained in terms of hydrolysis of the precursor either by ambient moisture or -OH groups present on the surface of LCO. They found that annealing of the coated LCO led to the diffusion of the coating into the particles as well as surface doping. Others used aluminium and lithium salts to coat LCO. For example, Chen et. al. used an $Al(NO_3)_3 \cdot 9H_2O$ and $LiNO_3$ solution in ethanol to coat nano-LCO with $LiAlO_2/Al_2O_3$.[249] Similarly, Han et al. used an aqueous $Al(NO_3)_3$ solution to coat both LCO and NMC523 and studied the evolution of the coating layer as a function of annealing temperature.[250] Dogan and coworkers have, in extensive and careful studies, built on this work and examined a variety of different nitrate and alkoxide precursors dissolved in different solvents and have compared the resulting coatings with those deposited with ALD.[100,238,245,250] Other recent studies have used TMA in organic solvents as the precursor solution.[101–103] TMA forms aluminium oxide by reaction with water through cleavage of the Al-C bonds (hydrolysis) generating methane.

In this chapter, a new method for coating cathode particles with Al_2O_3 is presented. By using a solution-deposition route and aluminium isopropoxide as a precursor, the cheap and scalable deposition of Al_2O_3 onto NMC811 is achieved. This precursor is deposited over the surface of the NMC811 particles and is decomposed by annealing, leading to a layer of oxide coating. This coating method differs from previously reported ones: as discussed above many previous studies have used conventional sol-gel approaches in which aqueous solutions with aluminium nitrate or aluminium alkoxides in organic solvents are used to coat cathode particles with Al_2O_3 by slow evaporation of the solvent.[220,238,251,252] However, because NMC811 is carbon dioxide- and moisture-sensitive this can potentially lead to degradation during the deposition process if it is not done under inert-atmosphere and dry conditions.[253] In contrast, the method described in this chapter allows deposition directly from solution by using a molecular precursor that reacts with the surface of the NMC under nitrogen, and that can be decomposed later by annealing leading to the metal oxide coating.[41] In this way, the presence of water and carbon dioxide can be avoided completely. Furthermore, this method should lead to thinner and more homogeneous coatings since, unlike in other synthetic routes, we

remove the solution containing the unreacted precursors. Here aluminium isopropoxide (AIP) in toluene is used as the precursor solution. AIP is an aluminium alkoxide which forms aluminium oxide by hydrolysis (e.g., by reaction with surface OH groups) or thermolysis, but is not pyrophoric, making it safer than TMA and more suitable for large-scale production. Compared to the aluminium ethylhexanodiisopropoxide used by Cho et. al.[97] AIP should hydrolyse more readily as alkoxide ligands are more basic than carboxylates. Furthermore, our coating process is followed by annealing of the coated particles.

The Al_2O_3 coatings deposited on NMC811 using the synthetic method described above are characterised in detail, focusing especially on the effects of different annealing temperatures on the structure and composition of the material. Scanning electron microscopy (SEM), transmission electron microscopy (TEM), energy dispersive X-ray spectroscopy (EDS), X-ray photoelectron spectroscopy (XPS) and ^{27}Al nuclear magnetic resonance (NMR) spectroscopy are applied to uncover the structural, morphological, and compositional changes of the coatings that take place at different annealing temperatures. Finally, these changes are related to the electrochemical performance of the coated cathode materials by performing long-term galvanostatic cycling of half cells and the results compared to previous coating studies.

3.3. Coating Deposition

The study of the effect of Al_2O_3 coatings on the degradation of NMC811 started by developing a solution-based method for the deposition of Al_2O_3 onto the surface of NMC secondary particles, which were roughly spherical aggregates of the NMC811 primary particles. Since AIP is known to react with water, the aim here was to exploit the trace amounts of water or hydroxyl groups, present on the NMC811 particles, to deposit an aluminium-based layer. The coating deposition was carried out under an inert, dry nitrogen atmosphere. In a typical procedure, 10 g of NMC811 and 100 mg of aluminium isopropoxide (AIP) were loaded into two separate Schlenk tubes inside a glovebox. The two flasks were connected to a nitrogen line and 50 mL of dry toluene was added to each flask. The precursor solution was then added to the NMC811 suspension, so that the precursor weight amounts to 1% of the total solid weight. Other weight % of AIP (2 and 40 wt%, the latter primarily for NMR studies) were tested initially, but it was found that the electrochemical performances of the 2 wt% and especially the 40 wt% precursor samples were poor, so only the results for the 1 wt% samples are reported here. The

mixture was left to react for 48 h at 80 ºC stirring and then allowed to cool to room temperature (Figure 3.1). The solvent was removed using a syringe and the resulting solid was washed three times with dry toluene in order to remove any unreacted precursor by adding 10 mL of toluene, stirring, and removing it with a syringe. The product was then dried at 100 ºC under vacuum (10^{-2} atm, 1 h). Further control samples were synthesized following the same procedure, but without the addition of AIP.

The next step was to anneal the coated particles to ensure the full decomposition of the precursor, induce changes in the structure of the coating, and achieve surface doping by diffusing aluminium ions into the sub-surface of the particles. This annealing step was performed for 4 h under air or oxygen (Figure 3.1). Several temperatures were used for the annealing step (200, 300, 400, 500, 600, 700 and 800 ºC). Uncoated samples annealed at 400 and 800 ºC under air were also prepared to investigate the effect of annealing under air on the structure and electrochemical cycling of NMC811, allowing the separation of this contribution from the effect the coating on the degradation of the material. These samples were treated with toluene at 80 ºC for 48 h under nitrogen but without adding AIP and then annealed at either 400 or 800 ºC under air for 4 h. Finally, since NMC811 is synthesized under oxygen atmosphere,[215] a coated sample annealed at 800 ºC under oxygen was synthesized to test whether annealing under air at high temperatures may be degrading the material, leading to faster capacity fade, and if the capacity retention of coated NMC811 can be improved further by annealing under oxygen.

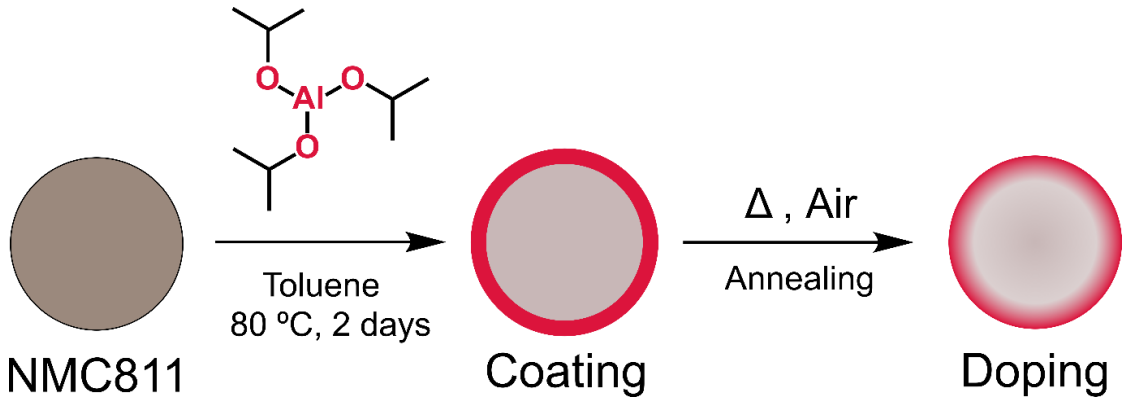

Figure 3.1. The coating process consists of two steps, the deposition of the precursors onto the surface of the NMC811 secondary particles from solution and the annealing of the resulting product.

3.4. Electron Microscopy Study of the Morphology and Composition of the Coatings

Scanning electron microscopy (SEM) and high-resolution transmission electron microscopy (HR-TEM) were used to verify the presence of a coating and to study its morphology as a function of annealing temperature. SEM images were taken in secondary electron (SE) mode with beam voltages of 2 kV for the pristine NMC and of 5 kV for the coated samples. The working distance was 6 mm for all SEM images and the samples were coated with 10 nm of Cr before imaging using a Turbo-Pumped Sputter Coater. Representative SEM images of the pristine and coated secondary particles are shown in Figure 3.2 and in appendix B (B7-B15).

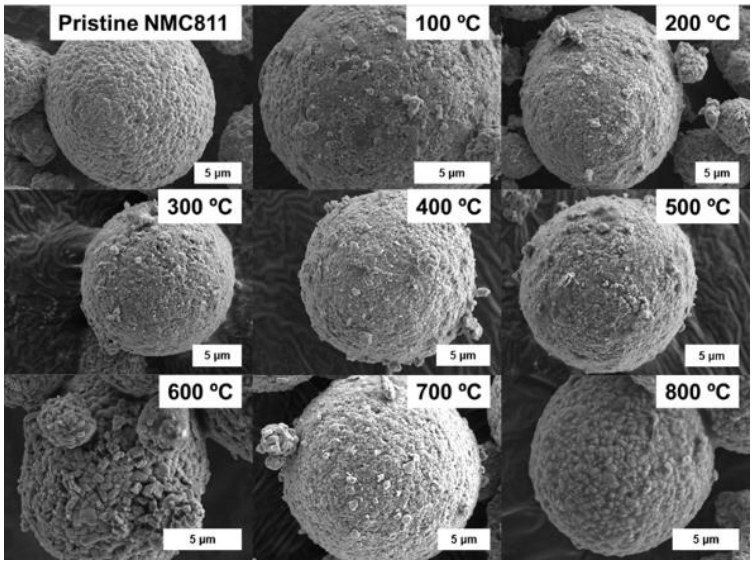

Figure 3.2. SEM images of uncoated (pristine) NMC811 particles and of NMC811 particles coated with Al_2O_3 and annealed at different temperatures, as given in the Figure. The sample labelled as "100 ºC" was only dried for 1 h under vacuum and not annealed under air.

From the SEM images it can be seen that the NMC811 primary particles are 100–200 nm in diameter and that they are agglomerated into spherical secondary particles of 5–20 µm in diameter. After coating and annealing up to 500 ºC, the primary particles are covered by a thin layer of material, with the surface becoming smoother and the primary particles being no longer as clearly visible. Small coating particles of 0.5–1 µm are also observed on top of the thin layer. At higher annealing temperatures, there is a further change in the surface morphology of the particles. The surface becomes rougher, and the primary particles are more clearly resolved.

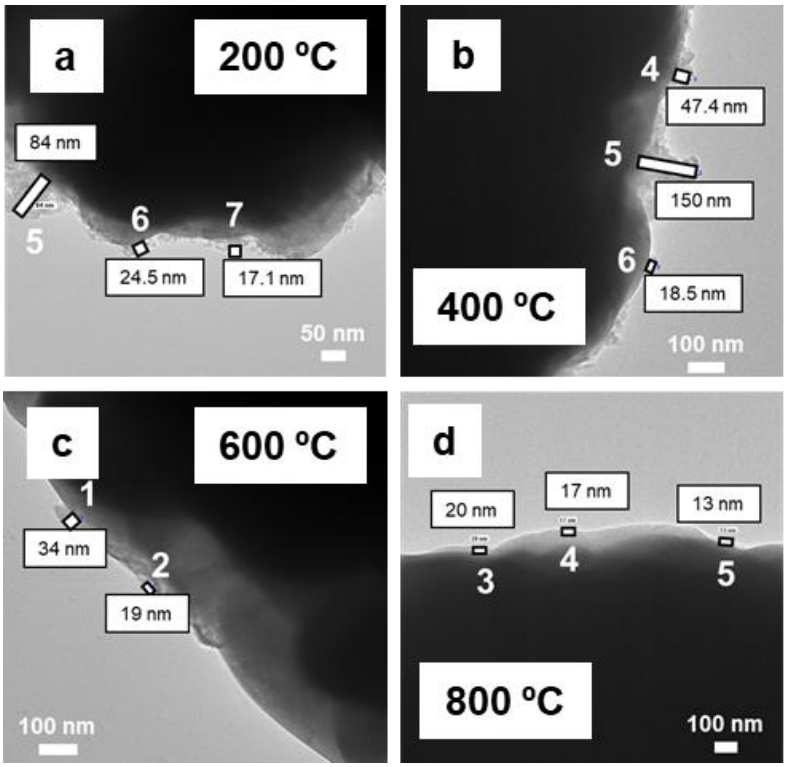

Figure 3.3. High resolution TEM images of the pristine and coated NMC811 particles annealed under air and coating thickness measurements. (a) Sample annealed at 200 °C. (b) Sample annealed at 400 °C. (c) Sample annealed at 600 °C. (d) Sample annealed at 800 °C.

To understand the morphological changes that the coating undergoes with increasing annealing temperature in more detail and to determine its thickness, HR-TEM measurements were carried out. The samples for TEM imaging were prepared by drop-casting a suspension of the NMC811 particles in ethanol onto a lacey carbon coated copper grid followed by solvent evaporation. Selected images and thickness measurements for the samples annealed at 200, 400, 600 and 800 °C are shown in Figure 3.3 and appendix B (B16-B26). The measurements were performed using an operating voltage of 200 kV and 5 µm aperture. The thickness of the coatings was estimated by measuring the coating thicknesses from TEM images taken on different regions of the sample and using both HR-TEM and STEM images. TEM shows the presence of a layer of material on top of the coated particles regardless of the annealing temperature but not in the pristine samples. It was found that the thickness varies greatly depending on the region of the sample under examination, but overall, fewer thick coating regions were found in the high-temperature annealing samples (Table 3.1). Both the SEM and HR-TEM results show that densification of the coating layer occurs at higher temperatures (>500 °C) and possible diffusion of the Al_2O_3 coating into the bulk of the NMC811.

Table 3.1. Measurements of coating thickness in different particles from TEM and STEM images. The thickness of the coating varies significantly between regions of the sample, but the maximum values observed decrease as annealing temperature is increased.

	Thickness / nm			
Measurement	**200 ºC**	**400 ºC**	**600 ºC**	**800 ºC**
1	63.2	98.5	34	34
2	116.4	47.0	19	36
3	4.3	38.3	-	20
4	9.6	47.4	-	17
5	84	150	-	13
6	24.5	18.5	-	-
7	17.1	152	-	-
8	106	112	-	-
9	24.4	130	-	-
10	67.9	-	-	-
11	45.5	-	-	-
12	52.5	-	-	-
13	30.4	-	-	-
14	16.7	-	-	-
15	18.4	-	-	-
16	36.4	-	-	-
17	19.4	-	-	-

Having studied the morphology of the coated NMC811 as a function of temperature, the changes in the composition of the coating with annealing temperature were then determined by elemental analysis using a combination of X-ray fluorescence (XRF), SEM-EDS point scans and scanning transmission electron microscopy (STEM) EDS mapping. All three techniques confirmed the presence of aluminium on the surface of the coated NMC811 and that the pristine NMC811 does not contain aluminium (Figures 3.4 and 3.5, Figures B27 and B28 and Tables B10–B14). To obtain Al : Ni ratios by SEM-EDS, between 20 and 100 EDS spectra were measured at multiple positions for each

sample (Figures B29-B38 and Tables B8 and B9). The Al : Ni ratios were calculated by averaging the values from these spectra. All SEM-EDS measurements were performed using a 15 keV electron beam and with a working distance of 15 mm. The XRF measurements were performed using an XRF spectrometer equipped with an Ag anode (X-ray energy of 50 kV) with help from Dr. Shutao Wang. The XRF Al : Ni ratios were obtained directly from a duplicate of the XRF measurement, and they show ratios between 0.012 ± 0.001 and 0.015 ± 0.002 (Table B15) for samples annealed at temperatures up to 500 ºC (Figure 3.4b). The Al : Ni ratios derived from EDS for this temperature range lie between 0.010 ± 0.002 and 0.022 ± 0.002, being generally larger compared with XRF except for the sample annealed at 200 ºC. This is not surprising considering that the measurement depth of the XRF is larger and so the relative amount of aluminium is lower.[254,255] The larger fluctuations in aluminium content between samples seen by EDS are attributed to inhomogeneities in the samples at a microscopic level. At 600 ºC, both EDS and XRF show a decrease in aluminium content with XRF measuring an Al : Ni ratio of 0.0079 ± 0.0001 at 600 ºC and EDS of 0.014 ± 0.001. The aluminium content measured by both techniques decreases further as the annealing temperature increases reaching comparable values for both techniques at 800 ºC of 0.004 ± 0.001 for XRF and 0.0052 ± 0.0009 for EDS (Tables B8-9 and B15). This strongly suggests that the Al in the coating is diffusing into the bulk of the particles beyond the depth of analysis of these techniques.

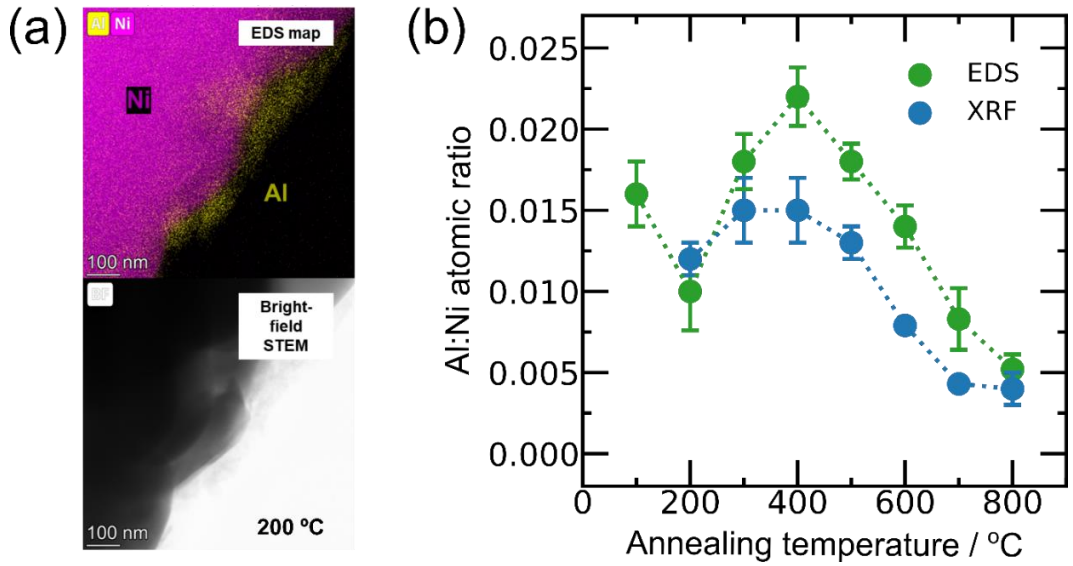

Figure 3.4. (a) EDS map and STEM image in bright field mode of the coated NMC811 annealed under air at 200 ºC. (b) Changes in aluminium to nickel atomic ratio as a function of annealing temperature as determined by EDS and XRF. The error bars are the 95% confidence intervals of measurements taken across several particles. Similar levels of aluminium content are detected up to a 500 ºC annealing temperature, but a decrease in aluminium content is seen at higher temperatures. Since both EDS and XRF measure the near-surface composition of the sample, this provides evidence for diffusion of aluminium into the bulk of the particles.

STEM-EDS maps were then obtained for samples annealed at 200, 400, 600 and 800 ºC to gain more detailed information about the elemental composition of the coating and the distribution of aluminium within the surface region of the particles (Figure 3.5 and Figures B39-B45). EDS maps were collected with an operating voltage of 200 kV and a spot size of 5 and 70 µm aperture for the bright-field (BF) imaging. Between 1 and 3 maps were collected in different regions of the sample for the as-coated and cycled samples (Figure 3.5 and Figures B39-B45, Appendix B). In order to obtain the STEM-EDS elemental quantification results, the Al : Ni ratios were calculated for each of the selected areas shown in Figures B39-B45 (Appendix B). Average values were calculated from at least two areas for each sample, and atomic errors were obtained from the fits of the EDS spectra as given by the Thermo Fischer Scientific Velox software. These values are tabulated in Tables B10-B13 and plotted in Figure 3.5. Of particular note, there is one outlier in the EDS measurement of the surface in the sample annealed at 400 °C (Figure B41, map 3, area 1). This region contained a significantly larger Al : Ni ratio (Al : Ni = 8) and is suggested to be a precipitated particle of aluminium oxide. This region was not included when calculating the average surface composition shown in Figure 3.5. Surface and bulk Al : Ni ratios were extracted from relevant areas of these maps. By measuring

the aluminium content at the surface regions (20–100 nm), it was possible to confirm that the aluminium signal seen in the SEM-EDS and XRF comes from the deposited layer, which has a much higher aluminium content compared to the bulk (Figures 3.4 and 3.5). Al : Ni ratios of 0.50 ± 0.07 and 0.40 ± 0.05 were calculated for the 200 and 400 ºC samples with a large decrease in aluminium content in the surface regions detected for the 600 and 800 ºC (0.02 ± 0.04 and 0.02 ± 0.05) samples, in agreement with the SEM-EDS and XRF results (Figure 3.5). The Al : Ni ratios on the surface are found to decrease after 400 °C, in line with the EDS study performed on the SEM as well as the XRF, XPS and NMR results. At 600 and 800 ºC, little difference in Al : Ni ratios was found between the surface and bulk regions.

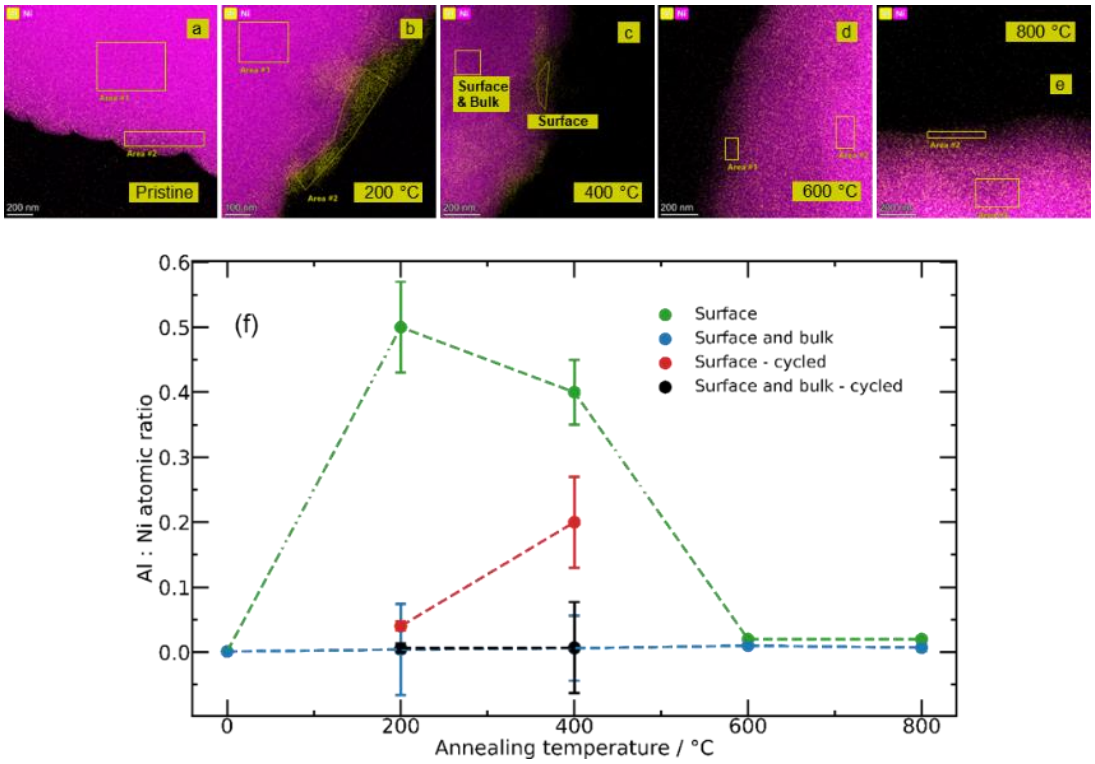

Figure 3.5. Al : Ni ratios and atomic errors obtained from TEM-EDS measurements of the as-coated and cycled samples annealed at various temperatures. (a-e) EDS maps and areas (yellow boxes) from where bulk and surface elemental information was extracted. (f) Scatter plot showing the change in Al : Ni ratio in the bulk and surface of the samples measured with TEM-EDS. The results further confirm the presence of a coating and its diffusion into the bulk with increasing annealing temperature. Furthermore, the analysis of the cycled cells shows that surface aluminium is still present after 300 cycles, although in less quantity.

The changes in the coating after long-term galvanostatic cycling (3–4.3 V, 250–300 cycles) were also studied by electron microscopy. To understand the evolution of the coating with cycling, SEM-EDS, TEM, and STEM-EDS were measured for the coated materials annealed at 200 and 400 ºC after 250 or 300 cycles in half cells, respectively. The cycled active material was recovered by opening the coin cells inside an argon-filled glovebox, washing the electrodes with dimethyl carbonate three times to remove the electrolyte, drying under vacuum, and scraping the electrode material off the current collector. SEM-EDS showed the presence of decomposed material (containing fluorine) and fragments of glass fibre separator on the surface which made it difficult to characterize the surface morphology of this material. SEM images of the samples annealed at 200 and 400 ºC after 250 and 300 electrochemical cycles show full secondary particles that retained the smooth morphology observed for the non-cycled samples (Figure 3.6 b and d, and B37-B38). However, less closely attached primary particles

compared to the pristine samples were also seen in both the SEM (B37, image 3 and B38 image 1) and in TEM (Figure B21c and B22 a and c).

SEM-EDS shows similar Al : Ni ratios after electrochemical cycling, while TEM shows lower Al : Ni ratios. Furthermore, less coated regions and thinner coatings were found using TEM after cycling, suggesting that the thicker regions of the coating can delaminate or detach after extensive cycling, or undergo chemical reaction during cycling (Figures 3.5 and 3.6, Figures B21-B22 and Table B13). There were some regions that still had a measurable surface coating and STEM-EDS elemental quantification was performed to investigate changes to the coated regions. The aluminum content on the surface was still greater than in the bulk but it was significantly decreased compared to that of the as-coated materials (i.e., before annealing) (Figure 3.5).

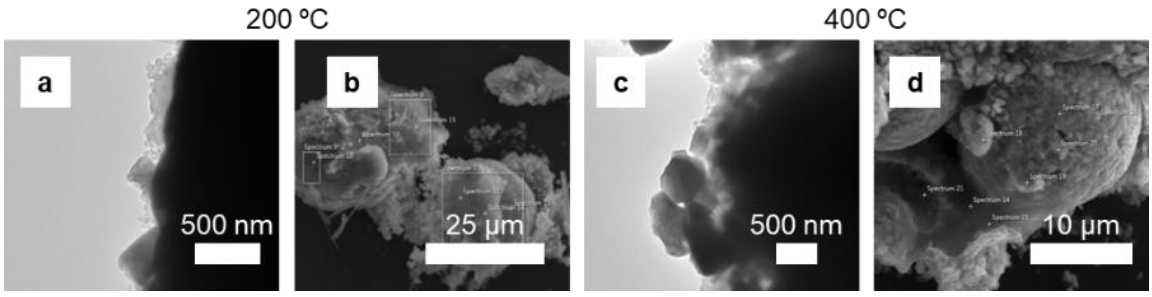

Figure 3.6. TEM (a, c) and SEM (b, d) images of the Al_2O_3 coated samples annealed at 200 and 400 °C under air after 250 and 300 cycles.

3.5. Powder XRD Characterisation of Al_2O_3 Coated NMC811 Materials

Powder X-ray diffraction (PXRD) was used next to determine whether the coating and annealing processes have an effect on the long-range structure of the material (with patterns and refinements reported in Figures 3.7 and 3.8, and Tables A2–A9). The PXRD data was collected on a Panalytical Empyrean powder X-ray diffractometer using CuK_α radiation (λ = 1.541 Å) over the 2θ range of 5-80º for 1 hour. Rietveld refinements were performed to obtain lattice parameters and site occupancies using the TOPAS program (V6).[256] NMC811 was refined in the $R\bar{3}m$ space group. The lattice parameters, cell volume and z diffraction coordinate of the oxygen atoms were refined. The remaining atomic coordinates are fixed by the symmetry conditions of the space group and were not refined. The site occupancies were calculated in order to obtain cation mixing values. This was done by fixing the total Ni occupancy to 80 % and then refine it between two Ni positions (one in the transition metal layer and one in the lithium layer, Tables A2-A9). Trials were made to carry this procedure using Co or Mn instead of Ni but no

preference for substitution of a specific transition metal by aluminium could be identified by PXRD, due to the similar scattering factors of the transition metals.

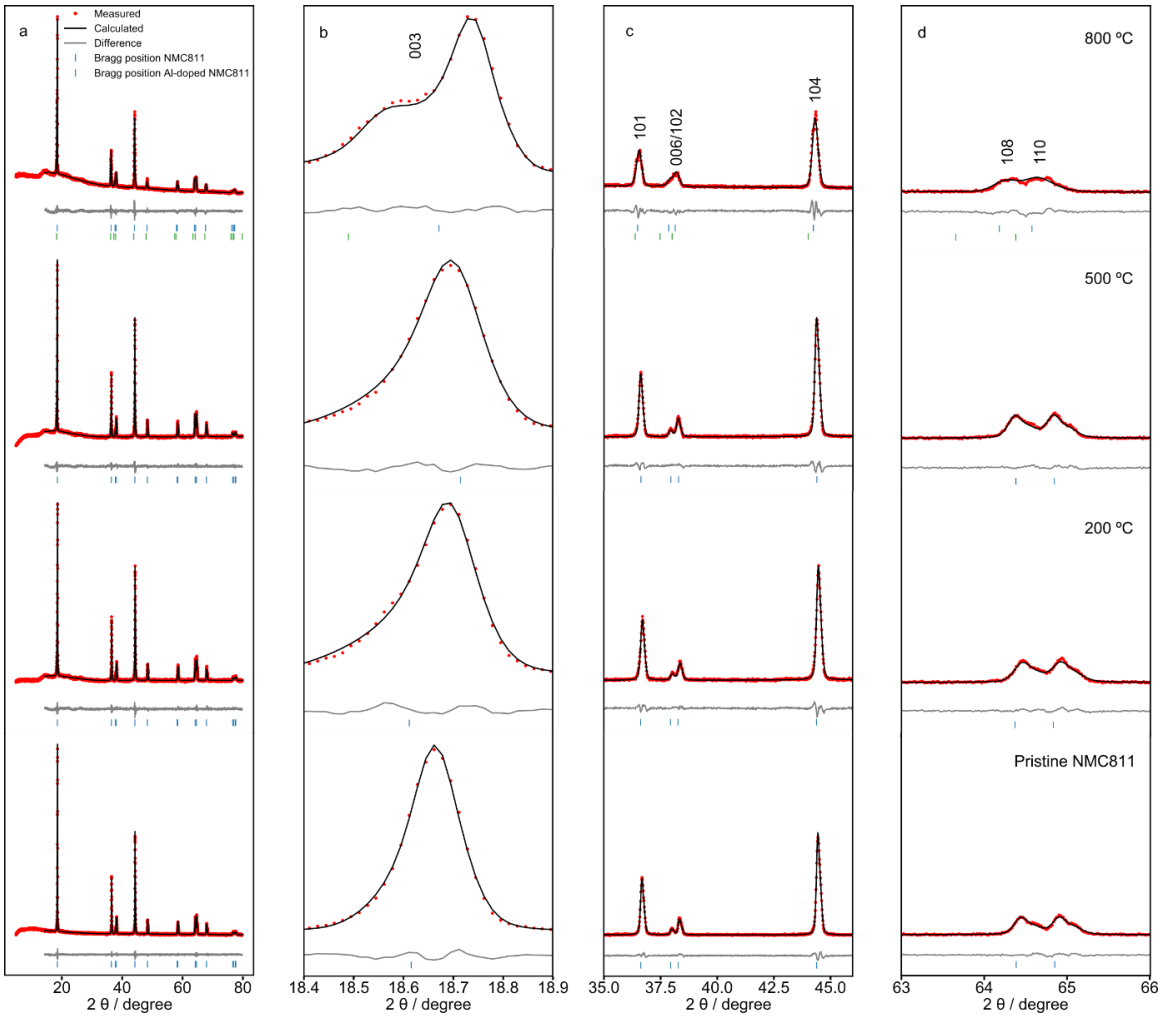

Figure 3.7. Powder X-ray diffraction (PXRD) patterns of the pristine NMC811 and the Al_2O_3 coated NMC811 materials annealed at 200, 500 and 800 °C under air. (a) View of the full PXRD pattern. (b) Expansion of the 003 reflection. (c) the 101, 006/102 and 104 reflections. (d) and the 108 and 110 reflections.

Pristine samples and coated samples annealed at 200, 500 and 800 ºC degrees (Figure 3.7) were compared with a coated samples annealed under oxygen at 800 ºC and with uncoated samples annealed under air at 400 and 800 ºC (Figure 3.8). For all these samples except for the coated NMC annealed under air at 800 ºC, Rietveld refinement shows that the reflections can be indexed to a single $R\bar{3}m$ phase with no significant differences in lattice parameters. The degree of anti-site mixing was also similar, increasing at higher annealing temperatures both for the coated and uncoated samples (Figure 3.9).

The coated sample annealed under air at 800 ºC, however, shows splitting of the 003, 101 and 104 reflections and the XRD pattern could not be fitted to a single phase (Figure 3.7). Introducing a second Al-rich phase with larger cell parameters ($a = b = 2.88$ Å and

c = 14.25 Å vs. a = b = 2.89 Å and c = 14.38 Å for the expanded phase) in which Al^{3+} ions substitute into the transition metal sites[242] gave good agreement with the measured data. Previous coating studies reported a single phase and only an increase in unit cell volume after annealing at 800 ºC for Al_2O_3 coated LCO and NMC532 in one report[250] and NMC622 and 811 in another (this study seeing additional peaks that were ascribed to stacking faults at high Al contents).[245] This behaviour may be due to the lower solubility of Al in high nickel-content materials.[245] The amount of this secondary phase was estimated to be 5 % of the total in the material, suggesting that this new phase is likely a near-surface modification and that the bulk of the NMC remains intact.

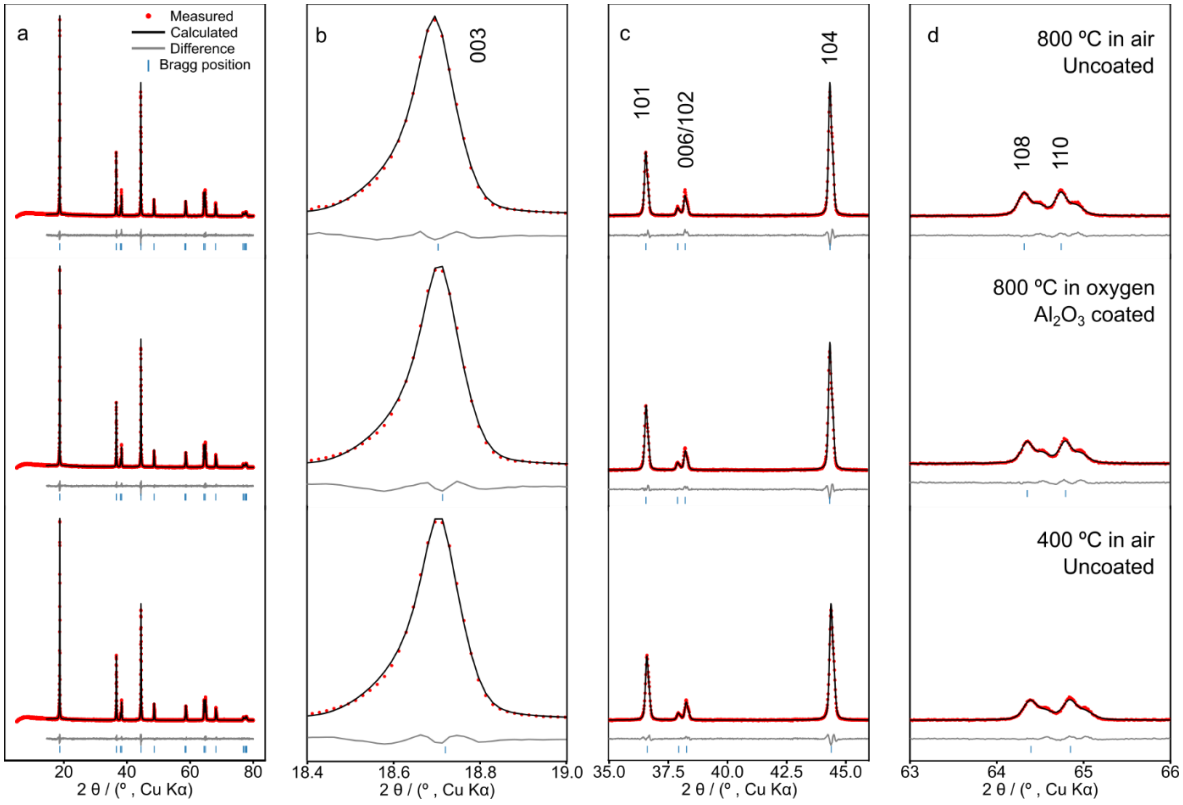

Figure 3.8. PXRD patterns of the control samples soaked in toluene and then annealed under air at 400 or 800 ºC as well as a coated sample annealed at 800 ºC under oxygen. (a) View of the full PXRD pattern. (b) Expansion of the 003 reflection. (c) Expansion of the 101, 006/102 and 104 reflections. (d) Expansion of the 108 and 110 reflections.

PXRD measurements of uncoated control samples soaked in toluene at 80 °C for 48 h and then annealed under air at 400 or 800 °C for 4 h were carried out to separate the effects of the synthetic conditions on the structure of the material from those that may result from the diffusion of the coating (Figure 3.8). No significant changes in (bulk) lattice parameters were observed for any of the control samples and the PXRD pattern of the control sample annealed at 800 °C could be described as a single NMC811 phase, supporting the assignment of the secondary Al-doped NMC811 phase (Figure 3.8). An

increase in cation mixing was seen after annealing under air at 800 ºC, with or without the coating, indicating that annealing under air at 800 ºC has, in itself, an effect on the structure of the material (Figure 3.9). The degree of mixing could be reduced by annealing under oxygen at 800 ºC, (3.2% vs. 4.5% for O_2 vs air, respectively; Tables A5, A6 and A9). Annealing at 400 ºC under air did not lead to an increase in cation mixing (1.5%, Table A7). Finally, the coated NMC811 sample annealed under O_2 at 800 °C shows no evidence of a secondary phase suggesting that the atmosphere in which the annealing is performed has a significant effect on the diffusion of the coating. This was consistent with the NMR results that show a larger amount of Al in paramagnetic environments for the coated sample annealed at 800 °C under air compared to oxygen (Figure 3.16).

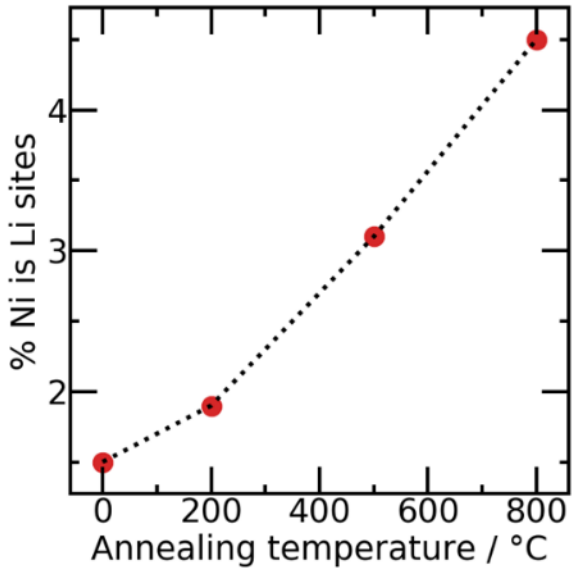

Figure 3.9. Increase in cation mixing with temperature as determined from Rietveld refinement of the powder XRD patterns of the Al_2O_3 coated NMC811 samples.

3.6. Investigating the Surface Chemistry of Coated NMC811 with XPS

In order to gain more detailed information on the chemical species present on the surface of the coated NMC811, X-ray photoelectron spectroscopy (XPS) measurements were carried out in collaboration with Dr. David S. Hall. These measurements were performed to understand the composition and chemical environments present and the temperature-induced changes in the coating in more detail. The XPS spectra were measured using an Escalab 250Xi spectrometer with an aluminium Kα X-ray source. The spot size was 500 μm for all measurements. For the high-resolution spectra, 20 eV of pass energy and 0.1 eV step size were used. A total of 60 and 20 scans were measured for the Al 2p and the C 1s spectra, respectively. The spectra were corrected with respect to the

carbon aliphatic peak for shifts in binding energies arising from the accumulation of electrostatic charge. In order to do this, the C 1s spectra were fitted to five peaks corresponding to aliphatic species (C-C, C-H), ethers and alcohols (C-OH, C-O-C), ketones (C=O), esters (O-C=O) and carbonates (CO_3^{2-}). The peaks were constrained to have equal width and their spacing was 1.5, 3.0, 4.1 eV and 4–5 eV, relative to the alkyl peak and the aliphatic peak was set to 284.8 eV.

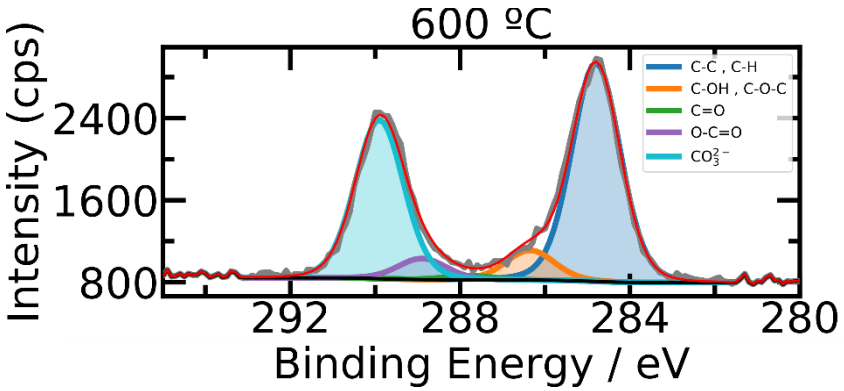

Figure 3.10. High-resolution C 1s spectrum of the sample annealed at 600 ºC. The sample was in powder form, hence no signals corresponding to C-F bonds are seen.

Samples annealed at 400 and 600 ºC were the as-coated/annealed powders. An example of C 1s high-resolution spectrum and XPS fitting used for charge correction is shown in Figure 3.10. Due to the consumption of all the available material during characterization, the samples annealed at 200 and 800 ºC were scraped from an electrode. Although this does not affect the conclusions, it explains the presence of additional peaks in the XPS spectra coming from the C-F chemical environment due to the PVDF binder. This peak was constrained to the same FWHM of the aliphatic carbon peak and allowed to fit freely in the 290–294 eV range while the other components were kept with the aforementioned constraints (Figure 3.11).

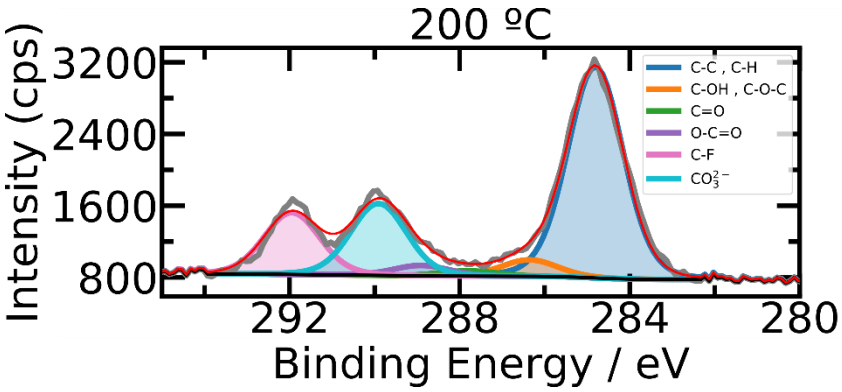

Figure 3.11. High-resolution C 1s spectrum of the sample annealed at 200 ºC. Because this sample was an electrode, a C-F peak from the PVDF binder is seen at higher binding energy.

The high-resolution XPS spectra of the aluminium 2p region which contains peaks corresponding to the transition metals (Ni, Co and Mn), lithium, and aluminium is shown in Figure 3.12. This region was hence fitted to eight components: Al 2p, Mn 3p, Li 1s, Co 3p, Co 3p satellite, Ni $3p_{3/2}$, Ni $3p_{1/2}$, Ni 3p satellite. Shirley background and Lorentzian asymmetric line-shapes were used. Al 2p, Mn 3p and Li 1s regions were each fitted to a single peak. The Ni, Co, and Mn peaks are split due to spin-orbit coupling into the $3p_{3/2}$ and $3p_{1/2}$ components. These two components appear in a 2:1 intensity ratio and separated by 2.2 eV in the case of Ni 3p.[257] Furthermore, a component corresponding to the satellite transition due to ligand-to-metal charge transfer is added at + 6 eV with respect to the $3p_{3/2}$ component in the case of nickel and +10 eV for cobalt.[257,258] It was not possible to deconvolute the Co 3p and Mn 3p peaks into the $3p_{3/2}$ and $3p_{1/2}$ components due to the low signal intensity but a peak corresponding to the Co 3p satellite transition was required. The area of the Co 3p satellite was constrained to be 10 % of that of the Co 3p main peak. The Ni 3p region was fitted to three peaks corresponding to Ni $3p_{3/2}$, Ni $3p_{1/2}$ and Ni 3p satellite. The Ni $3p_{1/2}$ peak was constrained to be half of the area of the Ni $3p_{3/2}$, with the same width and 2.2 eV above the position of the Ni $3p_{3/2}$ peak. The Ni 3p satellite was constrained to be 6 eV above the Ni $3p_{3/2}$ peak and with a FWHM of 3 to 5 eV.[257,258] (See Table 3.2 for details regarding the constraints applied in the fitting of the Al 2p region).

Small variations were detected in the binding energies of the nickel, cobalt, and manganese peaks between the samples, which are likely attributable to imperfect charge correction (Table C1). Such minor variations are typical of powders and complex nonuniform materials, where differential charging can occur.[259] That there are no clear trends or significant changes in the binding energies indicates that the oxidation states of

the transition metals on the surface remain the same after coating and annealing (Figure 3.12).

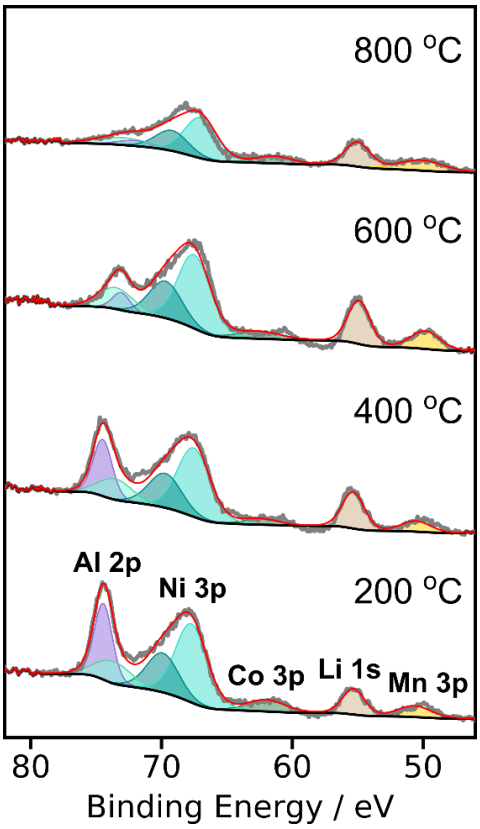

Figure 3.12. Al 2p region of the XPS spectra of Al_2O_3 coated NMC811 annealed at different temperatures, see Table C1 for the intensities and binding energies obtained by fitting these spectra. The binding energies of the Al 2p peak (purple) support the presence of aluminium oxide. Furthermore, the decrease in intensity of this peak supports the diffusion of the aluminium ions into the bulk of the particles.

The binding energy of the main Al 2p peak (74.45 eV) confirms that the material deposited onto the samples annealed at 200 and 400 ºC is an aluminium oxide.[260] A shift in the aluminium 2p peak to lower binding energies (approximately 73.09 eV) is observed at 600 ºC. This binding energy is only an approximation, because the overlap with the nickel 3p satellite, which gives rise to a broad peak centred at 73.72 eV (blue) makes it difficult to determine the exact position of the Al 2p peak in this sample. Nevertheless, this value matches well with the Al 2p binding energies that Appapillai et al.[261] measured for $LiAlO_2$, suggesting that lithiation of the coating has taken place at 600 ºC.

Table 3.2. Constraints used in fitting the aluminium 2p spectra.

Peak	BE / eV	FWHM / eV	Area constr.
Ni 3p 3/2	66.0–67.0	2.0–4.0	
Ni 3p 1/2	A + 2.2	A × 1.0	A × 0.50
Ni 3p satellite	A + 6.0	3.0–5.0	A × 0.31
Co 3p	60.0–62.0	2.0–4.0	
Co 3p satellite	D + 10.0	3.0–5.0	D × 0.1
Li 1s	53.0 – 55.0	2.0–4.0	
Mn 3p	49.0–51.0	2.0–4.0	
Al 2p	72.0–75.0	1.0–3.0	

Relative to the intensities of the peaks corresponding to Ni, Mn, and Co 2p orbitals, the Al 2p peak decreases in intensity with higher annealing temperature (Figure 3.12). In contrast, the intensity ratio of the Ni, Mn, and Co 2p peaks remains approximately constant, corresponding to the expected 8:1:1 elemental ratio. This is again consistent with the diffusion of the Al from the coating into the bulk of the particles and is mirrored by the lower aluminium contents detected at higher temperatures (600 and 800 ºC) from the survey scans (Table 3.3). As a result of the lower measurement depth of the XPS measurement (as determined by the inelastic mean free paths of the photoelectrons), the aluminium contents determined by XPS were two orders of magnitude higher than those determined by SEM-EDS and XRF and an order of magnitude higher than the TEM-derived values, with Al : Ni ratios of the order of 2.76–2.77 up to 400 ºC (Table 3.3). Above 400 ºC, the Al : Ni ratio decreases sharply to 0.87, decreasing further at 800 ºC to 0.14. This again shows that the proposed diffusion process does not occur below 400 ºC and that at 600 ºC there is significant diffusion taking place with even greater diffusion at higher temperatures (Table 3.3).

Table 3.3. XPS-derived atomic percentage values. The quantification was performed using Scofield's relative sensitivity factors.

		Annealing T			
		200 ºC	**400 ºC**	**600 ºC**	**800 ºC**
At. %	C 1s	32.2	32.3	31.9	59.7
	O 1s	46.6	58.0	59.1	16.3
	F 1s	9.7	0.77	0.94	20.6
	Mn 2p	1.5	1.4	2.6	0.63
	Co 2p	0.7	0.5	0.6	0.28
	Ni 2p	2.4	1.9	2.6	2.1
	Al 2s	6.8	5.2	2.2	0.3
	Al : Ni	2.8	2.76	0.87	0.14

Consistent with the XRF and EDS results, most of the aluminium has diffused past the measurement depth of XPS into the NMC at 800 ºC. The residual XPS signal found at 600 and 800 ºC could arise from either small amounts of coating that has not diffused into the particles or from surface Al-doped NMC phases. Lebens-Higgins et al. assigned the Al 2p signal from a $LiNi_{0.8}Al_{0.2}O_2$ (LNA) electrode with a binding energy of 72.7 eV[262] to a doped nickel oxide phase of the form $Li_{1-x}Ni_{1-y}Al_yO_2$, suggesting that the signal from our Al-doped NMC phase would be shifted to lower binding energies compared with Al 2p signal arising from a coating. This would increase the overlap with the Ni 3p peak complicating the XPS analysis of aluminium species in this case.

3.7. Solid-state NMR Characterisation

By using a combination of electron microscopy and X-ray spectroscopy it was possible to obtain accurate information on the composition and morphology of the coatings and confirm the presence of Al_2O_3 formed at low annealing temperatures. The next step involved the characterisation of the local structure and phase of the coatings using solid-state NMR (SSNMR). Furthermore, while the techniques discussed so far provided indirect evidence of diffusion of the coating into the bulk of the NMC811 particles, SSNMR is a direct probe for this process as it can distinguish between aluminium near diamagnetic or paramagnetic species (surface. vs. bulk). The SSNMR measurements were carried out in collaboration with Dr. Katharina Märker. All samples employed in

the NMR experiments were powders obtained after annealing, except for the one annealed at 800 ºC under air which was scraped from an electrode after cycling.

First, ^{7}Li NMR measurements were performed to determine if coating and annealing had any effect on the lithium local environments (Figure 3.13). The spectra are central slices of projection MATPASS spectra[263] which show only the isotropic resonance without spinning sidebands. The spectra were recorded at 4.7 T (200 MHz ^{1}H Larmor frequency) with 60 kHz MAS frequency to reduce the line broadening. Two distinct signals were identified in all the ^{7}Li NMR spectra for all annealing temperatures, a broad signal centered at 570 ppm and a narrower peak at ~ 0 ppm. Lithium in a diamagnetic environment is expected to resonate at about 0 ppm so the narrow peak is assigned to lithium salts that are known to occur upon exposure to air on the surface of the NMC811, such as Li_2CO_3 and LiOH.[253] The broad peak at 570 ppm originates from lithium environments with paramagnetic ions such as Ni^{2+} (d^8), Ni^{3+} (d^7) or Mn^{4+} (d^4) in their first coordination shell. Fermi contact interaction is known to shift the lithium signal under these circumstances by transfer of unpaired electron density from the transition metal ion to the Li 2s orbital through a bridging oxygen atom.[264] Due to the various possible combinations of paramagnetic ions in the first coordination shell of lithium, many overlapping resonances will be present that are seen experimentally as a broad peak centered at 570 ppm in agreement with previous literature.[265]

The fact that the shape and intensity of the signal arising from paramagnetic lithium environments is very similar between different samples suggests that there are no large changes in the bulk structure of the material induced by the coating and annealing process, in agreement with the PXRD experiments in which only small changes were seen between samples in terms of lattice parameters or anti-site mixing (Figure 3.7). However, a subtle broadening of this feature is observed as the annealing temperature is increased (Figure 3.13) which can be attributed to the formation of additional lithium local environments due to cation mixing which was seen to occur at higher annealing temperatures in the previous PXRD experiments. Finally, all the samples showed signals corresponding to surface lithium impurities. Although the relaxation delays used in these experiments were too short to quantify them (30 ms), they are also observed in the XPS measurements (Figures 3.10 and 3.11). This is expected for cathode materials of this type that were annealed under air.

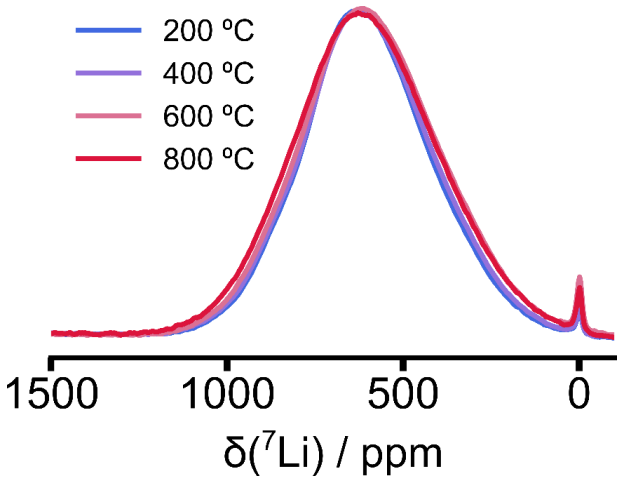

Figure 3.13. ^{7}Li SSNMR spectra of Al_2O_3 coated NMC811 annealed at various temperatures, as indicated in the Figure. The spectra were recorded at 4.7 T (200 MHz ^{1}H Larmor frequency) with 60 kHz MAS frequency and show the central slices of projection MATPASS spectra[263] in which the isotropic resonance without spinning sidebands is seen.

^{27}Al SSNMR measurements were next performed to examine the local structures of the coatings in more detail. While ^{27}Al NMR is a useful technique to characterize local structure, the interpretation of the results can be challenging due to the fact that ^{27}Al (I = $^{5}/_{2}$) is a quadrupolar nucleus and broad signals are often observed. This, coupled to the small amount of aluminium present in the alumina coated NMC811 particles, leads to difficulties in extracting accurate structural information. Furthermore, analogously to ^{7}Li chemical shifts, the ^{27}Al peak positions are affected by the presence of transition metal ions such as Ni^{2+}, Ni^{3+} and Mn^{4+} in the first coordination shell which can cause shifts in the aluminium signals via the Fermi contact interaction.[245] One way of overcoming these problems is to measure the samples at different magnetic fields. At low fields the effects of the paramagnetic ions is minimized which reduces the broadening of the signal, allowing the examination of ^{27}Al resonances that are shifted by paramagnetic ions through Fermi contact interactions. On the other hand, at low magnetic fields the quadrupolar broadening may dominate the line shape, which will cause signal broadening and distortions, complicating the phase assignment. At high magnetic fields the second-order quadrupolar interactions are reduced and the Boltzmann polarization increases, leading to sharper lines and better signal to noise ratio, respectively. Consequently, measurements at 200 MHz (4.7 T), 700 MHz (16.4 T) and 1GHz (23.5 T) were performed for the samples annealed at 200, 400, 600 and 800 °C to characterise temperature-dependent coating diffusion processes via the chemical shifts induced by the paramagnetic TM ions at low

magnetic fields and the structure of the coating layer present on the outer surface (diamagnetic environment) at high magnetic fields.

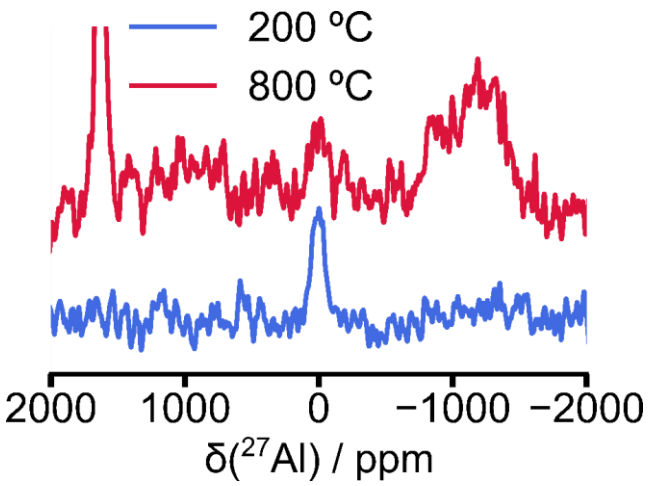

Figure 3.14. ^{27}Al SSNMR spectra of Al_2O_3 coated NMC811 annealed at various temperatures, as indicated in the Figure. These measurements were performed at 4.7 T (200 MHz ^{1}H Larmor frequency) with a 1.3 mm magic-angle spinning (MAS) NMR probe and 60 kHz MAS frequency, using a Hahn echo sequence with a recycle delay of 25 ms, a total echo length of two rotor periods and experimental times of about 20 hours.

Low-field experiments (4.7 T, 200 MHz, ^{1}H Larmor frequency) were performed on the Al_2O_3 coated NMC811 samples annealed at 200 and 800 °C under air (Figure 3.14) using a 1.3 mm magic-angle spinning (MAS) NMR probe and 60 kHz MAS frequency, a Hahn echo sequence with a recycle delay of 25 ms, a total echo length of two rotor periods and experimental times of about 20 hours. With these measurement conditions, the signal corresponding to Al ions near paramagnetic transition metals can be clearly distinguished in the red spectrum (top) at -1200 ppm (Figure 3.14) with a linewidth of more than 600 ppm. This ^{27}Al resonance compares well with the literature ^{27}Al spectra of NCA ($LiNi_{1-y-z}Co_yAl_zO_2$), confirming that the aluminium observed here is located in the TM layer largely nearby $Ni^{2+/3+}$ ions in the 1st cation coordination shell of Al^{3+}, giving rise to negative shifts.[266,267] Furthermore, a signal is seen at 1600 ppm due to Al metal from the current collector. The peak in the blue spectrum (bottom) originates from diamagnetic aluminium environments from alumina coating on the coated NMC811 sample annealed at 200 °C. The absence of the signal from Al in paramagnetic environments in this sample indicates that coating diffusion does not take place at such a low temperature.

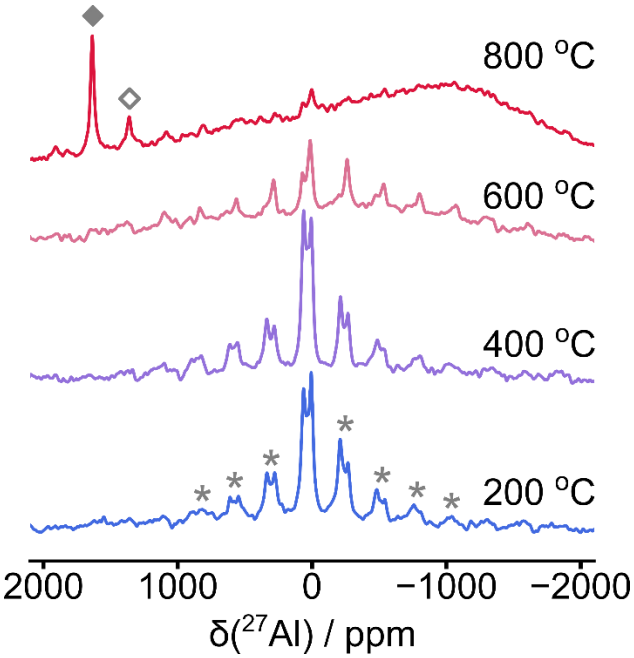

Figure 3.15. ^{27}Al SSNMR spectra of Al_2O_3 coated NMC811 annealed at various temperatures in air, recorded at a magnetic field strength of 16.5 T and a MAS frequency of 50 kHz. The spectra were scaled by the sample mass and the number of scans acquired. Spinning sidebands are marked with asterisks in the 200 ºC spectrum. All samples except 800 ºC were as-coated/annealed powders. The 800 ºC sample was scraped from an electrode, the small residues of aluminium current collector in the sample leading to an aluminium metal signal at 1636 ppm (the isotropic resonance and spinning sideband being marked with filled and empty diamonds, respectively)[268].

^{27}Al NMR spectra of Al_2O_3 coated NMC811 samples measured on a 16.44 T (700 MHz ^{1}H Larmor frequency) spectrometer are shown in Figure 3.15. These measurements were carried out using a 1.3 mm magic-angle spinning (MAS) probe at 50 kHz MAS frequency, a Hahn-echo pulse sequence with a 100 ms recycle delay and experimental times of between 14 and 17 hours. No difference in signal intensity in the diamagnetic region is seen on going from an annealing temperature of 200 to 400 ºC but changes in relative intensity at 600 ºC are seen and very little signal from the diamagnetic species remains by 800 ºC, again confirming that the diffusion process starts at temperatures higher than 400 ºC. Furthermore, a broad feature at -1200 ppm caused by aluminium near transition metal atoms appears at 600 ºC and grows in intensity at 800 ºC mirroring the results at 200 MHz and suggesting that the diffusion of Al starts at 600 ºC (in agreement with the EDS, XRF and XPS results). Dogan and co-workers have also observed a ^{27}Al NMR signal from aluminium nuclei nearby paramagnetic ions in Al_2O_3-coated NMC811 annealed at 800 ºC,[245] consistent with Al^{3+} incorporation into the bulk. In this earlier work, the aluminium oxide coating was deposited by evaporation of an aqueous $Al(NO_3)_3$

solution at 80 ºC.[245] In contrast to the present work, they observed an even broader signal at low ppm with discrete resonances at less negative ppm values (between 0 and -1000 ppm), the peaks being assigned to local environments containing more Co^{3+} ions in their local coordination shells.[245] The presence of these environments was ascribed to Co segregation at the surface of the NMC811 particles in the pristine material. However, no evidence for Co^{3+} segregation was seen in the present work.

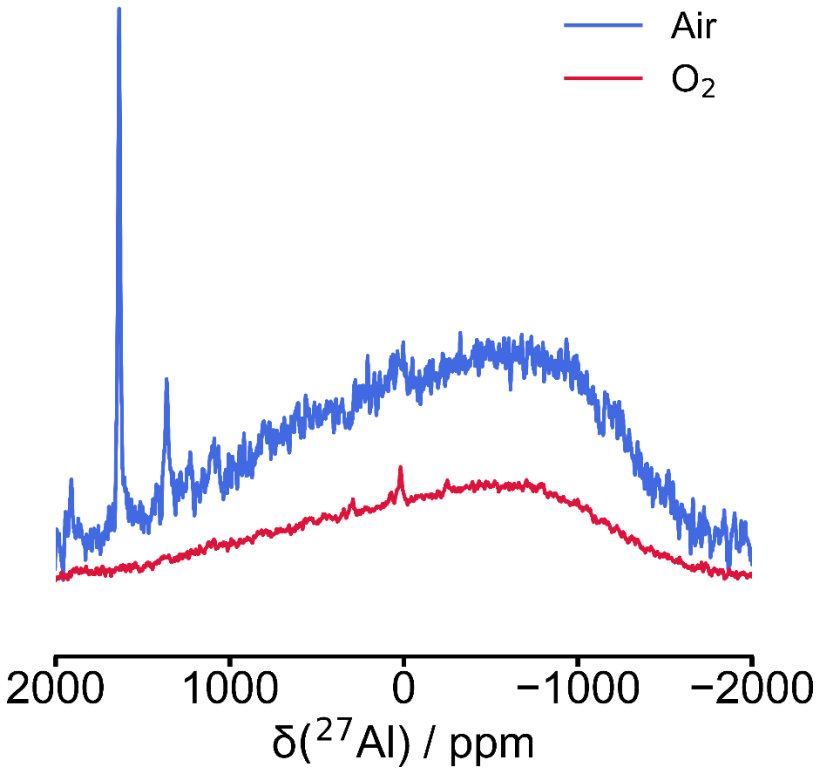

Figure 3.16. ^{27}Al solid-state NMR spectra of Al_2O_3 coated NMC811 annealed at 800 ºC under oxygen or air, as indicated in the Figure (The sample annealed under air is the same one as in Figure 3.14 and 3.15). The signals close to -1200 ppm correspond to Al ions near transition metal ions in the NMC and the signal observed at 1600 ppm for the sample annealed under air (top, blue trace) is assigned to Al metal from the current collector. The spectra were acquired at 50 kHz MAS frequency, using a Hahn echo sequence with a recycle delay of 25 ms and a total echo length of two rotor periods. The spectra were scaled by the number of scans and sample mass.

The ^{27}Al SSNMR spectrum of the sample annealed in oxygen at 800 °C was very similar to that of the sample annealed under air, confirming migration of most of the Al into the bulk (Figure 3.16). The intensity of the signal arising from Al^{3+} in paramagnetic environments was greater for the sample annealed under air than under oxygen which suggests that the oxygen atmosphere hinders the diffusion process to some extent. This is supported by PXRD that did not show any secondary phase when annealing under oxygen

at 800 ºC (Figure 3.8). Furthermore, it is clear from the PXRD results that annealing in less oxidising atmosphere (air) leads to more cation mixing than annealing under oxygen. This effect has been seen by other researchers and is thought to be mediated by the increase in oxygen vacancies when annealing under air.[269,270]

High-field NMR measurements were then performed on a 23.5 T spectrometer (1 GHz, ^{1}H Larmor frequency) with a 1.9 mm MAS probe. All the samples were as-coated annealed powders. Experiments were performed at 40 kHz MAS frequency for the samples annealed at 200 and 600 ºC and at 38 kHz MAS frequency for the sample annealed at 400 ºC. Again, a Hahn-echo sequence was used with a recycle delay of 100 ms and a total echo length of two rotor periods with experimental times of 21 - 23 hours. In order to deconvolute the spectra and quantify the amount of $^{[4]}$Al, $^{[5]}$Al, and $^{[6]}$Al aluminium present in the samples, the NMR spectra were fitted using the Czjzek model[271] for each peak. This model accounts for the distribution of quadrupolar interactions present in amorphous alumina due to its disordered structure, it describes the distribution of local environments and thus quadrupolar interactions leading to characteristic NMR signals with tails towards lower ppm values.[271] The central (isotropic) resonance of ^{27}Al SSNMR spectra and fittings are shown in Figure 3.17 and the fitting parameters and results are summarized in Table C6 in appendix C and in Figure 3.18. In these high field measurements, the various coordination environments of the Al_2O_3 coating are well resolved, making it possible to determine the phase and crystallinity of the coating. Three peaks are identified in this region which are assigned to the three possible coordination environments for the aluminium atoms in Al_2O_3 (4- , 5- and 6-coordinate sites (denoted $^{[4]}$Al, $^{[5]}$Al and $^{[6]}$Al, respectively)) that depend on the number of oxygen atoms coordinating to the aluminium. These environments give rise to distinct resonances with isotropic chemical shifts of approximately $^{[4]}$Al = 60 ppm , $^{[5]}$Al = 30 ppm and $^{[6]}$Al = 0 ppm[272] allowing the relative concentration of each site to be determined.

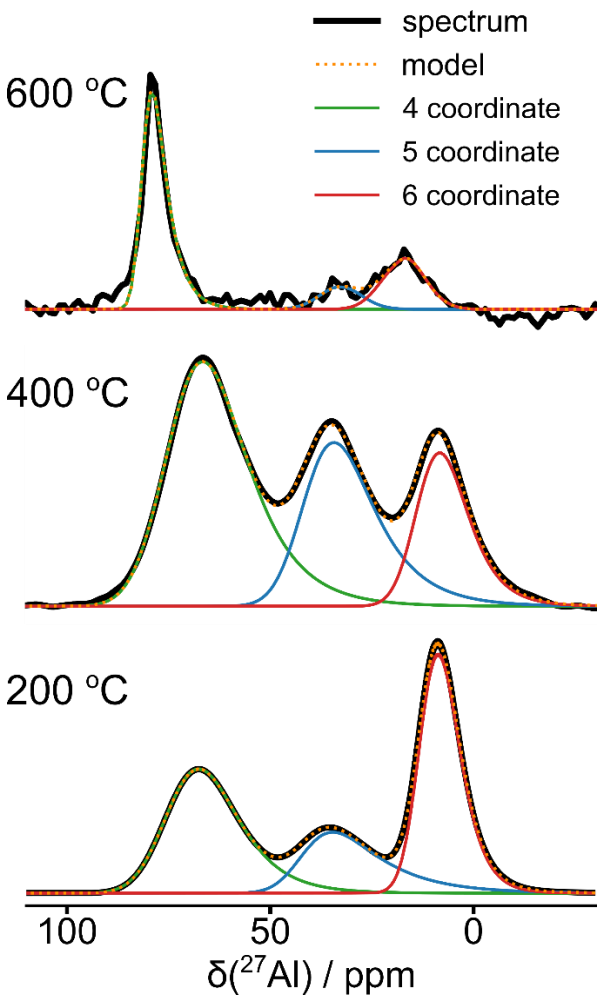

Figure 3.17. Central resonance of the ^{27}Al solid-state NMR spectra (black) of Al_2O_3-coated NMC811 annealed at various temperatures, as indicated in the Figure, along with fits applying the Czjzek model (orange dotted line).[271] The three aluminium environments are plotted under the curve and correspond to 4-(green) , 5-(blue) and 6-(red) coordinated aluminium. The spectra were acquired at 23.5 T and at a MAS frequency of 40 kHz for the samples annealed at 200 and 600 ºC and of 38 kHz for the sample annealed at 400 ºC.

There is a significant amount of aluminium in a five-coordinate environment in the 200 and 400 °C samples, which strongly suggests that the coating is amorphous, since no crystalline phase of aluminium oxide contains this local environment.[273] The percentages and absolute integrated intensities of the observed signals assigned to the $^{[4]}$Al, $^{[5]}$Al and $^{[6]}$Al sites are derived directly from the fit and shown in Figure 3.18. Typical amorphous alumina materials contain peaks at approx. 0 ppm for $^{[6]}$Al, 30 ppm for $^{[5]}$Al, and 60 ppm for $^{[4]}$Al.[272,274] Furthermore, amorphous alumina generally react first to form a γ-Al_2O_3-like phase, which contains both $^{[6]}$Al and $^{[4]}$Al, and much higher temperatures are required to form crystalline phases such as α-Al_2O_3, which are formed of octahedrally coordinated aluminium sites only. An increase in $^{[4]}$Al and $^{[5]}$Al and a

decrease in the $^{[6]}$Al signals is observed going from 200 to 400 ºC. A previous report on temperature-dependent structural evolution of amorphous alumina grown by a chemical vapor deposition method (CVD) also using AIP as a precursor shows a similar evolution of the aluminium environments with increasing deposition temperatures.[273] The signal intensity in the 200 and 400 ºC spectra remain comparable, while at 600 ºC a sharp decrease is seen, suggesting that a significant amount of aluminium diffusion has occurred at this temperature (Figure 3.18).

As the annealing temperature is increased, an increase in crystallinity of the aluminium oxide is normally expected, generally leading to γ-Al_2O_3, a process which should be accompanied by an increase in intensity of the $^{[6]}$Al signal.[273] Instead, however, an increase in the relative intensity of the $^{[4]}$Al signal is seen in our study, which is coupled to a marked decrease in $^{[6]}$Al signal and a slight increase in $^{[5]}$Al at 400 ºC. At 600 ºC, the relative intensity of the $^{[4]}$Al peak increases even further while the $^{[5]}$Al and $^{[6]}$Al environments remain low, with $^{[5]}$Al decreasing and $^{[6]}$Al increasing in relative intensity with respect to the 400 ºC spectrum. The $^{[4]}$Al and $^{[6]}$Al peaks shift from 75 to 82 ppm and 13 to 19 ppm, respectively (Table C6 in appendix C), supporting the formation of a lithiated alumina that contains a large proportion of $^{[4]}$Al. The low-pressure phase of $LiAlO_2$, γ-$LiAlO_2$, contains tetrahedrally coordinated Al sites and gives rise to shifts between 82 and 80 ppm.[275,276] The monoclinic phase β-$LiAlO_2$ also contains $^{[4]}$Al and gives rise to signals at 83 ppm,[275] while the high pressure phases α- and δ-$LiAlO_2$ contain $^{[6]}$Al sites with isotropic shifts of 15-17 ppm.[276] Our results are, therefore, consistent with a disordered/nanoparticulate γ-$LiAlO_2$ phase, or an amorphous phase with local structure similar to that found in γ-$LiAlO_2$ and a small amount of an α-alumina-like phases.[275,276] This formation of lithiated alumina phases after annealing Al_2O_3 coated NMCs to higher temperatures has also been observed by others[245,101] and could potentially lead to better lithium conductivity through the coating. In an earlier study,[245] small amounts of $^{[4]}$Al, $^{[5]}$Al and $^{[6]}$Al were detected after heating NMC811 coated with Al_2O_3 using an aqueous $Al(NO_3)_3$ solution at 800 ºC where the $^{[4]}$Al peak was observed at 69 ppm and thus cannot be assigned to crystalline γ-$LiAlO_2$ ($^{[4]}$Al peak at 80–82 ppm).[275] On the other hand, this shift is higher in ppm than expected for $^{[4]}$Al in Al_2O_3,[272,274] and in the previous work the authors assigned the peak to γ-$LiAlO_2$ at grain boundaries.[245] The residual diamagnetic species likely arise from the higher wt% Al contents of their films and the coating method, which likely leads to a less uniform deposition.

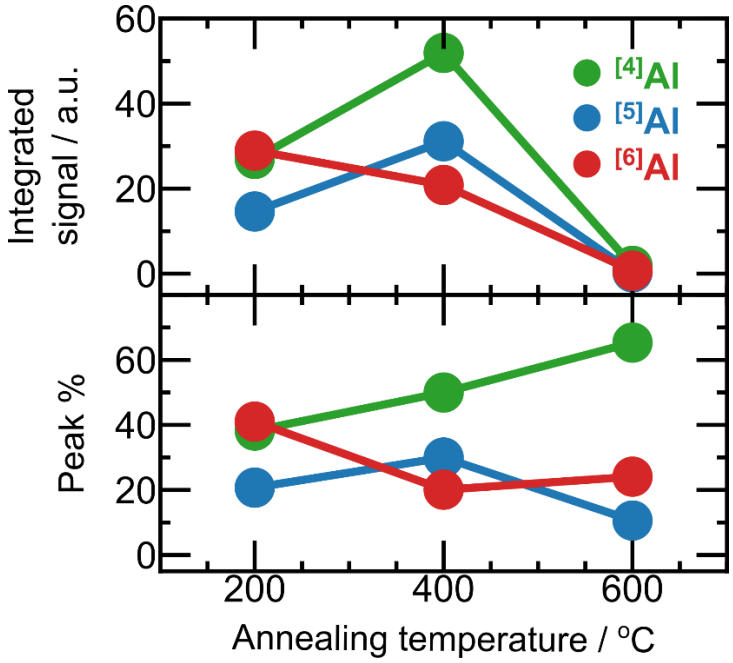

Figure 3.18. Evolution of the three aluminium coordination environments in the alumina coated NMC811 particles as a function of annealing temperature as obtained from the simulation of the ^{27}Al SSNMR spectra shown in Figure 3.17. The signal integration is shown in the top panel, indicating the evolution of the total quantity of $^{[4]}$Al, $^{[5]}$Al, and $^{[6]}$Al sites in the samples, and the relative distribution of the three alumina sites is shown in the bottom panel.

The formation of $LiAlO_2$ could be explained in part by the reaction of the Al_2O_3 coating with surface impurities such as Li_2CO_3 and LiOH, but it is unlikely that these impurities would provide enough lithium for the conversion of Al_2O_3 into $LiAlO_2$ on their own. On the other hand, previous reports suggest that Al_2O_3 coating under a variety of conditions extracts bulk Li^+ from NMCs to form $LiAlO_2$ after an annealing step.[100,250] The evidence presented in our study of diffusion of the coating into the bulk of the NMC suggests that diffusion of Li^+ from the bulk into the coating also occurs. If this lithiation of the coating proceeds by delithiation of the NMC, there are at least two possible reaction pathways: The NMC could be oxidized (Eq.1) or densified at this high annealing temperature (Eq. 2). While the lithium removal from the NMC bulk (Eq.1), might explain any lower capacity of a sample on the first charge, it should not result in a decrease in capacity on discharging in a half-cell. Furthermore, the XPS provides no clear evidence for any change of oxidation state of the transition metal ions. Thus, the reaction likely occurs via Eq. 2, but reactions with surface lithium carbonates may also occur in this temperature regime, providing another source of Li^+. Annealing in O_2 may favour reaction 1, perhaps explaining why no secondary phase is seen on annealing at 800 ºC in O_2.

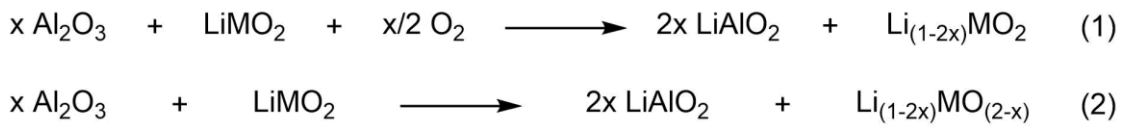

Previous SSNMR studied carried out by Dogan et. al. led to different conclusions regarding the evolution of Al_2O_3 coatings on Ni-rich NMCs deposited using aqueous wet-chemistry. In contrast to this work, where a large fraction of aluminium ions is in $^{[4]}$Al and $^{[5]}$Al sites, indicating the amorphous nature of the coatings, their Al_2O_3 coatings of NMC532, 622 and 811 annealed at 400 ºC showed a broad peak between 0 and approximately 25 ppm which was assigned to $^{[6]}$Al in an Al_2O_3 phase or α-$LiAlO_2$.[245] This suggests that aqueous processing and the use of $Al(NO_3)_3$ as the precursor leads to very different coating structures. The deposited coatings likely contain $^{[6]}$Al ions coordinated to hydroxyl groups and water molecules before drying and evolves differently on annealing. Perhaps more surprisingly, the same researchers observed only $^{[6]}$Al environments in coatings prepared when using 2 wt% AIP dissolved in either xylene or methanol as solvents and annealed at 400 ºC,[100] albeit on NMC532, suggesting that the removal of excess AIP (as in our method) may also be important in controlling the evolution of the Al^{3+} environments within the coatings.

3.8. Electrochemical Testing

After characterising the effect of temperature on the morphology, structure, and composition of the coated NMC811, the materials were tested as battery cathodes to understand how the coating phase, crystallinity (amorphous vs. γ-$LiAlO_2$) and surface Al doping affects electrochemical cycling. For this, galvanostatic cycling was performed for the coated and uncoated materials using a half-cell configuration (Figures 3.19–3.21, Table 3.4, and Figure D2). Cells were cycled between 3.0 and 4.3 V at C/2 for 250 cycles. The upper cut-off voltage of 4.3 V was chosen since cycling above 4.2 V results in more aggressive battery degradation.[217] Two slow cycles at C/20 were included every 50 cycles to assess if the observed capacity loss was intrinsic to the material or caused by slow kinetics. Electrochemical testing of the 700 ºC sample was inconclusive due to the much faster degradation observed for this sample, possibly in part due to the lower amount of active material available (approximately 50% less) meaning that it was difficult to produce good films for the electrochemistry and the results are therefore not reported here. A selection of representative specific capacity vs. cycling data is shown in Figure 3.19 (See Figure D2 and Table 3.4 for the full data). In this work, 1 C refers to the current needed to charge or discharge the cell in 1 h with an upper cut-off voltage of 4.3 V (corresponds to a cathode capacity of ~200 mA h / g). After electrochemical testing, the cells were stored in the discharged state for post-mortem analysis.

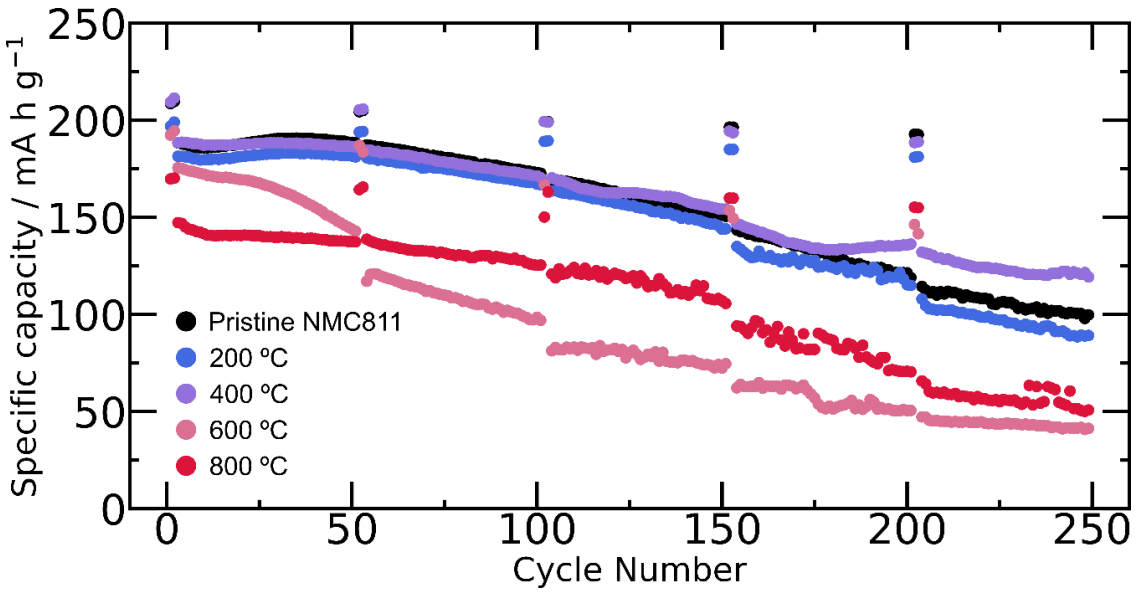

Figure 3.19. Selected long-term cycling data. After two formation cycles at C/20, the cells were cycled at C/2 between 3.0 and 4.3 V, with two slow cycles at C/20 every 50 cycles. Similar discharge capacities and capacity fade are observed for the pristine NMC811 and the coated samples up to 400 ºC, while lower capacities are observed at higher annealing temperatures.

The pristine NMC and the samples annealed at 200 and 400 ºC show similar initial discharge capacities ranging from 188.5 to 181.4 mA h g^{-1} at C/2. The sample annealed at 600 ºC has a slightly lower initial capacity of 175.5 mA h g^{-1} while the sample annealed at 800 ºC shows a significantly lower initial capacity of 147.3 mA h g^{-1}. The rate of capacity fade also changes as a function of annealing temperature. At slow rates (C/20), the capacity fade is similar for the pristine NMC811 and for the coated electrodes annealed at 200 and 400 ºC, while at faster rates (C/2), the coated sample annealed at 400 °C shows slightly better capacity retention compared to the pristine sample which loses 47 % of its specific discharge capacity after 250 cycles, samples annealed at 200 and 400 ºC losing 50% and 37% of their capacity, respectively. The samples annealed at higher temperatures show noticeably lower capacity retentions, the samples annealed at 600 and 800 ºC losing 77 and 66 % of their C/2 specific discharge capacity, respectively. Furthermore, the fade rate seems to be accelerated substantially after 25 cycles in the samples annealed at 600 ºC while for the samples annealed at 800 ºC there is a more gradual decay. The capacity of the 800 ºC sample fades at a similar rate to the pristine sample up to cycle 150 at which point it starts degrading faster than the pristine sample.

The rapid degradation even at slow rates for the 600 ºC sample is tentatively ascribed to the formation of a more crystalline γ-$LiAlO_2$-like coating phase, as seen in the SSNMR spectra. The crystalline γ-$LiAlO_2$ phase is a poor Li^+ conductor;[276] and given the coating

thicknesses of 19–34 nm observed by TEM it is possible that transport through the poorly conducting phase is impacting the capacity. Furthermore, the 600 ºC particle surfaces are rougher and the primary particles appear more distinct in the SEM images (Figure 3.2), and this morphology change may be associated with the γ-$LiAlO_2$ crystallization process. One hypothesis, that requires further experiments to confirm is that the morphological changes which may increase surface area could promote electrolyte degradation reactions and possibly more mechanical degradation. The fact that capacity at both high and low rates is only slightly worse than the uncoated electrode in the first 20 cycles further supports this idea. What is clear is that the γ-$LiAlO_2$-like coating formed here does not prevent significant growth in the Ohmic resistance during cycling.

When the aluminium from $LiAlO_2$ is incorporated into the transition metal layers of the NMC at 800 ºC, a recovery in the capacity retention is observed at low cycling rates. Both pristine NMC811 and the sample annealed at 800 ºC in air retain 91-92 % of their initial C/20 capacity after 203 cycles. The drop in the first and second capacity retention seen in the coated sample annealed at 800 ºC can be ascribed to Al substitution as the aluminium-doped NMC phase will have lower capacity than the pristine NMC because aluminium is electrochemically inactive. This is consistent with essentially all the literature on alumina-coated NMC samples heated to 800 ºC.[242,245] However, the Al substitution into the bulk and the formation of a second phase (as seen by XRD) again does not prevent the gradual increase in Ohmic resistance and reduced capacity seen at higher rates with cycle number, also consistent with prior work.[245] This suggests that Al^{3+} substitution into the bulk does little to reduce the extent of rock-salt formation in these high-nickel materials, which is one source of NMC degradation.[231]

Given the very different electrochemical performance of the samples annealed at 400, 600 and 800 ºC, samples annealed using smaller temperature steps of 100 ºC were studied and their voltage profiles and dQ/dV plots are plotted in Figure 3.20. Since there are only small differences in the dQ/dV profiles of the pristine sample and the samples annealed between 100 and 300 ºC, only the samples annealed at 400 to 800 ºC are compared in this Figure 3.20. The decrease in specific capacities is negligible in cycle 2 for the 200 and 400 ºC samples and small for samples annealed from 500 up to 600 ºC, but a much larger decrease in specific capacity is seen for the sample annealed at 800 ºC. By cycle 203, the poor performance of the 600 ºC sample is clearly visible in the voltage profile, along with a partial recovery in capacity for the 800 ºC sample.

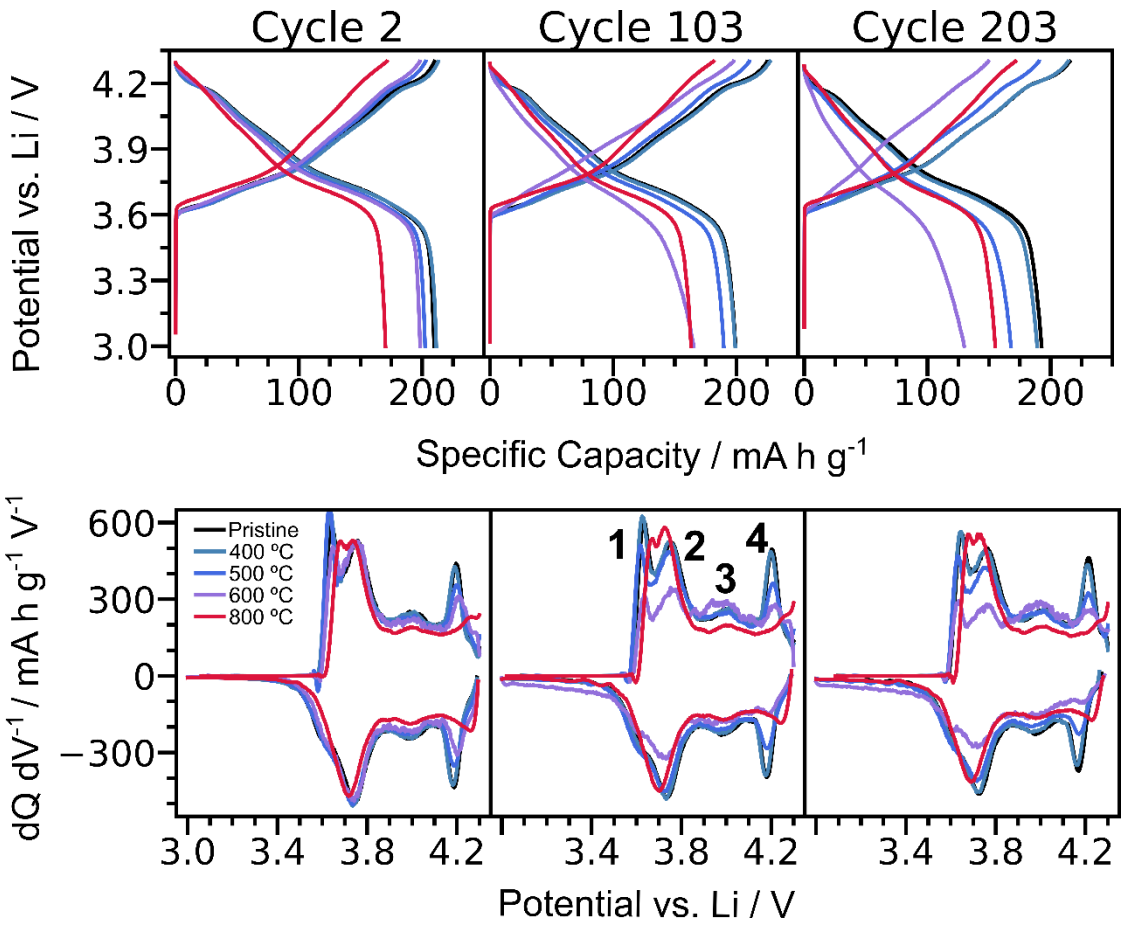

Figure 3.20. Voltage profiles and dQ/dV vs. voltage for half cells made with pristine NMC811 or Al_2O_3 coated NMC811 annealed at different temperatures. Cycles 2 (left), 103 (middle) and 203 (right) are shown, which were all performed at C/20.

A slow cycle rate data (C/20) was used to carry out the dQ/dV analysis and to separate the different electrochemical features and minimize impedance effects on the observed profiles. All samples show four peaks (labelled 1–4) on charge and discharge in their dQ/dV, as expected for NMC811.[265] The dQ/dV profiles are quite symmetric between charge and discharge in cycle 2, showing good reversibility of the charge/discharge cycle. Peak 4, which is associated with the flatter voltage process at close to 4.2 V, shifts to higher voltages on charge, and decreases in intensity as the annealing temperature increases, especially at 800 ºC where it almost vanishes. It is particularly clear from the dQ/dV plot of cycle 2 that much of the loss in capacity comes from the capacity associated with peak 4. This trend is observed also at higher cycle numbers. This peak is only observed in the nickel rich NMCs and LNO and has been associated with lattice collapse which occurs for NMC materials at high states of charge. It is at and above this voltage where much of the degradation is observed.[277] Interestingly, the sample annealed at 800

ºC shows a recovery of capacity retention and a partial merging of peaks 1 and 2 in its dQ/dV.

Having analysed the electrochemistry of the coated samples as compared to pristine NMC811, the effect on the electrochemistry of the conditions under which these coatings are synthesised was then explored. PXRD results revealed that the annealing step affected the structure of the NMC811 materials by increasing cation mixing so clearly the annealing step has an effect on the structure of the NMC811. It was therefore important to perform electrochemical testing on control samples that have been soaked in toluene and annealed at various temperatures and atmospheres to separate the effect of the solvents and heat treatments from those of the coating and surface doping. The results of these control experiments are shown in Figure 3.21 and Table 3.4. The uncoated NMC811 sample annealed at 400 ºC has similar initial capacities compared to the pristine NMC811, with an average of 186 and 179.9 mA h g^{-1} at C/2 and 206 and 199.9 mA h g^{-1} at C/20 for the pristine and control samples, respectively (Figure 3.21 and Table 3.4). However, the control sample has a better capacity retention than the pristine material at C/2 current rates after 200 cycles (19.7 % less C/2 capacity loss, Table 3.4), suggesting that washing with dry toluene and heating to 400 ºC under air has a beneficial effect on the capacity retention. In contrast to the 400 ºC control sample, the 800 ºC control sample showed a substantial decrease in initial capacity, both at C/2 (30.9 less mA h g^{-1}) and at C/20 (29.6 less mA h g^{-1}), which could result from the 2.9 % increase in Ni occupancy in the Li layer seen between control samples annealed at 400 and 800 ºC under air (Tables A7 and A8).[278] Nevertheless, better capacity retention than the pristine NMC811 (4.5 % less capacity loss at C/2) is still observed for this sample, again consistent with the idea that the coating process in itself (rather than the coating per se) results in better capacity retention. These improvements could be caused by the washing step, or by the heating, as it has been shown that surface Li_2CO_3 decomposes forming CO_2 at temperatures below 400 ºC for NMC811.[279]

By comparison with the uncoated sample annealed at 800 ºC, it is clear that the poor capacity and capacity retention observed for the coated sample annealed at 800 ºC cannot be attributed only to the heating under air and that the Al doping has a negative effect on the initial capacity and capacity retention of the material: there is nearly 10 mA h g^{-1} less initial capacity at C/2 and C/20 for the coated material and 22.7 % more capacity loss at C/2 after 200 cycles for the coated vs. non coated materials annealed in air at 800 ºC. The fact that the coated sample annealed at 800 ºC shows less capacity retention than the

pristine sample at C/2 rates but not at C/20 suggests that the capacity loss observed at high rates is a kinetic effect. This is surprising, given that at this temperature a large fraction of the Al^{3+} ions have diffused into the particles, but it may be associated with the secondary phase seen by XRD.

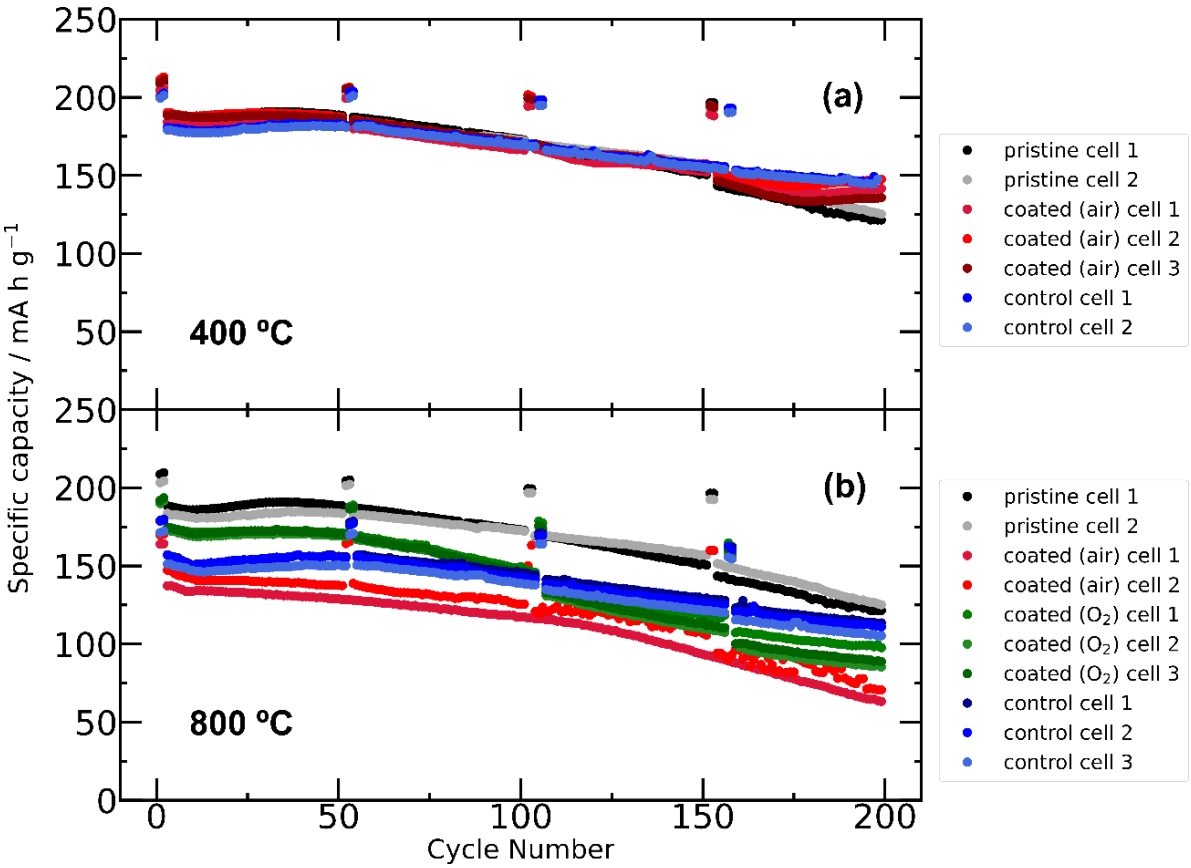

Figure 3.21. Long-term cycling data of NMC811/Li half cells, using pristine, Al_2O_3 coated, or control NMC811 electrodes. The coated samples were annealed in air (red) or oxygen (green), the control samples (blue) were treated with the same synthesis protocol as the coated samples and annealed in air, but without addition of aluminum isopropoxide. The annealing temperatures are given in the Figure.

To test if better capacity retention can be accessed by annealing under oxygen, a coated sample annealed under oxygen at 800 ºC was synthesized. The PXRD results (Figure 3.8 and Table A9) showed no secondary phases. Furthermore, less cation mixing was found compared to the sample annealed at 800 ºC under air (3.2 % of Ni in Li sites for the O_2 annealed sample and 4.5 % for the air-annealed sample, Tables A8 and A9, Appendix A). Electrochemically, this sample showed higher initial capacity than the coated sample annealed at 800 ºC under air (21.4–26.5 mA h g^{-1} difference) (Figure 3.21 and Table 3.4), which is attributed to the lower amount of cation mixing and possibly the lack of secondary phase. Both samples show similar rates of degradation at C/2, but 10% more degradation is seen at C/20 for the sample annealed under oxygen.

Table 3.4. Summary of initial capacities and capacity retention values for the pristine NMC811, coated NMC811 annealed at 400 and 800 ºC under air, 800 ºC under oxygen and control samples.

			Uncoated samples		Coated samples		
		Pristine NMC811	400 °C - Air	800 °C - Air	400 °C - Air	800 °C - Air	800 °C - O_2
Initial capacity C/20 (mA h g^{-1})	**average**	**206**	**199.9**	**176.4**	**208.5**	**169.8**	**191.2**
	max	208.6	200.3	179.1	211.6	169.8	192.1
	min	203.3	199.5	171.3	204.5	169.8	189.9
% Capacity loss C/20	**average**	**5.6**	**4.2**	**9.2**	**8**	**5.8**	**15.9**
	max	5.8	4.6	9.3	8.3	5.8	16.9
	min	5.3	3.7	7.6	7.6	5.8	7.6
Initial capacity C/2 (mA h g^{-1})	**average**	**186**	**179.9**	**155.1**	**187.6**	**147.3**	**173.8**
	max	188.4	188.4	157.1	190.2	188.4	174.6
	min	183.6	179.1	151.2	184.1	147.3	172.6
% Capacity loss C/2	**average**	**33.8**	**14.1**	**29.3**	**24.5**	**52**	**48**
	max	35.5	15.1	30.6	28	52	50.8
	min	32.1	13.1	28	22.4	52	43.9

These electrochemical trends can be partially explained by considering the insulating nature of the coating and the electrochemistry of aluminium-doped NMC phases. The coating is an electronic and ionic insulator and may hinder the extraction/insertion of lithium ions during the first charge/discharge. However, the NMC811 electrodes with amorphous coatings formed on annealing at 200 ºC and 400 ºC show good electrochemical performance both at high and low rates, the 400 ºC coating process resulting in marginally improved capacity retention over the uncoated at higher rates. This suggests that the amorphous alumina coating is better able to support Li^+ transport through it. By comparison, the AIP coatings formed in MeOH and xylene in earlier work at the same temperature, which contained $^{[6]}$Al only, were associated with poor capacity retention.[100] We note, however, that these results were obtained for NMC532, and the materials were cycled to 4.5V, a higher voltage being needed to extract a similar amount of Li.

Finally, we should compare our coating method to that of Neudeck et al.[102] who saw an improvement in capacity retention after coating wet (1000–1200 ppm of water) NMC811 with TMA in toluene, removing unreacted precursor before drying, but with no annealing step. Neudeck et al. tested their material in full (NMC811/graphite) pouch cells at 1C cycling rate and 45 ºC, and obtained impressive behaviour, extending the lifetimes of their batteries from 600 to over 1100 cycles (based on an 80% capacity retention). They speculate that their process removes water from the surface of the NMCs improving

capacity retention. Their coating must similarly be amorphous, their work motivating further studies of our 200 and 400 ºC annealed samples in full cells. More recent work on TMA coatings on $Li(Ni_{0.70}Co_{0.15}Mn_{0.15})O_2$ by Negi et. al. has also seen good performance for amorphous alumina coatings, but they see improved performance for a mixed amorphous $Al_2O_3/LiAlO_2$ coating layer, which they ascribed to increased lithium-ion conductivity.[101] These authors similarly use NMR to characterize their coatings, and the broadness of their ^{27}Al signals is consistent with an amorphous coating and the formation of $LiAlO_2$ at 600 ºC.

3.9. Conclusions

Although alumina coatings have been shown to increase the lifetime of a range of lower-nickel content NMCs, their efficacy for Ni rich materials such as NMC811 is less clear with various studies producing contradictory results. Since this could be a consequence of the different coating methods used in these studies, which result in different phases and uniformity of the alumina coatings, a new wet-chemistry method to deposit alumina on NMC811 is developed in this chapter. The result was a 30–100 nm thick coating, whose structure and electrochemistry was explored as a function of annealing temperature. High-field SSNMR spectroscopy, supported by XPS and microscopy was used to track the development of the alumina coating with temperature, an amorphous alumina-like coating being seen at low temperatures and a γ-lithium aluminate-like coating at 600 ºC. Essentially all the Al migrated into the bulk on annealing at 800 ºC. This evolution differs from a previous report on alumina coating of NMC811, albeit using a different wet-chemistry coating method, which found the presence of $^{[6]}Al$ environments at lower annealing temperatures, assigned to $Al(OH)_6$ or α-$LiAlO_2$ and the presence of $^{[4]}Al$ environments with lower frequency ^{27}Al NMR shifts than found in γ-$LiAlO_2$ at 800 ºC, which they tentatively assigned to environments in grain boundaries.[245]

The electrochemical findings were linked to the evolution of the coating induced by the annealing step by identifying the critical temperature at which doping of aluminium ions occurs in NMC811 and comparing samples that were not coated but still underwent the same annealing and washing steps. Annealing at 200–400 ºC resulted in similar capacity fade to pristine NMC811 on cycling the coated NMC materials in half-cells to 4.3V, with the washing and annealing steps but without the coating yielding similar results. Higher annealing temperatures led to faster degradation in half cells, with annealing at 600 ºC resulting in the greatest capacity fade. Interestingly, the degradation

at 800 ºC was slower than at 600 ºC but the overall capacity was reduced. This work highlights the fact that different coating conditions (solvents, precursor, wt.% of precursor, reaction times, atmosphere, temperatures, and the surface chemistry of the substrate) can have a noticeable effect on the structure of the resultant coating and its degree of crystallinity and the need to control the whole coating processes and suggests that alumina coatings do little to prevent degradation in half cells, motivating further studies of full cells and the role that coatings play in cross-over phenomena. Overall, our study provides fundamental information which should be of value in the development and analysis of NMC811 coatings. One implication of this work is that bimetallic oxide coatings with better lithium-ion conductivity should be of particular interest, motivating the next chapter of this thesis.

Chapter 4: Recovery of Long-term Capacity of NMC811 by Coating with Lithium Aluminate Using Mixed-metal Alkoxides

4.1. Abstract

Ni-rich $LiNi_xCo_yMn_zO_2$ (NMC) materials such as NMC811 (80% Ni) are one of the most promising candidates for next generation cathodes in Li-ion batteries due to their high energy densities and low costs. However, their reactive surface and poor mechanochemical properties pose a challenge for their practical handling and storage, due to their fast degradation under operation or storage in air. To solve these problems surface treatments such as coatings and washing as well as different morphologies with better mechanical integrity and lower surface area such as single-crystal NMC materials have been explored. In this chapter, a single-source precursor approach is applied for the first time to coat NMC811 with $LiAlO_2$. Three heterobimetallic alkoxides ($Li[Al(OCH_2Ph)_4]$, $Li[Al(O^iPr)_4]$ and $Li[Al(O^tBu)_4]$) are synthesised and their thermolysis and reactivity with NMC are studied by solution and solid-state nuclear magnetic resonance spectroscopy (NMR), thermogravimetric analysis (TGA), elemental analysis, powder X-ray diffraction (PXRD) and energy dispersive X-ray spectroscopy (EDS). The -OR group has a major influence on the properties of the precursors, $Li[Al(O^tBu)_4]$ resulting in the best coating deposition characteristics in terms of solubility, thermal decomposition, phases formed and reactivity with NMC. The effect of different morphologies and surface treatments on the solution deposition of $LiAlO_2$ onto NMC811 using these precursors is carefully evaluated by testing two different substrates: Pristine polycrystalline NMC811 (PC-NMC811) and Al_2O_3 coated single-crystal NMC811 (SC-NMC811). Furthermore, by studying the effect of soaking in water and coating on the surface, bulk structure, and electrochemistry of NMC811 it is found that the deposition reaction proceeds via a hydrolytic route, in which the precursor reacts with TM(O)-OH surface groups and adsorbed water. Finally, significant improvements in capacity retention and specific capacity were seen for the $LiAlO_2$ | Al_2O_3 | SC-NMC811 and the $LiAlO_2$ | H_2O soaked PC-NMC811 systems, which were attributed to the better Li-ion conductivity of $LiAlO_2$, surface Li enrichment and regeneration of degraded surfaces.

4.2. Introduction

In order for lithium-ion batteries to successfully replace fossil-fuels in transportation, their energy density and cycle life needs to increase and their cost should be reduced without compromising on safety.[280] Towards this end, Ni-rich $LiNi_xCo_yMn_zO_2$ (NMC) cathode active materials (CAM) were developed from the parent $LiCoO_2$ (LCO) material by partial substitution of Co by Ni and Mn. High Ni content NMC such as $LiNi_{0.8}Co_{0.1}Mn_{0.1}O_2$ (NMC811) show high energy density, thermal stability and low cobalt content, which should reduce costs and ethical mining concerns making it a promising candidate for applications in electric vehicles.[215]

The main obstacle for the use of NMC811 is its poor stability which leads to poor capacity retention and difficulties with practical handling, storage, and transportation. The underlying reasons for this decreased stability with increased Ni content have been investigated in great detail. Its surface is chemically active which leads to a host of surface reactions such as electrolyte oxidation,[27,281] reaction with CO_2 and moisture forming surface impurities (Li_2CO_3 and LiOH),[282] transition metal dissolution,[283,284] and reduction of the surface with the formation of an insulating rock salt layer (NiO) with oxygen evolution.[218,231,232] In addition to the surface reactivity, Ni-rich NMC materials have problematic chemomechanical properties. They display large anisotropic volume changes in the unit cell at high states of charge (SoC), which causes mechanical strain and leads to secondary particle cracking exposing fresh surfaces to electrolyte which aggravates the surface degradation.[29,277,285,286]

As noted above, when NMC811 is exposed to air it reacts with CO_2 and moisture forming surface impurities such as Li_2CO_3 and LiOH.[282] This leads to a decrease in specific capacity and capacity retention by depletion of surface Li which in turn encourages reduction of Ni^{3+} to Ni^{2+} and the formation of rock salt layers,[282,287] and increased gassing during cycling.[282] Furthermore, these surface impurities can increase the pH of the slurry during electrode preparation which prevents gelation and leads to poor casting properties.[288] To fully prevent the formation of these impurities, the exposure to air should be minimised. However, this is not always feasible for the storage and transportation of these materials in practical applications where large amounts will be used in electrode manufacture.

To mitigate surface degradation, synthetic modifications of the cathode surface have been developed with coating and surface doping being popular approaches towards this

end.[84,289,290] However, it is still unclear whether coating with monometallic oxides or surface doping can effectively mitigate the interfacial processes that lead to a loss of capacity in Ni-rich NMC materials.[291]

Washing and annealing steps have also been explored as strategies to eliminate the surface impurities and regenerate the surfaces of air-exposed CAM.[288,292–300] The most common approach to remove surface impurities is to wash the CAM with water, which was shown to be effective in improving capacity retention in $LiCoO_2$ (LCO).[294] However, it is unlikely that this method will work for NMCs, because of their sensitivity to water.[288] A large number of studies have addressed the effect of washing with water and annealing on the electrochemical properties of Ni-rich CAMs, but leading to very different conclusions due to the different conditions under which the CAM were synthesised, washed and tested. Some researchers have reported enhanced capacity retention after washing in water. In one study, an increase in the interlayer spacing and reduced cation mixing was seen after washing $LiNi_{0.88}Co_{0.11}Al_{0.01}O_2$ (NCA) in water which led to enhanced structural stability with cycling.[297] Others claimed that washing NCA that was exposed to air with water followed by annealing at 700 ºC led to improved capacity retention by removal of $LiOH/LiCO_3$.[293] Similarly some have reported an improvement in capacity retention after washing NMC811 in water for 20 min and then heating at 700 ºC, although with a loss in initial specific capacities.[292]

In contrast to those reports, Hofmann et al. carried out a systematic study of the effect of water soaking and aqueous electrode processing on the metal leaching and electrochemical properties of NMC111, 622, 811 and NCA.[296,301] They found that increasing Ni content led to more lithium leaching under the same conditions and further deteriorated the capacity retention. Interestingly, NCA was far more sensitive to water soaking than any NMC composition, due to more Li and Al leaching.[296,301] It is now becoming clear that treating Ni-rich NMC with water leads to a decrease in capacity retention due to lithium extraction by Li^+/H^+ exchange forming LiOH and TM(O)-OH species on the surface.[288] The delithiated surface is more reactive with the electrolyte,[302] which leads to more electrolyte degradation and rock-salt formation on cycling and the removal of surface impurities by washing creates more exposed surfaces.[299] Adding an annealing step after soaking NMC in water only leads to the formation of a NiO rock-salt layer which further deteriorates the long-term capacity retention.[288] However, if excess

lithium is added during this annealing step (for example in the form of Li_2CO_3), a more favourable surface which is less reactivity with the electrolyte can be obtained.[302]

Washing NMC811 with water also affects the mechanical properties of the material. In one study, washing for prolonged periods of 6 h in deionised water stirring led to significant particle cracking.[298] Furthermore, immersion in water for 6 h without stirring did not cause cracking but led to a decrease of the compressive load for failure to half of the value of pristine NMC811. Since water treatments are known to cause Li leaching in NMC811, the authors suggested that Li depleted surface regions and surface reconstruction produced a mismatch strain at grain boundaries, which decreased the mechanical integrity of the material.[298] It is also possible that the water treatment without stirring decreased the physical cohesion between the primary particles (through transition metal dissolution, for example), without causing cracking, which would also decrease the compressive load for failure.

Although other less damaging solvents such as alcohols have been used,[295] these are less effective in removing impurities (Li_2CO_3 particularly), less environmentally friendly and would need to be used dry to avoid water exposure.[302] Being able to wash Ni-rich NMCs in water and/or prepare water-based slurries is therefore an important research goal and although it has been shown that, by optimising the pH and mixing times, the damage caused to the materials can be limited,[300] effective surface treatments are still needed for the post-processing of water-washed NMC811 and the preparation of aqueous slurries.

Another strategy to mitigate degradation is to change the morphology of the particles. Monolithic Ni-rich NMCs, the so-called ‘single-crystal’ NMCs have received significant attention in recent years and they show promise of slower degradation compared to polycrystalline NMC.[303] Generally, single-crystal NMC811 (SC-NMC811) materials show more favourable properties such as less gassing with cycling, higher thermal stability and better capacity retention which stems from their reduced surface area compared to polycrystalline NMC811.[304,305] They also show less tendency to crack upon cycling which is proposed to be one of the degradation mechanisms of high Ni content NMC.[306] Some of the biggest challenges in developing viable SC-NMC materials are related to the difficulty of synthesising high-Ni content single-crystal particles with large (>1 μm) diameter.[307] Furthermore it is unclear whether fast charge/discharge rates will be

possible with SC-NMC due to the longer diffusion lengths of lithium caused by the larger size of the primary particles.[306]

Recently, there has been interest in ternary oxides,[105,249,308–311] fluorides,[224] phosphates,[312] and silicates [313,314] as coating materials for Ni-rich NMC due to the prospect of adding lithium-rich coatings which may display further advantages compared to the binary counterparts. In one study, Zr_xPO_y and $Li_xZr_yPO_z$ were deposited on NMC811 by ALD, showing that, while both increased capacity retention at low cycling rates, the lithium-rich coating allowed higher initial capacities and improved rate capabilities.[312] Li_2ZrO_3 coating has also been tested on a NMC with 70 % Ni.[310] Despite the fact that using two separate lithium and zirconium sources led to an inhomogeneous distribution of the elements on the surface, both by sol-gel and co-precipitation methods, improved capacity retention and rate capability were observed.[310] $LiAlF_4$ was also deposited by ALD onto NMC811 and it showed a good stability and improved capacity retention over 300 cycles in half cells without compromising rate capability.[224] Ternary oxides were also coated onto Ni-rich NMCs using mechanical mixing of nano-powders of the coating material with the CAM, generally obtaining positive results in capacity retention and rate capability.[309,311] In a recent report, improvements in cycle life of an NMC with 85% Ni content and LNO were seen by solution deposition of an aluminosilicate using trimethyl aluminium (TMA) and tetraethylorthosilicate (TEOS) as precursors.[314] However, it was necessary for the CAM to be wet in order for the coating reaction to take place, limiting the use of this method.[314]

Clearly the deposition of ternary coatings poses a synthetic challenge for conventional methods such as ALD, sol-gel, mechanical mixing, and co-precipitation. Most importantly, the need to use two precursors as the source of each of the metals leads to inhomogeneous composition of the coating. This is particularly true for ALD, were the two elements have to be deposited sequentially, in two separate cycles.[312] A suitable single-source precursor (SSP)[315] for the solution deposition of mixed-metal oxides onto NMC811 would be a step forward in solving this problem. The SSP must display a series of properties: It should decompose at a temperature below the diffusion of Al into NMC811 ($T < 500–600$ ºC), should be reactive with -OH groups or adsorbed water molecules present on the surface, and it should be soluble in innocent solvents (which do not react).

In this chapter, ternary metal oxide coatings are explored as a strategy to improve the capacity retention of NMC811 by developing mixed-metal alkoxides that are used as SSPs for coating deposition. In the previous chapter, it was shown that an Al_2O_3 coating deposited by a solution-based method was ineffective at improving the capacity retention in half cells. This was due to the insulating nature of Al_2O_3 which led to kinetic limitations, the extraction of Li from the NMC811 during annealing and the formation of a secondary phase containing electrochemically inactive Al^{3+} ions. Furthermore, the polycrystalline NMC811 (PC-NMC811) that was used in this previous chapter is expected to undergo significant cracking upon cycling, exposing fresh CAM surfaces to electrolyte and limiting the effects of the coating. These challenges prompted the search for other coating materials with more favourable properties. In this context, $LiAlO_2$ emerges as a promising option. Like Al_2O_3, it contains cheap, non-toxic, and abundant elements. However, it is a much better Li-ion conductor than Al_2O_3, specially in its amorphous form.[316] More importantly, since it already contains lithium, it is unlikely to extract Li from the surface of the NMC811 during annealing. Furthermore, recent research has shown that it may be possible to reverse rock-salt formation by a surface lithium treatment followed by annealing-induced lithium diffusion and oxidation of Ni^{2+} to Ni^{3+}.[317] Therefore, by annealing NMC811 coated with a lithium-rich layer, it may be possible to recover some of the capacity that has been lost due to exposure to air or water while also benefiting from having a surface coating. Furthermore, since SC-NMC811 is less prone to cracking than PC-NMC811, the effect of coating particles with different morphologies is investigated. This should provide more accurate information on the role of the coating in increasing the lifetime of the battery, as less fresh CAM surfaces are exposed to electrolyte during cycling SC-NMC811 potentially allowing further improvements in capacity retention. Finally, coating a pristine NMC surface vs. an Al_2O_3 coated surface will be explored to gain insight into the reactivity of the precursor with different oxide surfaces and clarify whether adding surface lithium can yield further benefits in terms of capacity retention compared to coating with Al_2O_3.

4.3. Precursor Synthesis

Heterobimetallic alkoxides have been used extensively in other areas for the synthesis of ternary oxide coatings.[315] This class of molecule is attractive due to their often simple synthesis, and favourable properties as SSPs such as the tendency to hydrolyse in the presence of water or thermolyze at relatively low temperatures. Consequently, lithium aluminium alkoxides were prepared by reaction of $LiAlH_4$ with different alcohols in dry THF. This was done to test the effect of different alkoxy groups (-OCH_2Ph, -O^iPr, -O^tBu) on the properties of the resulting molecules as precursors to $LiAlO_2$ coatings. By changing these groups, it is possible to change critical properties of the precursor such as solubility, decomposition temperatures and coating properties. The synthetic route employed in the current work was first used by Pauls et al. to synthesise $Li[Al(OCH_2Ph)_4]$ (**1**),[318] and in this work, is extended to two other heterobimetallic alkoxides: $Li[Al(O^iPr)_4]$ (**2**) and $Li[Al(O^tBu)_4]$ (**3**). The products are obtained by exothermic reaction (Scheme 4.1) of $LiAlH_4$ (1 M solution in THF) and the alcohol, dissolved in THF at room temperature giving H_2 and the mixed-metal alkoxide. This simple, one-step reaction is attractive from a practical perspective; it generates useful heat, requires simple and widely available starting materials and yields H_2(g) as the only side-product, which is essential for many industrial processes such as the synthesis ammonia and methanol.[120]

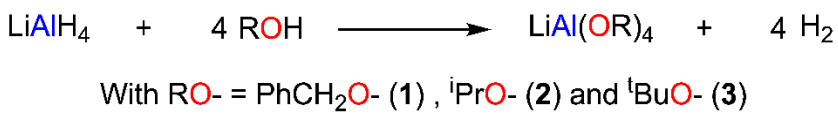

Scheme 4.1. Synthesis of the three lithium aluminate precursors used in this work. A 1 M solution of $LiAlH_4$ in THF is reacted with 4 equivalents of the alcohol to give hydrogen gas and the heterobimetallic alkoxide containing Li and Al.

It was found that the steric bulk of the alkoxy ligand (-OR) has a significant influence on the solubility of the precursors. The reactions to form **1** and **2** led to a white suspension that was filtered and the product was obtained by solvent evaporation under vacuum. Compound **1** was fully soluble in THF after filtration, but **2** was poorly soluble even after the filtration step. Synthesis of **3** led to a clear solution and required no filtration step, so the product was obtained directly by removing the THF solvent under vacuum. The resulting white powders were further dried under vacuum at 40 °C for 1 h and then stored for further analysis. The use of bulkier groups such as ^tBuOH or $PhCH_2OH$ led to products that were soluble in THF, but not fully soluble in any other solvents tested. This indicates

that THF coordination to Li^+ is playing an important role in solubilising these compounds (most likely by forming $Li(THF)_4^+$ counterions to the $Al(OR)_4^-$ anions).

Compounds **1** - **3** were characterised by elemental analysis and nuclear magnetic resonance (NMR) spectroscopy (both in solution, Figure 4.1 and in the solid state, Figures 4.2 and 4.3). Furthermore, many attempts to grow single crystals of **3** for X-ray diffraction were made, always resulting in the formation of white particles that did not diffract. Elemental analysis (Chapter 6, section 6.3.2.) indicates that the formulae of complexes **1**-**3** is $LiAl(OR)_4$ (with OR = OCH_2Ph, O^iPr or O^tBu) without any THF from the synthesis remaining after drying. The H content for compound **3** was consistently too high by around 0.7 % weight relative to the H content expected for $Li[Al(O^tBu)_4]$. It is unclear what the reason for this is - possibly the presence of some unreacted Al-H bonds from the $LiAlH_4$ used in its synthesis. However, bearing in mind the air sensitivity of all of the complexes **1**-**3** some hydrolysis occurring during isolation and/or analysis is the most likely explanation for this. To confirm that the reaction led to the desired bimetallic alkoxides, solution NMR measurements in d_8-THF were performed for compounds **1** and **3** (^{27}Al NMR, Figure 4.1, and Appendix C Fig. C3–C12 for the ^1H, ^{13}C, and ^7Li solution NMR of the compounds **1**-**3**). ^1H and ^{13}C solution NMR spectra of **1** and **3** are consistent with the presence of the expected alkoxy groups in the products ($-OCH_2Ph$ and $-O^tBu$ groups respectively). Furthermore, there is no evidence of THF from the synthesis coordinating to the compounds suggesting that the drying step at 40 ºC under vacuum fully removes all the coordinating THF molecules, in agreement with the elemental analysis results (See Appendix C, Figures C4-6 and C8-C11 for ^1H and ^{13}C solution NMR spectra).

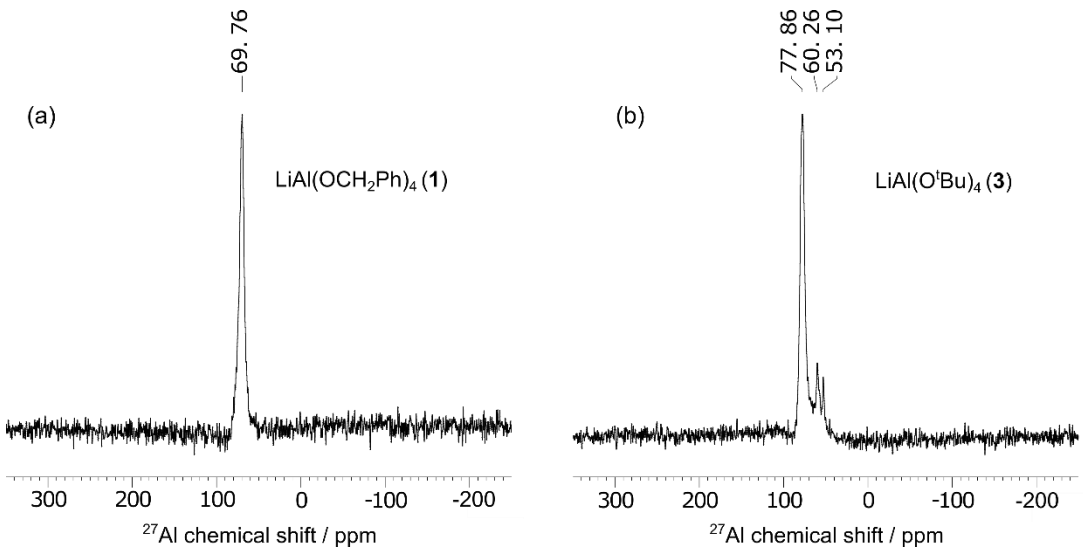

Figure 4.1. ^{27}Al solution NMR of **1** and **3**. The compounds were dissolved in d_8-THF, and the NMR measurements were performed at room temperature using a 9.4 T magnet (400 MHz ^{1}H Larmor frequency) and a solution of $Al(NO_3)_3$ in D_2O at 0 ppm was used as an external reference. The lack of solubility of compound **2** prevented its characterisation by solution NMR.

^{7}Li (Figures C3, C7 and C12, Appendix C) and ^{27}Al solution NMR measurements (Figure 4.1) confirmed the presence of both elements in **1** and **3,** thereby proving that bimetallic alkoxides were synthesised. ^{27}Al NMR spectra were background-subtracted to eliminate the contribution from the probe to the observed spectra (Figure 4.1). ^{27}Al NMR is a useful tool to investigate the structure of Al containing compounds because the chemical shift of the peaks can be related to the coordination number and chemical environment present. Aluminium is typically found in 4-, 5- or 6- coordination environments (denoted $^{[4]}$Al, $^{[5]}$Al and $^{[6]}$Al in this Chapter). No peaks from $LiAlH_4$ (sharp peak at 98 ppm)[319] were observed in these samples indicating that the $LiAlH_4$ is fully consumed during the synthesis. For precursor **1**, ^{27}Al solution NMR shows a single resonance centred at 69.76 ppm indicating the presence of a single $^{[4]}$Al environment in solution.[320] The ^{7}Li solution NMR spectrum of **1** (Appendix C, Figure C3) shows the presence of a main peak at -0.23 ppm and a broad peak at 0.35 possibly indicating dynamic behaviour. In contrast with **1**, compound **3** shows a single sharp resonance in the solution ^{7}Li NMR spectrum (-0.26 ppm, Appendix C, Figure C12) but three aluminium environments (77.68, 60.26 and 53.1 ppm, Figure 4.1) indicating the presence of two $^{[4]}$Al and one $^{[5]}$Al environment in solution.[320] The multiple aluminium or lithium environments suggest the presence of complicated equilibria in d^8-THF solutions, which are not uncommon for aluminates of this type (e.g., involving ion-pairing of $Li(THF)_n^+$ with $Al(OR)_4^-$, and potentially coordination of THF to Al^{3+}).[319]

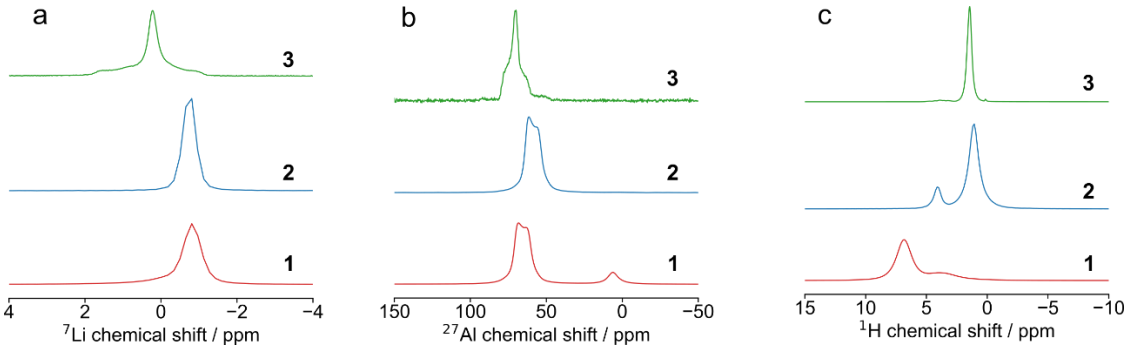

Figure 4.2. Solid-state NMR (SSNMR) spectra of the pristine precursors **1** (red), **2** (blue) and **3** (green). The ^{7}Li (a), ^{27}Al (b) and ^{1}H (c) NMR spectra are shown. The rotors were packed inside a N_2-filled glovebox to avoid hydrolysis of the precursors under air. The spectra of **3** were recorded at a magnetic field strength of 16.4 T and a MAS frequency of 50 kHz. The spectra of **1** and **2** were collected at a field strength of 11.7 T and a MAS frequency of 30 kHz. Only the central (isotropic) peaks are shown here.

Due to the insolubility of compound **2**, and to further characterise **1** and **3**, solid-state NMR (SSNMR) measurements were carried out on the three compounds (Figures 4.2, 4.3 and in Appendix C, Figures C23 and C24). The ^{7}Li SSNMR spectra are shown in Figure 4.2. Compounds **1** and **2** showed single resonances at -0.73 and -0.65 ppm, respectively. The main ^{7}Li NMR resonance of **3** was shifted to higher frequency compared to the other two (0.23 ppm). Furthermore, a broad feature centred at ca. 0 ppm and with a linewidth of 3 ppm is observed in the ^{7}Li NMR of compound **3**. The ^{27}Al SSNMR spectra also shows clear differences between the three compounds. The spectra were fitted as quadrupolar line shapes (Figure 4.3 and Appendix C, Figures C23 and C24) to obtain information about the number of environments present, their quadrupolar parameters (quadrupolar coupling constant, C_Q and the asymmetry parameter, η_Q) as well as the isotropic shift (δ_{iso}). Compound **1** has one $^{[4]}$Al environment at 72.9 ppm with a C_Q of 4.56 MHz and an η_Q of 0.111 while for **2,** the $^{[4]}$Al environment is centred at 65.9 ppm with a C_Q of 4.47 MHz and an η_Q of 0.108 (Table C7, Appendix C). The similar C_Q and η_Q of the $^{[4]}$Al peak in **1** and **2** suggest similar structure around the nucleus, while the isotropic shifts are consistent with Al coordinating to four oxygens.[319,320] Furthermore, compound **1** presents an additional peak at 6.4 ppm which corresponds to a single $^{[6]}$Al environment with an isotropic shift of 6.12 ppm and a C_Q of 0.055 MHz; the low C_Q suggesting a close to ideal octahedral geometry. Finally, the ^{1}H SSNMR spectra are consistent with the presence of the expected alkoxy groups for each compound. Compound **1** shows two resonances at 3.9 (-OCH_2-) and 6.9 ppm (-Ph). Meanwhile, **2**

presents two resonances at 4.12 (-OCH-) and 1.23 ppm ($-CH_3$) as expected for the $-O^iPr$ group and compound **3** showed only one proton peak at 1.45 ppm as there is only one proton environment in the $-O^tBu$ ligand.

The ^{27}Al SSNMR spectrum of compound **3** can be deconvoluted to two $^{[4]}Al$ environments centred at 79 and 61.2 ppm (Figure 4.3). This matches well with the solution NMR in which one intense peak is observed at 77.6 ppm and two smaller peaks are present at lower shifts, suggesting that the solid-state structure is at least partially retained in solution. The environment at higher shift is the major environment in this sample and it has a high C_Q of 6 MHz which indicates significant deviation from the ideal tetrahedral geometry, more so than the $^{[4]}Al$ environments found in **1** and **2**. The second $^{[4]}Al$ in **3** has a much lower C_Q of 0.055 MHz suggesting a tetrahedral geometry. Based on the chemical shifts and the C_Q values, the two peaks are assigned to $[Al(O^tBu)_3H]^-$ and $[Al(O^tBu)_4]^-$, respectively. Aluminium hydride peaks appear at higher shifts than aluminium alkoxides,[319] and the substitution of one $(O^tBu)^-$ group by an H^- would change the charge distribution (electrostatic interaction) around the aluminium nucleus thereby changing its C_Q value.[321] Furthermore, atmospheric solid analysis probe mass spectrometry (ASAP-MS) results (Chapter 6, Section 6.3.2.) confirmed the presence of the two anions $[Al(O^tBu)_4]^-$ and $[AlH(O^tBu)_3]^-$ in the solid state. Finally, deconvolution of the ^7Li spectrum shows that there are five lithium environments, one of them much more intense than the others. Simultaneously, 5 peaks are present in the ^1H NMR in the area corresponding to Al-H environments.[319] This suggests that all the possible combinations of $Li(O^tBu)_{4-n}H_n$ (with n = 0–4) are present, although one of them in much larger proportion. Based on the elemental analysis results this species could be n=0 i.e., $Li[Al(O^tBu)_4]$.

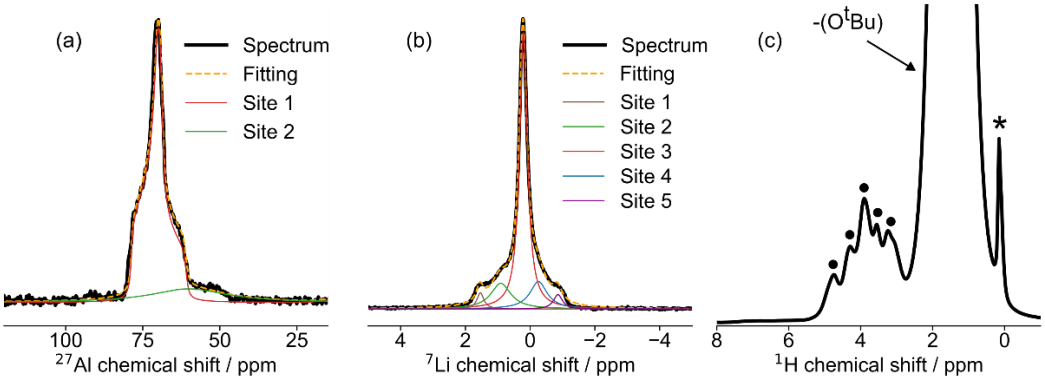

Figure 4.3. SSNMR and fittings for the ^{27}Al (a), ^{7}Li (b) and ^{1}H (c) spectra of precursor **3**. The spectra were acquired at a magnetic field strength of 16.4 T and a MAS frequency of 50 kHz. The circles mark the peaks arising from the five hydridic environments, and the asterisk marks the proton peak corresponding to vacuum grease.

4.4. Precursor Thermolysis

As in chapter three, the coating process involves the deposition of the precursors onto the surface of NMC811 particles from solution and the annealing of the coated materials to form $LiAlO_2$ by thermolysis of the precursors. Therefore, the thermolyses of the precursors **1-3** were studied first to determine their decomposition temperatures using thermogravimetric analysis (TGA) and to characterise the products formed by a combination of powder X-ray diffraction (PXRD) and SSNMR.

4.4.1. Thermogravimetric Analysis

TGA was performed to determine the decomposition temperature of the precursors, establish if the decomposition occurs in a single or multiple steps and to determine the weight loss during thermolysis which should provide evidence of $LiAlO_2$ formation. These measurements, shown in Figure 4.4, were performed under synthetic air flow as the annealing of the coated NMC811 samples after deposition is performed under air. To minimise precursor hydrolysis, a small amount of sample was quickly transferred from the glovebox to the TGA instrument where it was kept under synthetic (dry) air. The precursors were heated from 25 to 800 ºC at a rate of 10 ºC / min and the changes in sample masses were recorded.

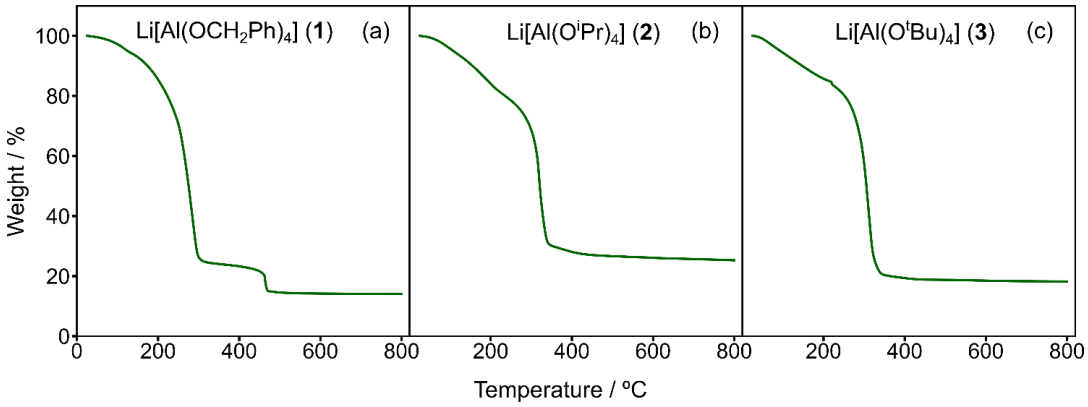

Figure 4.4. TGA curves of precursors **1** (a), **2** (b) and **3** (c) measured in air atmosphere between 25 and 800 °C with a heating rate of 10 °C/min.

TGA curves (Figure 4.4) show that the decomposition occurs in two steps for **1** with 70% of the mass is lost during the first step with an onset temperature of 236 ºC and an additional 8% is lost in a second decomposition step at ca. 470 ºC. Compounds **2** and **3** show TGA profiles with single decomposition steps at 302 and 283 ºC, respectively. Significant mass loss has already taken place before the main decomposition events for **2** and **3** (approx. 20%). This loss of mass starts at the beginning of heating and although some of this can be attributed to the desorption of THF molecules, it is unlikely that this accounts for 20 % mass loss as THF was not detected in the solution NMR. Therefore, it is likely that compounds **2** and **3** are quite sensitive to heat under dry air and start decomposing at temperatures below their main decomposition step. Finally, it should be noted that the % mass loss for the three compounds at 800 ºC corresponds to the formation of $LiAlO_2$ (Table 4.1), suggesting that all three of them can successfully form the desired coating material. The thermolysis could proceed by either elimination ($LiAl(OR)_4 \rightarrow LiAlO_2 + 2OR_2$) in dry atmosphere although in ambient conditions this is likely to occur by reaction with ambient moisture (following the equation $LiAl(OR)_4 + 2H_2O \rightarrow LiAlO_2 + 4ROH$). The aluminium and lithium content in samples after thermolysis was determined by inductively coupled plasma-optical emission spectroscopy (ICP-OES). The ICP-OES results clearly show that precursors **3** forms a solid with 1:1 Al to Li ratio, as expected for $LiAlO_2$. Compounds **1** and **2**, however, shows a Li : Al ratio of slightly less than 1 (0.876 - 0.976). Since the lithium does not sublime under these conditions for **3**, the Li deficiency could come from the precursor which could have a lower Li : Al ratio, or the formation of volatile $Li(OR)_n$ (OR=O^{i}Pr, OCH_2Ph) species.

Table 4.1. TGA decomposition temperature, % mass loss and Al : Ni ratios after decomposition. The decomposition temperatures were calculated from the extrapolated onset temperatures obtained from the main decomposition step. ICP-OES measurements were carried out on samples annealed at $T>T_d$.

Precursor	T_d / °C	Expected mass loss (%)	Measured mass loss (%)	Li : Al ratio (ICP)
$Li[Al(OCH_2Ph)_4]$ (**1**)	236	86	86	0.876 (400 ºC) 0.914 (800 ºC)
$Li[Al(O^iPr)_4]$ (**2**)	302	76	75	0.976 (400 ºC)
Li[Al(O^{t}Bu)4] (**3**)	283	80	82	1.003 (500 ºC)

4.4.2. Powder X-ray Diffraction

Samples for PXRD, SSNMR and elemental analysis were prepared by annealing the precursors in an alumina crucibles at 400–800 ºC for 4 h under air. Powder X-ray diffraction (PXRD) analysis was used to study the phases formed upon heating and the degree of crystallinity of the resulting materials (Figures 4.5 and 4.6).

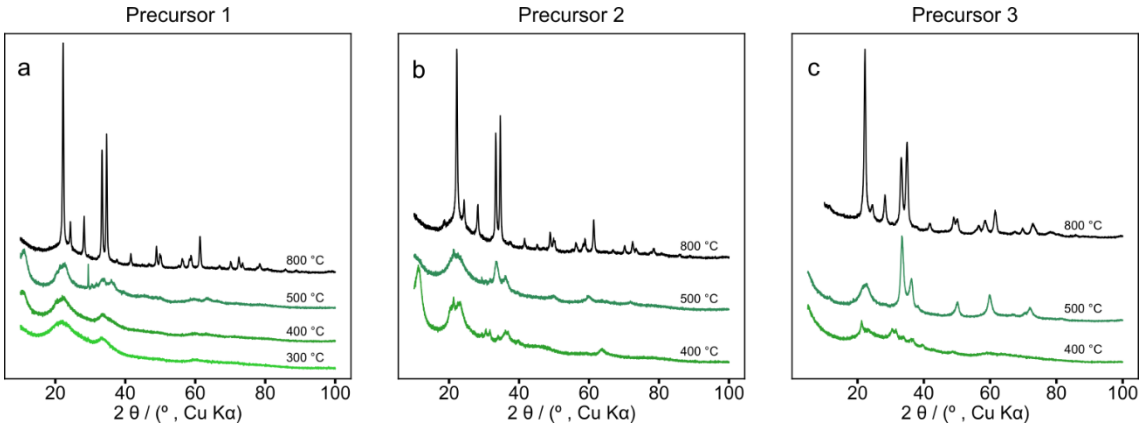

Figure 4.5. PXRD patterns of compounds **1**-**3** decomposed by annealing under air for 4 h at 300, 400, 500 and 800 ºC for compound **1** and 400, 500 and 800 ºC for compound **2** and **3**.

Generally, the PXRD patterns show broad peaks below 800 °C, indicating significant disorder (Figure 4.5). However, annealing **3** to 500 ºC led to the formation of sharper peaks in the PXRD pattern compared to **1** and **2**, suggesting that **3** starts to crystallise at this temperature. To determine the structure of the crystalline phases prepared at 800 ºC, Rietveld refinements of the PXRD patterns were performed.

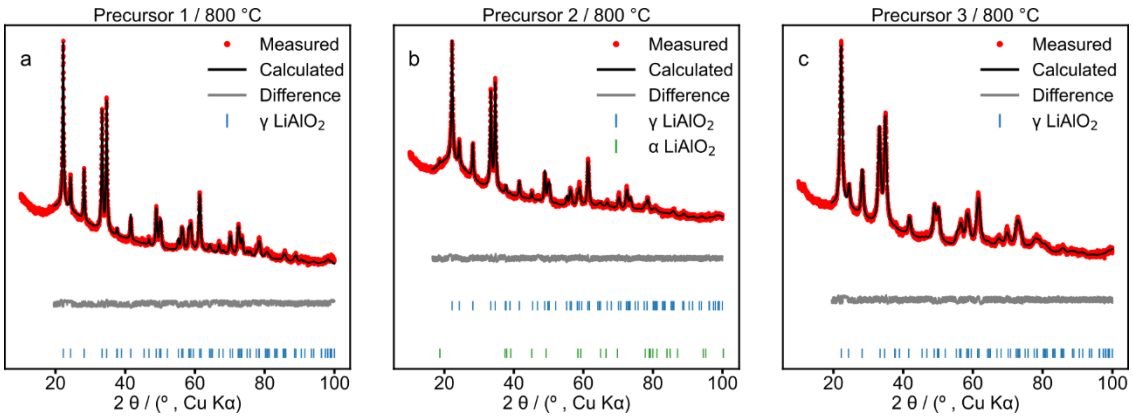

Figure 4.6. PXRD patterns of the **1**-**3** annealed under air at 800 ºC for 4 h together with the fittings obtained from Rietveld refinement.

There are three confirmed polymorphs of $LiAlO_2$; α-, δ, and γ-$LiAlO_2$ which crystallise forming hexagonal ($R\bar{3}m$), tetragonal ($I4_1/amd$), and tetragonal ($P4_12_12$) structures, respectively.[276,322] Out of these, γ- $LiAlO_2$ is particularly interesting as a lithium-ion conductor owing to the diffusion channels created by the 3D network of edge-sharing MO_4 tetrahedra.[322] Li-ion diffusion experiments have shown that the presence of defects, or even a mixture of amorphous and crystalline $LiAlO_2$, leads to an increase in lithium conductivity.[276,322] Rietveld refinement of the PXRD patterns confirmed the formation of γ-$LiAlO_2$ after annealing compounds **1**-**3** at 800 ºC (Figure 4.6). Materials **1** and **3** could be indexed to a single $P4_12_12$ γ-$LiAlO_2$ phase while for **2**, a secondary α-$LiAlO_2$ phase in the $R\bar{3}m$ space group (1.4 % by weight) was detected (Table 4.2). For the refinement of the γ-$LiAlO_2$ phase, the Li and Al atoms occupy the same site (4a) while the oxygen atoms are in a separate site (8b). Since Li and Al occupy the same site, the x and y coordinates were constrained to the same value and the z coordinate fixed to 0, as demanded by the Wyckoff positions of the $P4_12_12$ space group. The coordinates of the oxygen atom (8b site) were allowed to vary freely. The α-$LiAlO_2$ phase is described by a $R\bar{3}m$ space group and presents three different atomic positions 3a (Li), 3b (Al) and 6c (O). Only the z coordinate of the oxygen atom is refined, while the other atomic coordinates and site occupancies are fixed (see Appendix A, section A3 and Table 4.2). The occupancies were fixed to 1 in these refinements.

TGA and PXRD results show that the three precursors can be used to synthesise γ–$LiAlO_2$ by a simple thermolysis route at 800 ºC (See Table 4.2 for refined phases, and lattice parameters). This is in contrast to more conventional synthetic methods using alkoxide precursors via sol-gel or using ceramic synthesis which generally proceeds at

900–1000 ºC.[323–326] This presents advantages in the synthesis of pure $LiAlO_2$ samples, which is usually hampered by lithium sublimation at the temperatures at which the solid-state reaction takes place.[326] The lower temperature of γ-$LiAlO_2$ formation seen here can be attributed to the use of single-source precursors in which there is atomic mixing of Li and Al in the required 1:1 ratio before the start of the annealing process which should eliminate diffusion limitations. Not only can the desired composition be pre-formed in the SSP but also the structure. For example, **3** shows well defined $^{[4]}$Al environments in its pristine state (Figures 4.2 and 4.3). It also showed greater crystallinity at 500 ºC compared to **1** and **2**, demonstrating that the structure of the precursor can have a noticeable impact on the temperature at which the desired oxide phase starts to crystallise, which for **3** is ca. 500 ºC. Finally it was observed in further PXRD measurements (not shown here) that after prolonged exposure to air, γ-$LiAlO_2$ formed by thermolysis of **3** at 800 ºC partially decomposes forming $LiAl_2(OH)_7(H_2O)_2$ and Li_2CO_3, showing that this material is air-sensitive.[327] This has implications for the processing of the coated NMC particles, which should be carried out under dry atmosphere to prevent the conversion of the γ-$LiAlO_2$ coating into hydrated lithium alumina phases.

Table 4.2. Structure parameters obtained from Rietveld refinement of the PXRD patterns. The samples are compounds **1**-**3** annealed at 800 ºC for 4h.

Sample	R_{wp} / %	Refined phases	Space group	Wt %	a / Å	b / Å	c / Å
Precursor **1**	5.564	γ-$LiAlO_2$	$P4_12_12$	100	5.169	5.169	6.276
Precursor **2**	4.767	γ-$LiAlO_2$	$P4_12_12$	98.6	5.174	5.174	6.276
		α-$LiAlO_2$	$R\bar{3}m$	1.4	2.809	2.809	14.211
Precursor **3**	4.796	γ-$LiAlO_2$	$P4_12_12$	100	5.149	5.149	6.346

4.4.3. Solid-state NMR

The structures that **1**-**3** form below 800 ºC are of interest since these are the temperatures at which the annealing of the coated NMC811 particles will proceed. However, the fact that these materials are at least partially amorphous when annealing at these temperatures prevented the study of their structure by PXRD. For this reason, SSNMR spectroscopy was next used to determine their structures after annealing **1**-**3** at 500 ºC (Figure 4.7). Furthermore, since compound **3** showed the most promising properties as a precursor to γ-$LiAlO_2$, ^{27}Al-NMR of the sample annealed at 400 ºC was

also measured (the temperature at which annealing of the coated particles was carried out).

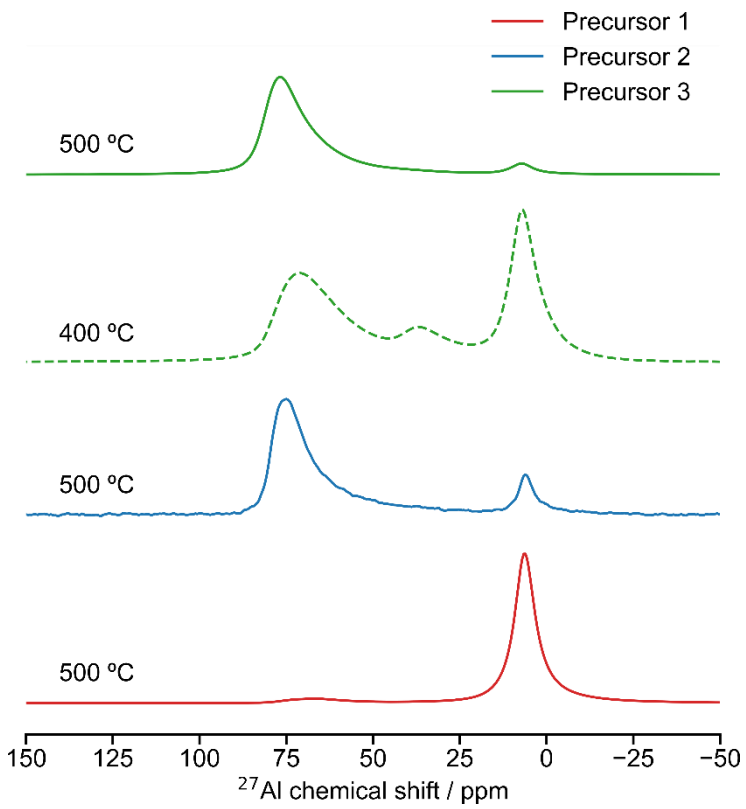

Figure 4.7. Solid-state ^{27}Al-NMR spectra of the annealed compounds **1-3** at 500 ºC and of **3** at 400 ºC are shown. The spectra of **3** were recorded at a magnetic field strength of 16.4 T and a MAS frequency of 50 kHz. The spectra of **1** and **2** were collected at a field strength of 11.7 T and a MAS frequency of 30 kHz. Only the central (isotropic) peaks are shown.

Compounds **2** and **3** form materials with very similar aluminium local environments. Both have mostly $^{[4]}$Al with a small amount of $^{[6]}$Al as expected for the formation of γ-$LiAlO_2$ type material. The lack of any $^{[5]}$Al peak, suggests the absence of amorphous Al_2O_3/$LiAlO_2$. On the other hand, the tailing of $^{[4]}$Al peaks to lower frequencies is a clear signature of disorder, in agreement with PXRD results, which showed broad peaks at annealing temperatures below 800 ºC. The $^{[6]}$Al environment in **2** can be assigned to the α-$LiAlO_2$ phase observed in the PXRD which may be already forming at 500 ºC. The amount of $^{[6]}$Al in **3** is lower compared to **2**, nevertheless it is possible that a small amount of α-$LiAlO_2$, which cannot be detected by laboratory PXRD is forming. Alternatively, it could be due to the $LiAl_2(OH)_7(H_2O)_2$ impurity which can form by contact with moisture. Heating **3** to 400 ºC leads to a clearly amorphous phase with a distribution of $^{[4]}$Al, $^{[5]}$Al and $^{[6]}$Al environments similar to those found in amorphous Al_2O_3, although at higher temperatures.[291] Finally, the product of decomposing **1** at 500 ºC has a very different

structure from that of the other two. It forms $^{[6]}$Al environments that only convert to the $^{[4]}$Al characteristic of γ-$LiAlO_2$ at higher temperatures, which are not being used here in order to avoid coating diffusion into the NMC811. The phase formed cannot be assigned to either of the high-pressure phases of α- or δ-$LiAlO_2$ due to the low crystallinity of the sample (Figure 4.5). Instead, it could be an amorphous $LiAlO_2$ with Al atoms in an octahedral geometry.

4.5. Coating NMC811 with $LiAlO_2$

4.5.1. Coating Deposition

In the previous sections, the structures of compounds **1-3** were studied in solution and in the solid state using NMR spectroscopy. Their thermolysis was also compared using TGA, PXRD and SSNMR. These studies showed that the three precursors can form a phase with composition $LiAlO_2$ when heated above their decomposition temperature (236-302 ºC) and that different structures and degrees of crystallinity can be obtained depending on the annealing temperature. The low solubility of **2** should in principle preclude its use in the solution deposition of $LiAlO_2$ coatings. Meanwhile, the two-steps decomposition mechanism of **1** (as observed by TGA) and the formation of a material containing mostly $^{[6]}$Al at 500 °C are less desirable properties compared with **3**, with its one step decomposition at 283 °C and lower-temperature crystallisation of γ-$LiAlO_2$. In any case, the three compounds will be tested in this section as coating agents to produce $LiAlO_2$ coatings onto NMC811 to see how the properties discussed affect the deposition.

A solution deposition method similar to the one employed in Chapter 3 was used to prepare the $LiAlO_2$-coated NMC811 with the whole process carried out under inert atmosphere. The same procedure was used to coat all the NMC811 materials discussed in this chapter, that is Al_2O_3 coated single-crystal NMC811 and uncoated polycrystalline NMC811. First, the precursor and NMC811 were loaded in a Schlenk flask so that the weight of the precursor corresponds to 1 % of the total solid weight. Dry THF was added, and the reaction mixture stirred under N_2 for 2 days at 60 ºC. To remove any unreacted precursor, the solvent was taken out by syringe, after which the sample was washed three times with dry THF (Figure 4.8). Finally, the coated NMC811 was dried under vacuum at 100 ºC for 2h and then annealed at 400 ºC under air for 4 h. This temperature was selected as it was found to lead to the best performing coatings in Chapter 3, due to the formation of an amorphous oxide layer, which should help with Li-ion conductivity

without increasing the cation mixing of the material or diffusing the coating in the near surface region.

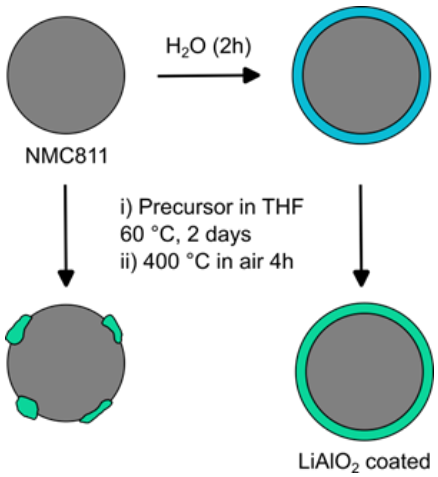

Figure 4.8. Scheme of the coating reactions. The pristine and water-treated NMC811 materials are coated by reaction with precursors **1**-**3** in dry THF for 2 days followed by annealing at 400 ºC under air for 4 h.

NMC811 with different morphologies and surface chemistries are used to test the scope of this coating procedure. In particular, single-crystal NMC811 (SC-NMC811) particles of 1 - 4 µm and polycrystalline NMC811 (PC-NMC811) particles of 10–20 µm are used. While the PC-NMC811 materials were pristine, EDS (Figure 4.10), and SS-NMR (Figure 4.16) showed that the SC-NMC811 used in this work was already coated with an Al_2O_3 layer (see Chapter 6 (experimental), section 6.3.1. for more information about the materials). Finally, SC- and PC-NMC811 samples that have been soaked in deionised water for 2 h while stirring and then dried under vacuum for 2 h at 50 ºC were coated following the same procedure (Figure 4.8). Electrochemical testing of these samples was then performed to help clarify if coating chemically degraded NMC811 with a lithium rich coating ($LiAlO_2$) could improve performance and how a pre-soaking step in water affects the coating deposition (Section 4.5.5.).

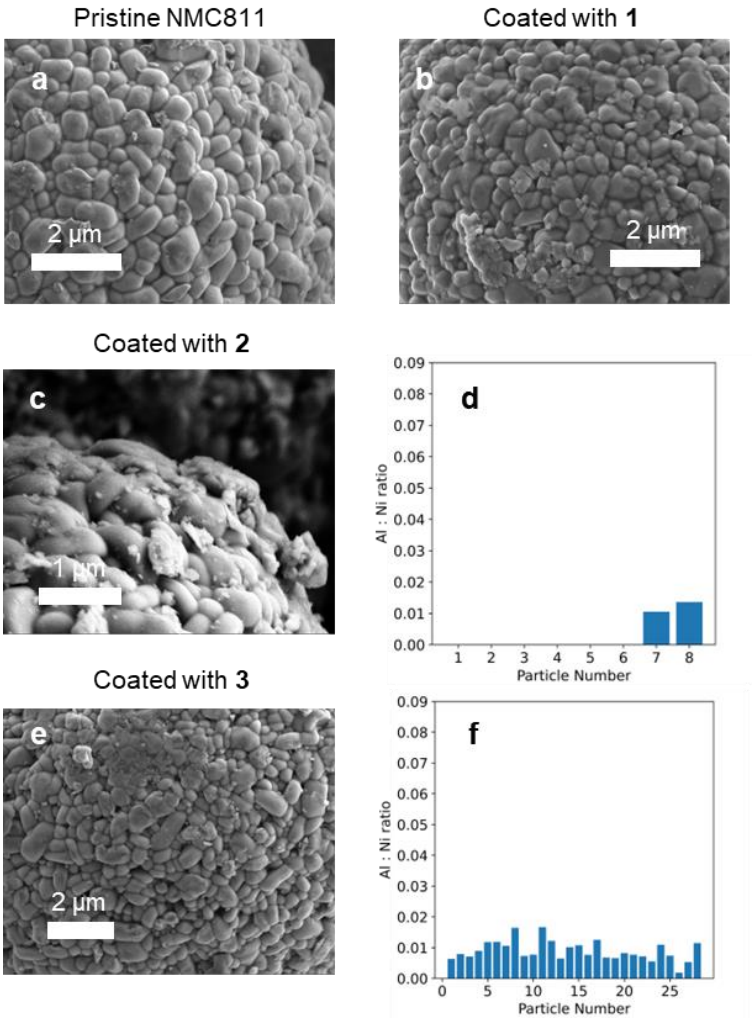

Figure 4.9. High-magnification SEM images of particles corresponding to pristine PC-NMC81 (a), PC-NMC811 coated with **1** (b), PC-NMC811 coated with **2** (c) and PC-NMC811 coated with **3** (e). The EDS Al : Ni ratios measured for individual particles are also shown for the PC-NMC811 coated with **2** (d) and **3** (f).

The SEM images in Figures 4.9 and 4.10 show that the pristine PC-NMC811 material is formed of 10–20 µm secondary particles that contain smaller 0.5–1 µm primary particles (same as Chapter 3). The surface morphology of the sample remains unchanged after coating PC-NMC811 with **1**. Furthermore, no aluminium signal could be observed by EDS. Coating with **2** on the other hand, led to significant coverage of some of the polycrystalline NMC811 secondary particles with chunks of material of 0.5–5 µm (Figure 4.9, c). Since **2** was not soluble in THF it can only be assumed that the dispersed particles of **2** aggregate on the surface of PC-NMC811 during the coating step. However, the EDS results of PC-NMC811 coated with **2** showed that the aluminium is localised in specific regions of the sample and that homogeneous deposition did not take place (Figure 4.9, d). Finally, coating with **3** led to subtle differences in the morphology of the of the

polycrystalline NMC811 particles with some areas covered by "patches" of coating (Figures 4.9e and 4.10b). The EDS measurements of PC-NMC811 coated with **3** showed that there is a consistent, although small, level of aluminium across different samples suggesting that the coating process was successful (Figure 4.9f).

Having characterised the thermolysis and solution deposition properties of compounds **1** - **3** in detail, it is now possible to compare them and decide which one has the best properties as a precursor to coat NMC811 with $LiAlO_2$. Compound **1** can be easily ruled out as it does not produce a coating on the surface of NMC811 as determined by SEM/EDS. Despite being fully soluble in THF, it did not react with NMC811 suggesting that the chemical stability of the precursor is also an important parameter that needs to be tuned by the choice of ligand. In this case benzoxy ligands lead to a precursor that does not react with the surface of the NMC811. This is presumably explained by the lower basicity of the alkoxide group due to the greater electron-withdrawing ability of the $PhCH_2$-group compared to aliphatic groups. Between **2** and **3** the choice is also clear based on the poor solubility of **2**, which leads to an uncontrolled, inhomogeneous deposition. It was therefore decided to continue with **3** for the water soaking / coating experiments, coating of SC-NMC811 and battery testing.

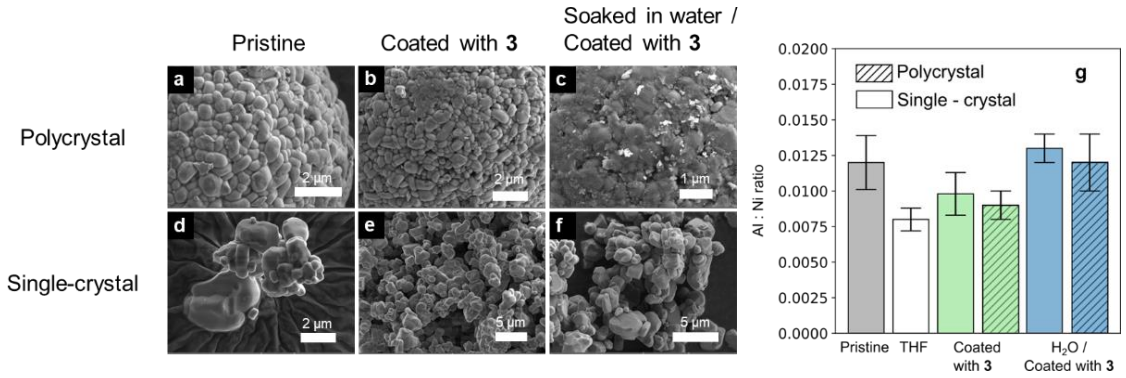

Figure 4.10. Representative SEM images of (a) pristine polycrystalline NMC811, (b) polycrystalline NMC811 coated **3,** (c) polycrystalline NMC811 soaked in water and coated with **3**, (d) Pristine single-crystal NMC811, (e) Single-crystal NMC811 coated with **3,** (f) Single-crystal NMC811 soaked in water and coated with **3**, (g) Bar-chart showing the Al : Ni ratios determined for each of the samples using energy-dispersive X-ray spectroscopy (EDS) data.

Figure 4.10 shows SEM images of PC-NMC811 and SC-NMC811 coated with **3** with and without a pre-soaking step in water. From the SEM images it can be seen that SC-NMC811 is formed of monolithic 1–4 µm primary particles that do not form secondary aggregates. PC-NMC811, on the other hand, is formed of smaller (<1 µm) primary

particles aggregated forming 10–20 μm secondary particles. This should make the SC-NMC811 more resistant to intergranular cracking while reducing the surface area. In comparison with the PC-NMC811, the SC-NMC811 material showed less obvious changes in morphology after coating with **3**. This could be an indication that the coating step was unsuccessful for SC-NMC811 or that, due to its smoother morphology, changes resulting from coating are more difficult to distinguish by SEM. The most striking change in morphology is seen for the PC-NMC811 sample soaked in water and coated with **3**. The surface of the particles is clearly covered by a thick surface layer and the primary particles of NMC811 can no longer be distinguished. This suggests that the pre-soaking in water is promoting coating deposition either by increasing the moisture levels on the surface of the NMC811 or by forming surface TM(O)-OH species that are more reactive with the precursor. This change in morphology was not as clear for the pre-soaked SC-NMC811.

Next, EDS was used to determine the changes in aluminium content after coating with **3** for the samples shown in Figure 4.10. First the Al : Ni ratios in the pristine materials were measured to determine the baseline levels. No Al was detected using EDS in the pristine PC-NMC811. On the other hand, the SC-NMC811 showed an aluminium signal (Al : Ni ratio 0.012 ± 0.019) suggesting that this commercial SC-NMC811 material was already coated or doped with aluminium during its synthesis process. Coating PC-NMC811 with **3** led to a consistent, small increase in aluminium content (Al : Ni ratio of 0.009 ± 0.001). For the SC-NMC811, similar Al : Ni values were observed for the pristine and coated with **3** materials. However, it should be noted that soaking SC-NMC811 in THF led to a decrease in the aluminium content on its own, so the Al : Ni ratio of the SC-NMC811 coated with **3** is greater than that of the SC-NMC811 soaked in THF suggesting that coating material has been deposited. The increase in Al content after coating is greater for PC-NMC811 than SC-NMC811 which could be due to the fact that the SC-NMC811 surface contains aluminium, probably in the form of a coating, hindering further deposition.

The EDS analysis of the coated samples pre-soaked in water showed that, compared to the coating of the pristine materials, a larger amount of aluminium is deposited for the soaked samples (both for the SC-NMC811 and the PC-NMC811) under the same conditions. In the case of the single-crystal NMC811, the changes in morphology after coating SC-NMC811 initially soaked in water are not as clear due to the smoother

morphology of the pristine SC-NMC811 material. Nevertheless, the Al : Ni ratio is clearly higher (0.013 ± 0.001) compared to the coated SC-NMC811 that has not been soaked in water. These SEM/EDS results suggest that the soaking in water and drying at 50 ºC under vacuum modifies the surface of the NMC811 and makes it more reactive with **3**. This could be a consequence of water molecules that are still adsorbed after the drying step and react with the precursor or the formation of additional reactive TM(O)-OH sites on the surface of the NMC811 after soaking in water.

4.5.2. XPS Characterisation

X-ray photoelectron spectroscopy (XPS) was next used to obtain a more detailed picture of the chemical species and elemental compositions of the surfaces. The XPS spectra were calibrated from the C 1s spectra (Figure 4.11), which were fitted following the procedure described in Chapters 2 and 3. In brief, the C 1s spectra were fitted to five components corresponding to aliphatic (C-C, C-H), ethers and alcohols (C-OH, C-O-C), ketones (C=O), esters (O-C=O) and carbonates (CO_3^{2-}) and the aliphatic peak was set to 284.8 eV. Unlike previous chapters, in this case all the samples were as-coated powders and so no contribution from a PVDF binder was seen in the C 1s spectra.

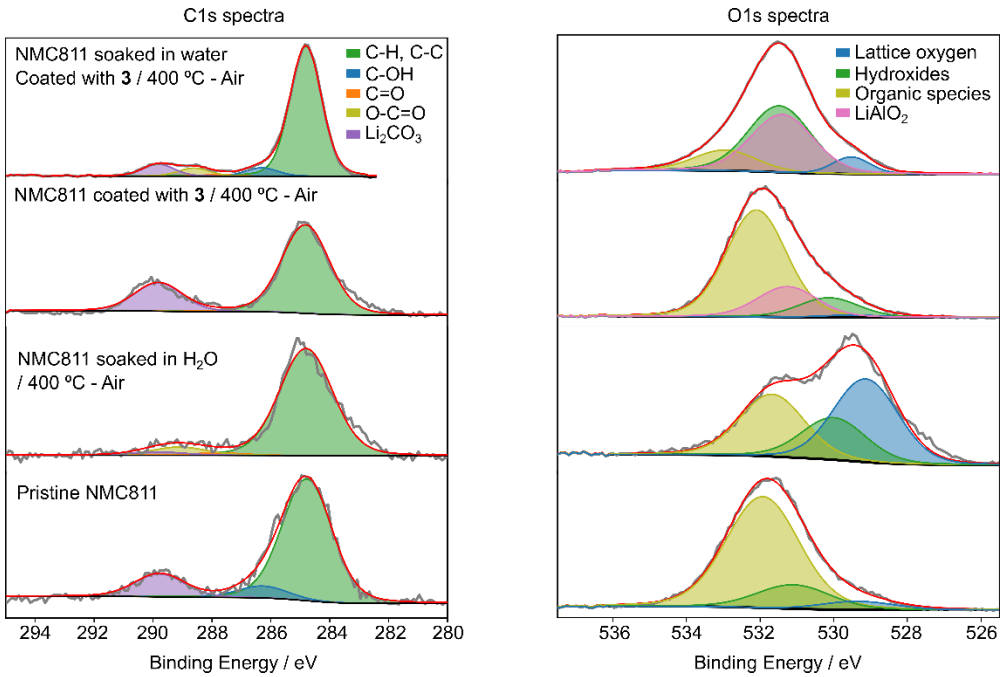

Figure 4.11. C 1s and O 1s high-resolution XPS spectra and fittings measured for the pristine PC-NMC811, PC-NMC811 soaked in water and annealed at 400 ºC, PC-NMC811 coated with **3**, and pre-soaked PC-NMC811 coated with **3**. All the coated samples undergo a post-annealing treatment at 400 ºC for 4 h after solution deposition of the coating.

Apart from being used for calibration, information about the surface chemistry of the samples can be extracted from the C 1s XPS spectra, especially when combined with the O 1s spectra (Figure 4.11). The O 1s spectra were fitted to three components for the case of pristine PC-NMC811 and PC-NMC811 soaked in water and annealed at 400 ºC: Lattice oxygen, hydroxides, and organic species. By comparing the O 1s and C 1s spectra it is possible to determine that the main oxygenated organic species contributing to the O 1s spectra is Li_2CO_3. An additional component was added for the coated samples to account for the presence of $LiAlO_2$. The organic species and $LiAlO_2$ components were constrained to the same full-width half maxima (FWHM). Since the lattice oxygen component tends to be narrower,[198] it was set as 0.6 times the FWHM of the other two as this gave the best fit for NMC811 soaked in water (Figure 4.11). Finally, the hydroxide component was allowed to vary freely in FWHM between 1 and 2. The position of the components was also constrained to the regions in which these peaks are expected to appear (values for the position constraints can be found in Table C2, Appendix C).[198]

The O 1s and C 1s spectra of the pristine PC-NMC811 show the presence of organic species on the surface. The lack of a lattice oxygen peak and the high intensity of the organic component of the O 1s spectrum suggest that the surface of the pristine NMC811

is significantly covered by Li_2CO_3. From the C 1s spectrum of the pristine PC-NMC811 we can conclude that the carbon species are mainly aliphatic with Li_2CO_3 also present in smaller amounts. After washing with water and annealing at 400 ºC under air, a decrease in organic species is observed in the O 1s XPS which also shows the emergence of a lattice oxygen peak, suggesting that this treatment cleans the surface of impurities. Furthermore, the C 1s spectrum shows that there is no Li_2CO_3 on the surface of the PC-NMC811 washed with water, confirming that the water treatment is decreasing the amount of Li_2CO_3 on the surface. The C 1s and O 1s spectra of the NMC811 coated with **3** are quite similar to those of the pristine NMC811 suggesting that the surface chemistry of the material was not affected by the coating step (low amounts of coating are present). On the other hand, the O 1s spectrum of the PC-NMC811 soaked in water and then coated using **3** is very different from that of the pristine PC-NMC811 or the pre-soaked NMC811 annealed without a coating step. Since these differences cannot be attributed to the change in measurement parameters, they must be due to the coating deposition. In fact, the position of the main O 1s component is 531.4 eV, close to literature values for $LiAlO_2$ O1s peak position (530.6 eV).[328]

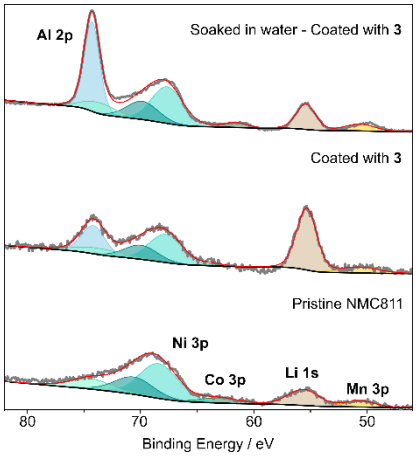

Figure 4.12. The Al 2p region of the XPS spectra of pristine PC-NMC811 and $LiAlO_2$ coated NMC (with and without a pre-soaking in water). The coating step results in the simultaneous deposition of aluminium and lithium on the surface of the particles as shown by the increased intensity of the Li 1s signal and the appearance of an Al 2p signal. The aluminium content of the coated NMC that was soaked in water is larger.

The Al 2p region of the XPS spectra (85–45 eV) is of particular interest as it contains information of the transition metals (Ni, Co, and Mn) as well as the aluminium and lithium bearing species present on the surface. Consequently, high-resolution spectra of the Al 2p region were recorded for pristine PC-NMC811, PC-NMC811 coated with **3** and PC-

NMC811 soaked in water and coated with **3** (Figure 4.12). The Al 2p region was fitted to 8 components. Al 2p, Mn 3p, Li 1s regions were fitted to a single peak each. The Co 3p was fitted to two peaks corresponding to the main peak and the satellite. The area of the Co 3p satellite was constrained to be 10% of that of the Co 3p main peak. The Ni 3p region was fitted to three peaks corresponding to Ni $3p_{3/2}$, Ni $3p_{1/2}$ and Ni 3p satellite. The Ni $3p_{1/2}$ was constrained to be half of the area of the Ni $3p_{3/2}$, same width and 2.2 eV above the position of the Ni $3p_{3/2}$ peak. The Ni 3p satellite was constrained to be 6eV above the Ni $3p_{3/2}$ peak and with a FWHM of 3 to 5 eV.[257,329]

The TM peaks remain in the same positions and relative intensities across the different samples indicated that there has not been any significant change in transition metals content or oxidation state induced by the washing or coating procedures. The Al 2p component is present in the sample coated with **3** further confirming the EDS results that the coating procedure results in the deposition of an aluminium-containing layer. The binding energy of the Al 2p peak is 74.18 eV, confirming the presence of Al^{3+} oxide species which typically appear at 73 - 74.5 eV.[105,316,328,330] The literature values for the Al 2p binding energy of $LiAlO_2$ coatings on NMC materials vary between 73.2 - 74.2 eV, whereas the values of Al_2O_3 coatings range between 73 - 73.5 eV. [105,316,328,330] These small differences in binding energy are typical for non-ideal surfaces where imperfect charge correction can occur. Nevertheless, $LiAlO_2$ tends to show at higher binding energies than Al_2O_3,[105,330] which suggest that the signal seen here (74.18 eV) could be from a lithiated alumina. More importantly, a sharp increase in the intensity of the Li 1s peak is observed for the sample coated with **3** compared to the pristine NMC811 material. This provides direct evidence that this precursor can successfully deposit Li and Al simultaneously, owing to its bimetallic nature.

The coated PC-NMC811 that has been soaked in water shows a much higher aluminium content compared to the coating of the untreated PC-NMC811. This is in line with the SEM/EDS measurements which showed that the soaking step induces the deposition of a thicker, more homogeneous coating layer. The binding energy of the Al 2p is 74.28 eV in this sample, indicating that the same Al^{3+} bearing material is deposited regardless of water pre-treatment. Finally, it is observed that the lithium content of the coated PC-NMC811 soaked in water is lower than that of the coated, untreated PC-NMC811 and similar to that of the pristine PC-NMC811. This may appear surprising considering that this precursor should lead to the simultaneous deposition of Li and Al. However, it should be remembered that the previous water treatment removed most of

the Li-bearing impurities from the surface, so the Li signal observed in this case comes solely from the coating whereas in the case of the coated, untreated PC-NMC811 the lithium signal had contributions from both the coating and the impurities. Furthermore, surface water could induce the preferential deposition of Al, leading to an Al_2O_3 / $LiAlO_2$ coating in which the Al : Li atomic ratio is higher than one.

4.5.3. Solid-state NMR Characterisation

A multinuclear SSNMR approach was then used to investigate the changes occurring in the surface and bulk of the material after soaking, annealing, and/or coating. First, ^{1}H and ^{7}Li SSNMR spectra of the pristine PC-NMC811 and PC-NMC811 soaked in water with and without an annealing step were measured to study how the proton environments change after the water-soaking treatment and if Li is extracted during soaking (Figure 4.13).

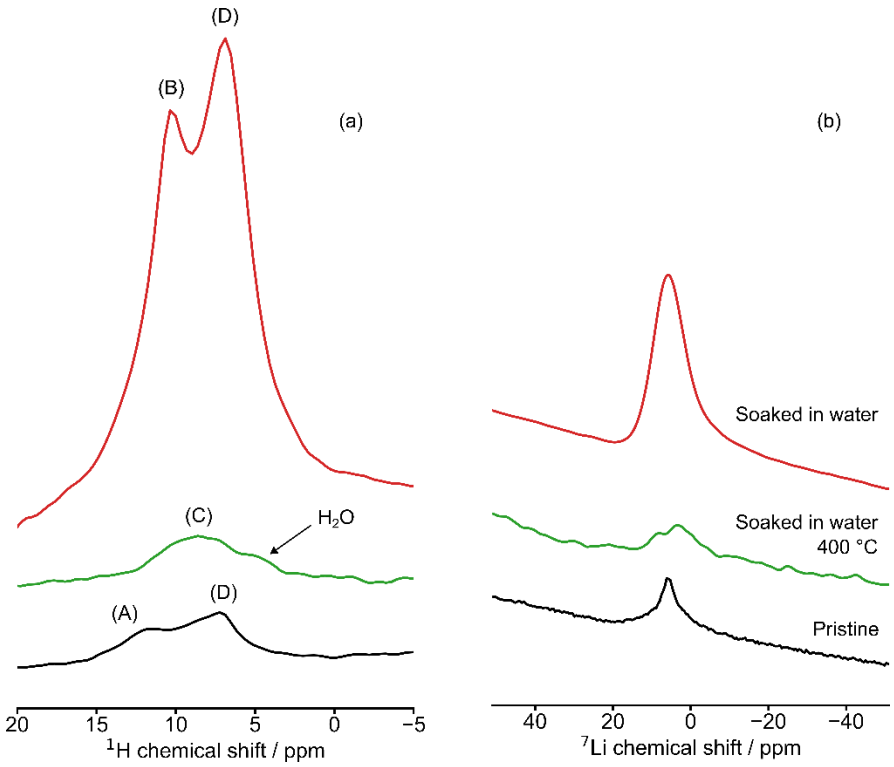

Figure 4.13. SSNMR spectra of pristine PC-NMC811 (black), PC-NMC811 soaked in water and dried at 50 ºC under vacuum (red), and PC-NMC811 soaked in water, dried at 100 ºC under vacuum and then annealed at 400 ºC under air for 4 h (green). The ^{1}H NMR (a) and ^{7}Li (b) spectra of these samples are shown in the Figure. Four different surface proton environments are seen: (A) 11.9 ppm and (B) 10.5 ppm, assigned here to carbonic acids, and (C) 8.9 ppm and (D) 7.1 ppm which are assigned to diamagnetic TM(O)-OH species. Additionally, a water environment is present in the soaked samples at ca. 5 ppm. The ^{7}Li spectra (b) show a peak at 6 ppm which is assigned to surface Li species. The spectra were recorded at a magnetic field strength of 16.4 T and a MAS frequency of 50 kHz and normalised to the sample mass and the number of scans. The recycle delay used for the ^{7}Li experiments is 100 ms whereas for the ^{1}H-NMR measurements, the optimal recycle delay was determined from a T_1 measurement using a saturation recovery experiment for each sample. All the spectra are normalised to the number of scans and mass of the sample. The slope in the baseline in (b) is due to the overlapping peak corresponding to bulk Li, which appears as a broad peak centred at 290 ppm with a linewidth of 1400 ppm due to shifting of the Li signal caused Fermi contact shift, induced by the various paramagnetic environments present in the bulk of NMC811 (See Appendix C, Figures C17–21 for the full spectra).

The ^{1}H SSNMR spectrum of the pristine PC-NMC811 is shown in Figure 4.13. All the proton NMR spectra showed a broad feature centred at 0 ppm and with a linewidth of approximately 200 ppm due to the probe background (Appendix C, section C6.1). Narrower peaks are due to protic surface species. The most likely surface species are water, LiOH, carbonic acids (such as $LiHCO_3$) and diamagnetic TM(O)-OH species. Since LiOH appears at negative ppm (-1 to -1.5 ppm),[331] the peaks observed here could

only be water, hydroxyl groups or carbonic acids. Water on oxide surfaces has a ^{1}H chemical shift of ca. 5 ppm,[332–334] and it is present in both soaked samples (with and without an annealing step, Figure 4.13). The peaks at higher shifts A and B are likely to be $LiHCO_3$, and the remaining peaks C and D are attributed to diamagnetic TM(O)-OH species where the TM are low-spin Co(III) and Ni(IV). These drastic changes in the ^{1}H NMR spectrum seen when the material is soaked in water and then dried at 50 ºC for 2 h suggest that water soaking promotes the formation of TM(O)-OH sites and that drying at 50 ºC under vacuum for 2 h does not fully remove adsorbed water from the surface. Furthermore, an increase in Li-containing surface species is seen after soaking in the ^{7}Li NMR, suggesting that the soaking step extracts Li from the particles forming surface Li species. After heating the PC-NMC811 soaked in water at 400 ºC, the ^{1}H and ^{7}Li spectra become less intense, suggesting that most of the surface water has been desorbed and that the surface lithium species have been re-incorporated in the lattice. These findings support previous literature which suggested that NMC811 forms TM(O)-OH surface species and LiOH upon exposure to water.[288] The authors observed that the heating step after washing had the biggest influence in the capacity retention of the material and proposed, through careful TGA-MS measurements, that the formed Ni(O)-OH evolves into NiO with H_2O and O_2 as side products.[288]

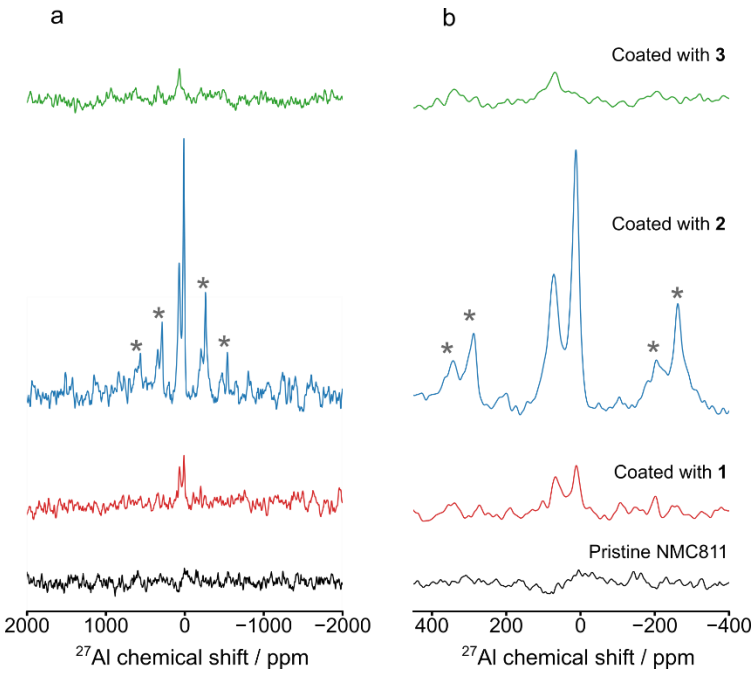

Figure 4.14. ^{27}Al NMR of PC-NMC811 coated with precursors **1**, **2** and **3**. (a) Full view of the spectra (b) Zoom-in on the isotropic region. The spectra were recorded at a magnetic field strength of 16.4 T and a MAS frequency of 50 kHz and normalised to the sample mass and the number of scans. The spinning-sidebands are marked with asterisks.

^{27}Al SSNMR spectroscopy was then used to investigate the coatings produced with **1**-**3** (Figure 4.14). Coating with any of the three precursors leads to the deposition of aluminium but the amount and structure of the coating changes significantly depending on the precursors used. Coatings from precursors **1** and **3** show low signal intensity while coating with precursor **2** leads to a more intense signal. Since precursor **2** was not soluble and the coating in this case was the result of the agglomeration of precursor particles on the NMC, it is expected that this uncontrolled deposition will result in higher aluminium content, although less homogeneously distributed throughout the sample surface as demonstrated in the EDS section. In contrast with the EDS results, which showed no Al content for the sample coated with precursor **1**, SSNMR shows the presence of two weak Al resonances at 67.6 and 11.9 ppm which are assigned to $^{[4]}$Al and $^{[6]}$Al environments, respectively. The fact that no aluminium was detected by EDS for coating with **1** suggests that the aluminium species observed here are not a surface coating but a more localised precipitate. Finally, coating with **3** leads to the deposition of a coating layer with a single $^{[4]}$Al environment at 68.2 ppm. Although the presence of $^{[4]}$Al is indicative of γ-$LiAlO_2$, this compound would show a $^{[4]}$Al signal at 80-82 ppm,[275,276] so the coating seen here is assigned to an amorphous $LiAlO_2$ phase bearing mostly $^{[4]}$Al environments.

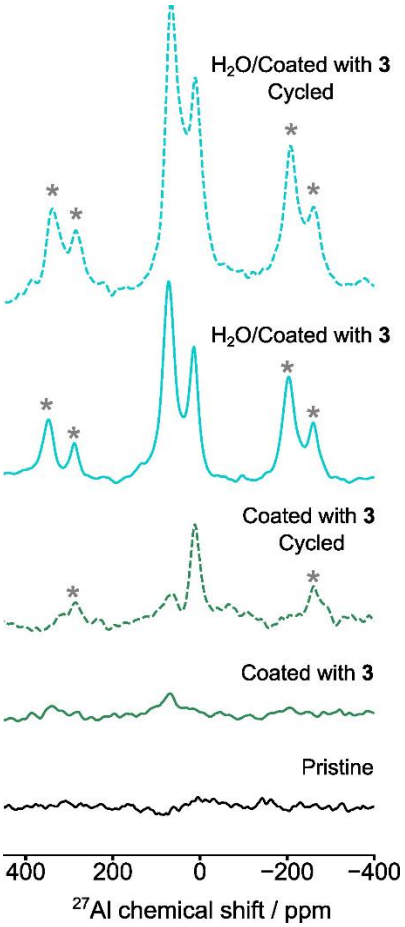

Figure 4.15. ^{27}Al NMR of coated polycrystalline NMC811 materials. The spectra were recorded at a magnetic field strength of 16.4 T and a MAS frequency of 50 kHz and normalised to the sample mass and the number of scans. The spinning sidebands are marked with asterisks.

Next the ^{27}Al NMR spectra of the coated PC-NMC811 with and without a pre-soaking step in water are discussed. Compared to the coated PC-NMC811, the coating of the PC-NMC811 soaked in water showed a much more intense aluminium signal which is in good agreement with the EDS and XPS results. The distribution of $^{[4]}$Al, $^{[5]}$Al and $^{[6]}$Al environments is very different from previous Al_2O_3 coating materials formed by annealing at the same temperature (400 ºC) that were discussed in Chapter 3. Two aluminium environments are seen at 72.6 and 14.1 ppm which are assigned to $^{[4]}$Al and $^{[6]}$Al, respectively. A weak $^{[5]}$Al signal is seen in this material and the predominant coordination environment is $^{[4]}$Al (Figure 4.15). This is assigned to an amorphous $LiAlO_2$ / Al_2O_3 with the aluminium occupying $^{[4]}$Al, $^{[5]}$Al and $^{[6]}$Al sites with $^{[5]}$Al < $^{[6]}$Al < $^{[4]}$Al. The assignment is based on the peak positions, the fact that annealing the precursor under air at this temperature led to an amorphous phase as determined by PXRD, and the higher Al content detected by XPS in the pre-soaked sample.

To investigate if long-term cycling had any effect on the coating structure, ^{27}Al SSNMR was measured on cycled electrodes (Figure 4.15). These were obtained after 300 charge-discharge cycles in half cells (more details on the electrochemical cycling in section 4.5.5.). The ^{27}Al SSNMR spectra of the cycled samples is almost identical to that of the as-coated materials both in intensity and in chemical shift and distribution of aluminium environments suggesting that the coating is quite stable under cycling conditions. The only difference was the appearance of a $^{[6]}$Al environment in the cycled PC-NMC811 coated with **3** (not soaked) which could be the result of scrapping some Al_2O_3 from the current collector or the deposition of some Al that was dissolved from the current collector into the electrolyte during cycling. In any case, the $^{[4]}$Al peak remains unchanged.

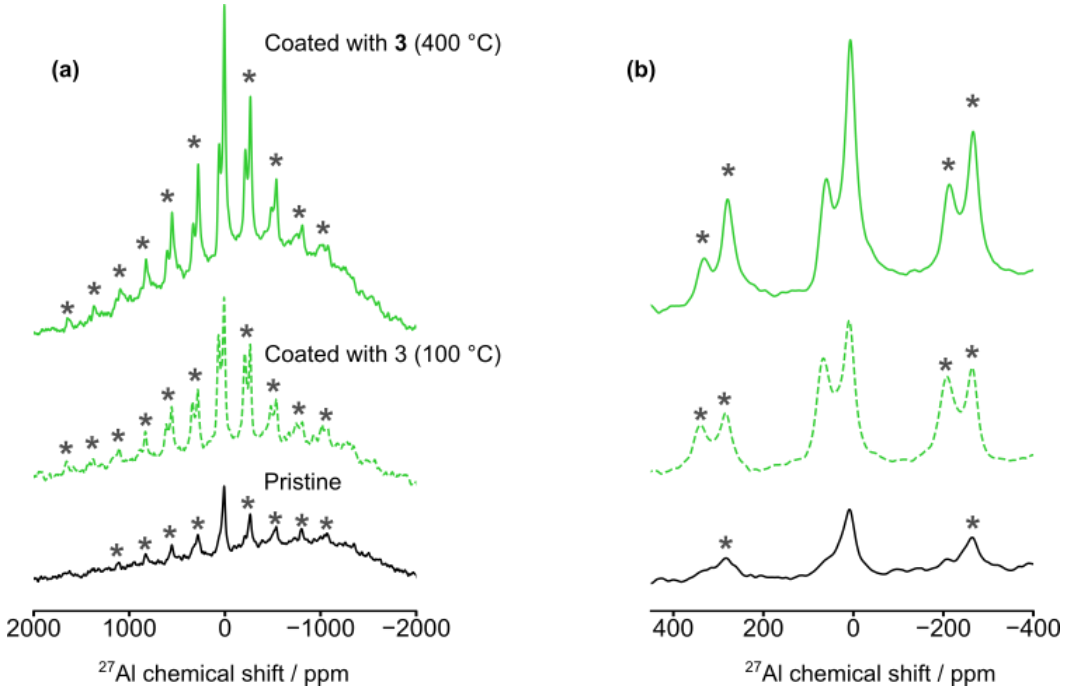

Figure 4.16. ^{27}Al SSNMR of the SC-NMC811 materials. (a) Full spectra, (b) zoom-in on the isotropic region. The spectra were recorded at a magnetic field strength of 16.4 T and a MAS frequency of 50 kHz and normalised to the sample mass and the number of scans. The spinning sidebands were marked with stars.

Pristine and coated SC-NMC811 materials were also studied by ^{27}Al SSNMR. In agreement with the EDS results, SSNMR shows that the pristine SC-NMC811 material contains aluminium. The line shape of the pristine SC-NMC811 spectrum is dominated by the $^{[6]}$Al environments at 9.4 ppm, consistent with the presence of a crystalline form of aluminium oxide, most likely boehmite (γ-AlOOH) based on the chemical shift.[335] Furthermore, an extremely broad resonance centred at -800 ppm is present. The position

and width of the peak is very similar to the one observed in Chapter 3, which resulted from diffusion of Al^{3+} ions from the Al_2O_3 coating into the NMC811 induced by high-temperature annealing. These results show that aluminium is present both in the surface of the pristine SC-NMC811 as a coating and in the bulk as dopant, suggesting that the as-received SC-NMC811 may have undergone a post-annealing treatment similar to the one developed in Chapter 3. The ^{27}Al SSNMR of the SC-NMC811 coated with **3** and dried at 100 ºC under vacuum shows a new $^{[4]}Al$ environment at 67.4 ppm that was not observed in the pristine SC-NMC811 material. This, combined with the EDS results which showed a uniform increase in surface aluminium content compared to the SC-NMC811 washed in THF, confirms that the coating deposition has taken place successfully. When the coated SC-NMC811 is heated under air at 400 ºC for 4 h, the paramagnetic Al signal increases in intensity indicating growth of the Al-doped NMC811 phase. It should be noted that this is below the temperature at which Al_2O_3 starts to diffuse into NMC811 (T > 500 ºC), however, this is a different case as the pristine NMC811 material already presented surface doping which may show a lower activation energy for this diffusion process with further annealing.

4.5.4. Powder XRD Characterisation of the Pristine and Coated Materials

PXRD measurements were performed on the pristine and coated SC-NMC811 and PC-NMC811. The aim of this was to characterise the long-range structure of these materials, to see if a secondary Al-doped NMC811 phase could be observed in the pristine SC-NMC811 and to determine whether the coating or soaking steps had any influence on the long-range structure of the materials.

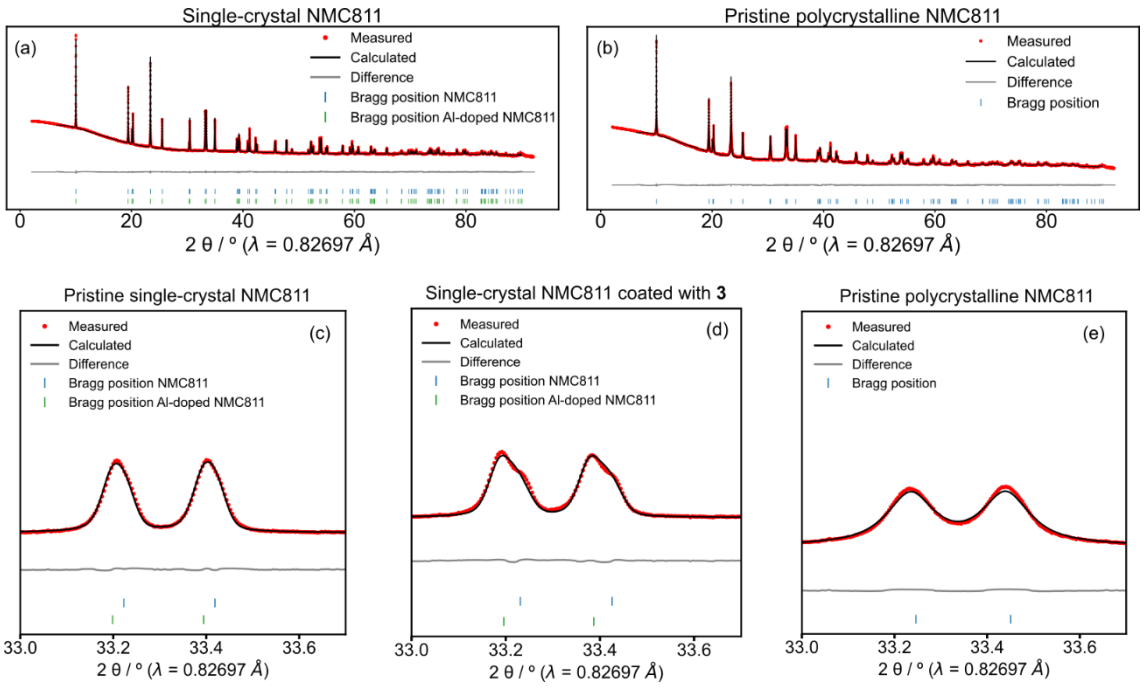

Figure 4.17. Synchrotron powder XRD patterns and Rietveld refinements of (a) pristine SC-NMC811, (b) pristine PC-NMC811, (c) zoom-in on 108 and 110 reflections of pristine SC-NMC811, (d) zoom-in on 108 and 110 reflections of SC-NMC811 coated with **3** and annealed at 400 ºC under air for 4 h. (e) zoom-in on 108 and 110 reflections of PC-NMC811.

The refinement of the PC-NMC811 structure showed the pattern of a single-phase material with a well-defined layered structure that could be indexed in the $R\bar{3}m$ space group. Furthermore, a low level of anti-site mixing (2.21% of Ni is Li sites) was observed. After coating with **3** and annealing, the PC-NMC811 structure shows a modest increase in cation mixing (3.58%) and a slight broadening of the peaks suggesting that the heat treatment induces some disorder. The pristine SC-NMC811 material showed splitting of all the reflections, particularly clear in reflections 108 and 110 showed in Figure 4.17. This is indicative of the presence of two phases and becomes more pronounced after coating and annealing at 400 ºC for 4h under air. Previous work has shown that doping NMC with increasing amounts of aluminium leads to an increase in the c lattice parameter.[336] The experimental data of SC-NMC811 obtained here was fitted to two phases by Rietveld refinement, and since one of the phases had a larger c lattice parameter they were assigned to NMC811 and an Al-doped NMC811 as in Chapter 3. The Al-doped NMC811 phase is formed by substituting TM sites with Al ions and has larger c parameters compared to the undoped phase (Table 4.3). In contrast to the Al-doped PC-NMC811 of Chapter 3, which showed 5% weight of secondary phase (which was assigned to Al-doped NMC), these SC-NMC811 materials show much larger extent of

doping according to the Rietveld refinement. Both the pristine SC-NMC811 and the coated SC-NMC811 dried at 100 ºC under vacuum show the same amount of Al-doped NMC811 phase (57% weight) but that annealing at 400 ºC under air for 4h leads to the growth of the Al-doped NMC phase which becomes 62% weight of the materials weight (Table 4.3), in good agreement with the SSNMR data which shows a growth in the signal from the paramagnetic Al environments. The cation mixing results for SC-NMC811 showed that the Al-doped NMC811 phase had generally a larger amount of Ni in Li sites compared to the undoped phase, which is consistent with the idea that the aluminium is displacing some of the Ni atoms. However, no clear differences in the cation mixing were seen before and after annealing for the SC-NMC811 material. Finally, no $LiAlO_2$ phase was observed in the synchrotron PXRD of the coated materials. This is not surprising, despite the high sensitivity of synchrotron PXRD, given the amorphous nature of the coatings at 400 ºC and the small amount in which they are present (< 1 wt%).

Taken together, the SSNMR and PXRD results suggest that the pristine SC-NMC811 was synthesised following a similar procedure to the one shown in Chapter 3. The material was probably first synthesised as SC-NMC811 without aluminium and then coated and annealed. This would explain why the synchrotron PXRD shows two phases; If the aluminium was introduced as a dopant during the synthesis of the SC-NMC811 then it would likely be a single Al-doped NMC811 phase. Furthermore, the higher weight percentage of the Al-doped NMC phase in the SC-NMC811 suggests that a higher Al_2O_3 wt % was used with longer annealing times or higher temperatures.

Table 4.3. Summary of the phases refined and lattice parameters and R_{wp} (%) obtained for each of the Rietveld refinements. All the phases were indexed to the space group $R\bar{3}m$.

Sample	R_{wp} / %	Refined phases	Wt %	a / Å	b / Å	c / Å
Polycrystalline (PC) NMC811	3.541	NMC811	100	2.87	2.87	14.188
PC-NMC811 coated with **3** / 400 °C (air)	4.898	NMC811	100	2.869	2.869	14.187
Single-crystal (SC)-NMC811	4.204	Al-NMC	57	2.875	2.875	14.205
		NMC	43	2.873	2.873	14.196
SC-NMC811 coated with 3 100 °C (vacuum)	4.114	Al-NMC	57	2.875	2.875	14.207
		NMC	43	2.873	2.873	14.196
SC-NMC811 coated with 3 400 °C (air)	3.118	Al-NMC	62	2.876	2.876	14.206
		NMC	38	2.872	2.872	14.192

In addition to the synchrotron PXRD data, other samples were measured using an in-house diffractometer (PC-NMC811 coated with **1** and **2**, soaked in water, and soaked in water / coated with **3**). The results are summarised in Table 4.4 and the PXRD patterns are shown in the (Appendix A, section A3.2). No differences in the lattice parameters were observed between the pristine sample and samples coated with precursors **1-3**, suggesting that the coating process did not affect the bulk structure significantly. No significant difference was observed in the cation mixing values between the pristine PC-NMC811 and the PC-NMC811 coated with **1-3** which had values between 1.47 and 1.74% (Appendix A, section A3.2.2). This further confirms that the structure of the NMC811 is not being affected by this treatment although it contradicts the previous synchrotron PXRD results which showed a modest increase in cation mixing after heating PC-NMC811 at 400 ºC under air in the presence of a coating. The reasons for this difference could be the lower resolution of the laboratory-based diffraction data and the well-defined peak shapes used in the refinement of the synchrotron-based data which allows detection of small changes in cation mixing.

Soaking NMC811 in water (both with and without a post-annealing step) did not lead to significant changes in lattice parameter (Table 4.4). This is consistent with the ^{7}Li SSNMR results that did not show any change in 'bulk lithium' signal in the ^{7}Li NMR spectra (Appendix C, section C6.2), suggesting that this delithiation is confined to the surface of NMC811 and does not disrupt the bulk of the material.

Table 4.4. R_{wp} and lattice parameters obtained from Rietveld refinement of laboratory data.

Sample	**R_{wp} / %**	**a / Å**	**b / Å**	**c / Å**
NMC811	1.906	2.873	2.873	14.212
Coated with **1** / 400 ºC (air)	5.076	2.874	2.874	14.213
Coated with **2** / 400 ºC (air)	5.112	2.874	2.874	14.212
Coated with **3** / 100 ºC (vacuum)	2.723	2.873	2.873	14.212
Soaked in water	4.873	2.874	2.874	14.207
Soaked in water / 400 ºC (air)	4.802	2.874	2.874	14.206
Soaked in water - Coated with **3** / 400 ºC (air)	3.032	2.874	2.874	14.214

4.5.5. Electrochemical Testing

The effect of soaking in water and coating with $LiAlO_2$ on the bulk and surface of NMC811 materials with different morphologies was investigated using multiple characterisation techniques (SEM-EDS, XPS, PXRD and SSNMR). These findings are now related to their electrochemical performance by testing in half cells (vs. Li).

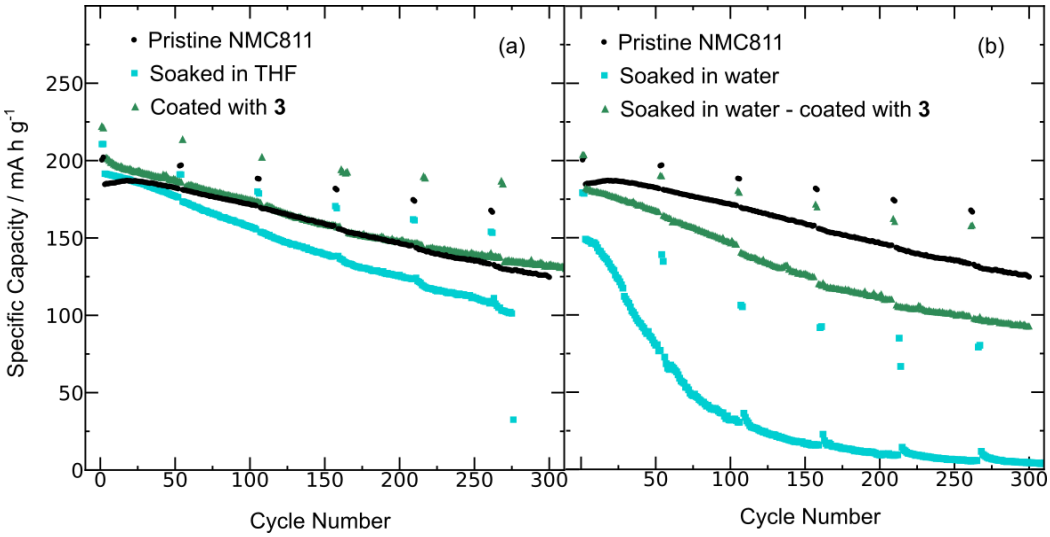

Figure 4.18. Long-term electrochemical cycling data (Specific Discharge Capacity/ mA h g^{-1} vs. cycle number). Results for the pristine PC-NMC811, PC-NMC811 coated with **3** and control uncoated sample (a). Results of PC-NMC811 soaked in water with and without a further coating step (b). These electrochemical measurements were carried out in half cell configuration (vs. Li) between 3 and 4.3 V. The cycling was performed at C/2 rate and slow C/20 cycles were included every 50 cycles.

Long-term galvanostatic cycling of PC-NMC811 treated under the various conditions described in this study is shown in Figure 4.18. First, the trends in capacity retention at slow (C/20) and fast (C/2) cycling rates will be discussed. The PC-NMC811 soaked in THF was a control in which PC-NMC811 was subjected to the same treatment as in the coating process but without addition of precursor, i.e., it was stirred in THF at 60 ºC for 2 days and then dried under vacuum at 100 ºC and annealed under air at 400 ºC for 4h. This was done to determine what the effect of THF soaking and annealing under air on its own is (without the coating). This showed consistently (four repeats, Appendix D, section D3) that the capacity retention is lower at C/2 (13.7% less) and C/20 rates (10% less) after THF treatment compared to the pristine NMC811 material. This is in contrast to the previous toluene washing experiments (Chapter 3) which showed that washing in toluene leads to a small improvement in capacity retention which was attributed to the removal of surface impurities. Unlike toluene, THF is a coordinating solvent with high affinity towards lithium so it may be extracting some of the lithium from the material.

Another possibility is that it is forming a passivating organic layer on the surface. The ^{7}Li SSNMR results do not support the lithium extraction hypothesis (Appendix C, Figure C17) as the surface lithium peak does not change in intensity after soaking in THF. On the other hand, XPS results for the sample coated with **3** showed an increase in surface organic species (Figure 4.11) which could not be attributed to the precursor as TGA analysis showed that the ethoxide ligands come off at temperatures below 400 ºC. Furthermore, ^{1}H SSNMR of the THF-soaked PC-NMC811 shows that an additional surface proton environment appears in between the TM(O)-OH signals after soaking in THF (ca. 10 ppm) and that the spinning sidebands increase in intensity suggesting that a new protic species has been deposited on the surface after THF washing (Appendix C, Figure C13). After annealing at 400 ºC under air, there is an increase in proton signal which was not seen for the water soaked samples. Heating THF at 500 ºC leads to decomposition to form aldehydes, and ethylene.[337] However, other studies have revealed that a range of metal-mediated ring-opening reactions of THF can occur at room temperature.[338] Although the precise species formed at 400 ºC over an NMC811 surface by THF decomposition are beyond the scope of this study, what is clear is that soaking in THF and heating at 400 ºC under air leads to an increase in protic surface species suggesting that the loss in capacity retention seen for the THF-soaked NMC811 comes from the deposition and decomposition of THF on the surface.

Coating PC-NMC811 with **3** led to more variable results in three repeats in terms of absolute capacity and capacity retention (see Appendix D, section D3). Nevertheless, in all the repeats the capacity retention at C/2 and C/20 was higher than or equal to that of pristine NMC811. For the data shown in Figure 4.18, similar capacity retention is seen at C/20 for the coated and pristine sample (82.7 and 86.2% respectively) whereas a small improvement in capacity retention is seen at C/2. Compared to the control THF samples, there is a clear improvement in capacity retention for the coated materials which showed 6.5% more capacity retention at C/20 and 5.3% at C/2. These results provide evidence that coating polycrystalline NMC811 with $LiAlO_2$ has a positive effect on the long-term capacity retention of the material during cycling in Li-ion half cells.

Compared to the coating and THF soaking experiments, water soaking and coating of the water soaked NMC811 led to a larger change in the capacity retention of the materials. Soaking PC-NMC811 in water for 2h at room temperature, followed by drying at 50 ºC under vacuum led to a decrease in initial capacities (Appendix D, section D3). Including an annealing step further decreases the capacity retention of the material with a 70.2% loss at C/2 and 47.3% at C/20 (Figure 4.18). These changes have been observed in literature,[288,298,299] and can be understood based on the lithium extraction that was seen by SSNMR. The long-term effect in the capacity retention indicates that the lithium extraction is accompanied by an irreversible structural change in the NMC811. Furthermore, although the rate of degradation is substantially increased both at C/2 and C/20 after soaking in water, it is much more marked at C/2 indicating that this loss of capacity is at least in part a kinetic effect, pointing at the formation of a resistive NiO layer on the surface. If water-soaked PC-NMC811 is then coated (mixed with a THF solution of **3** for 2 days at 60 ºC and annealing at 400 ºC under air), an impressive recovery of the capacity is observed (37.8 vs 78.8% capacity retention at C/20 and 22.8 vs. 58.2% at C/2). To ensure reproducibility, a duplicate of the measurement was performed in two different batches of PC-NMC811 materials subjected to the same soaking and coating treatment, and the same results were obtained (Appendix D3). Previous work has shown that mixing NMC622 with LiOH and annealing at 800 ºC under oxygen for 2h leads to the recovery of surface layered structure with Li insertion and oxidation of Ni^{2+} to Ni^{3+} which led to an increased specific capacity and capacity retention.[317] In order to see a recovery of capacity, the coating treatment must reverse some of the structural changes happening during the water soaking and annealing. It is proposed that the improved capacity retention seen in the $LiAO_2$ coated PC-NMC811 that has been pre-soaked with alumina proceeds by the same mechanism (NiO oxidation and Li re-insertion) although at lower annealing temperature (400 ºC) and with the simultaneous formation of a $LiAlO_2$ coating. Finally, although the performance recovery is not complete, it is possible that by optimising the precursor amounts and annealing step, further capacity retention can be regained.

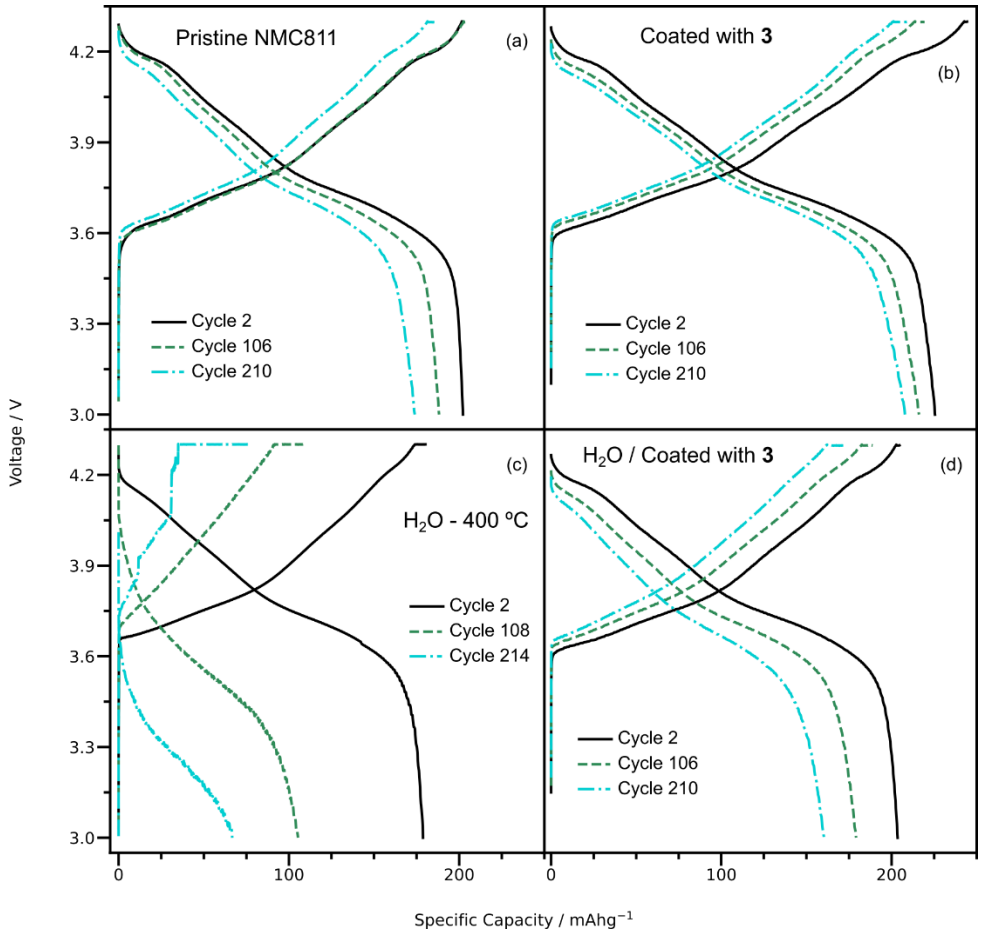

Figure 4.19. Voltage profiles measured for the slow cycles of PC-NMC811 samples. (a) Pristine PC-NMC811, (b) PC-NMC811 coated with **3**, (c) PC-NMC811 soaked in water and then annealed at 400 ºC under air. (d) PC-NMC811 soaked in water, coated with **3** and annealed under air at 400 ºC.

The voltage profiles at C/20 give insight into the electrochemical differences observed between samples in the long-term cycling plot (Figure 4.19). Compared to the pristine PC-NMC811 material, PC-NMC811 coated with **3** delivers higher capacity on charge and discharge on the second cycle without an increase in overpotential. The coating process allows more Li to be extracted and re-inserted in the NMC811 without showing any sign of interfacial resistance in the C/20 cycling profile of cycle 2. In cycle 106 and 210, the coated material displays more charge capacity loss than the pristine and requires a CCCV step to access the full charge capacity. Soaking in water followed by annealing under air leads to a very significant change in the voltage profiles. Generally, lower capacities are obtained from the first and second cycles, long CCCV steps at the end of charge and higher overpotentials are required both at charge and discharge (3.7 V start of charge vs. 3.6 V for the pristine PC-NMC811). The capacity loss is much more severe with almost half of the discharge capacity lost at cycle 108. The shape of the curves at cycles 108 is also different from the expected electrochemical cycling of NMC811 (without the 4

plateaus on charge and 3 on discharge), suggesting that the material is fully degraded. Coating a water soaked NMC811 (not annealed) leads to a recovery in capacity retention. The lower capacities and need for a CCCV step in cycle 2 indicate that the surface of the material has not been fully regenerated by the coating treatment. Nevertheless, higher capacities can be achieved in cycled 2 compared to the pre-soaked PC-NMC811 and voltage profiles with the expected features for NMC811 are observed also later in cycling, showing a significant improvement in cycling stability compared to the uncoated NMC811 soaked in water.

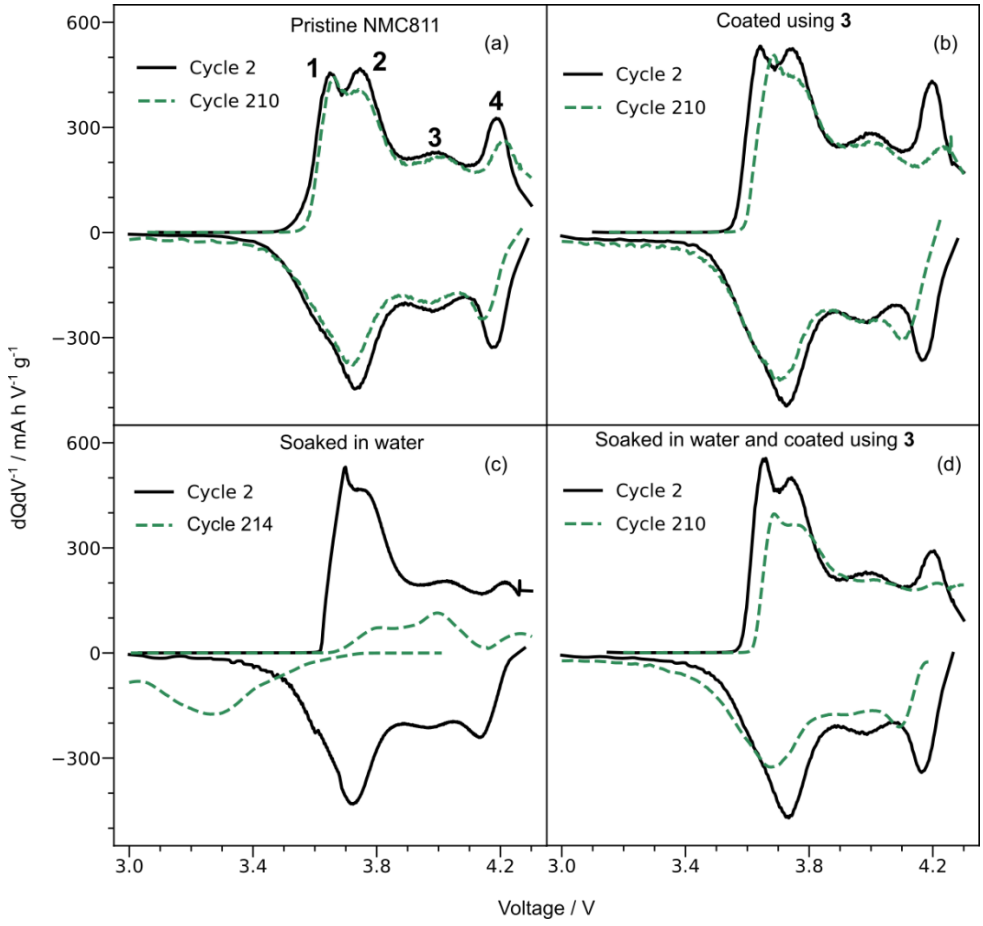

Figure 4.20. dQ/dV profiles measured for the slow (C/20) cycles of PC-NMC811 samples. (a) Pristine PC-NMC811, (b) PC-NMC811 coated with **3**, (c) PC-NMC811 soaked in water and then annealed at 400 ºC under air. (d) PC-NMC811 soaked in water, coated with **3** and annealed under air at 400 ºC.

The pristine PC-NMC811 shows good reversibility in the dQ/dV profile with highly symmetric charge-discharge curves. Clearly, most of the capacity fade in pristine PC-NMC811 comes from processes 2 and 4 (Figure 4.20). These coincide with the start and end of charge states, which are characterised by a lower Li mobility.[265] The dQ/dV plot of cycle 2 of PC-NMC811 coated with **3** shows very similar features to the pristine PC-NMC811 suggesting that the coating treatment has not changed the electrochemistry of the material significantly on the first cycles. The dQ/dV peaks are more intense in cycle 2 (particularly processes 1 and 4, Figure 4.20) compared to the pristine NMC811 sample meaning that more capacity is obtained out of these processes. These regions are more susceptible to capacity loss from the formation of insulating surface layers due to their inherent low Li mobility. The $LiAlO_2$ coating may be enhancing this Li transport across the NMC/electrolyte interface thereby allowing higher specific capacities.

Further differences between the coated and pristine PC-NMC811 electrochemistry can be observed upon cycling. Process 4 is suppressed to a greater extent after 210 cycles in the coated sample and the profile becomes less symmetric with the discharge peaks shifting to lower voltages. These results suggest that the coating is doing little to prevent the rock-salt formation which occurs spontaneously upon cycling. In fact, the greater polarisation seen for the coated sample suggests that a less ionically conductive surface forms after prolonged cycling. The improvements in capacity retention are likely to come from an initial rearrangement of the structure, with Li re-insertion and possibly less electrolyte oxidation, as the surface of the CAM is at least partially covered by $LiAlO_2$.

The dQ/dV analysis of the PC-NMC811 soaked in water and annealed under air shows that the loss in capacity comes mainly from the suppression of the high voltage process while process 1 is shifted to higher voltages (Figure 4.20). Furthermore, significant polarisation is observed even at cycle 2. This is all consistent with the hypothesis of the washing treatment creating a thick rock-salt layer on the surface. At cycle 214, a completely different dQ/dV profile is observed, suggesting that the material is fully degraded at that point. The peaks corresponding to processes 1 and 4 are almost fully suppressed on charge and presence of a broad peak only at low voltages on discharge. Coating the PC-NMC811 soaked in water using **3** leads to a recovery of the capacity and an electrochemistry that is again much closer to that of the pristine PC-NMC811. The recovery of capacity comes from processes 2 and 4 which were suppressed after soaking in water but reappear after coating with **3**. Like in the other cases, the discharge peaks

shift to lower voltages in cycle 210, and lower voltages need to be applied to achieve full discharge capacity (low-voltage discharge peak tailing towards the left). Nevertheless, reversible electrochemical behaviour with the expected NMC811 peaks is observed at cycle 210, in contrast to the water-soaked, uncoated PC-NMC811.

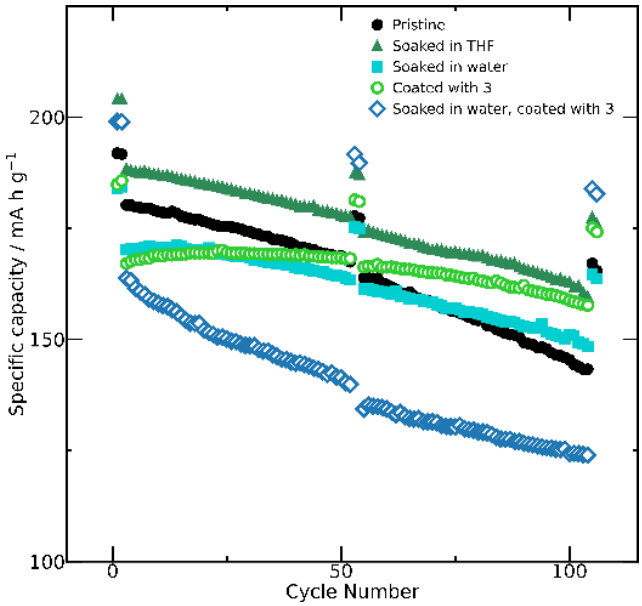

Figure 4.21. Long-term cycling of SC-NMC811 materials over 100 cycles. Pristine, soaked in THF, soaked in water, coated with **3** and soaked in water/coated with **3** (all annealed at 400 ºC) are shown in the Figure. The y axis (Specific capacity / mA h g^{-1}) starts at 100 mA h g^{-1} in this Figure to better visualise the differences in capacity retention between the samples.

Finally, the electrochemical cycling performance of the pristine SC-NMC811, SC-NMC811 coated with **3** and the soaked in water / coated SC-NMC811 were also compared in half cells (Figure 4.21). Specific discharge capacities as a function of cycle number are shown in Figure 4.21. The y-axis has been changed to 100 - 250 mA h g^{-1} (as opposed to 0 - 300 mA h g^{-1} in the previous Figure) to visualise the changes in specific capacity and capacity retention better. Due to the fact that the SC-NMC811 is surface coated with Al_2O_3 and also because of the differences in morphology, the response to the soaking and coating treatments is quite different from that observed for PC-NMC811.

In contrast to PC-NMC811, soaking in THF does not harm the capacity retention of the SC-NMC811. The capacity retention was the same at C/20 (84.3-84.4%) for the pristine and THF-soaked SC-NMC811 and slightly higher for the THF soaked SC-NMC811 at C/2 (78.2 vs. 75.6%). Since SC-NMC811 was already coated and surface doped, it is possible that it has a surface that is less reactive towards THF. The specific discharge capacities were ca. 10 mA h g^{-1} higher for the THF soaked SC-NMC811 over

three repeats (Figure D3, Appendix D). The EDS results (Figure 4.10) shown lower Al content in SC-NMC811 after washing in THF suggesting partial removal of the insulating Al_2O_3 layer, which may be helping with the cycling performance.

More surprisingly, soaking SC-NMC811 in water following the same procedure as for the PC-NMC811 did not lead to a deterioration of the cycling performance. There was a larger gap in between the C/20 and C/2 first cycles indicating that the surface of the SC-NMC811 has become more resistive after soaking in water therefore kinetically limiting the discharge capacity at C/2. Nevertheless, the capacity retention improved after soaking in water compared to pristine SC-NMC811, both at C/2 and C/20 C-rates (87.9 and 85.9 % for the soaked SC-NMC811 at C/20 and C/2 vs. 84.4 and 75.6% for the pristine SC-NMC811). It is thought that the mechanism of degradation of PC-NMC811 by soaking in water proceeds by a combination of lithium leaching from the particles, mechanical damage and cracking.[298] It is therefore possible that SC-NMC811 is less prone to degradation by soaking in water due to its better mechanical integrity. Furthermore, the Al_2O_3 coating and surface doping of the as-received SC-NMC811 may be preventing delithiation by H_2O and formation of TM(O)-OH sites therefore reducing the degree of degradation caused in this soaking step. Finally, soaking in water may be removing some of the soluble surface lithium salts (Li_2CO_3, LiOH) which are known to cause capacity fade in NMC materials.

The SSNMR studies showed that coating SC-NMC811 with **3** leads to the deposition of the amorphous $LiAlO_2$ layer on top of the Al_2O_3 coating. This double coating is expected to cause a kinetic limitation during cycling owing to the two interphases present (SC-NMC811|Al_2O_3|$LiAlO_2$) and the resulting increase in coating thickness. This is what is seen experimentally in the cycling data, where a larger gap between the first C/2 and C/20 cycles (similar to the soaked in water SC-NMC811) is seen for the material coated with **3** compared to the pristine material. Interestingly, the capacity retention improves both at C/2 and C/20 compared to both the pristine SC-NMC811 and the SC-NMC811 soaked in water (6.9% more capacity retention at C/2 and 6.1% more at C/20 compared to the SC-NMC811 soaked in water). It is possible that the coating deposition is covering regions of the particles that were not originally coated improving the surface coverage. Furthermore, the addition of surface Li may stabilise the structure improving the performance. Finally, in the same way as with PC-NMC811, soaking SC-NMC811 in water induces more coating deposition (as shown by EDS). This thick coating deposited

on a coated NMC811 material leads to a very substantial kinetic limitation in the electrochemical cycling with a large gap in C/2 - C/20 discharge capacity. This material still showed 3% more capacity retention than the pristine SC-NMC811 and the SC-NMC811 soaked in water at C/20, but similar capacity retention and lower specific capacities at C/2, owing to the thick double coating present.

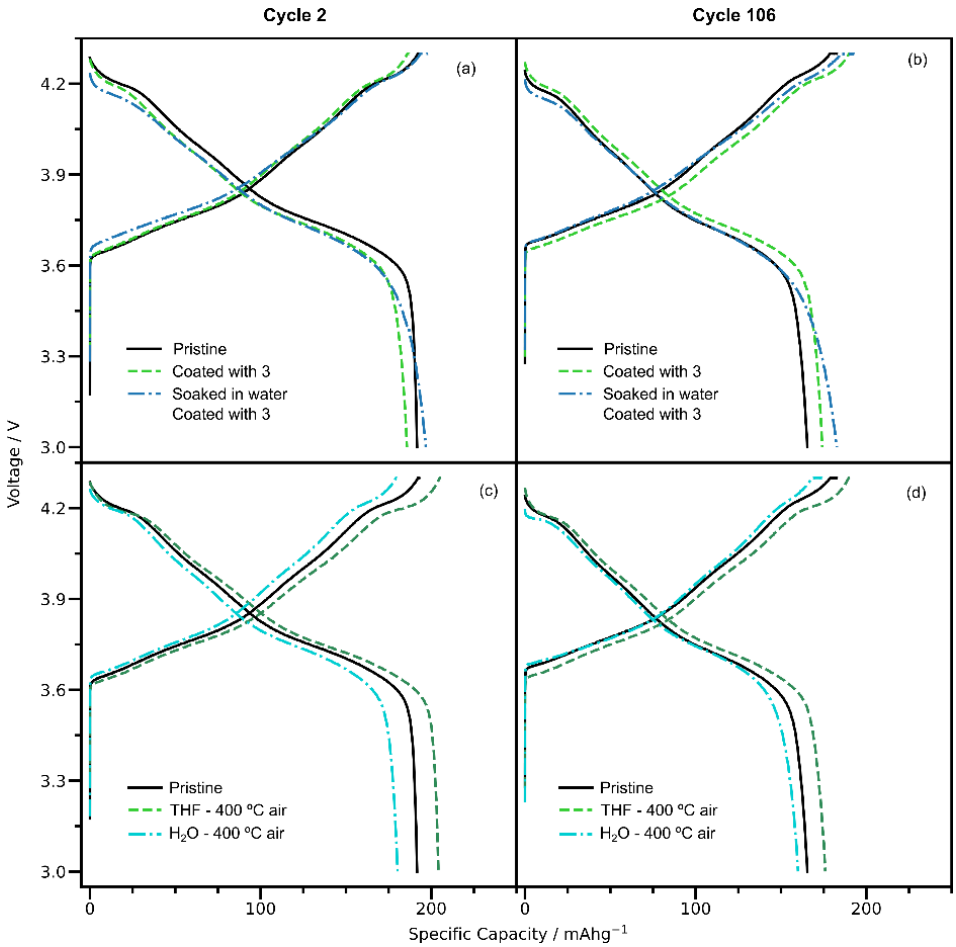

Figure 4.22. Voltage profiles obtained from the slow (C/20) cycles of the SC-NMC811 samples. (a) 2nd cycle of the pristine SC-NMC811, SC-NMC811 coated with **3** and SC-NMC811 soaked in water and coated with **3**. (b) 106th cycle of the pristine SC-NMC811, SC-NMC811 coated with **3** and SC-NMC811 soaked in water and coated with **3**. (c) 2nd cycle of pristine SC-NMC811, SC-NMC811 soaked in water and annealed at 400 ºC under air, SC-NMC811 soaked in THF and annealed at 400 ºC under air. (d) 106th cycle of pristine SC-NMC811, SC-NMC811 soaked in water and annealed at 400 ºC under air, SC-NMC811 soaked in THF and annealed at 400 ºC under air.

The voltage profiles obtained on the second and last (106th) C/20 cycles for the SC-NMC811 samples are analysed to determine the processes responsible for the differences in capacity retention. Comparing the voltage profiles of cycle 2 (Figure 4.22a) reveals that both the coated and soaked/coated SC-NMC811 display larger overpotentials compared to the pristine SC-NMC811. However, the pre-soaked and coated SC-NMC811

is able to deliver higher discharge capacities than the other two samples at C/20. In cycle 106 (Figure 4.22b), the pristine SC-NMC811 shows some signs of degradation as the overpotential grows more compared to the coated SC-NMC811 and is overlapping now with the pre-soaked and coated SC-NMC811 which still delivers the highest discharge capacity. This suggest that the coating is enhancing the cyclability of the material at higher cycle number by decreasing the resistance growth on the cathode which causes the overpotential increase with cycle number.

The effect of soaking in water or THF and annealing under air on the C/20 voltage profiles of the SC-NMC811 can be seen in bottom panels of Figure 4.22 (c and d). The THF-soaked SC-NMC811 shows lower overpotential in cycle 2 whereas the water soaked shows a higher overpotential compared to the pristine SC-NMC811. As discussed previously, THF soaking removes some of the aluminium from the surface, which should hinder lithium transport (Chapter 3). Meanwhile, the water treatment is expected to form some surface rock-salt. Although the SC-NMC811 is less affected by the water soaking than the PC-NMC811 (as determined from the long-term capacity retention) it still shows a higher resistance in its first cycles, indicating that the Al_2O_3 coating does not fully prevent the formation of rock-salt and suggesting that the gains in capacity retention observed are likely due to the removal of surface impurities and the better mechanical stability of SC-NMC811. At cycle 106 the voltage profile of pristine SC-NMC811 and SC-NMC811 soaked in water are almost superimposable, due to the greater degradation rate of the pristine sample. Meanwhile, the THF treated SC-NMC811 degrades slightly but continues to show higher capacities and lower overpotentials.

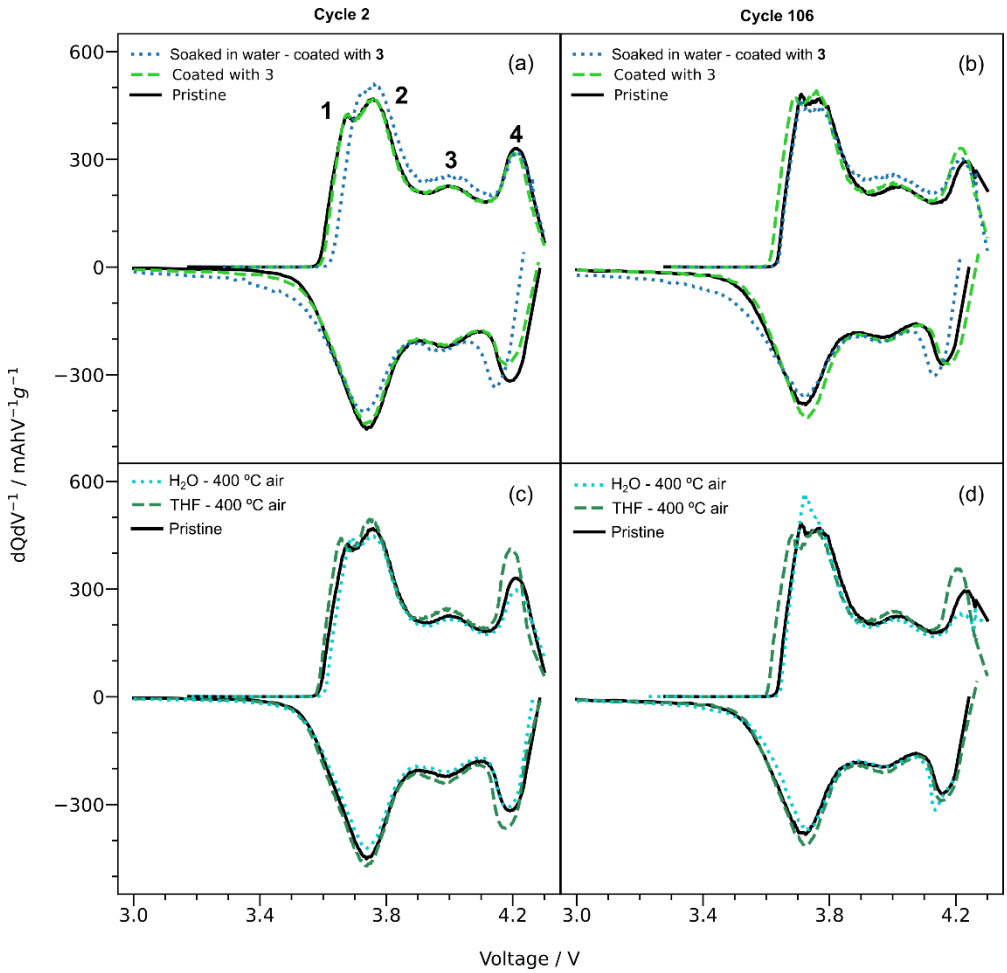

Figure 4.23. dQ/dV profiles obtained from the slow (C/20) cycles of the SC-NMC811 samples. (a) 2nd cycle of the pristine SC-NMC811, SC-NMC811 coated with **3** and SC-NMC811 soaked in water and coated with **3**. (b) 106th cycle of the pristine SC-NMC811, SC-NMC811 coated with **3** and SC-NMC811 soaked in water and coated with **3**. (c) 2nd cycle of pristine SC-NMC811, SC-NMC811 soaked in water and annealed at 400 ºC under air, SC-NMC811 soaked in THF and annealed at 400 ºC under air. (d) 106th cycle of pristine SC-NMC811, SC-NMC811 soaked in water and annealed at 400 ºC under air, SC-NMC811 soaked in THF and annealed at 400 ºC under air.

The dQ/dV profiles of the pristine SC-NMC811 and the SC-NMC811 coated with **3** are very similar (Figure 4.23 a, b), with the lower capacity of the coated material on the second cycle mainly coming from the high voltage process on discharge. In cycle 106 the symmetrical shape of the dQ/dV curve is mostly retained both for the pristine and the coated SC-NMC811 confirming the good cycling stability of both materials. The higher discharge capacity of the coated material at cycle 106 comes both from the high voltage charge process (4) and the low voltage discharge process (1). The SC-NMC811 soaked in water shows greater polarisation of its dQ/dV profile at cycle 2 and 106 compared to the other two, consistent with the findings of PC-NMC811 and the rock-salt formation hypothesis. The effect of water and THF soaking on the dQ/dV of the SC-NMC811 is

also considered (Figure 4.23 c, d). In general, the dQ/dV of the soaked samples have similar shape and are symmetric, like that of pristine SC-NMC811, confirming that neither soaking in water or THF has a negative effect on the cyclability of the SC-NMC811. The higher capacity of the sample soaked in THF comes from the high voltage process 4 which shows a more intense peak in the dQ/dV compared to the pristine SC-NMC811.

4.6. Conclusions

In this chapter, the surface of NMC811 is coated with $LiAlO_2$ to mitigate NMC811 degradation under electrochemical cycling conditions. $LiAlO_2$ is an excellent coating material, as it creates a lithium-rich surface and is a Li-ion conductor composed of cheap, non-toxic elements. However, current methods to deposit ternary oxides present limitations in terms of scalability, and homogeneity of the deposited layer. To overcome these problems, a new solution deposition method using heterobimetallic SSP is developed. First, the synthesis of the known alkoxide $Li[Al(OCH_2Ph)_4]$ was extended to two new compounds: $Li[Al(O^iPr)_4]$ and $Li[Al(O^tBu)_4]$. A study of the structure of the precursors as they thermolyze was then undertaken using solution and solid-state nuclear magnetic resonance (NMR), thermogravimetric analysis (TGA), powder X-ray diffraction (PXRD), elemental analysis and energy-dispersive X-ray spectroscopy (EDS). The -OR group ($-OCH_2Ph$, $-O^iPr$ and $-O^tBu$) was found to have a decisive influence on properties of the precursors such as solubility, thermal decomposition mechanism, crystallisation temperature, phases formed upon decomposition and reactivity with the NMC surface. Although the three precursors formed γ-$LiAlO_2$ at 800 ºC and amorphous phases below this temperature, only $Li[Al(O^tBu)_4]$ had the required properties to act as a precursor to $LiAlO_2$ coatings of NMC811.

The coating method was tested on NMC811 materials with different morphologies (single-crystal vs. polycrystalline NMC) and surface chemistries (Al_2O_3 coated vs. pristine surface). By a combination of X-ray photoelectron spectroscopy (XPS), synchrotron PXRD and solid-state nuclear magnetic resonance (SSNMR), the changes in the surface and bulk of the material with soaking in THF and H_2O, and after annealing at 400 °C under air were systematically investigated, in parallel to the surface changes due to the coating. ^1H and ^7Li SSNMR measurements showed that the surface of NCM811 is delithiated after soaking in water and that the number of TM(O)-OH sites increases. This surface change increased the amount of $LiAlO_2$ deposited under the same conditions

providing direct evidence that $LiAlO_2$ deposition proceeds via hydrolysis of the alkoxides with surface TM(O)-OH groups and adsorbed water. Finally, the electrochemical properties of the materials were evaluated in Li-ion half-cells by long-term galvanostatic cycling. It was found that the coating improved the specific capacity and capacity retention of Al_2O_3 coated single-crystal NMC811 significantly (17.2% more capacity retained at C/2 after 100 cycles), while having only a small effect on the polycrystalline material. Interestingly, coating polycrystalline NMC811 that was soaked in water allowed an impressive recovery of 50% of the capacity retention while also showing higher specific capacities, possibly by regeneration of the surface layered structures that were reduced to rock-salt by the water treatment. This work represents the first example of using heterobimetallic precursors to coat battery materials with $LiAlO_2$, providing a straightforward and scalable route to solution deposition of $LiAlO_2$ coatings that can increase cycle life and recover degraded NMC811. Furthermore, it provides insight into the complex relationship between morphology, surface chemistry and electrochemical lifetime in Ni-rich cathode materials for Li-ion batteries.

Chapter 5: Conclusions and Future Work

Rapid action is needed before climate change, caused by anthropogenic greenhouse gas emissions, becomes irreversible.[1] Since chemical synthesis underpins the development and improvement of emerging materials for renewable energy storage, great research efforts and resources are being directed towards the synthesis of materials that allow the transition to a sustainable society.[2,4,7] Nevertheless, many of the limitations of these materials, which are preventing their commercialisation, are not related to their intrinsic performance and bulk properties but have to do with their surface chemistry.[27,231,339] These surfaces can be optimised by applying coatings, which is the topic of this thesis.

Coating deposition using instrumental vapor deposition techniques such as atomic-layer deposition (ALD) and chemical vapor deposition (CVD) rely on metalorganic precursors, which react with the substrate of interest. The coatings are typically binary oxides, due to the limitations of the currently available precursors.[225,340] Solution deposition methods can rely on salts (nitrates, carbonates, etc.) or in alkoxide precursors for the sol-gel deposition of the coating and are often an attractive alternative to instrumental methods due to their low cost and ease of scalability.[88] However, rough and inhomogeneous coatings are often obtained by solution methods due to the lack of control of the deposition reactions (the coating is usually precipitated onto the surface of the particles by solvent evaporation).[24] Regardless of the deposition route, accessing homogeneous ternary oxides is challenging but could be the key to improve the surface properties of energy materials, due to the synergistic roles of the two metals in a heterobimetallic coating.[315]

The lack of suitable single source precursors (SSP) containing both metals and optimised coating deposition procedures are severely limiting research in ternary oxide coatings. Furthermore, the incomplete understanding of the relationship between molecular structure, deposition conditions, and coating structure is hampering their rational design. In this thesis, new precursors and deposition methods have been developed for the areas of Li-ion batteries and photoelectrocatalytic water electrolysis. The deposited coatings are characterised using a combination of surface and bulk techniques to understand the effect of the precursor and coating deposition conditions on the properties of the coating, and the link between those and the performance of the materials.

This general idea of using SSPs was first applied to the area of photoelectrocatalysis for water electrolysis in Chapter 2. The key process to optimise was the water oxidation reaction, which happens at the photoanode (see Chapter 1). In this context, $BiVO_4$ is a promising candidate because its band-gap energy allows it to absorb a significant part of the visible spectrum, its conduction band edge is at the thermodynamic potential for H_2 evolution and it is stable under neutral pH.[341] However, it suffers from surface charge recombination between the photogenerated holes and the electrons in the conduction band which sharply decreases its efficiency.[69] Adding a first-row (3d) transition metal (TM) catalyst coating has been shown to increase the performance of $BiVO_4$ by reducing charge recombination.[69] However, the use of heterobimetallic oxide coatings for this purpose has not been previously explored. In Chapter 2, the effect of coating $BiVO_4$ with a ternary 3d-TM doped ZrO_2 using a SSP was studied. Three novel Zr-oxo alkoxy precursors containing Cu, Co, and Fe were synthesised and used for the deposition of electrocatalytically active 3d-TM doped ZrO_2 films. In a linear-sweep voltammetry (LSV) test of the three catalysts, deposited on FTO by drop casting, the Co doped ZrO_2 (CoZr) was the best performing in terms of onset potentials, current density and Tafel slope. Therefore, CoZr was selected as co-catalyst for photoelectrochemical water oxidation. By spin-coating a solution of CoZr onto $BiVO_4$, an improvement in the performance of the photoanode was observed, lowering of the onset potentials by 0.1 V and increasing the photocurrent densities by 1.2 mA cm^{-2}.

Further improvements could potentially be obtained by optimising the fabrication of the CoZr|$BiVO_4$ composite. Post-annealing treatments could change the structure of the coating and improve the integrity of the film leading to better passivation of the surface electrons in the conduction band, increase the fraction of the dopant that is incorporated into the ZrO_2 matrix, and improved stability. Furthermore, although substrates with different surface areas were tested (carbon fibre paper, graphite paper and ITO-coated glass), optimising the morphology of the catalyst itself may lead to higher water oxidation activity.[46,58] This could be achieved for example by synthesising Co-doped ZrO_2 (nano)particles using a solvothermal, controlled hydrolysis or hot injection methods that then are deposited on FTO by drop casting with a binder or by electrophoresis.[46]

Many potential applications of SSP derived heterobimetallic coatings, beyond the ones discussed in this Thesis remain underexplored in the area of electrocatalysis. Due to the unique properties of SSP-derived coatings, they could be useful for other relevant

electrocatalytic transformations. For example, the activity of CO_2 reduction catalyst is strongly influenced by the local environment of the active metal sites,[342] but these effects have been studied primarily in polymeric organic systems and MOFs.[342,343] However, isolated 3d-TM sites in an amorphous oxide catalyst can be obtained by single-source deposition, but the effect of the oxide host on the CO_2 reduction activity of the catalytic site remains unexplored. Another potential application is in the fabrication of multijunction devices incorporating a photon conversion layer, coupled to a photoelectrode. This layer could convert photons that would normally be lost as thermal energy because of the energy mismatch with the bandgap of the semiconductor into usable photons, thereby increasing the quantum efficiency of the device.[344] Coating like lanthanide doped metal-oxides, can act as a spectral converter, and have been deposited from SSPs.[65]

In Chapters 3 and 4, it was considered whether oxide and heterobimetallic oxide coatings could be applied in the area of Li-ion batteries. Here new cathode materials with higher energy densities and lower costs, such as Ni-rich $LiNi_xMn_yCo_zO_2$ (NMC) suffer from surface instability with leads to side reactions with the battery electrolyte, surface degradation and rapid loss of battery capacity. Unlike the area of electrocatalysis, where coatings derived from SSPs have been extensively studied, the field of Li-ion batteries had not seen any previous applications of this surface coating approach. Therefore, a coating deposition method, driven by the reaction of an alkoxide with surface hydroxyl groups or adsorbed water is first developed in Chapter 3. First, the method was used to deposit Al_2O_3, one of the simplest, most widely studied coatings materials before extending it to heterobimetallic systems.

In Chapter 3, Al_2O_3 is deposited by reacting the Ni-rich NMC811 material with aluminium isopropoxide (AIP). Afterwards, the materials are annealed at temperatures of 100–800 ºC to achieve changes in the coating structure and surface Al-doping by coating diffusion into the NMC811. A clear relationship between the extent of doping and decrease in specific capacity of the NMC811 is found and no improvement in capacity retention were seen in half-cells, even for the samples annealed at low temperature. Although it is possible that subtle differences in long-term capacity retention are not being seen due to the use of half cells (vs. Li) in which the capacity loss due to the Li chip may be masking the capacity loss of the NMC. It is clear that neither Al_2O_3 coatings, nor Al doping are very effective strategies to increase the lifetime of polycrystalline NMC811.

The ionically insulating nature of Al_2O_3 and the Al-doped NMC layers, as well as the cracking of secondary NMC811 particles with cycling were considered important factors explaining the results.

Following on from these findings, $LiAlO_2$ was used in Chapter 4 as a coating for NMC811. In contact with air and moisture, NMC811 forms surface impurities such as Li_2CO_3 and LiOH.[282] This creates a Li-depleted surface region that is more prone to degrade by forming NiO.[282] By coating with a Li-rich coating and annealing at low temperatures, it is in theory possible recover the surface lithium increasing capacity retention. Furthermore, $LiAlO_2$ has higher Li-ion conductivity than Al_2O_3. Finally, using single-crystal NMC811 can improve the capacity retention by reducing particle cracking with cycling,[304] but the interplay between particle morphologies and coatings are not yet well explored. In Chapter 4, these ideas were tested experimentally by developing new SSP molecules for the deposition of $LiAlO_2$ coatings onto NMC811. Coating Al_2O_3 doped single-crystal NMC811 with $LiAlO_2$ leads to an improvement in capacity retention, suggesting that the enrichment in surface lithium plays an important role in improving the stability of the surface. Furthermore, the specific capacity and capacity retention of a polycrystalline NMC811 that was artificially degraded by soaking in water, could be partially recovered by coating with $LiAlO_2$, supporting the idea that the formation of a surface rock-salt layer can be reversed by coating with a lithium-rich material.

The approach followed in Chapter 4 was limited by the poor solubility of the SSP, $Li[Al(O^tBu)_4]$, which wasn't fully soluble in solvents other than THF. This solvent was shown to have a negative effect in the capacity retention of NMC811 so it would be desirable to design other SSPs containing ligand groups that increase solubility. For example, organometallic complexes with less polar Al-C bonds which would also be more reactive towards water,[345] or alkoxides with bulkier organic ligands (although this last strategy may lead to poor thermolysis properties). Moving forward, it would be interesting to test the effects of coatings with higher Li content by using precursors with an Li : Al ratio higher than 1. It might be possible to prepare these by adapting the reaction conditions used in Chapter 4, using less sterically bulky alcohol groups or/and different stoichiometry of the reagents. Another option is the controlled hydrolysis of $Li[Al(O^tBu)_4]$ (with or without solvothermal conditions) which could result in the formation of higher nuclearity heterobimetallic clusters with different ratios of the two metals.[346]

Further work in the coating deposition of $LiAlO_2$ may also lead to improvements in capacity retention. Although the coating conditions used in Chapter 4 were borrowed from the previous Chapter, it is possible that small adjustments in annealing temperature and time or weight % of precursor could further improve the electrochemistry by allowing more Li to diffuse into the NMC811. Now that the role of water in the coating-deposition reaction has become clearer, it would be possible to optimise the surface water content while minimising the degradation. For example, by decreasing the water soaking time, or by adding stoichiometric amounts of water to a NMC811 suspension in THF before the addition of the precursor. Finally, $LiAlO_2$ coating of pristine (uncoated) single-crystal NMC811 could be explored as they may lead to further improvements in capacity retention compared to the $LiAlO_2/Al_2O_3$ coated NMC811.Looking beyond the coating applications discussed in this Thesis, there are many other potential uses of SSP coatings in the battery area. So far, most coatings applied to battery electrodes were not redox active. On the other hand, SSPs for the synthesis of cathode materials such as LCO have already been prepared.[80] It should then be possible to coat a Ni-rich cathodes with another layered oxide that is more stable obtaining coatings that conducts Li, contribute to the capacity of the material and have a more compatible crystal structure, while still passivating the surface of the Ni-rich cathode.

An obvious intersection between the area of electrochemical energy storage (batteries) and electrocatalysis is the oxygen electrochemistry, which is the key to (photo)electrocatalytic water splitting and plays an important role in the development of lithium-air batteries.[347] The later are usually formed of a lithium metal anode, an organic electrolyte, and a porous cathode material. The working principle of these batteries is the reversible oxygen reduction to peroxide species at the cathode on discharge that combine with Li from the electrolyte to form Li_2O and Li_2O_2 species.[348] Addition of an oxygen evolution reaction (OER) or oxygen reduction reaction (ORR) catalysts to the cathode has been shown to increase the capacity of the cell by enhancing the kinetics of the cathodic processes. However, there are only a handful of examples of this, mainly using noble metals.[349] On the other hand, bifunctional catalysts based on more abundant elements can be obtained from SSPs,[55] and they could be easily integrated in Li-O_2 cathodes by solution deposition.

In summary, this Thesis demonstrates the potential of molecular precursors to create new functional interphases in energy materials. This rapidly evolving field is always

presenting us with new surfaces to passivate and reactions to catalyse. The design possibilities allowed by molecular chemistry mean that new precursors and coating materials will emerge to meet these challenges. This, coupled to an improved understanding of solution coating deposition, the effects of morphology, crystallinity, and synergies in ternary and quaternary oxide coatings, is sure to contribute significantly to the development of new-generation energy technologies.

Chapter 6: Experimental Details

6.1. Experimental Details for Chapter 2

6.1.1. Synthesis and Characterisation of Precursors 1, 2 and 3

Precursor Reagents: Zirconium(IV) ethoxide ($Zr(OEt)_4$, Sigma-Aldrich, 98%), iron(II) chloride ($FeCl_2$, Sigma-Aldrich, 98%), cobalt(II) chloride ($CoCl_2$, Sigma-Aldrich, ≥ 97%), copper(II) chloride ($CuCl_2$, Sigma-Aldrich, ≥ 97%), dimethyl sulfoxide (DMSO, Alfa Aesar, ≥99%), anhydrous ethanol (EtOH, Sigma-Aldrich), dry tetrahydrofuran (THF, Sigma-Aldrich), potassium hydroxide (KOH, Sigma-Aldrich, semiconductor grade, ≥ 99%), Nafion® 117 solution, bismuth nitrate pentahydrate ($Bi(NO)_3 \cdot 5H_2O$, Sigma-Aldrich, 98%), sodium iodide (NaI, laboratory reagent grade, Fischer Scientific), p-benzoquinone (≥ 98%, Sigma-Aldrich), vanadyl acetylacetonate (≥ 97%, Fluka).

Precursor Synthesis: Strict inert-atmospheric conditions were used throughout all of the syntheses of **1**-**3**. Anhydrous chloride salts $M^{II}Cl_2$ with M = Co, Cu, Fe and $ZrOEt_4$ (98%) were acquired from Aldrich chemical company. EtOH was distilled over Mg turnings and tetrahydrofuran (THF) over sodium/benzophenone under nitrogen atmosphere. Teflon-lined (23 mL capacity) autoclaves (model 4749, Parr) were used for all experiments. Autoclaves were heated using a Binder ED53 53 L oven with natural convection. The reactions were loaded with the solvents and reagents inside a Saffron Scientific (type β) glovebox, equipped with a closed loop recirculation system for the removal of moisture and oxygen (operating at ca. 0.1–0.5 ppm O_2). Storage of the products, and analytical and spectroscopic samples were prepared inside the glovebox.

*Synthesis of $[Zr_4O(EtO)_{15}Co^{II}Cl]$ (**1**):* Zirconium(IV) ethoxide (1.132 g, 4.18 mmol), cobalt(II) chloride (102 mg, 0.78 mmol), and anhydrous EtOH (5 mL, 85.7 mmol) were placed in a Teflon-lined autoclave and heated at 100 °C for 1 day. After cooling down to room temperature, the EtOH was evaporated, and residue was crystallized from 5 mL dry THF at -14 °C, to produce purple crystals of **1** which were dried under vacuum (0.53 g, 27 % yield on the basis of $CoCl_2$ supplied). Elemental analysis found C 29.9, H 5.7, calc. for **1** C 31.3, H 6.5.

*Synthesis of $[Zr_4(O)_2(EtO)_{16}Fe^{III}_2Cl_2]$ (**2**):* Zirconium(IV) ethoxide (1.132g, 4.18 mmol), iron(II) chloride (99 mg, 0.78 mmol), and anhydrous EtOH (5 ml, 85.7 mmol) were placed in a Teflon-lined autoclave and heated at 100 °C for 1 day. After cooling to room temperature, the EtOH was evaporated, and the residue was crystallized from 5 mL dry THF at -14 °C to produce pink crystals of the solvate **2**·2THF which were dried under

vacuum (0.13 g, 11% yield on the basis of providing $FeCl_2$). Elemental analysis found C 29.0, H 5.9, calc. for **2** C 29.5, H 6.1. The elemental analysis shows that the THF present in the crystalline lattice is completely removed under vacuum, which also leads to the loss of crystallinity.

Synthesis of $[Zr_4(O)_2(EtO)_{18}Cu^{II}_4Cl_4]$ *(**3**):* Zirconium(IV) ethoxide (1.132g, 4.18 mmol), copper(II) chloride (105 mg, 0.78 mmol), and anhydrous EtOH (5 mL, 85.7 mmol) were placed in a Teflon-lined autoclave and heated at 100 ℃ for 1 day. After cooling to room temperature, the EtOH was evaporated, and the residue was crystallized in 5 mL of dry THF at -14 ºC to produce blue crystals of **3**·EtOH (0.41 g, 62 % yield on the basis of $CuCl_2$ provided). Elemental analysis found C 25.7, H 5.3, calc. for **2** C 26.9, H 5.6. The elemental analysis shows that the EtOH present in the crystalline lattice is completely removed under vacuum, which also leads to the loss of crystallinity.

IR spectroscopy measurements: IR spectra were recorded as Nujol mulls using a Perkin-Elmer 1000 spectrophotometer with a universal ATR using NaCl windows.

UV-VIS spectroscopy measurements: The spectra were measured using a Varian Cary 50 spectrophotometer at 25 °C using quartz crystal cells. UV-diffuse reflectance spectroscopy (UV-DRS) was measured using a Harrick Scientific Video Barrelino probe. *Elemental Analysis*: Elemental CHN analysis was obtained using an Exeter Analytical, Inc. CE-440 Elemental Analyzer with a combustion temperature of 975 °C.

ICP-OES measurements: An iCAP 7400 Series ICP Spectrometer from Thermo Fisher Scientific was used to detect the Co, Cu, Fe content in the film samples. Samples for analysis were dissolved in 2% HNO_3 to an estimated 1 ppm (mg/L) concentration (5 to 10 mL total volume).

Single-crystal X-ray diffraction: All single-crystal X-ray data were collected at 180(2) K using a Nonius KappaCCD diffractometer equipped with MoKα radiation (λ = 0.7107 Å). Crystallographic data in CIF format have been deposited with the Cambridge Crystallographic Data Centre (CCDC 2011723-2011725).

6.1.2. Characterisation of the Catalysts

Materials Characterization: Scanning electron microscopy/energy dispersive X-ray spectroscopy (SEM/EDS) were obtained using a TESCAN MIRA3 FEG-SEM (FEG = field emission gun). SEM images were acquired at 5 kV or 15 kV acceleration voltages, and EDS spectra were acquired at a 30 kV acceleration voltage. X-ray photoelectron spectroscopy (XPS) was measured on a ThermoFisher Scientific EscaLab 250Xi equipped with a monochromatic Al Kα X-ray source (hν = 1486.68 eV) and a spot size of 500 μm × 500 μm. Survey spectra were measured at a pass energy of 100 eV and high-resolution spectra were measured at a pass energy of 20 eV. On account of closures due to the pandemic, the free-standing CuZr was measured at another facility, using a ThermoFisher Scientific K-Alpha XPS system, also equipped with a monochromatic Al Kα X-ray source (hν = 1486.69 eV). The survey spectrum was measured at a pass energy of 160 eV and the high-resolution spectra were measured at a pass energy of 20 eV.

Electrochemical and Photoelectrochemical Measurements:

The PEC measurements were performed with a Newport Oriel 67005 solar light simulator with an AM 1.5G solar filter. The irradiance (i.e., flux density) was calibrated to 100 mW m^{-2} using a Newport 116-R optical power meter. Since $BiVO_4$ is not stable under alkaline conditions, 0.1 M potassium borate (KBi) buffer (pH 8.5) with 0.1 M K_2SO_4 as supporting electrolyte was used for the PEC measurements. Prior to the PEC measurements, the electrolyte solution was purged with N_2 for 20 minutes. The CV scans (chopped, light and dark) were run between 0.1 V and 1.4 V vs. RHE at a low scan rate of 10 mV s^{-1}. The scans were performed under back-illumination to ensure efficient light absorption. The O_2 quantification was conducted for the best performing system CoZr in the anodic compartment of a gas-tight (photo)electrochemical cell using an Ocean Optics fluorescence oxygen probe (Forpor-R). A constant potential was applied for 4 h. The O_2 baseline was also recorded before and after the chronoamperometry. The amount of oxygen in solution was obtained using Henry's law.

6.2. Experimental Details for Chapter 3

6.2.1. Reagents and Materials

NMC811 (Targray), aluminium isopropoxide (Sigma-Aldrich, ≥ 98%), toluene was dried under nitrogen over sodium and freshly distilled before use.

6.2.2. Characterisation of the Pristine and Coated NMC811

6.2.2.1. Electron Microscopy and Elemental Quantification by EDS/XRF

Images were taken with a TESCAN MIRA3 Field emission gun (FEG)-SEM in secondary electron (SE) mode with beam voltages ranging from 2 kV for the pristine NMC and 5 kV for the coated samples. The working distance was 6 mm for all images. All samples were coated with 10 nm of Cr before imaging using a Quorum Technologies Q150T ES Turbo-Pumped Sputter Coater/Carbon Coater.

TEM images, Scanning Transmission Electron microscopy (STEM) and Energy Dispersive X-ray spectroscopy (EDS) spectra and maps were collected using a Thermo Scientific (FEI) Talos F200X G2 TEM operating at 200 kV with a spot size of 5 and 70 μm aperture for the bright-field (BF) imaging. TEM images were acquired using a Ceta 16M CMOS camera. EDS was performed in STEM mode with images acquired using the High Angle Annular Dark Field (HAADF) and Bright Field (BF) detectors and EDS spectra/maps collected using the Super-X EDS detector system which consists of 4 windowless silicon drift detectors.

X-ray Fluorescence Measurements were performed using an Epsilon 4 Malvern Panalytical XRF spectrometer with an Ag anode (X-ray energy of 50 kV) and a SDD30 silicon drift detector.

6.2.2.2. Solid-state NMR (SSNMR) Measurements

Sample quantities ranged between 7.6 and 9.3 mg.

a) ^{7}Li NMR Measurements at 200 MHz

The spectra were recorded on a 4.7 T Bruker Avance III spectrometer (200 MHz ^{1}H Larmor frequency), using a Bruker 1.3 mm magic-angle spinning (MAS) NMR probe and spinning at 60 kHz MAS frequency. The spectra are central slices of projection MATPASS spectra,[263] which show only the isotropic resonance without spinning sidebands. Eight t_1 increments were recorded for each spectrum, with a recycled delay of 30 ms and 5120 transients acquired per t_1 increment. Li_2CO_3 was used as external reference for these measurements (0 ppm).

b) ^{27}Al NMR Measurements at 200 MHz

A 4.7 T Bruker Avance III spectrometer (200 MHz ^{1}H Larmor frequency), with a Bruker 1.3 mm magic-angle spinning (MAS) NMR probe was used. The spectra were acquired at 60 kHz MAS frequency, using a rotor-synchronized Hahn echo pulse sequence with a recycle delay of 25 ms. 1127040 transients were acquired per spectrum, leading to an experimental time of about 20 hours. AlF_3 was used as external reference (-17 ppm relative to 1 M $Al(NO_3)_3$ in D_2O at 0 ppm).

c) ^{27}Al NMR Measurements at 700 MHz

Measurements were carried out on a 16.4 T Bruker Avance III spectrometer (700 MHz ^{1}H Larmor frequency), using a Bruker 1.3 mm magic-angle spinning (MAS) probe. Experiments were performed at 50 kHz MAS frequency, using a rotor-synchronized Hahn-echo pulse sequence with a 100 ms recycle delay. Between 372,000 and 402,000 scans were acquired, leading to experimental times between 14 and 17 hours. AlF_3 (-17.0 ppm relative to 1 M $Al(NO_3)_3$ in D_2O at 0 ppm) was used as an external reference to calibrate the ^{27}Al chemical shift. For the sample annealed under air, which had a mass of 5.8 mg, 308,832 scans were recorded leading to a measurement time of 5 h. The sample annealed under oxygen had a mass of 7.33 mg and was measured for 20 h (1293,168 scans were measured).

d) ^{27}Al NMR Measurements at 1 GHz

The high-field NMR measurements were performed on a 23.5 T Bruker Avance Neo spectrometer (1 GHz ^{1}H Larmor frequency) with a Bruker 1.9 mm MAS probe. All samples were as-coated powders. Experiments were performed at 40 kHz MAS frequency for the samples annealed at 200 and 600 ºC and at 38 kHz MAS frequency for the sample annealed at 400 ºC. A rotor-synchronised Hahn-echo sequence was used with a recycle delay of 100 ms. Between 684,416 and 715,520 transients were collected, leading to experimental times between 21 and 23 hours. The spectra were simulated and fit using a Czjzek distribution.[271]

6.2.3. Electrode Fabrication and Cell Assembly

Electrodes were prepared by mixing 88 wt % NMC811 powder with 6 wt % carbon black (Super-P Carbon, Timcal) and 6 wt % PVDF binder (Kynar, HSV-900). The total amounts of the coated and uncoated solids ranged between 250 and 400 mg. The solid mixture was ground for 5 minutes under air using a pestle and mortar. Then 0.85 mL of N-methyl-2-pyrrolidone (NMP) per gram of solid was added, the slurry was mixed in a planetary centrifugal mixer (Thinky, ARM/310 CE) at 2000 rpm for 10 minutes and transferred to a nitrogen-filled glovebox. Here, the slurry was cast on aluminium foil with a doctor-blade to 150 μm thickness. The cast electrode was then dried under vacuum at room temperature overnight and cut into electrode disks of 12.7 mm diameter. These were dried under vacuum at 120 ºC for 24 h before being transferred to an argon-filled glovebox with oxygen and water levels below 10 ppm. The resulting electrodes had active mass loadings of 6.4 ± 1.4 mg / cm^2.

Coin cells were assembled inside an argon filled glovebox with water and oxygen levels below 10 ppm. The cell components were a lithium disk of 16 mm diameter, purchased from LTS Research Laboratories, Inc. as the counter electrode, one 0.5 mm thick spacer, a steel spring, a glass fibre separator (GF/B, Whatman,16 mm diameter) soaked with 100 μL of electrolyte and the cathode disk. The electrolyte used was 1.0 M $LiPF_6$ in ethylene carbonate (EC) and ethyl methyl carbonate (EMC) mixed in a 3:7 w/w ratio (SoulBrain, USA).

6.3. Experimental Details for Chapter 4

6.3.1. Reagents and Materials

Polycrystalline NMC811 (Targray), Single-crystal NMC811 (Li-FUN), 1.0 M $LiAlH_4$ solution in THF (Sigma-Aldrich). Benzyl alcohol (Sigma-Aldrich ≥ 99 %), isopropanol (Sigma-Aldrich ≥ 99 %), tert-butanol (Alfa Aesar ≥ 99 %).

6.3.2. Synthetic Procedures

General synthetic considerations: All the solvents were dried over activated molecular sieves for 48 h before used and all the operations were carried out under strict inert atmosphere.

Synthesis of $Li[Al(OCH_2Ph)_4]$ (**1**): Addition of 4 mL of a 1M $LiAlH_4$ solution in THF over 1.66 mL of a benzyl alcohol solution in 10 mL of THF (4 equivalents) led to evolution of H_2(g) and the formation of a white suspension. After 1h, a clear solution is obtained by removing the solids by filtration and the product (white powder) is obtained by removing the solvent under vacuum. The product is then dried under vacuum at 40 ºC for 1h. Yield: 500 mg, 1.08 mmol, 27 %.

^{1}H NMR (400 MHz, d_8-THF, 295K) δ/ppm: 7.34 (s, 1H, Ph-**H** *ortho*), 7.19 (s, 1H, Ph-**H** *meta*), 7.09 (s, 1H, Ph-**H**, *para*), 4.81 (s, 2H, -C**H$_2$**Ph). **^{13}C{^{1}H} NMR** (400 MHz, d^8-THF, 295K) δ/ppm: 146.6 (1C, Ph(**C**)-C), 128.6 (2C, Ph(**C**) *meta*), 128.2 (2C, Ph(**C**) para), 127.1 (2C, Ph(**C**) ortho), 65.6 (1C, -**C**H_2Ph). **^{7}Li NMR** (400 MHz, d_8-THF, 295K) δ/ppm: 0.35 (s, b), -0.23 (s). **^{27}Al NMR** (400 MHz, d_8-THF, 295K) δ/ppm: 69.76 (s). **CHN analysis** $LiAlC_{28}H_{28}O_4$: 72.73; H, 6.06; N, 0.0. Found: C, 71.93; H, 6.08; N, 0.0.

Synthesis of $Li[Al(O^iPr)_4]$ (**2**): Addition of 4 mL of a 1M $LiAlH_4$ solution in THF over 1.22 mL of isopropanol solution in 10 mL of THF (4 equivalents) leads to H_2 (g) formation and the precipitation of a white solid. After 1h, the solid is filtered and the solvent is removed from the resulting white suspension under vacuum. A white powder is obtained and dried under vacuum at 40 ºC for 1h. Yield: 300 mg, 1.11 mmol, 12.3 %.

^{7}Li NMR (400 MHz, d_8-THF, 295K) δ/ppm: -0.27 (s). **CHN analysis** $LiAlC_{12}H_{28}O_4$: C, 50.06; H, 10.01; N, 0.0. Found: C, 50.32; H, 9.91; N, 0.0.

Synthesis of Li[Al(O^{t}Bu)$_4$] (**3**): Addition of 4 mL of a 1M $LiAlH_4$ solution in THF over 1.52 mL of tert-butanol solution in 10 mL of THF (4 equivalents) leads to H_2(g) formation and a clear solution (no precipitate is observed). After 1h, the solvent is removed under vacuum and the resulting white powder is dried under vacuum at 40 ºC for 1h. Yield: 1.08 g, 3.31 mmol, 83 %.

^{1}H NMR (400 MHz, d_8-THF, 295K) δ/ppm: 1.23 (s, -C(C**H**$_3$)$_3$, 9H), 1.21 (s, -C(C**H**$_3$)$_3$, 9H). **^{13}C{^{1}H} NMR** (400 MHz, d^8-THF, 295K) δ/ppm: 68.32 (s, -**C**(CH$_3$)$_3$, 1C), 34.16 (s, -C(**C**H$_3$)$_3$, 3C), 34.05 (s, -C(**C**H$_3$)$_3$, 3C). **^{7}Li NMR** (400 MHz, d_8-THF, 295K) δ/ppm: -0.26 (s). **^{27}Al NMR** (400 MHz, d_8-THF, 295K) δ/ppm: 77.86 (s), 60.26 (s), 53.1 (s). **CHN analysis** $LiAlC_{16}H_{36}O_4$: C, 58.91; H, 11.04; N, 0.0. Found: C, 58.1; H,11.74; N, 0.0. **HRMS** (ASAP$^-$) m/z calculated for $[M]^-$ $[C_{16}H_{36}Al_1O_4]^-$: 319.240 found: 319.2422. $[C_{12}H_{28}Al_1O_3]^-$: 247.190, found: 247.1855.

Thermolysis of compounds **1**-**3**. The precursors were loaded in alumina crucibles and heated under air with a heating rate of 10 ºC / min to 300, 400, 500 or 800 ºC (**1**) or 400, 500 or 800 ºC (**2** and **3**) for 4 h and then allowed to cool down to room temperature.

Water soaking step. NMC811 is loaded in a Schlenk flask inside the glovebox and transferred to a Schlenk line and put under nitrogen. Deionised water is then added (10 mL water / g of NMC) and stirred for 2h at room temperature. The water is then removed by syringe and the sample is dried under vacuum at 50 ºC for 2h. The resulting product is kept under inert atmosphere for the coating deposition step. Part of this sample is annealed under air at 400 ºC to study the effect of annealing on a water soaked NMC without a coating (control experiment).

Coating deposition. The coating was deposited onto NMC811 using this same procedure regardless of the precursor used (compounds **1**–**3**) or the NMC sample (Al_2O_3 coated single-crystal NMC811 or uncoated polycrystalline NMC811). The precursor and NMC811 are loaded in a Schlenk flask inside the glovebox (precursor wt. is 1 % of the total solid wt %). The reaction vessel is connected to a Schlenk line and put under nitrogen. Dry THF (10 mL / g of NMC) is added, and the reaction proceeds at 60 ºC for 48 h stirring. After that, the solvent is removed by syringe and the product is washed three times with 10 mL of THF each. Finally, the product is dried under vacuum at 100 ºC for 2h. The same procedure was employed for the NMC811 that was pre-soaked in water (water soaking step) and for the control samples but without the addition of precursor for the control experiments.

6.3.3. Characterisation of the NMC811 Materials

6.3.3.1. Electron Microscopy

Details of the SEM/EDS are the same as in chapter 3, see section 6.2.2.1. for more information. Details of the XPS measurements can be found in the main text.

6.3.3.2. XPS Characterisation

The XPS spectra were collected using a Phi Versaprobe instrument with Al Kα radiation using a facility from the Henry Royce institute. A spot size of 100 µm, a step size of 0.1 eV and a pass energy of 55 eV were used. Due to the relatively short amount of time for the measurements available in the previous facility, the XPS data of the pre-soaked PC-NMC811 coated with **3** was measured in a HarwellXPS facility using a Kratos SUPRA instrument with a pass energy of 40 eV, a spot size of 700 x 300 µm and a step size of 0.1 eV.

6.3.3.3. Powder XRD Characterisation

The laboratory diffraction measurements were performed using a diffractometer equipped with a Cu Kα radiation source (λ = 1.541 Å) and over the 10–100° 2θ range of for 1 h. The synchrotron PXRD patterns were measured at I11 (Diamond Light Source, UK). For the synchrotron measurements, samples were packed in a quartz capillary and sealed with epoxy resin before shipping and the peak-shapes were obtained directly from a silicon refinement. All the refinements were performed using the TOPAS program (V6).

6.3.3.4. SSNMR Measurements of the Precursors

Most of the spectra were recorded on a 11.7 T Bruker Avance III spectrometer (500 MHz ^{1}H Larmor frequency), using a Bruker 2.5 mm magic-angle spinning (MAS) NMR probe and spinning at 30 kHz MAS frequency. Only the pristine compound **3** annealed at 400 and 500 °C samples were recorded using a 16.4 T Bruker Avance III spectrometer (700 MHz ^{1}H Larmor frequency), with a Bruker 1.3 mm magic-angle spinning (MAS) probe and spinning at 50 kHz MAS frequency. The spin lattice relaxation time constant (T_1) was determined for each sample using a saturation recovery experiment. The spectra shown in this work were acquired using a rotor-synchronized Hahn-echo pulse sequence. The recycle delay (d_1) was determined directly from the T_1 values ($d_1 = T_1*5$). Sample quantities ranged between 1.15 and 14.15 mg for the 500 MHz measurements and between 1.84 and 8.53 mg for the 700 MHz measurements.

^{27}Al-NMR measurements. AlF_3 (-17.0 ppm) was used as an external reference to calibrate the ^{27}Al chemical shift, between 256 and 376,320 scans were recorded.

^{1}H-NMR measurements. Adamantane ($C_{10}H_{16}$, 1.9 ppm) was used as an external reference to calibrate the ^{1}H chemical shift, between 16 and 256 scans were recorded.

^{7}Li-NMR measurements. Li_2CO_3 (0 ppm) was used as an external reference to calibrate the ^{7}Li chemical shift and between 16 and 32 scans were recorded.

6.3.3.5. SSNMR Measurements of the NMC811 Materials

The spectra were acquired using a 16.4 T Bruker Avance III spectrometer (700 MHz ^{1}H Larmor frequency), with a Bruker 1.3 mm magic-angle spinning (MAS) probe and spinning at 50 kHz MAS frequency. Sample quantities ranged between 4 and 8.53 mg. The spin lattice relaxation constant (T_1) for the ^{1}H measurements was determined for each sample using a saturation recovery experiment. The spectra were then acquired using a rotor-synchronized Hahn-echo pulse sequence. The recycle delay (d_1) was determined directly from the T_1 values ($d_1 = T_1*5$) in the case of the ^{1}H measurements. For the ^{27}Al NMR measurements, the d_1 was set to 25 ms and for the ^{7}Li NMR to 100 ms. Same references were used for external calibration as in the previous section. To prepare the SSNMR samples of the cycled electrodes, the cycled cells were transferred to an argon-filled glovebox, opened and the electrode was washed one time with dimethyl carbonate (DMC) and dried under vacuum for 15 minutes. The material was then scrapped from the aluminium current collector and packed in 1.3 mm SSNMR rotors.

6.3.4. Electrode Fabrication, Cell Assembly and Electrochemical Cycling

Electrodes were prepared by mixing 90 wt % NMC811 powder with 5 wt% carbon black (Super-P Carbon, Timcal) and 5 wt % PVDF binder (Kynar, HSV-900). The total amounts of the coated and uncoated solids ranged between 250 and 400 mg. The solid mixture was ground for 5 minutes under air using a pestle and mortar. Then 0.5-0.8 mL of N-methyl-2-pyrrolidone (NMP) was added, the slurry was mixed in a planetary centrifugal mixer (Thinky, ARM/310 CE) at 2000 rpm for at least 10 minutes and transferred to an argon-filled glovebox. Here, the slurry was cast on aluminium foil with a doctor-blade to 150 μm thickness. The cast electrode was then dried under atmospheric pressure overnight at room temperature and then under vacuum for 4-5h at room temperature. The electrodes were then cut into disks of 12.7 mm diameter. These were dried under vacuum at 120 ºC for 24 h before being transferred to an argon-filled glovebox with oxygen and water levels below 10 ppm. The resulting electrodes had active mass loadings of 6.7 ± 1.7 mg / cm^2. Coin cells were assembled inside an argon filled glovebox with water and oxygen levels below 10 ppm. The cell components were a lithium disk of 16 mm diameter, purchased from LTS Research Laboratories, Inc. as the counter electrode, one 0.5 mm thick spacer, a steel spring, a polypropylene separator (Celgard 3031) soaked with 60 μL of electrolyte and the cathode disk. The Celgard separators had been previously cut into 16 mm disks, washed with ethanol, and dried under vacuum at 50 ºC overnight. The electrolyte used was 1.0 M $LiPF_6$ in ethylene carbonate (EC) and ethyl methyl carbonate (EMC) mixed in a 3:7 w/w ratio (SoulBrain, USA). Details on the charge-discharge protocols can be found in Chapter 4. The electrochemical cycling was performed using an Arbin LTB or a LAND CT2001A cycler.

All the NMC811 materials in Chapter 4 were tested using the same conditions. The voltage window was 3 to 4.3 V vs. Li with a constant current, constant voltage (CCCV) step at the end of charge. The testing was done at C/2 rate with two C/20 formation cycles and then two C/20 cycles every 50 cycles. In this work, 1C refers to the current needed to charge or discharge the cell in 1 h with an upper cut-off voltage of 4.3 V (corresponds to a cathode capacity of ~200 mA h/g). The purpose of the slow cycles was to test if the observed decrease in specific capacity was caused by kinetic limitations which could be eliminated at slow rates.

Appendix A: X-ray Diffraction

A1. Refinements of the Single-Crystal XRD Data (Chapter 2)

A1.1. Precursor 1: [{$Zr_4(\mu_4\text{-}O)(OEt)_{15}$}$Co^{II}Cl$]

A space group C2/c was used to describe the complex. The structure is situated on a crystallographic 2-fold rotation axis (passing through atoms O1 and O5) and necessitates 50% site occupancy for atoms Co1 and Cl1. This was confirmed by refinement of the site occupancies. Lowering the symmetry to *Cc* or $P2_1/n$ does not resolve this disorder, so the $C2/c$ description is retained. An anisotropic model with geometrical and ISOR restraints was applied. Alternative trials with the displacement parameters linked to common isotropic values led to quite significant increases in the *R*-factors, so the restrained anisotropic model was finally preferred.

A1.2. Precursor 2: [{$Zr_4(\mu_4\text{-}O)_2(EtO)_{16}$}$(Fe^{III}Cl)_2$]

Geometrical and ISOR restraints were applied to all ethoxide groups, some of which are modelled as disordered**.** Assignment of the O atom within the 5-membered ring was based on initial indications from the displacement parameters, but it is highly uncertain. The geometry of the ring is restrained, and isotropic displacement parameters are constrained to a single common value in the final refinement.

A1.3. Precursor 3: [{$Zr_4(\mu_4\text{-}O)_2(EtO)_{16}$}{$(Cu^{II}Cl)_2(OEt)$}$_2$]

The final structure was obtained by a 2-component HKLF-5 refinement using PLATON/TWINROTMAT (A. Spek, Utrecht University). The additional electron density found in spaces between the complexes was modelled as one disordered ethanol molecule per void. Omitting this molecule and applying SQUEEZE corrects for 130 electrons per unit cell, which gives ca. 32 electrons per void space, broadly consistent with the 26 electrons expected for EtOH. Since the obtained structure is a dication with no balancing anions, three possibilities were considered for charge balancing within the crystal structure:

1. Two H^+ associated with the complex: there is no clear location to accommodate these protons. In the *SQUEEZE* result (which provides the highest precision for the main complex), the two non-bridging EtO^- ligands have Zr–O = 1.907 (6) and 1.917 (6) Å, compared to protonated examples in the CSD with mean Zr–O ≈ 2.25 Å. Likewise, the geometry of the bridging EtO^- ligands and the central [O] atoms do not indicate any protonation sites.

2. Exchange of some Cu–Cl groups for Cu–H_2O: although the solvents used were nominally dried, it is possible that H_2O could be present. Cu–Cl/H_2O exchange is quite commonly seen in crystal structures, with the Cl and O atoms occupying essentially the same atomic site. However, the X-ray data do not support this hypothesis. Producing mixed Cl/O sites and refining site occupancy factors invariably produced fully occupied Cl atoms. The displacement ellipsoids of Cl show no indication of partial occupancy.

3. Exchange of some EtO^- ligands for H_2O: this seems the most probable mechanism for charge balance, given the X-ray data. In the X-ray refinement, the coordinated O atoms would be largely unaffected (although Zr–OH_2 bond distances would be longer than Zr–OEt), but the displacement parameters of the C atoms of EtO^- should indicate partial site occupancy. This is very difficult to assess, since the EtO^- ligands are anyway poorly resolved, and the displacement parameters of the C atoms are all large. Some are clearly larger than others, but it is difficult to distinguish potential fractional occupancy from positional disorder. Short contacts do exist between some EtO^- ligands in neighbouring complexes (most notably atoms C82 and C102). Bridging Zr–H_2O–Zr units are rare in the CSD (only one example), while non-bridging Zr–OH_2 is common. It is possible that some terminal EtO^- ligands are replaced by water in a manner that does not produce crystallographic order. Replacement of the ethoxide ligand in Cu–OEt–Cu might also be possible; this is difficult to assess from the geometry (since 5-coordinate Cu^{II} is highly variable), and the displacement ellipsoids are not clearly larger than any of the other EtO^- ligands.

A1.4. Crystallographic Data and Refinement of Complexes 1, 2 and 3.

Table A1. Details of the refinements performed on the single-crystal X-ray diffraction (SC-XRD) data obtained for complexes 1,2 and 3.

	1	2	3
CCDC number	2011723	2011724	2011725
Cambridge data number	DW_K1_0004	DW_K1_0007	DW_K1_0006
Chemical formula	$C_{30}H_{75}ClCoO_{16}Zr_4$	$C_{40}H_{96}Cl_2Fe_2O_{20}Zr_4$	$C_{38}H_{96}Cl_4Cu_4O_{21}Zr_4$
Formula weight	1151.16	1444.64	1649.98
Temperature / K	180(2)	180(2)	180(2)
Crystal system	monoclinic	triclinic	monoclinic
Space group	*C*2/*c*	*P*–1	*C*2/*c*
a / Å	22.2252(6)	10.8605(4)	27.6397(7)
b / Å	11.1515(4)	11.8055(4)	13.3575(4)
c / Å	22.8685(8)	13.4100(5)	18.1081(6)
α / deg	90	95.6906(13)	90
β / deg	118.2860(13)	92.7536(13)	101.0883(12)
γ / deg	90	112.3541(15)	90
Unit-cell volume / Å^3	4991.0(3)	1575.42(10)	6560.7(3)
Z	4	1	4
Calc. density / g cm^{-3}	1.532	1.523	1.670
F(000)	2348	742	3344

Radiation type	MoKα	MoKα	MoKα
Absorption coefficient / mm^{-1}	1.241	1.231	2.103
Crystal size / mm^3	0.35 x 0.23 x 0.12	0.32 x 0.28 x 0.06	0.28 x 0.18 x 0.14
2θ range / deg	7.05-43.93	7.03-50.00	7.36-43.97
Completeness to max 2θ	0.986	0.982	0.991
No. of reflections measured	11821	13683	14557
No. of independent reflections	3000	5421	14557
R(int)	0.0403	0.0461	0.0636
No. parameters / restraints	250 / 120	316 / 160	335 / 159
Final $R1$ values (I > 2σ(I))	0.0868	0.0409	0.0526
Final $wR(F^2)$ values (all data)	0.1001	0.0568	0.0774
Goodness-of-fit on F^2	1.079	1.029	0.977
Largest difference peak & hole / e $Å^{-3}$	1.097, -0.605	0.724, -0.506	0.931, -0.477

A2. PXRD Rietveld Refinements (Chapter 3)

All Rietveld refinements of NMC811 materials were carried out in the $R\bar{3}m$ space group.

A2.1. Pristine NMC811

Table A2. Atom positions and occupancies of the pristine NMC811 used in this work. Fitting quality: R_{wp} = 1.883 %, R_{exp} = 1.461 %, goodness of fit = 1.288. Lattice parameters: a = b = 2.87327 Å, c = 14.2122.

Site	Atom	x	y	z	Occupancy
3a	Ni1	0	0	0	0.015
	Li1	0	0	0	0.985
3b	Ni2	0	0	0.5	0.785
	Co1	0	0	0.5	0.1
	Mn1	0	0	0.5	0.1
6c	O1	0	0	0.24232	1

A2.2. Al_2O_3 Coated NMC811 Annealed at 200 º C

Table A3. Atom positions and occupancies of Al_2O_3 / NMC811 annealed at 200 ºC. Fitting quality: R_{wp} = 2.191 %, R_{exp} = 1.491 %, goodness of fit = 1.469. Lattice parameters: a = b = 2.87399 Å, c = 14.2151 Å.

Site	Atom	x	y	z	Occupancy
3a	Ni1	0	0	0	0.019
	Li1	0	0	0	0.981
3b	Ni2	0	0	0.5	0.781
	Co1	0	0	0.5	0.1
	Mn1	0	0	0.5	0.1
6c	O1	0	0	0.2432	1

A2.3. NMC811 Al_2O_3 Coated and Annealed at 500 º C

Table A4. Atom positions and occupancies of Al_2O_3 / NMC811 annealed at 500 ºC. Fitting quality: R_{wp} = 2.137 %, R_{exp} = 1.449 %, goodness of fit = 1.469 Lattice parameters: a = b = 2.87347 Å, c = 14.2132 Å.

Site	Atom	x	y	z	Occupancy
3a	Ni1	0	0	0	0.031
	Li1	0	0	0	0.969
3b	Ni2	0	0	0.5	0.769
	Co1	0	0	0.5	0.1
	Mn1	0	0	0.5	0.1
6c	O1	0	0	0.24394	1

A2.4. NMC811 Al_2O_3 Coated and Annealed at 800 º C

Phase 1: NMC811 (94.64 %)

Table A5. Atom positions and occupancies of Al_2O_3 / NMC811 annealed at 800 ºC for the pristine NMC811 phase. Fitting quality: R_{wp} = 2.969 %, R_{exp} = 1.795 %, goodness of fit = 1.654. Lattice parameters: a = b = 2.88418 Å, c = 14.2457 Å.

Site	Atom	x	y	z	Occupancy
3a	Ni1	0	0	0	0.045
	Li1	0	0	0	0.955
3b	Ni2	0	0	0.5	0.755
	Co1	0	0	0.5	0.1
	Mn1	0	0	0.5	0.1
6c	O1	0	0	0.23719	1

Phase 2: Al-doped NMC811 (5.36 %)

Table A6. Atom positions and occupancies of Al_2O_3 / NMC811 annealed at 800 ºC for the aluminium-doped NMC811 phase. Fitting quality: R_{wp} = 2.969 %, R_{exp} = 1.795 %, goodness of fit = 1.654. Lattice parameters: a = b = 2.89199 Å, c = 14.3845 Å.

Site	Atom	x	y	z	Occupancy
3a	Ni1	0	0	0	0.0
	Li1	0	0	0	1.0
3b	Ni2	0	0	0.5	0.8
	Co1	0	0	0.5	0.011
	Al1	0	0	0.5	0.089
	Mn1	0	0	0.5	0.1
6c	O1	0	0	0.52802	1

A2.5. Uncoated NMC811 Annealed at 400 ºC under Air

Table A7. Atom positions and occupancies of uncoated NMC811 annealed at 400 ºC. Fitting quality: R_{wp} = 1.915 %, R_{exp} = 1.309 %, goodness of fit = 1.462. Lattice parameters: a = b = 2.87326 Å, c = 14.20989 Å.

Site	Atom	x	y	z	Occupancy
3a	Ni1	0	0	0	0.0152
	Li1	0	0	0	0.985
3b	Ni2	0	0	0.5	0.785
	Co1	0	0	0.5	0.1
	Mn1	0	0	0.5	0.1
6c	O1	0	0	0.24253	1

A2.6. Uncoated NMC811 Annealed at 800 ºC under Air

Table A8. Atom positions and occupancies of uncoated NMC811 annealed at 800 ºC. Fitting quality: R_{wp} = 1.99147 %, R_{exp} = 1.33093 %, goodness of fit = 1.49629. Lattice parameters: a = b = 2.87746 Å, c = 14.22219 Å.

Site	Atom	x	y	z	Occupancy
3a	Ni1	0	0	0	0.044
	Li1	0	0	0	0.956
3b	Ni2	0	0	0.5	0.77
	Co1	0	0	0.5	0.1
	Mn1	0	0	0.5	0.1
6c	O1	0	0	0.24254	1

A2.7. Al_2O_3 Coated NMC811 Annealed at 800 ºC under Oxygen

Table A9. Atom positions and occupancies of uncoated NMC811 annealed at 800 ºC. Fitting quality: R_{wp} = 1.92709 %, R_{exp} = 1.32253 %, goodness of fit = 1.45712. Lattice parameters: a = b = 2.87509 Å, c = 14.215 Å.

Site	Atom	x	y	z	Occupancy
3a	Ni1	0	0	0	0.03
	Li1	0	0	0	0.97
3b	Ni2	0	0	0.5	0.78
	Co1	0	0	0.5	0.1
	Mn1	0	0	0.5	0.1
6c	O1	0	0	0.24252	1

A3. PXRD data and Rietveld Refinements (Chapter 4)

A3.1. Precursor Thermolysis: Rietveld Refinement Parameters

Table A10. Atomic coordinates and site occupancies of precursor **1** annealed at 800 ºC.

Site	Atom	x	y	z	Occupancy
4a	Li1	0.795	0.795	0	1
	Al1	0.186	0.186	0	1
8b	O1	0.353	0.295	0.778	1

Table A11. Atomic coordinates and site occupancies of the γ-$LiAlO_2$ phase formed after decomposition of precursor **2** at 800 ºC under air.

Site	Atom	x	y	z	Occupancy
4a	Li1	0.838	0.838	0	1
	Al1	0.178	0.178	0	1
8b	O1	0.338	0.286	0.779	1

Table A12. Atomic coordinates and site occupancies of the α-$LiAlO_2$ phase formed after decomposition of precursor **2** at 800 ºC under air.

Site	Atom	x	y	z	Occupancy
3a	Li1	0	0	0	1
3b	Al1	0	0	0.5	1
6c	O1	0	0	0.249	1

Table A13. Atomic coordinates and site occupancies of precursor **3** annealed at 800 ºC.

Site	Atom	x	y	z	Occupancy
4a	Li1	0.815	0.815	0	1
	Al1	0.184	0.184	0	1
8b	O1	0.351	0.282	0.783	1

A3.2. Diffraction Patterns and Refinements of NMC811 Materials (Chapter 4)

A3.2.1. Laboratory PXRD data

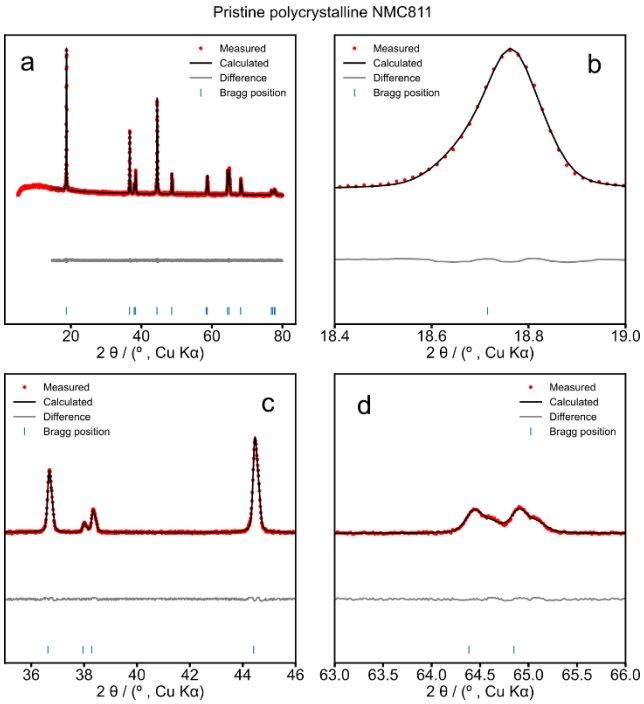

Figure A1. Polycrystalline NMC811 (pristine).

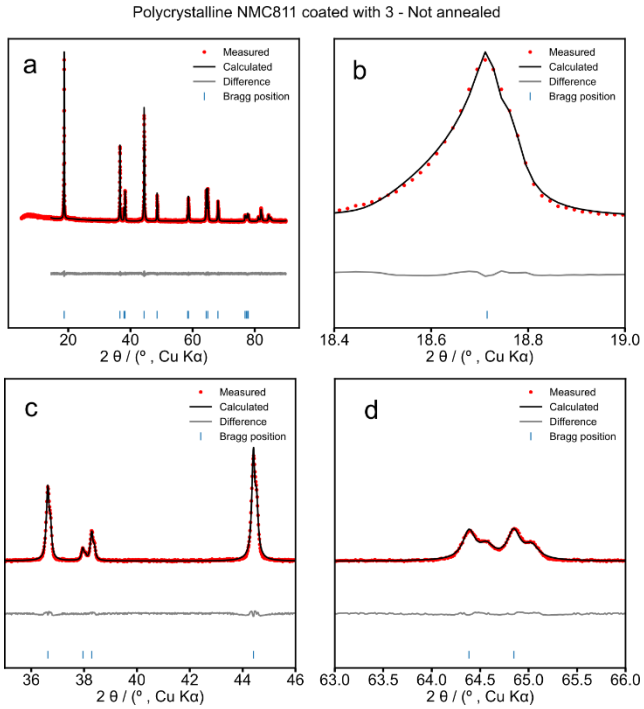

Figure A2. Polycrystalline NMC811 coated with **3** not annealed.

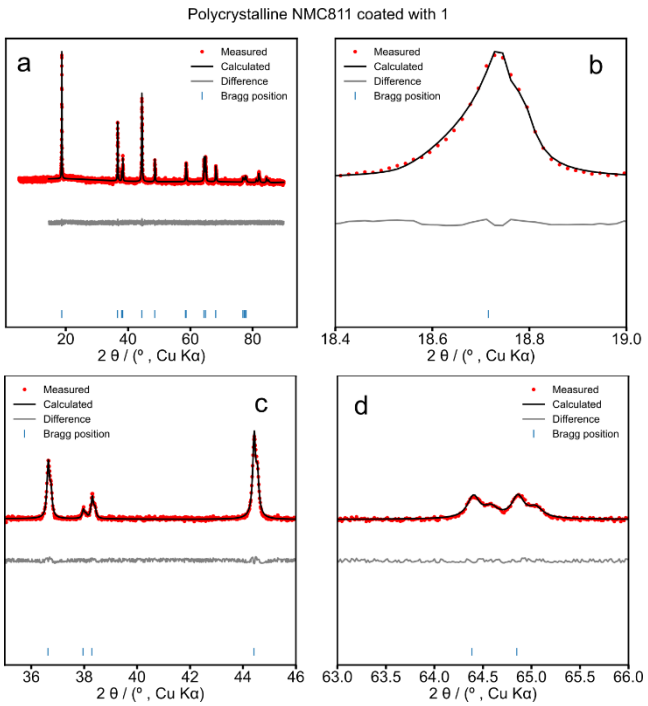

Figure A3. Polycrystalline NMC811 coated with **1**.

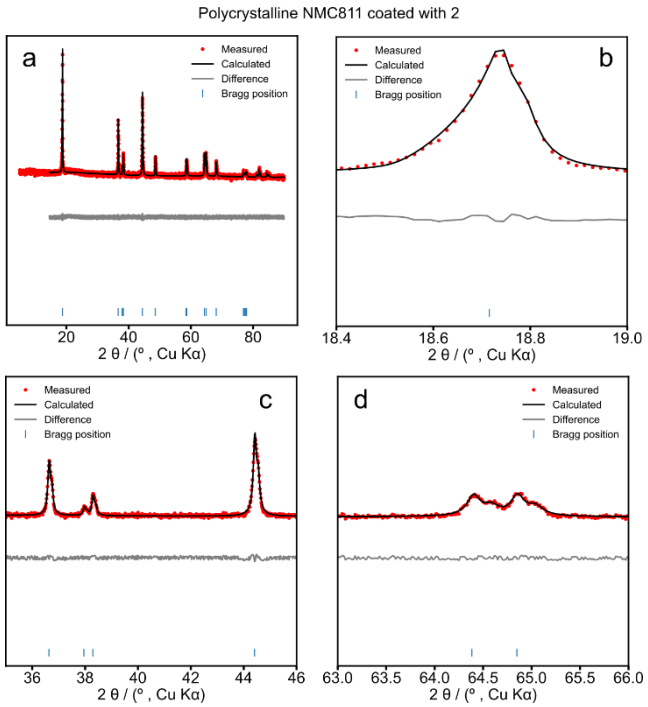

Figure A4. Polycrystalline NMC811 coated with **2**.

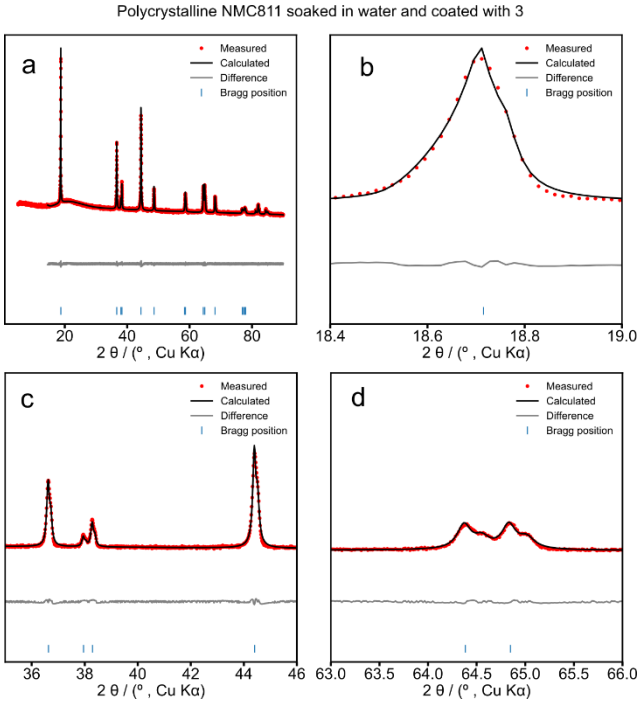

Figure A5. Polycrystalline NMC811 soaked in water and coated with **3**.

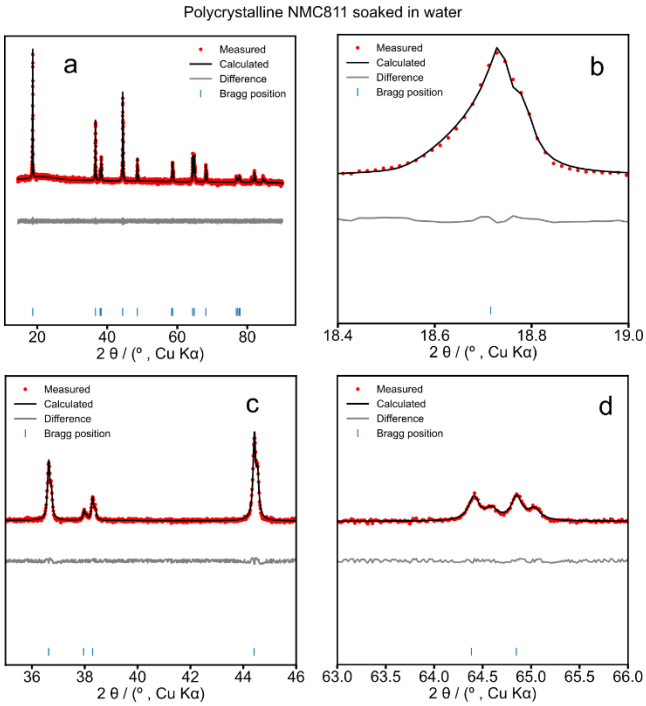

Figure A6. Polycrystalline NMC811 soaked in water (not annealed).

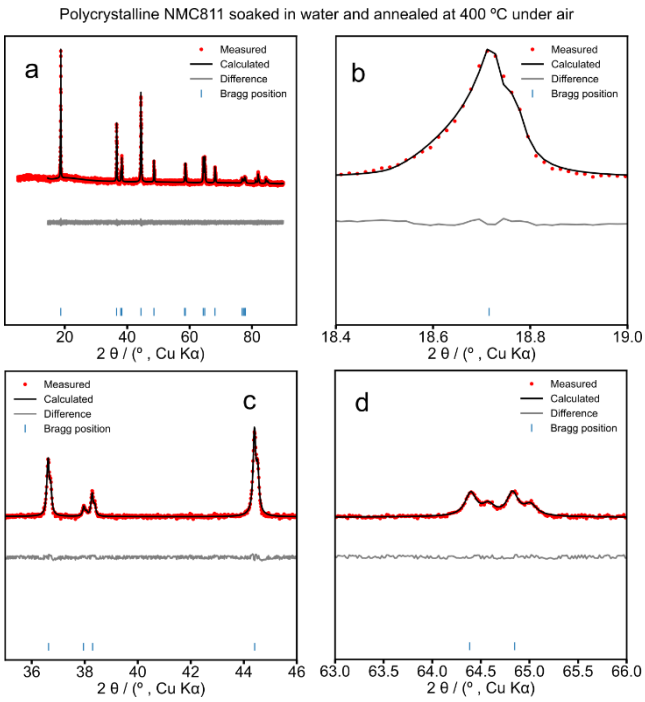

Figure A7. Polycrystalline NMC811 soaked in water annealed at 400 ºC.

A3.2.2. Refinement Results for the Laboratory PXRD data

Table A14. Pristine polycrystalline NMC811 atomic coordinates and site occupancies.

Site	Atom	x	y	z	Occupancy
3a	Li1	0	0	0	0.985
	Ni1	0	0	0	0.0152
3b	Ni2	0	0	0.5	0.785
	Co1	0	0	0.5	0.1
	Mn1	0	0	0.5	0.1
6c	O1	0	0	0.242	1

Table A15. Atomic coordinates and site occupancies polycrystalline NMC811 coated using precursor **1** and annealed under air at 400 ºC.

Site	Atom	x	y	z	Occupancy
3a	Li1	0	0	0	0.984
	Ni1	0	0	0	0.0164
3b	Ni2	0	0	0.5	0.784
	Co1	0	0	0.5	0.1
	Mn1	0	0	0.5	0.1
6c	O1	0	0	0.243	1

Table A16. Atomic coordinates and site occupancies polycrystalline NMC811 coated using precursor **2** and annealed under air at 400 ºC.

Site	Atom	x	y	z	Occupancy
3a	Li1	0	0	0	0.985
	Ni1	0	0	0	0.0147
3b	Ni2	0	0	0.5	0.785
	Co1	0	0	0.5	0.1
	Mn1	0	0	0.5	0.1
6c	O1	0	0	0.243	1

Table A17. Atomic coordinates and site occupancies polycrystalline NMC811 coated using precursor **3** and dried under vacuum at 100 ºC.

Site	Atom	x	y	z	Occupancy
3a	Li1	0	0	0	0.983
	Ni1	0	0	0	0.0174
3b	Ni2	0	0	0.5	0.783
	Co1	0	0	0.5	0.1
	Mn1	0	0	0.5	0.1
6c	O1	0	0	0.242	1

Table A18. Atomic coordinates and site occupancies NMC811 soaked in water and dried under vacuum at 100 ºC.

Site	Atom	x	y	z	Occupancy
3a	Li1	0	0	0	0.984
	Ni1	0	0	0	0.0158
3b	Ni2	0	0	0.5	0.784
	Co1	0	0	0.5	0.1
	Mn1	0	0	0.5	0.1
6c	O1	0	0	0.243	1

Table A19. Atomic coordinates and site occupancies NMC811 soaked in water and annealed under air at 400 ºC.

Site	Atom	x	y	z	Occupancy
3a	Li1	0	0	0	0.978
	Ni1	0	0	0	0.0216
3b	Ni2	0	0	0.5	0.778
	Co1	0	0	0.5	0.1
	Mn1	0	0	0.5	0.1
6c	O1	0	0	0.242	1

Table A20. Atomic coordinates and site occupancies NMC811 soaked in water, coated with **3** and annealed under air at 400 ºC.

Site	Atom	x	y	z	Occupancy
3a	Li1	0	0	0	0.98
	Ni1	0	0	0	0.0202
3b	Ni2	0	0	0.5	0.78
	Co1	0	0	0.5	0.1
	Mn1	0	0	0.5	0.1
6c	O1	0	0	0.244	1

A3.2.3. Synchrotron PXRD data

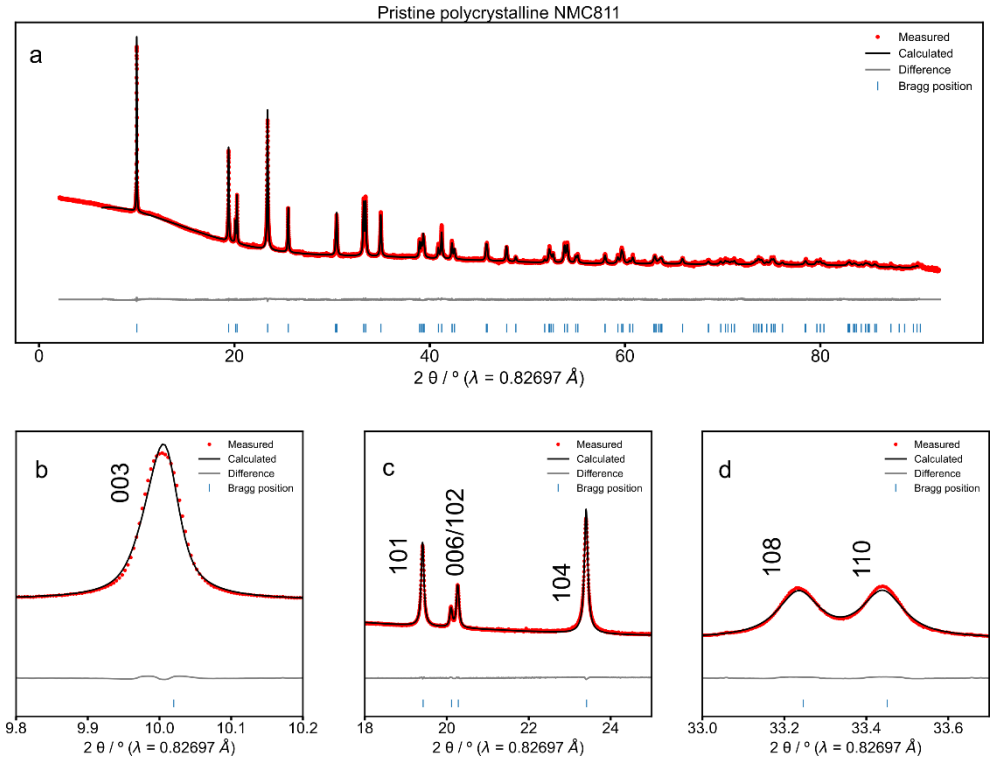

Figure A8. Polycrystalline NMC811

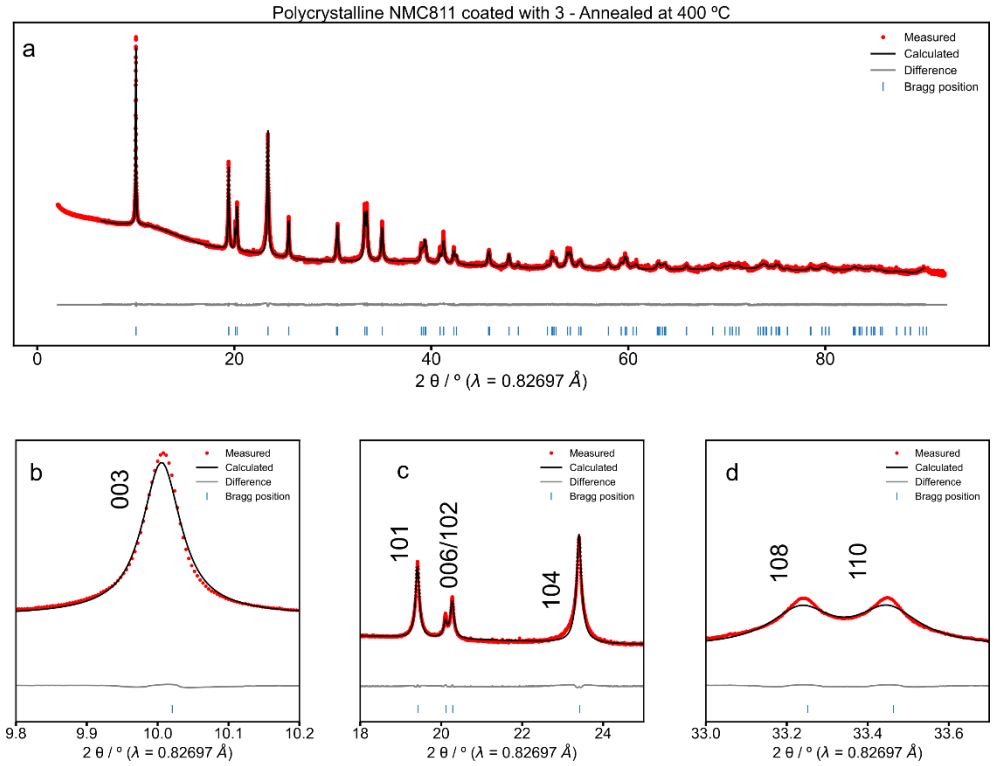

Figure A9. Polycrystalline NMC811 coated with **3** and annealed at 400 ºC under air.

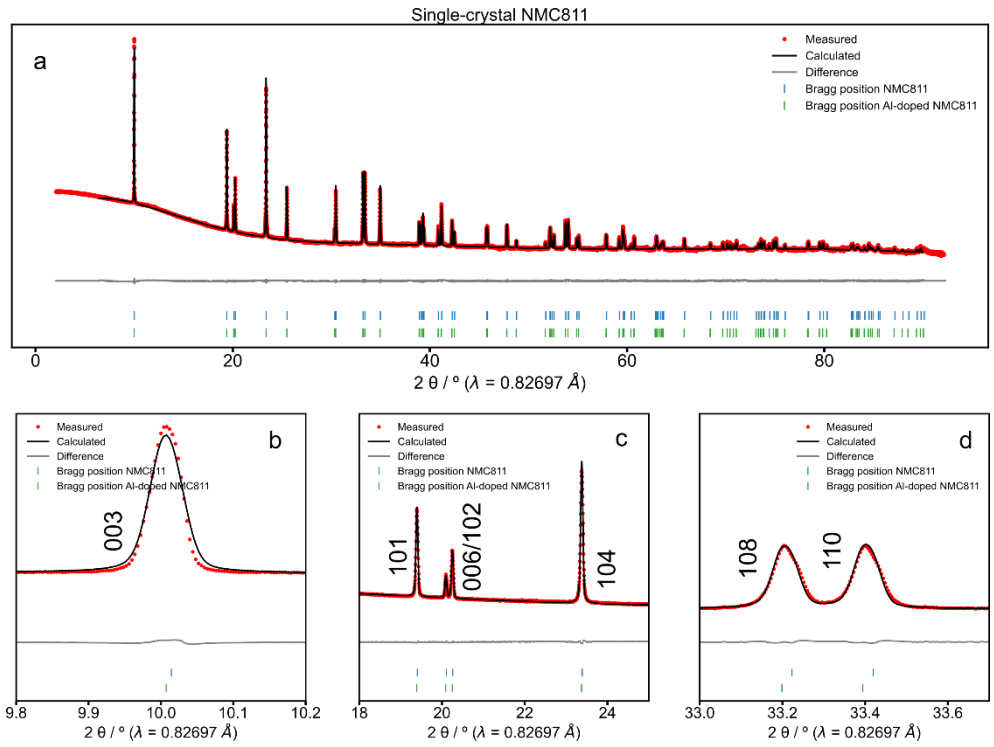

Figure A10. Single-crystal NMC811.

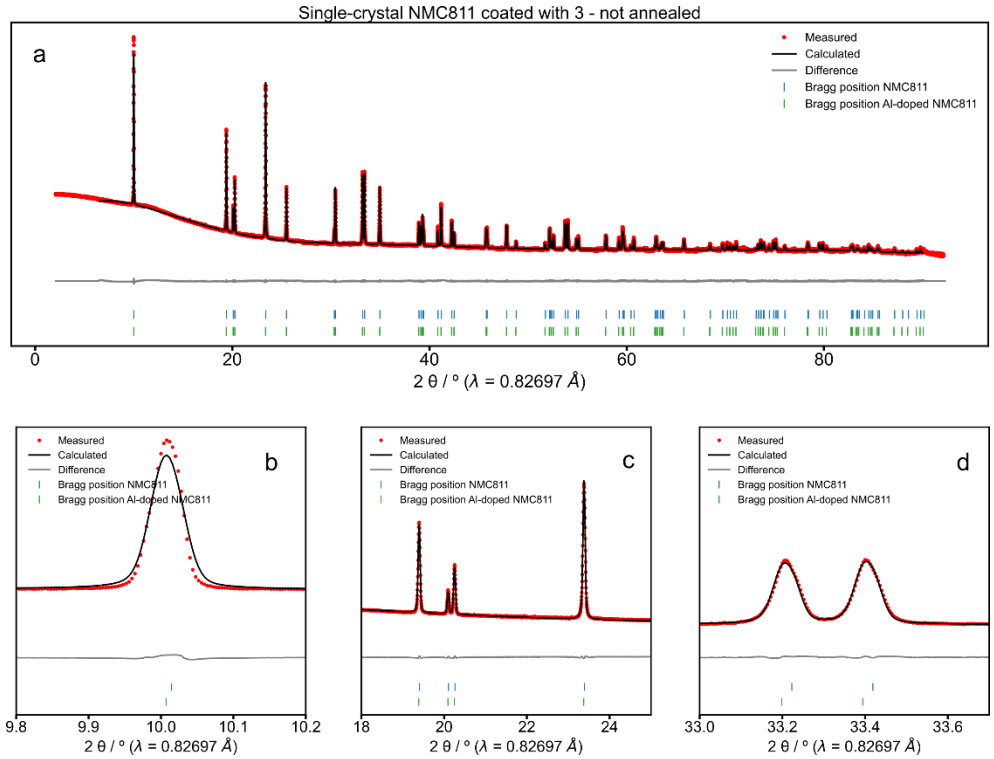

Figure A11. Single-crystal NMC811 coated with **3** and dried at 100 ºC under vacuum.

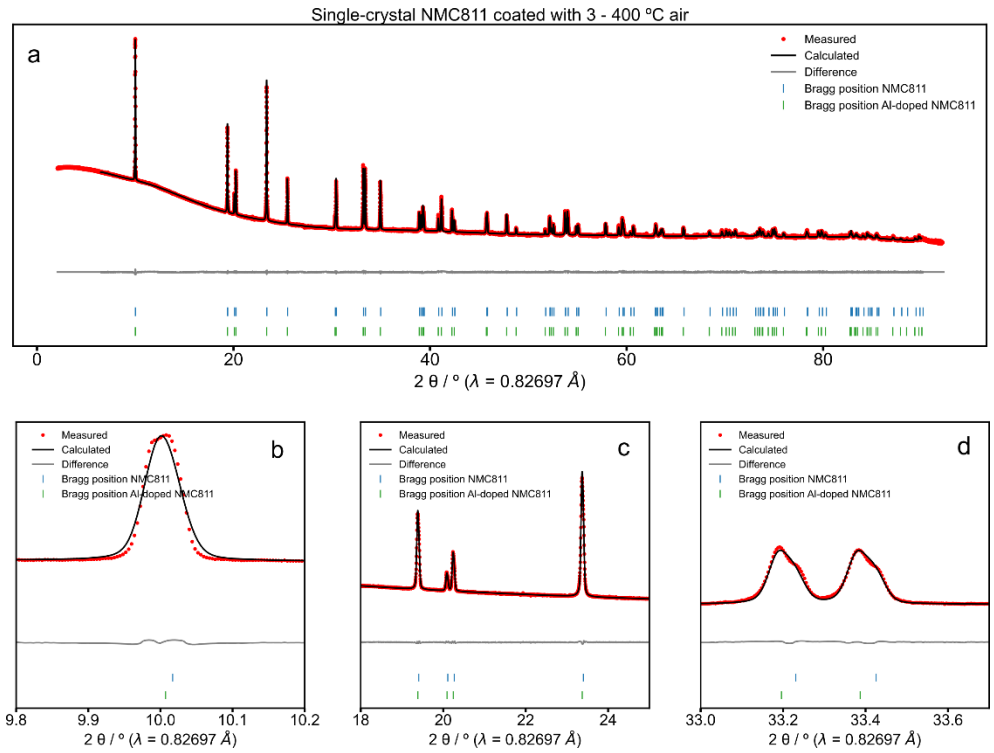

Figure A12. Single-crystal NMC811 coated with **3** and annealed at 400 ºC under air.

A3.2.4. Refinement Results for the Synchrotron PXRD data

Table A21. R_{wp} and lattice parameters from Rietveld refinement of laboratory data.

Sample	R_{wp} / %	Refined phases	Wt %	a / Å	b / Å	c / Å
Polycrystalline (PC) NMC811	3.541	NMC811	100%	2.87	2.87	14.188
PC-NMC811 coated with **3** / 400 °C (air)	4.898	NMC811	100%	2.869	2.869	14.187
Single-crystal (SC)-NMC811	4.204	Al-NMC	57%	2.875	2.875	14.205
		NMC	43%	2.873	2.873	14.196
SC-NMC811 coated with 3 100 °C (vacuum)	4.114	Al-NMC	57%	2.875	2.875	14.207
		NMC	43%	2.873	2.873	14.196
SC-NMC811 coated with 3 400 °C (air)	3.118	Al-NMC	62%	2.876	2.876	14.206
		NMC	38%	2.872	2.872	14.192

Table A22. Polycrystalline NMC811

Site	Atom	x	y	z	Occupancy
3a	Li1	0	0	0	0.978
	Ni1	0	0	0	0.0221
3b	Ni2	0	0	0.5	0.778
	Co1	0	0	0.5	0.1
	Mn1	0	0	0.5	0.1
6c	O1	0	0	0.242	1

Table A23. Polycrystalline NMC811 coated with **3** and annealed under air at 400 °C.

Site	Atom	x	y	z	Occupancy
3a	Li1	0	0	0	0.964
	Ni1	0	0	0	0.0358
3b	Ni2	0	0	0.5	0.764
	Co1	0	0	0.5	0.1
	Mn1	0	0	0.5	0.1
6c	O1	0	0	0.242	1

Table A24. Aluminium-doped NMC811 phase in the pristine single-crystal NMC811.

Site	Atom	x	y	z	Occupancy
3a	Li1	0	0	0	0.957
	Ni1	0	0	0	0.0434
3b	Ni2	0	0	0.5	0.738
	Mn1	0	0	0.5	0.1
	Co1	0	0	0.5	0.1
	Al1	0	0	0.5	0.0188
6c	O1	0	0	0.243	1

Table A25. NMC811 phase in the pristine single-crystal NMC811.

Site	Atom	x	y	z	Occupancy
3a	Li1	0	0	0	0.998
	Ni1	0	0	0	0.002
3b	Ni2	0	0	0.5	0.798
	Co1	0	0	0.5	0.1
	Mn1	0	0	0.5	0.1
6c	O1	0	0	0.238	1

Table A26. Aluminium-doped NMC811 phase in the single-crystal NMC811 coated with **3** and dried at 100 ºC under vacuum.

Site	Atom	x	y	z	Occupancy
3a	Li1	0	0	0	0.957
	Ni1	0	0	0	0.0434
3b	Ni2	0	0	0.5	0.743
	Mn1	0	0	0.5	0.1
	Co1	0	0	0.5	0.1
	Al1	0	0	0.5	0.0134
6c	O1	0	0	0.243	1

Table A27. NMC811 phase in the single-crystal NMC811 coated with **3** and dried at 100 ºC under vacuum.

Site	Atom	x	y	z	Occupancy
3a	Li1	0	0	0	0.998
	Ni1	0	0	0	0.00178
3b	Ni2	0	0	0.5	0.798
	Co1	0	0	0.5	0.1
	Mn1	0	0	0.5	0.1
6c	O1	0	0	0.238	1

Table A28. Aluminium-doped NMC811 phase in the single-crystal NMC811 coated with **3** and annealed at 400 ºC under air.

Site	Atom	x	y	z	Occupancy
3a	Li1	0	0	0	0.983
	Ni1	0	0	0	0.0165
3b	Ni2	0	0	0.5	0.73
	Mn1	0	0	0.5	0.1
	Co1	0	0	0.5	0.1
	Al1	0	0	0.5	0.0536
6c	O1	0	0	0.24	1

Table A29. NMC811 phase in the single-crystal NMC811 coated with **3** and annealed at 400 ºC under air.

Site	Atom	x	y	z	Occupancy
3a	Li1	0	0	0	0.993
	Ni1	0	0	0	0.00711
3b	Ni2	0	0	0.5	0.793
	Co1	0	0	0.5	0.1
	Mn1	0	0	0.5	0.1
6c	O1	0	0	0.24	1

Appendix B: Electron Microscopy and Elemental Analysis by X-ray Spectroscopy

B1. Characterisation of the Catalyst Films using SEM-EDS (Chapter 2)

To analyse the elemental composition and distribution of elements in the catalysts, EDS point scans were taken across the sample. The normalized atomic percentage of each of the elements detected by EDS is presented and the dopant : Zr ratio is calculated. Outliers were removed using a Dixon's Q test with 80 % confidence. The 95 % confidence intervals were calculated.

B1.1. EDS Analysis of CoZr Electrode before Catalysis:

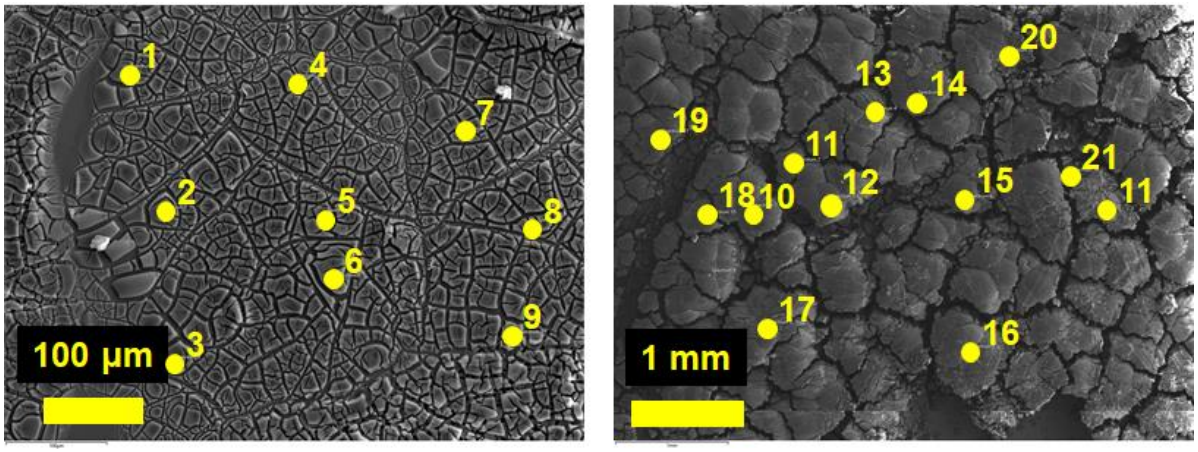

Figure B1. Location of the point scans measured on the CoZr electrode before catalysis.

Table B1. Normalized atomic percentages of the elements detected in the CoZr electrode before catalysis.

	Atomic %					
Spectrum	O	C	Zr	Cl	Co	Co : Zr
1	63.7	17.2	11.9	5.4	1.8	0.15
2	63.5	15.3	13.2	5.9	2.0	0.15
3	63.6	15.0	13.4	6.1	1.9	0.14
4	62.8	21.8	9.7	4.2	1.5	0.15
5	59.5	15.8	15.5	6.7	2.5	0.16
6	58.4	16.7	15.8	6.7	2.4	0.15
7	59.2	23.6	10.8	4.7	1.6	0.15
8	59.7	19.2	13.5	5.5	2.1	0.16
9	58.1	21.7	12.7	5.7	1.9	0.15
10	69.1	21.4	6.9	2.3	0.2	0.03
11	61.1	17.5	14.0	4.8	2.5	0.18
12	75.6	15.7	6.6	2.1	0.1	0.02
13	66.9	19.1	9.7	3.7	0.6	0.06
14	62.7	16.1	14.2	5.7	1.3	0.090
15	70.1	17.4	8.8	3.2	0.4	0.05
16	65.9	17.4	11.1	4.3	1.2	0.11
17	59.8	16.8	15.5	6.0	1.8	0.12
18	61.9	18.0	13.5	4.7	1.9	0.14
19	62.8	15.0	14.5	6.0	1.6	0.11

20	60.6	19.8	12.6	4.7	2.3	0.18
21	58.6	22.8	12.5	4.4	1.7	0.14
Average	63.0	18.3	12.2	4.9	1.6	0.10
Confidence interval	1.67	1.00	1.0	0.49	0.27	0.02

B1.2. EDS Analysis of CoZr Electrode after Catalysis

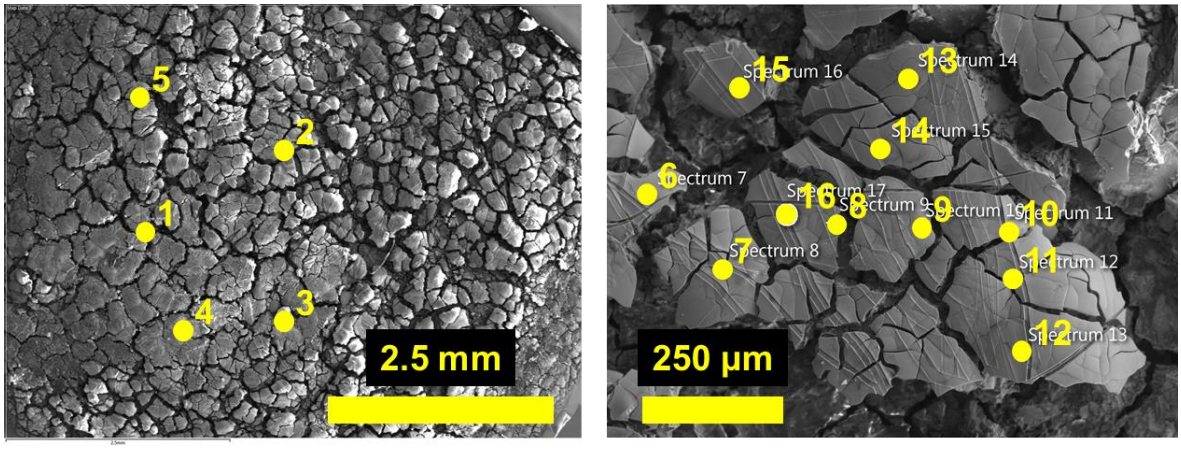

Figure B2. Location where the point scans were measured on the CoZr electrode after catalysis.

Table B2. Normalized atomic percentages of the elements detected in the CoZr electrode after catalysis.

	Atomic %						
Spectrum	O	C	Zr	K	F	Co	Co :Zr
1	48	19.5	18.8	4.9	5.5	3.4	0.18
2	33.7	0	11.1	5.2	47.1	2.7	0.24
3	34.4	0	12.4	6.1	41.9	4.5	0.36
4	25.1	0	10.5	4.1	58.4	1.9	0.18
5	40.1	31.5	8.7	3.5	15	1.2	0.14
6	69.8	11.3	14.9	1.8	0	2.2	0.15
7	64.4	17	10.4	3.4	0	4.8	0.46
8	53.5	28	14.1	2.1	0	2.4	0.17
9	68.1	10	17.2	2.1	0	2.6	0.15
10	63.6	16.5	15.4	2.2	0	2.3	0.15
11	53.9	26.4	13.5	2.8	0	3.4	0.25
12	46.8	31.3	16.5	2.5	0	2.8	0.17
13	62.2	10.3	21.2	2.9	0	3.3	0.16
14	64.5	12.3	18.2	2.3	0	2.7	0.15
15	56.7	11.3	24.4	3.1	0	4.5	0.18
16	62.5	16.9	15.9	2.2	0	2.6	0.16
Average	53	15.1	15.2	3.2	10.5	3	0.2
Confidence interval	5.88	4.47	1.81	0.55	19.8	0.43	0.04

B1.3. EDS Analysis of CuZr Electrode before Catalysis

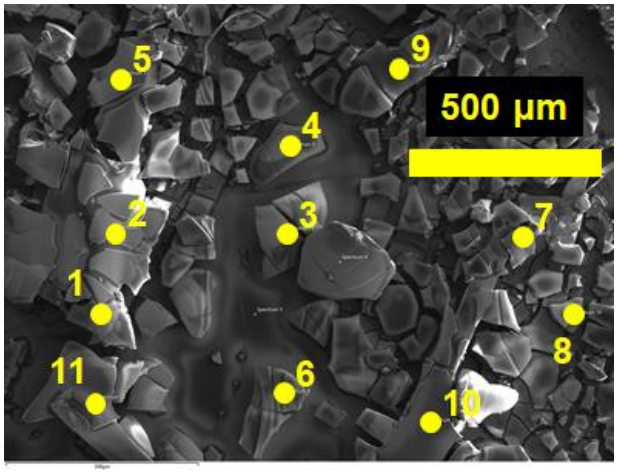

Figure B3. Location where the point scans were measured on the CuZr electrode before catalysis.

Table B3. Normalized atomic percentages of the elements detected in the CuZr electrode before catalysis.

	Atomic %					
Spectrum	O	C	Zr	Cl	Cu	Cu : Zr
1	64.9	25.6	6.5	1.2	1.8	0.28
2	69.6	15.6	10.6	2.1	2.2	0.21
3	23.8	65.1	8.7	1.7	0.6	0.07
4	49.4	37.4	9.6	1.7	1.9	0.2
5	70.0	17.6	8.6	1.6	2.2	0.26
6	47.8	42.5	7.1	1.1	1.5	0.21
7	47.3	46.4	4.1	0.6	1.7	0.41
8	60.6	23.5	11.6	2.2	2.1	0.18
9	33.3	57.7	6.9	1.0	1.1	0.16
10	73.2	15.2	8.5	1.8	1.2	0.14
11	69.3	19	8.3	1.6	1.9	0.23
Average	55.4	33.2	8.2	1.5	1.7	0.2
Confidence interval	8.88	9.58	1.1	0.26	0.28	0.04

B1.4. EDS Analysis of CuZr Electrode after Catalysis

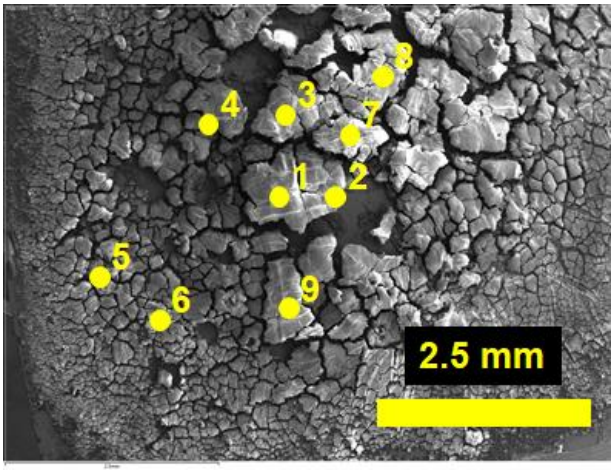

Figure B4. Location where the point scans were measured on the CuZr electrode after catalysis.

Table B4. Normalized atomic percentages of the elements detected in the CuZr electrode after catalysis.

	Atomic %					
Spectrum	O	C	Zr	K	Cu	Cu : Zr
1	57.9	30.1	6.6	4.8	0.5	0.08
2	57.9	20.6	14.1	6.1	1.2	0.085
3	57.4	24.4	11.8	5.3	1.2	0.10
4	59.7	28.7	7.6	2.7	1.3	0.17
5	54.7	25.8	13.2	5.0	1.3	0.10
6	75.1	0	17.6	5.3	2.0	0.11
7	58.6	27.7	12.4	0	1.3	0.10
8	54.3	24.3	14.5	5.8	1.1	0.076
9	59.0	15.9	17.9	5.9	1.4	0.078
Average	59.4	21.9	13	4.5	1.0	0.10
Confidence interval	3.87	5.84	2.4	1.3	0.3	0.04

B1.5. EDS Analysis of FeZr Electrode before Catalysis

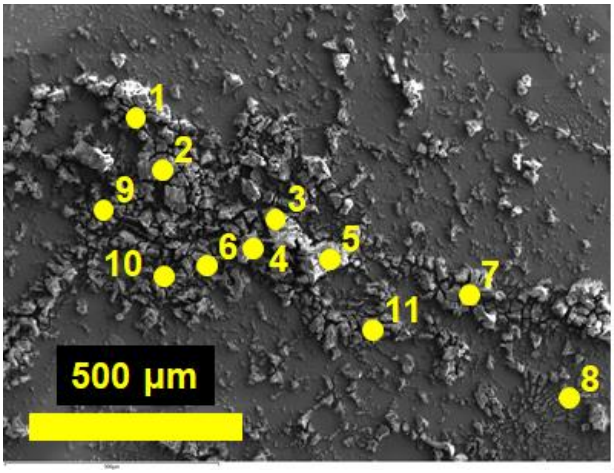

Figure B5. Location where the point scans were measured on the FeZr electrode before catalysis.

Table B5. Normalized atomic percentages of the elements detected in the FeZr electrode before catalysis.

	Atomic %				
Spectrum	O	Cl	Zr	Fe	Fe : Zr
1	63.7	7.2	25.1	4.0	0.16
2	74.4	6.0	17.1	2.5	0.15
3	78.1	5.7	14.8	1.4	0.095
4	66.1	6.7	23.0	4.2	0.18
5	64.7	7.5	24.4	3.4	0.14
6	67.2	7.3	22.5	2.9	0.13
7	79.6	5.6	13.5	1.3	0.096
8	77.3	5.9	15.3	1.5	0.098
9	73.8	6.2	17.9	2.1	0.12
10	69.2	7.3	20.8	2.7	0.13
11	69.5	7.0	21.4	2.1	0.098
Average	71.2	6.6	19.6	2.6	0.13
Confidence intervals	3.06	0.39	2.2	0.54	0.031

B1.6. EDS Analysis of FeZr Electrode after Catalysis

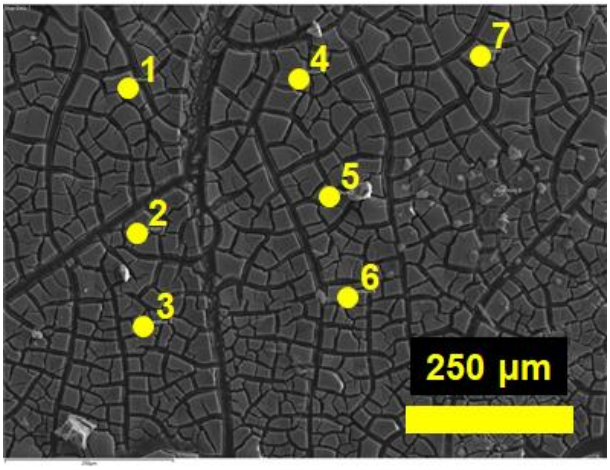

Figure B6. Location where the point scans were measured on the FeZr electrode after catalysis.

Table B6. Normalized atomic percentages of the elements detected in the FeZr electrode after catalysis.

	Atomic %					
Spectrum	O	Zr	C	K	Fe	Fe : Zr
1	71.8	21.0	0	4.9	2.4	0.11
2	60.6	16.3	17.5	3.8	1.8	0.11
3	60.2	15.6	18.8	3.7	1.7	0.11
4	61.5	15.5	17.9	3.6	1.5	0.10
5	56.9	16.2	21.3	3.7	1.9	0.12
6	59.6	14.8	20.3	3.6	1.6	0.11
7	62.7	16.5	15.3	3.8	1.7	0.10
Average	61.9	16.6	15.9	3.9	1.8	0.11
Confidence intervals	3.38	1.46	5.20	0.33	0.21	0.016

B1.7. Summary of the EDS Results and Dopant : Zr Ratio

Table B7. Summary of EDS-derived dopant : Zr ratios

Sample	TM : Zr ratio	Confidence interval
Co : Zr precursor	0.25	-
Co : Zr before	0.12	0.02
Co : Zr after	0.2	0.04
Cu : Zr precursor	1	-
Cu : Zr before	0.2	0.04
Cu : Zr after	0.1	0.04
Fe : Zr precursor	0.5	-
Fe : Zr before	0.13	0.031
Fe : Zr after	0.11	0.016

B.2. Characterisation of the Pristine and Al_2O_3 Coated NMC811 (Chapter 3)

B2.1. SEM Images

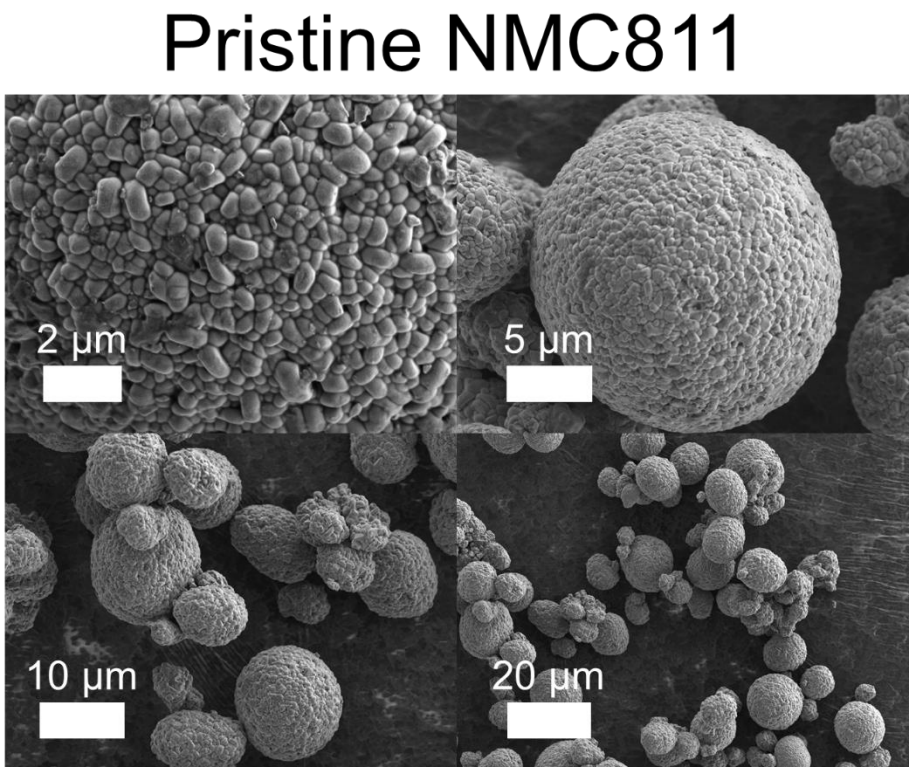

Figure B7. SEM images of pristine NMC811.

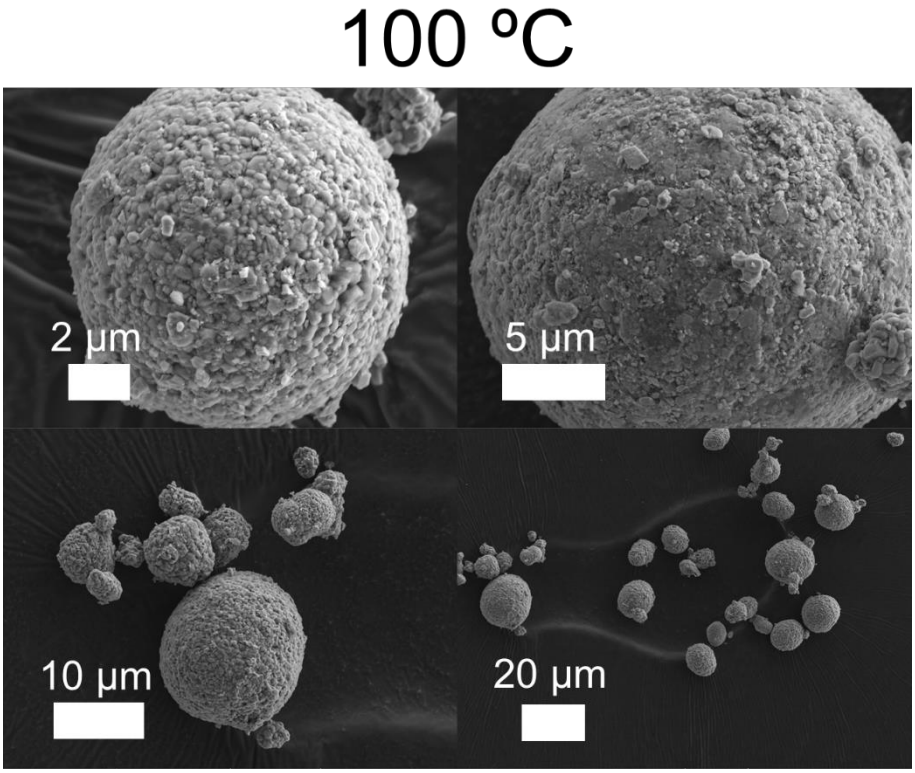

Figure B8. SEM images of Al_2O_3 coated NMC811 dried under vacuum at 100 ºC.

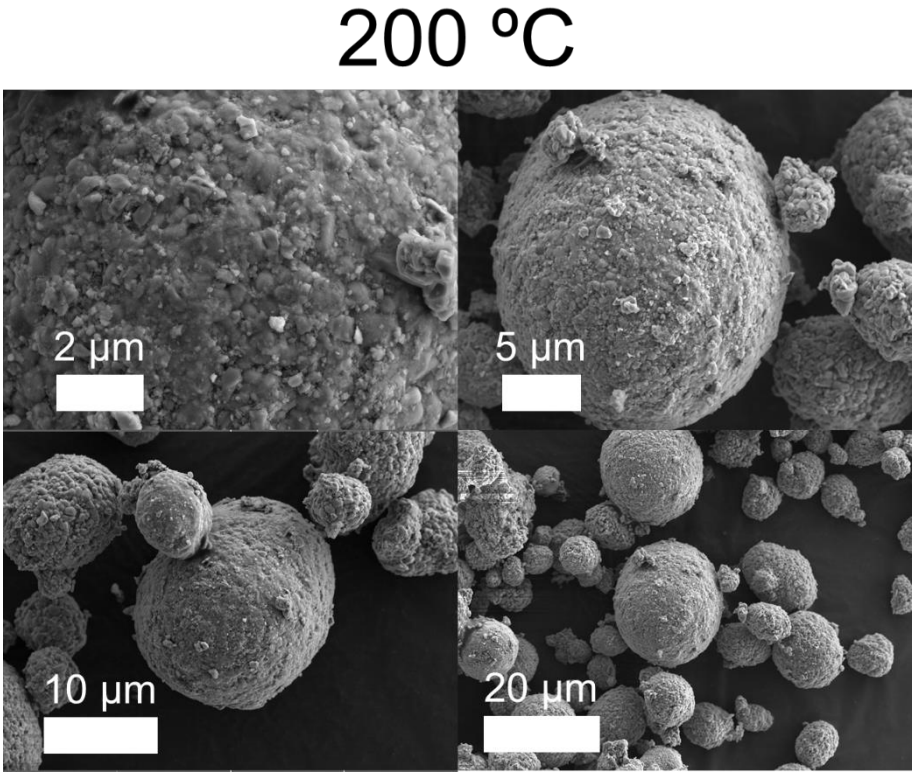

Figure B9. SEM images of Al_2O_3 coated NMC811 dried and then annealed under air at 200 ºC.

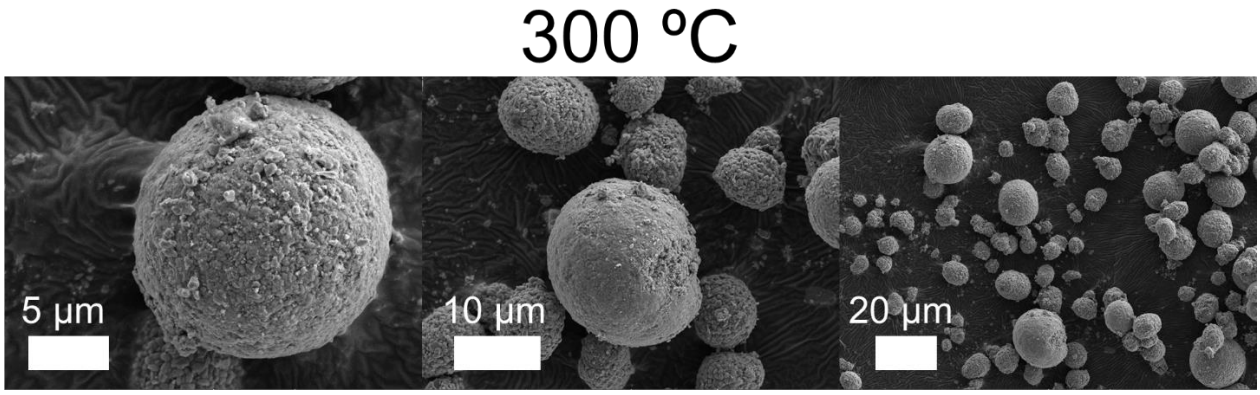

Figure B10. SEM images of Al_2O_3 coated NMC811 dried and then annealed under air at 300 ºC.

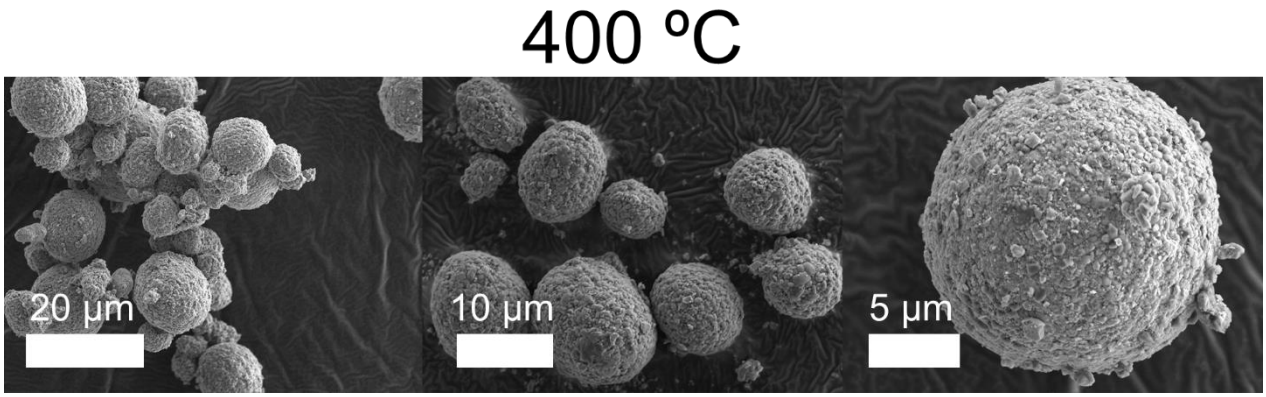

Figure B11. SEM images of Al_2O_3 coated NMC811 dried and then annealed under air at 400 ºC.

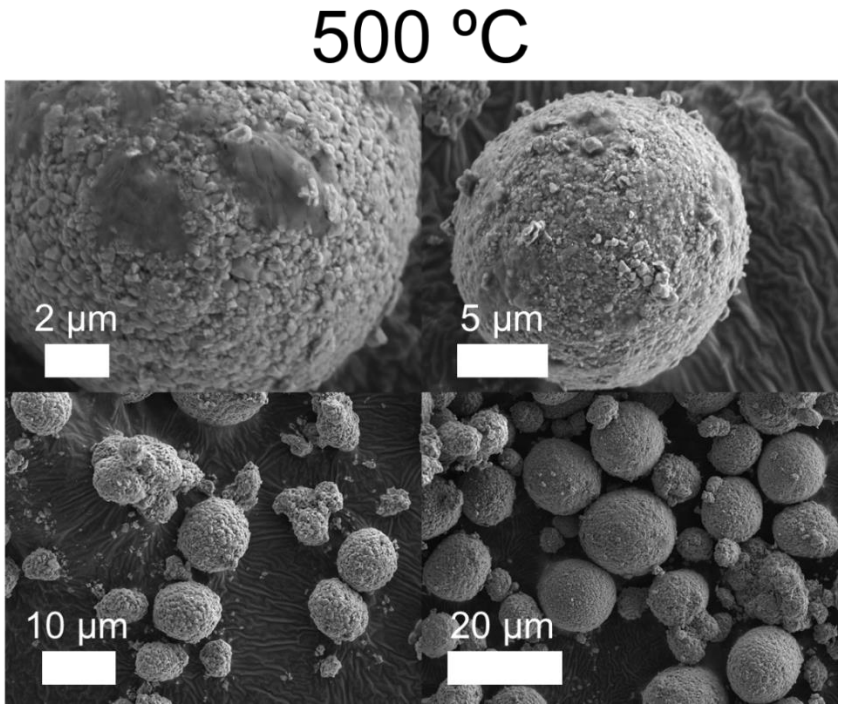

Figure B12. SEM images of Al_2O_3 coated NMC811 dried and then annealed under air at 500 ºC.

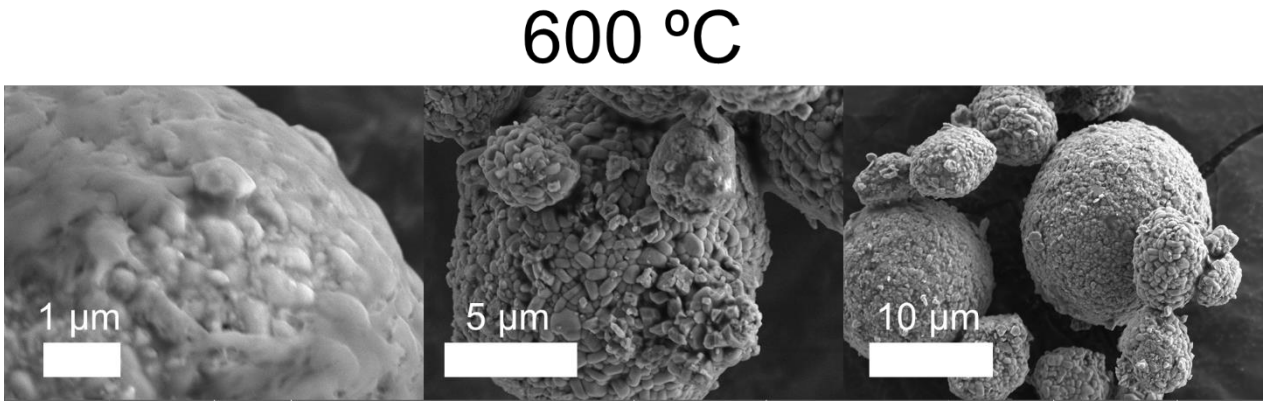

Figure B13. SEM images of Al_2O_3 coated NMC811 dried and then annealed under air at 600 ºC.

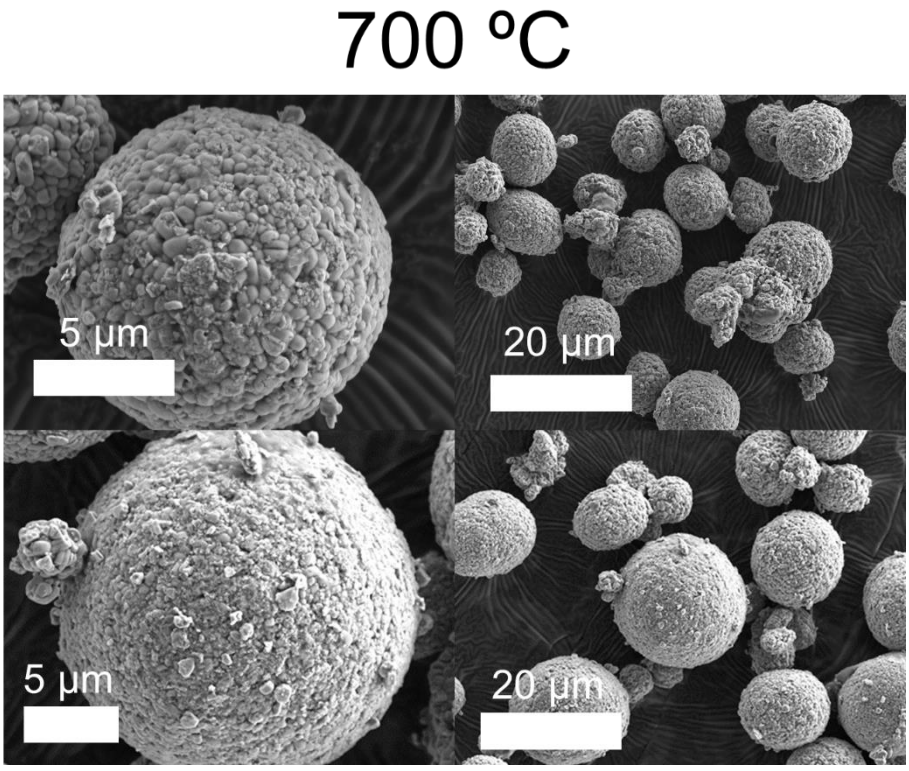

Figure B14. SEM images of Al_2O_3 coated NMC811 dried and then annealed under air at 700 ºC.

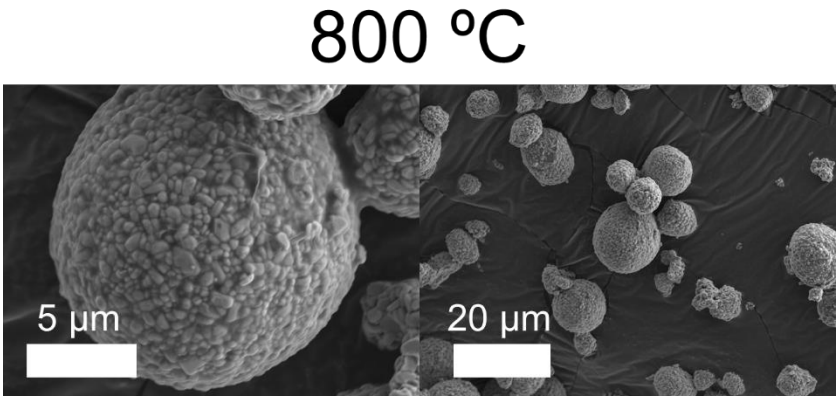

Figure B15. SEM images of Al_2O_3 coated NMC811 dried and then annealed under air at 800 ºC.

B2.2. High-resolution TEM Images

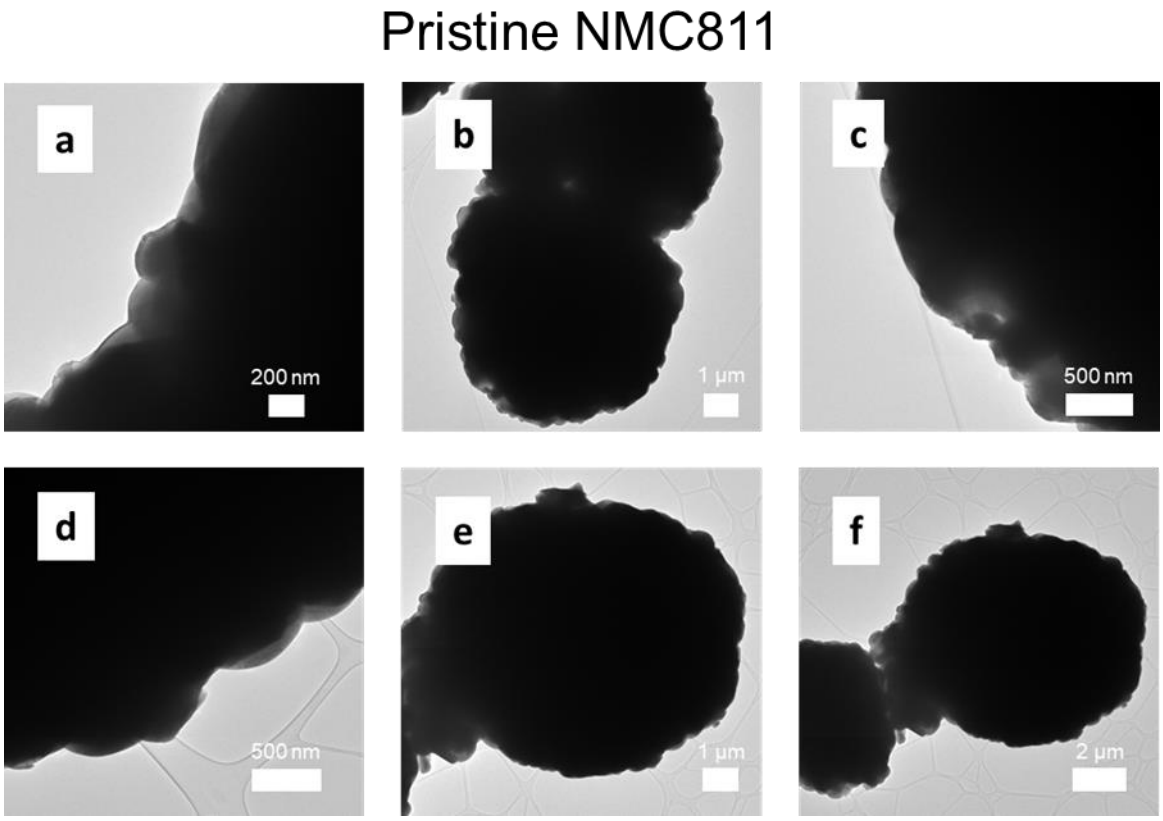

Figure B16. High-resolution TEM images of the pristine NMC811.

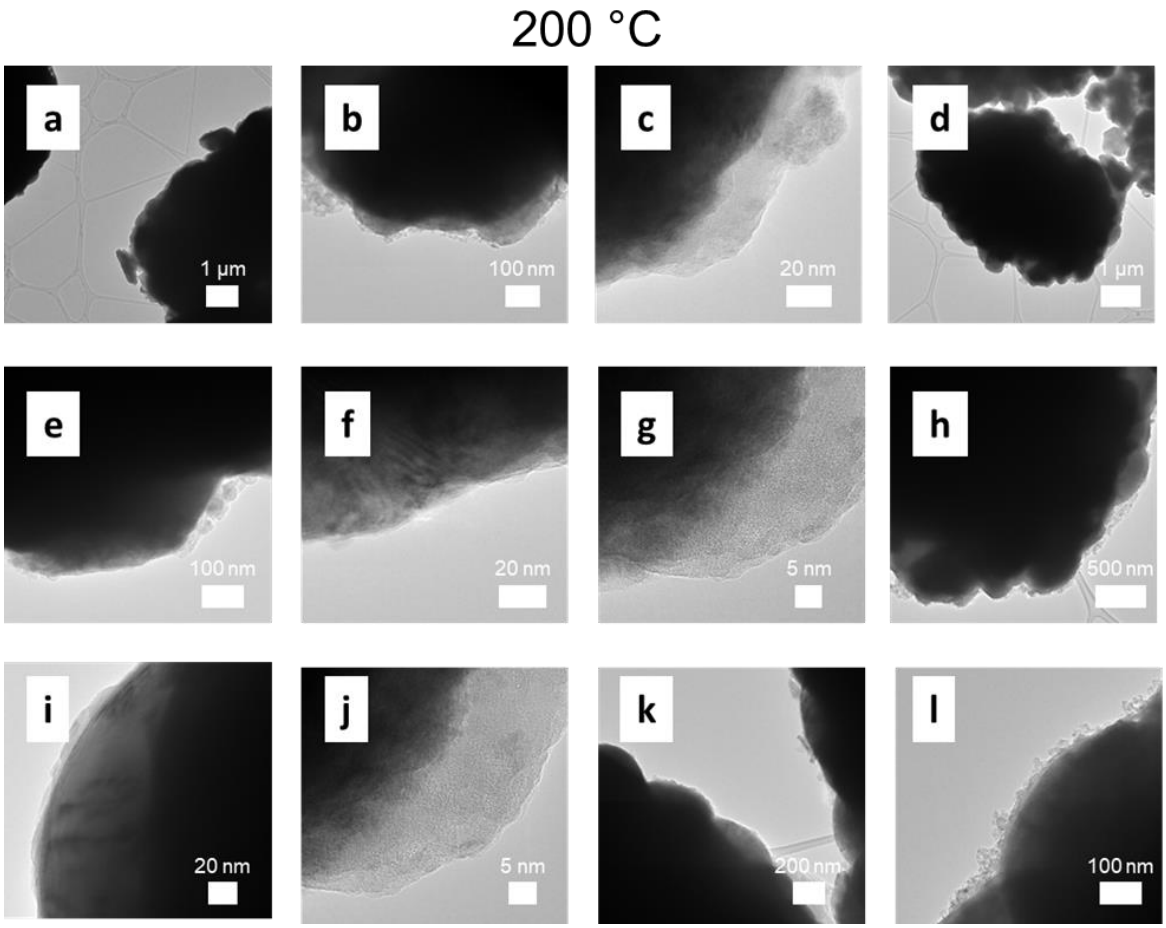

Figure B17. High-resolution TEM images of the Al_2O_3 coated NMC811 annealed at 200 ºC under air.

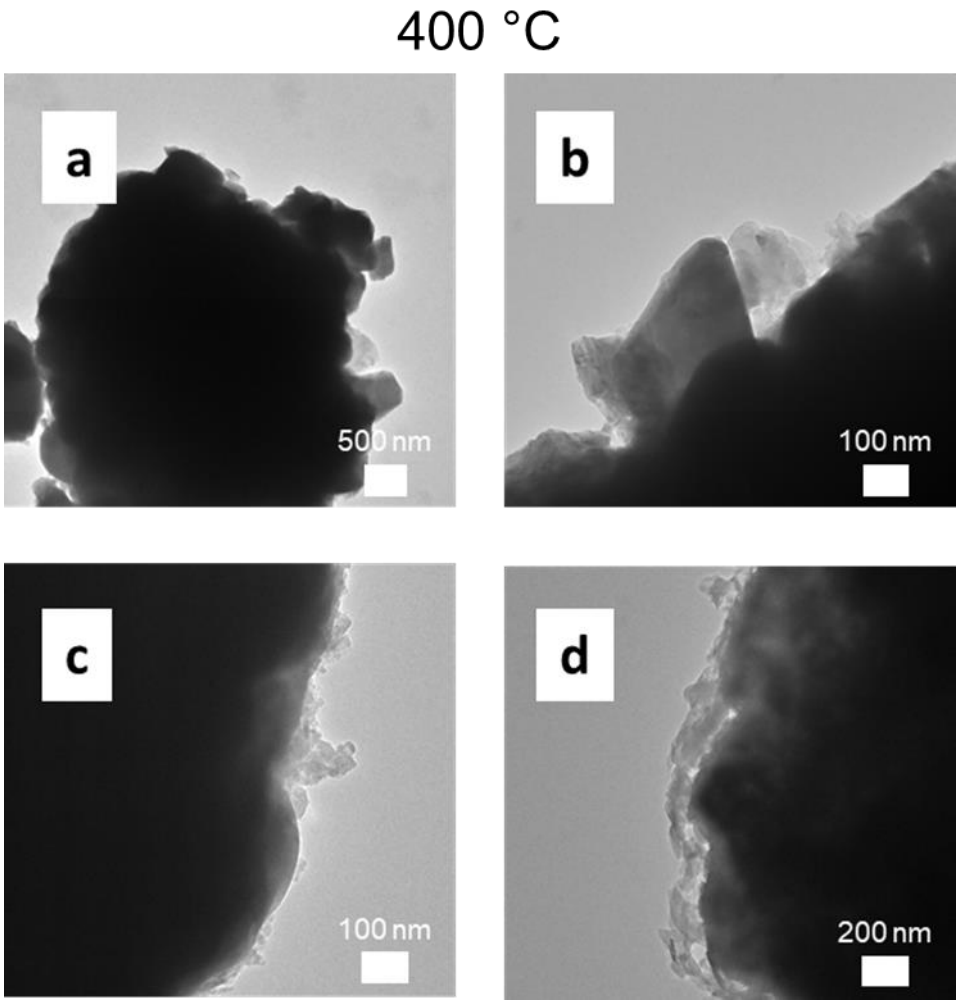

Figure B18. High-resolution TEM images of the Al_2O_3 coated NMC811 annealed at 400 ºC under air.

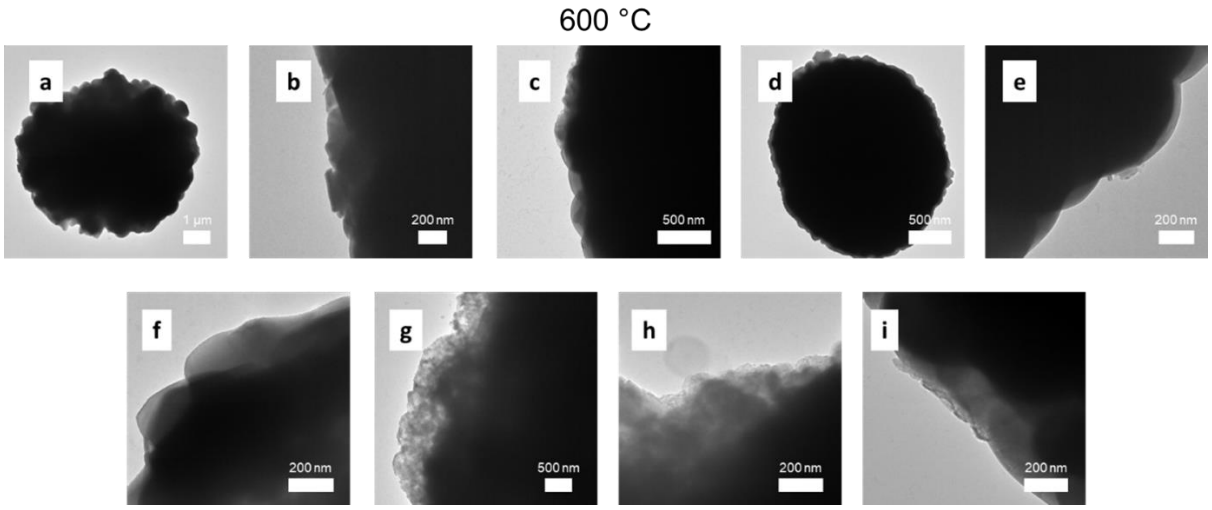

Figure B19. High-resolution TEM images of the Al_2O_3 coated NMC811 annealed at 600 ºC under air.

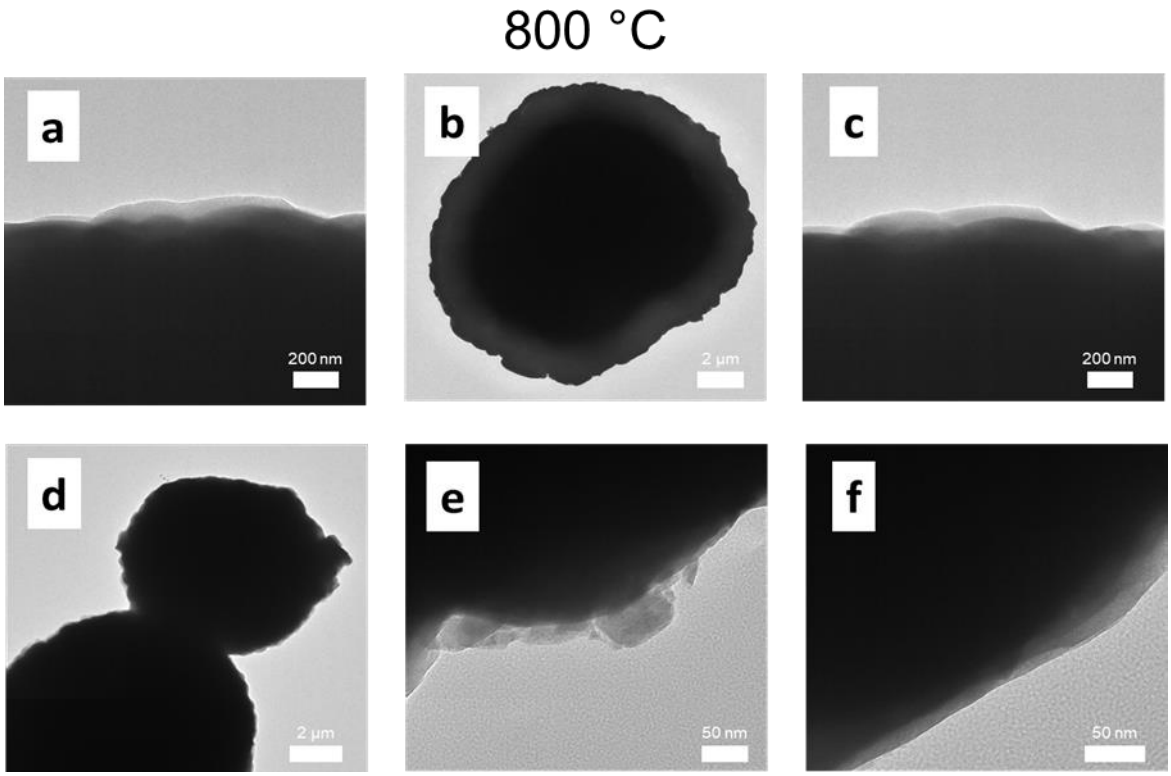

Figure B20. High-resolution TEM images of the Al_2O_3 coated NMC811 annealed at 800 ºC under air.

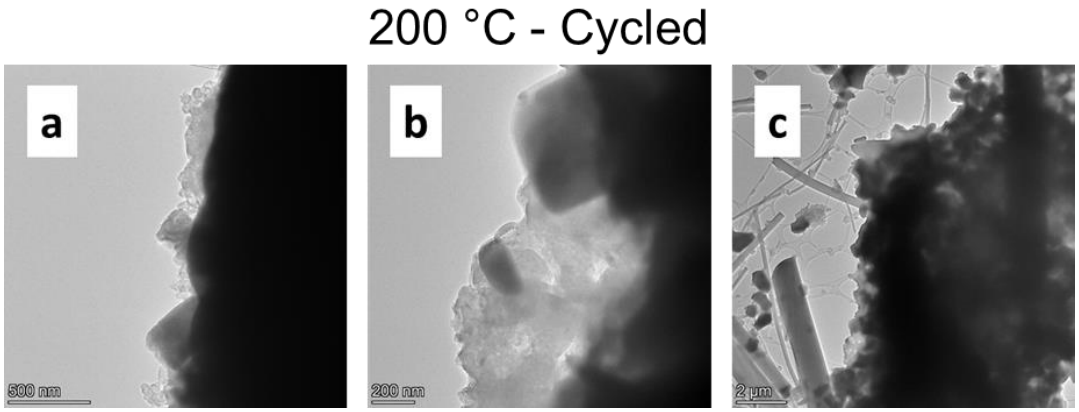

Figure B21. High-resolution TEM images of the Al_2O_3 coated NMC811 annealed at 200 ºC under air after 250 cycles.

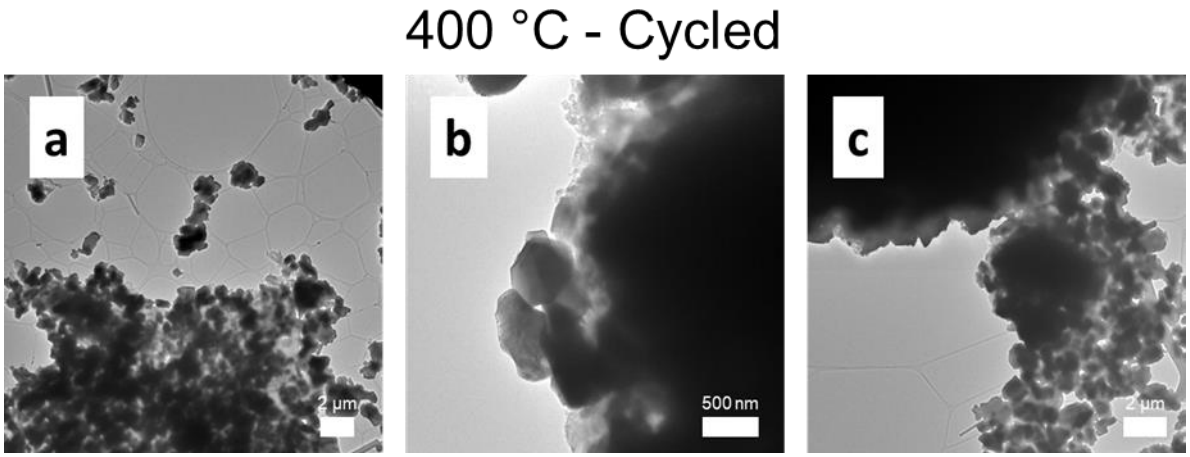

Figure B22. High-resolution TEM images of the Al_2O_3 coated NMC811 annealed at 400 ºC under air after 300 cycles.

B.2.3. Coating Thickness Measurements with TEM

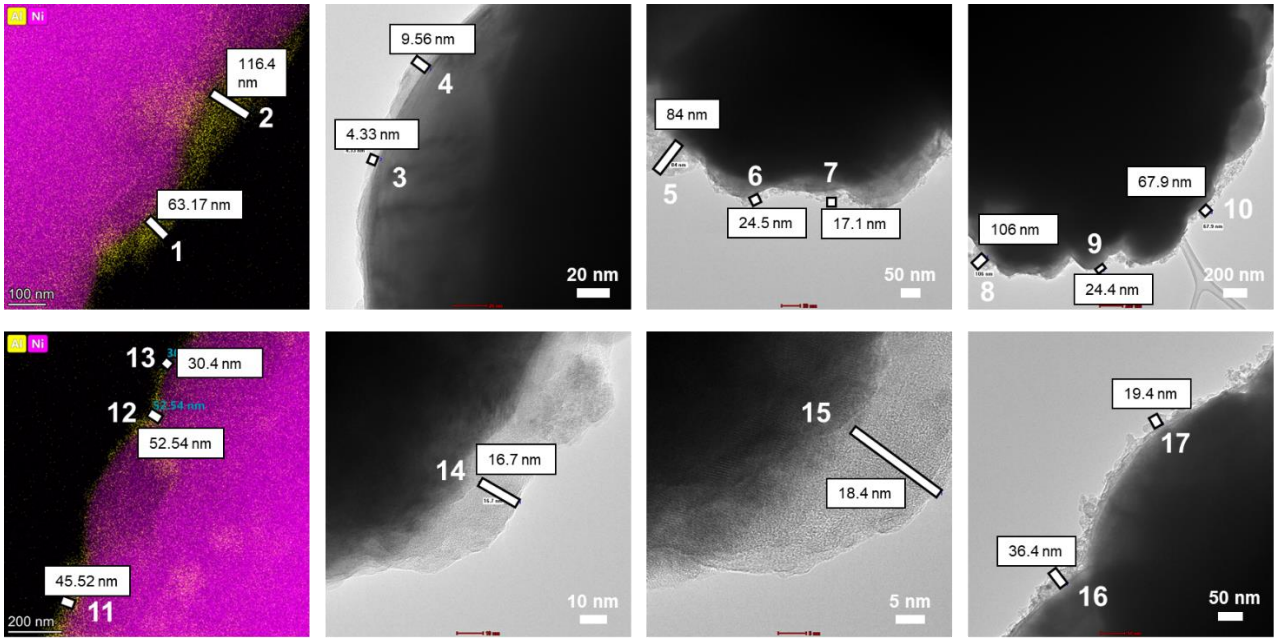

Figure B23. TEM images and EDS maps from where the coating thicknesses of the 200 ºC annealed sample were obtained, the locations where the thickness measurement were taken, and the thicknesses measured are indicated in the Figure.

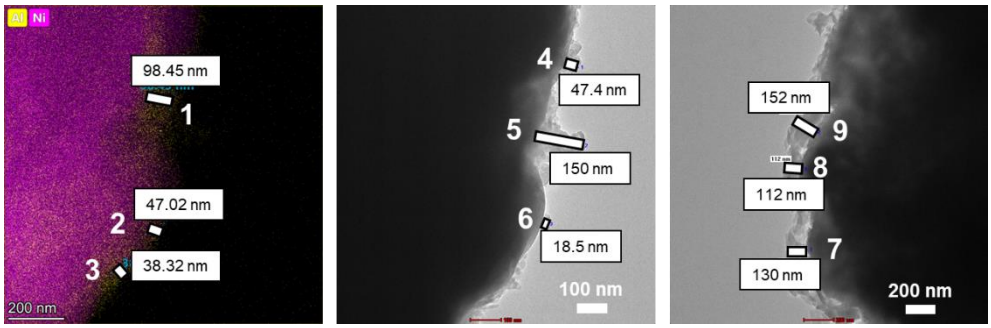

Figure B24. TEM images and EDS maps from where the coating thicknesses of the 400 ºC annealed sample were obtained, the locations where the thickness measurement were taken, and the thicknesses measured are indicated in the Figure.

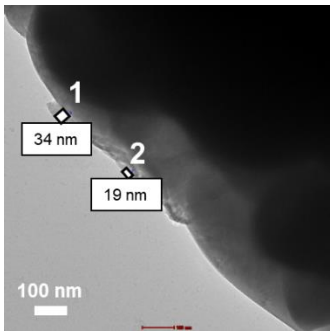

Figure B25. TEM images from where the coating thicknesses of the 600 ºC annealed sample were obtained, the locations where the thickness measurement were taken, and the thicknesses measured are indicated in the Figure.

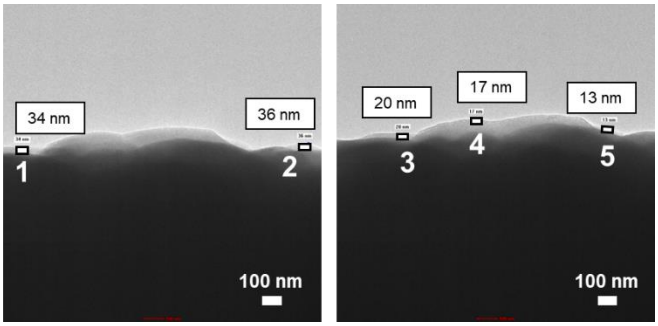

Figure B26. TEM images from where the coating thicknesses of the 800 ºC annealed sample were obtained, the locations where the thickness measurement were taken, and the thicknesses measured are indicated in the Figure.

B.2.4. SEM-EDS Characterisation

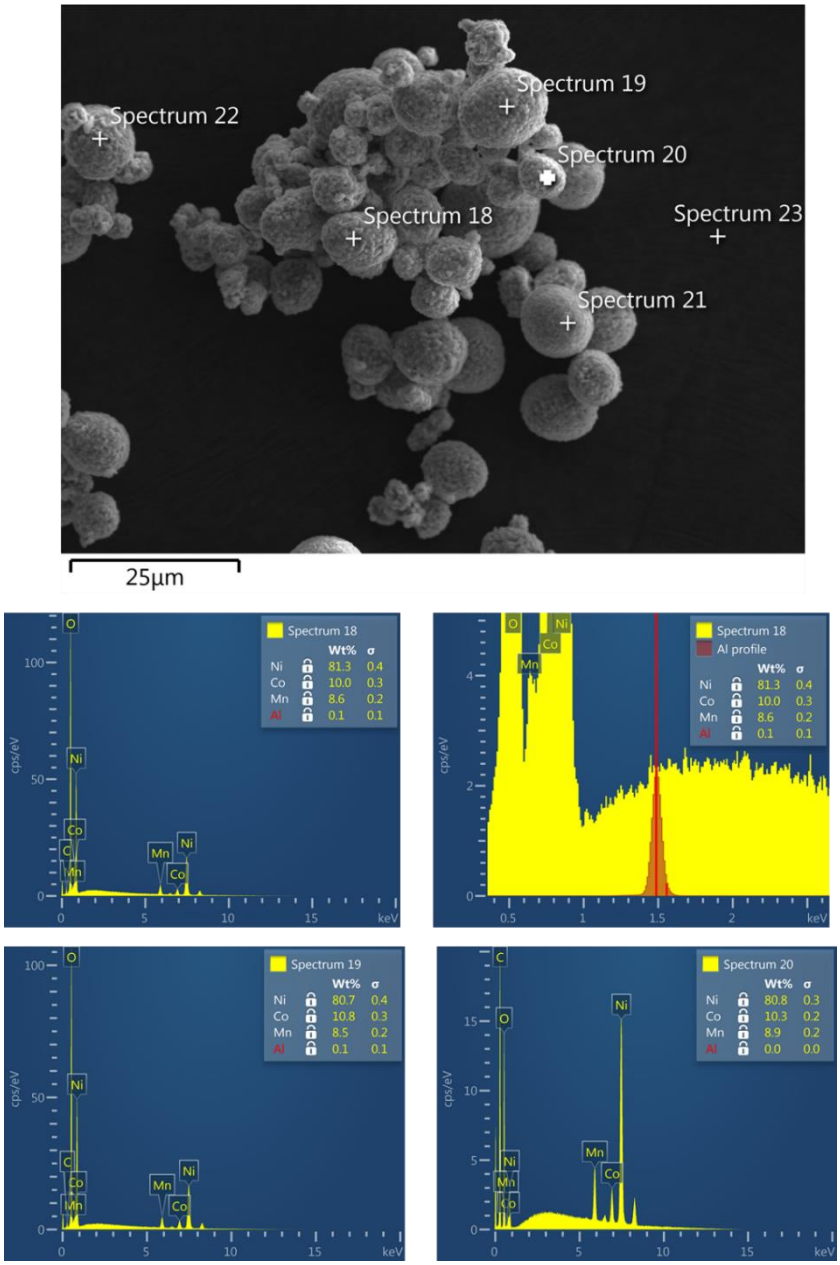

Figure B27. Three EDS spectra and location of the point scans taken on the pristine NMC811 sample. No aluminium signal can be detected within the limits of this technique.

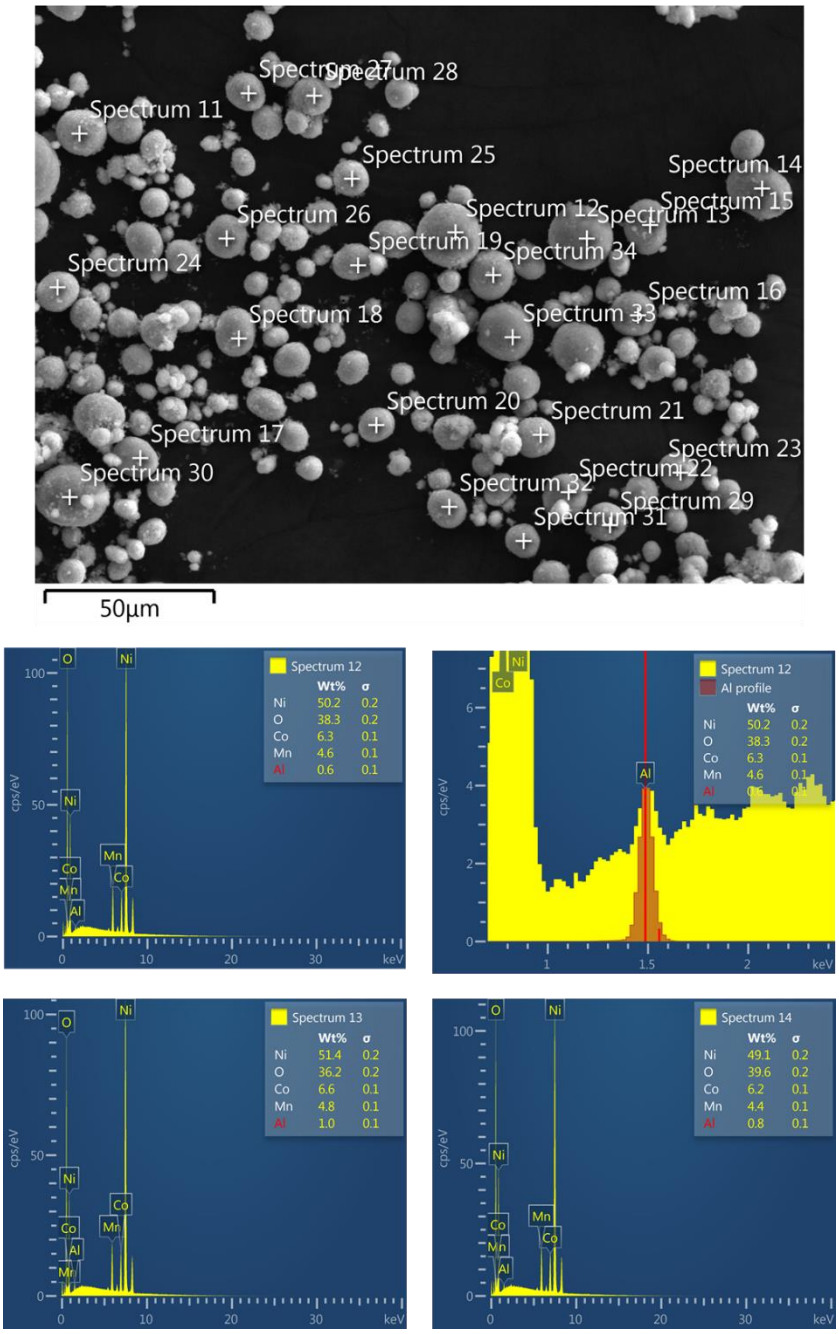

Figure B28. Three EDS spectra and location of the point scans taken on the as-coated (not annealed) NMC811 sample. Significant aluminium signal can be detected in all the measurements (0.6–1 weight %).

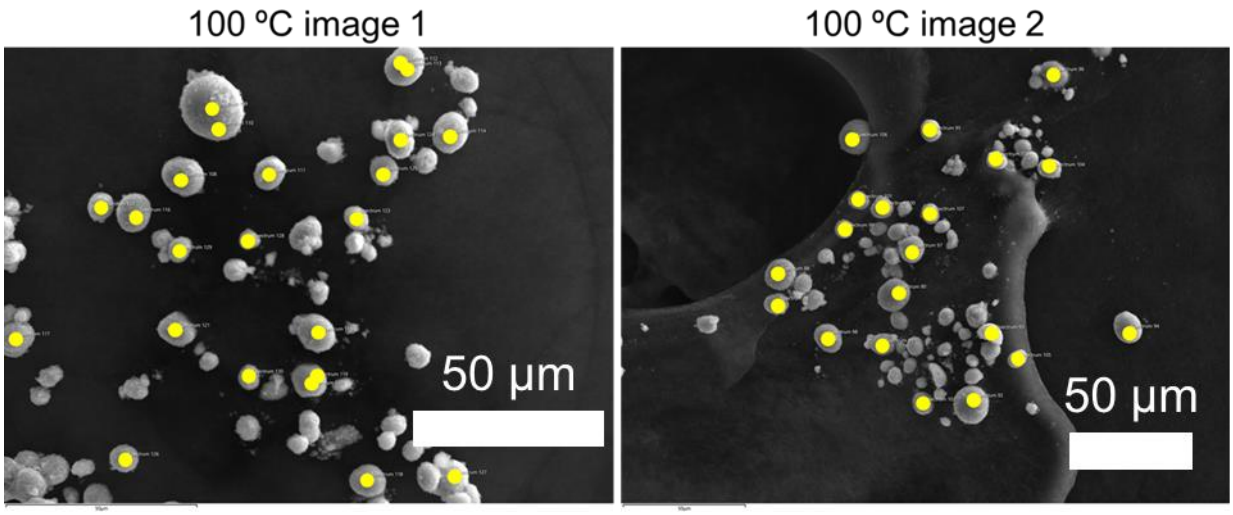

Figure B29. SEM images and EDS point scans of the Al_2O_3 coated NMC811 dried under vacuum at 100 ºC.

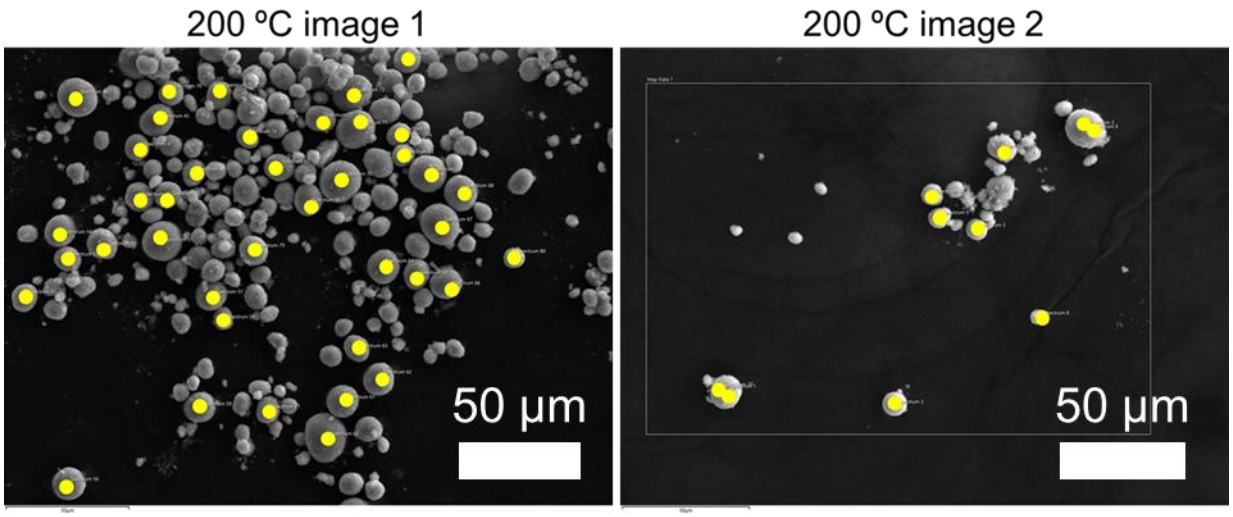

Figure B30. SEM images and EDS point scans of the Al_2O_3 coated NMC811 annealed at 200 ºC.

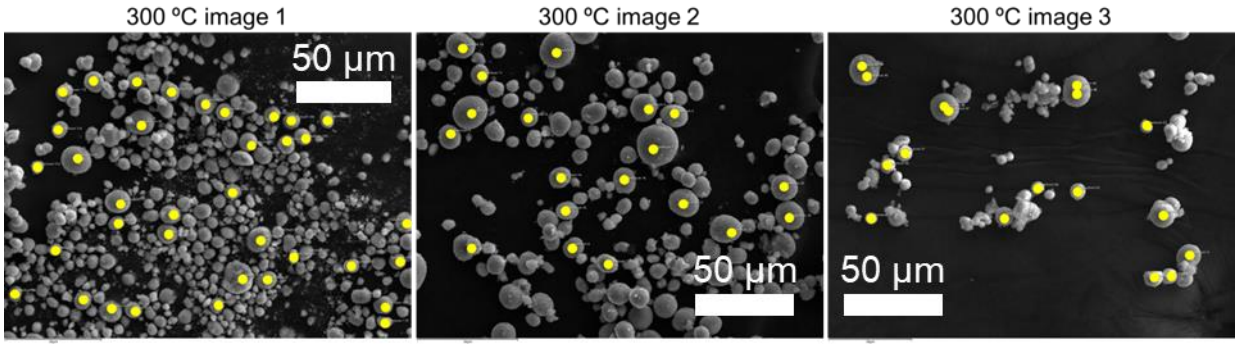

Figure B31. SEM images and EDS point scans of the Al_2O_3 coated NMC811 annealed at 300 ºC.

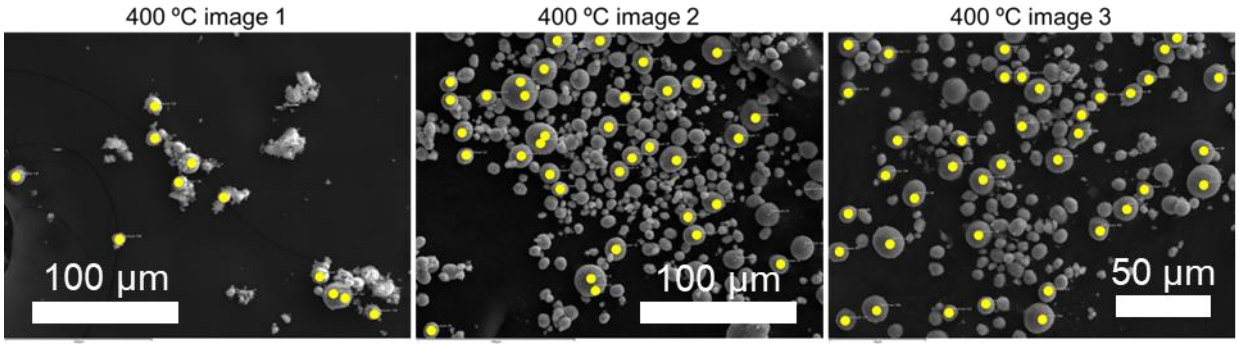

Figure B32. SEM images and EDS point scans of the Al_2O_3 coated NMC811 annealed at 400 ºC.

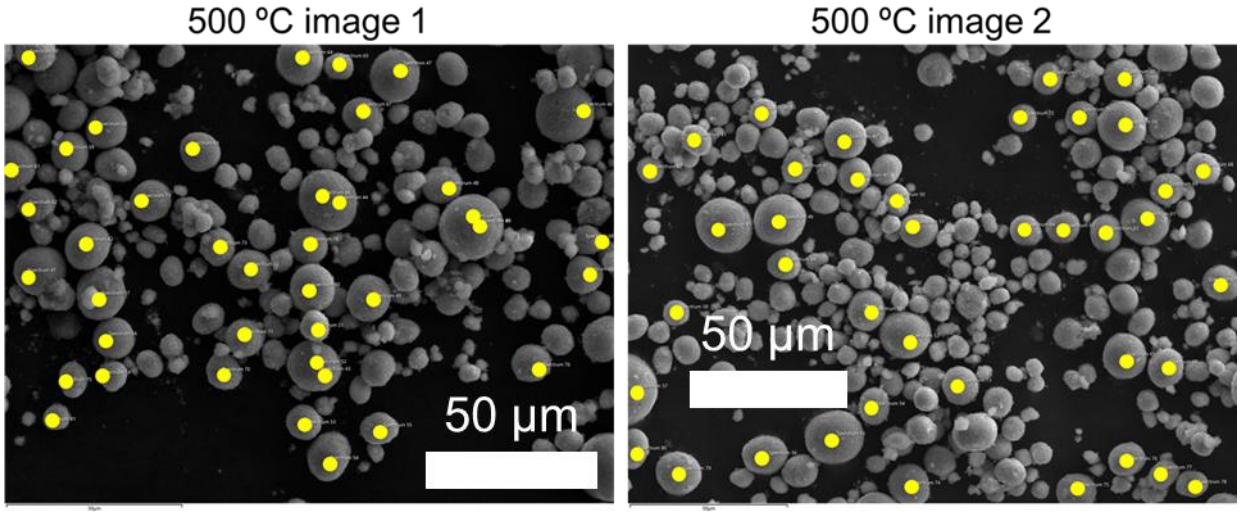

Figure B33. SEM images and EDS point scans of the Al_2O_3 coated NMC811 annealed at 500 ºC.

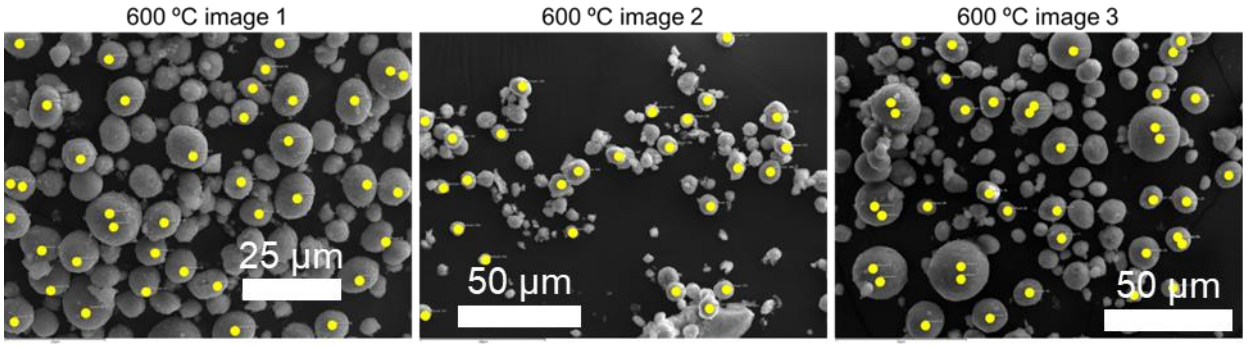

Figure B34. SEM images and EDS point scans of the Al_2O_3 coated NMC811 annealed at 600 ºC.

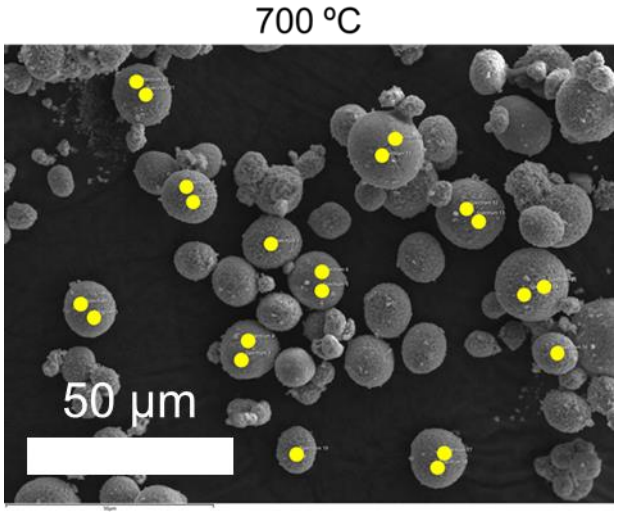

Figure B35. SEM images and EDS point scans of the Al_2O_3 coated NMC811 annealed at 700 ºC.

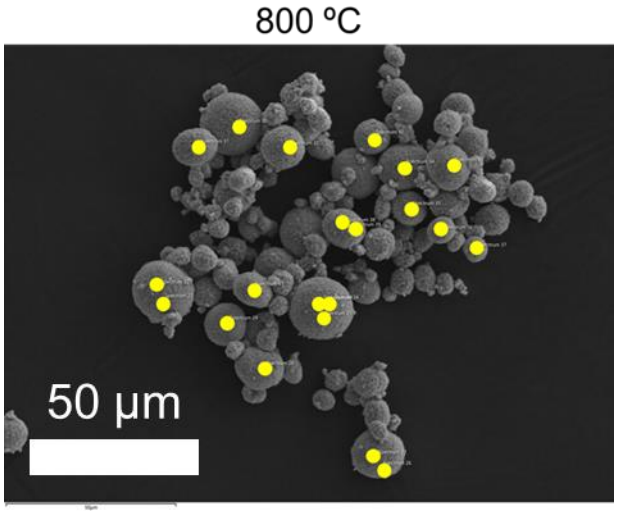

Figure B36. SEM images and EDS point scans of the Al_2O_3 coated NMC811 annealed at 800 ºC.

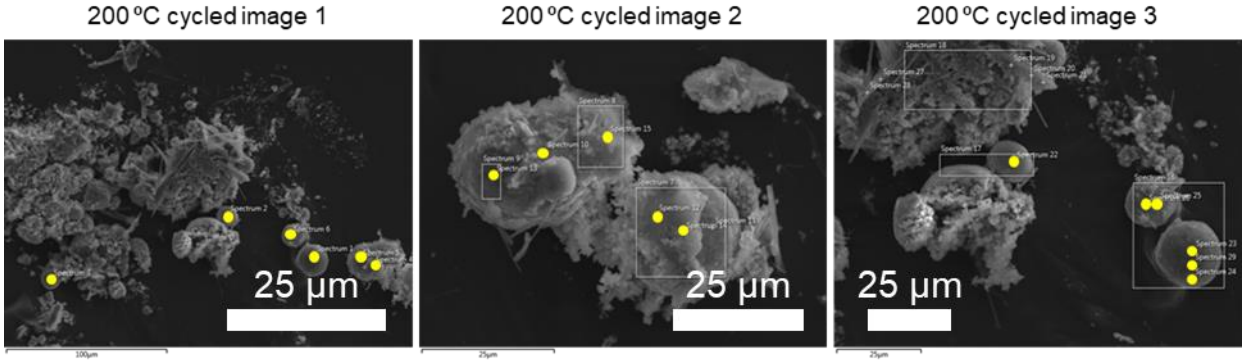

Figure B37. SEM images and EDS point scans of the Al_2O_3 coated NMC811 annealed at 200 ºC after 300 galvanostatic cycles.

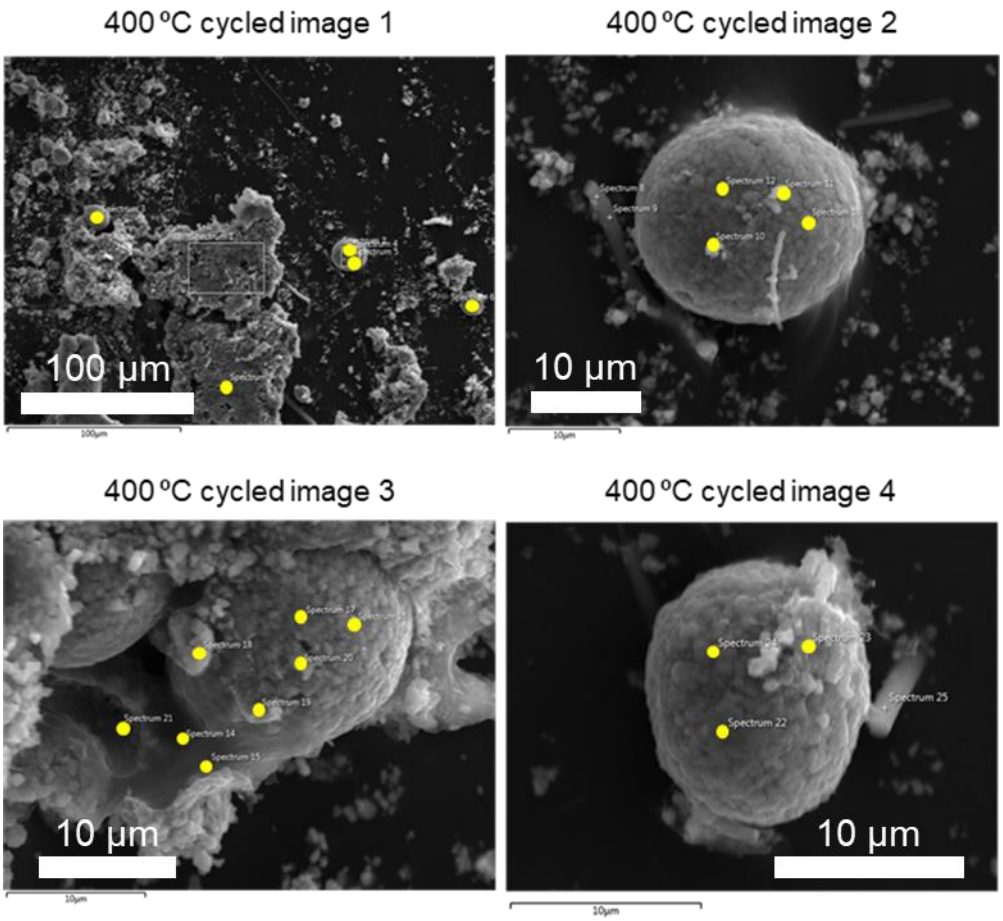

Figure B38. SEM images and EDS point scans of the Al_2O_3 coated NMC811 annealed at 400 ºC after 250 galvanostatic cycles.

Table B8. EDS-derived atomic percentages of the representative elements, Al : Ni rations, the 95 % confidence intervals and the number of spectra taken for each sample.

Annealing T / ºC		**C**	**O**	**Al**	**Mn**	**Co**	**Ni**	**Al : Ni**	**Number of spectra**
100	At %	30	49	0.25	1.88	2.00	15	0.016	43
	CI	3	3	0.03	0.11	0.14	1	0.002	
200	At %	34	40	0.30	2.30	2.65	20	0.010	50
	CI	5	3	0.04	0.20	0.23	2	0.002	
300	At %	20	55	0.35	2.34	2.57	20	0.018	76
	CI	2	2	0.03	0.11	0.13	1	0.002	
400	At %	17	57	0.45	2.27	2.62	20.3	0.022	91
	CI	2	1	0.03	0.08	0.10	0.8	0.002	
500	At %	13	59	0.40	2.49	2.8	21.7	0.018	81
	CI	1	1	0.02	0.08	0.1	0.8	0.001	
600	At %	29	49	0.25	2.15	2.31	17.9	0.014	100
	CI	2	2	0.02	0.09	0.12	0.9	0.001	
700	At %	9	52	0.26	3.3	4.0	32	0.008	21
	CI	1	6	0.04	0.4	0.6	5	0.002	
800	At %	6	31	0.27	5.5	6.6	51	0.0052	21
	CI	1	2	0.04	0.2	0.2	2	0.0009	

Table B9. EDS-derived atomic percentages for aluminium and nickel as well as the Al : Ni ratio with 95 % confidence intervals and the number of spectra taken for the Al_2O_3 coated NMC811 annealed at 200 ºC and 400 ºC after 250 or 300 cycles.

Annealing Temperature / ºC		**Ni**	**Al**	**Al : Ni**	**Number of spectra**
200 - cycled	At %	17.4	0.20	0.02	15
	CI	3.10	0.10	0.01	
400 - cycled	At %	17.1	0.20	0.01	20
	CI	3.54	0.08	0.004	

B2.5. STEM-EDS Characterisation

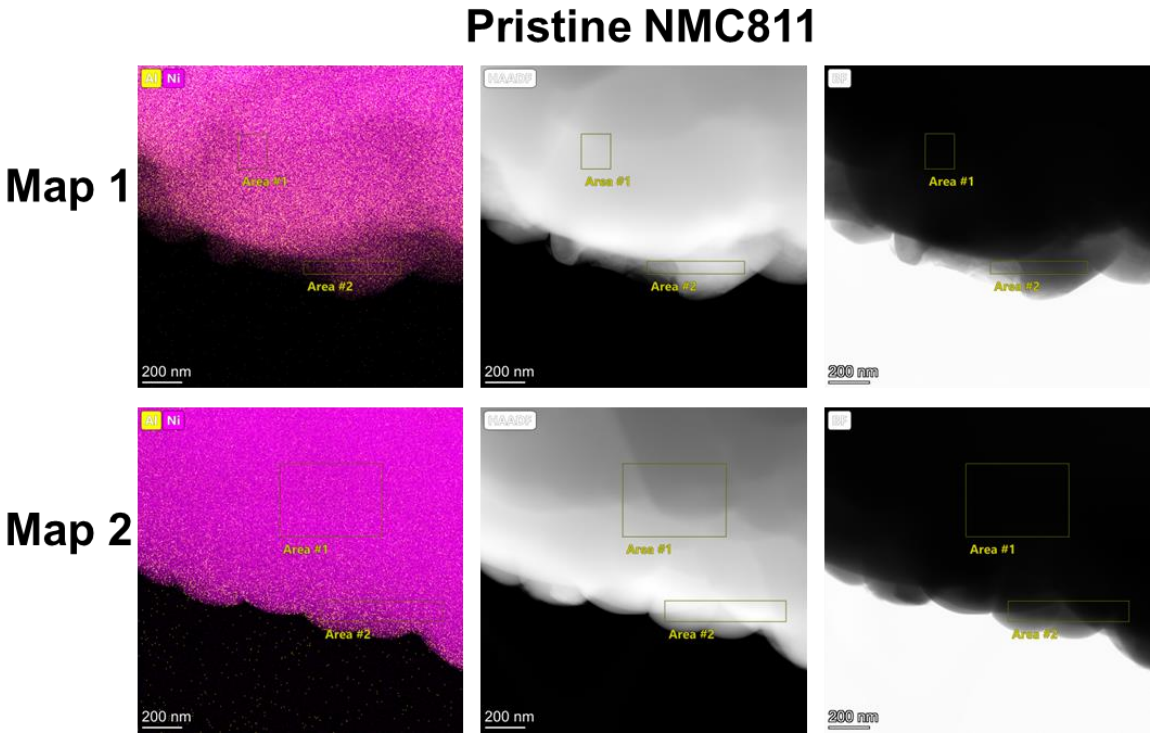

Figure B39. EDS map and high-angle annular dark field (HAAD) / bright field (BF) images of pristine NMC811. The areas used for the EDS quantification are shown.

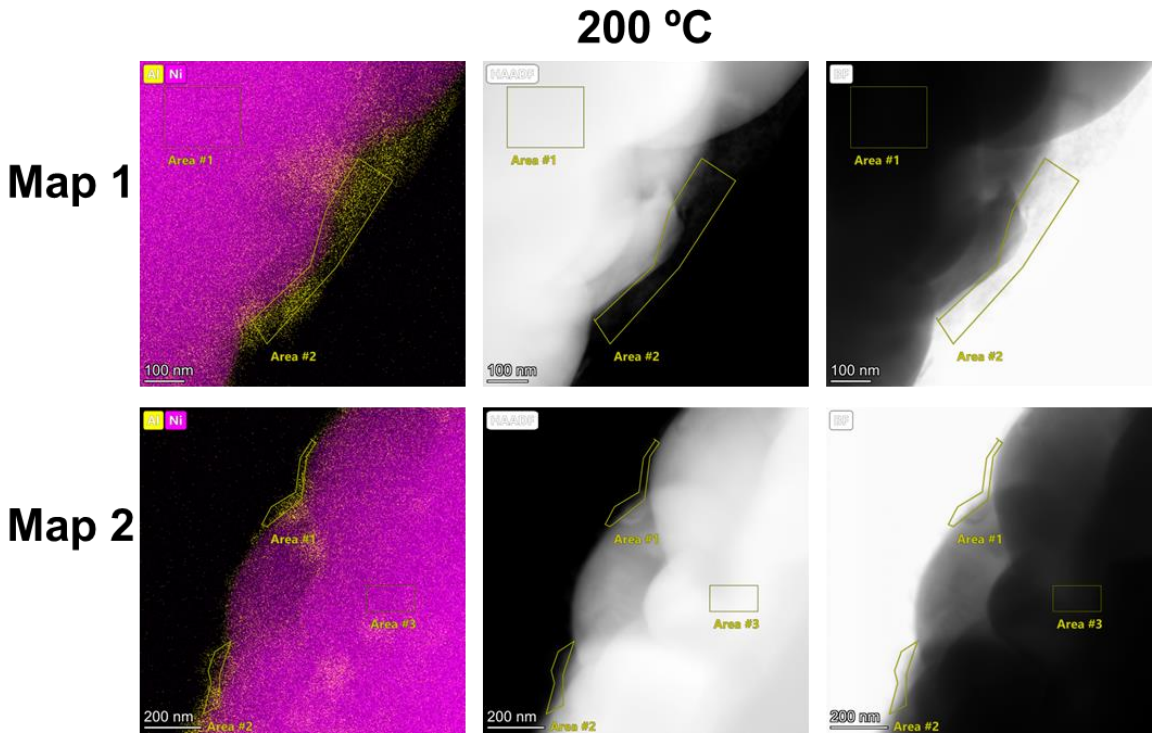

Figure B40. EDS map and high-angle annular dark field (HAAD) / bright field (BF) images of the Al_2O_3 coated NMC811 annealed at 200 ºC. The areas used for the EDS quantification are shown.

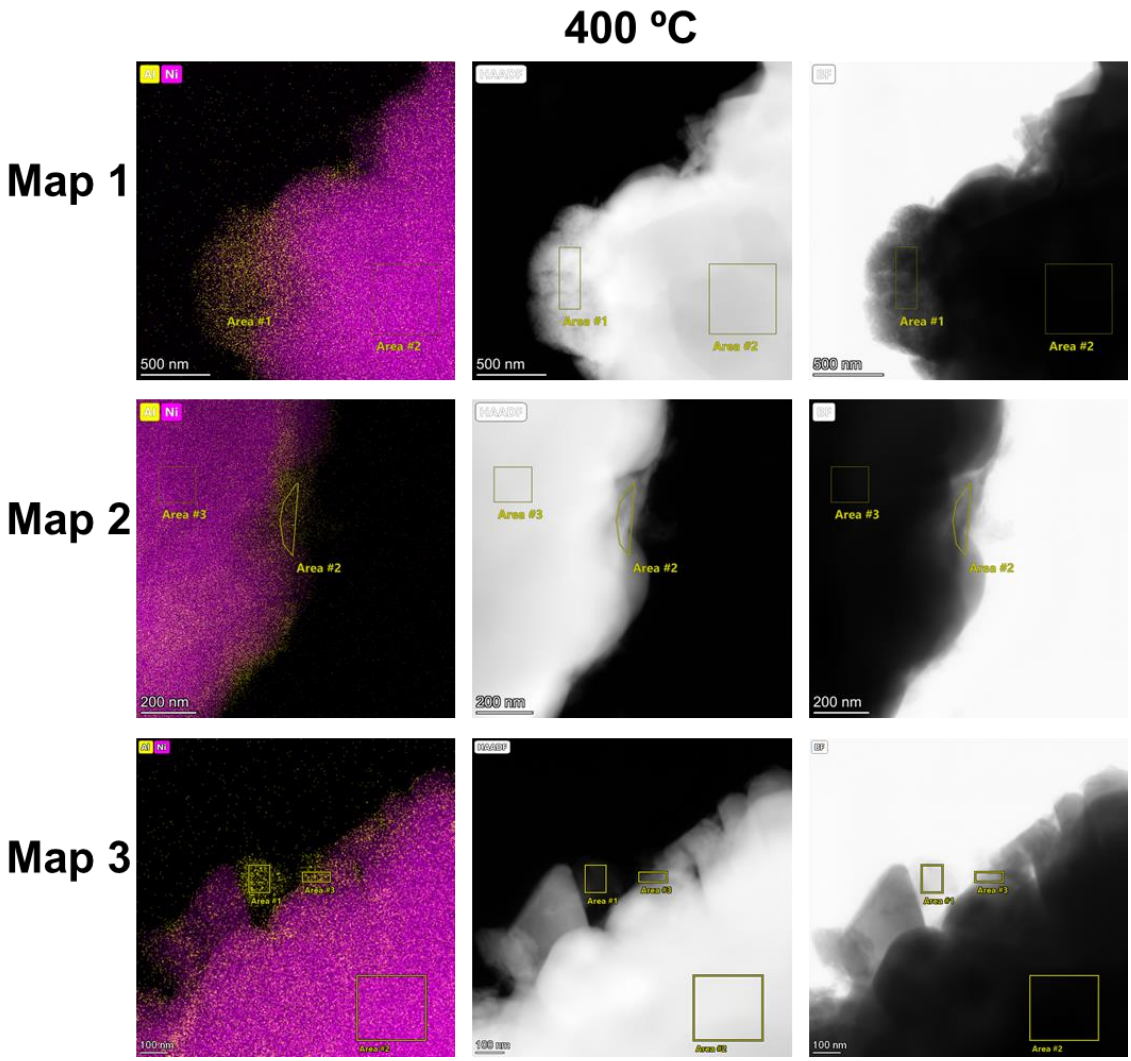

Figure B41. EDS map and high-angle annular dark field (HAAD) / bright field (BF) images of the Al_2O_3 coated NMC811 annealed at 400 ºC. The areas used for the EDS quantification are shown.

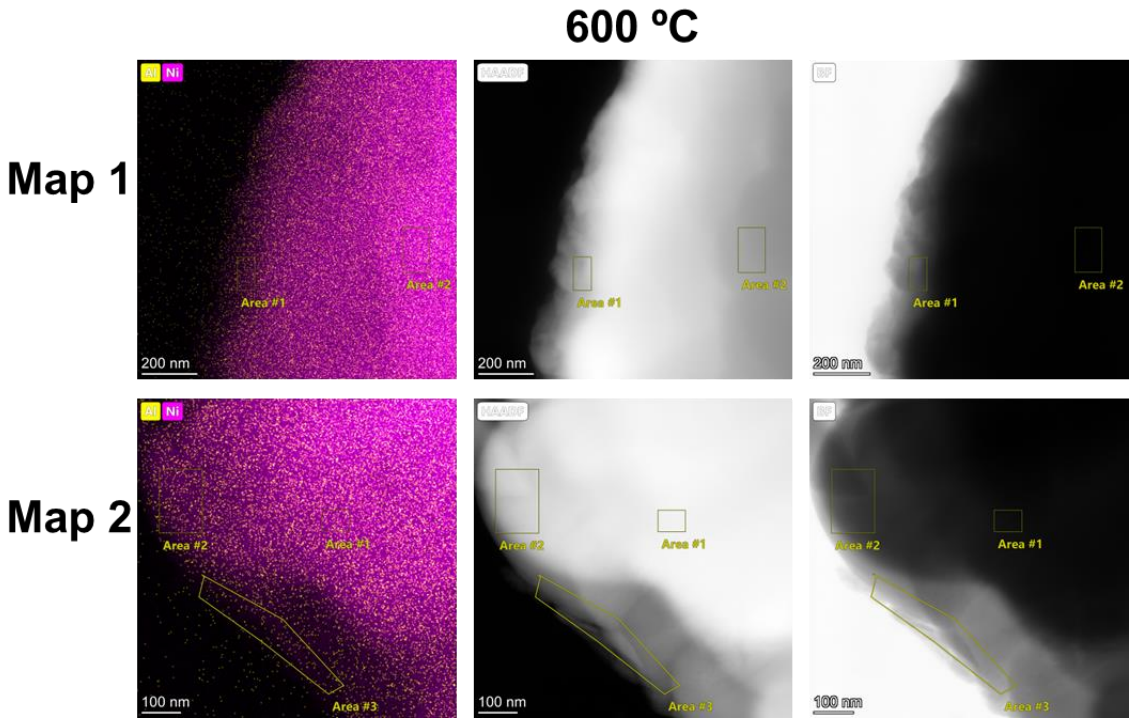

Figure B42. EDS map and high-angle annular dark field (HAAD) / bright field (BF) images of the Al_2O_3 coated NMC811 annealed at 600 ºC. The areas used for the EDS quantification are shown.

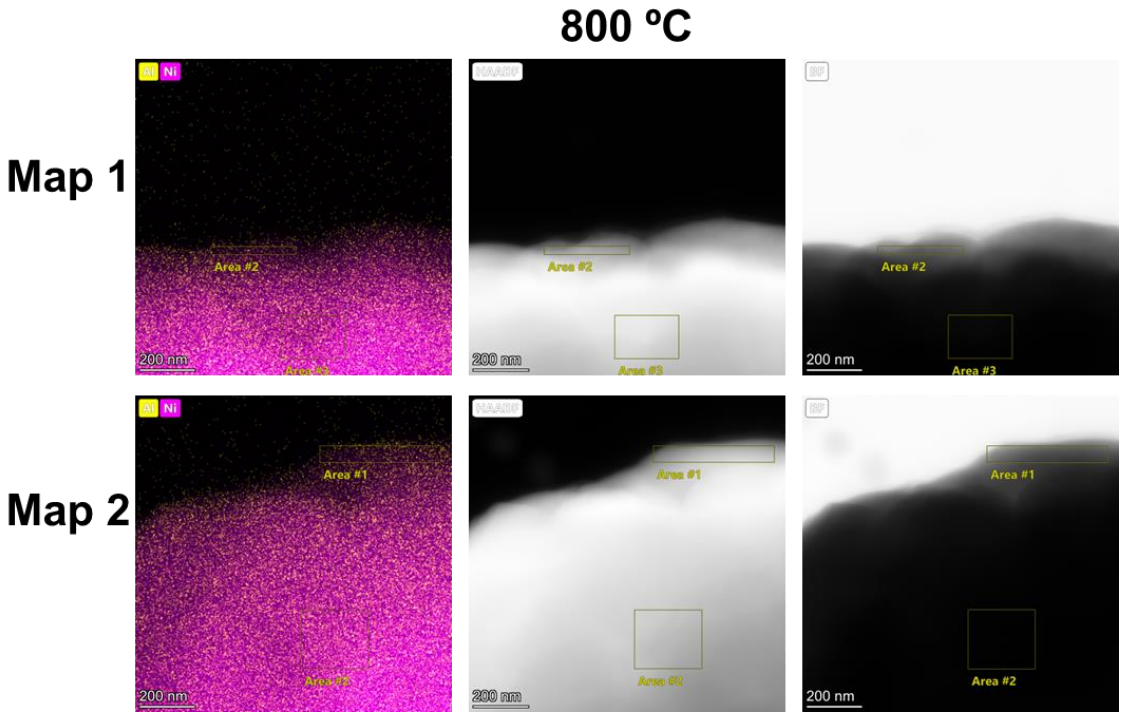

Figure B43. EDS map and high-angle annular dark field (HAAD) / bright field (BF) images of the Al_2O_3 coated NMC811 annealed at 800 ºC. The areas used for the EDS quantification are shown.

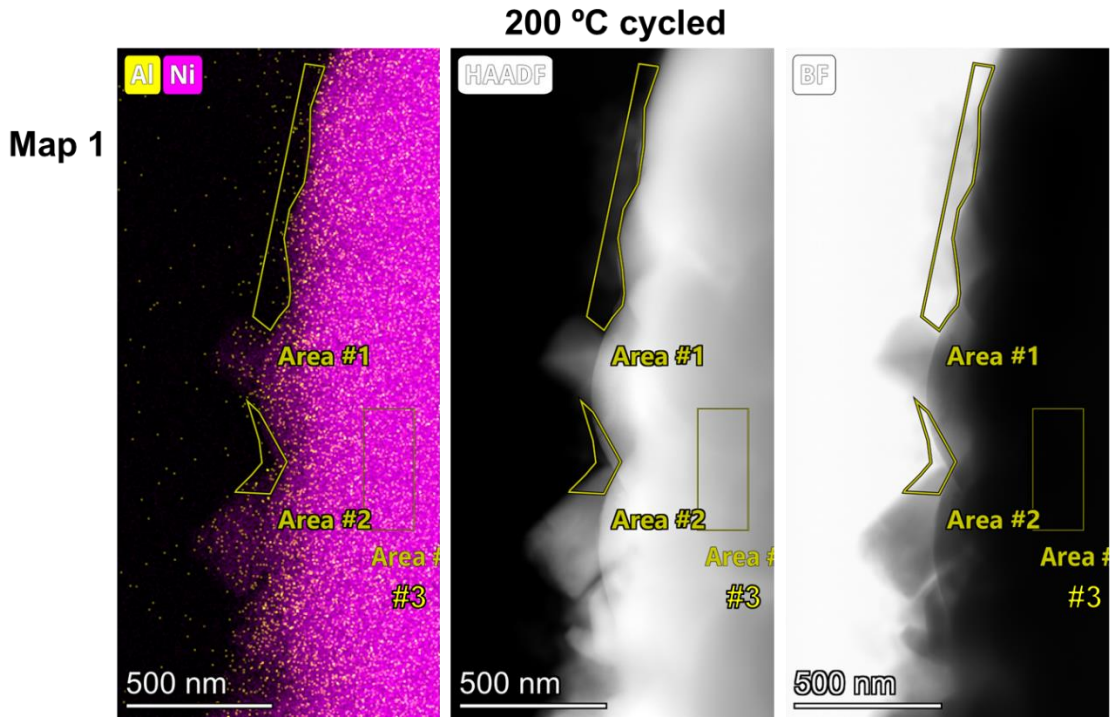

Figure B44. EDS map and high-angle annular dark field (HAAD) / bright field (BF) images of the Al_2O_3 coated NMC811 annealed at 200 ºC under air which has been cycled 250 times. The areas used for the EDS quantification are shown.

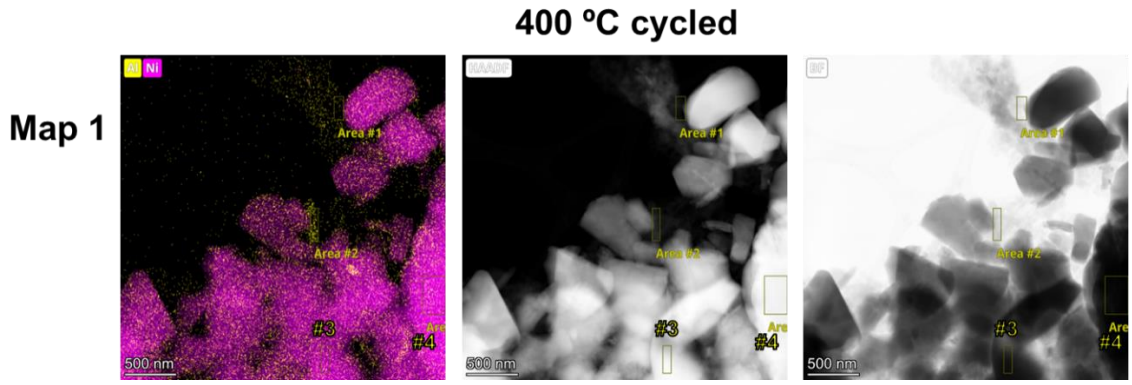

Figure B45. EDS map and high-angle annular dark field (HAAD) / bright field (BF) images of the Al_2O_3 coated NMC811 annealed at 400 ºC under air which has been cycled 300 times. The areas used for the EDS quantification are shown.

B2.5.1. Atomic Percentages Determined by STEM-EDS Mapping

Table B10. TEM-EDS atomic % of aluminium, manganese, cobalt and nickel and error in the atomic % and the fitting for the pristine NMC811 sample taken on representative bulk and surface areas of the sample.

Sample	Area		Al	Ni
pristine NMC811 map 1 (Figure B39)	1 (Bulk)	Atomic Fraction (%)	0.09	77.16
		Atomic Error (%)	0.02	17.47
	2 (Surface)	Atomic Fraction (%)	0.11	78
		Atomic Error (%)	0.03	17.76
Pristine NMC811 map 2 (Figure B39)	1 (Bulk)	Atomic Fraction (%)	0.14	78.6
		Atomic Error (%)	0.03	17.97
	2 (Surface)	Atomic Fraction (%)	0.11	78.82
		Atomic Error (%)	0.02	18.04
200 ºC map 1 (Figure B40)	1 (Bulk)	Atomic Fraction (%)	0.38	76.28
		Atomic Error (%)	0.07	17.17
	2 (Surface)	Atomic Fraction (%)	40	47
		Atomic Error (%)	5	9
200 ºC map 2 (Figure B40)	1 (Surface)	Atomic Fraction (%)	22	60
		Atomic Error (%)	3	12

	2 (Surface)	Atomic Fraction (%)	22	63
		Atomic Error (%)	4	13
	3 (Bulk)	Atomic Fraction (%)	0.29	78
		Atomic Error (%)	0.06	18

Table B11. TEM-EDS atomic % of aluminium, manganese, cobalt and nickel and error in the atomic % for the coated NMC811 sample annealed at 400 ºC measured on representative bulk and surface areas of the sample.

Sample	Area		Al	Ni
400 ºC map 1 Figure B41	1 (Surface)	Atomic Fraction (%)	27.15	53
		Atomic Error (%)	4.1	10
	2 (Bulk)	Atomic Fraction (%)	0.36	81
		Atomic Error (%)	0.07	19
400 ºC map 2 Figure B41	2 (Surface)	Atomic Fraction (%)	22	61
		Atomic Error (%)	3	13
	3 (Bulk)	Atomic Fraction (%)	0.45	77
		Atomic Error (%)	0.09	17
400 ºC map 3 Figure B41	1 (Surface)	Atomic Fraction (%)	84.6	10.6
		Atomic Error (%)	5.6	1.8
	2 (Bulk)	Atomic Fraction (%)	0.64	77
		Atomic Error (%)	0.12	17
	3 (Surface)	Atomic Fraction (%)	24	60.2
		Atomic Error (%)	4	12.5

Table B12. TEM-EDS atomic % of aluminium, manganese, cobalt and nickel and error in the atomic % and the fitting for the coated NMC811 annealed at 600 and 800 ºC measured on representative bulk and surface areas of the sample.

Sample	Area		Al	Ni
600 ºC map 1 Figure B42	1 (Surface)	Atomic Fraction (%)	0.89	81.1
		Atomic Error (%)	0.23	18.9
	2 (Bulk)	Atomic Fraction (%)	0.35	82.4
		Atomic Error (%)	0.07	19.3
600 ºC map 2 Figure B42	1 (Bulk)	Atomic Fraction (%)	2.08	86.3
		Atomic Error (%)	0.49	20.9
	2 (Surface)	Atomic Fraction (%)	2.08	87.5
		Atomic Error (%)	0.44	21.4
	3 (Surface)	Atomic Fraction (%)	1.64	87.8
		Atomic Error (%)	0.39	21.5
800 ºC map 1 Figure B43	2 (Surface)	Atomic Fraction (%)	0.73	79.6
		Atomic Error (%)	0.24	18.4
	3 (Bulk)	Atomic Fraction (%)	0.55	80.4
		Atomic Error (%)	0.11	18.6
800 ºC map 2 Figure B43	1 (Surface)	Atomic Fraction (%)	1.84	79.7
		Atomic Error (%)	0.36	18.4
	2 (Bulk)	Atomic Fraction (%)	0.52	80.2
		Atomic Error (%)	0.1	18.5

Table B13. TEM-EDS atomic % of aluminium, manganese, cobalt and nickel and error in the atomic % and the fitting for the cycled NMC811 samples coated and annealed at 200 and 400 ºC measured on representative bulk and surface areas of the sample.

Sample	Area		Al	Ni
200 ºC cycled map 1 Figure B44	1 (Surface)	Atomic Fraction (%)	3.58	76.2
		Atomic Error (%)	0.92	3.3
	2 (Surface)	Atomic Fraction (%)	2.11	79.0
		Atomic Error (%)	0.68	3.0
	3 (Bulk)	Atomic Fraction (%)	0.46	82.1
		Atomic Error (%)	0.06	2.6
400 ºC cycled map 1 Figure B45	4 (Bulk)	Atomic Fraction (%)	0.65	80.8
		Atomic Error (%)	0.09	2.8
	2 (Surface)	Atomic Fraction (%)	36.0	48.0
		Atomic Error (%)	4.6	5.2
	5 (Surface)	Atomic Fraction (%)	9.0	67.2
		Atomic Error (%)	4.9	6.1
	3 (Bulk)	Atomic Fraction (%)	0.52	80.6
		Atomic Error (%)	0.13	2.8
	1 (Surface)	Atomic Fraction (%)	7.0	75.2
		Atomic Error (%)	4.1	5.5
	6 (Surface)	Atomic Fraction (%)	2.8	76.2
		Atomic Error (%)	1.4	3.5

B2.6. XRF Characterisation

Table B14. Atomic percentages of manganese, cobalt, nickel, and aluminium for the pristine NMC811 sample used in this work as determined by XRF.

Element	**Mn**	**Co**	**Ni**	**Al**
atomic %	0.14	0.19	1.36	0

Table B15. The atomic percentages of aluminium and nickel as determined by XRF. A duplicate of each measurement was performed, and the mean and 95 % confidence interval (CI) are reported.

Annealing T / ºC		**Al**	**Ni**	**Al : Ni**
200	At %	0.97	79.19	0.012
	CI	0.09	0.02	0.001
300	At %	1.2	78	0.015
	CI	0.1	1	0.002
400	At %	1.2	79	0.015
	CI	0.1	1	0.002
500	At %	0.97	77.4	0.013
	CI	0.08	0.5	0.001
600	At %	0.622	79.1	0.0079
	CI	0.007	0.7	0.0001
700	At %	0.34	79.2	0.0043
	CI	0.01	0.5	0.0002
800	At %	0.35	79	0.004
	CI	0.08	2	0.001

B3. Characterisation of the NMC811 Materials Discussed in Chapter 4

B3.1. Scanning Electron Microscopy Images

B3.1.1. Polycrystalline NMC811

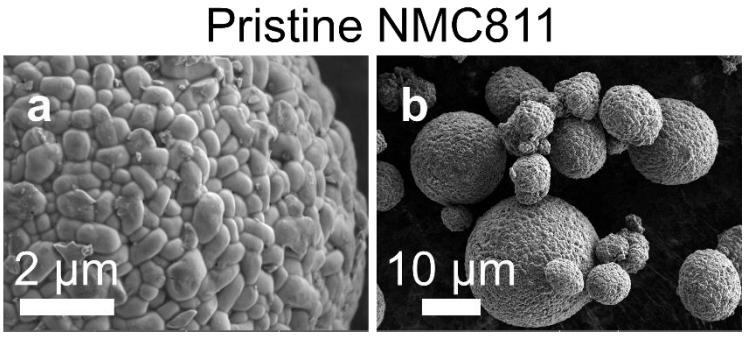

Figure B46. SEM images of pristine NMC811.

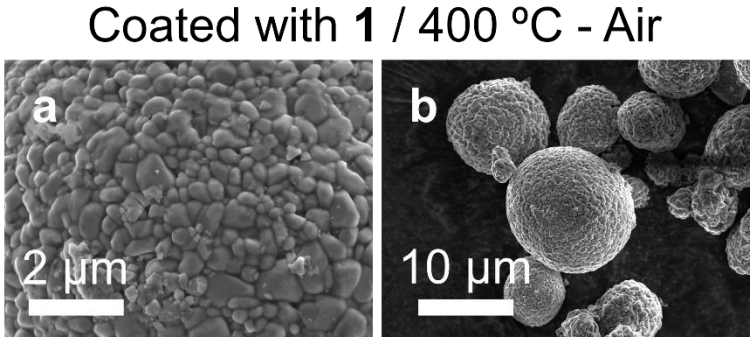

Figure B47. SEM images of NMC811 coated using precursor **1** and then annealed at 400 ºC under air.

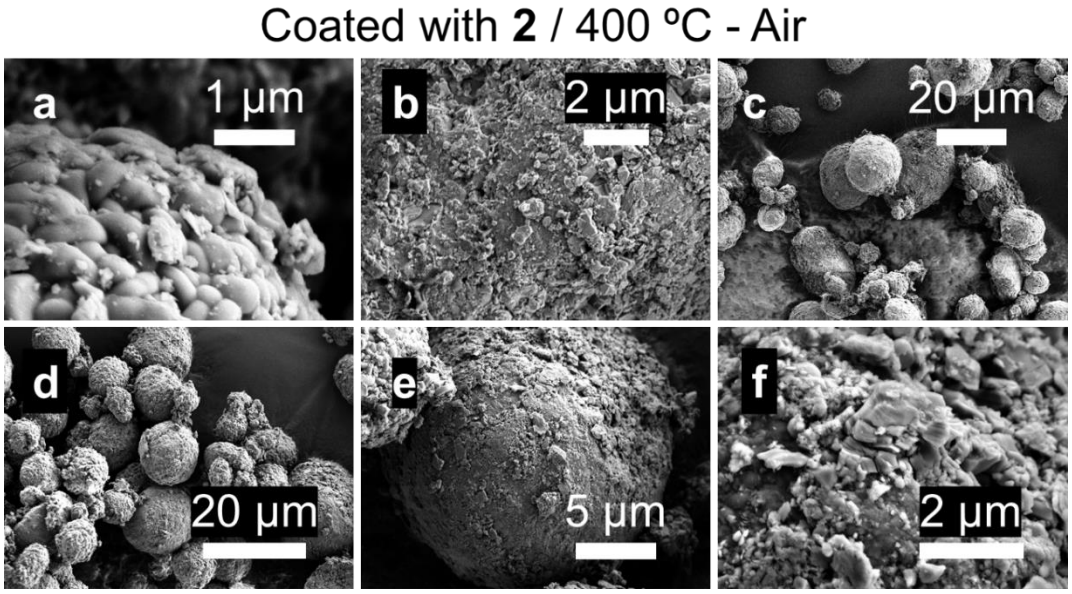

Figure B48. SEM images of NMC811 coated using precursor **2** and then annealed at 400 ºC under air.

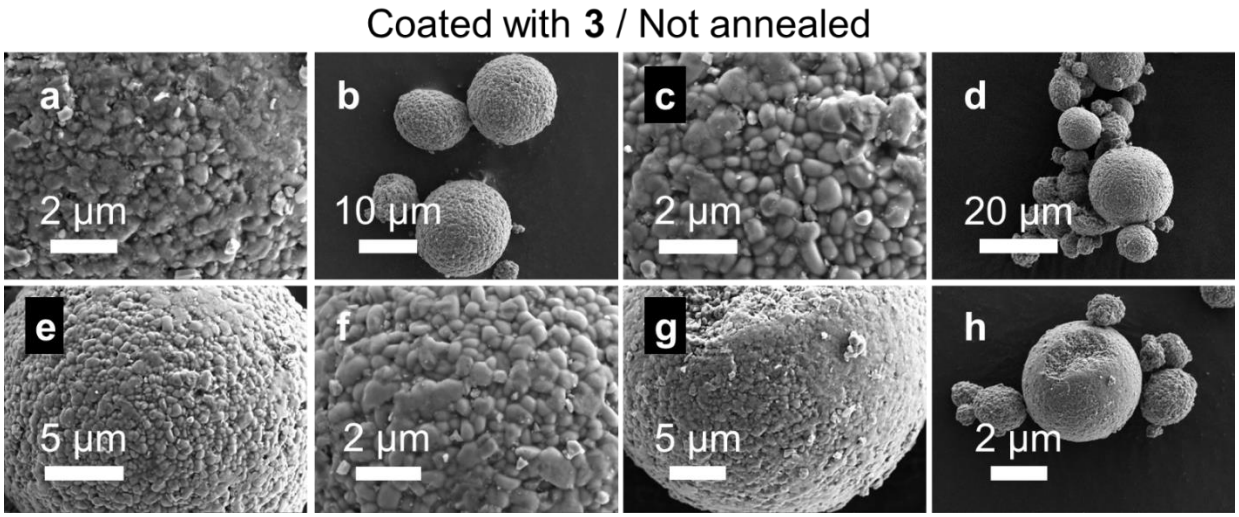

Figure B49. SEM images of NMC811 coated using precursor **3**.

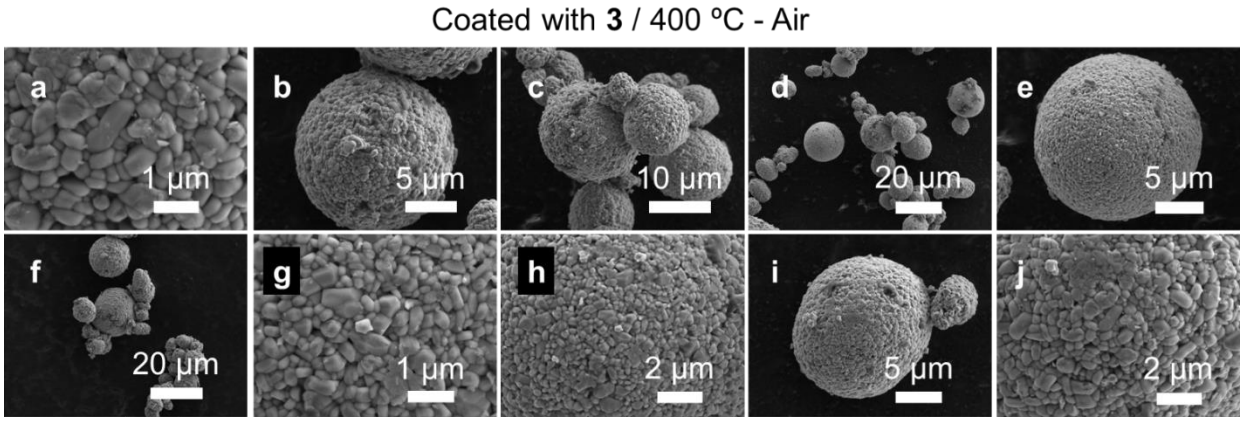

Figure B50. SEM images of NMC811 coated using precursor **3** and then annealed at 400 ºC under air.

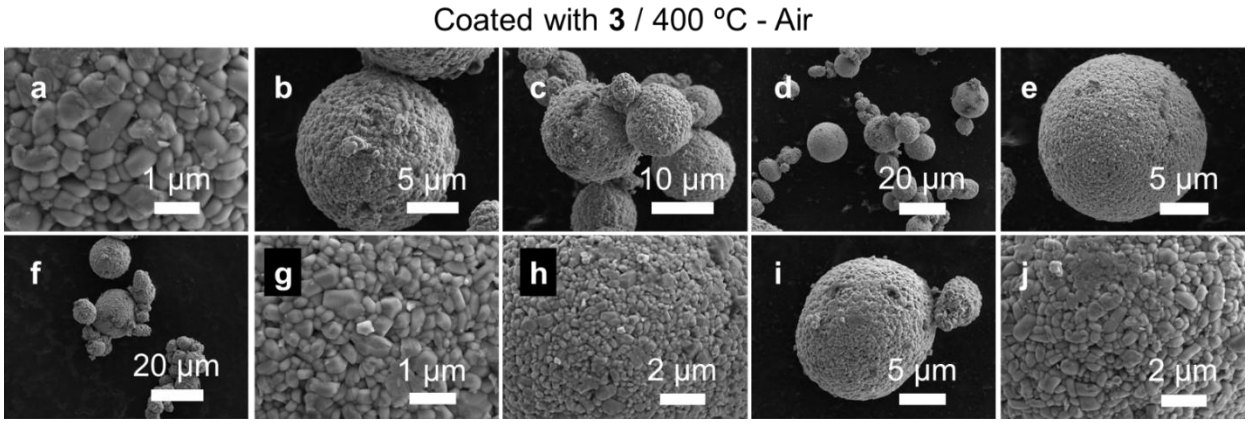

Figure B51. SEM images of NMC811 coated using precursor **3** and then annealed at 400 ºC under oxygen.

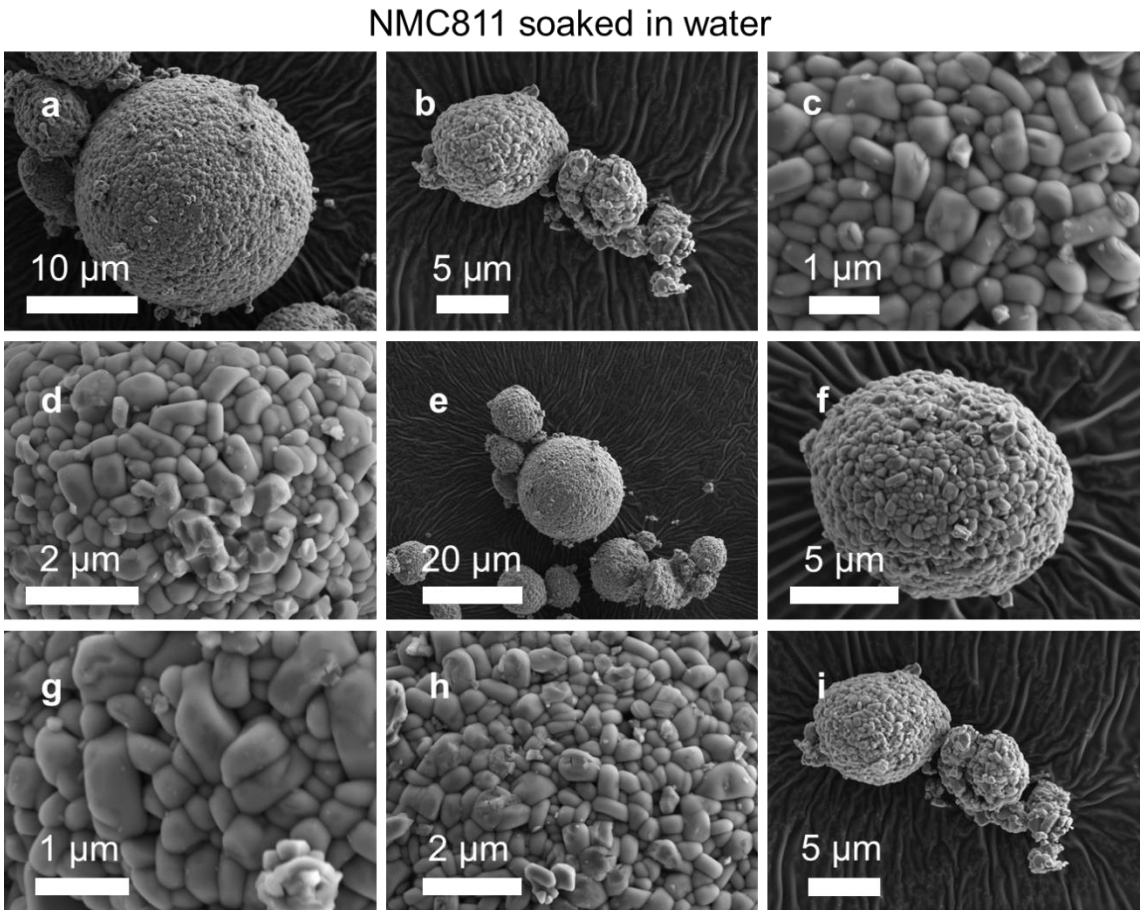

Figure B52. SEM images of NMC811 soaked in water.

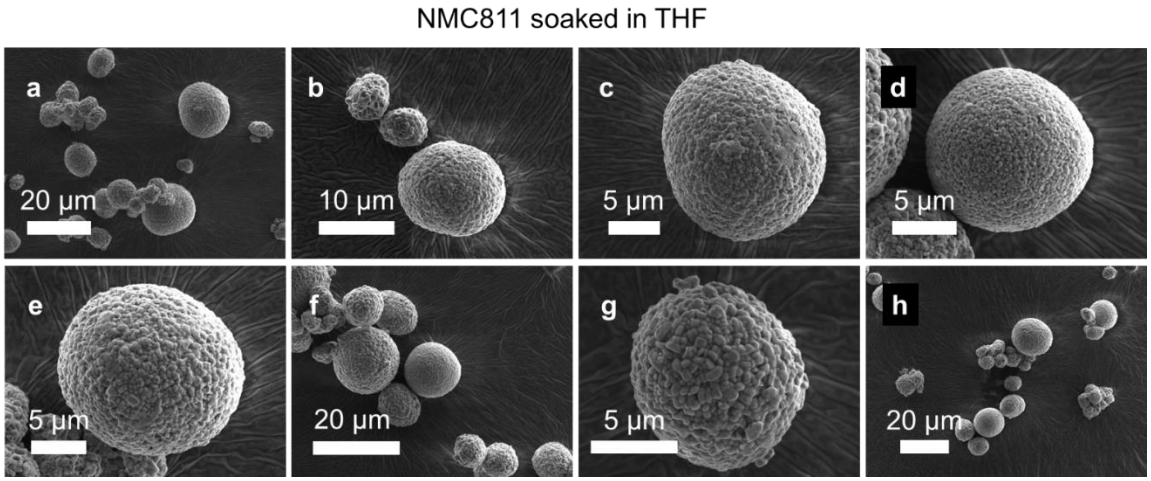

Figure B53. SEM images of NMC811 soaked in THF.

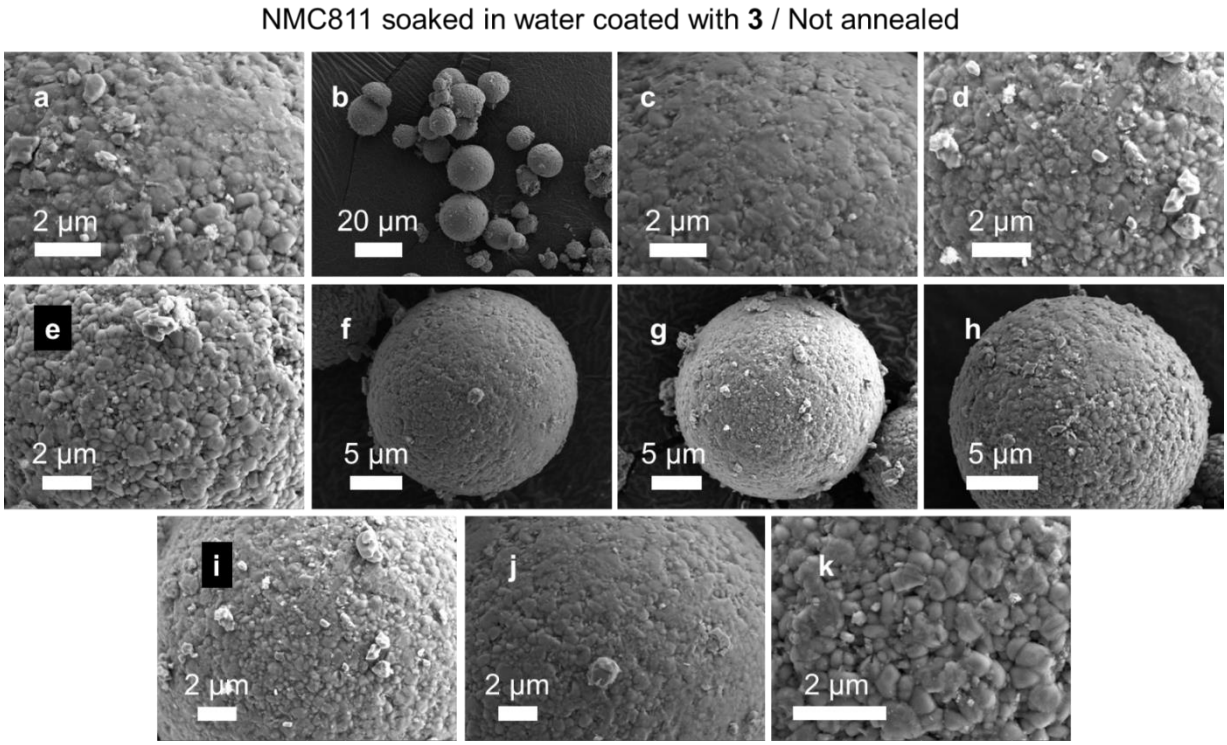

Figure B54. SEM images of NMC811 soaked in water, coated using precursor **3**.

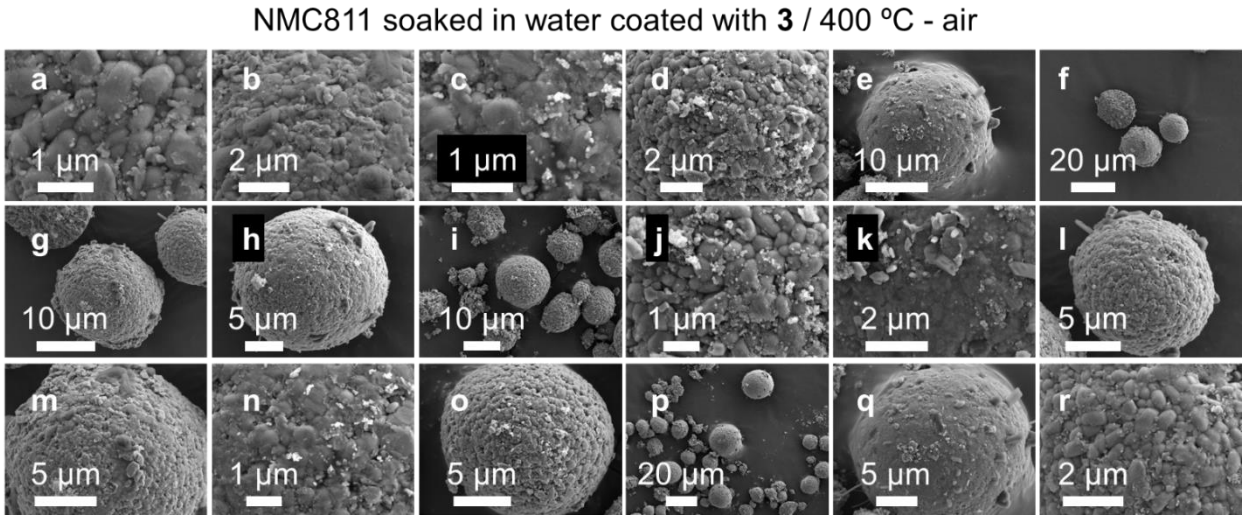

Figure B55. SEM images of NMC811 soaked in water, coated using precursor **3** and annealed at 400 ºC under air.

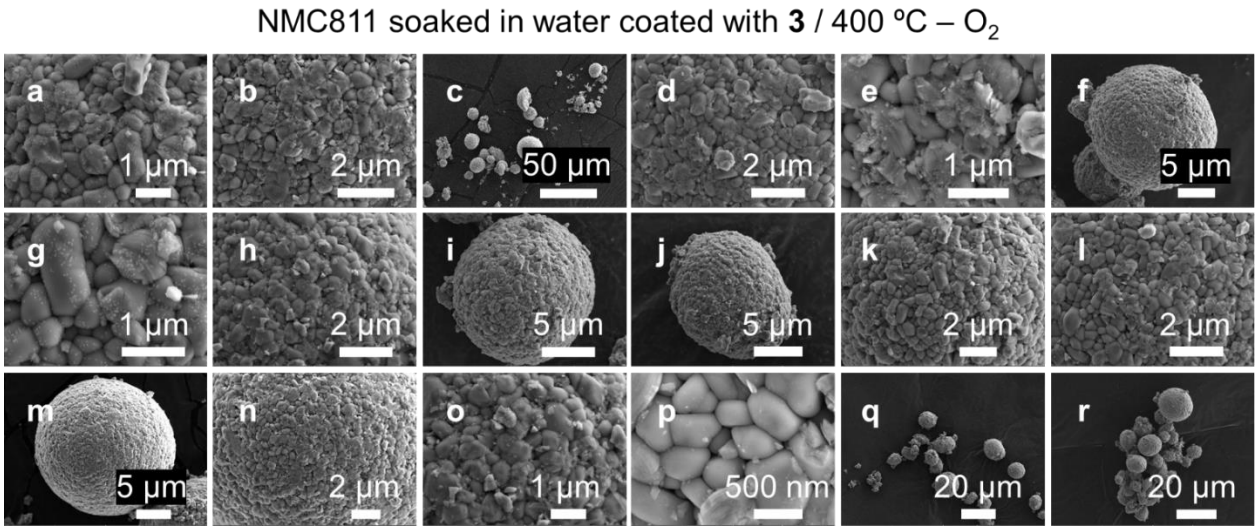

Figure B56. SEM images of NMC811 soaked in water, coated using precursor **3** and annealed at 400 ºC under oxygen.

B3.1.2. Single-crystal NMC811

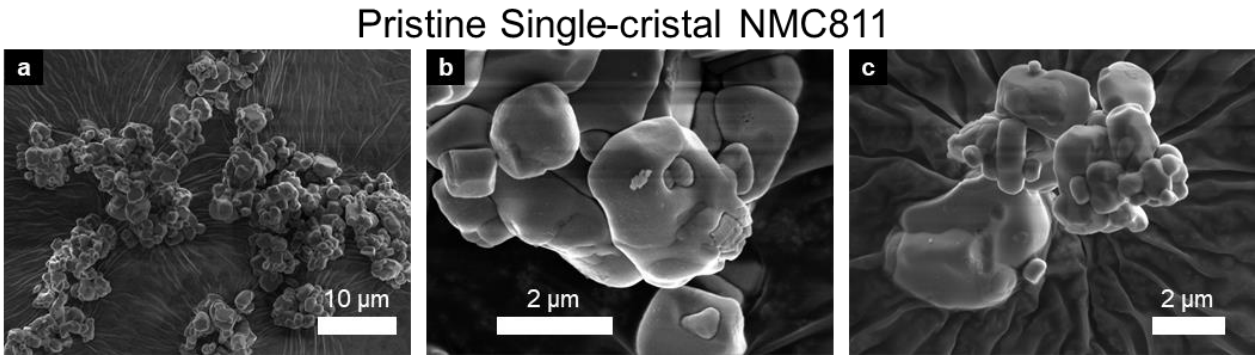

Figure B57. SEM images of pristine (Al_2O_3 coated) single-crystal NMC811.

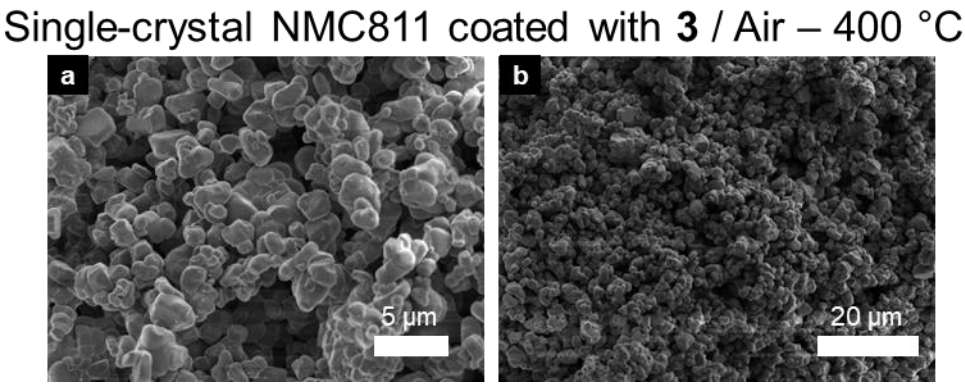

Figure B58. SEM images of (Al_2O_3 coated) single-crystal NMC811 coated with **3** without a pre-soaking in water.

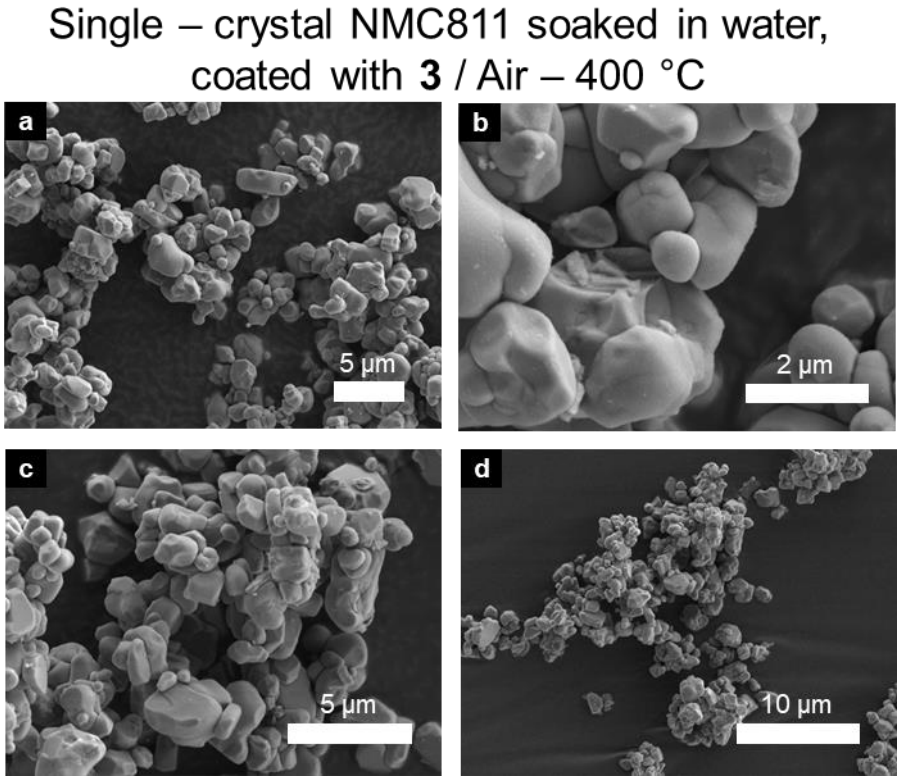

Figure B59. SEM images of (Al_2O_3 coated) single-crystal NMC811 soaked in water and coated with **3**.

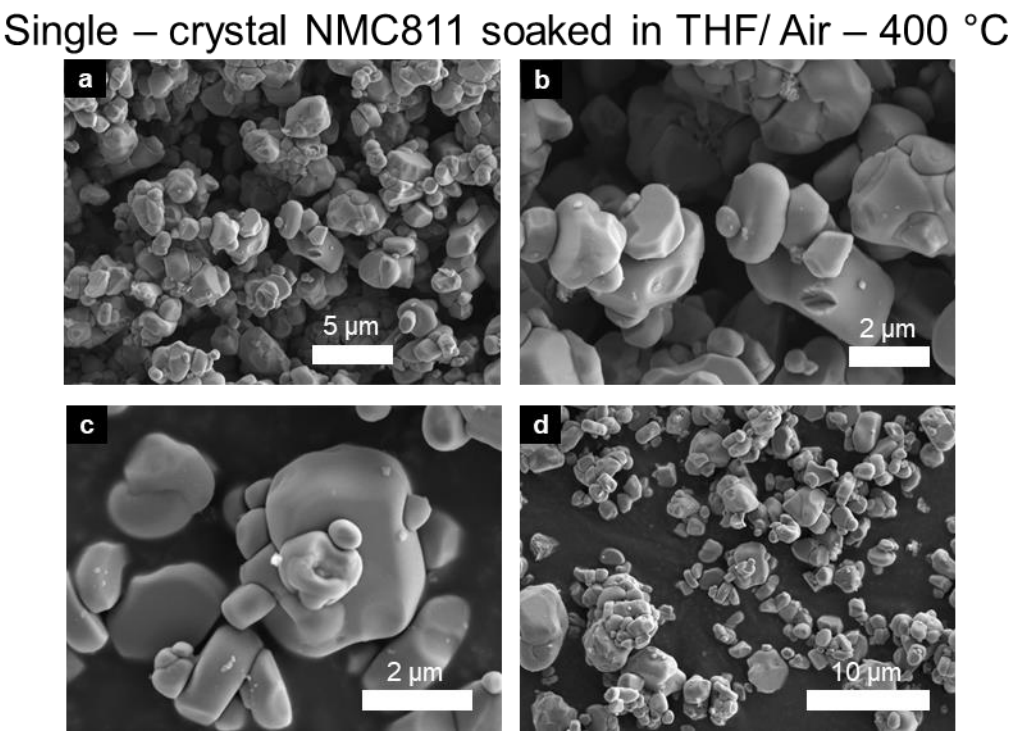

Figure B60. SEM images of the control (Al_2O_3 coated) single-crystal NMC811 sample soaked in THF and annealed at 400 ºC under air.

B3.2. EDX Analysis

B3.2.1. Polycrystalline NMC811

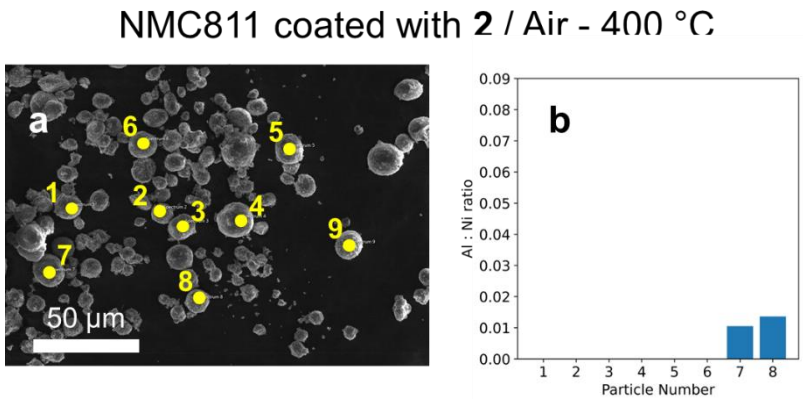

Figure B61. (a) SEM images and locations of the EDS point scans taken for NMC811 using precursor **2** and annealed at 400 ºC under air. (b) Al : Ni ratios calculated for each of the particles.

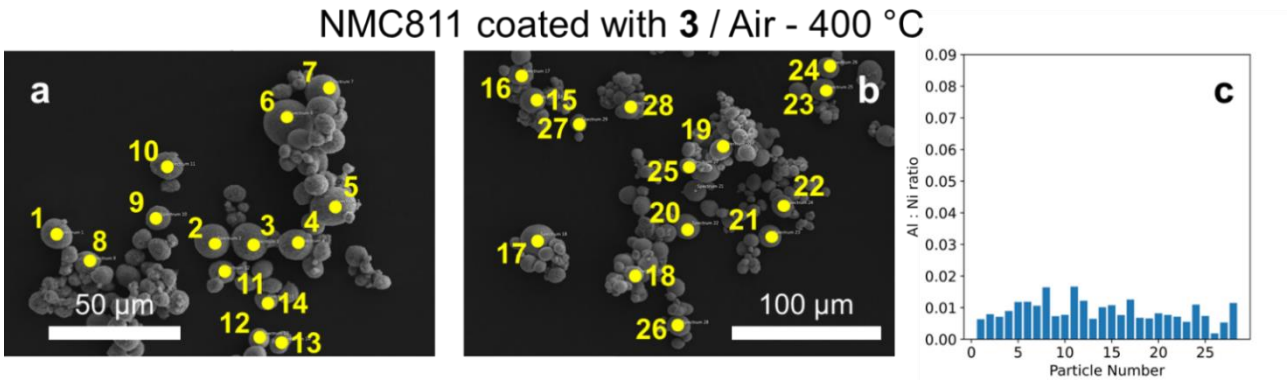

Figure B62. (a, b) SEM images and locations of the EDS point scans taken for NMC811 using precursor **3** and annealed at 400 ºC under air. (c) Al : Ni ratios calculated for each of the particles.

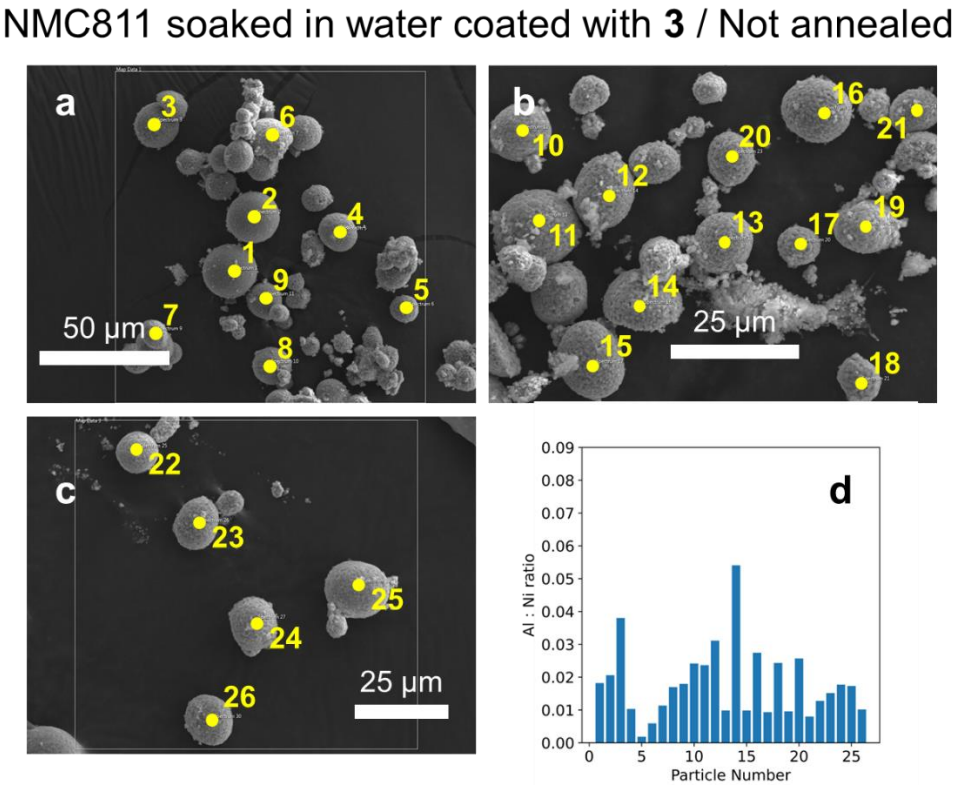

Figure B63. (a-c) SEM images and locations of the EDS point scans taken for NMC811 soaked in water and coated using precursor **3**. (d) Al : Ni ratios calculated for each of the particles.

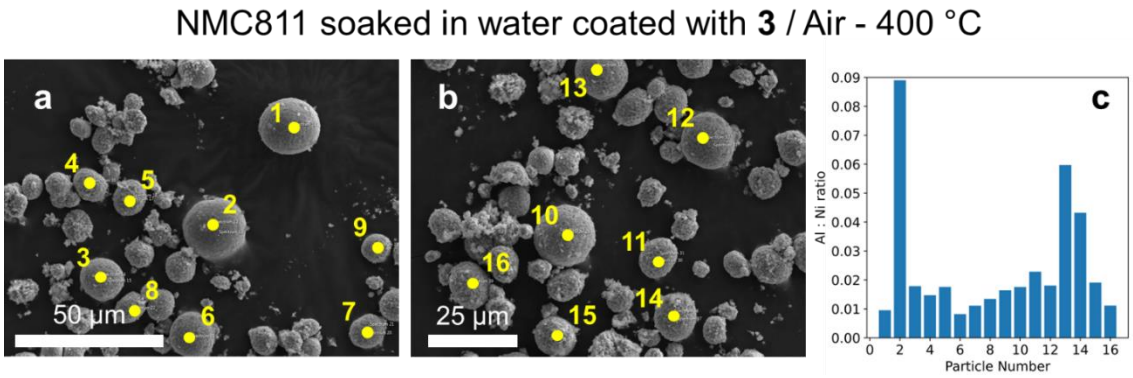

Figure B64. (a-b) SEM images and locations of the EDS point scans taken for NMC811 soaked in water, coated using precursor **3** and annealed at 400 ºC under air. (c) Al : Ni ratios calculated for each of the particles.

B3.2.2. Single-crystal NMC811

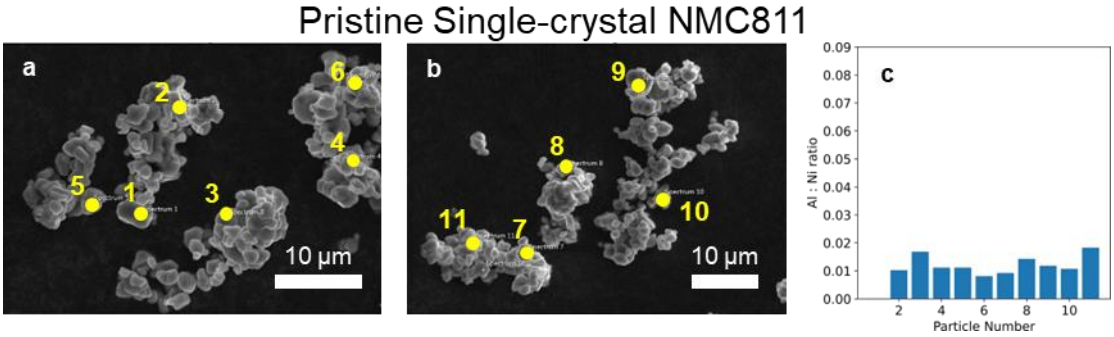

Figure B65. (a, b) SEM images and locations of the EDS point scans taken for the pristine (Al_2O_3 coated) single crystal NMC811. (c) Al : Ni ratios calculated for each of the particles.

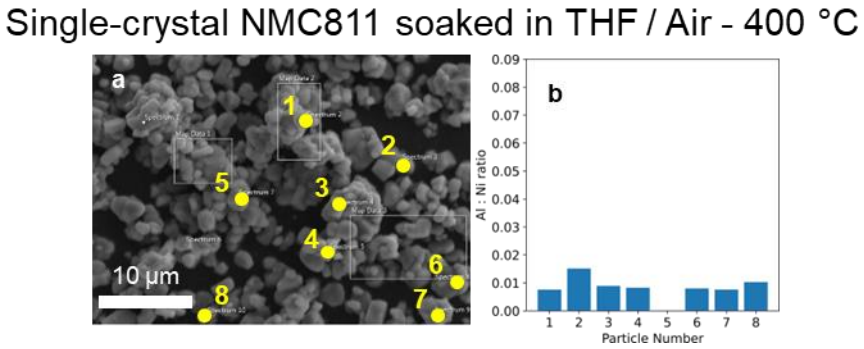

Figure B66. (a) SEM images and locations of the EDS point scans taken for the pristine (Al_2O_3 coated) single crystal NMC811. (b) Al : Ni ratios calculated for each of the particles.

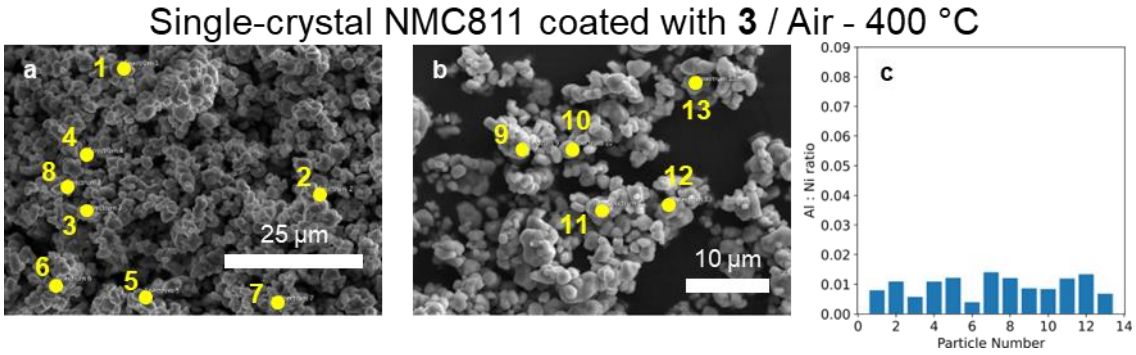

Figure B67. (a, b) SEM images and locations of the EDS point scans taken for (Al_2O_3 coated) single crystal NMC811 coated with **3**. (c) Al : Ni ratios calculated for each of the particles.

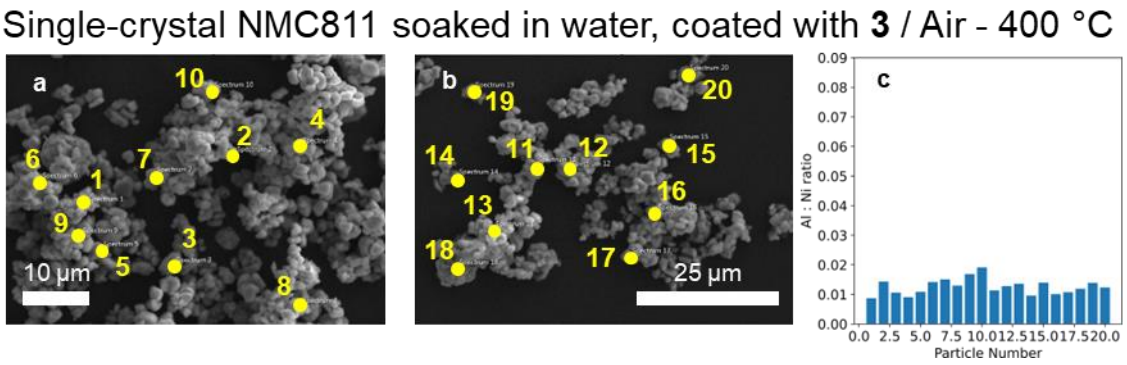

Figure B68. (a, b) SEM images and locations of the EDS point scans taken for (Al_2O_3 coated) single crystal NMC811 soaked in water and coated with **3**. (c) Al : Ni ratios calculated for each of the particles.

Appendix C: Spectroscopy

C1. XPS Survey Spectra of the Catalysts Discussed in Chapter 2

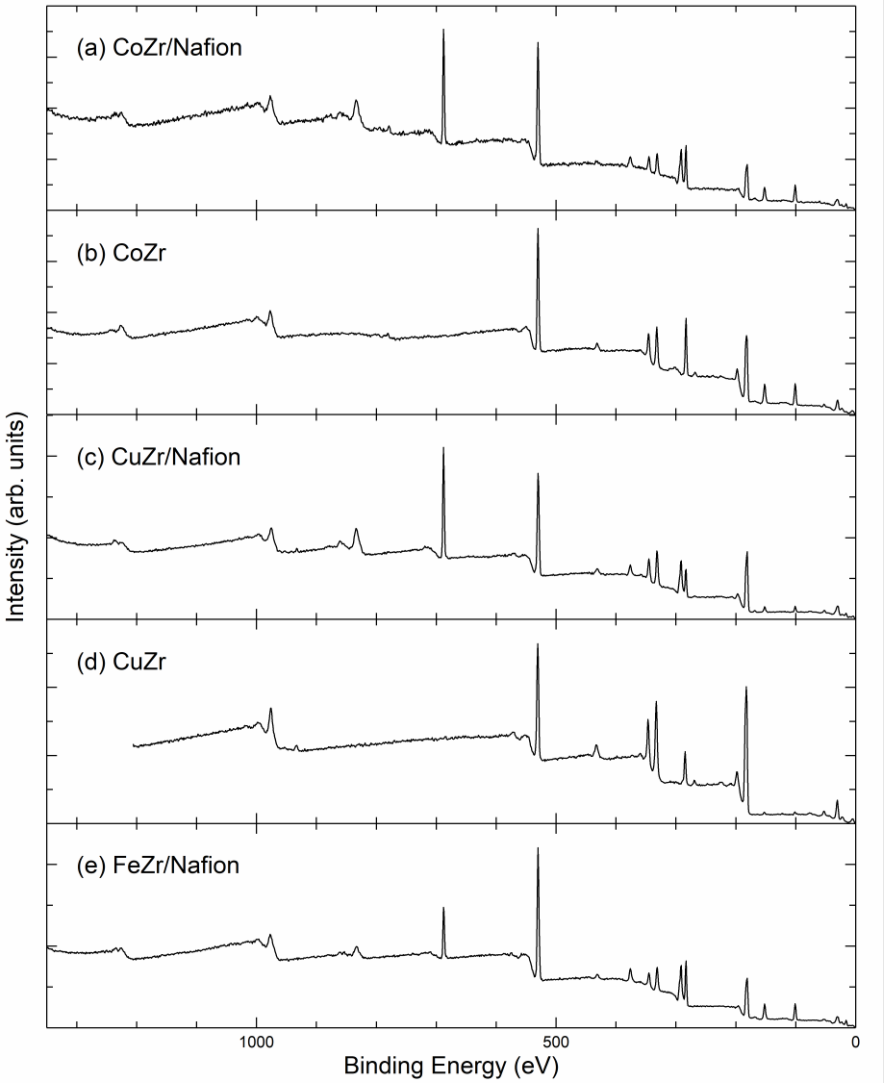

Figure C1. XPS survey spectra for the materials characterized in this work. Note that (d) was measured on a different instrument. During the fabrication of the electrocatalyst film, a 1:1 Nafion : EtOH mixture was drop-casted over the catalytic films to improve their adherence to the FTO glass. For the XPS measurements, samples with and without Nafion were used. The Zr 3d spectra shown in the main text correspond to the samples treated with a 1:1 solution of Nafion in ethanol.

C2. XPS Survey Scans and Fitting Parameters for the High-resolution Al 2p Region (Chapter 3)

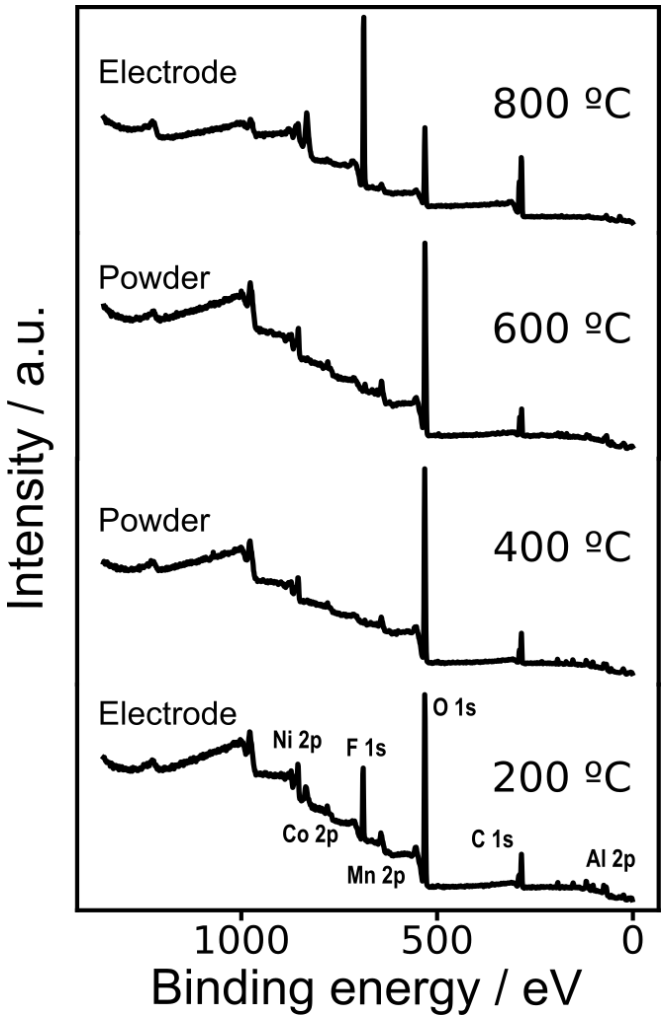

Figure C2. XPS survey scans of the samples discussed in Chapter 3.

Table C1. Position and area of the peaks used in the fitting of the Al 2p spectra.

	200 °C		400 °C		600 °C		800 °C	
Component	B.E./eV	Area	B.E./eV	Area	B.E./eV	Area	B.E./eV	Area
Al 2p	74.45	757.4	74.52	632.5	73.09	168.2	72	99.51
Mn 3p	50.63	204	50.52	203.3	49.81	288.1	50.11	254.3
Li 1s	55.31	311.1	55.35	458.2	54.9	527.2	54.99	328.5
Co 3p	61.94	230.8	62.24	142.8	62.51	166.2	61.35	135.3
Co 3p sat	71.94	23.08	72.24	14.28	72.51	16.62	71.35	13.53
Ni 3p 3/2	67.72	1371	67.55	1293	67.5	1313	67	728.7
Ni 3p 1/2	69.92	686	69.75	646.7	69.7	656.4	69.2	364.4
Ni 3p sat	73.72	425.3	73.55	401	73.5	407	73	226

C3. Fitting of the High-resolution XPS Spectra in Chapter 4

Table C2. Position and area of the peaks used in the fitting of the C 1s spectra.

	Pristine		Soaked annealed		Soaked coated		coated	
Component	B.E./eV	Area	B.E./eV	Area	B.E./eV	Area	B.E./eV	Area
C-C, C-H	284.78	1334.25	284.8	1175.5	284.81	21765.4	284.8	2566.22
C-OH , C-O-C	286.28	130.79	286.3	0	286.31	1400.37	286.3	0
C=O	287.78	0	287.8	116.17	287.81	264.93	287.8	19.39
O-C=O	289.08	0	289.1	12.51	288.61	1347.75	289.1	53.48
LiCO3	289.78	250.66	289.8	217.62	289.81	1983.69	289.8	602.99

Table C3. Position and area of the peaks used in the fitting of the O 1s spectra.

	Pristine		H_2O soaked/ annealed		Coated with **3**		Soaked coated	
Component	B.E./eV	Area	B.E./eV	Area	B.E./eV	Area	B.E./eV	Area
Lattice oxygen	529.35	418.3	529.39	3091.16	529.3	287.67	529.52	7710.16
Hydroxides	531.09	1232.29	531.31	487.18	530.69	2774	531.45	50945.72
Organic species	531.93	5697.1	531.76	1970.38	532.12	6127.19	532.94	15757.67
$LiAlO_2$	-	-	-	-	530.99	584.18	531.42	42971.25

Table C4. Position and area of the peaks used in the fitting of the Al 2p spectra.

	H_2O soaked / coated with **3**		Coated with **3**		Pristine NMC811	
Component	B.E./eV	Area	B.E./eV	Area	B.E./eV	Area
Al 2p	74.28	2974.24	74.18	166.47	-	-
Mn 3p	50.63	435.7	50.63	56.6	50.63	85.13
Li 1s	55.4	1055.5	55.33	317.63	55.61	230.68
Co 3p	61.65	229.62	63.63	10.4	63.07	91.28
Co 3p sat	71.65	22.96	73.63	1.04	73.07	9.13
Ni 3p 3/2	67.63	2499.81	67.77	241.01	68.39	625.76
Ni 3p 1/2	69.83	1249.9	69.97	120.5	70.59	312.88
Ni 3p sat	73.63	774.94	73.77	74.71	74.39	193.98

Table C5. Constraints used to fit the O 1s spectra.

Component	**FWHM**	**Position / eV**
Lattice Oxygen	= Hydroxides	529.6–528.5
Hydroxides	1 - 3	531.5–530
Organic Species	= Hydroxides	533.7–531.5
$LiAlO_2$	= Hydroxides	531.5–530

C4. Fitting Parameters 1 GHz Solid-state ^{27}Al NMR Measurements (Chapter 3)

Table C6. Parameters used in the fitting of the high-field NMR measurements (Figures 3.17 and 3.18 in Chapter 3) using a Czjzek distribution (Gaussian Isotropic Model, d = 5). δ_{iso} is the isotropic chemical shift, Δ_{CS} is the full width at half maximum of the isotropic chemical shift Gaussian distribution, and C_Q is the peak value of the quadrupolar coupling of the Czjzek distribution.[271]

T / ºC	Al coord. number	δ_{iso} / ppm	Δ_{CS} / ppm	$\underline{C}_Q$ / kHz
200	4	75.5	15.6	9504
	5	43.8	12.7	11490
	6	13.4	9.1	6786
400	4	75.3	16.8	10227
	5	42.6	13.8	10126
	6	14.4	11.1	8019
600	4	82.4	4.3	6242
	5	35.4	11.6	3918
	6	18.6	12.2	2010

C5. Solution NMR Spectra (Chapter 4)

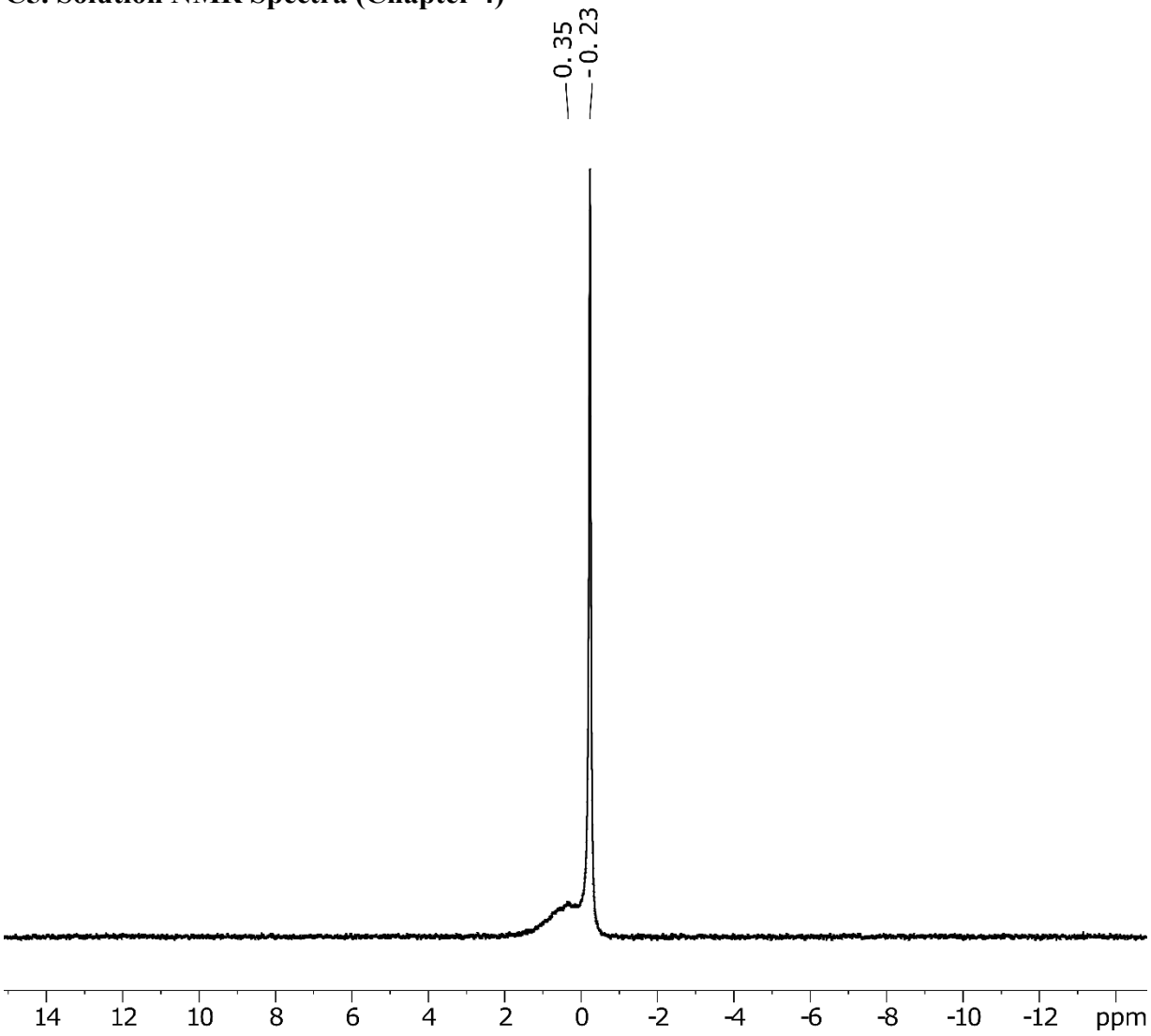

Figure C3. ^{7}Li NMR (400 MHz, THF, 295 K) spectrum of $LiAl[OCH_2Ph)_4]$ (**1**).

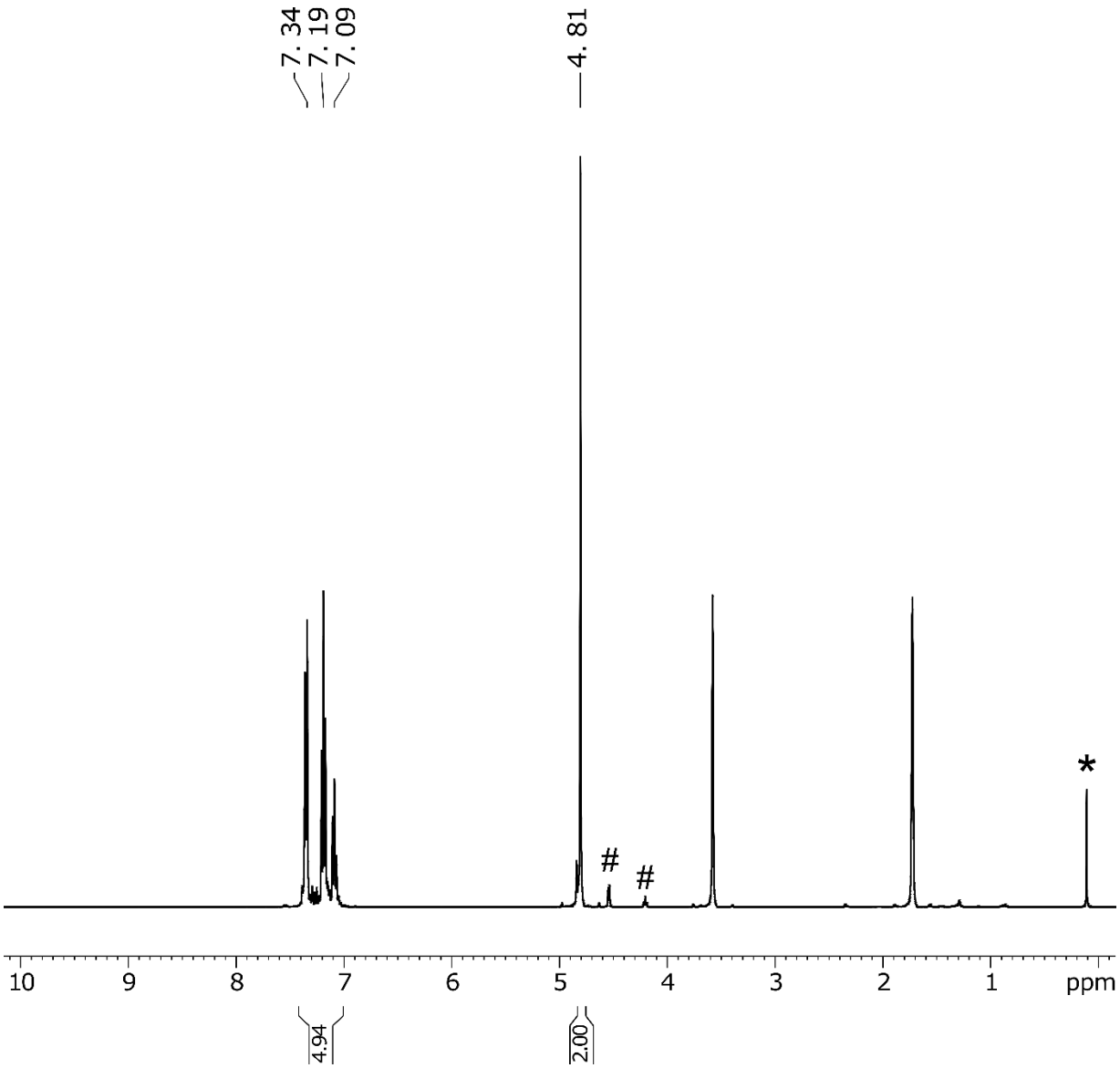

Figure C4. ^{1}H NMR (400 MHz, THF, 295 K) spectrum of $LiAl[OCH_2Ph)_4]$ (**1**). The peak due to silicone grease is marked with (*). Peaks marked with an # are assigned to unreacted alcohol.

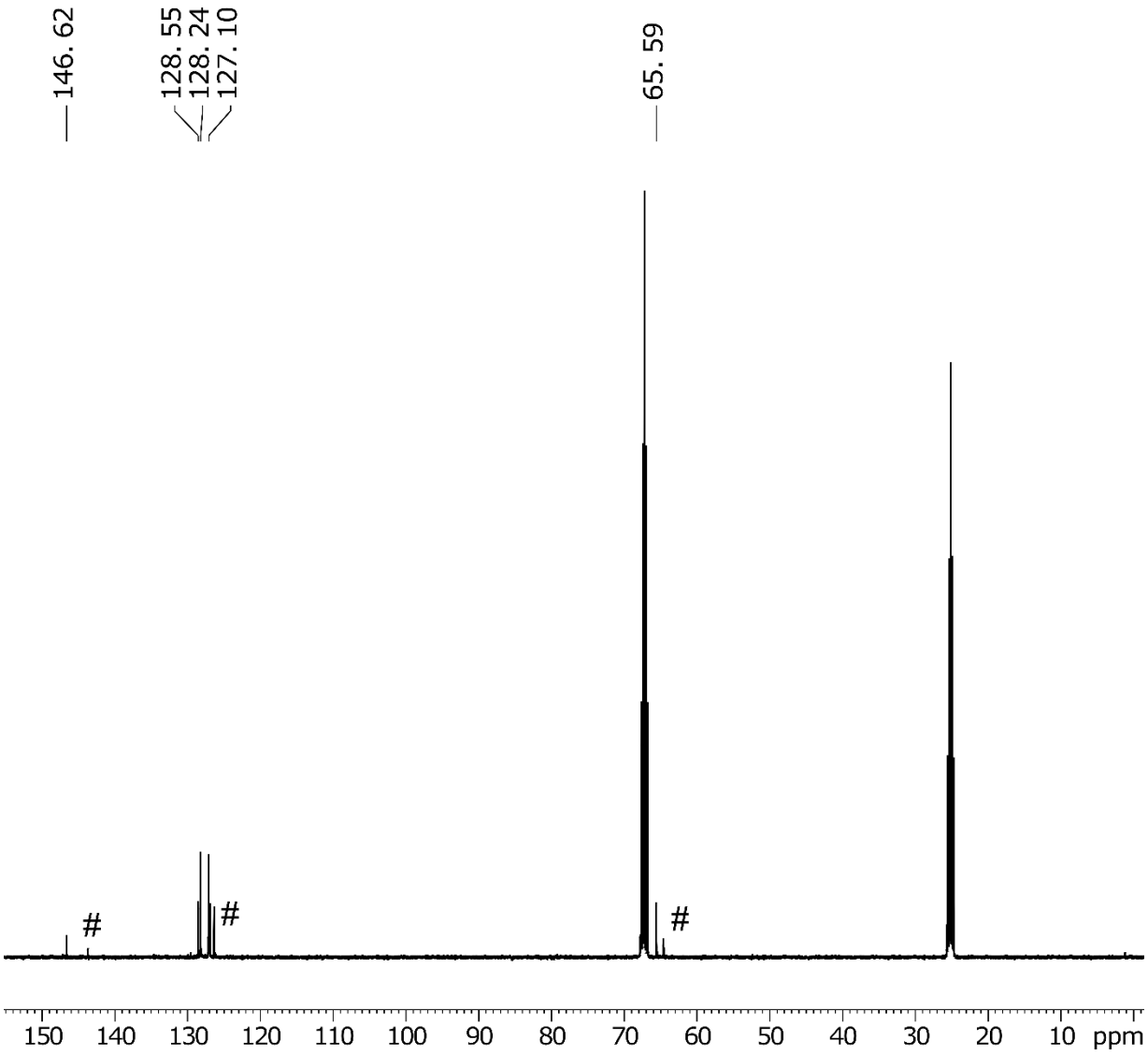

Figure C5. ^{13}C NMR (400 MHz, THF, 295 K) spectrum of $LiAl[OCH_2Ph)_4]$ (**1**). Peaks marked with an # are assigned to unreacted alcohol.

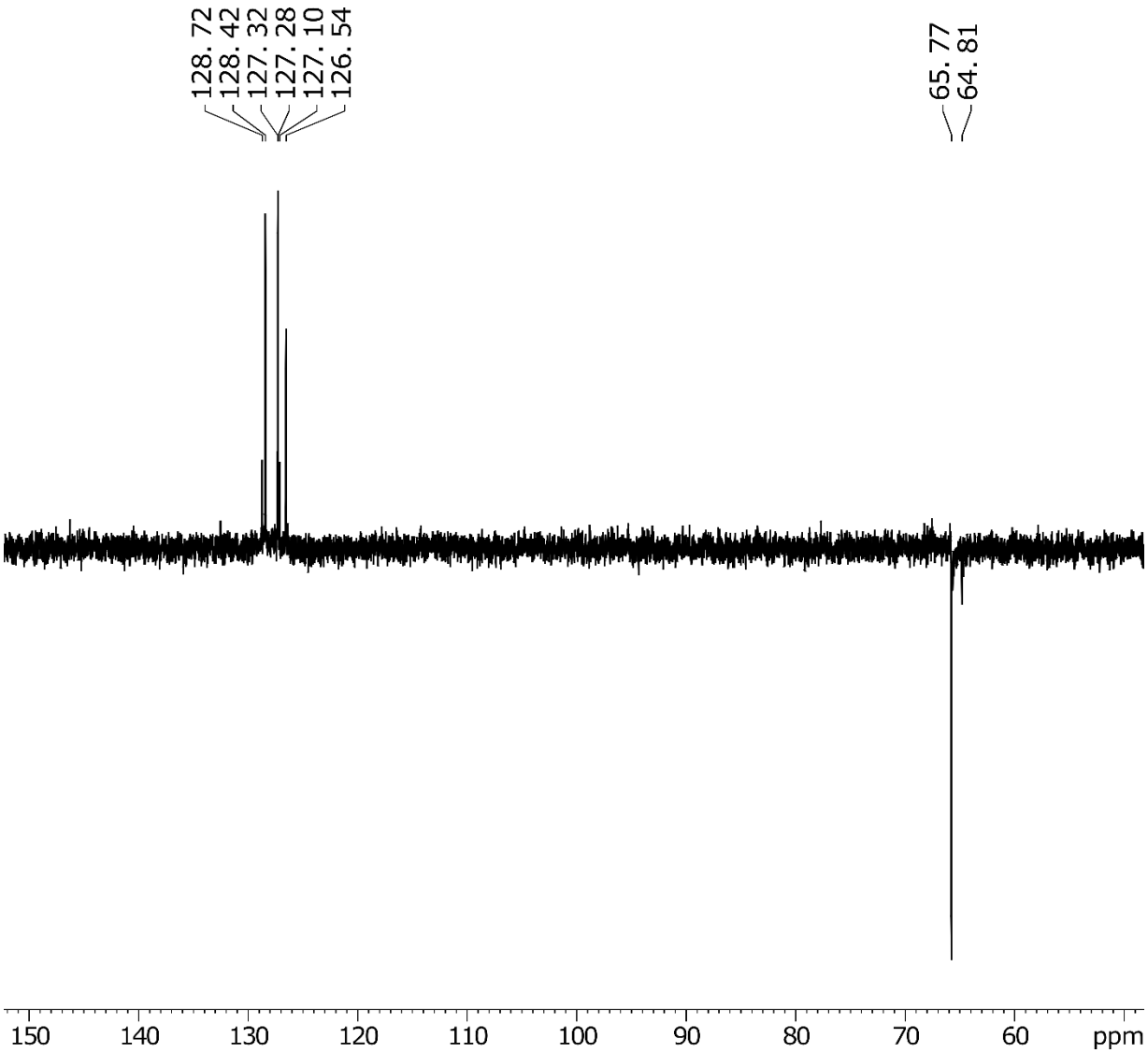

Figure C6. ^{13}C NMR DEPT 135 (400 MHz, THF, 295 K) spectrum of $LiAl[OCH_2Ph)_4]$ (**1**).

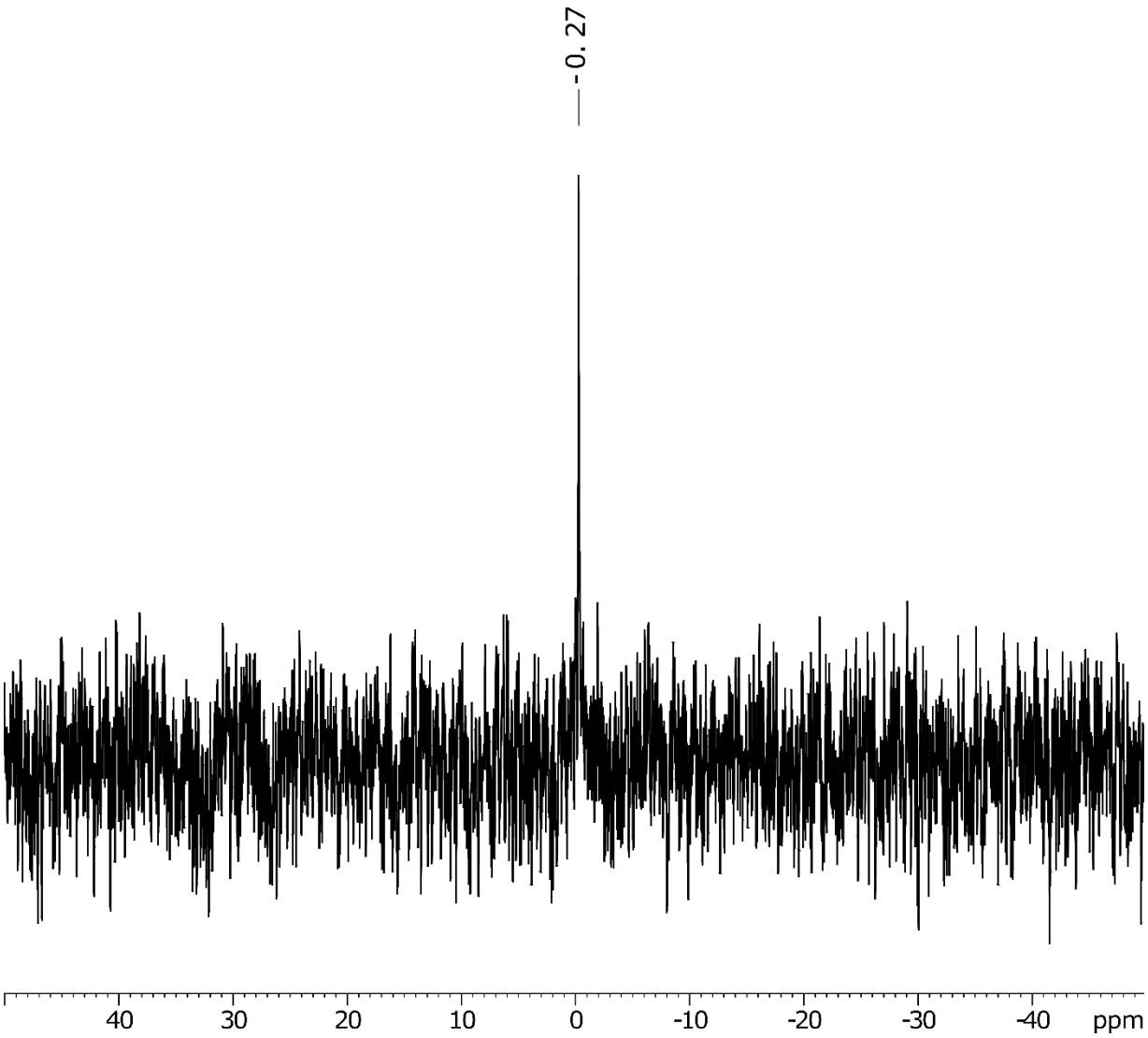

Figure C7. ^{7}Li NMR (400 MHz, THF, 295 K) spectrum of LiAl[(O^{i}Pr)$_4$] (**2**).

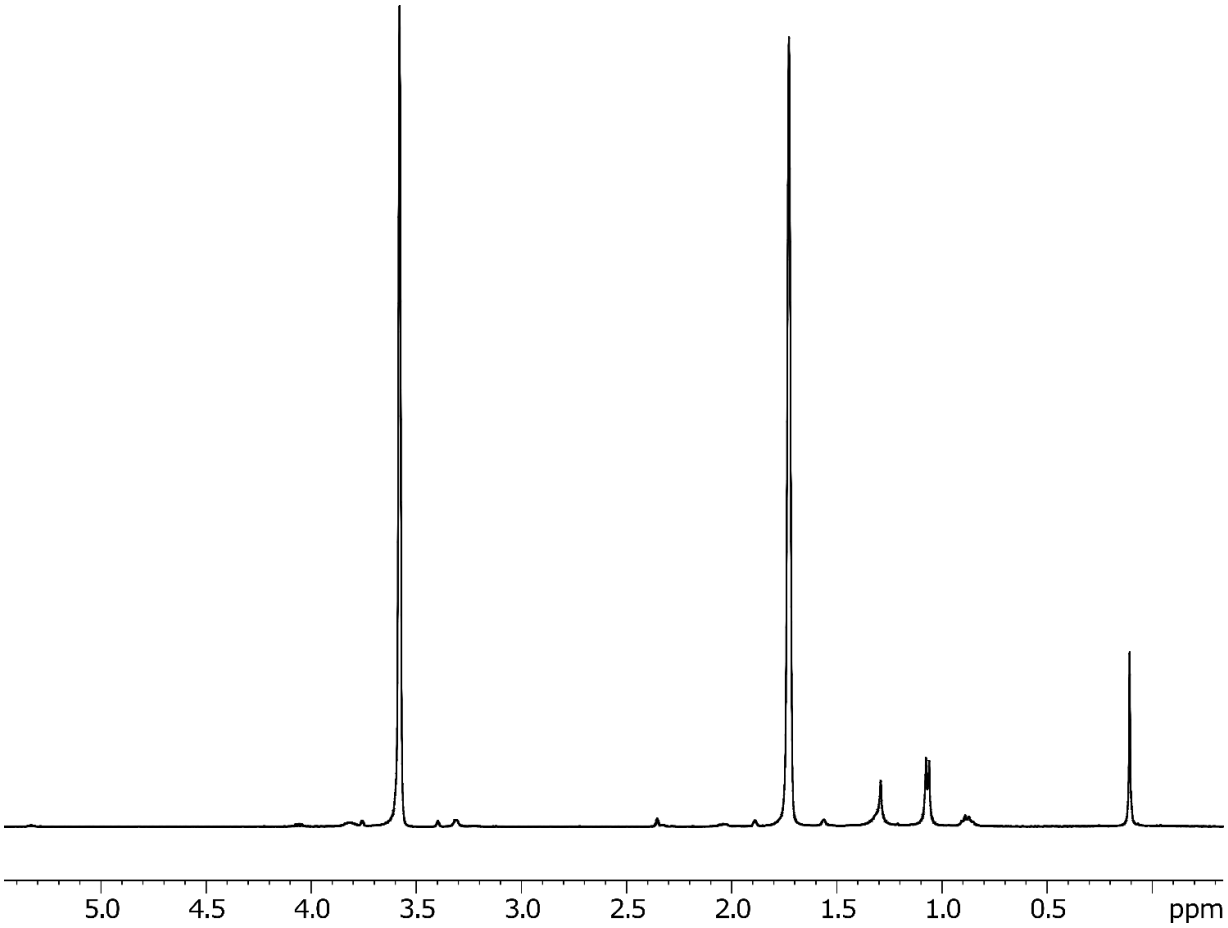

Figure C8. ^{1}H NMR (400 MHz, THF, 295 K) spectrum of LiAl[(O^{i}Pr)$_4$] (**2**).

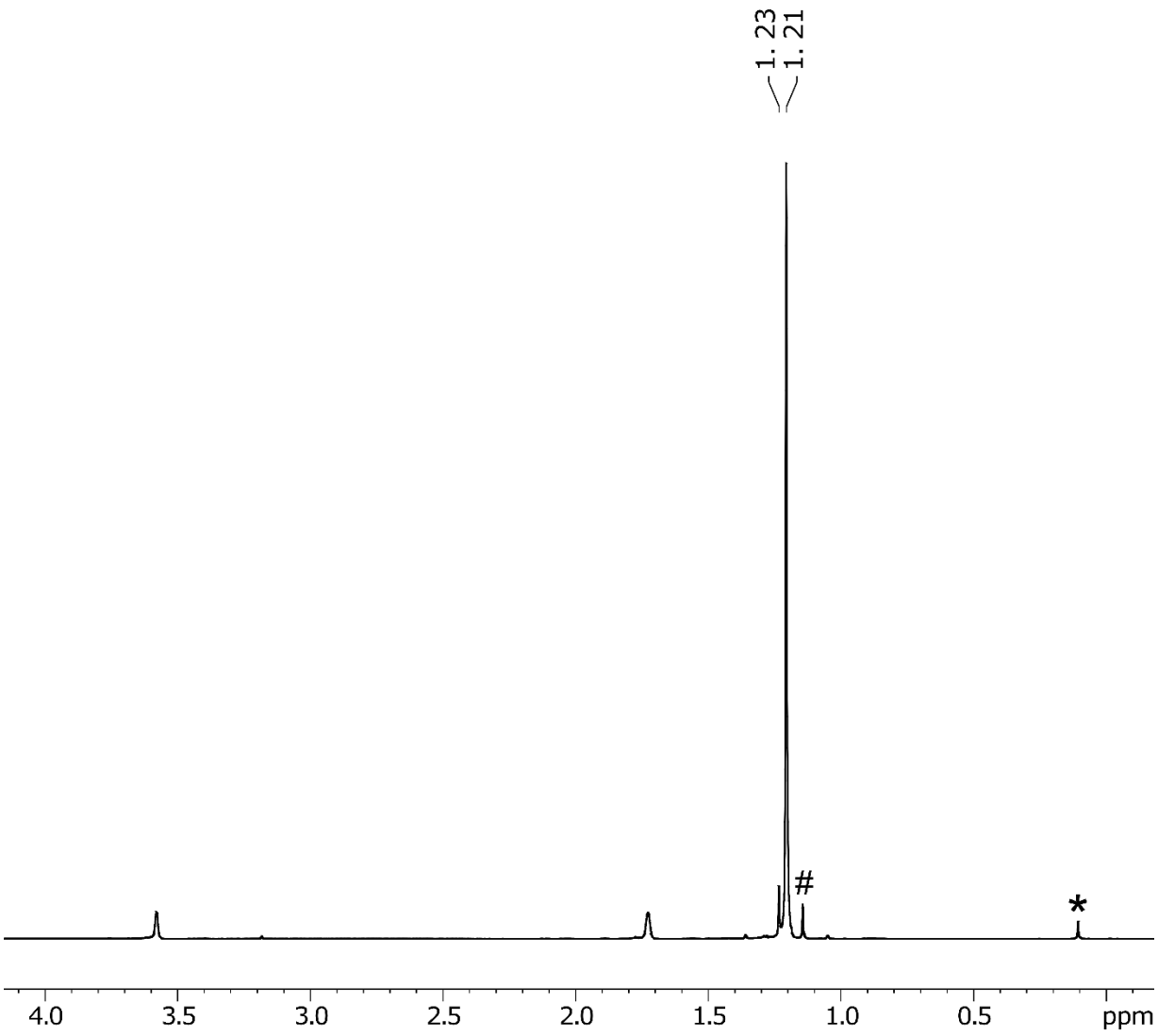

Figure C9. ^{1}H NMR (400 MHz, THF, 295 K) spectrum of LiAl[(O^{t}Bu)$_4$] (**3**). In addition of the THF solvent peaks, one signal arises due to the presence of silicone grease (*) and one due to unreacted tert-butanol (#).

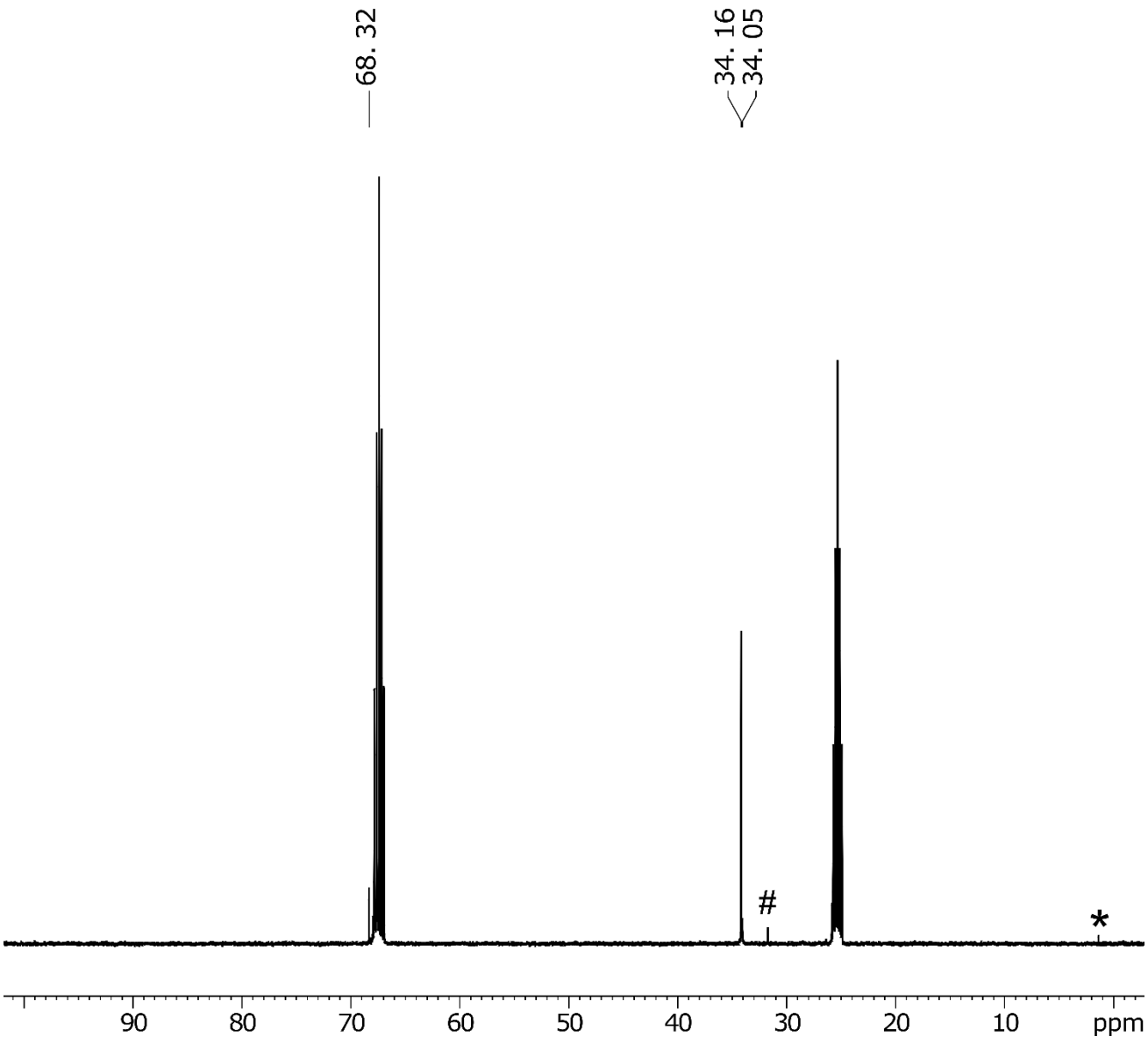

Figure C10. ^{13}C NMR (400 MHz, THF, 295 K) spectrum of $LiAl[O^tBu)_4]$ (**3**). Apart from the THF solvent peaks found at 67.21 and 25.12 ppm, one signals arise due to the presence of silicone grease (*) and two due to unreacted tert-butanol (#).

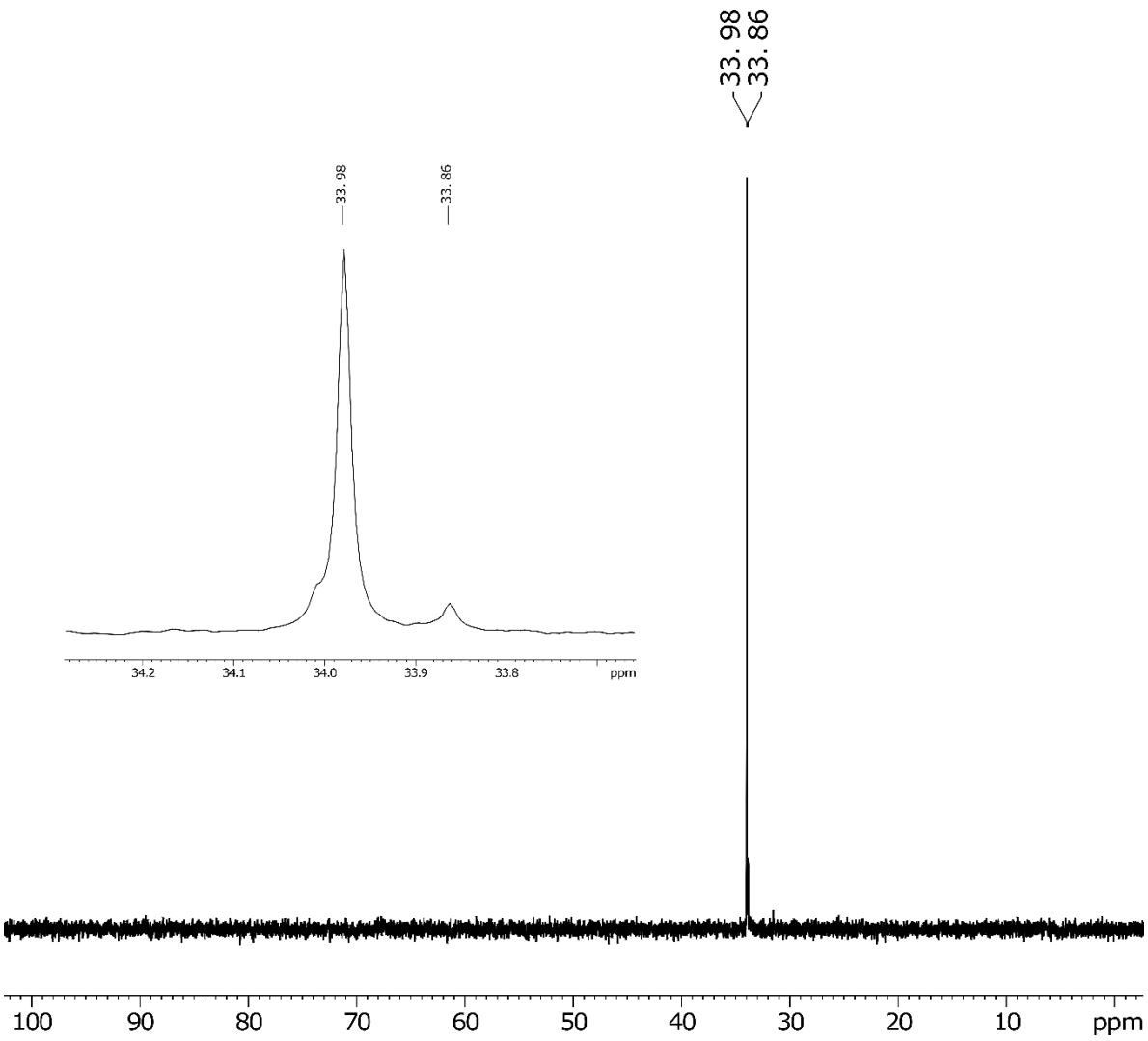

Figure C11. ^{13}C NMR DEPT 135 (400 MHz, THF, 295 K) spectrum of $LiAl[O^tBu)_4]$ (**3**).

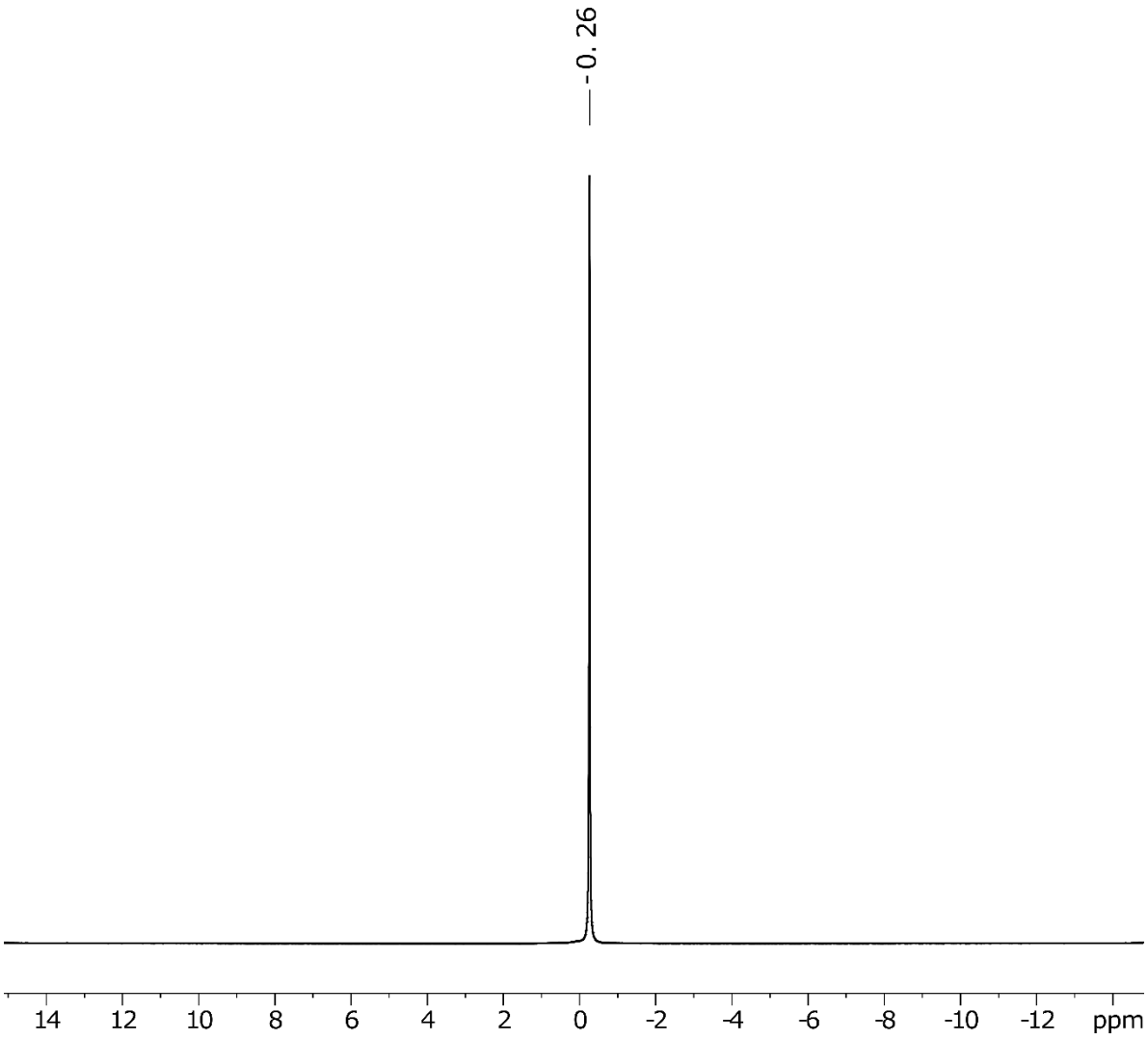

Figure C12. ^{7}Li NMR (400 MHz, THF, 295 K) spectrum of LiAl[O^{t}Bu)$_4$] (**3**).

C6. Solid-state NMR Spectra from Chapter 4

The spectra shown in this section were recorded at a magnetic field strength of 16.4 T and a MAS frequency of 50 kHz and normalised to the sample mass and the number of scans. The spinning side-bands are marked with stars. The recycle delay (D1) used for the ^{7}Li and ^{27}Al experiments is 100 ms and 25 ms respectively whereas for the ^{1}H-NMR measurements it was determined from a saturation recovery experiment for each sample. All the spectra are normalised to the number of scans and mass of the sample.

C6.1. ^{1}H SSNMR Measurements

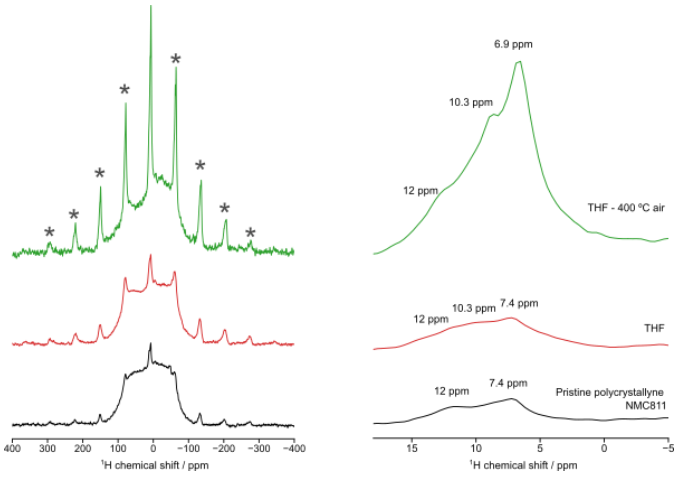

Figure C13. ^{1}H SSNMR of the pristine PC-NMC811, PC- NMC811 soaked in THF and dried at 100 °C under vacuum for 2 h and THF soaked NMC811 annealed under air. Full spectra and zoom-in on the central transition are shown. The spinning sidebands are marked with stars.

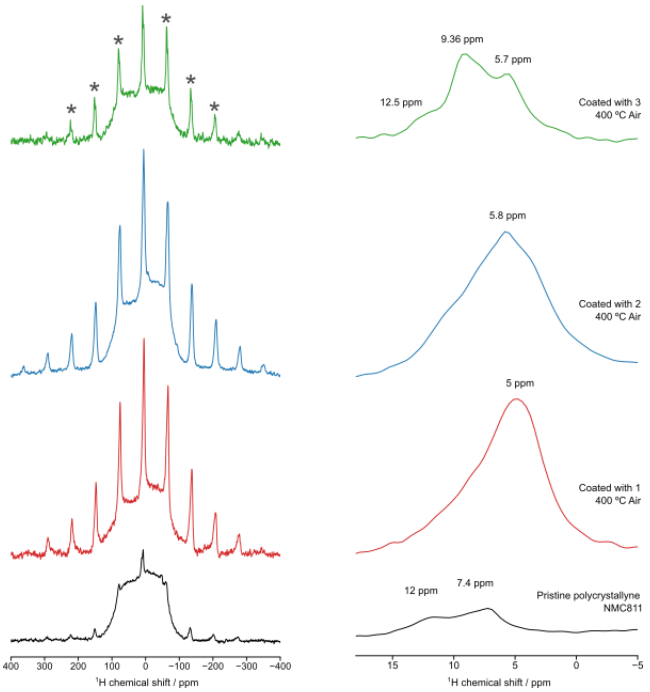

Figure C14. ^{1}H SSNMR of pristine PC-NMC811, PC-NMC811 coated with **1**, PC-NMC811 coated with **2** and PC-NMC811 coated with **3**. Full spectra and zoom-in on the central transition are shown. The spinning sidebands are marked with stars.

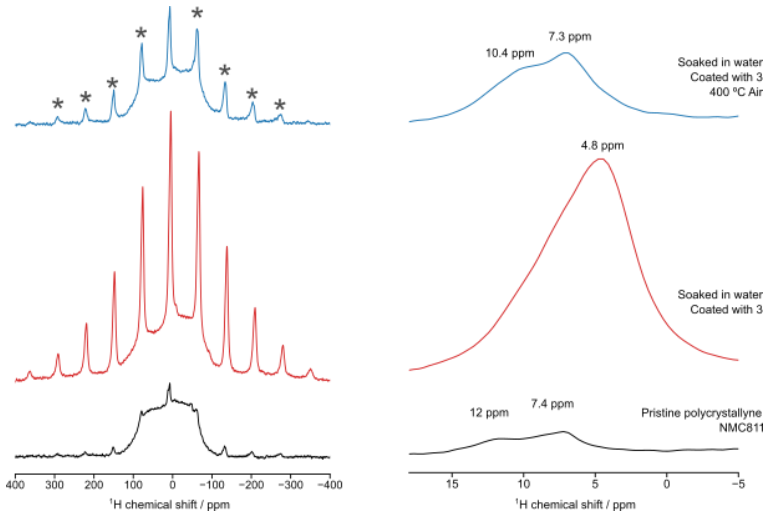

Figure C15. ^{1}H SSNMR of pristine PC-NMC811, PC-NMC811 soaked in water and drying under vacuum at 50 °C for 2h, PC-NMC811 soaked in water, dried under vacuum at 50 °C for 2h and the annealed at 400 °C under air for 4 h. Full spectra and zoom-in on the central transition are shown. The spinning sidebands are marked with stars.

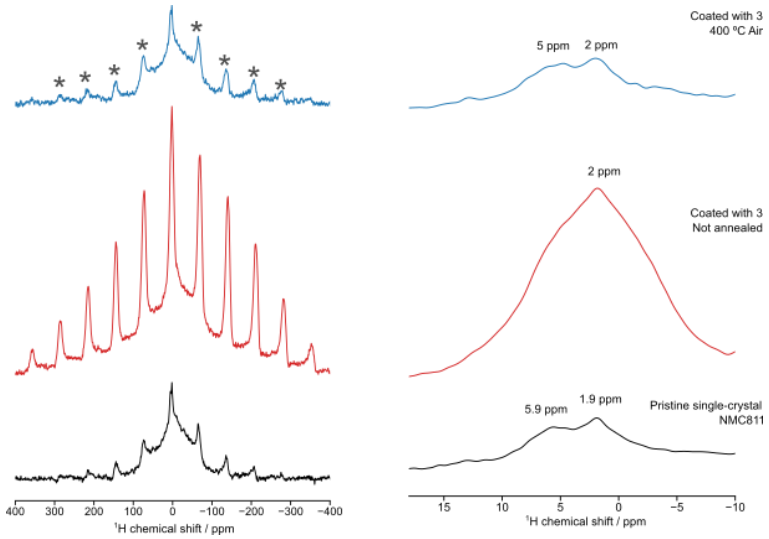

Figure C16. ^{1}H SSNMR of pristine SC-NMC811, SC-NMC811 coated with **3** before annealing, SC-NMC811 coated with **3** and annealed at 400 °C under air for 4 h. Full spectra and zoom-in on the central transition are shown. The spinning sidebands are marked with stars.

C6.2. ^{7}Li SSNMR Measurements

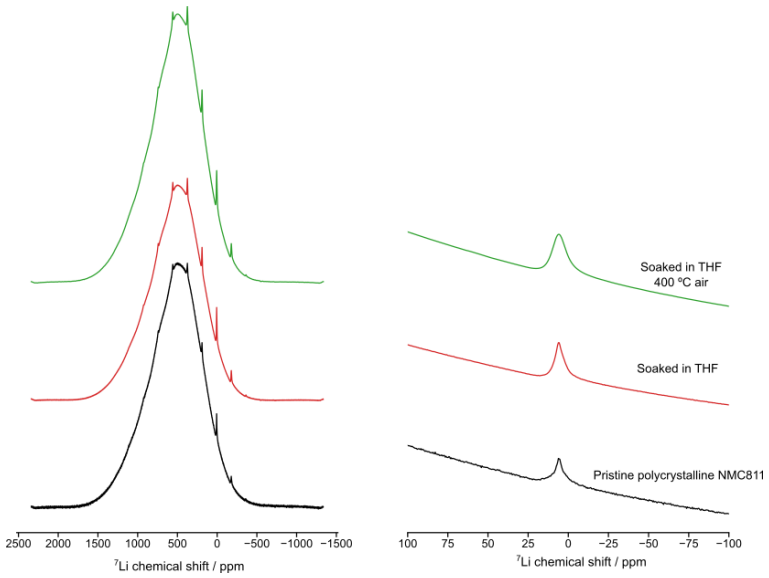

Figure C17. ^{7}Li SSNMR of pristine PC-NMC811, PC-NMC811 soaked in THF, PC-NMC811 soaked in THF and then annealed at 400 °C for 4 h. Full spectra and zoom-in on the central transition are shown.

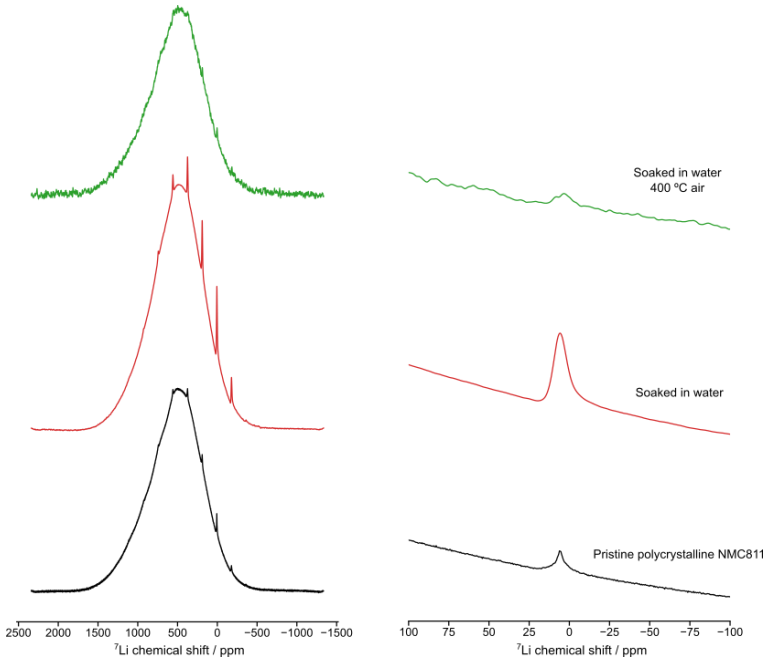

Figure C18. ^{7}Li SSNMR of pristine PC-NMC811, PC-NMC811 soaked in water, PC-NMC811 soaked in water and then annealed at 400 °C for 4 h. Full spectra and zoom-in on the central transition are shown.

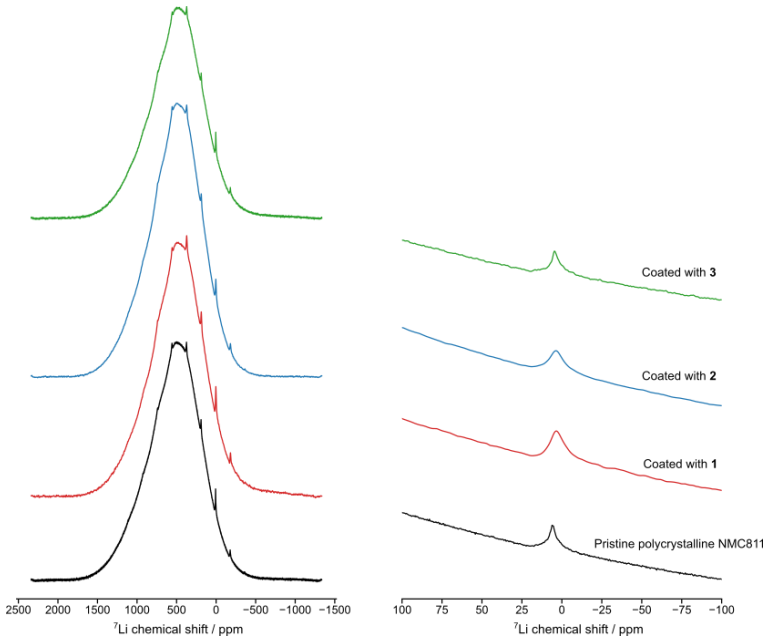

Figure C19. ^{7}Li SSNMR of pristine PC-NMC811, PC-NMC811 coated with **1**, PC-NMC811 coated with **2** and PC-NMC811 coated with **3**. Full spectra and zoom-in on the central transition are shown.

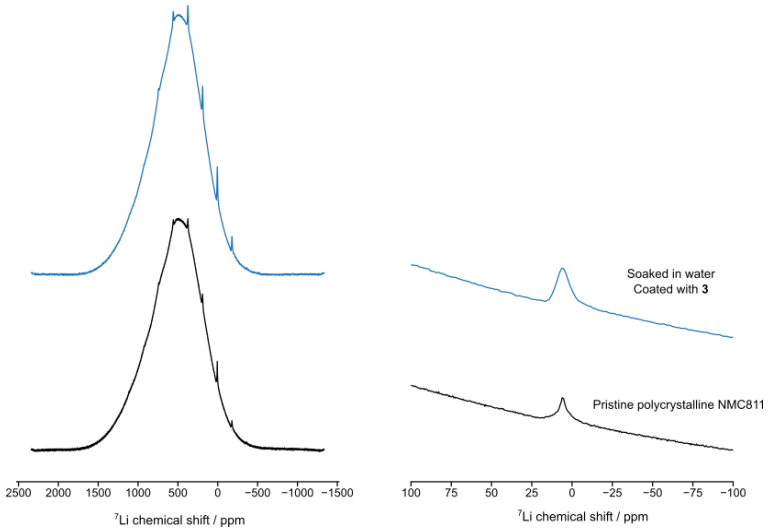

Figure C20. ^{7}Li SSNMR of pristine PC-NMC811, PC-NMC811 soaked in water and coated with **3**.

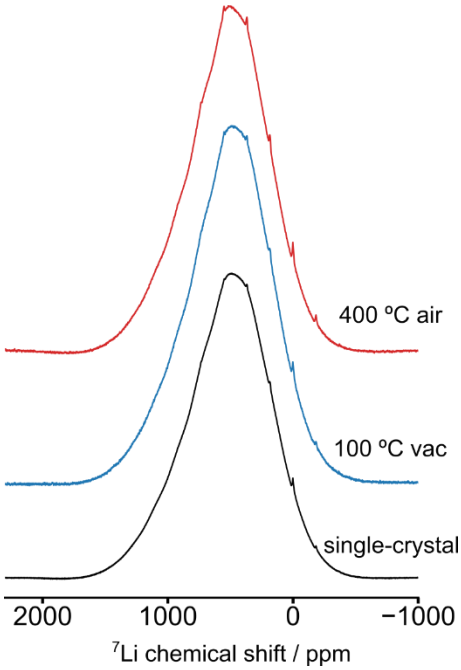

Figure C21. ^{7}Li SSNMR of pristine SC-NMC811, SC-NMC811 coated with **3** and dried under vacuum at 100 °C and SC-NMC811 coated with **3** and annealed at 400 °C under air.

C6.3. ^{27}Al SSNMR Measurements

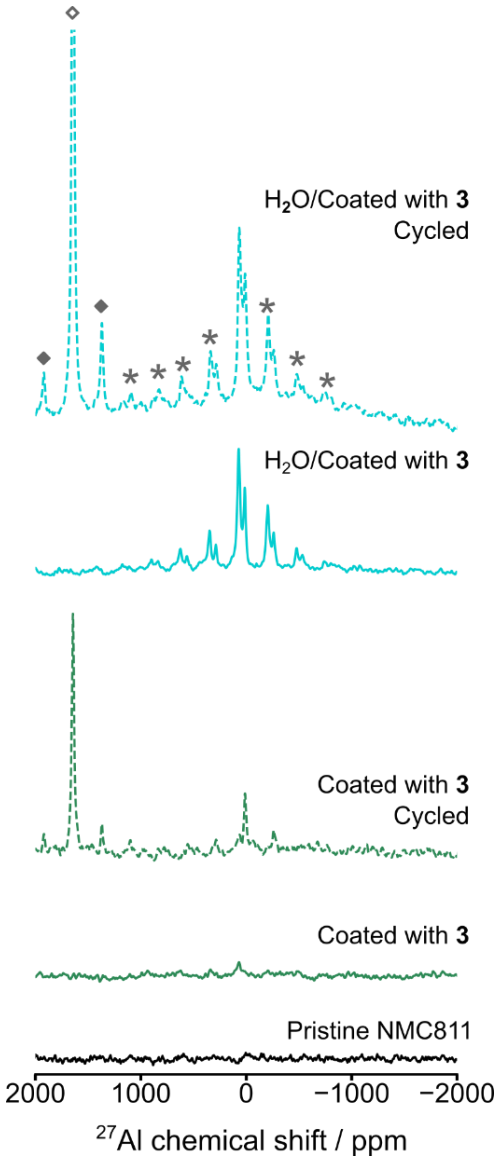

Figure C22. ^{27}Al SSNMR of pristine PC-NMC811, PC-NMC811 coated with **3**, PC-NMC811 coated with **3** after 300 cycles, PC-NMC811 soaked in water and coated with **3**, PC-NMC811 soaked in water and coated with **3** after 300 cycles.

C6.4. Fittings of the SSNMR Spectra of the Precursors

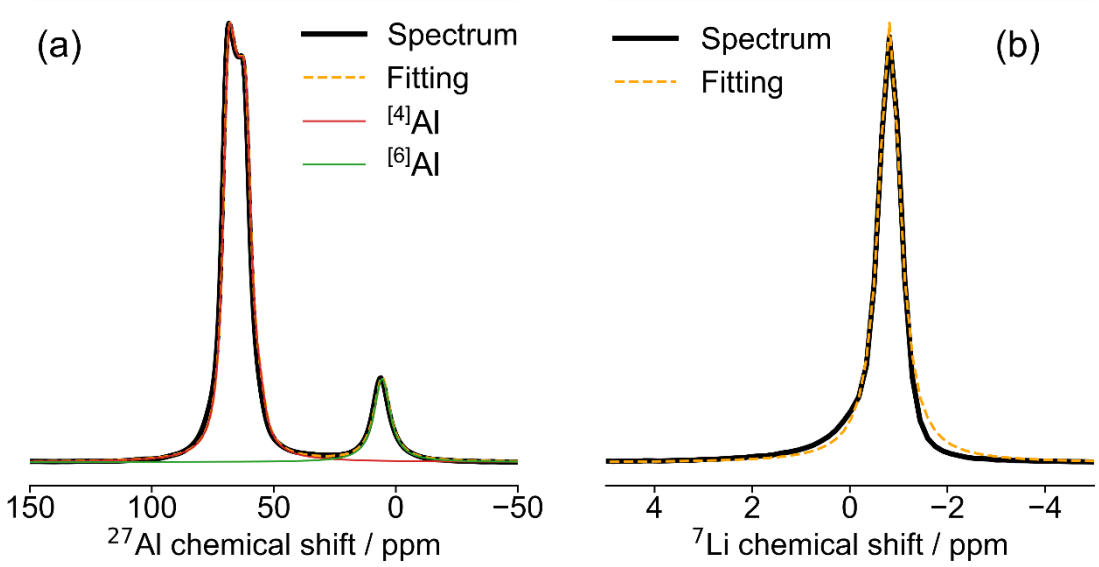

Figure C23. SSNMR spectra and fittings obtained for compound **1**. (a) ^{27}Al SSNMR spectrum and fitting. (b) ^{7}Li SSNMR spectrum and fitting.

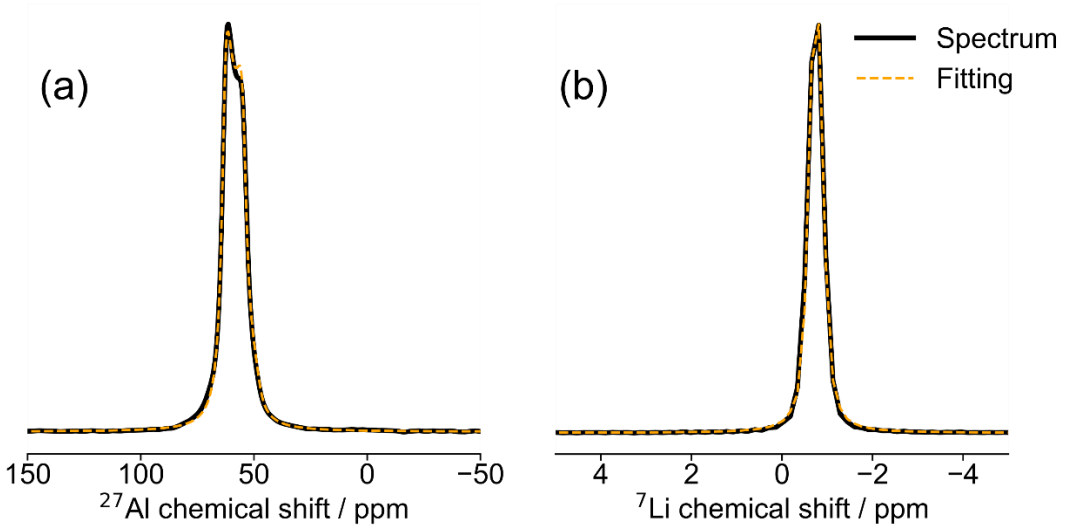

Figure C24. SSNMR spectra and fittings obtained for compound **2**. ^{27}Al SSNMR spectrum and fitting. (b) ^{7}Li SSNMR spectrum and fitting.

Table C7. SSNMR fitting parameters (Chapter 4)

Nucleus	Compound	Site	δ_{iso}	C_Q / kHz	ν_Q / kHz	η_Q
^{27}Al	1	1	72.9	4559	684	0.111
		2	6.12	55	8	0.058
	2	1	65.9	4471	671	-0.108
	3	1	79.0	5961	894	-0.912
		2	61.2	55	8	0.152
^{7}Li	1	1	-0.803	78	39	0
	2	1	-0.499	533	266	0.02
	3	1	1.53	75	38	0.06
		2	0.926	73	37	0.019
		3	0.232	0	0	0
		4	-0.221	140	70	0.09
		5	-0.807	71	35	0.07

Appendix D: Electrochemistry

D1. Determination of Ohmic Resistance, R_Ω, for IR Correction in Chapter 2

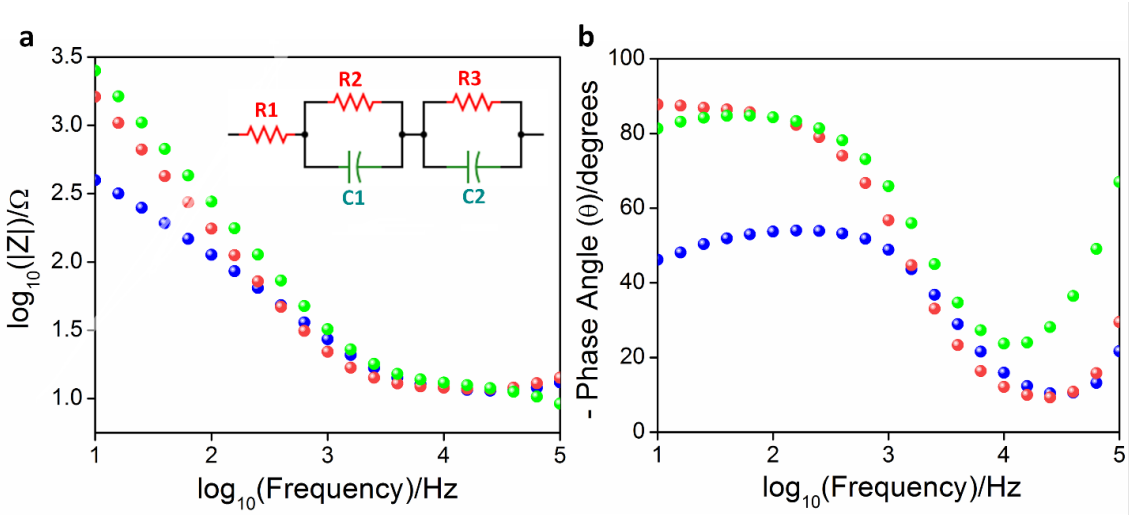

Figure D1. Electrochemical impedance spectroscopy data for CoZr (blue), FeZr (red) and CuZr (green) systems. (a) Bode plots showing the variation of log |Z| vs. log (frequency) with the (inset) equivalent circuit (R indicates resistance, C indicates capacitance). (b) Variation of the phase angle with log (frequency) for the respective systems. Measurements were performed in degassed 1 M $KOH_{(aq)}$ solutions at room temperature.

To account for solution resistance and other Ohmic contributions to the applied potential the following correction was applied:

$$E_{IR-corrected} = E_{applied} - IR_\Omega \quad (1)$$

R_Ω was set to be the same as the R1 values from the fitting of the electrochemical impedance spectra represented in Figure D1. The following series of resistance and capacitors connected in parallel (R2/C1) and (R3/C2) represent the electrode-catalyst and the catalyst-solution interfaces. The value of R1 was of the order of 10 Ω for all samples.

D2. Long-term Galvanostatic Cycling of Al_2O_3-coated NMC811 in Chapter 3

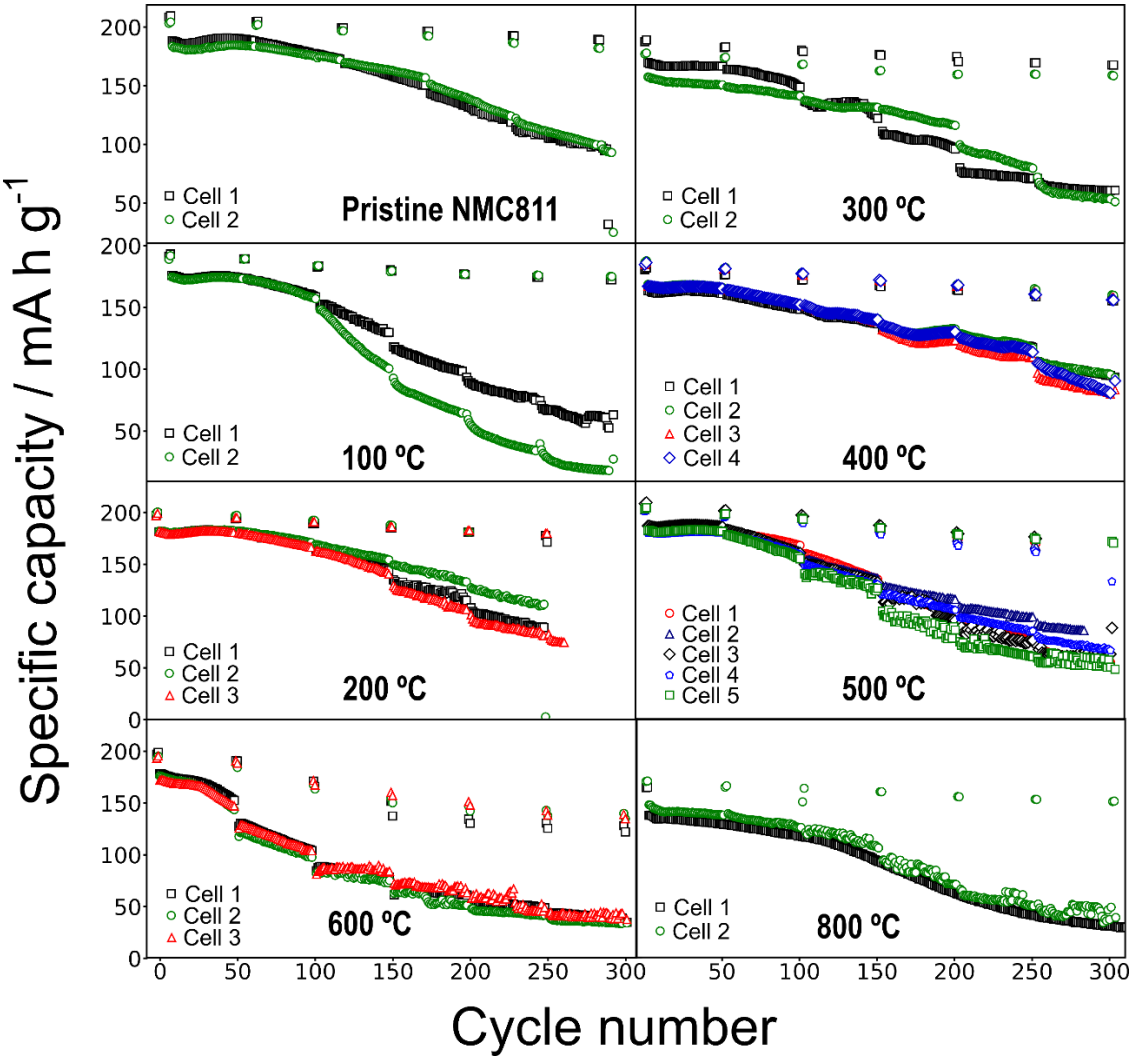

Figure D2. Full set of long-term cycling data of NMC811/Li coin cells, using pristine or Al_2O_3 coated NMC811 electrodes. The coated samples were annealed under air at the temperatures given in the Figure. Data of multiple cells is plotted for each sample. Cells were prepared with 1.0 M $LiPF_6$ in a 3:7 mixture of ethylene carbonate and ethylmethyl carbonate. Cells were cycled at room temperature (~25 °C) and at a nominal rate of C/2, with two slow diagnostic C/20 cycles every 50 cycles.

D3. Long-term Cycling of the NMC811 Materials Discussed in Chapter 4

D3.1. Polycrystalline NMC811 Materials

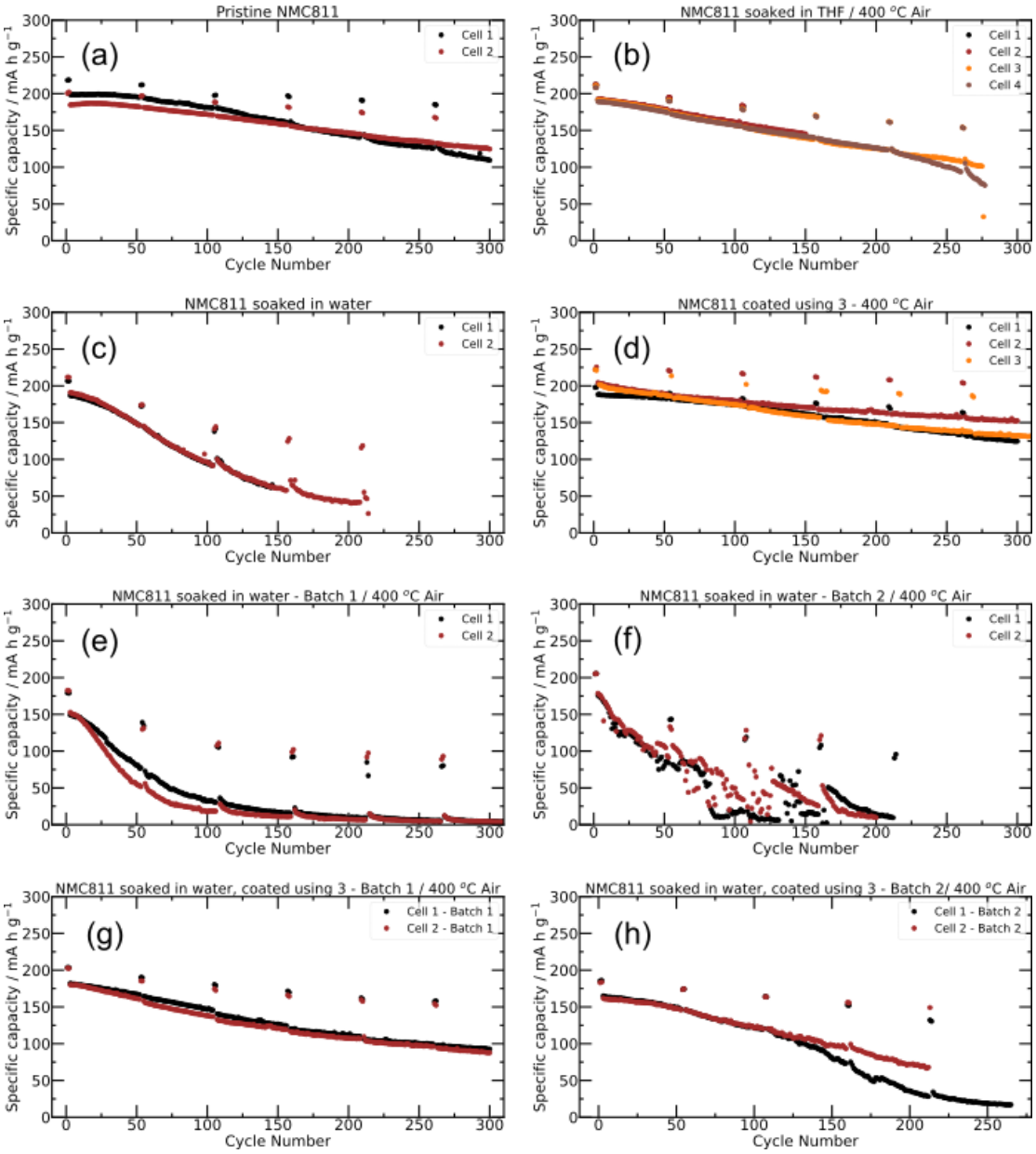

Figure D3. Full long-term cycling dataset for polycrystalline NMC811 materials. (a) Pristine NMC811. (b) NMC811 soaked in THF and annealed at 400 ºC under air. (c) NMC811 soaked in water. (d) NMC811 coated using precursor **3** and annealed under air at 400 ºC. (e) First batch of NMC811 soaked in water and annealed under air at 400 ºC. (f) Second batch of NMC811 soaked in water and annealed under air at 400 ºC. (g) First batch of NMC811 soaked in water and then coated with precursor **3** and annealed under air at 400ºC. (h) Second batch of NMC811 soaked in water and then coated with precursor **3** and annealed under air at 400ºC.

D3.2. Single-crystal NMC811 Materials

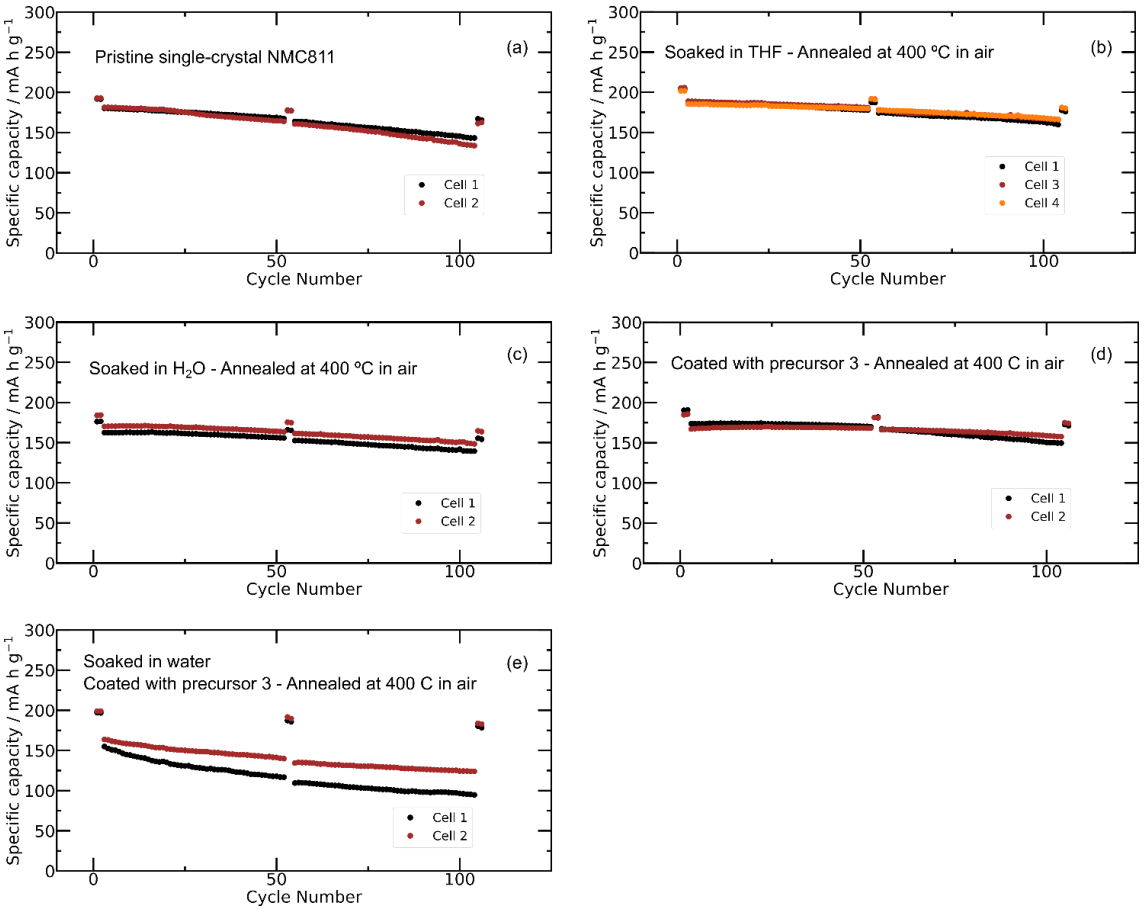

Figure D4. Full long-term cycling dataset for single-crystal NMC811 materials. (a) Pristine NMC811. (b) NMC811 soaked in THF and annealed at 400 ºC under air. (c) NMC811 soaked in water. (d) NMC811 coated using precursor **3** and annealed under air at 400 ºC. (e) NMC811 soaked in water and annealed under air at 400 ºC.

References

(1) Chu, S.; Majumdar, A. Opportunities and Challenges for a Sustainable Energy Future. *Nature* **2012**, *488* (7411), 294–303. https://doi.org/10.1038/nature11475.

(2) Goodenough, J. B. Electrochemical Energy Storage in a Sustainable Modern Society. *Energy Environ. Sci.* **2014**, *7* (1), 14–18. https://doi.org/10.1039/C3EE42613K.

(3) Yang, Z.; Zhang, J.; Kintner-Meyer, M. C. W.; Lu, X.; Choi, D.; Lemmon, J. P.; Liu, J. Electrochemical Energy Storage for Green Grid. *Chem. Rev.* **2011**, *111* (5), 3577–3613. https://doi.org/10.1021/cr100290v.

(4) Seh, Z. W.; Kibsgaard, J.; Dickens, C. F.; Chorkendorff, I.; Nørskov, J. K.; Jaramillo, T. F. Combining Theory and Experiment in Electrocatalysis: Insights into Materials Design. *Science* **2017**, *355* (6321), eaad4998. https://doi.org/10.1126/science.aad4998.

(5) Jiao, K.; Xuan, J.; Du, Q.; Bao, Z.; Xie, B.; Wang, B.; Zhao, Y.; Fan, L.; Wang, H.; Hou, Z.; Huo, S.; Brandon, N. P.; Yin, Y.; Guiver, M. D. Designing the next Generation of Proton-Exchange Membrane Fuel Cells. *Nature* **2021**, *595* (7867), 361–369. https://doi.org/10.1038/s41586-021-03482-7.

(6) Goodenough, J. B.; Manthiram, A. A Perspective on Electrical Energy Storage. *MRS Communications* **2014**, *4* (4), 135–142. https://doi.org/10.1557/mrc.2014.36.

(7) Armand, M.; Tarascon, J.-M. Building Better Batteries. *Nature* **2008**, *451* (7179), 652–657. https://doi.org/10.1038/451652a.

(8) Lewis, N. S.; Nocera, D. G. Powering the Planet: Chemical Challenges in Solar Energy Utilization. *Proc. Natl. Acad. Sci. U.S.A.* **2006**, *103* (43), 15729–15735. https://doi.org/10.1073/pnas.0603395103.

(9) Olah, G. A. Beyond Oil and Gas: The Methanol Economy. *Angew. Chem. Int. Ed.* **2005**, *44* (18), 2636–2639. https://doi.org/10.1002/anie.200462121.

(10) MacFarlane, D. R.; Cherepanov, P. V.; Choi, J.; Suryanto, B. H. R.; Hodgetts, R. Y.; Bakker, J. M.; Ferrero Vallana, F. M.; Simonov, A. N. A Roadmap to the Ammonia Economy. *Joule* **2020**, *4* (6), 1186–1205. https://doi.org/10.1016/j.joule.2020.04.004.

(11) Tilley, S. D. Recent Advances and Emerging Trends in Photo-Electrochemical Solar Energy Conversion. *Adv. Energy Mater.* **2019**, *9* (2), 1802877. https://doi.org/10.1002/aenm.201802877.

(12) Goodenough, J. B.; Kim, Y. Challenges for Rechargeable Li Batteries. *Chem. Mater.* **2010**, *22* (3), 587–603. https://doi.org/10.1021/cm901452z.

(13) Goodenough, J. B.; Park, K.-S. The Li-Ion Rechargeable Battery: A Perspective. *J. Am. Chem. Soc.* **2013**, *135* (4), 1167–1176. https://doi.org/10.1021/ja3091438.

(14) Peled, E.; Menkin, S. Review—SEI: Past, Present and Future. *J. Electrochem. Soc.* **2017**, *164* (7), A1703–A1719. https://doi.org/10.1149/2.1441707jes.

(15) Edström, K.; Gustafsson, T.; Thomas, J. O. The Cathode–Electrolyte Interface in the Li-Ion Battery. *Electrochimica Acta* **2004**, *50* (2–3), 397–403. https://doi.org/10.1016/j.electacta.2004.03.049.

(16) Björklund, E.; Xu, C.; Dose, W. M.; Sole, C. G.; Thakur, P. K.; Lee, T.-L.; De Volder, M. F. L.; Grey, C. P.; Weatherup, R. S. Cycle-Induced Interfacial Degradation and Transition-Metal Cross-Over in $LiNi_{0.8}Mn_{0.1}Co_{0.1}O_2$-Graphite Cells. *Chem. Mater.* **2022**, *34* (5), 2034–2048. https://doi.org/10.1021/acs.chemmater.1c02722.

(17) He, J.; Manthiram, A. A Review on the Status and Challenges of Electrocatalysts in Lithium-Sulfur Batteries. *Energy Storage Materials* **2019**, *20*, 55–70. https://doi.org/10.1016/j.ensm.2019.04.038.

(18) Maiyalagan, T.; Jarvis, K. A.; Therese, S.; Ferreira, P. J.; Manthiram, A. Spinel-Type Lithium Cobalt Oxide as a Bifunctional Electrocatalyst for the Oxygen Evolution and Oxygen Reduction Reactions. *Nat Commun* **2014**, *5* (1), 3949. https://doi.org/10.1038/ncomms4949.

(19) Li, T.; Yuan, X.-Z.; Zhang, L.; Song, D.; Shi, K.; Bock, C. Degradation Mechanisms and Mitigation Strategies of Nickel-Rich NMC-Based Lithium-Ion Batteries. *Electrochem. Energ. Rev.* **2020**, *3* (1), 43–80. https://doi.org/10.1007/s41918-019-00053-3.

(20) McKone, J. R.; Lewis, N. S.; Gray, H. B. Will Solar-Driven Water-Splitting Devices See the Light of Day? *Chem. Mater.* **2014**, *26* (1), 407–414. https://doi.org/10.1021/cm4021518.

(21) Lewis, N. S. Developing a Scalable Artificial Photosynthesis Technology through Nanomaterials by Design. *Nature Nanotech.* **2016**, *11* (12), 1010–1019. https://doi.org/10.1038/nnano.2016.194.

(22) Lu, H.; Andrei, V.; Jenkinson, K. J.; Regoutz, A.; Li, N.; Creissen, C. E.; Wheatley, A. E. H.; Hao, H.; Reisner, E.; Wright, D. S.; Pike, S. D. Single-Source Bismuth (Transition Metal) Polyoxovanadate Precursors for the Scalable Synthesis of

Doped $BiVO_4$ Photoanodes. *Advanced Materials* **2018**, *30* (46), 1804033. https://doi.org/10.1002/adma.201804033.

(23) Lai, Y.-H.; Park, H. S.; Zhang, J. Z.; Matthews, P. D.; Wright, D. S.; Reisner, E. A Si Photocathode Protected and Activated with a Ti and Ni Composite Film for Solar Hydrogen Production. *Chem. Eur. J.* **2015**, *21* (10), 3919–3923. https://doi.org/10.1002/chem.201406566.

(24) Cabana, J.; Kwon, B. J.; Hu, L. Mechanisms of Degradation and Strategies for the Stabilization of Cathode–Electrolyte Interfaces in Li-Ion Batteries. *Acc. Chem. Res.* **2018**, *51* (2), 299–308. https://doi.org/10.1021/acs.accounts.7b00482.

(25) Chen, Z.; Qin, Y.; Amine, K.; Sun, Y.-K. Role of Surface Coating on Cathode Materials for Lithium-Ion Batteries. *J. Mater. Chem.* **2010**, *20* (36), 7606. https://doi.org/10.1039/c0jm00154f.

(26) Myung, S.-T.; Amine, K.; Sun, Y.-K. Surface Modification of Cathode Materials from Nano- to Microscale for Rechargeable Lithium-Ion Batteries. *J. Mater. Chem.* **2010**, *20* (34), 7074. https://doi.org/10.1039/c0jm00508h.

(27) Rinkel, B. L. D.; Vivek, J. P.; Garcia-Araez, N.; Grey, C. P. Two Electrolyte Decomposition Pathways at Nickel-Rich Cathode Surfaces in Lithium-Ion Batteries. *Energy Environ. Sci.* **2022**, *15* (8), 3416–3438. https://doi.org/10.1039/D1EE04053G.

(28) Zheng, J. M.; Zhang, Z. R.; Wu, X. B.; Dong, Z. X.; Zhu, Z.; Yang, Y. The Effects of AlF_3 Coating on the Performance of $Li[Li_{0.2}Mn_{0.54}Ni_{0.13}Co_{0.13}]O_2$ Positive Electrode Material for Lithium-Ion Battery. *Journal of The Electrochemical Society*, **155** (10) A775-A782 (2008). https:// doi.org/ 10.1149/1.2966694.

(29) Ryu, H.-H.; Park, K.-J.; Yoon, C. S.; Sun, Y.-K. Capacity Fading of Ni-Rich $Li[Ni_xCo_yMn_{1-x-y}]O_2$ ($0.6 \le x \le 0.95$) Cathodes for High-Energy-Density Lithium-Ion Batteries: Bulk or Surface Degradation? *Chemistry of Materials* **2018**, *30* (3), 1155–1163. https://doi.org/10.1021/acs.chemmater.7b05269.

(30) Xin, F.; Zhou, H.; Chen, X.; Zuba, M.; Chernova, N.; Zhou, G.; Whittingham, M. S. Li–Nb–O Coating/Substitution Enhances the Electrochemical Performance of the $LiNi_{0.8}Mn_{0.1}Co_{0.1}O_2$ (NMC811) Cathode. *ACS Appl. Mater. Interfaces* **2019**, *11* (38), 34889–34894. https://doi.org/10.1021/acsami.9b09696.

(31) Xin, F.; Zhou, H.; Zong, Y.; Zuba, M.; Chen, Y.; Chernova, N. A.; Bai, J.; Pei, B.; Goel, A.; Rana, J.; Wang, F.; An, K.; Piper, L. F. J.; Zhou, G.; Whittingham, M. S. What Is the Role of Nb in Nickel-Rich Layered Oxide Cathodes for Lithium-Ion

Batteries? *ACS Energy Lett.* **2021**, 1377–1382. https://doi.org/10.1021/acsenergylett.1c00190.

(32) Hu, S.; Lewis, N. S.; Ager, J. W.; Yang, J.; McKone, J. R.; Strandwitz, N. C. Thin-Film Materials for the Protection of Semiconducting Photoelectrodes in Solar-Fuel Generators. *J. Phys. Chem. C* **2015**, *119* (43), 24201–24228. https://doi.org/10.1021/acs.jpcc.5b05976.

(33) Zhong, M.; Hisatomi, T.; Kuang, Y.; Zhao, J.; Liu, M.; Iwase, A.; Jia, Q.; Nishiyama, H.; Minegishi, T.; Nakabayashi, M.; Shibata, N.; Niishiro, R.; Katayama, C.; Shibano, H.; Katayama, M.; Kudo, A.; Yamada, T.; Domen, K. Surface Modification of CoO_x Loaded $BiVO_4$ Photoanodes with Ultrathin *p*-Type NiO Layers for Improved Solar Water Oxidation. *J. Am. Chem. Soc.* **2015**, *137* (15), 5053–5060. https://doi.org/10.1021/jacs.5b00256.

(34) McDowell, M. T.; Lichterman, M. F.; Spurgeon, J. M.; Hu, S.; Sharp, I. D.; Brunschwig, B. S.; Lewis, N. S. Improved Stability of Polycrystalline Bismuth Vanadate Photoanodes by Use of Dual-Layer Thin TiO_2 / Ni Coatings. *J. Phys. Chem. C* **2014**, *118* (34), 19618–19624. https://doi.org/10.1021/jp506133y.

(35) Zhong, D. K.; Choi, S.; Gamelin, D. R. Near-Complete Suppression of Surface Recombination in Solar Photoelectrolysis by "Co-Pi" Catalyst-Modified W:$BiVO_4$. *J. Am. Chem. Soc.* **2011**, *133* (45), 18370–18377. https://doi.org/10.1021/ja207348x.

(36) Lewis, N. S. Chemical Control of Charge Transfer and Recombination at Semiconductor Photoelectrode Surfaces. *Inorg. Chem.* **2005**, *44* (20), 6900–6911. https://doi.org/10.1021/ic051118p.

(37) Lu, H.; Wright, D. S.; Pike, S. D. The Use of Mixed-Metal Single Source Precursors for the Synthesis of Complex Metal Oxides. *Chem. Commun.* **2020**, *56* (6), 854–871. https://doi.org/10.1039/C9CC06258K.

(38) Li, N.; Pranantyo, D.; Kang, E.-T.; Wright, D. S.; Luo, H.-K. In Situ Self-Assembled Polyoxotitanate Cages on Flexible Cellulosic Substrates: Multifunctional Coating for Hydrophobic, Antibacterial, and UV-Blocking Applications. *Adv. Funct. Mater.* **2018**, *28* (23), 1800345. https://doi.org/10.1002/adfm.201800345.

(39) Li, N.; Pranantyo, D.; Kang, E.-T.; Wright, D. S.; Luo, H.-K. A Simple Drop-and-Dry Approach to Grass-Like Multifunctional Nanocoating on Flexible Cotton Fabrics Using In Situ-Generated Coating Solution Comprising Titanium-Oxo

Clusters and Silver Nanoparticles. *ACS Appl. Mater. Interfaces* **2020**, *12* (10), 12093–12100. https://doi.org/10.1021/acsami.9b22768.

(40) Li, N.; Matthews, P. D.; Leung, J. J.; King, T. C.; Wood, P. T.; Luo, H.-K.; Wright, D. S. Synthesis, Structure and Properties of the Manganese-Doped Polyoxotitanate Cage [$Ti_{18}MnO_{30}(OEt)_{20}(MnPhen)_3$] (Phen = 1,10-Phenanthroline). *Dalton Trans.* **2015**, *44* (44), 19090–19096. https://doi.org/10.1039/C5DT03617H.

(41) Veith, M. Molecular Precursors for (Nano) Materials — a One Step Strategy. *Journal of the Chemical Society, Dalton Transactions* **2002**, No. 12, 2405–2412. https://doi.org/10.1039/b201383p.

(42) Marchand, P.; Carmalt, C. J. Molecular Precursor Approach to Metal Oxide and Pnictide Thin Films. *Coordination Chemistry Reviews* **2013**, *257* (23–24), 3202–3221. https://doi.org/10.1016/j.ccr.2013.01.030.

(43) Mishra, S.; Daniele, S. Molecular Engineering of Metal Alkoxides for Solution Phase Synthesis of High-Tech Metal Oxide Nanomaterials. *Chem. Eur. J.* **2020**, *26* (42), 9292–9303. https://doi.org/10.1002/chem.202000534.

(44) Panda, C.; Menezes, P. W.; Driess, M. Nano-Sized Inorganic Energy-Materials by the Low-Temperature Molecular Precursor Approach. *Angew. Chem. Int. Ed.* **2018**, *57* (35), 11130–11139. https://doi.org/10.1002/anie.201803673.

(45) Menezes, P. W.; Indra, A.; González-Flores, D.; Sahraie, N. R.; Zaharieva, I.; Schwarze, M.; Strasser, P.; Dau, H.; Driess, M. High-Performance Oxygen Redox Catalysis with Multifunctional Cobalt Oxide Nanochains: Morphology-Dependent Activity. *ACS Catal.* **2015**, *5* (4), 2017–2027. https://doi.org/10.1021/cs501724v.

(46) Yao, S.; Forstner, V.; Menezes, P. W.; Panda, C.; Mebs, S.; Zolnhofer, E. M.; Miehlich, M. E.; Szilvási, T.; Ashok Kumar, N.; Haumann, M.; Meyer, K.; Grützmacher, H.; Driess, M. From an Fe_2P_3 Complex to FeP Nanoparticles as Efficient Electrocatalysts for Water-Splitting. *Chem. Sci.* **2018**, *9* (45), 8590–8597. https://doi.org/10.1039/C8SC03407A.

(47) Menezes, P. W.; Indra, A.; Littlewood, P.; Schwarze, M.; Göbel, C.; Schomäcker, R.; Driess, M. Nanostructured Manganese Oxides as Highly Active Water Oxidation Catalysts: A Boost from Manganese Precursor Chemistry. *ChemSusChem* **2014**, *7* (8), 2202–2211. https://doi.org/10.1002/cssc.201402169.

(48) Ranade, M. R.; Navrotsky, A.; Zhang, H. Z.; Banfield, J. F.; Elder, S. H.; Zaban, A.; Borse, P. H.; Kulkarni, S. K.; Doran, G. S.; Whitfield, H. J. Energetics of

Nanocrystalline TiO_2. *Proc. Natl. Acad. Sci. U.S.A.* **2002**, *99*, 6476–6481. https://doi.org/10.1073/pnas.251534898.

(49) Levchenko, A. A.; Li, G.; Boerio-Goates, J.; Woodfield, B. F.; Navrotsky, A. TiO_2 Stability Landscape: Polymorphism, Surface Energy, and Bound Water Energetics. *Chem. Mater.* **2006**, *18* (26), 6324–6332. https://doi.org/10.1021/cm061183c.

(50) Yang, J.; Akbarzadeh, J.; Maurer, C.; Peterlik, H.; Schubert, U. Sol-Gel Synthesis of $ZnTiO_3$ Using a Single-Source Precursor Based on *p*-Carboxybenzaldehyde Oxime as a Linker. *J. Mater. Chem.* **2012**, *22* (45), 24034. https://doi.org/10.1039/c2jm35355e.

(51) Regue, M.; Armstrong, K.; Walsh, D.; Richards, E.; Johnson, A. L.; Eslava, S. Mo-Doped TiO_2 Photoanodes Using $[Ti_4Mo_2O_8(OEt)_{10}]_2$ Bimetallic Oxo Cages as a Single Source Precursor. *Sustainable Energy Fuels* **2018**, *2* (12), 2674–2686. https://doi.org/10.1039/C8SE00372F.

(52) Walter, C.; Kalra, S.; Beltrán-Suito, R.; Schwarze, M.; Menezes, P. W.; Driess, M. Manganese Sulfide Enables the Formation of a Highly Active β-MnOOH Electrocatalyst for Effective Alkaline Water Oxidation. *Materials Today Chemistry* **2022**, *24*, 100905. https://doi.org/10.1016/j.mtchem.2022.100905.

(53) Polarz, S.; Strunk, J.; Ischenko, V.; van den Berg, M. W. E.; Hinrichsen, O.; Muhler, M.; Driess, M. On the Role of Oxygen Defects in the Catalytic Performance of Zinc Oxide. *Angew. Chem. Int. Ed.* **2006**, *45* (18), 2965–2969. https://doi.org/10.1002/anie.200503068.

(54) Shevchenko, D.; Anderlund, M. F.; Styring, S.; Dau, H.; Zaharieva, I.; Thapper, A. Water Oxidation by Manganese Oxides Formed from Tetranuclear Precursor Complexes: The Influence of Phosphate on Structure and Activity. *Phys. Chem. Chem. Phys.* **2014**, *16* (24), 11965. https://doi.org/10.1039/c3cp55125c.

(55) Beltrán-Suito, R.; Menezes, P. W.; Driess, M. Amorphous Outperforms Crystalline Nanomaterials: Surface Modifications of Molecularly Derived CoP Electro(Pre)Catalysts for Efficient Water-Splitting. *J. Mater. Chem. A* **2019**, *7* (26), 15749–15756. https://doi.org/10.1039/C9TA04583J.

(56) Beltrán-Suito, R.; Forstner, V.; Hausmann, J. N.; Mebs, S.; Schmidt, J.; Zaharieva, I.; Laun, K.; Zebger, I.; Dau, H.; Menezes, P. W.; Driess, M. A Soft Molecular 2Fe–2As Precursor Approach to the Synthesis of Nanostructured FeAs for Efficient Electrocatalytic Water Oxidation. *Chem. Sci.* **2020**, *11* (43), 11834–11842. https://doi.org/10.1039/D0SC04384B.

(57) Panda, C.; Menezes, P. W.; Walter, C.; Yao, S.; Miehlich, M. E.; Gutkin, V.; Meyer, K.; Driess, M. From a Molecular 2Fe-2Se Precursor to a Highly Efficient Iron Diselenide Electrocatalyst for Overall Water Splitting. *Angew. Chem. Int. Ed.* **2017**, *56* (35), 10506–10510. https://doi.org/10.1002/anie.201706196.

(58) Eslava, S.; Reynal, A.; Rocha, V. G.; Barg, S.; Saiz, E. Using Graphene Oxide as a Sacrificial Support of Polyoxotitanium Clusters to Replicate Its Two-Dimensionality on Pure Titania Photocatalysts. *J. Mater. Chem. A* **2016**, *4* (19), 7200–7206. https://doi.org/10.1039/C5TA09989G.

(59) Tong, L.; Wu, W.; Kuepper, K.; Scheurer, A.; Meyer, K. Electrochemically Deposited Nickel Oxide from Molecular Complexes for Efficient Water Oxidation Catalysis. *ChemSusChem* **2018**, *11* (16), 2752–2757. https://doi.org/10.1002/cssc.201800971.

(60) Baktash, E.; Littlewood, P.; Pfrommer, J.; Schomäcker, R.; Driess, M.; Thomas, A. Controlled Formation of Nickel Oxide Nanoparticles on Mesoporous Silica Using Molecular Ni_4O_4 Clusters as Precursors: Enhanced Catalytic Performance for Dry Reforming of Methane. *ChemCatChem* **2015**, *7* (8), 1280–1284. https://doi.org/10.1002/cctc.201402983.

(61) Suseno, S.; McCrory, C. C. L.; Tran, R.; Gul, S.; Yano, J.; Agapie, T. Molecular Mixed-Metal Manganese Oxido Cubanes as Precursors to Heterogeneous Oxygen Evolution Catalysts. *Chem. Eur. J.* **2015**, *21* (38), 13420–13430. https://doi.org/10.1002/chem.201501104.

(62) Nocera, D. G. The Artificial Leaf. *Acc. Chem. Res.* **2012**, *45* (5), 767–776. https://doi.org/10.1021/ar2003013.

(63) Andrei, V.; Wang, Q.; Uekert, T.; Bhattacharjee, S.; Reisner, E. Solar Panel Technologies for Light-to-Chemical Conversion. *Acc. Chem. Res.* **2022**, *55* (23), 3376–3386. https://doi.org/10.1021/acs.accounts.2c00477.

(64) Matthews, P. D.; King, T. C.; Wright, D. S. Structure, Photochemistry and Applications of Metal-Doped Polyoxotitanium Alkoxide Cages. *Chem. Commun.* **2014**, *50* (85), 12815–12823. https://doi.org/10.1039/C4CC04421E.

(65) Lv, Y.; Yao, M.; Holgado, J. P.; Roth, T.; Steiner, A.; Gan, L.; Lambert, R. M.; Wright, D. S. A Low-Temperature Single-Source Route to an Efficient Broad-Band Cerium(III) Photocatalyst Using a Bimetallic Polyoxotitanium Cage. *RSC Adv.* **2013**, *3* (33), 13659. https://doi.org/10.1039/c3ra41524d.

(66) Lai, Y.-H.; Lin, C.-Y.; Lv, Y.; King, T. C.; Steiner, A.; Muresan, N. M.; Gan, L.; Wright, D. S.; Reisner, E. Facile Assembly of an Efficient CoO_x Water Oxidation Electrocatalyst from Co-Containing Polyoxotitanate Nanocages. *Chem. Commun.* **2013**, *49* (39), 4331–4333. https://doi.org/10.1039/C2CC34934E.

(67) Lutterman, D. A.; Surendranath, Y.; Nocera, D. G. A Self-Healing Oxygen-Evolving Catalyst. *J. Am. Chem. Soc.* **2009**, *131* (11), 3838–3839. https://doi.org/10.1021/ja900023k.

(68) Park, Y.; McDonald, K. J.; Choi, K.-S. Progress in Bismuth Vanadate Photoanodes for Use in Solar Water Oxidation. *Chem. Soc. Rev.* **2013**, *42* (6), 2321–2337. https://doi.org/10.1039/C2CS35260E.

(69) Zachäus, C.; Abdi, F. F.; Peter, L. M.; van de Krol, R. Photocurrent of $BiVO_4$ Is Limited by Surface Recombination, Not Surface Catalysis. *Chem. Sci.* **2017**, *8* (5), 3712–3719. https://doi.org/10.1039/C7SC00363C.

(70) Crespo-Quesada, M.; Reisner, E. Emerging Approaches to Stabilise Photocorrodible Electrodes and Catalysts for Solar Fuel Applications. *Energy Environ. Sci.* **2017**, *10* (5), 1116–1127. https://doi.org/10.1039/C7EE00777A.

(71) Lai, Y.-H.; King, T. C.; Wright, D. S.; Reisner, E. Scalable One-Step Assembly of an Inexpensive Photoelectrode for Water Oxidation by Deposition of a Ti- and Ni-Containing Molecular Precursor on Nanostructured WO_3. *Chem. Eur. J.* **2013**, *19* (39), 12943–12947. https://doi.org/10.1002/chem.201302641.

(72) Uchiyama, H.; Puthusseri, D.; Grins, J.; Gribble, D.; Seisenbaeva, G. A.; Pol, V. G.; Kessler, V. G. Single-Source Alkoxide Precursor Approach to Titanium Molybdate, $TiMoO_5$, and Its Structure, Electrochemical Properties, and Potential as an Anode Material for Alkali Metal Ion Batteries. *Inorg. Chem.* **2021**, *60* (6), 3593–3603. https://doi.org/10.1021/acs.inorgchem.0c03087.

(73) Fröschl, T.; Hörmann, U.; Kubiak, P.; Kučerová, G.; Pfanzelt, M.; Weiss, C. K.; Behm, R. J.; Hüsing, N.; Kaiser, U.; Landfester, K.; Wohlfahrt-Mehrens, M. High Surface Area Crystalline Titanium Dioxide: Potential and Limits in Electrochemical Energy Storage and Catalysis. *Chem. Soc. Rev.* **2012**, *41* (15), 5313. https://doi.org/10.1039/c2cs35013k.

(74) Tyagi, A.; Karmakar, G.; Mandal, B. P.; Dutta Pathak, D.; Wadawale, A.; Kedarnath, G.; Srivastava, A. P.; Jain, V. K. Di- *Tert*-Butyltin(IV) 2-Pyridyl and 4,6-Dimethyl-2-Pyrimidyl Thiolates: Versatile Single Source Precursors for the Preparation of SnS Nanoplatelets as Anode Material for Lithium Ion Batteries.

Dalton Trans. **2021**, *50* (37), 13073–13085. https://doi.org/10.1039/D1DT01142A.

(75) Boyle, T. J.; Rodriguez, M. A.; Ingersoll, D.; Headley, T. J.; Bunge, S. D.; Pedrotty, D. M.; De'Angeli, S. M.; Vick, S. C.; Fan, H. A Novel Family of Structurally Characterized Lithium Cobalt Double Aryloxides and the Nanoparticles and Thin Films Generated Therefrom. *Chem. Mater.* **2003**, *15* (20), 3903–3912. https://doi.org/10.1021/cm020902u.

(76) Wei, Z.; Han, H.; Filatov, A. S.; Dikarev, E. V. Changing the Bridging Connectivity Pattern within a Heterometallic Assembly: Design of Single-Source Precursors with Discrete Molecular Structures. *Chem. Sci.* **2014**, *5* (2), 813–818. https://doi.org/10.1039/C3SC52657G.

(77) Han, H.; Zhou, Z.; Carozza, J. C.; Lengyel, J.; Yao, Y.; Wei, Z.; Dikarev, E. V. From Lithium to Sodium: Design of Heterometallic Molecular Precursors for the $NaMO_2$ Cathode Materials. *Chem. Commun.* **2019**, *55* (50), 7243–7246. https://doi.org/10.1039/C9CC02836F.

(78) Han, H.; Carozza, J. C.; Zhou, Z.; Zhang, Y.; Wei, Z.; Abakumov, A. M.; Filatov, A. S.; Chen, Y.-S.; SantaLucia, D. J.; Berry, J. F.; Dikarev, E. V. Hetero *Tri* Metallic Precursor with 2:2:1 Metal Ratio Requiring at Least a Pentanuclear Molecular Assembly. *J. Am. Chem. Soc.* **2020**, *142* (29), 12767–12776. https://doi.org/10.1021/jacs.0c05139.

(79) Han, H.; Wei, Z.; Barry, M. C.; Carozza, J. C.; Alkan, M.; Rogachev, A. Y.; Filatov, A. S.; Abakumov, A. M.; Dikarev, E. V. A Three Body Problem: A Genuine Hetero *Tri* Metallic Molecule *vs.* a Mixture of Two Parent Hetero *Bi* Metallic Molecules. *Chem. Sci.* **2018**, *9* (21), 4736–4745. https://doi.org/10.1039/C8SC00917A.

(80) Tey, S. L.; Reddy, M. V.; Subba Rao, G. V.; Chowdari, B. V. R.; Yi, J.; Ding, J.; Vittal, J. J. Synthesis, Structure, and Magnetic Properties of $[Li(H_2O)M(N_2H_3CO_2)_3]\cdot 0.5H_2O$ (M = Co,Ni) as Single Precursors to $LiMO_2$ Battery Materials. *Chem. Mater.* **2006**, *18* (6), 1587–1594. https://doi.org/10.1021/cm0523891.

(81) Xu, K. Electrolytes and Interphases in Li-Ion Batteries and Beyond. *Chemical Reviews* **2014**, *114* (23), 11503–11618. https://doi.org/10.1021/cr500003w.

(82) Myung, S.-T.; Izumi, K.; Komaba, S.; Sun, Y.-K.; Yashiro, H.; Kumagai, N. Role of Alumina Coating on Li−Ni−Co−Mn−O Particles as Positive Electrode Material

for Lithium-Ion Batteries. *Chem. Mater.* **2005**, *17* (14), 3695–3704. https://doi.org/10.1021/cm050566s.

(83) Jurng, S.; Heiskanen, S. K.; Chandrasiri, K. W. D. K.; Abeywardana, M. Y.; Lucht, B. L. Minimized Metal Dissolution from High-Energy Nickel Cobalt Manganese Oxide Cathodes with Al_2O_3 Coating and Its Effects on Electrolyte Decomposition on Graphite Anodes. *J. Electrochem. Soc.* **2019**, *166* (13), A2721–A2726. https://doi.org/10.1149/2.0101913jes.

(84) Li, C.; Zhang, H. P.; Fu, L. J.; Liu, H.; Wu, Y. P.; Rahm, E.; Holze, R.; Wu, H. Q. Cathode Materials Modified by Surface Coating for Lithium Ion Batteries. *Electrochimica Acta* **2006**, *51* (19), 3872–3883. https://doi.org/10.1016/j.electacta.2005.11.015.

(85) Cabana, J.; Kwon, B. J.; Hu, L. Mechanisms of Degradation and Strategies for the Stabilization of Cathode–Electrolyte Interfaces in Li-Ion Batteries. *Accounts of Chemical Research* **2018**, *51* (2), 299–308. https://doi.org/10.1021/acs.accounts.7b00482.

(86) Liu, Y.; Lin, X.; Sun, Y.; Xu, Y.; Chang, B.; Liu, C.; Cao, A.; Wan, L. Precise Surface Engineering of Cathode Materials for Improved Stability of Lithium-Ion Batteries. *Small* **2019**, 1901019. https://doi.org/10.1002/smll.201901019.

(87) Zuo, D. Recent Progress in Surface Coating of Cathode Materials for Lithium Ion Secondary Batteries. *Journal of Alloys and Compounds* **2017**, 706, 24–40. http://doi.org/10.1016/j.jallcom.2017.02.230.

(88) Kalluri, S.; Yoon, M.; Jo, M.; Park, S.; Myeong, S.; Kim, J.; Dou, S. X.; Guo, Z.; Cho, J. Surface Engineering Strategies of Layered $LiCoO_2$ Cathode Material to Realize High-Energy and High-Voltage Li-Ion Cells. *Adv. Energy Mater.* **2017**, *7* (1), 1601507. https://doi.org/10.1002/aenm.201601507.

(89) Hsiao, Y.-S.; Chang, L.-Y.; Hu, C.-W.; Lu, C.-Z.; Wu, N.-J.; Chen, Y.-L.; Hsieh, T.-H.; Huang, J.-H.; Hsu, S.-C.; Weng, H.-C.; Chen, C.-P. Cr^{3+}-Doped $TiNb_2O_7$ as an Advanced Anode Material for High-Performance Lithium-Ion Batteries. *Applied Surface Science* **2023**, *614*, 156155. https://doi.org/10.1016/j.apsusc.2022.156155.

(90) Kim, S.-S.; Kadoma, Y.; Ikuta, H.; Uchimoto, Y.; Wakihara, M. Electrochemical Performance of Natural Graphite by Surface Modification Using Aluminum. *Electrochem. Solid-State Lett.* **2001**, *4* (8), A109. https://doi.org/10.1149/1.1379829.

(91) Neuhold, S.; Vaughey, J. T.; Grogger, C.; López, C. M. Enhancement in Cycle Life of Metallic Lithium Electrodes Protected with Fp-Silanes. *Journal of Power Sources* **2014**, *254*, 241–248. https://doi.org/10.1016/j.jpowsour.2013.12.057.

(92) Kottegoda, I. R. M.; Kadoma, Y.; Ikuta, H.; Uchimoto, Y.; Wakihara, M. Enhancement of Rate Capability in Graphite Anode by Surface Modification with Zirconia. *Electrochem. Solid-State Lett.* **2002**, *5* (12), A275. https://doi.org/10.1149/1.1516410.

(93) Zhao, Y.; Liang, J.; Sun, Q.; Goncharova, L. V.; Wang, J.; Wang, C.; Adair, K. R.; Li, X.; Zhao, F.; Sun, Y.; Li, R.; Sun, X. *In Situ* Formation of Highly Controllable and Stable Na_3PS_4 as a Protective Layer for Na Metal Anode. *J. Mater. Chem. A* **2019**, *7* (8), 4119–4125. https://doi.org/10.1039/C8TA10174D.

(94) Neudeck, S.; Mazilkin, A.; Reitz, C.; Hartmann, P.; Janek, J.; Brezesinski, T. Effect of Low-Temperature Al_2O_3 ALD Coating on Ni-Rich Layered Oxide Composite Cathode on the Long-Term Cycling Performance of Lithium-Ion Batteries. *Sci Rep* **2019**, *9* (1), 5328. https://doi.org/10.1038/s41598-019-41767-0.

(95) Fey, G. T.-K.; Yang, H.-Z.; Prem Kumar, T.; Naik, S. P.; Chiang, A. S. T.; Lee, D.-C.; Lin, J.-R. A Simple Mechano-Thermal Coating Process for Improved Lithium Battery Cathode Materials. *Journal of Power Sources* **2004**, *132* (1–2), 172–180. https://doi.org/10.1016/j.jpowsour.2004.01.033.

(96) Han, B.; Key, B.; Lapidus, S. H.; Garcia, J. C.; Iddir, H.; Vaughey, J. T. From Coating to Dopant: How the Transition Metal Composition Affects Alumina Coatings on Ni-Rich Cathodes. *ACS Appl. Mater. Interfaces* **2017**, *9*, 41291-41302. https://doi.org/10.1021/acsami.7b13597.

(97) Cho, J.; Kim, Y. J.; Park, B. LiCoO2 Cathode Material That Does Not Show a Phase Transition from Hexagonal to Monoclinic Phase. *Journal of The Electrochemical Society* **2001**, *148* (10), A1110–A1115. https://doi.org/10.1149/1.1397772.

(98) Cho, J.; Kim, Y. J.; Park, B. Novel $LiCoO_2$ Cathode Material with Al_2O_3 Coating for a Li Ion Cell. *Chemistry of Materials* **2000**, *12* (12), 3788–3791. https://doi.org/10.1021/cm000511k.

(99) Fey, G. T.-K.; Chen, J.-G.; Kumar, T. P. Enhanced Cyclability of $LiCoO_2$ Cathodes Coated with Alumina Derived from Carboxylate-Alumoxanes. *Journal of Applied Electrochemistry* **2005**, *35* (2), 177–184. https://doi.org/10.1007/s10800-004-5822-7.

(100) Han, B.; Dunlop, A. R.; Trask, S. E.; Key, B.; Vaughey, J. T.; Dogan, F. Tailoring Alumina Based Interphases on Lithium Ion Cathodes. *J. Electrochem. Soc.* **2018**, *165* (14), A3275–A3283. https://doi.org/DOI 10.1149/2.0211814jes.

(101) Negi, R. S.; Celik, E.; Pan, R.; Stäglich, R.; Senker, J.; Elm, M. T. Insights into the Positive Effect of Post-Annealing on the Electrochemical Performance of Al_2O_3-Coated Ni-Rich NCM Cathodes for Lithium-Ion Batteries. *ACS Appl. Energy Mater.* **2021**, *4* (4), 3369–3380. https://doi.org/10.1021/acsaem.0c03135.

(102) Neudeck, S.; Strauss, F.; Garcia, G.; Wolf, H.; Janek, J.; Hartmann, P.; Brezesinski, T. Room Temperature, Liquid-Phase Al_2O_3 Surface Coating Approach for Ni-Rich Layered Oxide Cathode Material. *Chemical Communications* **2019**, *55* (15), 2174–2177. https://doi.org/10.1039/C8CC09618J.

(103) Negi, R. S.; Culver, S. P.; Mazilkin, A.; Brezesinski, T.; Elm, M. T. Enhancing the Electrochemical Performance of $LiNi_{0.70}Co_{0.15}Mn_{0.15}O_2$ Cathodes Using a Practical Solution-Based Al_2O_3 Coating. *ACS Appl. Mater. Interfaces* **2020**, *12*, 31392-31400. https://doi.org/10.1021/acsami.0c06484.

(104) Li, L.; Chen, Z.; Zhang, Q.; Xu, M.; Zhou, X.; Zhu, H.; Zhang, K. A Hydrolysis-Hydrothermal Route for the Synthesis of Ultrathin $LiAlO_2$-Inlaid $LiNi_{0.5}Co_{0.2}Mn_{0.3}O_2$ as a High-Performance Cathode Material for Lithium Ion Batteries. *Journal of Materials Chemistry A* **2015**, *3* (2), 894–904. https://doi.org/10.1039/C4TA05902F.

(105) Liu, W.; Li, X.; Xiong, D.; Hao, Y.; Li, J.; Kou, H.; Yan, B.; Li, D.; Lu, S.; Koo, A.; Adair, K.; Sun, X. Significantly Improving Cycling Performance of Cathodes in Lithium Ion Batteries: The Effect of Al_2O_3 and $LiAlO_2$ Coatings on $LiNi_{0.6}Co_{0.2}Mn_{0.2}O_2$. *Nano Energy* **2018**, *44*, 111–120. https://doi.org/10.1016/j.nanoen.2017.11.010.

(106) Martens, A.; Bolli, C.; Hoffmann, A.; Erk, C.; Ludwig, T.; El Kazzi, M.; Breddemann, U.; Novák, P.; Krossing, I. Coating of NCM851005 Cathode Material with $Al^0@Al_2O_3$ and Subsequent Treatment with Anhydrous HF. *J. Electrochem. Soc.* **2020**, *167* (7), 070510. https://doi.org/10.1149/1945-7111/ab68d0.

(107) Phattharasupakun, N.; Geng, C.; Johnson, M. B.; Väli, R.; Liu, A.; Liu, Y.; Sawangphruk, M.; Dahn, J. R. Impact of Al Doping and Surface Coating on the Electrochemical Performances of Li-Rich Mn-Rich $Li_{1.11}Ni_{0.33}Mn_{0.56}O_2$ Positive

Electrode Material. *J. Electrochem. Soc.* **2020**, *167* (12), 120531. https://doi.org/10.1149/1945-7111/abb282.

(108) Xu, M.; Chen, Z.; Li, L.; Zhu, H.; Zhao, Q.; Xu, L.; Peng, N.; Gong, L. Highly Crystalline Alumina Surface Coating from Hydrolysis of Aluminum Isopropoxide on Lithium-Rich Layered Oxide. *Journal of Power Sources* **2015**, *281*, 444–454. https://doi.org/10.1016/j.jpowsour.2015.02.019.

(109) Walther, F.; Strauss, F.; Wu, X.; Mogwitz, B.; Hertle, J.; Sann, J.; Rohnke, M.; Brezesinski, T.; Janek, J. The Working Principle of a $Li_2CO_3/LiNbO_3$ Coating on NCM for Thiophosphate-Based All-Solid-State Batteries. *Chem. Mater.* **2021**, *33* (6), 2110–2125. https://doi.org/10.1021/acs.chemmater.0c04660.

(110) Lee, J. S.; Park, Y. J. Comparison of $LiTaO_3$ and $LiNbO_3$ Surface Layers Prepared by Post- and Precursor-Based Coating Methods for Ni-Rich Cathodes of All-Solid-State Batteries. *ACS Appl. Mater. Interfaces* **2021**, *13* (32), 38333–38345. https://doi.org/10.1021/acsami.1c10294.

(111) Schipper, F.; Bouzaglo, H.; Dixit, M.; Erickson, E. M.; Weigel, T.; Talianker, M.; Grinblat, J.; Burstein, L.; Schmidt, M.; Lampert, J.; Erk, C.; Markovsky, B.; Major, D. T.; Aurbach, D. From Surface ZrO_2 Coating to Bulk Zr Doping by High Temperature Annealing of Nickel-Rich Lithiated Oxides and Their Enhanced Electrochemical Performance in Lithium Ion Batteries. *Adv. Energy Mater.* **2018**, *8* (4), 1701682. https://doi.org/10.1002/aenm.201701682.

(112) Hu, S.-K.; Cheng, G.-H.; Cheng, M.-Y.; Hwang, B.-J.; Santhanam, R. Cycle Life Improvement of ZrO_2-Coated Spherical $Li[Ni_{1/3}Co_{1/3}Mn_{1/3}]O_2$ Cathode Material for Lithium Ion Batteries. *Journal of Power Sources* **2009**, *188* (2), 564–569. https://doi.org/10.1016/j.jpowsour.2008.11.113.

(113) Liu, S.; Su, J.; Zhang, C.; Chen, X.; Zhao, J.; Huang, T.; Wu, J.; Yu, A. Understanding the Effects of Surface Modification on Improving the High-Voltage Performance of Ni-Rich Cathode Materials. *Materials Today Energy* **2018**, *10*, 40–47. https://doi.org/10.1016/j.mtener.2018.08.013.

(114) Hildebrand, S.; Vollmer, C.; Winter, M.; Schappacher, F. M. Al_2O_3, SiO_2 and TiO_2 as Coatings for Safer $Li[Ni_{0.8}Co_{0.15}Al_{0.05}]O_2$ Cathodes: Electrochemical Performance and Thermal Analysis by Accelerating Rate Calorimetry. *J. Electrochem. Soc.* **2017**, *164* (9), A2190–A2198. https://doi.org/10.1149/2.0071712jes.

(115) Rastgoo-Deylami, M.; Javanbakht, M.; Omidvar, H. Enhanced Performance of Layered $Li_{1.2}[Mn_{0.54}Ni_{0.13}Co_{0.13}]O_2$ Cathode Material in Li-Ion Batteries Using Nanoscale Surface Coating with Fluorine-Doped Anatase TiO_2. *Solid State Ionics* **2019**, *331*, 74–88. https://doi.org/10.1016/j.ssi.2018.12.025.

(116) Liu, S.; Zhang, C.; Su, Q.; Li, L.; Su, J.; Huang, T.; Chen, Y.; Yu, A. Enhancing Electrochemical Performance of $Li[Ni_{0.6}Co_{0.2}Mn_{0.2}]O_2$ by Lithium-Ion Conductor Surface Modification. *Electrochimica Acta* **2017**, *224*, 171–177. https://doi.org/10.1016/j.electacta.2016.12.024.

(117) Wu, N.; Wu, H.; Liu, H.; Zhang, Y. Solvothermal Coating $Li[Ni_{0.8}Co_{0.15}Al_{0.05}]O_2$ Microspheres with Nanoscale Li_2TiO_3 Shell for Long Lifespan Li-Ion Battery Cathode Materials. *Journal of Alloys and Compounds* **2016**, *665*, 48–56. https://doi.org/10.1016/j.jallcom.2016.01.044.

(118) Gao, H.; Zeng, X.; Hu, Y.; Tileli, V.; Li, L.; Ren, Y.; Meng, X.; Maglia, F.; Lamp, P.; Kim, S.-J.; Amine, K.; Chen, Z. Modifying the Surface of a High-Voltage Lithium-Ion Cathode. *ACS Appl. Energy Mater.* **2018**, *1* (5), 2254–2260. https://doi.org/10.1021/acsaem.8b00323.

(119) Mylavarapu, S. K.; Ulu Okudur, F.; Yari, S.; De Sloovere, D.; D'Haen, J.; Shafique, A.; Van Bael, M. K.; Safari, M.; Hardy, A. Effect of TiO_x Surface Modification on the Electrochemical Performances of Ni-Rich (NMC-622) Cathode Material for Lithium-Ion Batteries. *ACS Appl. Energy Mater.* **2021**, *4* (10), 10493–10504. https://doi.org/10.1021/acsaem.1c01309.

(120) The Future of Hydrogen; IEA: Paris, **2019**. https://www.iea.org/ reports/the-future-of-hydrogen.

(121) Chu, S.; Majumdar, A. Opportunities and Challenges for a Sustainable Energy Future. *Nature* **2012**, *488* (7411), 294–303. https://doi.org/10.1038/nature11475.

(122) Reece, S. Y.; Hamel, J. A.; Sung, K.; Jarvi, T. D.; Esswein, A. J.; Pijpers, J. J. H.; Nocera, D. G. Wireless Solar Water Splitting Using Silicon-Based Semiconductors and Earth-Abundant Catalysts. *Science* **2011**, *334* (6056), 645–648. https://doi.org/10.1126/science.1209816.

(123) Tilley, S. D. Recent Advances and Emerging Trends in Photo-Electrochemical Solar Energy Conversion. *Advanced Energy Materials* **2019**, *9* (2), 1802877. https://doi.org/10.1002/aenm.201802877.

(124) Montoya, J. H.; Seitz, L. C.; Chakthranont, P.; Vojvodic, A.; Jaramillo, T. F.; Nørskov, J. K. Materials for Solar Fuels and Chemicals. *Nature Mater.* **2017**, *16* (1), 70–81. https://doi.org/10.1038/nmat4778.

(125) Shiva Kumar, S.; Lim, H. An Overview of Water Electrolysis Technologies for Green Hydrogen Production. *Energy Reports* **2022**, *8*, 13793–13813. https://doi.org/10.1016/j.egyr.2022.10.127.

(126) Das, S.; Bhattacharjee, S.; Mondal, S.; Dutta, S.; Bothra, N.; Pati, S. K.; Bhattacharyya, S. Bimetallic Zero-Valent Alloy with Measured High-Valent Surface States to Reinforce the Bifunctional Activity in Rechargeable Zinc-Air Batteries. *ACS Sustainable Chem. Eng.* **2021**, *9* (44), 14868–14880. https://doi.org/10.1021/acssuschemeng.1c04970.

(127) Kärkäs, M. D.; Åkermark, B. Water Oxidation Using Earth-Abundant Transition Metal Catalysts: Opportunities and Challenges. *Dalton Trans.* **2016**, *45* (37), 14421–14461. https://doi.org/10.1039/C6DT00809G.

(128) Sun, K.; Moreno-Hernandez, I. A.; Schmidt, W. C.; Zhou, X.; Crompton, J. C.; Liu, R.; Saadi, F. H.; Chen, Y.; Papadantonakis, K. M.; Lewis, N. S. A Comparison of the Chemical, Optical and Electrocatalytic Properties of Water-Oxidation Catalysts for Use in Integrated Solar-Fuel Generators. *Energy Environ. Sci.* **2017**, *10* (4), 987–1002. https://doi.org/10.1039/C6EE03563A.

(129) Jiao, Y.; Zheng, Y.; Jaroniec, M.; Qiao, S. Z. Design of Electrocatalysts for Oxygen- and Hydrogen-Involving Energy Conversion Reactions. *Chem. Soc. Rev.* **2015**, *44* (8), 2060–2086. https://doi.org/10.1039/C4CS00470A.

(130) Lee, S. W.; Carlton, C.; Risch, M.; Surendranath, Y.; Chen, S.; Furutsuki, S.; Yamada, A.; Nocera, D. G.; Shao-Horn, Y. The Nature of Lithium Battery Materials under Oxygen Evolution Reaction Conditions. *J. Am. Chem. Soc.* **2012**, *134* (41), 16959–16962. https://doi.org/10.1021/ja307814j.

(131) Tan, T.; Han, P.; Cong, H.; Cheng, G.; Luo, W. An Amorphous Cobalt Borate Nanosheet-Coated Cobalt Boride Hybrid for Highly Efficient Alkaline Water Oxidation Reaction. *ACS Sustainable Chem. Eng.* **2019**, *7* (6), 5620–5625. https://doi.org/10.1021/acssuschemeng.9b00258.

(132) Lyu, F.; Wang, Q.; Choi, S. M.; Yin, Y. Noble-Metal-Free Electrocatalysts for Oxygen Evolution. *Small* **2019**, *15* (1), 1804201. https://doi.org/10.1002/smll.201804201.

(133) McCrory, C. C. L.; Jung, S.; Ferrer, I. M.; Chatman, S. M.; Peters, J. C.; Jaramillo, T. F. Benchmarking Hydrogen Evolving Reaction and Oxygen Evolving Reaction Electrocatalysts for Solar Water Splitting Devices. *J. Am. Chem. Soc.* **2015**, *137* (13), 4347–4357. https://doi.org/10.1021/ja510442p.

(134) Gao, M.; Sheng, W.; Zhuang, Z.; Fang, Q.; Gu, S.; Jiang, J.; Yan, Y. Efficient Water Oxidation Using Nanostructured α-Nickel-Hydroxide as an Electrocatalyst. *J. Am. Chem. Soc.* **2014**, *136* (19), 7077–7084. https://doi.org/10.1021/ja502128j.

(135) Gerken, J. B.; McAlpin, J. G.; Chen, J. Y. C.; Rigsby, M. L.; Casey, W. H.; Britt, R. D.; Stahl, S. S. Electrochemical Water Oxidation with Cobalt-Based Electrocatalysts from pH 0–14: The Thermodynamic Basis for Catalyst Structure, Stability, and Activity. *J. Am. Chem. Soc.* **2011**, *133* (36), 14431–14442. https://doi.org/10.1021/ja205647m.

(136) Chen, S.; Duan, J.; Jaroniec, M.; Qiao, S.-Z. Nitrogen and Oxygen Dual-Doped Carbon Hydrogel Film as a Substrate-Free Electrode for Highly Efficient Oxygen Evolution Reaction. *Advanced Materials* **2014**, *26* (18), 2925–2930. https://doi.org/10.1002/adma.201305608.

(137) Song, F.; Bai, L.; Moysiadou, A.; Lee, S.; Hu, C.; Liardet, L.; Hu, X. Transition Metal Oxides as Electrocatalysts for the Oxygen Evolution Reaction in Alkaline Solutions: An Application-Inspired Renaissance. *J. Am. Chem. Soc.* **2018**, *140* (25), 7748–7759. https://doi.org/10.1021/jacs.8b04546.

(138) Lv, L.; Yang, Z.; Chen, K.; Wang, C.; Xiong, Y. 2D Layered Double Hydroxides for Oxygen Evolution Reaction: From Fundamental Design to Application. *Advanced Energy Materials* **2019**, *9* (17), 1803358. https://doi.org/10.1002/aenm.201803358.

(139) Lu, H.; Andrei, V.; Jenkinson, K. J.; Regoutz, A.; Li, N.; Creissen, C. E.; Wheatley, A. E. H.; Hao, H.; Reisner, E.; Wright, D. S.; Pike, S. D. Single-Source Bismuth (Transition Metal) Polyoxovanadate Precursors for the Scalable Synthesis of Doped $BiVO_4$ Photoanodes. *Advanced Materials* **2018**, *30* (46), 1804033. https://doi.org/10.1002/adma.201804033.

(140) Park, Y.; McDonald, K. J.; Choi, K.-S. Progress in Bismuth Vanadate Photoanodes for Use in Solar Water Oxidation. *Chem. Soc. Rev.* **2013**, *42* (6), 2321–2337. https://doi.org/10.1039/C2CS35260E.

(141) Andrei, V.; Hoye, R. L. Z.; Crespo-Quesada, M.; Bajada, M.; Ahmad, S.; Volder, M. D.; Friend, R.; Reisner, E. Scalable Triple Cation Mixed Halide Perovskite–

$BiVO_4$ Tandems for Bias-Free Water Splitting. *Advanced Energy Materials* **2018**, *8* (25), 1801403. https://doi.org/10.1002/aenm.201801403.

(142) Andrei, V.; Reuillard, B.; Reisner, E. Bias-Free Solar Syngas Production by Integrating a Molecular Cobalt Catalyst with Perovskite–$BiVO_4$ Tandems. *Nat. Mater.* **2020**, *19* (2), 189–194. https://doi.org/10.1038/s41563-019-0501-6.

(143) Rettie, A. J. E.; Lee, H. C.; Marshall, L. G.; Lin, J.-F.; Capan, C.; Lindemuth, J.; McCloy, J. S.; Zhou, J.; Bard, A. J.; Mullins, C. B. Combined Charge Carrier Transport and Photoelectrochemical Characterization of $BiVO_4$ Single Crystals: Intrinsic Behavior of a Complex Metal Oxide. *J. Am. Chem. Soc.* **2013**, *135* (30), 11389–11396. https://doi.org/10.1021/ja405550k.

(144) Zachäus, C.; Abdi, F. F.; Peter, L. M.; Krol, R. van de. Photocurrent of $BiVO_4$ Is Limited by Surface Recombination, Not Surface Catalysis. *Chem. Sci.* **2017**, *8* (5), 3712–3719. https://doi.org/10.1039/C7SC00363C.

(145) Tolod, K. R.; Hernández, S.; Russo, N. Recent Advances in the $BiVO_4$ Photocatalyst for Sun-Driven Water Oxidation: Top-Performing Photoanodes and Scale-Up Challenges. *Catalysts* **2017**, *7* (1), 13. https://doi.org/10.3390/catal7010013.

(146) Kim, T. W.; Choi, K.-S. Nanoporous $BiVO_4$ Photoanodes with Dual-Layer Oxygen Evolution Catalysts for Solar Water Splitting. *Science* **2014**, *343* (6174), 990–994. https://doi.org/10.1126/science.1246913.

(147) Chang, X.; Wang, T.; Zhang, P.; Zhang, J.; Li, A.; Gong, J. Enhanced Surface Reaction Kinetics and Charge Separation of p–n Heterojunction Co_3O_4/$BiVO_4$ Photoanodes. *J. Am. Chem. Soc.* **2015**, *137* (26), 8356–8359. https://doi.org/10.1021/jacs.5b04186.

(148) Lai, Y.-H.; Palm, D. W.; Reisner, E. Multifunctional Coatings from Scalable Single Source Precursor Chemistry in Tandem Photoelectrochemical Water Splitting. *Advanced Energy Materials* **2015**, *5* (24), 1501668. https://doi.org/10.1002/aenm.201501668.

(149) Yang, Q.; Li, Z.; Zhang, R.; Zhou, L.; Shao, M.; Wei, M. Carbon Modified Transition Metal Oxides/Hydroxides Nanoarrays toward High-Performance Flexible All-Solid-State Supercapacitors. *Nano Energy* **2017**, *41*, 408–416. https://doi.org/10.1016/j.nanoen.2017.09.049.

(150) Bates, M. K.; Jia, Q.; Doan, H.; Liang, W.; Mukerjee, S. Charge-Transfer Effects in Ni–Fe and Ni–Fe–Co Mixed-Metal Oxides for the Alkaline Oxygen Evolution

Reaction. *ACS Catal.* **2016**, *6* (1), 155–161. https://doi.org/10.1021/acscatal.5b01481.

(151) Smith, R. D. L.; Prévot, M. S.; Fagan, R. D.; Zhang, Z.; Sedach, P. A.; Siu, M. K. J.; Trudel, S.; Berlinguette, C. P. Photochemical Route for Accessing Amorphous Metal Oxide Materials for Water Oxidation Catalysis. *Science* **2013**, *340* (6128), 60–63. https://doi.org/10.1126/science.1233638.

(152) Browne, M. P.; Vasconcelos, J. M.; Coelho, J.; O'Brien, M.; Rovetta, A. A.; McCarthy, E. K.; Nolan, H.; Duesberg, G. S.; Nicolosi, V.; Colavita, P. E.; Lyons, M. E. G. Improving the Performance of Porous Nickel Foam for Water Oxidation Using Hydrothermally Prepared Ni and Fe Metal Oxides. *Sustainable Energy Fuels* **2017**, *1* (1), 207–216. https://doi.org/10.1039/C6SE00032K.

(153) Lu, H.; Wright, D. S.; Pike, S. D. The Use of Mixed-Metal Single Source Precursors for the Synthesis of Complex Metal Oxides. *Chem. Commun.* **2020**, *56* (6), 854–871. https://doi.org/10.1039/C9CC06258K.

(154) Lai, Y.-H.; Lin, C.-Y.; Lv, Y.; King, T. C.; Steiner, A.; Muresan, N. M.; Gan, L.; Wright, D. S.; Reisner, E. Facile Assembly of an Efficient CoO_x Water Oxidation Electrocatalyst from Co-Containing Polyoxotitanate Nanocages. *Chem. Commun.* **2013**, *49* (39), 4331–4333. https://doi.org/10.1039/C2CC34934E.

(155) Lai, Y.-H.; King, T. C.; Wright, D. S.; Reisner, E. Scalable One-Step Assembly of an Inexpensive Photoelectrode for Water Oxidation by Deposition of a Ti- and Ni-Containing Molecular Precursor on Nanostructured WO_3. *Chemistry – A European Journal* **2013**, *19* (39), 12943–12947. https://doi.org/10.1002/chem.201302641.

(156) Lai, Y.-H.; Park, H. S.; Zhang, J. Z.; Matthews, P. D.; Wright, D. S.; Reisner, E. A Si Photocathode Protected and Activated with a Ti and Ni Composite Film for Solar Hydrogen Production. *Chemistry – A European Journal* **2015**, *21* (10), 3919–3923. https://doi.org/10.1002/chem.201406566.

(157) Yang, Y.; Yang, Y.; Pei, Z.; Wu, K.-H.; Tan, C.; Wang, H.; Wei, L.; Mahmood, A.; Yan, C.; Dong, J.; Zhao, S.; Chen, Y. Recent Progress of Carbon-Supported Single-Atom Catalysts for Energy Conversion and Storage. *Matter* **2020**, *3* (5), 1442–1476. https://doi.org/10.1016/j.matt.2020.07.032.

(158) Matthews, P. D.; King, T. C.; Wright, D. S. Structure, Photochemistry and Applications of Metal-Doped Polyoxotitanium Alkoxide Cages. *Chem. Commun.* **2014**, *50* (85), 12815–12823. https://doi.org/10.1039/C4CC04421E.

(159) Ji, P.; Feng, X.; Oliveres, P.; Li, Z.; Murakami, A.; Wang, C.; Lin, W. Strongly Lewis Acidic Metal–Organic Frameworks for Continuous Flow Catalysis. *J. Am. Chem. Soc.* **2019**, *141* (37), 14878–14888. https://doi.org/10.1021/jacs.9b07891.

(160) Rorrer, J. E.; Toste, F. D.; Bell, A. T. Mechanism and Kinetics of Isobutene Formation from Ethanol and Acetone over $Zn_xZr_yO_z$. *ACS Catal.* **2019**, *9* (12), 10588–10604. https://doi.org/10.1021/acscatal.9b03045.

(161) Nikoofar, K.; Khademi, Z. A Review on Green Lewis Acids: Zirconium(IV) Oxydichloride Octahydrate ($ZrOCl_2 \cdot 8H_2O$) and Zirconium(IV) Tetrachloride ($ZrCl_4$) in Organic Chemistry. *Res Chem Intermed* **2016**, *42* (5), 3929–3977. https://doi.org/10.1007/s11164-015-2260-6.

(162) Liu, Y.; Lau, T.-C. Activation of Metal Oxo and Nitrido Complexes by Lewis Acids. *J. Am. Chem. Soc.* **2019**, *141* (9), 3755–3766. https://doi.org/10.1021/jacs.8b13100.

(163) Devi, T.; Lee, Y.-M.; Nam, W.; Fukuzumi, S. Metal Ion-Coupled Electron-Transfer Reactions of Metal-Oxygen Complexes. *Coordination Chemistry Reviews* **2020**, *410*, 213219. https://doi.org/10.1016/j.ccr.2020.213219.

(164) Vrettos, J. S.; Stone, D. A.; Brudvig, G. W. Quantifying the Ion Selectivity of the Ca^{2+} Site in Photosystem II: Evidence for Direct Involvement of Ca^{2+} in O_2 Formation. *Biochemistry* **2001**, *40* (26), 7937–7945. https://doi.org/10.1021/bi010679z.

(165) Yamaguchi, K.; Shoji, M.; Isobe, H.; Miyagawa, K.; Nakatani, K. Theory of Chemical Bonds in Metalloenzymes XXII: A Concerted Bond-Switching Mechanism for the Oxygen–Oxygen Bond Formation Coupled with One Electron Transfer for Water Oxidation in the Oxygen-Evolving Complex of Photosystem II. *Molecular Physics* **2019**, *117* (17), 2320–2354. https://doi.org/10.1080/00268976.2018.1552799.

(166) Brudvig, G. W. Water Oxidation Chemistry of Photosystem II. *Philosophical Transactions of the Royal Society B: Biological Sciences* **2008**, *363* (1494), 1211–1219. https://doi.org/10.1098/rstb.2007.2217.

(167) Matsui, K.; Yoshida, H.; Ikuhara, Y. Review: Microstructure-Development Mechanism during Sintering in Polycrystalline Zirconia. *International Materials Reviews* **2018**, *63* (6), 375–406. https://doi.org/10.1080/09506608.2017.1402424.

(168) Heuer, A. H. Transformation Toughening in ZrO_2-Containing Ceramics. *J American Ceramic Society* **1987**, *70* (10), 689–698. https://doi.org/10.1111/j.1151-2916.1987.tb04865.x.

(169) Ramos-Garcés, M. V.; Sanchez, J.; Luz-Rivera, K. L.; Toro-Pedrosa, D. E. D.; Jaramillo, T. F.; Colón, J. L. Morphology Control of Metal-Modified Zirconium Phosphate Support Structures for the Oxygen Evolution Reaction. *Dalton Trans.* **2020**, *49* (12), 3892–3900. https://doi.org/10.1039/C9DT04135D.

(170) Ramos-Garcés, M. V.; Sanchez, J.; Del Toro-Pedrosa, D. E.; Alvarez, I. B.; Wu, Y.; Valle, E.; Villagrán, D.; Jaramillo, T. F.; Colón, J. L. Transition Metal-Modified Exfoliated Zirconium Phosphate as an Electrocatalyst for the Oxygen Evolution Reaction. *ACS Appl. Energy Mater.* **2019**, *2* (5), 3561–3567. https://doi.org/10.1021/acsaem.9b00299.

(171) Barraza Alvarez, I.; Wu, Y.; Sanchez, J.; Ge, Y.; Ramos-Garcés, M. V.; Chu, T.; Jaramillo, T. F.; Colón, J. L.; Villagrán, D. Cobalt Porphyrin Intercalation into Zirconium Phosphate Layers for Electrochemical Water Oxidation. *Sustainable Energy Fuels* **2021**, *5* (2), 430–437. https://doi.org/10.1039/D0SE01134G.

(172) Sanchez, J.; Ramos-Garcés, M. V.; Narkeviciute, I.; Colón, J. L.; Jaramillo, T. F. Transition Metal-Modified Zirconium Phosphate Electrocatalysts for the Oxygen Evolution Reaction. *Catalysts* **2017**, *7* (12), 132. https://doi.org/10.3390/catal7050132.

(173) Mete, B.; Peighambardoust, N. S.; Aydin, S.; Sadeghi, E.; Aydemir, U. Metal-Substituted Zirconium Diboride (Zr1-TMB2; TM = Ni, Co, and Fe) as Low-Cost and High-Performance Bifunctional Electrocatalyst for Water Splitting. *Electrochimica Acta* **2021**, *389*, 138789. https://doi.org/10.1016/j.electacta.2021.138789.

(174) Huang, L.; Chen, D.; Luo, G.; Lu, Y.; Chen, C.; Zou, Y.; Dong, C.; Li, Y.; Wang, S. Zirconium-Regulation-Induced Bifunctionality in 3D Cobalt–Iron Oxide Nanosheets for Overall Water Splitting. *Adv. Mater.* **2019**, *31* (28), 1901439. https://doi.org/10.1002/adma.201901439.

(175) Yang, G.; Zhu, B.; Fu, Y.; Zhao, J.; Lin, Y.; Gao, D.; Li, J. High-Valent Zirconium-Doping Modified Co_3O_4 Weave-like Nanoarray Boosts Oxygen Evolution Reaction. *Journal of Alloys and Compounds* **2021**, *886*, 161172. https://doi.org/10.1016/j.jallcom.2021.161172.

(176) Sanchez, J.; Stevens, M. B.; Young, A. R.; Gallo, A.; Zhao, M.; Liu, Y.; Ramos-Garcés, M. V.; Ben-Naim, M.; Colón, J. L.; Sinclair, R.; King, L. A.; Bajdich, M.; Jaramillo, T. F. Isolating the Electrocatalytic Activity of a Confined NiFe Motif within Zirconium Phosphate. *Adv. Energy Mater.* **2021**, *11* (20), 2003545. https://doi.org/10.1002/aenm.202003545.

(177) Yang, Y.; Yang, Y.; Liu, Y.; Zhao, S.; Tang, Z. Metal–Organic Frameworks for Electrocatalysis: Beyond Their Derivatives. *Small Science* **2021**, *1* (12), 2100015. https://doi.org/10.1002/smsc.202100015.

(178) Zhao, S.; Tan, C.; He, C.-T.; An, P.; Xie, F.; Jiang, S.; Zhu, Y.; Wu, K.-H.; Zhang, B.; Li, H.; Zhang, J.; Chen, Y.; Liu, S.; Dong, J.; Tang, Z. Structural Transformation of Highly Active Metal–Organic Framework Electrocatalysts during the Oxygen Evolution Reaction. *Nat Energy* **2020**, *5* (11), 881–890. https://doi.org/10.1038/s41560-020-00709-1.

(179) Steunou, N.; Dromzee, Y.; Robert, F.; Sanchez, C. Synthesis and Characterization of Titanium Oxo-Alkoxides through Solvatothermal Process. *MRS Online Proceedings Library (OPL)* **1996**, *435*. https://doi.org/10.1557/PROC-435-487.

(180) Eslava, S.; McPartlin, M.; Thomson, R. I.; Rawson, J. M.; Wright, D. S. Single-Source Materials for Metal-Doped Titanium Oxide: Syntheses, Structures, and Properties of a Series of Heterometallic Transition-Metal Titanium Oxo Cages. *Inorg. Chem.* **2010**, *49* (24), 11532–11540. https://doi.org/10.1021/ic101687m.

(181) Eslava, S.; Hengesbach, F.; McPartlin, M.; Wright, D. S. Heterometallic Cobalt(II)–Titanium(IV) Oxo Cages; Key Building Blocks for Hybrid Materials. *Chem. Commun.* **2010**, *46* (26), 4701. https://doi.org/10.1039/c0cc00016g.

(182) Eslava, S.; Goodwill, B. P. R.; McPartlin, M.; Wright, D. S. Extending the Family of Titanium Heterometallic–Oxo–Alkoxy Cages. *Inorg. Chem.* **2011**, *50* (12), 5655–5662. https://doi.org/10.1021/ic200350j.

(183) Hegemann, C.; Tyrra, W.; Neudörfl, J.-M.; Mathur, S. Synthetic and Structural Investigations on the Reactivity of the Cd–I Bond in $[ICd\{Zr_2(O^iPr)_9\}]$ to Construct New Mixed-Metal Alkoxides. *Organometallics* **2013**, *32* (6), 1654–1664. https://doi.org/10.1021/om301053b.

(184) Seisenbaeva, G. A.; Gohil, S.; Kessler, V. G. Influence of Heteroligands on the Composition, Structure and Properties of Homo- and Heterometallic Zirconium Alkoxides. Decisive Role of Thermodynamic Factors in Their Self-Assembly. *J. Mater. Chem.* **2004**, *14* (21), 3177. https://doi.org/10.1039/b404303k.

(185) Mehrotra, R. C.; Singh, A.; Sogani, S. Homo- and Hetero-Metallic Alkoxides of Group 1, 2 and 12 Metals. *Chemical Society Reviews.* **1994**, *23*, 215–225. https://doi.org/10.1039/CS9942300215.

(186) Samuels, J. A.; Vaartstra, B. A.; Huffman, J. C.; Trojan, K. L.; Hatfield, W. E.; Caulton, K. G. A Planar Oxocuprate(II) Array via Heterometallic Alkoxide Chemistry. *J. Am. Chem. Soc.* **1990**, *112* (26), 9623–9624. https://doi.org/10.1021/ja00182a023.

(187) Piszczek, P.; Richert, M.; Wojtczak, A. Crystal Structure and Spectral Characterization of Hexanuclear Oxo Titanium(IV) Clusters: $[Ti_6O_6(OSi(CH_3)_3)_6(OOCR)_6]$ (R=But, CH_2But, $C(CH_3)_2$Et). *Polyhedron* **2008**, *27* (2), 602–608. https://doi.org/10.1016/j.poly.2007.10.018.

(188) Samuel, E.; Ferner, R.; Bigorgne, M. Low-Frequency Infrared and Raman Spectra of Pi-Cyclopentadienyl Compounds of Titanium, Zirconium, and Hafnium. *Inorg. Chem.* **1973**, *12* (4), 881–887. https://doi.org/10.1021/ic50122a035.

(189) Navío; Hidalgo; Colón, G.; Botta, S. G.; Litter, M. I. Preparation and Physicochemical Properties of ZrO_2 and Fe/ZrO_2 Prepared by a Sol−Gel Technique. *Langmuir* **2001**, *17* (1), 202–210. https://doi.org/10.1021/la000897d.

(190) Kanan, M. W.; Nocera, D. G. In Situ Formation of an Oxygen-Evolving Catalyst in Neutral Water Containing Phosphate and Co^{2+}. *Science* **2008**, *321* (5892), 1072–1075. https://doi.org/10.1126/science.1162018.

(191) Zhao, S.; Yang, Y.; Tang, Z. Insight into Structural Evolution, Active Sites, and Stability of Heterogeneous Electrocatalysts. *Angew. Chem. Int. Ed.* **2022**, *61* (11). https://doi.org/10.1002/anie.202110186.

(192) Miller, D. J.; Biesinger, M. C.; McIntyre, N. S. Interactions of CO_2 and CO at Fractional Atmosphere Pressures with Iron and Iron Oxide Surfaces: One Possible Mechanism for Surface Contamination? *Surf. Interface Anal.* **2002**, *33* (4), 299–305. https://doi.org/10.1002/sia.1188.

(193) *NIST X-Ray Photoelectron Spectroscopy Database, NIST Standard Reference Database Number 20*; National Institute of Standards and Technology: Gaithersburg MD, USA, 2012.

(194) Dillard, J. G.; Glasbrenner, H.; Pfennig, G.; Klewe-Nebenius, H.; Ache, H. J. Surface Analysis Studies of Zr-Co Alloy and Zr-Co Alloy Films. *Journal of the Less Common Metals* **1990**, *166* (2), 233–239. https://doi.org/10.1016/0022-5088(90)90005-5.

(195) Chen, C.; Levitin, G.; Hess, D. W.; Fuller, T. F. XPS Investigation of Nafion® Membrane Degradation. *Journal of Power Sources* **2007**, *169* (2), 288–295. https://doi.org/10.1016/j.jpowsour.2007.03.037.

(196) Ardizzone, S.; Cattania, M. G.; Lugo, P. Interfacial Electrostatic Behaviour of Oxides: Correlations with Structural and Surface Parameters of the Phase. *Electrochimica Acta* **1994**, *39* (11–12), 1509–1517. https://doi.org/10.1016/0013-4686(94)85128-X.

(197) Kim, J. S.; Kim, B.; Kim, H.; Kang, K. Recent Progress on Multimetal Oxide Catalysts for the Oxygen Evolution Reaction. *Adv. Energy Mater.* **2018**, *8* (11), 1702774. https://doi.org/10.1002/aenm.201702774.

(198) Biesinger, M. C.; Payne, B. P.; Grosvenor, A. P.; Lau, L. W. M.; Gerson, A. R.; Smart, R. St. C. Resolving Surface Chemical States in XPS Analysis of First Row Transition Metals, Oxides and Hydroxides: Cr, Mn, Fe, Co and Ni. *Applied Surface Science* **2011**, *257* (7), 2717–2730. https://doi.org/10.1016/j.apsusc.2010.10.051.

(199) Biesinger, M. C. Advanced Analysis of Copper X-Ray Photoelectron Spectra: Advanced Analysis of Copper X-Ray Photoelectron Spectra. *Surf. Interface Anal.* **2017**, *49* (13), 1325–1334. https://doi.org/10.1002/sia.6239.

(200) Majee, R.; Kumar, A.; Das, T.; Chakraborty, S.; Bhattacharyya, S. Tweaking Nickel with Minimal Silver in a Heterogeneous Alloy of Decahedral Geometry to Deliver Platinum-like Hydrogen Evolution Activity. *Angew. Chem. Int. Ed.* **2020**, *59* (7), 2881–2889. https://doi.org/10.1002/anie.201913704.

(201) Bhattacharjee, S.; Andrei, V.; Pornrungroj, C.; Rahaman, M.; Pichler, C. M.; Reisner, E. Reforming of Soluble Biomass and Plastic Derived Waste Using a Bias-Free $Cu_{30}Pd_{70}$ |Perovskite|Pt Photoelectrochemical Device. *Adv. Funct. Mater.* **2021**, 2109313. https://doi.org/10.1002/adfm.202109313.

(202) Suryanto, B. H. R.; Wang, Y.; Hocking, R. K.; Adamson, W.; Zhao, C. Overall Electrochemical Splitting of Water at the Heterogeneous Interface of Nickel and Iron Oxide. *Nat Commun* **2019**, *10* (1), 5599. https://doi.org/10.1038/s41467-019-13415-8.

(203) Wang, X.-D.; Chen, H.-Y.; Xu, Y.-F.; Liao, J.-F.; Chen, B.-X.; Rao, H.-S.; Kuang, D.-B.; Su, C.-Y. Self-Supported $NiMoP_2$ Nanowires on Carbon Cloth as an Efficient and Durable Electrocatalyst for Overall Water Splitting. *J. Mater. Chem. A* **2017**, *5* (15), 7191–7199. https://doi.org/10.1039/C6TA11188B.

(204) Du, J.; Chen, Z.; Ye, S.; Wiley, B. J.; Meyer, T. J. Copper as a Robust and Transparent Electrocatalyst for Water Oxidation. *Angew. Chem.* **2015**, *127* (7), 2101–2106. https://doi.org/10.1002/ange.201408854.

(205) Man, I. C.; Su, H.; Calle-Vallejo, F.; Hansen, H. A.; Martínez, J. I.; Inoglu, N. G.; Kitchin, J.; Jaramillo, T. F.; Nørskov, J. K.; Rossmeisl, J. Universality in Oxygen Evolution Electrocatalysis on Oxide Surfaces. *ChemCatChem* **2011**, *3* (7), 1159–1165. https://doi.org/10.1002/cctc.201000397.

(206) Iqbal, B.; Saleem, M.; Arshad, S. N.; Rashid, J.; Hussain, N.; Zaheer, M. One-Pot Synthesis of Heterobimetallic Metal–Organic Frameworks (MOFs) for Multifunctional Catalysis. *Chem. Eur. J.* **2019**, *25* (44), 10490–10498. https://doi.org/10.1002/chem.201901939.

(207) Bayatsarmadi, B.; Zheng, Y.; Casari, C. S.; Russo, V.; Qiao, S.-Z. Pulsed Laser Deposition of Porous N-Carbon Supported Cobalt (Oxide) Thin Films for Highly Efficient Oxygen Evolution. *Chem. Commun.* **2016**, *52* (80), 11947–11950. https://doi.org/10.1039/C6CC04776A.

(208) Su, P.; Ma, S.; Huang, W.; Boyjoo, Y.; Bai, S.; Liu, J. Ca^{2+}-Doped Ultrathin Cobalt Hydroxyl Oxides Derived from Coordination Polymers as Efficient Electrocatalysts for the Oxidation of Water. *J. Mater. Chem. A.* **2019**, *7* (33), 19415–19422. https://doi.org/10.1039/C9TA05882F.

(209) Morales-Guio, C. G.; Liardet, L.; Hu, X. Oxidatively Electrodeposited Thin-Film Transition Metal (Oxy)Hydroxides as Oxygen Evolution Catalysts. *J. Am. Chem. Soc.* **2016**, *138* (28), 8946–8957. https://doi.org/10.1021/jacs.6b05196.

(210) Kim, J. S.; Park, I.; Jeong, E.-S.; Jin, K.; Seong, W. M.; Yoon, G.; Kim, H.; Kim, B.; Nam, K. T.; Kang, K. Amorphous Cobalt Phyllosilicate with Layered Crystalline Motifs as Water Oxidation Catalyst. *Adv. Mater.* **2017**, *29* (21), 1606893. https://doi.org/10.1002/adma.201606893.

(211) Jiang, C.; Yang, J.; Han, X.; Qi, H.; Su, M.; Zhao, D.; Kang, L.; Liu, X.; Ye, J.; Li, J.; Guo, Z.-X.; Kaltsoyannis, N.; Wang, A.; Tang, J. Crystallinity-Modulated $Co_{2-x}V_xO_4$ Nanoplates for Efficient Electrochemical Water Oxidation. *ACS Catal.* **2021**, *11* (24), 14884–14891. https://doi.org/10.1021/acscatal.1c04618.

(212) Harada, M.; Kotegawa, F.; Kuwa, M. Structural Changes of Spinel MCo_2O_4 (M = Mn, Fe, Co, Ni, and Zn) Electrocatalysts during the Oxygen Evolution Reaction Investigated by In Situ X-Ray Absorption Spectroscopy. *ACS Appl. Energy Mater.* **2022**, *5* (1), 278–294. https://doi.org/10.1021/acsaem.1c02824.

(213) Boonlha, S.; Chakthranont, P.; Kityakarn, S. 3DOM Cerium Doped $LaCoO_3$ Bifunctional Electrocatalysts for the Oxygen Evolution and Reduction Reactions. *ChemCatChem* **2022**, *14* (3). https://doi.org/10.1002/cctc.202101398.

(214) Whittingham, M. S. Lithium Batteries and Cathode Materials. *Chem. Rev.* **2004**, *104* (10), 4271–4302. https://doi.org/10.1021/cr020731c.

(215) Li, W.; Erickson, E. M.; Manthiram, A. High-Nickel Layered Oxide Cathodes for Lithium-Based Automotive Batteries. *Nat Energy* **2020**, *5* (1), 26–34. https://doi.org/10.1038/s41560-019-0513-0.

(216) Noh, H.-J.; Youn, S.; Yoon, C. S.; Sun, Y.-K. Comparison of the Structural and Electrochemical Properties of Layered $Li[Ni_xCo_yMn_z]O_2$ (x = 1/3, 0.5, 0.6, 0.7, 0.8 and 0.85) Cathode Material for Lithium-Ion Batteries. *Journal of Power Sources* **2013**, *233*, 121–130. https://doi.org/10.1016/j.jpowsour.2013.01.063.

(217) Dose, W. M.; Xu, C.; Grey, C. P.; De Volder, M. F. L. Effect of Anode Slippage on Cathode Cutoff Potential and Degradation Mechanisms in Ni-Rich Li-Ion Batteries. *Cell Reports Physical Science* **2020**, *1* (11), 100253. https://doi.org/10.1016/j.xcrp.2020.100253.

(218) Jung, R.; Metzger, M.; Maglia, F.; Stinner, C.; Gasteiger, H. A. Oxygen Release and Its Effect on the Cycling Stability of $LiNi_xMn_yCo_zO_2$ (NMC) Cathode Materials for Li-Ion Batteries. *J. Electrochem. Soc.* **2017**, *164* (7), A1361–A1377. https://doi.org/10.1149/2.0021707jes.

(219) Eldesoky, A.; Logan, E. R.; Louli, A. J.; Song, W.; Weber, R.; Hy, S.; Petibon, R.; Harlow, J. E.; Azam, S.; Zsoldos, E.; Dahn, J. R. Impact of Graphite Materials on the Lifetime of NMC811/Graphite Pouch Cells: Part II. Long-Term Cycling, Stack Pressure Growth, Isothermal Microcalorimetry, and Lifetime Projection. *J. Electrochem. Soc.* **2022**, *169* (1), 010501. https://doi.org/10.1149/1945-7111/ac42f1.

(220) Myung, S.-T.; Izumi, K.; Komaba, S.; Sun, Y.-K.; Yashiro, H.; Kumagai, N. Role of Alumina Coating on Li−Ni−Co−Mn−O Particles as Positive Electrode Material for Lithium-Ion Batteries. *Chemistry of Materials* **2005**, *17* (14), 3695–3704. https://doi.org/10.1021/cm050566s.

(221) Cho, W.; Kim, S.-M.; Song, J. H.; Yim, T.; Woo, S.-G.; Lee, K.-W.; Kim, J.-S.; Kim, Y.-J. Improved Electrochemical and Thermal Properties of Nickel Rich $LiNi_{0.6}Co_{0.2}Mn_{0.2}O_2$ Cathode Materials by SiO_2 Coating. *Journal of Power Sources* **2015**, *282*, 45–50. https://doi.org/10.1016/j.jpowsour.2014.12.128.

(222) Wang, Z.; Liu, E.; He, C.; Shi, C.; Li, J.; Zhao, N. Effect of Amorphous $FePO_4$ Coating on Structure and Electrochemical Performance of $Li_{1.2}Ni_{0.13}Co_{0.13}Mn_{0.54}O_2$ as Cathode Material for Li-Ion Batteries. *Journal of Power Sources* **2013**, *236*, 25–32. https://doi.org/10.1016/j.jpowsour.2013.02.022.

(223) Sun, Y.-K.; Lee, M.-J.; Yoon, C. S.; Hassoun, J.; Amine, K.; Scrosati, B. The Role of AlF_3 Coatings in Improving Electrochemical Cycling of Li-Enriched Nickel-Manganese Oxide Electrodes for Li-Ion Batteries. *Advanced Materials* **2012**, *24* (9), 1192–1196. https://doi.org/10.1002/adma.201104106.

(224) Xie, J.; Sendek, A. D.; Cubuk, E. D.; Zhang, X.; Lu, Z.; Gong, Y.; Wu, T.; Shi, F.; Liu, W.; Reed, E. J.; Cui, Y. Atomic Layer Deposition of Stable $LiAlF_4$ Lithium Ion Conductive Interfacial Layer for Stable Cathode Cycling. *ACS Nano* **2017**, *11* (7), 7019–7027. https://doi.org/10.1021/acsnano.7b02561.

(225) Shi, Y.; Zhang, M.; Qian, D.; Meng, Y. S. Ultrathin Al_2O_3 Coatings for Improved Cycling Performance and Thermal Stability of $LiNi_{0.5}Co_{0.2}Mn_{0.3}O_2$ Cathode Material. *Electrochimica Acta* **2016**, *203*, 154–161. https://doi.org/10.1016/j.electacta.2016.03.185.

(226) Cho, J.; Kim, T.-J.; Kim, Y. J.; Park, B. High-Performance ZrO_2-Coated $LiNiO_2$ Cathode Material. *Electrochemical and Solid-State Letters* **2001**, *4* (10), A159–A161. https://doi.org/10.1149/1.1398556.

(227) Beltrop, K.; Klein, S.; Nölle, R.; Wilken, A.; Lee, J. J.; Köster, T. K.-J.; Reiter, J.; Tao, L.; Liang, C.; Winter, M.; Qi, X.; Placke, T. Triphenylphosphine Oxide as Highly Effective Electrolyte Additive for Graphite/NMC811 Lithium Ion Cells. *Chem. Mater.* **2018**, *30* (8), 2726–2741. https://doi.org/10.1021/acs.chemmater.8b00413.

(228) Li, J.; Liu, H.; Xia, J.; Cameron, A. R.; Nie, M.; Botton, G. A.; Dahn, J. R. The Impact of Electrolyte Additives and Upper Cut-off Voltage on the Formation of a Rocksalt Surface Layer in $LiNi_{0.8}Mn_{0.1}Co_{0.1}O_2$ Electrodes. *J. Electrochem. Soc.* **2017**, *164* (4), A655–A665. https://doi.org/10.1149/2.0651704jes.

(229) Li, J.; Downie, L. E.; Ma, L.; Qiu, W.; Dahn, J. R. Study of the Failure Mechanisms of $LiNi_{0.8}Mn_{0.1}Co_{0.1}O_2$ Cathode Material for Lithium Ion Batteries. *J. Electrochem. Soc.* **2015**, *162* (7), A1401–A1408. https://doi.org/10.1149/2.1011507jes.

(230) Jung, S.-K.; Gwon, H.; Hong, J.; Park, K.-Y.; Seo, D.-H.; Kim, H.; Hyun, J.; Yang, W.; Kang, K. Understanding the Degradation Mechanisms of $LiNi_{0.5}Co_{0.2}Mn_{0.3}O_2$

Cathode Material in Lithium Ion Batteries. *Advanced Energy Materials* **2014**, *4* (1), 1300787. https://doi.org/10.1002/aenm.201300787.

(231) Xu, C.; Märker, K.; Lee, J.; Mahadevegowda, A.; Reeves, P. J.; Day, S. J.; Groh, M. F.; Emge, S. P.; Ducati, C.; Layla Mehdi, B.; Tang, C. C.; Grey, C. P. Bulk Fatigue Induced by Surface Reconstruction in Layered Ni-Rich Cathodes for Li-Ion Batteries. *Nat. Mater.* **2020**. https://doi.org/10.1038/s41563-020-0767-8.

(232) Lin, F.; Markus, I. M.; Nordlund, D.; Weng, T.-C.; Asta, M. D.; Xin, H. L.; Doeff, M. M. Surface Reconstruction and Chemical Evolution of Stoichiometric Layered Cathode Materials for Lithium-Ion Batteries. *Nat Commun* **2014**, *5* (1), 3529. https://doi.org/10.1038/ncomms4529.

(233) Moryson, Y.; Walther, F.; Sann, J.; Mogwitz, B.; Ahmed, S.; Burkhardt, S.; Chen, L.; Klar, P. J.; Volz, K.; Fearn, S.; Rohnke, M.; Janek, J. Analyzing Nanometer-Thin Cathode Particle Coatings for Lithium-Ion Batteries—The Example of TiO_2 on NCM622. *ACS Appl. Energy Mater.* **2021**, acsaem.1c01255. https://doi.org/10.1021/acsaem.1c01255.

(234) Cho, J.; Kim, T.-J.; Kim, J.; Noh, M.; Park, B. Synthesis, Thermal, and Electrochemical Properties of $AlPO_4$-Coated $LiNi_{0.8}Co_{0.1}Mn_{0.1}O_2$ Cathode Materials for a Li-Ion Cell. *J. Electrochem. Soc.* **2004**, *151* (11), A1899. https://doi.org/10.1149/1.1802411.

(235) Shi, S. J.; Tu, J. P.; Mai, Y. J.; Zhang, Y. Q.; Tang, Y. Y.; Wang, X. L. Structure and Electrochemical Performance of CaF_2 Coated $LiMn_{1/3}Ni_{1/3}Co_{1/3}O_2$ Cathode Material for Li-Ion Batteries. *Electrochimica Acta* **2012**, *83*, 105–112. https://doi.org/10.1016/j.electacta.2012.08.029.

(236) Hall, D. S.; Gauthier, R.; Eldesoky, A.; Murray, V. S.; Dahn, J. R. New Chemical Insights into the Beneficial Role of Al_2O_3 Cathode Coatings in Lithium-Ion Cells. *ACS Applied Materials & Interfaces* **2019**, acsami.8b22743. https://doi.org/10.1021/acsami.8b22743.

(237) David, L.; Dahlberg, K.; Mohanty, D.; Ruther, R. E.; Huq, A.; Chi, M.; An, S. J.; Mao, C.; King, D. M.; Stevenson, L.; Wood, D. L. Unveiling the Role of Al_2O_3 in Preventing Surface Reconstruction During High-Voltage Cycling of Lithium-Ion Batteries. *ACS Applied Energy Materials* **2019**. https://doi.org/10.1021/acsaem.8b01877.

(238) Han, B.; Key, B.; Lipton, A. S.; Vaughey, J. T.; Hughes, B.; Trevey, J.; Dogan, F. Influence of Coating Protocols on Alumina-Coated Cathode Material: Atomic

Layer Deposition versus Wet-Chemical Coating. *J. Electrochem. Soc.* **2019**, *166* (15), A3679–A3684. https://doi.org/10.1149/2.0681915jes.

(239) Karayaylali, P.; Tatara, R.; Zhang, Y.; Chan, K.-L.; Yu, Y.; Giordano, L.; Maglia, F.; Jung, R.; Lund, I.; Shao-Horn, Y. Editors' Choice—Coating-Dependent Electrode-Electrolyte Interface for Ni-Rich Positive Electrodes in Li-Ion Batteries. *J. Electrochem. Soc.* **2019**, *166* (6), A1022–A1030. https://doi.org/10.1149/2.0461906jes.

(240) Chen, Z.; Qin, Y.; Amine, K.; Sun, Y.-K. Role of Surface Coating on Cathode Materials for Lithium-Ion Batteries. *Journal of Materials Chemistry* **2010**, *20* (36), 7606. https://doi.org/10.1039/c0jm00154f.

(241) Guilmard, M.; Croguennec, L.; Denux, D.; Delmas, C. Thermal Stability of Lithium Nickel Oxide Derivatives. Part I: $Li_xNi_{1.02}O_2$ and $Li_xNi_{0.89}Al_{0.16}O_2$ (x = 0.50 and 0.30). *Chem. Mater.* **2003**, *15* (23), 4476–4483. https://doi.org/10.1021/cm030059f.

(242) Croguennec, L.; Bains, J.; Bréger, J.; Tessier, C.; Biensan, Ph.; Levasseur, S.; Delmas, C. Effect of Aluminum Substitution on the Structure, Electrochemical Performance and Thermal Stability of $Li_{1+x}(Ni_{0.4}Mn_{0.4}Co_{0.2-z}Al_z)_{1-x}O_2$. *J. Electrochem. Soc.* **2011**, *158* (6), A664. https://doi.org/10.1149/1.3571479.

(243) Zhou, F.; Zhao, X.; Lu, Z.; Jiang, J.; Dahn, J. R. The Effect of Al Substitution on the Reactivity of Delithiated $LiNi_{1/3}Mn_{1/3}Co_{(1/3-z)}Al_zO_2$ with Non-Aqueous Electrolyte. *Electrochemistry Communications* **2008**, *10* (8), 1168–1171. https://doi.org/10.1016/j.elecom.2008.05.036.

(244) Wilcox, J. D.; Rodriguez, E. E.; Doeff, M. M. The Impact of Aluminum and Iron Substitution on the Structure and Electrochemistry of $Li(Ni_{0.4}Co_{0.2-y}M_yMn_{0.4})O_2$ Materials. *J. Electrochem. Soc.* **2009**, *156* (12), A1011. https://doi.org/10.1149/1.3237100.

(245) Han, B.; Key, B.; Lapidus, S. H.; Garcia, J. C.; Iddir, H.; Vaughey, J. T.; Dogan, F. From Coating to Dopant: How the Transition Metal Composition Affects Alumina Coatings on Ni-Rich Cathodes. *ACS Applied Materials & Interfaces* **2017**, *9* (47), 41291–41302. https://doi.org/10.1021/acsami.7b13597.

(246) Xiong, D. J.; Hynes, T.; Ellis, L. D.; Dahn, J. R. Effects of Surface Coating on Gas Evolution and Impedance Growth at $Li[Ni_xMn_yCo_{1-x-y}]O_2$ Positive Electrodes in Li-Ion Cells. *J. Electrochem. Soc.* **2017**, *164* (13), A3174–A3181. https://doi.org/10.1149/2.0991713jes.

(247) Zhu, W.; Huang, X.; Liu, T.; Xie, Z.; Wang, Y.; Tian, K.; Bu, L.; Wang, H.; Gao, L.; Zhao, J. Ultrathin Al_2O_3 Coating on $LiNi_{0.8}Co_{0.1}Mn_{0.1}O_2$ Cathode Material for Enhanced Cycleability at Extended Voltage Ranges. *Coatings* **2019**, *9* (2), 92. https://doi.org/10.3390/coatings9020092.

(248) Cho, J.; Kim, Y. J.; Park, B. Novel $LiCoO_2$ Cathode Material with Al_2O_3 Coating for a Li Ion Cell. *Chemistry of Materials* **2000**, *12* (12), 3788–3791. https://doi.org/10.1021/cm000511k.

(249) Chen, C.; Yao, W.; He, Q.; Ashuri, M.; Kaduk, J.; Liu, Y.; Shaw, L. Tunable $LiAlO_2/Al_2O_3$ Coating through a Wet-Chemical Method To Improve Cycle Stability of Nano-$LiCoO_2$. *ACS Appl. Energy Mater.* **2019**, *2* (5), 3098–3113. https://doi.org/10.1021/acsaem.8b02079.

(250) Han, B.; Paulauskas, T.; Key, B.; Peebles, C.; Park, J. S.; Klie, R. F.; Vaughey, J. T.; Dogan, F. Understanding the Role of Temperature and Cathode Composition on Interface and Bulk: Optimizing Aluminum Oxide Coatings for Li-Ion Cathodes. *ACS Appl. Mater. Interfaces* **2017**, *9* (17), 14769–14778. https://doi.org/10.1021/acsami.7b00595.

(251) Wen, X.; Liang, K.; Tian, L.; Shi, K.; Zheng, J. Al_2O_3 Coating on $Li_{1.256}Ni_{0.198}Co_{0.082}Mn_{0.689}O_{2.25}$ with Spinel-Structure Interface Layer for Superior Performance Lithium Ion Batteries. *Electrochimica Acta* **2018**, *260*, 549–556. https://doi.org/10.1016/j.electacta.2017.12.120.

(252) Chen, B.; Ma, X.; Chen, M.; Bullen, D.; Wang, J.; Arsenault, R.; Wang, Y. Systematic Comparison of Al^{3+} Modified $LiNi_{0.6}Mn_{0.2}Co_{0.2}O_2$ Cathode Material from Recycling Process. *ACS Appl. Energy Mater.* **2019**, *2* (12), 8818–8825. https://doi.org/10.1021/acsaem.9b01814.

(253) Jung, R.; Morasch, R.; Karayaylali, P.; Phillips, K.; Maglia, F.; Stinner, C.; Shao-Horn, Y.; Gasteiger, H. A. Effect of Ambient Storage on the Degradation of Ni-Rich Positive Electrode Materials (NMC811) for Li-Ion Batteries. *Journal of The Electrochemical Society* **2018**, *165* (2), A132–A141. https://doi.org/10.1149/2.0401802jes.

(254) *Handbook of Practical X-Ray Fluorescence Analysis*; Beckhoff, B., Ed.; Springer: Berlin ; New York, 2006.

(255) Boyes, E. D. Analytical Potential of EDS at Low Voltages. *Microchimica Acta* **2002**, *138* (3–4), 225–234. https://doi.org/10.1007/s006040200026.

(256) Coelho, A. A. *TOPAS* and *TOPAS-Academic*: An Optimization Program Integrating Computer Algebra and Crystallographic Objects Written in C++. *J Appl Crystallogr* **2018**, *51* (1), 210–218. https://doi.org/10.1107/S1600576718000183.

(257) Andreu, N.; Flahaut, D.; Dedryvère, R.; Minvielle, M.; Martinez, H.; Gonbeau, D. XPS Investigation of Surface Reactivity of Electrode Materials: Effect of the Transition Metal. *ACS Appl. Mater. Interfaces* **2015**, *7* (12), 6629–6636. https://doi.org/10.1021/am5089764.

(258) Dahéron, L.; Dedryvère, R.; Martinez, H.; Ménétrier, M.; Denage, C.; Delmas, C.; Gonbeau, D. Electron Transfer Mechanisms upon Lithium Deintercalation from $LiCoO_2$ to CoO_2 Investigated by XPS. *Chem. Mater.* **2008**, *20* (2), 583–590. https://doi.org/10.1021/cm702546s.

(259) Baer, D. R.; Artyushkova, K.; Cohen, H.; Easton, C. D.; Engelhard, M.; Gengenbach, T. R.; Greczynski, G.; Mack, P.; Morgan, D. J.; Roberts, A. XPS Guide: Charge Neutralization and Binding Energy Referencing for Insulating Samples. *Journal of Vacuum Science & Technology A* **2020**, *38* (3), 031204. https://doi.org/10.1116/6.0000057.

(260) Verdier, S.; Ouatani, L. E.; Dedryvère, R.; Bonhomme, F.; Biensan, P.; Gonbeau, D. XPS Study on Al_2O_3- and $AlPO_4$-Coated $LiCoO_2$ Cathode Material for High-Capacity Li Ion Batteries. *Journal of The Electrochemical Society* **2007**, *154* (12), A1088–A1099. https://doi.org/10.1149/1.2789299.

(261) Appapillai, A. T.; Mansour, A. N.; Cho, J.; Shao-Horn, Y. Microstructure of $LiCoO_2$ with and without "$AlPO_4$" Nanoparticle Coating: Combined STEM and XPS Studies. *Chem. Mater.* **2007**, *19* (23), 5748–5757. https://doi.org/10.1021/cm0715390.

(262) Lebens-Higgins, Z.; Faenza, N.; Mukherjee, P.; Sallis, S.; Badway, F.; Pereira, N.; Schlueter, C.; Lee, T.-L.; Cosandey, F.; Amatucci, G.; Piper, L. F. J. Electrochemical and Thermal Stress of $LiNi_{0.8}Co_{0.15}Al_{0.05}O_2$ Electrodes: Evolution of Aluminum Surface Environments. *ECS Trans.* **2017**, *80* (10), 197–206. https://doi.org/10.1149/08010.0197ecst.

(263) Hung, I.; Zhou, L.; Pourpoint, F.; Grey, C. P.; Gan, Z. Isotropic High Field NMR Spectra of Li-Ion Battery Materials with Anisotropy >1 MHz. *J. Am. Chem. Soc.* **2012**, *134* (4), 1898–1901. https://doi.org/10.1021/ja209600m.

(264) Grey, C. P.; Dupre, N. NMR Studies of Cathode Materials for Lithium-Ion Rechargeable Batteries. Chem. Rev. **2004**, *104*, 4493-4512. https://doi.org/10.1021/cr020734p.

(265) Märker, K.; Reeves, P. J.; Xu, C.; Griffith, K. J.; Grey, C. P. Evolution of Structure and Lithium Dynamics in $LiNi_{0.8}Mn_{0.1}Co_{0.1}O_2$ (NMC811) Cathodes during Electrochemical Cycling. *Chem. Mater.* **2019**, *31* (7), 2545–2554. https://doi.org/10.1021/acs.chemmater.9b00140.

(266) Dogan, F.; Vaughey, J. T.; Iddir, H.; Key, B. Direct Observation of Lattice Aluminum Environments in Li Ion Cathodes $LiNi_{1-y-z}Co_yAl_zO_2$ and Al-Doped $LiNi_xMn_yCo_zO_2$ via ^{27}Al MAS NMR Spectroscopy. *ACS Applied Materials & Interfaces* **2016**, *8* (26), 16708–16717. https://doi.org/10.1021/acsami.6b04516.

(267) Trease, N. M.; Seymour, I. D.; Radin, M. D.; Liu, H.; Liu, H.; Hy, S.; Chernova, N.; Parikh, P.; Devaraj, A.; Wiaderek, K. M.; Chupas, P. J.; Chapman, K. W.; Whittingham, M. S.; Meng, Y. S.; Van der Van, A.; Grey, C. P. Identifying the Distribution of Al^{3+} in $LiNi_{0.8}Co_{0.15}Al_{0.05}O_2$. *Chemistry of Materials* **2016**, *28* (22), 8170–8180. https://doi.org/10.1021/acs.chemmater.6b02797.

(268) Leifer, N.; Srur-Lavi, O.; Matlahov, I.; Markovsky, B.; Aurbach, D.; Goobes, G. $LiNi_{0.8}Co_{0.15}Al_{0.05}O_2$ Cathode Material: New Insights via ^{7}Li and ^{27}Al Magic-Angle Spinning NMR Spectroscopy. *Chemistry of Materials* **2016**, *28* (21), 7594–7604. https://doi.org/10.1021/acs.chemmater.6b01412.

(269) Bi, Y.; Yang, W.; Du, R.; Zhou, J.; Liu, M.; Liu, Y.; Wang, D. Correlation of Oxygen Non-Stoichiometry to the Instabilities and Electrochemical Performance of $LiNi_{0.8}Co_{0.1}Mn_{0.1}O_2$ Utilized in Lithium Ion Battery. *Journal of Power Sources* **2015**, *283*, 211–218. https://doi.org/10.1016/j.jpowsour.2015.02.095.

(270) Shim, J.-H.; Kim, C.-Y.; Cho, S.-W.; Missiul, A.; Kim, J.-K.; Ahn, Y. J.; Lee, S. Effects of Heat-Treatment Atmosphere on Electrochemical Performances of Ni-Rich Mixed-Metal Oxide ($LiNi_{0.8}Co_{0.15}Mn_{0.05}O_2$) as a Cathode Material for Lithium Ion Battery. *Electrochimica Acta* **2014**, *138*, 15–21. https://doi.org/10.1016/j.electacta.2014.06.079.

(271) d'Espinose de Lacaillerie, J.-B.; Fretigny, C.; Massiot, D. MAS NMR Spectra of Quadrupolar Nuclei in Disordered Solids: The Czjzek Model. *Journal of Magnetic Resonance* **2008**, *192* (2), 244–251. https://doi.org/10.1016/j.jmr.2008.03.001.

(272) Lee, S. K.; Park, S. Y.; Yi, Y. S.; Moon, J. Structure and Disorder in Amorphous Alumina Thin Films: Insights from High-Resolution Solid-State NMR. *The*

Journal of Physical Chemistry C **2010**, *114* (32), 13890–13894. https://doi.org/10.1021/jp105306r.

(273) Sarou-Kanian, V.; Gleizes, A. N.; Florian, P.; Samélor, D.; Massiot, D.; Vahlas, C. Temperature-Dependent 4-, 5- and 6- Fold Coordination of Aluminum in MOCVD-Grown Amorphous Alumina Films: A Very High Field ^{27} Al-NMR Study. *The Journal of Physical Chemistry C* **2013**, *117* (42), 21965–21971. https://doi.org/10.1021/jp4077504.

(274) Lee, S. K.; Lee, S. B.; Park, S. Y.; Yi, Y. S.; Ahn, C. W. Structure of Amorphous Aluminum Oxide. *Physical Review Letters* **2009**, *103* (9). https://doi.org/10.1103/PhysRevLett.103.095501.

(275) Müller, D.; Gessner, W.; Scheler, G. Chemical Shift and Quadrupole Coupling of the ^{27}Al NMR Spectra of $LiAlO_2$ Polymorphs. *Polyhedron* **1983**, *2* (11), 1195–1198. https://doi.org/10.1016/S0277-5387(00)84356-9.

(276) Wohlmuth, D. Order vs. Disorder—a Huge Increase in Ionic Conductivity of Nanocrystalline $LiAlO_2$ Embedded in an Amorphous-like Matrix of Lithium Aluminate. *Journal of Materials Chemistry A* **2014**, *2*, 20295–20306. https://doi.org/10.1039/c4ta02923b.

(277) Li, H.; Liu, A.; Zhang, N.; Wang, Y.; Yin, S.; Wu, H.; Dahn, J. R. An Unavoidable Challenge for Ni-Rich Positive Electrode Materials for Lithium-Ion Batteries. *Chem. Mater.* **2019**, *31* (18), 7574–7583. https://doi.org/10.1021/acs.chemmater.9b02372.

(278) Zheng, J.; Ye, Y.; Liu, T.; Xiao, Y.; Wang, C.; Wang, F.; Pan, F. Ni/Li Disordering in Layered Transition Metal Oxide: Electrochemical Impact, Origin, and Control. *Acc. Chem. Res.* **2019**, *52* (8), 2201–2209. https://doi.org/10.1021/acs.accounts.9b00033.

(279) Sicklinger, J.; Metzger, M.; Beyer, H.; Pritzl, D.; Gasteiger, H. A. Ambient Storage Derived Surface Contamination of NCM811 and NCM111: Performance Implications and Mitigation Strategies. *J. Electrochem. Soc.* **2019**, *166* (12), A2322–A2335. https://doi.org/10.1149/2.0011912jes.

(280) Schmuch, R.; Wagner, R.; Hörpel, G.; Placke, T.; Winter, M. Performance and Cost of Materials for Lithium-Based Rechargeable Automotive Batteries. *Nat Energy* **2018**, *3* (4), 267–278. https://doi.org/10.1038/s41560-018-0107-2.

(281) Rinkel, B. L. D.; Hall, D. S.; Temprano, I.; Grey, C. P. Electrolyte Oxidation Pathways in Lithium-Ion Batteries. *J. Am. Chem. Soc.* **2020**, *142* (35), 15058–15074. https://doi.org/10.1021/jacs.0c06363.

(282) Jung, R.; Morasch, R.; Karayaylali, P.; Phillips, K.; Maglia, F.; Stinner, C.; Shao-Horn, Y.; Gasteiger, H. A. Effect of Ambient Storage on the Degradation of Ni-Rich Positive Electrode Materials (NMC811) for Li-Ion Batteries. *J. Electrochem. Soc.* **2018**, *165* (2), A132–A141. https://doi.org/10.1149/2.0401802jes.

(283) Jung, R.; Linsenmann, F.; Thomas, R.; Wandt, J.; Solchenbach, S.; Maglia, F.; Stinner, C.; Tromp, M.; Gasteiger, H. A. Nickel, Manganese, and Cobalt Dissolution from Ni-Rich NMC and Their Effects on NMC622-Graphite Cells. *J. Electrochem. Soc.* **2019**, *166* (2), A378–A389. https://doi.org/10.1149/2.1151902jes.

(284) Ruff, Z.; Xu, C.; Grey, C. P. Transition Metal Dissolution and Degradation in NMC811-Graphite Electrochemical Cells. *J. Electrochem. Soc.* **2021**, *168* (6), 060518. https://doi.org/10.1149/1945-7111/ac0359.

(285) Kondrakov, A. O.; Schmidt, A.; Xu, J.; Geßwein, H.; Mönig, R.; Hartmann, P.; Sommer, H.; Brezesinski, T.; Janek, J. Anisotropic Lattice Strain and Mechanical Degradation of High- and Low-Nickel NCM Cathode Materials for Li-Ion Batteries. *J. Phys. Chem. C* **2017**, *121* (6), 3286–3294. https://doi.org/10.1021/acs.jpcc.6b12885.

(286) Schweidler, S.; de Biasi, L.; Garcia, G.; Mazilkin, A.; Hartmann, P.; Brezesinski, T.; Janek, J. Investigation into Mechanical Degradation and Fatigue of High-Ni NCM Cathode Material: A Long-Term Cycling Study of Full Cells. *ACS Appl. Energy Mater.* **2019**, *2* (10), 7375–7384. https://doi.org/10.1021/acsaem.9b01354.

(287) Faenza, N. V.; Bruce, L.; Lebens-Higgins, Z. W.; Plitz, I.; Pereira, N.; Piper, L. F. J.; Amatucci, G. G. Editors' Choice—Growth of Ambient Induced Surface Impurity Species on Layered Positive Electrode Materials and Impact on Electrochemical Performance. *J. Electrochem. Soc.* **2017**, *164* (14), A3727–A3741. https://doi.org/10.1149/2.0921714jes.

(288) Pritzl, D.; Teufl, T.; Freiberg, A. T. S.; Strehle, B.; Sicklinger, J.; Sommer, H.; Hartmann, P.; Gasteiger, H. A. Editors' Choice—Washing of Nickel-Rich Cathode Materials for Lithium-Ion Batteries: Towards a Mechanistic Understanding. *J. Electrochem. Soc.* **2019**, *166* (16), A4056–A4066. https://doi.org/10.1149/2.1351915jes.

(289) Chen, Z.; Qin, Y.; Amine, K.; Sun, Y.-K. Role of Surface Coating on Cathode Materials for Lithium-Ion Batteries. *Journal of Materials Chemistry* **2010**, *20* (36), 7606. https://doi.org/10.1039/c0jm00154f.

(290) Myung, S.-T.; Amine, K.; Sun, Y.-K. Surface Modification of Cathode Materials from Nano- to Microscale for Rechargeable Lithium-Ion Batteries. *Journal of Materials Chemistry* **2010**, *20* (34), 7074. https://doi.org/10.1039/c0jm00508h.

(291) Riesgo-González, V.; Hall, D. S.; Märker, K.; Slaughter, J.; Wright, D. S.; Grey, C. P. Effect of Annealing on the Structure, Composition, and Electrochemistry of NMC811 Coated with Al_2O_3 Using an Alkoxide Precursor. *Chem. Mater.* **2022**, *34* (21), 9722–9735. https://doi.org/10.1021/acs.chemmater.2c02580.

(292) Xiong, X.; Wang, Z.; Yue, P.; Guo, H.; Wu, F.; Wang, J.; Li, X. Washing Effects on Electrochemical Performance and Storage Characteristics of $LiNi_{0.8}Co_{0.1}Mn_{0.1}O_2$ as Cathode Material for Lithium-Ion Batteries. *Journal of Power Sources* **2013**, *222*, 318–325. https://doi.org/10.1016/j.jpowsour.2012.08.029.

(293) Kim, J.; Hong, Y.; Ryu, K. S.; Kim, M. G.; Cho, J. Washing Effect of a $LiNi_{0.83}Co_{0.15}Al_{0.02}O_2$ Cathode in Water. *Electrochem. Solid-State Lett.* **2006**, *9* (1), A19. https://doi.org/10.1149/1.2135427.

(294) Jeong, S.; Kim, J.; Mun, J. Self-Generated Coating of $LiCoO_2$ by Washing and Heat Treatment without Coating Precursors. *J. Electrochem. Soc.* **2019**, *166* (3), A5038–A5044. https://doi.org/10.1149/2.0071903jes.

(295) Zheng, X.; Li, X.; Wang, Z.; Guo, H.; Huang, Z.; Yan, G.; Wang, D. Investigation and Improvement on the Electrochemical Performance and Storage Characteristics of $LiNiO_2$-Based Materials for Lithium Ion Battery. *Electrochimica Acta* **2016**, *191*, 832–840. https://doi.org/10.1016/j.electacta.2016.01.142.

(296) Hofmann, M.; Kapuschinski, M.; Guntow, U.; Giffin, G. A. Implications of Aqueous Processing for High Energy Density Cathode Materials: Part II. Water-Induced Surface Species on $LiNi_{0.8}Co_{0.15}Al_{0.05}O_2$. *J. Electrochem. Soc.* **2020**, *167* (14), 140535. https://doi.org/10.1149/1945-7111/abc6ca.

(297) Lee, W.; Lee, D.; Kim, Y.; Choi, W.; Yoon, W.-S. Enhancing the Structural Durability of Ni-Rich Layered Materials by Post-Process: Washing and Heat-Treatment. *J. Mater. Chem. A* **2020**, *8* (20), 10206–10216. https://doi.org/10.1039/D0TA01083A.

(298) Azhari, L.; Zhou, X.; Sousa, B.; Yang, Z.; Gao, G.; Wang, Y. Effects of Extended Aqueous Processing on Structure, Chemistry, and Performance of Polycrystalline $LiNi_xMn_yCo_zO_2$ Cathode Powders. *ACS Appl. Mater. Interfaces* **2020**, *12* (52), 57963–57974. https://doi.org/10.1021/acsami.0c20105.

(299) Lee, W.; Lee, S.; Lee, E.; Choi, M.; Thangavel, R.; Lee, Y.; Yoon, W.-S. Destabilization of the Surface Structure of Ni-Rich Layered Materials by Water-Washing Process. *Energy Storage Materials* **2022**, *44*, 441–451. https://doi.org/10.1016/j.ensm.2021.11.006.

(300) Wood, M.; Li, J.; Ruther, R. E.; Du, Z.; Self, E. C.; Meyer, H. M.; Daniel, C.; Belharouak, I.; Wood, D. L. Chemical Stability and Long-Term Cell Performance of Low-Cobalt, Ni-Rich Cathodes Prepared by Aqueous Processing for High-Energy Li-Ion Batteries. *Energy Storage Materials* **2020**, *24*, 188–197. https://doi.org/10.1016/j.ensm.2019.08.020.

(301) Hofmann, M.; Kapuschinski, M.; Guntow, U.; Giffin, G. A. Implications of Aqueous Processing for High Energy Density Cathode Materials: Part I. Ni-Rich Layered Oxides. *J. Electrochem. Soc.* **2020**, *167* (14), 140512. https://doi.org/10.1149/1945-7111/abc033.

(302) Renfrew, S. E.; Kaufman, L. A.; McCloskey, B. D. Altering Surface Contaminants and Defects Influences the First-Cycle Outgassing and Irreversible Transformations of $LiNi_{0.6}Mn_{0.2}Co_{0.2}O_2$. *ACS Appl. Mater. Interfaces* **2019**, *11* (38), 34913–34921. https://doi.org/10.1021/acsami.9b09992.

(303) Logan, E. R.; Hebecker, H.; Ma, X.; Quinn, J.; HyeJeong, Y.; Kumakura, S.; Paulsen, J.; Dahn, J. R. A Comparison of the Performance of Different Morphologies of $LiNi_{0.8}Mn_{0.1}Co_{0.1}O_2$ Using Isothermal Microcalorimetry, Ultra-High Precision Coulometry, and Long-Term Cycling. *J. Electrochem. Soc.* **2020**, *167* (6), 060530. https://doi.org/10.1149/1945-7111/ab8620.

(304) Zhang, H.; He, X.; Chen, Z.; Yang, Y.; Xu, H.; Wang, L.; He, X. Single-Crystalline Ni-Rich $LiNi_xMn_yCo_{1-x-y}O_2$ Cathode Materials: A Perspective. *Advanced Energy Materials* **2022**, *12* (45), 2202022. https://doi.org/10.1002/aenm.202202022.

(305) Huang, Q.; Ma, L.; Liu, A.; Ma, X.; Li, J.; Wang, J.; Dahn, J. R. The Reactivity of Charged Positive $Li_{1-n}[Ni_xMn_yCo_z]O_2$ Electrodes with Electrolyte at Elevated Temperatures Using Accelerating Rate Calorimetry. *Journal of Power Sources* **2018**, *390*, 78–86. https://doi.org/10.1016/j.jpowsour.2018.04.036.

(306) Trevisanello, E.; Ruess, R.; Conforto, G.; Richter, F. H.; Janek, J. Polycrystalline and Single Crystalline NCM Cathode Materials—Quantifying Particle Cracking, Active Surface Area, and Lithium Diffusion. *Adv. Energy Mater.* **2021**, 2003400. https://doi.org/10.1002/aenm.202003400.

(307) Bi, Y.; Tao, J.; Wu, Y.; Li, L.; Xu, Y.; Hu, E.; Wu, B.; Hu, J.; Wang, C.; Zhang, J.-G.; Qi, Y.; Xiao, J. Reversible Planar Gliding and Microcracking in a Single-Crystalline Ni-Rich Cathode. *Science* **2020**, *370* (6522), 1313–1317. https://doi.org/10.1126/science.abc3167.

(308) Maiti, S.; Sclar, H.; Sharma, R.; Vishkin, N.; Fayena-Greenstein, M.; Grinblat, J.; Talianker, M.; Burstein, L.; Solomatin, N.; Tiurin, O.; Ein-Eli, Y.; Noked, M.; Markovsky, B.; Aurbach, D. Understanding the Role of Alumina (Al_2O_3), Pentalithium Aluminate (Li_5AlO_4), and Pentasodium Aluminate (Na_5AlO_4) Coatings on the Li and Mn-Rich NCM Cathode Material $0.33Li_2MnO_3 \cdot 0.67Li(Ni_{0.4}Co_{0.2}Mn_{0.4})O_2$ for Enhanced Electrochemical Performance. *Adv. Funct. Mater.* **2021**, *31* (8), 2008083. https://doi.org/10.1002/adfm.202008083.

(309) Herzog, M. J.; Gauquelin, N.; Esken, D.; Verbeeck, J.; Janek, J. Increased Performance Improvement of Lithium-Ion Batteries by Dry Powder Coating of High-Nickel NMC with Nanostructured Fumed Ternary Lithium Metal Oxides. *ACS Appl. Energy Mater.* **2021**, acsaem.1c00939. https://doi.org/10.1021/acsaem.1c00939.

(310) Song, B.; Li, W.; Oh, S.-M.; Manthiram, A. Long-Life Nickel-Rich Layered Oxide Cathodes with a Uniform Li_2ZrO_3 Surface Coating for Lithium-Ion Batteries. *ACS Appl. Mater. Interfaces* **2017**, *9* (11), 9718–9725. https://doi.org/10.1021/acsami.7b00070.

(311) Cangaz, S.; Hippauf, F.; Takata, R.; Schmidt, F.; Dörfler, S.; Kaskel, S. Surface Functionalization of $LiNi_{7.0}Co_{0.15}Mn_{0.15}O_2$ with Fumed Li_2ZrO_3 via a Cost-Effective Dry-Coating Process for Enhanced Performance in Solid-State Batteries. *Batteries & Supercaps* **2022**, *5* (9). https://doi.org/10.1002/batt.202200100.

(312) Akella, S. H.; Taragin, S.; Wang, Y.; Aviv, H.; Kozen, A. C.; Zysler, M.; Wang, L.; Sharon, D.; Lee, S. B.; Noked, M. Improvement of the Electrochemical Performance of $LiNi_{0.8}Co_{0.1}Mn_{0.1}O_2$ via Atomic Layer Deposition of Lithium-Rich Zirconium Phosphate Coatings. *ACS Appl. Mater. Interfaces* **2021**, *13* (51), 61733–61741. https://doi.org/10.1021/acsami.1c16373.

(313) Seenivasan, M.; Yang, C.; Wu, S.; Li, Y.-J. J.; Chien, W.-C.; Piraman, S.; Lue, S. J. Improving Structural and Thermal Stability of $LiNi_{0.8}Co_{0.15}Al_{0.05}O_2$ by a Fast-Ionic-Conductive $LiAlSiO_4$ Surface Coating for Li-Ion Batteries. *Electrochimica Acta* **2021**, *387*, 138620. https://doi.org/10.1016/j.electacta.2021.138620.

(314) Dreyer, S. L.; Kretschmer, K. R.; Tripković, Đ.; Mazilkin, A.; Chukwu, R.; Azmi, R.; Hartmann, P.; Bianchini, M.; Brezesinski, T.; Janek, J. Multi-Element Surface Coating of Layered Ni-Rich Oxide Cathode Materials and Their Long-Term Cycling Performance in Lithium-Ion Batteries. *Adv Materials Inter* **2022**, *9* (8), 2101100. https://doi.org/10.1002/admi.202101100.

(315) Lu, H.; Wright, D. S.; Pike, S. D. The Use of Mixed-Metal Single Source Precursors for the Synthesis of Complex Metal Oxides. *Chem. Commun.* **2020**, 10.1039.C9CC06258K. https://doi.org/10.1039/C9CC06258K.

(316) Park, J. S.; Meng, X.; Elam, J. W.; Hao, S.; Wolverton, C.; Kim, C.; Cabana, J. Ultrathin Lithium-Ion Conducting Coatings for Increased Interfacial Stability in High Voltage Lithium-Ion Batteries. *Chem. Mater.* **2014**, *26* (10), 3128–3134. https://doi.org/10.1021/cm500512n.

(317) Zhang, F.; Lou, S.; Li, S.; Yu, Z.; Liu, Q.; Dai, A.; Cao, C.; Toney, M. F.; Ge, M.; Xiao, X.; Lee, W.-K.; Yao, Y.; Deng, J.; Liu, T.; Tang, Y.; Yin, G.; Lu, J.; Su, D.; Wang, J. Surface Regulation Enables High Stability of Single-Crystal Lithium-Ion Cathodes at High Voltage. *Nat Commun* **2020**, *11* (1), 3050. https://doi.org/10.1038/s41467-020-16824-2.

(318) Pauls, J. Synthesen und Reaktionen von Aluminiumalkoxid-Verbindungen. Z. Anorg. Allg. Chem. **2000**, *626*, 270-279. https://doi.org/10.1002/(SICI)1521-3749(200001)626:1<270::AID-ZAAC270>3.0.CO;2-O.

(319) Nöth, H.; Schlegel, A.; Knizek, J.; Krossing, I.; Ponikwar, W.; Seifert, T. Lithium and Sodium Alkoxy- and Aryloxyhydridoaluminates in Solution and in the Solid State. *Chem. Eur. J.* **1998**, *4* (11), 2191–2203. https://doi.org/10.1002/(SICI)1521-3765(19981102)4:11<2191::AID-CHEM2191>3.0.CO;2-Y.

(320) Haouas, M.; Taulelle, F.; Martineau, C. Recent Advances in Application of ^{27}Al NMR Spectroscopy to Materials Science. *Progress in Nuclear Magnetic Resonance Spectroscopy* **2016**, *94–95*, 11–36. https://doi.org/10.1016/j.pnmrs.2016.01.003.

(321) Lam, E.; Comas-Vives, A.; Copéret, C. Role of Coordination Number, Geometry, and Local Disorder on ^{27}Al NMR Chemical Shifts and Quadrupolar Coupling

Constants: Case Study with Aluminosilicates. *J. Phys. Chem. C* **2017**, *121* (36), 19946–19957. https://doi.org/10.1021/acs.jpcc.7b07872.

(322) Wiedemann, D.; Nakhal, S.; Rahn, J.; Witt, E.; Islam, M. M.; Zander, S.; Heitjans, P.; Schmidt, H.; Bredow, T.; Wilkening, M.; Lerch, M. Unravelling Ultraslow Lithium-Ion Diffusion in γ-$LiAlO_2$: Experiments with Tracers, Neutrons, and Charge Carriers. *Chem. Mater.* **2016**, *28* (3), 915–924. https://doi.org/10.1021/acs.chemmater.5b04608.

(323) Carrera, L. M.; Jimenez-Becerril, J.; Bosch, P.; Bulbulian, S. Effect of Synthesis Techniques on Crystallite Size and Morphology of Lithium Aluminate. *J American Ceramic Society* **1995**, *78* (4), 933–938. https://doi.org/10.1111/j.1151-2916.1995.tb08417.x.

(324) Kinoshita, K.; Sim, J. W.; Ackerman, J. P. Preparation and Characterization of Lithium Aluminate. *Materials Research Bulletin* **1978**, *13* (5), 445–455. https://doi.org/10.1016/0025-5408(78)90152-6.

(325) Valenzuela, M. A.; Jimenez-Becerril, J.; Bosch, P.; Bulbulian, S.; Lara, V. H. Sol-Gel Synthesis of Lithium Aluminate. *J American Ceramic Society* **1996**, *79* (2), 455–460. https://doi.org/10.1111/j.1151-2916.1996.tb08144.x.

(326) Hirano, S.-I.; Hayashi, T.; Kageyama, T. Synthesis of $LiAlO_2$ Powder by Hydrolysis of Metal Alkoxides. *J American Ceramic Society* **1987**, *70* (3), 171–174. https://doi.org/10.1111/j.1151-2916.1987.tb04953.x.

(327) Beckerman, S. J.; Ford, R. B.; Nemeth, M. T. Conversion of Gamma Lithium Aluminate to Lithium Aluminum Carbonate Hydroxide Hydrate. *Powder Diffr.* **1996**, *11* (4), 312–317. https://doi.org/10.1017/S0885715600009325.

(328) Appapillai, A. T.; Mansour, A. N.; Cho, J.; Shao-Horn, Y. Microstructure of $LiCoO_2$ with and without "$AlPO_4$" Nanoparticle Coating: Combined STEM and XPS Studies. *Chem. Mater.* **2007**, *19* (23), 5748–5757. https://doi.org/10.1021/cm0715390.

(329) Dahéron, L.; Dedryvère, R.; Martinez, H.; Ménétrier, M.; Denage, C.; Delmas, C.; Gonbeau, D. Electron Transfer Mechanisms upon Lithium Deintercalation from $LiCoO_2$ to CoO_2 Investigated by XPS. *Chem. Mater.* **2008**, *20* (2), 583–590. https://doi.org/10.1021/cm702546s.

(330) Shu, Y.; Xie, Y.; Yan, W.; Meng, S.; Sun, D.; Jin, Y.; Xiang, L. Tuning the Ratio of Al_2O_3 to $LiAlO_2$ in the Composite Coating Layer for High Performance

$LiNi_{0.5}Mn_{1.5}O_4$ Materials. *Ceramics International* **2020**, *46* (10), 14840–14846. https://doi.org/10.1016/j.ceramint.2020.03.009.

(331) Leskes, M.; Moore, A. J.; Goward, G. R.; Grey, C. P. Monitoring the Electrochemical Processes in the Lithium–Air Battery by Solid State NMR Spectroscopy. *J. Phys. Chem. C* **2013**, *117* (51), 26929–26939. https://doi.org/10.1021/jp410429k.

(332) Shen, L.; Wang, Y.; Du, J.; Chen, K.; Lin, Z.; Wen, Y.; Hung, I.; Gan, Z.; Peng, L. Probing Interactions of Γ-Alumina with Water via Multinuclear Solid-State NMR Spectroscopy. *ChemCatChem* **2020**, *12* (6), 1569–1574. https://doi.org/10.1002/cctc.201901838.

(333) Liu, F.; Feng, N.; Wang, Q.; Xu, J.; Qi, G.; Wang, C.; Deng, F. Transfer Channel of Photoinduced Holes on a TiO_2 Surface As Revealed by Solid-State Nuclear Magnetic Resonance and Electron Spin Resonance Spectroscopy. *J. Am. Chem. Soc.* **2017**, *139* (29), 10020–10028. https://doi.org/10.1021/jacs.7b04877.

(334) Mogilevsky, G.; Karwacki, C. J.; Peterson, G. W.; Wagner, G. W. Surface Hydroxyl Concentration on $Zr(OH)_4$ Quantified by ^1H MAS NMR. *Chemical Physics Letters* **2011**, *511* (4–6), 384–388. https://doi.org/10.1016/j.cplett.2011.06.072.

(335) MacKenzie, K. J. D.; Temuujin, J.; Smith, M. E.; Angerer, P.; Kameshima, Y. Effect of Mechanochemical Activation on the Thermal Reactions of Boehmite (γ - AlOOH) and γ-Al_2O_3. *Thermochimica Acta* **2000**, *359*(2000) 87-94. https://doi.org/10.1016/S0040-6031(00)00513-X.

(336) Dogan, F.; Vaughey, J. T.; Iddir, H.; Key, B. Direct Observation of Lattice Aluminum Environments in Li Ion Cathodes $LiNi_{1-y-z}Co_yAl_zO_2$ and Al-Doped $LiNi_xMn_yCo_zO_2$ via ^{27} Al MAS NMR Spectroscopy. *ACS Appl. Mater. Interfaces* **2016**, *8* (26), 16708–16717. https://doi.org/10.1021/acsami.6b04516.

(337) Klute, C. H.; Walters, W. D. The Thermal Decomposition of Tetrahydrofuran. *J. Am. Chem. Soc.* **1946**, *68* (3), 506–511. https://doi.org/10.1021/ja01207a045.

(338) Kennedy, A. R.; Klett, J.; Mulvey, R. E.; Wright, D. S. Synergic Sedation of Sensitive Anions: Alkali-Mediated Zincation of Cyclic Ethers and Ethene. *Science* **2009**, *326* (5953), 706–708. https://doi.org/10.1126/science.1178165.

(339) Stamenkovic, V. R.; Strmcnik, D.; Lopes, P. P.; Markovic, N. M. Energy and Fuels from Electrochemical Interfaces. *Nature Mater* **2017**, *16* (1), 57–69. https://doi.org/10.1038/nmat4738.

(340) Karayaylali, P.; Tatara, R.; Zhang, Y.; Chan, K.-L.; Yu, Y.; Giordano, L.; Maglia, F.; Jung, R.; Lund, I.; Shao-Horn, Y. Editors' Choice—Coating-Dependent Electrode-Electrolyte Interface for Ni-Rich Positive Electrodes in Li-Ion Batteries. *J. Electrochem. Soc.* **2019**, *166* (6), A1022–A1030. https://doi.org/10.1149/2.0461906jes.

(341) Kim, T. W.; Choi, K.-S. Nanoporous $BiVO_4$ Photoanodes with Dual-Layer Oxygen Evolution Catalysts for Solar Water Splitting. *Science* **2014**, *343* (6174), 990–994. https://doi.org/10.1126/science.1246913.

(342) Liu, Y.; McCrory, C. C. L. Modulating the Mechanism of Electrocatalytic CO_2 Reduction by Cobalt Phthalocyanine through Polymer Coordination and Encapsulation. *Nat Commun.* **2019**, *10* (1), 1683. https://doi.org/10.1038/s41467-019-09626-8.

(343) Nam, D.-H.; Bushuyev, O. S.; Li, J.; De Luna, P.; Seifitokaldani, A.; Dinh, C.-T.; García de Arquer, F. P.; Wang, Y.; Liang, Z.; Proppe, A. H.; Tan, C. S.; Todorović, P.; Shekhah, O.; Gabardo, C. M.; Jo, J. W.; Choi, J.; Choi, M.-J.; Baek, S.-W.; Kim, J.; Sinton, D.; Kelley, S. O.; Eddaoudi, M.; Sargent, E. H. Metal–Organic Frameworks Mediate Cu Coordination for Selective CO_2 Electroreduction. *J. Am. Chem. Soc.* **2018**, *140* (36), 11378–11386. https://doi.org/10.1021/jacs.8b06407.

(344) Wang, Q.; Pornrungroj, C.; Linley, S.; Reisner, E. Strategies to Improve Light Utilization in Solar Fuel Synthesis. *Nat Energy* **2021**, *7* (1), 13–24. https://doi.org/10.1038/s41560-021-00919-1.

(345) Jung, E.; Yoo, S. H.; Chung, T.-M.; Kim, C. G.; Kim, Y.; Jung, D. Y. Heterobimetallic Lithium Organoaluminum and Organogallium Complexes: Potential Single Precursors for MOCVD of $LiMO_2$ Thin Films. *Inorganic Chemistry Communications* **2002**, *5* (6), 439–441. https://doi.org/10.1016/S1387-7003(02)00438-0.

(346) Veith, M.; Valtchev, K.; Huch, V. Ein neuer Aluminium/Nickel/Oxo-Cluster: $[Ni(acac)OAl(O^tBu)_2]_4$. *Z. anorg. allg. Chem.* **2003**, *629* (3), 569–574. https://doi.org/10.1002/zaac.200390092.

(347) Lu, Y.-C.; Gasteiger, H. A.; Parent, M. C.; Chiloyan, V.; Shao-Horn, Y. The Influence of Catalysts on Discharge and Charge Voltages of Rechargeable Li–Oxygen Batteries. *Electrochemical and Solid-State Letters*. **2010**, *13*(6) A69-A72. https://doi.org/10.1149/1.3363047.

(348) Aurbach, D.; McCloskey, B. D.; Nazar, L. F.; Bruce, P. G. Advances in Understanding Mechanisms Underpinning Lithium–Air Batteries. *Nat Energy* **2016**, *1* (9), 16128. https://doi.org/10.1038/nenergy.2016.128.

(349) Lu, Y.-C.; Xu, Z.; Gasteiger, H. A.; Chen, S.; Hamad-Schifferli, K.; Shao-Horn, Y. Platinum−Gold Nanoparticles: A Highly Active Bifunctional Electrocatalyst for Rechargeable Lithium−Air Batteries. *J. Am. Chem. Soc.* **2010**, *132* (35), 12170–12171. https://doi.org/10.1021/ja1036572.